University of Strathclyde
Department of Civil and Environmental Engineering

Kinematics of Soft Soil Landslides Based on the Analysis of Microseismic Monitoring Data

Georgios Yfantis

A thesis presented in fulfilment of the requirements for the degree of Doctor of Philosophy

2015

This thesis is the result of the author's original research. It has been composed by the author and has not been previously submitted for examination which has led to the award of a degree.

Signed:  Date: 17/06/15

Abstract

Landslide failures are a worldwide problem claiming human lives and causing catastrophic damages to infrastructure, with their impact able to reach that of war conflicts. For these reasons this thesis is going to investigate on the use of microseismic monitoring to study the kinematic behaviour of landslides and help towards the design of an optimised early or real time warning system. All findings are based in field experiments, using 1D and 3D short period seismometers, designed to understand the capabilities and limitations of microseismic monitoring in order to enhance the first and minimize the last.

The first goal of this thesis is to understand accuracy of microseismic monitoring in locating weak seismic events. The effect of the seismic velocity model is studied against common seismological assumptions, while different aperture sizes of microseismic arrays are put into test for achieving optimum location results.

Next, in order to allow the study of the expected landslide seismicity during a future landslide failure, a novel methodology, an up-scaled shear box, is designed to induce landslide like seismic signals. The proposed methodology can recreate soil slip events allowing control over different geotechnical conditions, such as stress levels, thus reproducing different landslide failure scenarios.

The up-scaled shear box methodology is then used to test a novel engineered seismic source: glass shard piles placed inside the landslide's mass, triggered from the landslide's displacements. The material characteristics of glass shards don't change in time, e.g. due to saturation, and have a stable seismic signature during displacement. For these reasons glass shard piles can act as the common seismic source, overcoming the time consuming process of identifying landslide complex failure mechanisms.

Finally, failure is induced to two landslide vertical faces under controlled conditions. Both landslides have identical characteristics, e.g. size and geology, with the only difference that in one of them a glass shard pile was incorporated. Visual observations, displacement and loading observations of the landslide faces, timed with a GPS clock, allowing for their detection on the seismic recordings and the characterisation of failure events. The collected data are found to correlate well with the experiments conducted with the up-scaled shear box methodology, allowing for their validation.

Acknowledgements

I can't thank enough Dr. Stella Putharouli and Prof. Rebecca Lunn for accepting me as their PhD candidate and leading me through the process these years. Under their guidance, I formed my research identity and gained skills I probably cannot yet comprehend. I will never forget that their first action as my supervisors, before even officially registering, was to mention the possibility (and finally arranging) to cross the Atlantic and visit Brazil for 2 months. After that kind of introduction it was made clear that working with them was at least going to be exciting. Endless meetings and tons of mails followed, as well as more research related travels. I hope that all these years I made the most of their academic knowhow.

I would like to thank Dr. Aderson Farias do Nascimento, of the Universidade Federal do Rio Grande do Norte. The meetings with him regarding seismic analysis techniques were revealing. The arrangements for me to be trained by Dr. Mario K. Takeya and work along his research group, as well as for conducting one of my first field experiments where much appreciated and always remembered. During those field days I tasted coconut water picked straight from the tree and chicken feet, normal Brazilian delicacies. The first one was delicious, the second not so much.

I need to specially thank Dr. Hernan Eduardo Martinez Carvajal, of the Universidade de Brasília. He took great interest in my research work after attending a talk I gave and started brainstorming with me what was to be my main experimental work. Little did he know what he was in for. His hospitality, his trust, his help, his resources awarded to me were unexpected all the way of our collaboration. I am grateful for all the experiences I shared with him: from the dusty field sandwiches to eating at rodizios and drinking kashasha, from talking hard core science to conversations about life.

I would like to thank Dr. Gregório Luís Silva Araújo for his advice and help. He was always there with a smile and a much needed tool from the lab.

Many thanks to Fundex and Embre, the two Brazilian companies that helped towards conducting my experiments with hardware as well as with manpower. Their friendly, loosen approach made everything seem easy and trivial.

Many thanks to Jorge de la Rosa Gonzalez, Marcelo Alejandro Lano Serna, Diego Alexander Ocampo, Raydel Lorenzo Reinaldo, Julián Buriticá García, Eduardo Botero, as well as Mr João and Savio, for their assistance during the field experiments. Without their help I couldn't have lifted, dug, pulled, moved and drank all the things that needed to be lifted, dug, pulled, moved and drank.

I have to thank Dr. Manoel Neto for being my protector during both of my trips to Brazil. He was my tour guide in Brasilia the first time I visited the city, and what a tour it was. He was my getaway expert during the final passport control at the end of my second visit to Brazil. If not for him the Brazilian, non-English speaking, custom officers might have added a small imprisonment experience to my PhD achievements.

Many thanks to all the friends who these past few years shared with me my crazy excitement, as well as my moderate moody moments, over food and drinks. Mostly food. Sanity was thus achieved. Partly.

I have to thank my older sister and younger brother for supporting me when needed. It was fun to see that the fighting during our early years in life, transformed into fighting with breaks of meaningful conversations. Who would knew.

Finally, many many many, many many thanks to my mother and father. To begin with, they created me and formed who I am. During my PhD adventure, they were there for me from the beginning of the application process, to this last point of submission. I am sure they will continue to be only a thought away.

This was the last section of this thesis that I wrote. It was recommended to do so by a Doctor, as the best rehabilitation technique towards the "World After the PhD".

World: I am free

(I think)

Table of Contents

List of Tables

List of Figures

List of Acronyms

D: epicentre distance (source-to-sensor)

dB: ratio of two values of the same physical meaning (usually power) expressed at a logarithmic scale.

f_s: sampling frequency

F: force (kN)

FT1: Failure Type 1 (Crack Formation/Propagation Events)

FT2: Failure Type 2 (Soil Block Topple and Fall Events)

FT3: Failure Type 3 (Soil Block Fall Events)

FFT: Fast Fourier Transformation

g: the gravitational acceleration

H: Focal depth

L1: Landslide Experiment 1

L2: Landslide Experiment 1

NFFT: number of points in the FFT

P-wave: primary or pressure wave

PSD: Power Spectral Density

S-wave: shear wave

t_P, t_S: P- and S- wave arrival time to the sensor

t_0: origin time

t_s :sample time intervals

T_i: Arrival time of wavefront to "Sensor i".

T_{event}: Time that the seismic event occurred.

V_P, V_S: P-wave and S-wave velocity respectively

VF1, VF2: Vertical Face 1 (or 2) of Landslide Experiment 1 (or 2)

VM: velocity model

X: epicentre distance from seismometers

z: depth (m)

γ_{soil}*: specific weight (kN/m^3) of soil*

θ_P, θ_S: angle of incidence/refraction of P-waves and S-waves respectively

σ_v*: vertical stress (kN/m^2) at depth z*

ω: angular frequency measured at rads/sec

Chapter 1
Introduction

1.1 Research Question

The focus of this research is to increase our understanding of landslide kinematics and its emitted seismicity using microseismic monitoring. The term landslide indicates any gravitational movement of soil, rock and organic material down a slope and the changed topography of the area (Highland and Bobrowsky, 2008). Mass movements and slope failures are global phenomena characterized as natural hazards, threatening human activities. Such events can claim human lives, destroy infrastructure and affect every aspect of economic activity.

One of the most famous disasters around the world caused by a landslide is the Vajont dam failure case, taking place in the Italian Alps 80km from Venice, on October 9, 1963. An estimated volume of 280×10^6 m^3 landslide debris, one of the largest debris volumes ever mobilized in history, fell into the water aquifer leading to a 220m tall wave of displaced water that passed above the dam destroying only the bridge topping the dam (Alonso et.al, 2010). The incident left the dam intact but destroyed several villages downstream with the death toll being above 2000 people (Alonso et.al, 2010). The slope that collapsed on that day was known to undergo small displacements from the 1960's which were monitored using surface markers (Alonso et.al, 2010). The accumulated displacement of the surface markers from their installation up to the landslide reached 2.5m-4m with displacement rate reaching 20-30cm per day prior to the final failure (Alonso et.al, 2010). Precipitation levels, as well as water pressure at four boreholes were also monitored, but the collected data, their interpretation and the actions taken did not prevent the catastrophe nor mitigate the risk.

Suwa et al. (2008) studied a landslide event taking place at a quarry in Okayama, Japan, that led to the death of three quarry workers on June 22, 2000. On the day of the event an eyewitness report raised awareness of small landslide failures prior to the start of any quarry works. The quarry company's head visited the site and confirmed new landslide debris deposits in the range of a few cubic meters. Quarry workers came

after at their usual time to start working and found that small landslides occurred frequently. All quarry works stopped to observe the evolution of the phenomenon with work personnel staying inside the quarry yard. The risk was miscalculated, evacuation was thought to be unnecessary and the landslide of 800,000 m^3 volume surprised them.

Other deadly examples are the Las Colinas landslide (fig. 1.1) in El Salvador that killed 944 people and destroyed 108,000 houses on January 13, 2001 (Konagai et.al, 2002) and the landslides occurring in the Vargas and Miranda state, Venezuela, that killed between 10,000 to 50,000 people and left over 150,000 homeless in December 1999 (fig. 1.2) (information from IRIS PASSCAL Instrument Centre). There are many more individual examples that one can reference. In general, there were 32,322 recorded deaths caused by landslides worldwide during the period 2004-2010, a number that might be underestimated (Petley, 2012).

Figure 1.1: The Las Collinas landslide which killed 944 people and destroyed 108,000 houses on January the 13th 2001 (picture from http://www.mindfully.org/Heritage/El-Salvador-Quake-Ignored3.jpg).

Figure 1.2: Debris flow in Venezuela during the month of December 1999 (picture from http://www.iris.edu/gifs/eno/venz1999.jpg).

In Scotland there are many examples of landslides affecting human activities. "The Times" reported a train serviced from Glasgow to Oban was derailed on June 6, 2010, with one wagon bursting into flames, due to large rock boulders lying on the train tracks. The boulders were the result of a rockslide that happened earlier that day and due to low visibility, the collision couldn't be avoided. Only 8 people were injured. A more recent example, as reported by the BBC was the landslide at the "Rest and be thankful" site that led to road closure of route A83 for four days on March the 6th 2014. Route A83 had to remain closed for more than 30 days in 2012 due landslide failures on the same site as reported by the Sunday Post.

Landslides pose a constant threat to the built environment and can claim human lives in numbers that can reach levels found in war conflicts. Large landslides consisting of thousands of cubic meters of debris traveling kilometres away from their original

position are very impressive and catastrophic. It is common though that such landslides commence with smaller displacement or failure events as seen in the quarry example (Suwa et.al, 2008). In addition, small events can be catastrophic, as in the case of the train derailment in Scotland presented previously. It is these small events (centimetre soil displacements and failures involving a few m^3) that are the focus of this thesis. They can be destructive and pose a great danger, as well as being indicative of larger events.

Landslides have proven to be complex phenomena that have been studied from many points of view (geological, geophysical, geotechnical, hydrological). Their investigation involves collecting multiple data sets jointly analysed before one can conclude about the state of the slope. The implementation of the optimum solution for landslide prevention can be a very expensive and time consuming process. The location and timing of landslides remain difficult to predict and it is hard to achieve a high level safety from landslide failure events especially under extreme conditions, e.g. an extremely long-duration rainfall event with a return period (recurrence interval) of greater than a hundred years.

No matter the reason that leads to a landslide, deaths can be avoided if the landslide behaviour is properly understood in real time and evacuation is imminent. Therefore, it may be of great value to provide a monitoring methodology that enables understanding of landslide behaviour, reduces risk, is efficient and is low cost in time and effort. This thesis is going to propose the use of microseismic monitoring techniques, through field experiments, in an effort to shed some light on the kinematics and the emitted seismicity of landslides, and potentially for use as an early warning system for landslide failure.

The reason for choosing microseismic monitoring is firstly, its ability to record very weak sources of seismic energy. Such sources could be millimetres of soil displacement or landslide failures involving less than $1m^3$ of soil debris. Implementing microseismic monitoring and understanding its limitations in recording landslide displacements and failure events will be a goal of this thesis.

A second advantage of using microseismic monitoring is that seismometer deployment is easy and rapid in any environment, and the sensors are able to provide information even if they are not placed on the active landslide body. Optimizing the deployment geometry to monitor small displacement and failure events will be a second goal of this thesis.

Finally the last advantage of microseismic monitoring is that it can provide continuous data remotely. If seismometers are connected with a constant power source, e.g. a battery rechargeable from solar panels, then data can be recorded and transmitted in real time to any part of the world. This means that a seismic network requires staff on-site only for its installation and its maintenance. The final goal will be to identify signals that could provide advance warning of landslide failure as part of a real-time monitoring network.

1.2 Types of landslides

In order to understand the physics involved during landslide displacement or failure events is it necessary to review the possible types of landslides and the mechanisms involved. Since natural phenomena can have endless combinations, the goal of this section is to review the basic landslide types, that when combined, create all possible outcomes.

There are many categorization systems of landslide types and many trigger mechanisms. Landslides can be divided in categories using two methods (Varnes, 1978, Highland and Bobrowsky, 2008). The first method uses material criteria and distinguishes landslides into “rock” or “soil” or both. Then continues in dividing “soil” into two parts; 1) “earth” is when the material involved are equal or smaller in size than sand particles and 2) “debris” if they are bigger. The second method uses the type of material displacement as criterion. That way mass movement is divided into “fall”, “topple”, “slide”, “spread” or “flow”. It is usual for these two methods to be combined

(Table 1.1), e.g. rock-fall. If more than two categories are involved then they are written in a sequence e.g. rock fall – debris flow.

-/-		Rock	**Debris** soil consisting of less than 80% from sand and finer material	**Earth** soil consisting of more than 80% from sand and finer material
Slides	**Rotational**	Rock Slide	Debris Slide	Earth Slide
	Translational			
Falls		Rock Fall	Debris Fall	Earth Fall
Topples		Block Topple	Debris Topple-	Block Topple
Flows		Rock Creep	Debris Avalanche, Debris Flow, Debris Creep	Rapid Earth Flow, Earth Flow, Earth Creep
Spreads		Rock Spread	Debris Spread	Earth Spread
Complex		Combination of at least two landslide types e.g. Rock Fall - Debris Flow		

Table 1.1: Landslide classification based on material involved and failure mechanisms.

1.2.1 Slides

The process of soil or rock material moving down a slope, with the failure plane forming on thin areas of high shear stress is defined as a slide (fig. 1.3a, b, c) (Highland and Bobrowsky, 2008). Slides are divided in rotational (fig. 1.3a) when the failure plane is curved upwards and translational (fig. 1.3b) when the failure plane is rather flat (Highland and Bobrowsky, 2008).

1.2.2 Falls

Soil or rock blocks that detach from a slope and are displaced mainly by falling, bouncing or rolling where no or very little shearing forces are involved in the process are characterized as falls (fig. 1.3d), (Highland and Bobrowsky, 2008).

1.2.3 Topples

Soil or rock material rotating around a point located in their lower area, are characterized as topples (fig. 1.3e) (Highland and Bobrowsky, 2008).

1.2.4 Flows

The displacement of soil or rock material behaving as liquid is characterized as a flow (fig. 1.3f, g, h, i) (Highland and Bobrowsky, 2008). Depending on the landslide's displacement velocity going from extremely rapid ($5x10^{3}$ mm/sec) to extremely slow ($5x10^{-7}$ mm/sec), this type of landslide failure can be divided into avalanche ((fig. 1.3g), flow (fig. 1.3f, h) or creep (fig. 1.3i). Special naming is given to the rapid displacement of tephra and other volcanic small grained material called "lahars" (volcanic debris flows). Flows in permafrost occur when the ice of the upper layer of ground (usually the first meter) in areas where the ground is at a permanent frozen state melts. The saturated soil is able to move on the frozen layer under low friction conditions.

1.2.5 Spreads

Spreads occur when the surficial soil or rock layer is submerged into a softer deeper layer (fig. 1.3j), (Highland and Bobrowsky, 2008).

1.2.6 Complex Landslides

Complex are characterized the landslides that combine two or more of the above presented failure mechanisms. For example a landslide combining Rock-Fall and a Debris-Flow (fig. 1.4a) or Rock-Topple and Debris-Flow (fig. 1.4b)

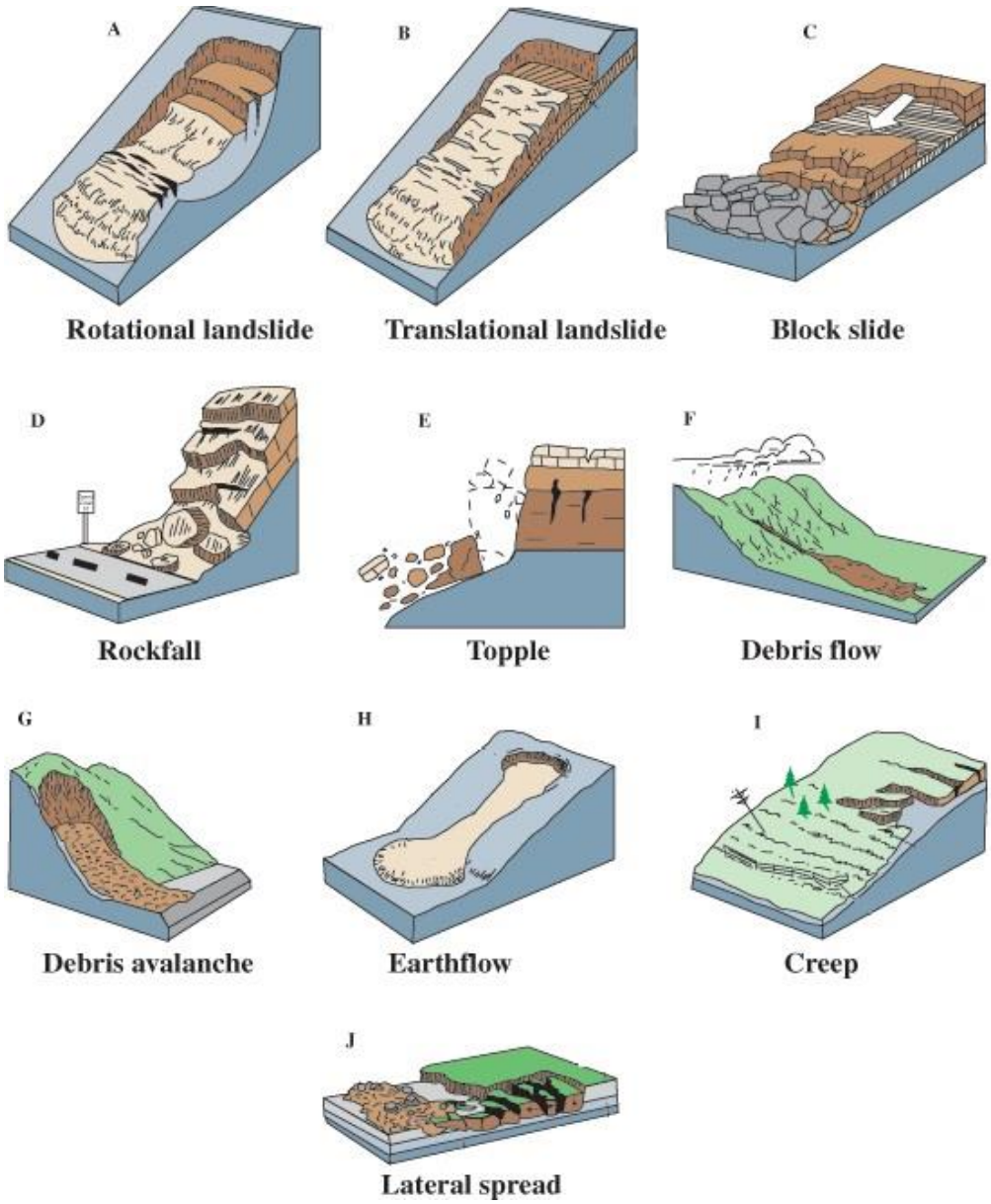

Figure 1.3: Schematic examples of the main displacement types of landslide material (photo from: http://pubs.usgs.gov/fs/2004/3072/images/Fig3grouping-2LG.jpg).

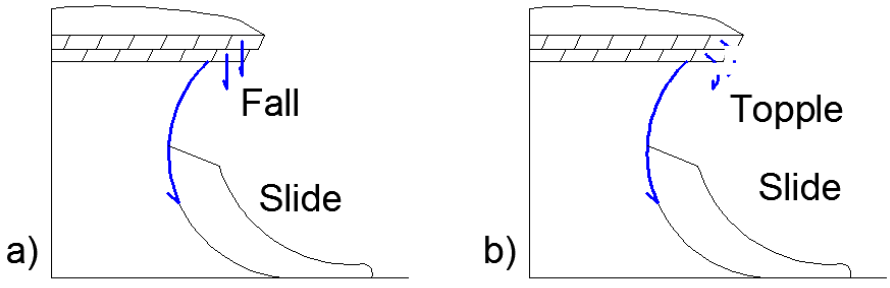

Figure 1.4: Schematic examples of two landslide complex failure mechanisms.

1.3 Trigger mechanisms of landslides

In this thesis triggering mechanisms are characterized as the events that are not caused by the landslide's mass, but affect the landslide's behaviour by initiating failure. Trigger mechanisms can be attributed to natural phenomena (Table 1.2), e.g. rainfall, or as a result of human activities (Table 1.3), such as a slope excavation. Increase in the geology's saturation due to precipitation is the most common triggering mechanism, though increasing saturation alone does not always lead to landslide failure.

Identifying a landslide's trigger mechanism is not an easy task and there may be several parameters involved, such us the loosening of the soil or rock from tree roots, which are difficult to observe. Trigger mechanisms can combine to initiate a landslide failure.

Rainfall	Snow melt
Flooding	Earthquake
Volcanic Eruption	Thawing
Freeze and Thaw weathering	Shrink and Swell weathering

Table 1.2: Physical causes acting as trigger mechanisms of landslides (Highland and Bobrowsky, 2008)

Changing landslide's topography by excavation	Use of soil or rock material in an unstable way for construction
Increasing load on slope, e.g. house construction	Changing water levels in natural or manmade reservoirs
Strong vibrations due to human activities, e.g. pile driving	Mining
Deforestation	River diversion
Increase of landslide saturation due to leakage of utilities, e.g. water pipes	

Table 1.3: Human causes acting as trigger mechanisms of landslides (Highland and Bobrowsky, 2008)

Understanding landslide triggering mechanisms through microseismic monitoring will not be part of this thesis. The main goal is to identify and understand the emitted seismicity during landslide failures that range from a few millimetres to a few meters, involving a few cm^3 to a few m^3 of landslide material. The literature review will reveal that there is little work in detecting and validating such failures. Whilst these types of events are considered to pose the minimum threat to human lives and activities, they are small enough to be precursory events of larger failures, thus making them particularly important in predicting a catastrophic landslide failure event.

1.4 Landslide monitoring methodologies

All landslide monitoring techniques, apart from visual reconnaissance, can be classified into three main categories: geodetic, geotechnical and geophysical. The choice among the different types of monitoring depends on various factors e.g. budget restrictions, site conditions (e.g. steepness of the slope) and environmental parameters. Choosing the optimum technique, or a combination of them, is not an easy task.

1.4.1 Initial Site Visit

The first step towards understand a landslide's behaviour and its monitoring needs is a site visit for basic evaluation and mapping. A measuring tape or a GPS system and a photograph are helpful for this first site visit. If erosion and/or vegetation hasn't wiped clean any displacement evidence, the displacement rate can be measured. In cases where failure material is properly exposed, the landslide's depth can be determined (Wieczorek and Snyder, 2009). An initial site visit saves time in planning the needed monitoring approach by providing insight on what type, and at which location, monitoring instrumentation can be deployed. It cannot though be used as a continuous monitoring method and must be conducted within days of the landslide event in cases where health and safety conditions allow it.

1.4.2 Geodetic Monitoring

Geodetic monitoring aims to measure surficial displacement and can be divided in three main categories; a) Passive optical sensors which are devices recording natural radiation emitted or reflected by objects, e.g., light (Ground base, aerial and satellite imaging) (SafeLand deliverable 4.1, 2010, Wieczorek. & Snyder, 2009), b) Active optical sensors or LASERs which describe all sensors emitting beams and afterwards recording their reflection (Electronic distance meters –EDMs & Total Stations-, Terrestrial and Aerial Laser Scanners –TLS or LiDAR-)) (SafeLand deliverable 4.1, 2010, Schulz, 2007, Wieczorek & Snyder, 2009), c) Active microwave sensors which are all sensors emitting electromagnetic waves and recording their reflection to produce images of objects (Ground, aerial or satellite based InSAR, DInSAR) (SafeLand deliverable 4.1, 2010, Riedel & Walther, 2008, Wieczorek & Snyder, 2009). An alternative to using a total station can be a GPS antenna (SafeLand deliverable 4.1, 2010).

Each of the three categories and the individual monitoring technique have their advantages and disadvantages. In general, the main advantage of the geodetic methods is the large area coverage and their remote sensing nature (SafeLand deliverable 4.1, 2010). In contrast, their main disadvantage is that geodetic monitoring cannot track displacements of underground points to understand the landslide's behaviour at depth and usually cannot be used as a continuous real time monitoring method (SafeLand deliverable 4.1, 2010). A key difference between the three categories is that active microwave sensors are affected very little by atmospheric conditions, e.g. fog or rain, unlike passive or active optical sensors (SafeLand deliverable 4.1, 2010).

1.4.3 Geotechnical Monitoring

Geotechnical monitoring is very valuable in landslide studies as it can provide information regarding the slope both in terms of ground displacement but also in terms of geological engineering parameters that affect ground displacement. Extensometers (probe, fixed borehole or wire extensometers) and inclinometers (probe, in-place inclinometers) can be used to monitor landslide displacement (Kandawasvika &

Reinhardt, 2005, Fujisawa et al., 2007, Wieczorek & Snyder, 2009), piezometers can monitor ground water level and pressure (Wieczorek & Snyder, 2009, Kane & Beck, 2000), and finally earth pressure cells can record stress levels in soils. In addition core logging of the landslide's mass gives direct information regarding the properties of local geology with depth. The main advantage of geotechnical monitoring is the high accuracy of data provided and the fact that they can provide geological parameters other than deformation (SafeLand deliverable 4.1, 2010). The disadvantage of geotechnical methods is the low spatial coverage (point measurements) and the usual need for drilling that increases the installation time and cost (SafeLand deliverable 4.1, 2010).

1.4.4 Geophysical Monitoring

Geophysical monitoring techniques can provide information on subsurface conditions related to the landslide's geology and behaviour (SafeLand deliverable 4.1, 2010). They can be categorized into electrical methods measuring electric resistivity and potential (Barta et.al, 2005, Jongmans and Garambois, 2007), electromagnetic methods measuring electromagnetic waves such as ground penetrating radar (Maurer et.al., 2010), gravimetry measuring differences in the gravitational field (Del Gaudio et.al., 2010) and seismic methods using the reflection/refraction or dispersion properties of seismic waves (Pugin et.al, 2004, Meric et.al, 2005, Jongmans and Garambois, 2007). All the above methods are used to produce 2D or 3D images of the near surface geology of landslides (SafeLand deliverable 4.1, 2010). If used at steady time increments the images produced can reveal geological changes in time due to landslide movement. Deciding on the time lapse has to be based on the evolution of the landslide e.g. creeps are very slow so one campaign per month is probably more than enough.

The main advantages of geophysical monitoring methods are their non-invasive nature and that they can usually monitor large areas with relatively little effort (SafeLand deliverable 4.1, 2010). On the contrary, main disadvantage is the fact that the provided

data have a non-unique interpretation, leading in different conclusions (SafeLand deliverable 4.1, 2010).

In addition to producing images of a landslide's geology to understand its behaviour, recording the landslide's emitted microseismicity allows direct information to be derived regarding the landslide's failure mechanisms. Phenomena like displacements, crack propagation and falls produce seismic waves that can in principle be detected and located with the use of seismic sensors (Walter et al., 2009, Senfaute et.al, 2009). Microseismicity can potentially provide real time continuous information of large areas regarding landslide behaviour, characteristics that are the main advantages of the method. It should be noted however that, the high attenuation of the weathered landslide material and the low emitted seismic energy of small failure events reduce the event detectability. Furthermore, the heterogeneity of the landslide's geology can lead to large event location errors. The use of microseismicity in landslide monitoring is going to be extensively presented in the literature review chapter.

1.5 Aim of this thesis

This thesis will investigate the potential for microseismic monitoring to provide reliable information as a continuous landslide monitoring method. Focus will be given to soil landslides, as the most attenuating geological material, and to small failure events. Experimental results will be presented on a novel methodology that can recreate landslide seismicity at field scale, as well as on a new technology that has been found to track the landslide displacements emitting distinct seismic signals. Main goal will be to characterise the emitted seismicity from different landslide failure mechanisms and validate their distinct frequency patterns. Finally, all data will be jointly compared in order to prove the consistency of all findings.

Chapter 2
Literature Review

2.1 Introduction

The knowledge on landslide failure mechanisms comes from monitoring and observation. In the introduction chapter a number of landslide monitoring techniques have been presented that provide information on the kinematics of existing landslides (the mechanisms describing the motion of the landslide's body). This chapter focuses on presenting the state of the art applications of seismic monitoring.

Seismic monitoring was chosen for this research to be advantageous over other monitoring methods because: (a) seismometers can be deployed inside or outside the landslide borders to record landslide events and used as (b) a continuous monitoring method, (c) with data that can be transmitted in real-time and (d) analysed automatically by software routines providing information regarding the behaviour of the landslide.

The oldest studies that were reviewed and that use seismometers to monitor landslides where those of Galitzin (1915) and Jeffreys (1923) (Suriñach et.al, 2005). Research on the emitted seismicity of landslides was more systematic from the 90's due to advances in seismic instrumentation technology as well as in the analysis capabilities of computers. There have been many studies on different landslide types proving that seismic signals are emitted due processes such as joint formation and displacements inside rock masses (Amitrano et al, 2007), rock-fall events (Deparis et al, 2008), failure of softer soil materials found in mudslides (Walter et al., 2009), pyroclastic and volcanic flows (Calder et.al, 2002, Zobin et.al, 2009), snow and ice avalanches (Kishimura and Izumi, 1997, Surinach et.al, 2000, Caplan-Auerbach and Huggel, 2007), or processes during glacier displacement (Stuart et.al., 2005, Roux et.al., 2008).

This chapter is structured as follows: Firstly, a short description of how seismometers work is given along with different deployment methodologies. The main focus though is given to known seismic signal characteristics of landslide displacement and failure

events as well as reported precursory signals. There are many landslide categories with each one having unique characteristics, e.g. failure mechanism, type of material involved. This literature review will only consider landslide case studies involving rock or/and soft soil material. These are the most common around the world with potential of posing danger to humans and the built environment. As well, this research is focused only on soft soil landslides.

2.2 Seismic instrumentation

A seismometer is a device that allows measurements of the Earth's ground motion (Wielandt, 2002). Since seismometers are placed on the Earth, they do not have a reference plane independent from its movement, thus they cannot measure ground movement directly (Havskov and Alguacil, 2010). Most seismometers have a suspended mass using a swinging system and they measure the relative motion between that mass and the ground (Havskov and Alguacil, 2010). This relative motion should have a non-negative acceleration, to comply with the inertia principle, and be observable (Havskov and Alguacil, 2010).

Classical mechanical seismometers allow observation of the relative movement with the help of a velocity transducer which is either 1) a fixed coil where the seismometer's mass that has an attached magnet on it is free to move inside the coil or 2) a fixed magnet and a coil that moves along with the seismometer's mass (Havskov and Alguacil, 2010). The final output of the seismometer is an electric signal proportional to the velocity of the seismometer's mass (Havskov and Alguacil, 2010). Since the velocity transducer has a low sensitivity at low frequencies (<0.2Hz) an alternative design is to use a displacement transducer where the mass of the seismometer is kept at a nearly stationary state by cancelling external forces with the help of an opposite electronically generated force (Havskov and Alguacil, 2010). More information on how seismometers are build can be found in Borman (2002) and Havskov&Alguacil (2010).

There are three main categories of seismometers: broadband, short period and accelerometers. Broadband sensors can record low frequent ground movements starting from 0.01Hz up to some tens of Hz (Havskov and Alguacil, 2010). Short period sensors record ground movements usually in the range of 1Hz to 100Hz, while accelerometers record strong ground motions usually >10Hz up to 1000Hz (Havskov and Alguacil, 2010). There are piezoelectric transducers that can record higher frequencies but are usually used in the lab and are of no interest in this study (Dixon et.al, 2003).

2.3 Seismic Sensor Deployment

The deployment of seismometers can be divided into three main categories. The first one is deploying a single seismic station. The seismometer records the earth's tremor but limited conclusions can be drawn from looking at isolated seismograms. With a single seismometer one can mostly detect seismic events and analyse their frequency content.

The second deployment category is the seismic network (Havskov and Alguacil, 2010). A seismic network is the combination of many seismometers, deployed usually a few to a couple of hundred kilometres apart, for locating strong seismic events (e.g. earthquakes) and obtaining information regarding the earth's crust (Trnkoczy et.al, 2012). Their most important characteristic is that the data of each seismic station is transmitted in real time to a central location, with data being synchronised at a common time reference system (Trnkoczy et.al, 2012).

The third main category of seismic sensor deployment is the seismic array (Rost and Thomas, 2002). The main difference between seismic arrays and networks is the analysis techniques used on the collected data, e.g. determining the back azimuth of the recorded wavefront. Thus a seismic network can be used as a seismic array and vice versa (Schweitzer et.al., 2002**)**. Array analysis techniques though require high signal coherency constraining the sensor spacing and data quality (Schweitzer et.al, 2002, Rost and Thomas, 2002). For this reason seismic array seismometers are closely

spaced compared to those in seismic networks. A large array example is LASA (1965-1978) with a sensor spacing of 2-3km (Rost and Thomas, 2002) meaning that sensor spacing at arrays is usually smaller. Seismic arrays are used as a tool to reduce the detection threshold of earthquakes, nuclear explosions and increase the resolution of imaging the earth's structure (Rost and Thomas, 2002).

Microseismic monitoring is the study of ground tremor with magnitude smaller than 3 in the Richter scale (Lee and Stewart, 1981). The Richter scale is defined by the equation $M_L=\log(A) - \log(A_0)$, with (A) being the maximum trace amplitude (recorded in mm) when a Wood-Anderson seismometer is used and with $(-\log(A_0))$ accounting for the amplitude attenuation due to source-to-sensor distance (Lee and Stewart, 1981). Microseismic monitoring can be conducted either by seismic networks or arrays as long as they allow for detection and analysis of microseismic events.

2.4 Seismic monitoring of Landslides dominated by rock material

Seismic monitoring of landslides has been mostly focused at cases where dominating material was rock. This is because rock is a brittle material that during failure or displacement emits a considerable amount of seismic energy. The latter, along with the small attenuation properties of rock give make seismic monitoring of rock slopes advantageous over using seismometers to monitor soil dominated landslides.

2.4.1 Studies based on seismometers spaced at distances >1km

Without installing additional instrumentation researchers have searched the seismic recordings of local seismic networks designed for earthquake monitoring in order to detect landslide events. The smallest landslides recorded from such a network, according to the reviewed literature, were $103m^3$ (Deparis et.al, 2008) and $106m^3$ (Schneider et.al, 2010) going up to impressive landslides with mass in the range of 10^5m^3 (Deparis et.al, 2008) and even 10^6m^3 (Feng, 2011). Seismic networks have also been capable of recording teleseismic signals of very large catastrophic rockslides with source-to-sensor distances of thousands of kilometres (Ekström and Stark, 2013).

Sensors usually used in such networks are broadband seismometers but they can also be short period seismometers (Deparis et.al, 2008). The spacing of sensors in seismic networks is in the range of a few to a couple of hundred kilometres apart, e.g. 3km (Burtin et.al, 2009), 8km (Schneider et.al, 2010), 30km (Deparis et.al, 2008, Dammeier et.al, 2011).

Landslide related signals recorded from such networks are generally found to be of low frequency content (<25Hz). This is due to the large source-to-sensor distances and the fact that high frequencies are attenuated easier than low frequencies. More specific frequency content has been found to be in the range of 1-20Hz (Schneider et.al, 2010), 1-10Hz (Deparis et.al, 2008), 2-22Hz (Burtin et.al, 2009), up to 8-9Hz (Suriñach et.al, 2005), 3-10Hz (Dammeier et.al, 2011), 0.5-5Hz (Feng, 2011, Kao et.al, 2012).

Location analysis of landslide signals recorded by local networks designed to record earthquakes was found to be possible but problematic. Absolute error between the calculated and true location of the landslide was found to be 10.9km (Dammeier et.al, 2011), 8km (Lin et.al, 2010) or in the range of a few kilometres (Kao et.al, 2012). Location analysis of these seismic recordings is difficult and involves large errors mainly because they are small in magnitude when compared to earthquakes (events these local seismic networks were designed for), resulting in unclear wave phases (Suriñach et.al, 2005, Kao et.al, 2012). Even if P-waves have a clear on-set, S-waves overlap with the P-wave coda leading to unclear S-wave time on-sets (Deparis et.al, 2008). Finally there are cases where the deployment geometry of the seismic network does not surround the source of the landslide, creating a data set unable to properly constrain a location solution (Burtin et.al, 2009). The landslide events detected by the studies referenced above are catastrophic and very large in size with their true location reported by the local population.

2.4.2 Studies based on seismometers spaced at distances between 0.1-1km

There are a number of studies where seismometers were deployed closer to landslide sites with sensor spacing (SeSp) between 100m to 1000m and source-to-sensor

distances (StSD) smaller than 1000m. Specifically, studies were found to have 500m to 1000m SeSp and StSD from ~100m to ~500m (Brückl and Mertl, 2006), ~300m SeSp and 50m to 2100m StSD (Hibert et.al, 2011), 150m SeSp and 200m StSD (Vilajosana et.al, 2008), 500m to 2000m SeSp and <1000m StSD (Zimmer et.al, 2012), and 200m to 500m SeSp and 500m to 1000m StSD (Chen et.al, 2005). These networks were able to record free rock falls of estimated volume ranging from 10 to $10^4 m^3$ (Hibert et.al, 2011) and $75m^3$ rock falls (Vilajosana et.al, 2008) up to impressive events of $46700m^3$ rock falls (Zimmer et.al., 2012). These seismic networks were also used in combination with sensors deployed for earthquake monitoring (Zimmer et.al, 2012).

Sensors at these studies varied from short period seismometers of 1Hz (Chen et.al, 2005, Vilajosana et.al, 2008, Hibert et.al, 2011) to 4.5Hz (Brückl and Mertl, 2006, Zimmer et.al, 2012) and even broadband seismometers (Brückl and Mertl, 2006).

The frequency content of landslide induced seismic events recorded on these proximal networks was found to be below 50Hz, a higher frequency threshold than that found in studies using earthquake seismic networks. This is due to the smaller source-to-sensor distances and the smaller spacing between sensors. Specifically landslide seismicity was found to be up to 30Hz due to mass movement events (Brückl and Mertl, 2006), up to 15Hz by rock fall impacts (Zimmer et.al., 2012), between 2Hz and 10Hz with seismic energy centred around 5Hz for granular rock flows (Hibert et.al, 2011), with up to 40Hz with seismic energy centred around 7Hz for free fall rock fall events (Hibert et.al, 2011), and up to 50Hz for rock falls and flow events (Vilajosana et.al, 2008).

Large uncertainties in detecting and characterizing landslide related events among the seismic recordings can come up if the seismic sensors are not focused on the landslide site. In general, monitoring of seismicity over a large area (e.g. monitoring processes occurring in mine tunnelling or due to tectonic activities) without prior knowledge of the signal characteristics makes it difficult to attribute a source mechanism in the

recorded signal (Chen et.al., 2005). Finally, detection of small rock fall events and precursory failure signals might still be unsuccessful (Zimmer et.al, 2012).

Locating landslide related events by picking P and S-wave first arrivals, using data obtained from medium sized networks is still problematic. There have been cases where location was not possible (Brückl and Mertl, 2006) or it was only possible to estimate a probable area of origin (Chen at.al, 2005). Other studies have reported successfully locating rock fall events but without giving an error estimation (Hibert et.al, 2011, Zimmer et.al, 2012). The main problem in locating landslide seismic signals is, as before, the low signal to noise ratios resulting in unclear wave phase on-sets (Brückl and Mertl, 2006).

2.4.3 Studies based on seismometers spaced at distances <0.1km

The studies presented in the previous sections reveal that different source-to-sensor distances produce different seismic recordings. For this reason researchers deploy seismic sensors on landslides a few meters or tenths of meters away from the landslide mass undergoing displacement. There have been cases that sensor spacing has been as small as 10m with sensors placed just above the part of the rock cliff undergoing failure with source-to-sensor slant distances between 3m to 67m (Wust-Bloch, 2010). These small seismic networks have been deployed with the hope of recording seismic signals emitted during small rock failures and crack formation/propagation within rock mass comparable to larger seismic networks.

Sensors used in such studies are seismometers with flat frequency response over 40Hz to 1.5kHz (Amitrano et.al, 2005, Senfaute et.al, 2009), geophones with a flat response above 40Hz (Myers 2000), accelerometers with flat response over 2Hz to 10kHz (Amitrano et.al, 2005, Senfaute et.al, 2009), short period seismometers with a flat response between 1-100Hz (Wust-Bloch, 2010), short period seismometers with a flat response above 2Hz (Levy et.al, 2011), geophones with a flat response above 100Hz (Amitrano et.al, 2010), seismometers with a flat response above 4.5Hz (Helmstetter and Garambois 2010, Got et.al, 2010), geophones able to detect frequencies between

8Hz to 1500Hz (Huang et.al, 2007), broadband velocimeters with a flat response above 0.05Hz (Helmstetter and Garambois 2010).

Findings of the frequency content of landslide failure related signals vary with study. In general seismicity related to landslide dominated by rock was found to be below 1000Hz. Detection of possible landslide related events was decided based on the knowledge of noise source signals and then locating them to see whether they originate from the landslide's body (Spillmann et al, 2007). As it will be presented in the next paragraph, seismic recordings revealed signals of different frequency content. Possible reasons for this behaviour can be the different geology found at different sites, different source mechanisms causing the recorded seismicity and different types of sensors as well as deployment geometry and source-to-sensor distances when monitoring the sites under investigation.

More specific, signals with frequencies between 10Hz and 75Hz with most of the seismic energy concentrated above 20Hz were recorded during failure process, crack formation/propagation, of a cliff (Wust-Bloch, 2010). Seismicity recorded from these small source-to-sensor distances are capable of recording precursory failure signals. Signals with frequencies between 100Hz and 1000Hz recorded before a rock fall were attributed to crack formation, with frequencies between 100Hz and 500Hz recorded several minutes before a rock fall were attributed to propagation of existing cracks, while the final rock fall events produced signals with frequencies below 100Hz (Senfaute et.al, 2009). Other studies recorded signals with frequency content below 120Hz with dominant frequencies around 25Hz, as well as between 40Hz and 50Hz (Got et.al, 2010), frequencies between 10Hz and 150Hz for natural rock falls, and frequencies between 10Hz and 80Hz for rock thrown manually from the cliff (Levy et.al, 2011). Seismicity emitted by a rock slide was never observed above 100Hz with few events above 50Hz (Helmstetter and Garambois, 2010). Signals emitted during debris flows changed their frequency content depending on the position of the flow compared to the sensors: a) At start, the forefront of the debris flow produced seismicity below 50Hz, b) when it was closest to the sensors frequency content was between 10Hz and 250Hz, while c) seismicity was between 50Hz and 100Hz when the

debris flow passed the sensor (Huang et.al, 2007). In general frequency content of debris flows was between 10Hz and 150Hz with larger events producing lower frequencies (Huang et.al. 2007). Increase in the noise levels was also proven to be a precursory indicator of landslide failure (Amitrano et.al, 2005). Despite these findings, some studies conclude that most of landslide deformation occurs aseismically (Spillmann et al, 2007).

Locating landslide related seismic signals was found to be a difficult task for large and medium sized seismic networks as discussed earlier, and is reported to also be difficult for small seismic arrays/networks. The reasons are similar. Most signals do not emit or are not recorded with clear wave onsets that allow precise time picking and thus an accurate location analysis (Helmstetter and Garambois, 2010). In addition the S wave coda overlap with the P wave coda due to small source-to-sensor distances thus not allowing the use of S wave onsets as an additional location restrain (Helmstetter and Garambois, 2010).

Finally small seismic arrays were able to record landslide failure kilometres away from their deployment area they were meant to monitor. Seismic arrays consisting of four short-period (1Hz) seismometers were able to record and locate a 15000m^3 rock fall 5000m away from the monitoring area, as well as some precursory signals to the main failure that were attributed to smaller rock fall events (Walter et.al., 2012). The frequency content of the main failure signal was up to 20Hz, while the signals prior to the main failure up to 150Hz. The calculated location uncertainty of the events was estimated to be around 500m, 10% of the epicentre distance from the sensors. Another study reports that a large rockfall (50,000m^3 to 100,000 m^3) was recorded by two seismic arrays deployed 400m and 13400m away from the location of the event (Moran et.al, 2008).

2.5 Seismic monitoring of Landslides dominated by soil material

There have been case studies dealing with the seismicity emitted by landslides dominated by soft sediments (soil). A number of different seismic sensors have been

used to monitor such sites. Seismometers with flat response over 0.1Hz to 80Hz and over 2Hz to 80Hz (Tonnellier et.al, 2013), short period seismometers with flat response above 2Hz (Gomberg et.al, 1995, Gomberg et.al, 2011), broadband seismometers (Amitrano et.al, 2007), short period seismometers with flat response above 1Hz (Gomberg et.al, 1995, Walter and Joswig, 2008, Walter et.al., 2009, Walter et.al, 2011, Walter et.al, 2012, Rothmund and Joswig, 2012) and seismometers with flat response above 4.5Hz (Gomberg et.al, 1995).

It was shown from landslide monitoring of slopes dominated by rock that when seismometers were deployed densely, landslide events were recorded clearer. For this reason seismometers were closely spaced when used for monitoring slopes dominated by soil material ranging with sensor spacing. from 20m to 40m (Tonnellier et.al, 2013) or up to 50m (Gomberg et.al, 2011, Walter et.al., 2011). At such cases, the achieved landslide event detection threshold could range up to a few hundred meters away (Rothmund and Joswig, 2012).

Different types of signals were reported from these studies and attributed to different source mechanisms. Signals characterized as quakes had a frequency content <10Hz and were associated with internal friction of the landslide material or fissure opening/closing. Rock falls detached from the head of the landslide or debris flows had a frequency content between 2Hz to 30Hz (Tonnellier et.al, 2013). Increase in the background noise levels between frequencies 0.01Hz and 10Hz, with a more sensitive frequency band being between 0.1Hz and 1Hz, was found to correlate with landslide displacement (Amitrano et.al, 2007). Slide quakes with frequency content between 1Hz to 200Hz have been recorded and located a few hundred meters away from the sensors recording (Rothmund and Joswig, 2012). Events described as fracture processes within the landslide's body generated during the landslide's material deformation were reported to have frequency content between 10Hz to 120Hz (Walter et.al, 2011, Walter et.al, 2012). The same fracture events are reported to have frequency content between 10Hz to 80Hz, while events classified as "scratch events" caused by friction between the bedrock and the landslide material have frequency content up to 150Hz (Walter et.al, 2009, Walter and Joswig 2009). Seismic sensors

were able to record fissure development within clay material at frequencies up to 150Hz at very small source-to-sensor distances of a few meters (Walter et.al, 2012).

Detection of landslide related events is not an easy task. Reports have been made of most landslide deformation occurring aseismically (Gomberg et.al, 2011). In Gomberg's et.al, (2011) study 88 short period seismometers were deployed along the landslide's body with sensor spacing reaching a maximum of 50m. In addition, his results concluded that there was no possible way to correlate seismic signals with landslide displacement or failure events. Most of the studies have used knowledge of noise source signals to emit outliers and then tried to locate the remaining events (Gomberg et.al, 2011). Separation between noise sources, e.g. wild life, and possible candidates for landslide related events was made using 1) the event being recorded from multiple sensors at similar magnitudes, excluding the high frequent bursts, 2) minimum and maximum duration of events, 3) the frequency content of sources (Walter et.al., 2011).

Location of landslide emitted seismic events has also proven to be hard, with uncertainties starting in identifying landslide related events. It was found that locating events in a plane (without depth determination) was possible using 4 seismometers (Tonnellier et.al, 2013). It was found that locating events by creating hyperbolas using P-wave first arrivals produces more accurate results since S-wave arrival times are hard to identify (Tonnellier et.al, 2013). There were case studies that the arrival times of wave phases were used successfully for location analysis (Gomberg et.al, 1995). At others though the source location could only be estimated without concluding whether the recorded signals originated from the landslide's body or the surrounding area (Gomberg et.al, 2011). In other studies, successful location results were produced at a source-to-sensor distance location threshold of 200m (Rothmund and Joswig, 2012), 140m (Walter et.al, 2009) and 350m (Walter and Joswig, 2008, Walter et.al., 2011) depending on the event magnitude and the degree of attenuating due to the local geology. The only error estimation given is in the range of 10% of the source-to-sensor distance which is the expected accuracy of the beam formation location technique (Walter et.al, 2011, Walter et.al, 2012). In general though location error estimation is

hard because the true location of the landslide related sources are unknown and usually not visible since they occur within the landslide's body.

The problems involved in locating the emitted seismicity of soil dominated landslides are many. First of all P and S waves as seen in the rock slides are not separated due to the small source-to-sensor distances (Tonnellier et.al, 2013). In addition true first arrivals of P-waves are not always visible in the recordings (Helmstetter & Garambois 2010). It was also found that the number of sensors monitoring the landslide under investigation played a major role, since the greater the area coverage with a dense seismic network the better the obtained data (Tonnellier et.al, 2013). That way seismometers had a greater chance in recording landslide related events. That is not always the case since studies with seismic networks following the previous guidline were not able to produce accurate location results (Gomberg et.al., 2011). Also the heterogeneity of the landslide's geology along with irregular topographies add to the complexity of the location analysis increasing the uncertainties involved in the produced results (Gomberg et.al, 2011).

Seismic recordings of slidequakes and other slope related events published in the literature review were not conclusive regarding their source mechanisms and how they relate to the slope's behaviour, implying that additional monitoring technologies are needed (Rothmund and Joswig, 2012). This might be due to low signal-to-noise ratios, meaning that the emitted landslide signals are masked from the local noise conditions (Tonnellier et.al, 2013). The latter might not necessary be due to high background noise levels, but due to a high attenuating geology and to weak seismic landslide signals (Tonnellier et.al, 2013).

2.6 Other studies of seismic monitoring of landslides

So far studies trying to capture distinct signals related to landslide displacement of failure events deploying short period or broadband seismic sensors were presented. The same types of sensors have been used in other cases to monitor background noise (Meric et.al, 2007, Jongmans et.al, 2009, Renalier et.al, 2010, Maisant et.al, 2012). The simplest application is that increase in the noise level means increased activity in

the landslide under investigation (Amitrano et al, 2007). More complex analysis involve those calculating the S-wave velocity profile of the local landslide geology using noise recordings, e.g. using the SPAC method. These results lead to identification of the surface between soft soil material and bedrock, a possible failure plane (Meric et.al, 2007). Researchers have also noticed a decrease in S-wave velocity during the "damaging" (deconsolidation) process of the landslide material indicating the possibility of landslide failure (Jongmans et.al, 2009, Renalier et.al, 2010, Maisant et.al, 2012).

Finally, another interesting concept is the use of passive or active waveguides in combination with acoustic seismic sensors for landslide monitoring purposes (Rouse et.al, 1991, Dixon et.al, 2003, Shiotani, 2006, Dixon and Spriggs, 2007, Cheon et.al, 2011). A waveguide is usually a long bar or pipe made from steel or a material with less attenuating behaviour than the landslide's geology (Rouse et.al, 1991, Dixon et.al, 2003). Attached to these waveguides are seismic sensors able to record high frequencies, e.g. from 1kHz to 7kHz (Rouse et.al, 1991), sensors with resonant frequencies (upper frequency limit of sensor) of 30kHz (Dixon et.al, 2003), 50kHz (Dixon and Spriggs, 2007), 60kHz (Shiotani, 2006, Cheon et.al, 2011). Passive wave guides are in direct contact with the landslide's body and are used as a shorter, less attenuating travel path between source and sensor: during landslide displacement, the landslide's body interacts with the waveguide and tremors are transmitted to the sensor. Active wave guides are usually pipes filled with fine granular material like sand or gravel: during landslide displacement the active waveguide is being displaced and so is its filled material. Interactions between the fine granular material are transmitted through the pipe to the acoustic sensor indicating landslide displacement. The main problem of the passive and active waveguide is distinguishing between background landslide noise, electric noise and signals (Rouse et.al, 1991, Dixon et.al, 2003, Shiotani, 2006, Dixon and Spriggs, 2007).

2.7 Summary

Case studies of rock and soil dominated landslides were presented in this chapter. It was shown that the characteristics of seismic signals emitted during landslide deformation or failure depend on a large number of parameters such as the local geology, and the deformation characteristics. Great progress has been made in using seismic monitoring for understanding landslide behaviour. Many types of events have been identified with their seismicity mapped. Problems in using seismometers to monitor landslides exist especially to those dominated by soil material compared to those by rock. There are limitless combinations of the above, creating two main problems. Firstly, it is difficult to identify landslide related seismic signals if no a priori knowledge for the landslide seismicity exists. And secondly, it is difficult to find the same seismic signal recorded at all landslide sites, meaning that the optimisation of sensor deployment in order to achieve maximum event detection, must be case sensitive.

Active landslides have a complex, time variant, geology. Materials involved in slope deformation can be of various soil types, mixed with small or large rock boulders, moving against a stable soil or/and rock layer. In time, the geological profile of the material involved changes due to the displacement of the slope. As a result, mechanical properties of the local geology alter, e.g. stress conditions. Fluctuation in weather conditions, e.g. precipitation, also adds to the complexity of the problem by changing the saturation of the geological layers. All the above mean that the travel path of seismic waves between a source and a seismometer is complex due to a) refractions/reflections of the signal, b) variable attenuation and c) variable seismic velocity.

Studying a natural phenomenon such as a landslide, where there is no control over the parameters involved and no a priori knowledge of the seismic signal's characteristics, is very difficult and involves large uncertainties e.g. variations in the mechanical conditions of the geology in time. Additional landslide monitoring technologies can be used simultaneously with the seismic sensors, e.g. rain gauges, inclinometers or video recordings, in order to constrain the problem by identifying the location and

origin time of an event. Each monitoring methodology used though, has uncertainties in the data interpretation.

It is those problems that this research work has addressed through controlled field experiments where the source mechanisms and the origin time of the seismic events are known a priori.

Chapter 3
Seismic Theory

3.1 Introduction

Seismometers are used in this thesis as the investigation tool in order to enhance our understanding and monitoring capabilities of landslides. In this chapter a brief description of the seismic wave types, as well as the methods available to calculate a velocity model and the location of a seismic source is presented.

3.2 Seismic waves

Seismic waves are elastic waves created and radiated away from a seismic source (Kearey et.al, 2002). They also represent the propagation of mechanical force perturbations of a material (Santamarina et.al, 2001). Any phenomenon that can create seismic waves that travel though the earth, e.g. explosion, earthquake, footstep, can be characterized as a seismic source. All seismic waves are elastic meaning that as they propagate though a material they don't cause permanent deformation to it.

3.2.1 Categories and Types of Seismic Waves

There are two categories of seismic waves; a) body waves (P-waves and S-waves) and b) surface waves (Rayleigh and Love waves) (fig. 3.1). There are three main differences between the two categories; 1) body waves can propagate throughout the whole body of the earth while surface waves propagate along to the earth's surface or the contact surface between two different geological materials, 2) Body waves propagate at higher velocities than surface waves though the same material, 3) Body waves are non-dispersive while surface waves are. A wave is dispersive when its frequency components propagate at different velocities, with lower frequencies traveling faster. Each category contains more than one type of seismic waves and are presented below. In this thesis only the properties of the body wave are going to be utilised.

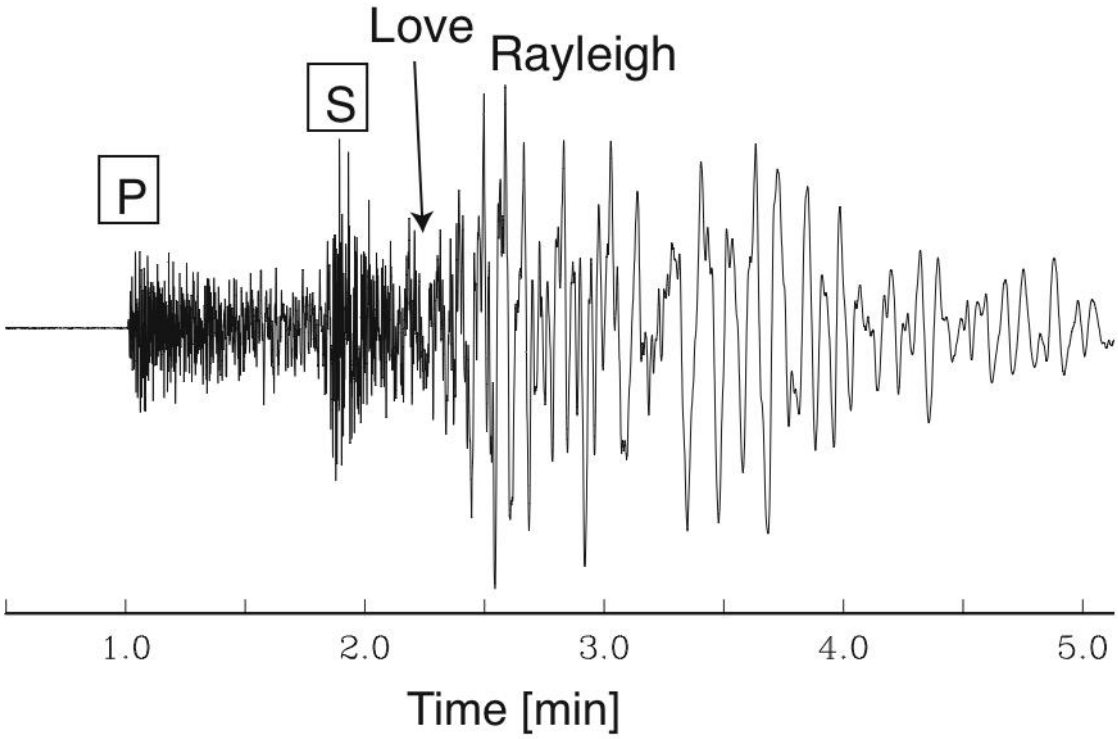

Figure 3.1: Seismogram showing the arrival times of body waves (P-wave & S-wave) and surface waves (Love & Rayleigh waves). (image from http://quakeinfo.ucsd.edu/~gabi/sio15/supps/ seismogram.png)

Body waves

Two wave types can be categorized as body waves; 1) Compressional waves or P-waves (from the word primary since they are recorded first) and 2) Shear waves or S-waves (from the word secondary since they are recorded after the P-wave). Their main differences are that P-waves travel faster than S-waves when both waves propagate through the same material and that they propagate with a different mechanism which allows P-waves to travel in liquids, e.g. lava or water (fig. 3.2). As P-waves travel they compress and dilate elastically the particles of a material along their direction of propagation (fig. 3.2a), while as S-waves travel they shear elastically the particles of a material perpendicular to their direction of propagation (fig. 3.2b) (Kearey et.al, 2002). S-waves can be divided into SH (H for horizontal) and SV (V for vertical) waves based on the particle motion they induce.

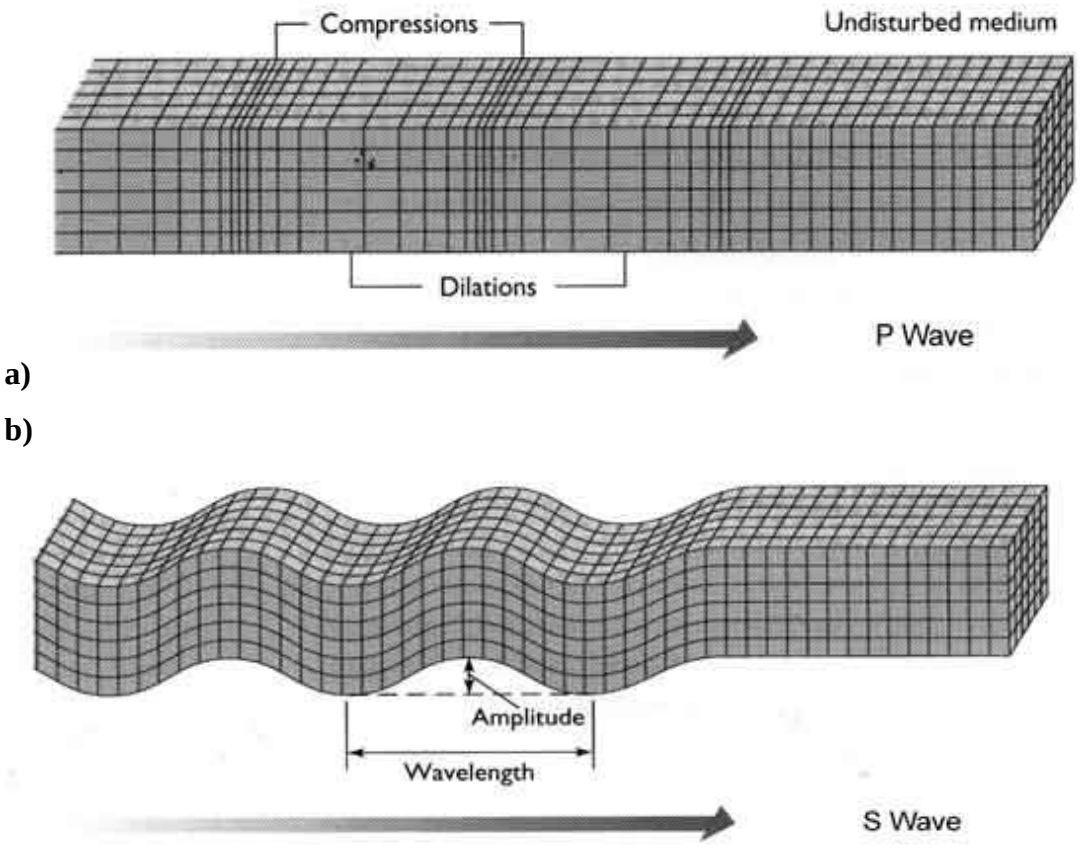

Figure 3.2: Propagation mechanism of **(a)** P-waves and **(b)** SV-waves (shearing along the vertical plane). (images from http://allshookup.org/quakes/wavetype.htm)

Surface Waves

Two wave types can be categorized as body waves; 1) Rayleigh waves and 2) Love waves. Their main difference is that Rayleigh wave can travel through water and are slower compared to Love waves. As Rayleigh waves travel the displacement is elliptical with a plane normal to the surface and the direction of propagation (fig. 3.3a). Love waves can be found only within a surface layer that overlies a faster shear wave velocity layer (Kearey et.al, 2002). As Love waves travel they displace sideways, parallel to the free surface and perpendicular to the direction of propagation (fig. 3.3b) (Kearey et.al, 2002).

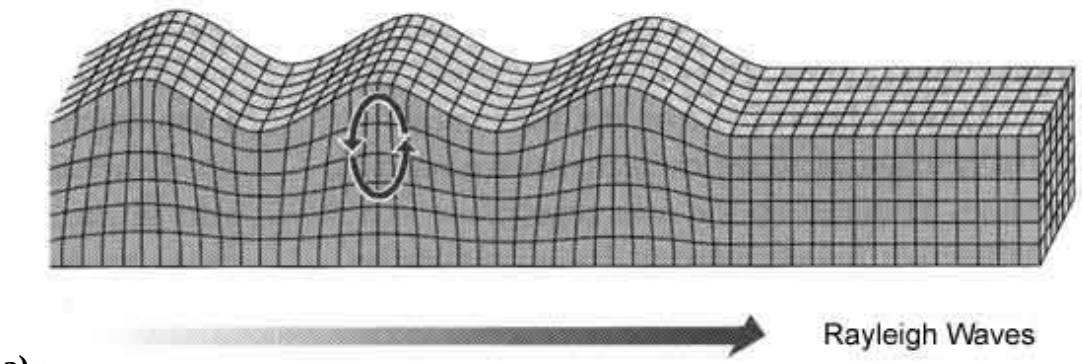

a)

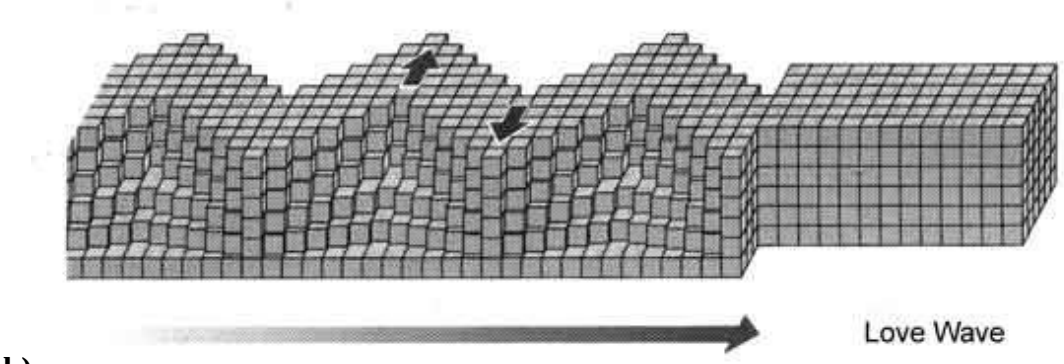

b)

Figure 3.3: Rayleigh-wave (a) and Love-wave (b) propagation mechanism. (images from http://allshookup.org/quakes/wavetype.htm)

3.2.2 Propagation of Seismic Body Waves

The work in this thesis is going to be based on body waves so their propagation through a medium will be briefly presented. When a seismic source is active it emits seismic waves or pulses that travel away from the source's location in all possible directions. The starting points of those waves propagating through the geology are referred to as wavefront (fig. 3.4). Seismic rays mark the path seismic energy travels and are always perpendicular to the wavefront in isotropic media. The velocity of the waves or wavefront depends on the properties of the propagation material (geology), e.g. density and porosity. When waves travel through isotropic, homogeneous materials, they have a constant propagation velocity and a spherical wavefront.

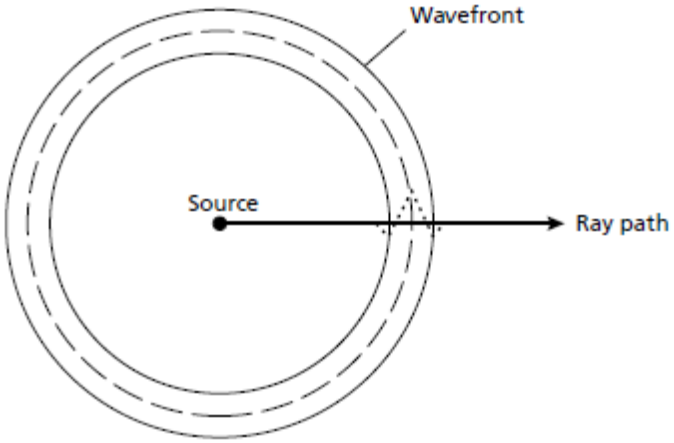

Figure 3.4: Sketch of a source, its wavefront and a ray path through an isotropic medium (after Kearey et.al, 2002).

Geological materials are very rarely isotropic and homogeneous. Their properties change since the earth's geology is heterogeneous at all scales; a) the structure of the earth is layered (crust, mantle, etc.), b) the crust consists of different rock materials, e.g. granite or basalts, or soil materials, e.g. clay or sand, c) with rock or soil layers to also be heterogeneous, e.g. a soil layer having different saturation values or a rock layer having different fracture geometries throughout their mass. These changes result in different seismic velocities; material with different elastic and bulk modulus and/or densities have different seismic velocities (Kearey et.al, 2002). In addition, as the confining pressure of a geological material increases, so does its seismic velocity properties (Kearey et.al, 2002). This increase in velocity is the result of cracks, flaws or grain boundaries closing by the increase in pressure.

There are two directions a wave can hit an interface between two different geological materials; a) with a normal incidence angle and b) with an oblique incidence angle to the direction of propagation. The simple case of a 2D space is going to be presented below.

a) Normal Incidence Angle

As a wave hits the interface of two geological materials with a normal incidence angle to the direction of propagation the original seismic wave splits its energy into a reflected wave and a refracted wave (fig. 3.5) (Santamarina et.al, 2001). The portion of energy divided into the two new waves depends on the difference between the acoustic impedance (= density x seismic velocity of a geological material) of the two materials (Kearey et.al, 2002). In general, the larger their difference the more energy is reflected (Kearey et.al, 2002).

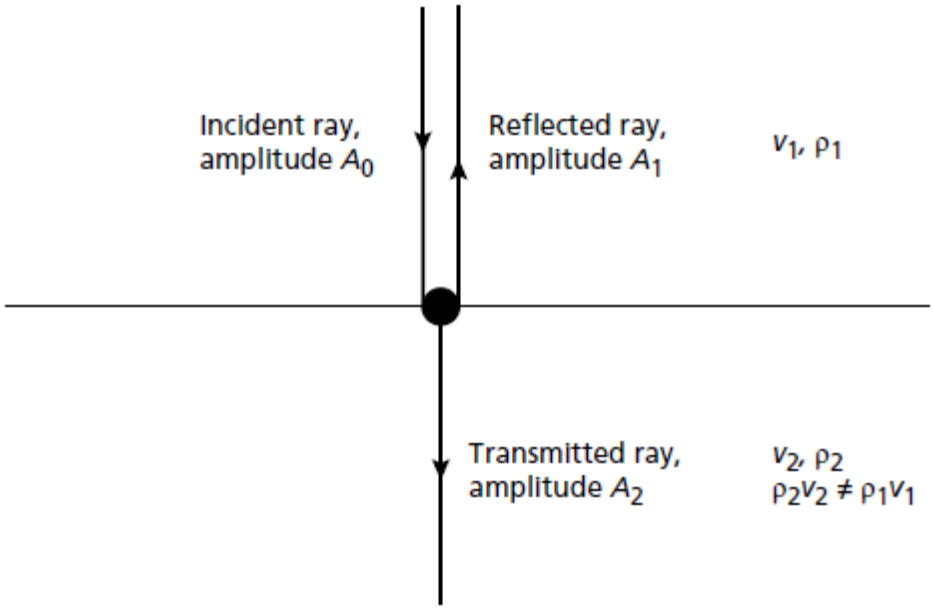

Figure 3.5: Representation of the refraction and reflection of a wave hitting the interface of two different geological materials (picture after Kearey et.al, 2002).

b) Oblique Incidence Angle

When a wave hits the interface of two different geological material with an oblique incidence angle it is divided into reflected and refracted waves and can also undergo mode change (fig. 3.6) (Santamarina et.al, 2001). Waves undergo a mode change when their particle motion changes and different wave types are created. This can happen

when a P-wave or an SV-wave hits such an interface because they induce particle motion in both x- (horizontal) and y- (vertical) directions of the interface. The reflection and refraction angles can be calculated using the generalized Snell's law from the equation below (Santamarina et.al, 2001):

$$\frac{\sin\theta_{P1}}{V_{P1}} = \frac{\sin\theta_{P2}}{V_{P2}} = \frac{\sin\theta_{S1}}{V_{S1}} = \frac{\sin\theta_{S2}}{V_{S2}},$$

where: V_P, V_S: P-wave and S-wave velocity respectively and
θ_P, θ_S: angle of incidence/refraction of P-waves and S-waves respectively.

A special case of a ray hitting an interface is at the critical angle of incidence when the refracted ray travels along the interface with the higher velocity. The critical angle can be calculated from the above equation, e.g. if θ_{P2} is replaced with 90°.

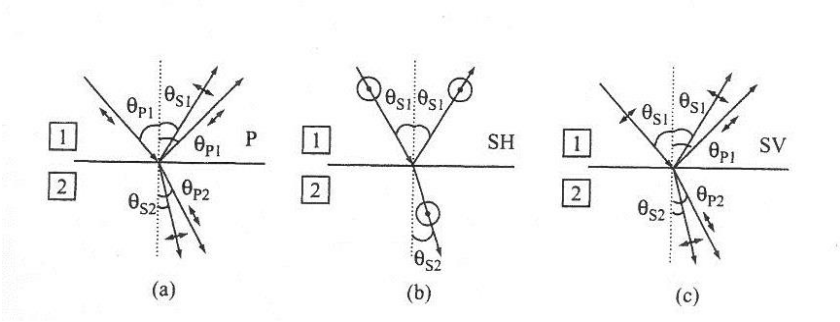

Figure 3.6: Reflection, refraction and mode change of **a)** P-waves, **b)** SH-waves, **c)** SV waves (image from Santamarina et.al, 2001)

In figure 3.7 the ray paths of waves emitted by a seismic source within a heterogeneous medium are presented without taking into account any mode conversion. The wave velocities have a constant gradient making the rays of the seismic waves to be continuously refracted, thus curved.

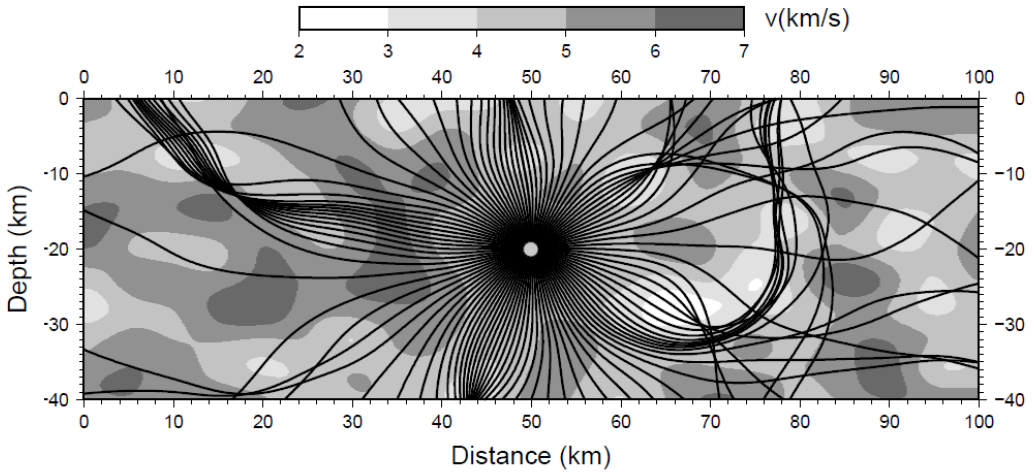

Figure 3.7: Representation of a source and the ray paths of the emitted waves through a heterogeneous medium where wave velocities have a smoothed gradient (after Rawlinson et.al, 2007).

Wave propagation becomes more complex when the medium is no longer homogeneous. When media have an object of different material inside them, e.g. a boulder inside a layer of clay or interfaces have abrupt discontinuities, e.g. edge of a fault, the geology has characteristics such that Snell's law is not applicable anymore for characterising propagated seismic waves (Kearey et.al, 2002). A wave hitting such structures is diffracted meaning that his energy is scattered radially (Kearey et.al, 2002).

A heterogeneous geological material is commonly assumed as homogeneous layer, e.g. the seismic velocity model IASP91 used for global seismology where the geology of the earth is divided into homogeneous layers (Kennett and Engdahl, 1991). In essence a real geological material is replaced with its equivalent homogeneous material having its 'effective properties' derived from the variance of the properties of the original material. There are three reasons why to go through this process; 1) Computation constrains meaning that taking into account all existing heterogeneities can lead into non convergence thus no solution, e.g. location search algorithms, or because the computational capability is not available. 2) Lack of knowledge regarding

the true geological structure that can lead to bias errors and false belief of the final's solution achieved accuracy. 3) Taking into account local heterogeneities has very little effect on the final solution. Homogenisation of a geological material must always be applied carefully taking great care that the final result of the process is close to the real represented geology. In this thesis homogeneous layers (same P-wave velocity) will be used in Chapter 5 to model the change in geotechnical parameters of a single geological material along with depth.

3.2.3 Attenuation of Seismic Waves

The last characteristic of seismic wave propagation through the earth's geology is the attenuation of seismic energy. Attenuation has three aspects; a) geometrical spreading of energy, b) apparent attenuation (due to wave transmitting and scattering through geological interfaces) and c) intrinsic attenuation (due to non-elastic geological properties) (Santamarina et.al, 2001).

a) Geometrical Spreading of Energy

Geometrical spreading is the effect of seismic waves radiated away from a seismic source. The wavefront in an isotropic material is spherical with a surface of $4\pi r^2$ that is constantly expanding, thus the seismic energy per unit area of the wavefront $E/4\pi r^2$ is constantly decreasing (Kearey et.al, 2002). The same principle applies to heterogeneous media despite the fact that the seismic wavefront has a complex surface. This scattering effect is elastic and preserves the original energy (Rotman, 2011).

b) Apparent Attenuation

When a wave hits an interface of two different geological materials it is divided into a reflected and refracted wave, while in cases it can change modes resulting in the creation of a different wave type that is also reflected and refracted (fig. 3.6). The seismic energy of the original wave is conserved but divided into all of these new waves. This means that each one of the transmitted new waves has lower energy than the original.

c) Intrinsic Attenuation (due to Geological Properties)

Seismic energy attenuation is also a result of the material properties of the geology through which seismic waves propagate: the geology of the Earth is not perfectly elastic and internal friction phenomena lead to transformation of the seismic energy into heat, thus attenuation (Santamarina et.al, 2001, Kearey et.al, 2002, Rotman, 2011). Saturation levels, porosity and the confining pressure of a soil material (Santamarina et.al, 2001) or cracks and saturation in rocks (Rotman, 2011) are some of the parameters affecting intrinsic attenuation.

The understanding of attenuation is critical in designing the deployment geometry of seismometers. The expected high attenuation of soils was the reason the seismic sensors used during experiments were densely spaced (5-50m apart). Knowledge of the attenuation effect over seismic recordings is gained experimentally from the first location experiment discussed in Chapter 5 leading to the final deployment geometry used to monitor the artificially induced landslides (Chapter 8).

3.3 Seismic Analysis

Two very important tasks regarding microseismicity is the calculation of a velocity model representing the local geology and the location of microseismic events. In this section the main techniques of both analysis categories are going to be presented along. The ones used in this thesis will be explained more deeply and their selection justified.

3.3.1 Calculation of Velocity Models

The seismic representation of the local geology is achieved through the velocity model. The velocity model is necessary for locating detected seismic events, with an accurate representation of the geology through the velocity model producing accurate location results. Wave velocities are attributed to geological material based on their type characteristics. In general, seismic waves travel faster in rock formations than soft soils.

Location analysis utilizes mostly first P and S-wave arrivals. It is very common for the first arrivals of S-waves to overlap with the P-wave coda. This means that location analysis in landslide monitoring expeditions cannot depend explicitly on S-wave recordings. In addition, all site investigation needed prior to having a fully functional seismic monitoring system of slopes prone to failure, need to be achieved at relatively low cost in time. The latter attribute in the methodology used for conducting an accurate velocity model is necessary for two main reasons. 1) Landslides can be a fast evolving natural phenomenon. Within hours their behaviour can change completely, e.g. due to a strong rainfall event, leading to destabilization and failure. 2) It is impossible to equip all landslides with seismic sensors to monitor continuously their behaviour. This means that short time duration does not allow for an extended geophysical characterization using techniques that are time consuming, e.g. the refraction/reflection methodology. Seismic monitoring of landslides has to be a fast monitoring technology that provides reliable information regarding the slope's behaviour and stability. For this reason a fast methodology for creating a P-wave velocity is going to be used. Fast, regarding the low cost in time needed for data collection in the field and the analysis process, without though losing in accuracy.

The techniques presented in this section are widely used for the calculation of a P- or S-wave velocity model. Many of these techniques require deployment of seismometers at geometries not optimum for a microseismic monitoring designed for event location. It is common, for example, to deploy sensors linearly for velocity model data acquisition, a geometry that has a poor special coverage of the monitoring area. This means that the investigator needs to deploy sensors twice on the landslide which is a time consuming and potentially dangerous task. The optimum methodology found in the literature review used in landslide monitoring that fulfils the above characteristics is the calculation of the P-wave velocity model using calibration shots (Gomberg et.al, 1995, Myers, 2000, Walter and Joswig, 2009, Wust-Bloch, 2010, Walter et.al, 2012, Tonnellier et.al, 2013).

Calibration Shots

Data acquisition is based on active seismic sources that are usually explosives. Seismometers are deployed on the slope based on the need of the landslide monitoring campaign with explosives distributed at various positions on the site under investigation with the location of both known a-priory. The more explosives used and the denser they are distributed, the better the calculation of the final P-wave velocity model. Finally the explosives are triggered separately at a known time so identification of the seismic waves created by each explosion is easily done.

Once all explosives are triggered and all data are collected, the calculation of the velocity model can start. First step is to pick the P-wave arrivals from all sensors created by one explosion. Since the P-wave velocity model is unknown a single value or a layered velocity model (layers each having their own velocity value) is attributed based on the site's previous geological knowledge. Using the arrival time information and the estimated velocity model, the explosion can be located. Since the velocity model used for the location process is known to be inaccurate, discrepancies between the real and calculated location exist. By a trial and error procedure the single velocity or layered velocity model has to change in order for the calculated location of the explosion to match the real location. The same procedure is repeated for all explosions. The final velocity model chosen must produce the minimum location errors between the calculated and real locations of the explosions. The error is an indication of how accurate the chosen velocity model represents the site's geology and whether or not the first time arrivals of the recorded P-waves were picked correctly.

Refraction Technique

The method uses P- or S-wave time arrivals of wave that are critically refracted waves along discontinuities from active seismic sources, e.g. explosions or shear wave vibrator, recorded by seismometers deployed linearly on the earth's surface. The refraction method is used to map distinct interfaces between two different geological materials, e.g. top soil layer over bedrock.

Seismic Tomography

Seismic tomography also uses arrival times of P- or S-waves with sensors deployed linearly on the surface or at different depths (in boreholes). It can be used to provide a smoother velocity model of the geology under investigation compared to the ones from a refraction technique.

Reflection Technique

The reflection technique differs from the refraction technique in that it utilizes the whole recorded signal of waves reflected from discontinuities that are originally emitted from active seismic sources.

Ambient Noise (Microtremor) Measurements

Another technique in constructing an S-wave velocity model involves utilizing ambient noise recordings. The advantage being that active sources are not required. This most common technique is the Spatial Autocorrelation Method (SPAC) method that utilizes the vertical component of ambient noise to provide an S-wave velocity model (Okada, 2006).

3.3.2 Location Methods

The location problem consists of four unknown parameters; the spatial coordinate of the source (X, Y, Z) and the origin time of the event (T_0). Location analysis is subjected to two major error sources; a) accuracy of the velocity model used, and b) errors in determining the arrival times of waves. The accuracy of the velocity model used is connected to how accurate the existing knowledge of the local geology is and whether it is modelled correctly. Determination of the time when different wave phases were recorded from a seismometer can be difficult due to attenuation effects and high noise conditions.

The need for a robust location technique that determines the coordinate of a seismic event with low computational cost has led to the creation of many location techniques. First the ts-tp circle location method and the tp-tp hyperbola method are going to be

presented as two of the oldest techniques and most commonly used while the rest can are organized as in Figure 3.8 by Che (2003).

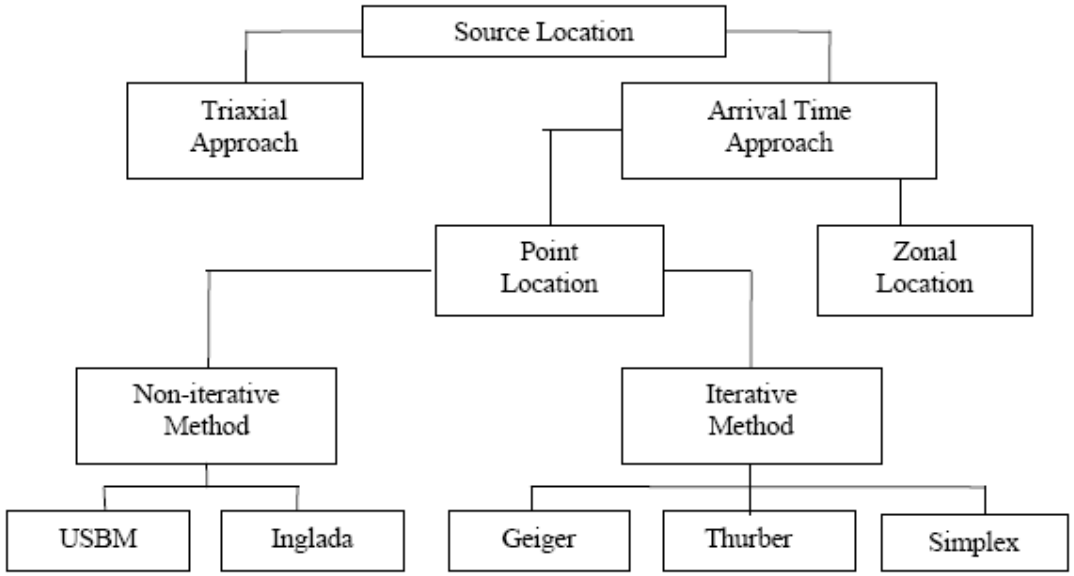

Figure 3.8: The most common source location methods used in seismology (after Che, 2003).

P & S Time Arrival Circle Method

A very old and most common location method used to explain the basic concepts of earthquake location is the circle method that uses P- and S-wave time arrivals (Stamps and Smalley, 2006). Using the equation shown below, using the wave velocity and travel time, a radius *D* having as centre the location of one seismometer is calculated. If three or more stations record the same event with clear arrival times of the P- and S-waves then the epicentre (the event's location in the surface of the earth) can be located as shown in Figure 3.9b.

$$\left.\begin{aligned} D &= V_P(t_P - t_0) \\ D &= V_S(t_S - t_0) \end{aligned}\right\} \quad D = \left(\frac{V_P V_S}{V_P - V_S}\right)(t_S - t_P),$$

where

D:	epicentre distance (source-to-sensor)
V_P, V_S:	P- and S- wave velocity
t_P, t_S:	P- and S- wave arrival time to the sensor
t_0:	origin time.

The circles shown in Figure 3.9b do not have a single contact point but seem to define an area where the epicentre is likely to be (given uncertainties). That is because the depth is not well defined. Once the epicentre is chosen, depth can be estimated using the equation below and the hypocentre of the seismic event can be defined (fig. 3.9a),

$$H = \sqrt{D^2 - X^2},$$

where

H:	Focal depth
X:	epicentre distance from seismometers.

The description above is valid for a homogeneous velocity model. If the velocity model is layered the spheres are deformed due to the refraction path of the seismic waves as they pass through the different geological material (fig. 3.10)

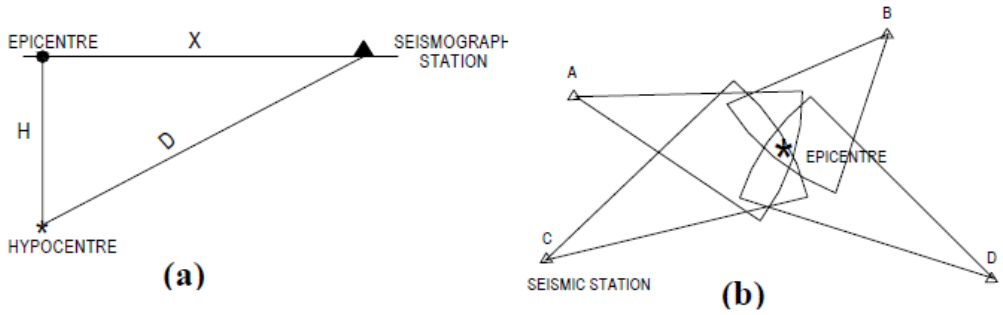

Figure 3.9: Circle's location technique: a) Sketch of seismic station, epicentre and hypocentre of the seismic event. b) A circle (or arch) is drawn around each seismic station using the seismic velocities along with the P- and S- wave arrival times of each station. The epicentre of the earthquake lies in the area where all three circles almost meet. When the epicentre is defined, the focal depth can be calculated and the hypocentre of the seismic event estimated (image after Kayal, J.R., 2008).

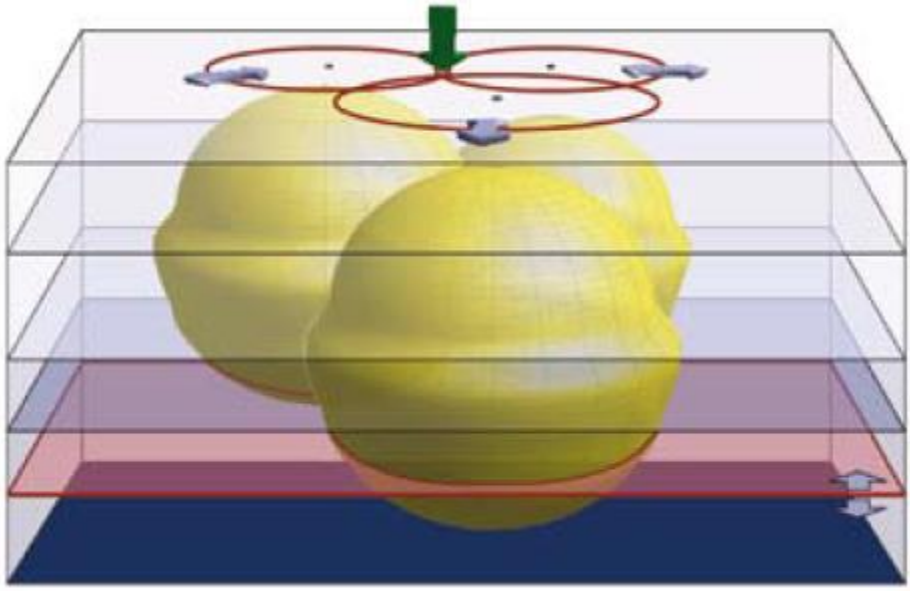

Figure 3.10: Deformed spheres calculated using P- and S-wave time arrivals of seismometers buried at a layered geology. Three seismometers are deployed at the centre of the spheres buried below ground surface. Spheres are deformed due to the layered velocity model used that causes seismic waves to refract as they propagate through the different geological material. The red horizontal plane cuts the spheres into the focal depth of the seismic event with the projection of the circles and sensors presented at the surface (image after Joswig, 2008).

Hyperbola Method

Another very common location method involved generating hyperbolic P-wave time arrivals (fig. 3.11) (Mohorovicic, 1915, Rydelek and Pujol, 2004, Pujol, 2004). For a hyperbola to be created two P-wave arrival times are needed from two seismometers located at distances d_1 and d_2 from the source. The curve represents the points where a source can lie in order to have the same difference of P-wave arrival times (t_{p1}-t_{p2}) at a certain depth. If depth changes, so does the geometry of the curve. If V_P is the P-wave velocity and t_1, t_2 the P-wave arrival times recorded at two seismometers then the equation of the hyperbola is:

$$d_2 - d_1 = V_P(t_2 - t_1).$$

A location is calculated with the use of a minimum of four stations recordings creating 6 hyperbolas in total. All hyperbolas theoretically meet at a single point. Discrepancies between the velocity model and the real local geology as well as errors in picking the true P-wave arrival times result in location errors or in no convergence of the hyperbolas thus no location result.

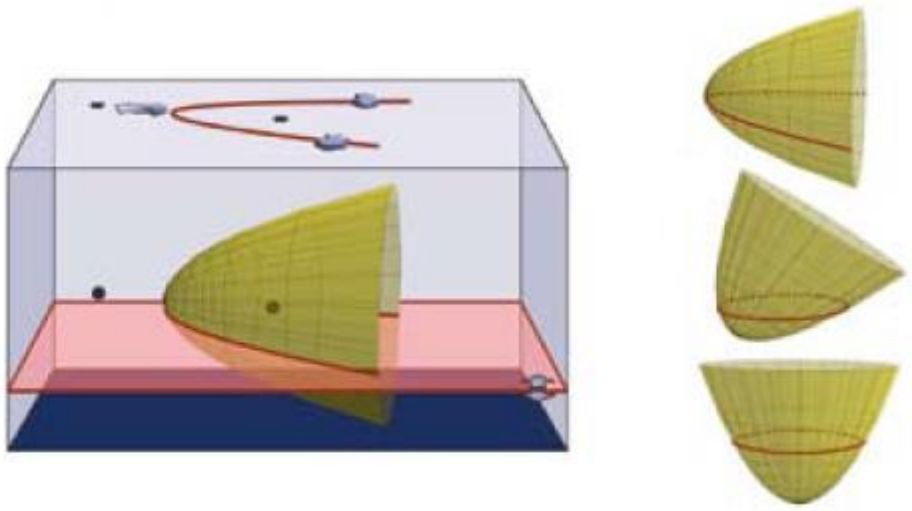

Figure 3.11: Sketch of a hyperboloid created from the P-wave arrival times of two seismic sensors buried at the same depth in a homogeneous geology. The red plane cuts the geology at a depth with the sensors and hyperboloid projection shown at the surface as black dots and hyperbola respectively. On the right of the picture three different hyperboloids are shown for the case when the sensors are buried at different depths (after Joswig, 2008).

Triaxial Sensor Approach

This method uses two types of data coming from one 3D seismometer: event amplitude as well as the P- and S-wave arrival times (Che, 2003). The source location is defined by the relative distance and azimuth to the known location of the sensor. The advantage of the method is that only one sensor is needed to achieve a source location solution. A problem though lies in the use of amplitudes as input data. Their values depend greatly on material properties (attenuation) and local geological conditions (site amplification). Using this method in landslide monitoring is hard since the arrival time determination of S-waves was found to be difficult because they usually overlap with the P-wave coda (Helmstetter and Garambois, 2010).

Zonal Source Location Method

This method is the simplest way of estimating the seismic source (Che, 2003). In figure 3.12 a schematic array geometry is presented. The location is first considered to be in the vicinity of the sensor that first recorded the event. Then this area is divided into smaller parts judging from the order that the remaining the sensors recording the same event. The technique has no need for a velocity model, utilizes only P-wave arrivals and has no restrictions on how many sensors have recorded the event. On the other hand, the location solution is only estimated in the horizontal plane since no depth estimation can be made and needs a large number of seismometers densely spaced for a good estimation.

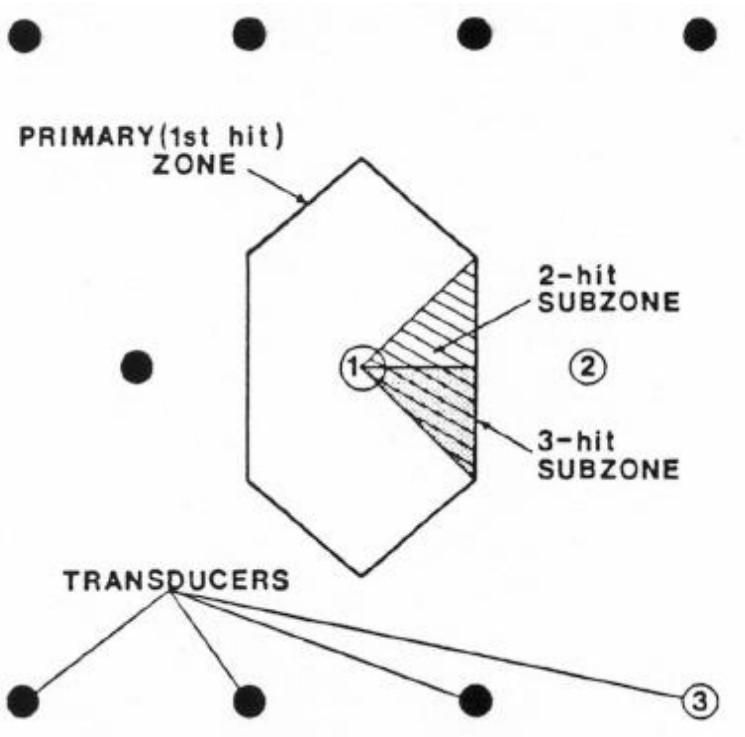

Figure 3.12: The zonal location method array (after Che M, 2003). "1" stands for the sensor that recorded the event first. From this the polygon can be drawn, marking the area of the epicentre. By knowing which sensor recorded the event next ("2" sensor), the area of the event's location can be constrained further.

Non-iterative methods

These methods solve the location problem with a direct mathematical solution of a defined system of equations. They have no computational difficulties and can deliver a solution quickly. Their major disadvantage is that they assume a uniform velocity model for the propagation of the seismic waves. Two methods are representative in this category: a) Inglada's and b) the USBM method (Che, 2003).

a) Inglada's Method

The Inglada's method needs four different seismometers recording the P-wave arrival time of the same source. Arrival time data and a single P-wave velocity is used in the following equation to create a nonlinear system that results in a unique location

solution (Che, 2003). The geometrical explanation is locating the source as the common centre of 4 spheres representing the wavefront at the time the sensors recorded the event (fig. 3.13),

$$(A_i - X)^2 + (B_i - Y)^2 + (C_i - Z)^2 = (T_i - T_{event})^2 \times V_P^2 ,$$

where:

T_i:	Arrival time of wavefront to "Sensor i".
T_{event}:	Time that the seismic event occurred.
V_p:	P-wave velocity.

b) USBM method

The USBM method was developed at the United States Bureau of Mines (USBM) and solves the same equation shown in Inglada's method in a different way (Che, 2003). The main difference is that it utilizes five P-wave arrival times. If more arrival time data are available, statistical analysis can be used to solve the system of equations (superstatic problem, least squares method).

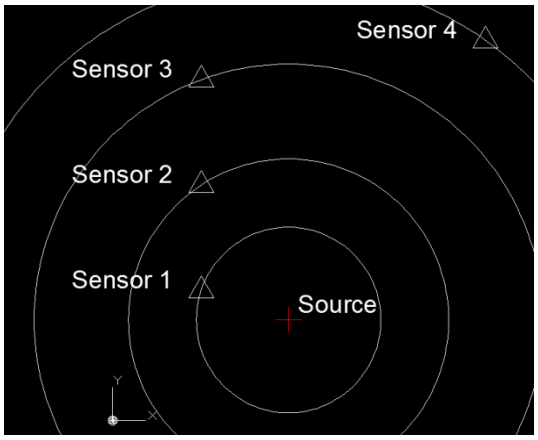

Figure 3.13: Geometrical explanation of Inglada's location method with the four circle representing the wave front of the source at the time it was recorded by the four different seismometers.

Iterative Methods

These methods utilize arrival times, a velocity model and an initial possible location solution usually selected by the user. By calculating the signal's source to sensors travel times and comparing them with the recorded arrival times, the initial chosen location solution is corrected. The process is repeated and provides a new location solution each time until an accepted error is reached. Iterative methods are trial and error procedures that can be divided based on their search algorithm into a) derivative, b) sequential, c) genetic and d) Simplex methods.

a) Derivative approach

The Geiger method (Geiger 1912) and Thurber's method (Thurber, 1985) are the most famous methods in this category, with the only difference between the two being that Geiger uses only the first derivative while Thurber uses the first and second derivative. The major problem of these methods is the stability of the solution. Many factors such as poor sensor coverage of the monitoring area or an unsuccessful initial trial solution can lead to a never ending loop (solution does not converge) as the convergence criteria cannot be satisfied. The Geiger method is expressed mathematical for one sensor

$$f_i(x) = f_i(x_0 + \delta x) = f_i(x_0) + \frac{\partial f_i}{\partial x}\delta x + \frac{\partial f_i}{\partial y}\delta y + \frac{\partial f_i}{\partial z}\delta z + \frac{\partial f_i}{\partial t}\delta t\,,$$

$$f_i(x) - f_i(x_0) = \frac{\partial f_i}{\partial x}\delta x + \frac{\partial f_i}{\partial y}\delta y + \frac{\partial f_i}{\partial z}\delta z + \frac{\partial f_i}{\partial t}\delta t\,,$$

where:

$f_i(x)$: real time function (observed time arrivals)

$f_i(x_0)$: chosen time function (calculated arrival times from the trial solution)

$\frac{\partial f_i}{\partial x}\delta x + \frac{\partial f_i}{\partial y}\delta y + \frac{\partial f_i}{\partial z}\delta z + \frac{\partial f_i}{\partial t}\delta t$: correction vector of the chosen solution calculated by the time difference between the observed and the calculated time arrivals.

b) Sequential Searching Algorithms

Sequential searching algorithms cover the methodologies that divide the monitoring area into smaller ones which are represented by their centre point or other key points (Horiuchi et al, 2005). These points are considered as the source location solution. Travel times are calculated from them to the sensors and are compared to the observed ones. A better estimation is usually achieved by further dividing a block with the process finalizing when the needed accuracy is achieved.

c) Simplex algorithm

Derivative methods give a solution very quickly but are unstable and might not give one at all, while sequential searching algorithms are very stable but slow. A solution in-between these two is the Simplex algorithm that is stable, will never diverge and uses simpler mathematical processes (Prugger and Gendzwill, 1989; Gendzwill and Prugger, 1989).

Initially an error space defined from five vertices is chosen around the sensor that first recorded first the seismic event under investigation. Its dimensions can be a third or half of the array size used, in general though it can be arbitrarily chosen. Each vertex point is considered as a possible location and its theoretical arrival to the recorded sensor is calculated and compared to the measured one. Through a relocation process of the vertices the initial error space is relocated and eventually decreased towards the minimum error space. The search is stopped when the volume of the simplex space is lower than a selected threshold.

Master Event Techniques

In addition to the methods presented above that provide location based on recordings of the event under investigation, the master event techniques utilize the wave form (seismic recordings) and solution of a successfully located event (master event) to provide a location solution of a weaker event (slave event) that has no clear P-wave arrivals. The location calculated for the slave event is based on the correlation of its

seismic recordings with the master event's recordings and on the master location, and not to a location solution through standard means (e.g. using the Simplex algorithm). To apply a master event technique two assumptions must be valid: a) Sources have small in-between distance compared to their source-to-sensor distance, thus have similar travel paths, b) Sources share similar physical processes, and thus the seismic waveforms emitted share common characteristics.

A graphical implementation of the master event technique is given by Häge and Joswig (2009). The clear wave forms of a master event are correlated with the wave forms of a weak source. More specifically, the waveforms of both events recorded at the same seismometer are adjusted to overlap. Picking the first P-wave arrivals of the slave event is now easier or at worst case scenario they can be better estimated. Hyperbolas can then be calculated for both events. From the location point of the master event, perpendicular vectors are calculated towards the closest points of each hyperbola of the slave event. The combination of these vectors produce the final vector having as a start the location point of the master event and as an end the location point of the slave event.

3.4 Methods used in this thesis for the calculation of velocity models and location of microseismic events

The basic need for successful landslide monitoring is the deployment of the monitoring equipment and the retrieval of information related to the landslide's behaviour with the lowest possible time cost. Considering these characteristics, the calibration shot method is the chosen method in calculating a velocity model. The same technique was implemented by many landslide monitoring surveys for the same reason (Gomberg et.al, 1995, Walter and Joswig, 2009, Tonnellier et.al, 2013).

The location method chosen for a landslide monitoring is restricted to methods capable of providing accurate results based on only P-wave time arrivals, the waves that are usually clearly identifiable in landslide monitoring as mentioned in the literature review. In addition, the implementation of the location method should allow the user

to understand how sensitive the final result is to the chosen parameters; (P-wave arrival times and velocity model). The engineer needs to understand how the hypocentre of a seismic event shifts in space. This is necessary because the emitted signals during landslide failure events are found to be weak (see literature review). This characteristic increases the possibility of the chosen P-wave arrival times to be erroneous due to attenuation or amplitude below the background noise levels. In addition, landslides consist of heterogeneous geology varying through time making the velocity model used inaccurate. If small changes in the location parameters create large shifts of the hypocentre in space the solution uncertainties are high.

The seismic software "Hypoline" (Joswig, 2008) can combine the above characteristics; it can implement the hyperbola location method and the master event technique. In addition it can implement the circle method when S-wave arrival times are available, that can be used additionally to the other location techniques in order to further constrain the location solution. Finally, the software provides a graphical display of the location results. If the user changes the arrival times of waves or the velocity mode the graphical representation is updated in real time, allowing the user to understand how stable the final location solution is.

3.5 Summary

The basics of seismic theory were presented in this chapter. First a description of the seismic wave types and their propagation through geological medium was given. Seismic velocity models were presented next along with available methodologies allowing their calculation. Finally some of the most known seismic location techniques were presented.

Chapter 4
Signal Processing Techniques

4.1 Introduction

In this chapter a short description about different signal analysis tools that are used in this thesis is provided. In the first sections the term signal (seismic signal) and the efficient process to record them is discussed. The Fourier transformation is presented next, along with the spectrogram and power spectral density plots. Finally the parameters used in the subsequent signed analysis of soft soil landslides are given.

The term "signal" refers to a time varying process that represents a vibration traveling through geological materials (seismic signal). In nature, signals are continuous in time, with their amplitudes able to span in a continuous domain. Recording signals can be done by sampling them at discrete time increments. The equation below expresses a sinusoidal wave in the continuous time domain and in the discrete time domain after sampling (fig. 4.1),

$$x(t) = \sin(2\pi f_0 t) \rightarrow sampling \rightarrow x(n) = \sin(2\pi f_0 nt),$$

where; t: time, n: index number representing the sample number (integer).

Seismic signals are sampled at constant time increments with the help of a datalogger (or digitizer) connected to seismometers. The oscillation of a mass inside a seismometer is translated to an electrical signal that is recorded in the discrete time domain (sampled) by a datalogger. The sampled data are digitized in binary format and include the number of the sample with the corresponding signal amplitude. The amplitude resolution of the recorded signal is not infinite and depends on the construction of the datalogger (fig. 4.1c).

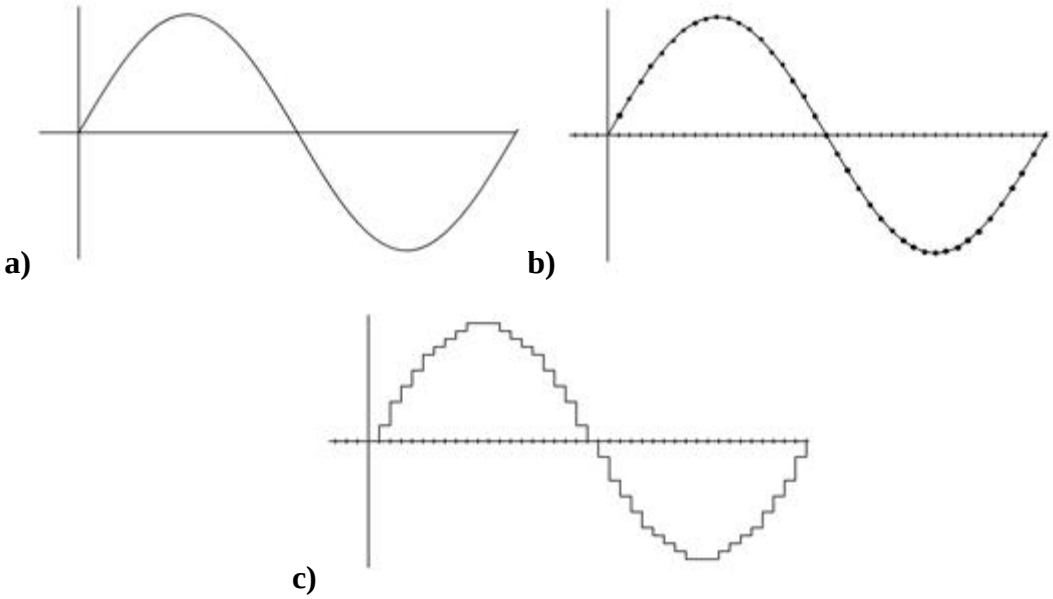

Figure 4.1: a) A continuous sinusoidal wave in time and amplitude, **b)** A sin wave sampled, **c)** Representation of a sampled sin wave in the discrete time domain. If samples were collected at smaller time and amplitude increments the representation of the sin wave would be smoother. (image from http://www.jiscdigitalmedia.ac.uk/guide/an-introduction-to-digital-audio)

Signals can be also presented in the frequency domain. Such representations of signals allow for further characterization of their properties and discrimination with other signals. Frequency patterns of seismic signals help in distinguishing between different seismic events, e.g. a local earthquake from a landslide. Transition of a signal from the time to the frequency domain takes place through the Fourier transformation (discussed in a following section).

4.2 Sampling a Signal

4.2.1 Aliasing

Our ability to record seismic signals is limited in sampling them at discrete intervals in the time domain. This raises the question of how to choose a sampling rate that will allow accurate representation of the recorded signal. The answer involves understanding the frequency domain ambiguity due to sampling (discretising) a

continuous signal; the samples recorded from a datalogger of a signal can be misinterpreted for other signals, e.g. a 7kHz sinusoidal wave sampled at 6kHz can be misinterpreted to a 1kHz sinusoidal wave (fig. 4.2). This misinterpretation of the true frequency content of a sampled signal is called aliasing.

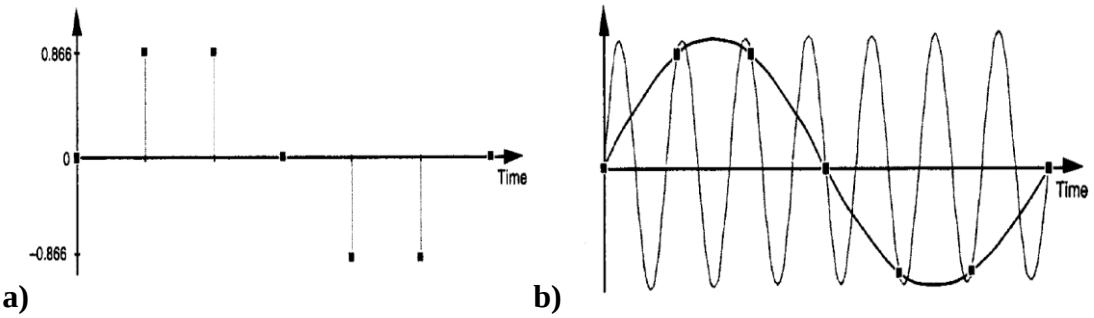

a) **b)**

Figure 4.2: a) Samples recorded from a datalogger of a 7kHz sin wave at 6kHz sampling rate, **b)** Two of the possible sinusoidal waves of 1kHz and 7kHz fitting the samples (image after Lyons, 2011).

The equations explaining this phenomenon for the simple case of a sinusoidal wave ($x(n)$) with frequency (f_0) that is sampled every (t_s), thus has a sampling frequency of (f_s), are shown below.

$$x(n) = \sin(2\pi f_0 n t_s) = \sin(2\pi f_0 n t_s + 2\pi m) = \sin(2\pi(f_0 + \frac{m}{nt_s})nt_s),$$

with (m) being an integer. If (m) is expanded as an multiplication product of two integers ($m=kn$) and by replacing (t_s) with ($1/f_s$) then;

$$x(n) = \sin(2\pi(f_0 + \frac{k}{t_s})nt_s) = \sin(2\pi(f_0 + kf_s)nt_s) = \sin(2\pi f_0 nt_s),$$

meaning that

$$(2\pi(f_0 + kf_s)nt_s) = (2\pi f_0 nt_s) \rightarrow (f_0 + kf_s) = f_0$$

thus a sampled sequence of a sinusoidal wave of (f_0) can be interpreted by all sinusoidal waves with frequencies (f_0+kf_s). Note that (k) is an integer and can take both positive and negative values.

There are two implications of the aliasing effect on signals (fig. 4.3). Both can be tackled using the sampling theorem and an antialiasing filter, that when combined lead to accurate sampling (recording) of signals and allow the accurate calculation of signal's frequency content, are presented in 4.2.2 and 4.2.3.

4.2.2 Sampling Theorem

Let's study a seismic signal (continuous in the real time domain) that has its frequency content band limited within (-B) to (B) Hz (fig. 4.3a). This signal is the only one existing in the geology under study. Capturing the signal means recording it using a sampling rate (f_s). Sampling though leads to replications of the real frequency content of the recorded signal (due to $f_0=(f_0+kf_s)$ shown above) (Lyons, 2011). The chosen sampling rate (f_s) can fall into two categories; a) when $f_s<2B$ the created frequency replications will overlap with the real frequency content of the signal creating distortions (fig. 4.3b), b) when $f_s\geq 2B$ where the created frequency replications will be distinct (fig. 4.3c) (Lyons, 2011).

For this reason the sampling theorem states that in order to sample correctly a signal with no frequency content higher than (B) the sampling rate must be $f_s\geq 2B$ (Lyons, 2011).

a)

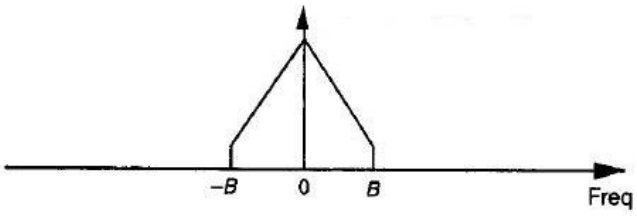

b)

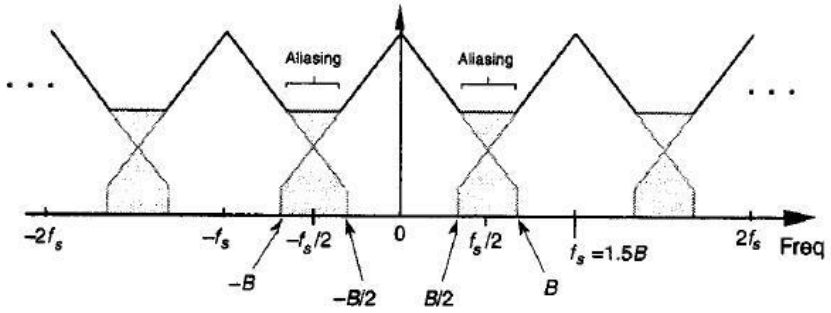

c)

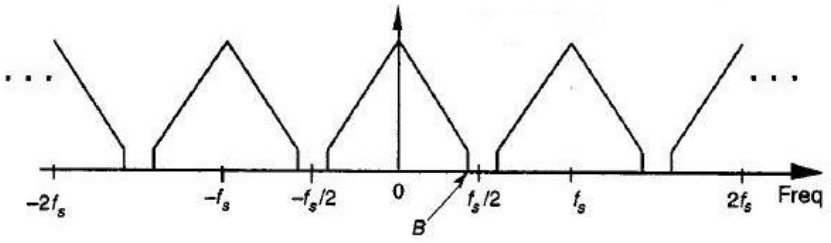

Figure 4.3: a) Real frequency content of a seismic signal existing alone in the geology under study, **b)** The analysed frequency content of signal sampled with $f_s<2B$, **c)** The analysed frequency content of signal sampled with $f_s \geq 2B$ (image after Lyons, 2011).

4.2.3 Antialiasing Filter

The second category ($f_s \geq 2B$) seems to provide better results but can be equally disturbing to the real signal as the first ($f_s<2B$). Let's study the case of having the same signal with band limited frequency content within (-*B*) to (*B*) Hz along with noise existing in the geology under study (fig. 4.4a). This scenario represents better a real monitoring case. The signal and noise is recorded with a sampling rate of $f_s \geq 2B$. The frequency content of the signal and noise at such cases have separate replications as in Figure 4.3c, that if combined lead to the result presented in Figure 4.4b: the frequency content of the real signal is contaminated with the frequency content of noise (Lyons, 2011). To avoid this phenomenon, an antialiasing filter is used in dataloggers when

recording data. An antialiasing filter is a low-pass filter deleting all frequencies above $f_s/2$ (Lyons, 2011).

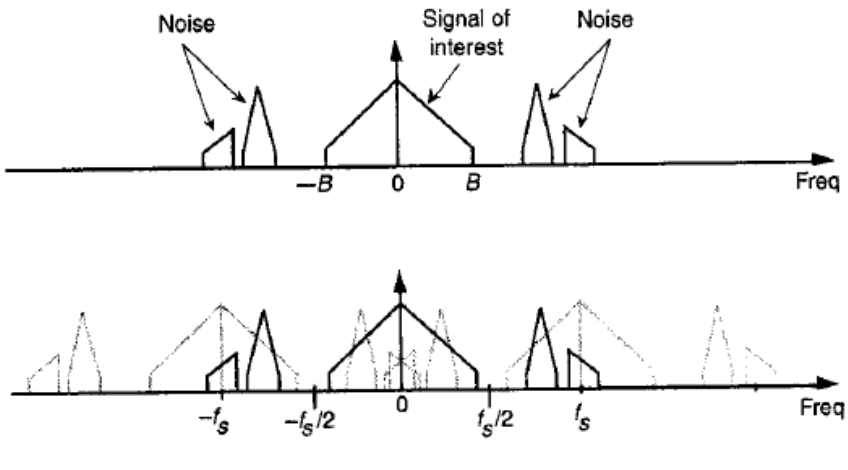

Figure 4.4: **a)** Real frequency content of a seismic signal existing along with noise in the geology under study, **b)** The analysed frequency content of the recorded signal and noise sampled with $f_s \geq 2B$ leading to the contamination of the signal's frequency content with noise (image after Lyons, 2011).

Following the sampling theorem, if a signal is sampled with a sampling rate that is double the upper limit of the signal's frequency content limit ($f_s \geq 2B$) then its frequency content can be resolved without distortions using an antialiasing filter. This means that the upper limit of the signal's frequency content should be known before recording. For this reason the sampling rate is always chosen to be higher than the doubled expected upper limit of the frequency content of the signal. Even if the chosen sampling rate is lower than the optimum one ($f_s/2 < B$), calculating the frequency spectrum of the recorded data will not result in distortions when an antialiasing filter is used (Lyons, 2011). The set back is that the calculated frequency spectrum of the collected data does not resolve the full frequency content of the recorded data (Lyons, 2011).

4.3 Window functions, Smearing and Spectral Leakage

In order to calculate the frequency spectrum of a sampled time signal it is assumed that the signal is periodic (Stoica & Moses, 2005). A periodic signal can be one that repeats itself endlessly over time or one that starts and ends from 0 at the beginning and end of the time window used to calculate the frequency spectra. Signals recorded with seismometers do not fulfil such requirements and some data manipulation and assumptions need to be made.

In order to calculate the frequency spectrum of a seismic signal, a time windowed signal is truncated from the recordings containing the full seismic signal under analysis assuming that it is periodic. This simple act of isolating a part of the seismogram from the rest of the seismic recordings means that we apply a rectangular window (Stoica & Moses, 2005). Its equation is defined below:

$$w_R(k) = \begin{cases} 1, \text{ when } k = 0, \ldots, (N-1) \\ 0, \text{ otherwise} \end{cases}$$

Or

$$W_R(\omega) = \frac{\sin\left[\left(N - \frac{1}{2}\right)\omega\right]}{\sin\left(\frac{\omega}{2}\right)}, \text{ with } \omega = 2\pi f,$$

where:

ω: angular frequency measured at rad/sec).

Using the second mathematical description, the rectangular window function can be visualized as shown in Figure 4.5.

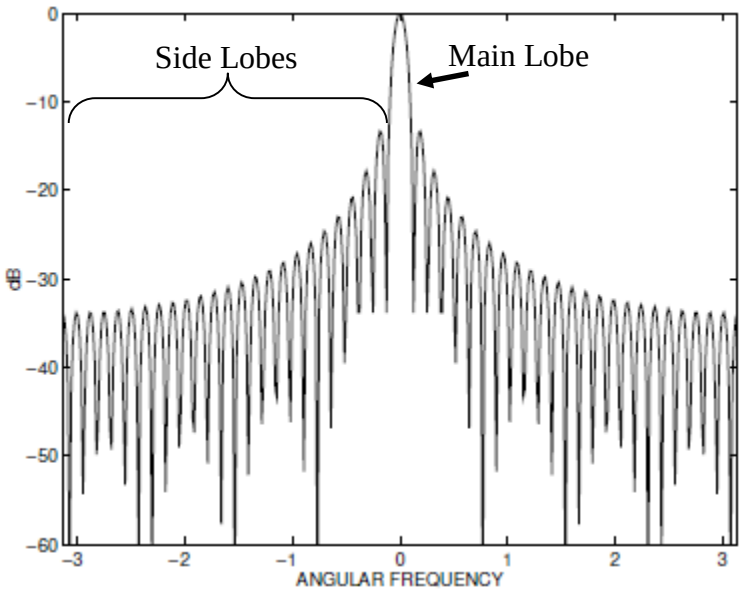

Figure 4.5: The rectangular window visualization when WR(ω)/WR(0) for 25 samples (N=25). Annotated is the main lobe and side lobe (image from Stoica & Moses, 2005).

Annotated in Figure 4.5 is the main lobe of the rectangular window. Similar representations exist for all window functions. The width of the main lobe is very import since it represents the frequency resolution of the window (Stoica & Moses, 2005). Frequencies spaced closer than the width of the main lobe cannot be resolved and are represented as one frequency. For example, if the frequency resolution of the window used is 1Hz then it will be impossible to resolve the spectral amplitude of frequencies 0.9Hz and 1.1Hz with their spectral amplitude added to the 1Hz frequency. This effect is known as smearing. The width of the main lobe is dependent only the number of samples a window function has (Stoica & Moses, 2005).

In addition to the main lobe, window functions have side lobes (fig. 4.5). These are artefacts of spectral energy transferred from the resolved frequency of the main lobe. This effect is called spectral leakage and it is the result of calculating the frequency spectrum of non-periodic signals. The effect of spectral leakage is easier understood using monochromatic signals, signals having energy contained within one frequency

only. Transforming monochromatic signals from the time domain to the frequency domain, more than one frequency will appear to have energy. The same effect takes place with each frequency of more complex (non-periodic) signals. This way the final frequency representation of a signal is distorted.

There are other window functions used in spectral analysis that reduce the first and last samples of the recorded signal to zero and allow for the final signal to be characterized as periodic, e.g. the Hamming window function used in this thesis for the power spectral density (PSD) and spectrogram calculation. These are more sophisticated windows that can be used to reduce the spectral leakage phenomenon. The mathematical description of the rectangular window and others along with their main characteristics of the main and side lobes is summarized below to allow comparison.

- The Rectangular window function (fig. 4.5) (Stoica & Moses, 2005)

$$w_R(k) = 1, \quad \text{for } k = 0,...,(M-1)$$

$$w_R(k) = 0, \quad \text{for } k > (M-1)$$

Approximate Main Lobe width (in Hz): $\frac{1}{\mathrm{M}}$

First Sidelobe level is 13dB lower than the main lobe. Note that dB is the ratio of two values of the same physical meaning (usually power) expressed at a logarithmic scale.

- The Hamming window function (fig. 4.6) (Stoica & Moses, 2005)

$$w_R(k) = 0.54 + 0.46\cos(\frac{\pi k}{M-1}), \quad \text{for } k = 0,...,(M-1)$$

$$w_R(k) = 0, \quad \text{for } k > (M-1)$$

Approximate Main Lobe width: $\frac{2}{\mathrm{M}}$

First Side Lobe level is 41dB lower than the main lobe.

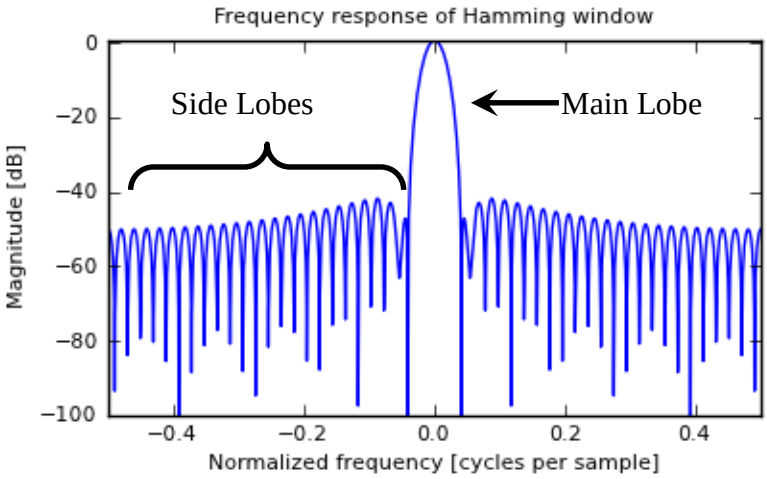

Figure 4.6: The Hamming window visualization when $W_R(\omega)/W_R(0)$ for 25 samples (N=25). Annotated is the main lobe and side lobes (image from Stoica & Moses, 2005). (image from https://docs.scipy.org/doc/numpy-1.6.0/reference/generated/numpy.hamming.html)

Despite the fact that the Hamming window function has a larger width for its main lobe compared to the Rectangular window function (2 times wider), its side lobe level is much lower (3.15 times lower) meaning that leakage of signals is minimized. Furthermore the Hamming window might have the same lobe width with other window functions, e.g. the Hanning and Bartlett window, but its side lobe is much lower than its main lobe thus reducing further the spectral leakage (Stoica & Moses, 2005). For the above reasons the Hamming window was chosen as a good compromise between frequency resolution, smearing effect and its ability to reduce the spectral leakage compared to other window functions for the analysis in this thesis. More information on windows and their characteristics can be found in (Harris, 1978, Stoica & Moses, 2005).

4.4 Spectral Analysis

The spectral analysis of a seismic signal is the understanding of its frequency content. Such analysis can be done in the frequency domain using techniques such as the Fast Fourier Transformation (FFT), Spectrograms or the Power Spectral Density (PSD). These techniques are all based on the FFT and are discussed below.

4.4.1 Spectral Analysis in the Frequency Domain

Fast Fourier Transformation (FFT)

Transformation of a time signal to its equivalent in the frequency domain takes place through the FFT. Figure 4.7 represents a sinusoidal wave in the time and frequency domain with the latter being calculated through Fourier analysis. More complex periodic signals though, can be formed using a series of sinusoidal waves (Kearey et.al, 2002). The combination of sinusoidal waves that can form the complex periodical signal under focus can be calculated with the Fourier analysis (Kearey et.al, 2002). The Fourier equations for a signal in the continuous and discrete time domain are given below respectively (Press et.al., 1992):

$$H(f_n) = \int_{-\infty}^{+\infty} h(t) e^{2\pi i f_n t}\, dt\,, \qquad H(n) = \sum_{k=0}^{N-1} h_k e^{2\pi i k n / N}$$

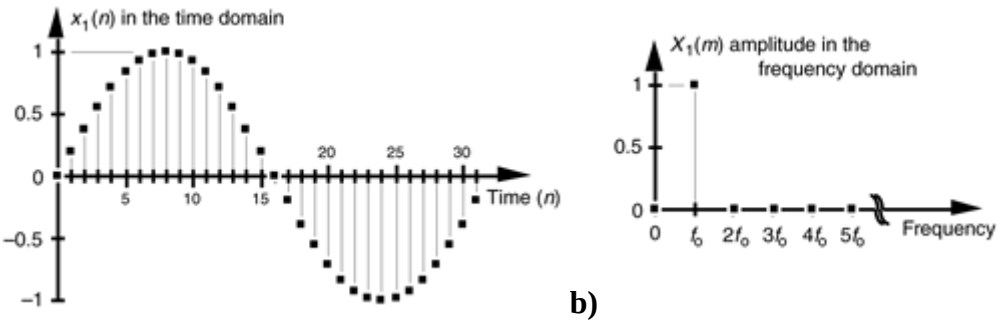

Figure 4.7: a) Sampled sinusoidal wave (discrete time domain), **b)** Representation of the sin wave in the frequency domain. (image from http://flylib.com/books/en/2.729.1.12/1/**)**

The FFT is an algorithm that can transform a signal sampled in the time domain to its equivalent representation in the frequency domain (fig. 4.8). Its difference from the Fourier equation is that it is less costly in computational memory when calculating a frequency spectrum (Press et.al., 1992).

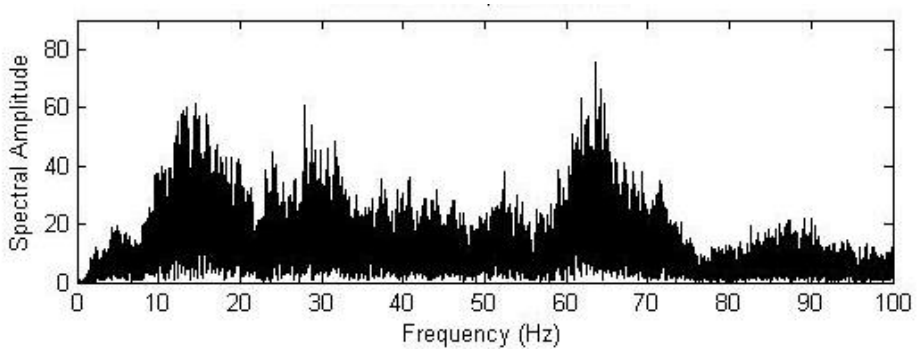

Figure 4.8: Fourier spectrum of a seismic event showing the spectral amplitude over frequency for seismic recordings of finite duration.

Computing the frequency spectrum of a signal using the FFT requires (1) the signal (x(n)), (2) the number of points in the FFT (NFFT) and (3) the sampling rate used to record the data. (1) The FFT is based on the Fourier transformation that can be used for periodical signals only. Seismic signals though do not fit that description. In order to overcome that problem it is assumed that the signal of n samples has a period of n samples. (2) The NFFT is the number of frequency "bins" used to calculate the spectral amplitude over. Since the representation of the signal in the frequency domain is discrete (as in the time domain), the x-axis representing frequency is divided into parts or bins. If the sampling rate of a signal is Fs then the x-axis from 0 Hz to Fs Hz is divided in (NFFT) bins. The useful frequency information of a signal sampled with Fs is up to Fs/2 (sampling theorem) and so the x-axis at a FFT plot would be from 0 Hz to Fs/2 and would be divided into NFFT/2 bins starting from N=0 to N=NFFT/2-1 (Press et.al., 1992). If the NFFT is larger than the signal's samples (NFFT>n) then the

signal is padded with zeroes from x(n+1) to x(NFFT) to allow computation of the frequency spectrum. Finally, if NFFT is a power of 2 then computations are much simpler and faster (Press et.al., 1992). (3) The sampling frequency as said above is used to define the limit of the x-axis and avoid aliasing.

The FFT analysis is applied on a signal of finite length, meaning that it is truncated from the rest of the recordings. This procedure implies that a window function called rectangular window is applied to the seismogram. More information regarding window functions were given at section 4.3.

Power Spectral Density

The PSD, like the FFT, can be used for revealing the frequency pattern of a signal (fig. 4.9) (Vaseghi, 2000). In other words, the power spectrum of a seismic signal is the calculation of its power over its frequency content (fig. 4.9) (Stoica & Moses, 2005). In this thesis the Welch method was used for the calculation of the PSD of signal because it involves fewer computations than other methods and so facilitates a more efficient analysis (Welch, 1967).

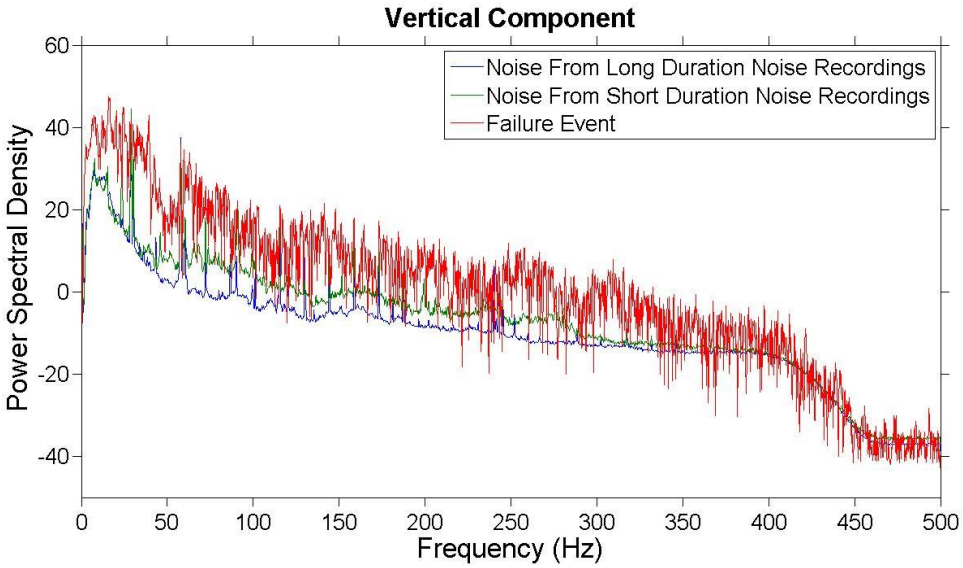

Figure 4.9: Power Spectral Density plot of a falling block of soil recorded by the vertical component of a seismometer at source-to-sensor distance of ~10m.

The method needs as input a sampled signal (X(j)) in the time domain. The signal is divided into K time segments of equal length (e.g. $X_1(j)$ with j=0, …, L-1, $X_2(j)$ with j=L, …, 2L-1 and so on). These segments can overlap. Each one of these segments is multiplied by a window function of equal length (W(j) with j=0, …, L-1) creating K such products ($X_K(j)W(j)$), (Welch, 1967). The window function used for the implementation of the Welch method in this thesis was the Hamming window (section 4.3). For each product of this multiplication process a FFT is calculated,

$$A_K(n) = \frac{1}{L}\sum_{j=0}^{L-1} X_K(j)W(j)e^{-2kijn/L} \text{ , where } i = \sqrt{-1}\,.$$

These amplitude spectra undergo the modification shown below in order to calculate their PSD (Welch, 1967):

$$I_k(f_n) = \frac{L}{U}\left|A_K(n)\right|^2,\ U = \frac{1}{L}\sum_{j=0}^{L-1} W^2(j)\,.$$

The final PSD estimation is given by the average of all the $I_K(f_n)$ (Welch, 1967):

$$\hat{p}(f_n) = \frac{1}{K}\sum_{k=1}^{K} I_k(f_n)\,.$$

4.4.2 Analysis in the Time/Frequency Domain

When analysing a signal in the frequency domain, all information in the time domain is lost. Analysis in the time/frequency domain overcomes this problem. This analysis is the representation of the frequency spectrum of a signal sampled in the time domain. Such representation is possible through the spectrogram. Spectrograms are 3D plots with the x-axis representing the frequency content of the signal, the y-axis representing time and the z-axis representing the spectral amplitude the recorded signal has over its frequency content (fig. 4.10). The third axis is usually colour scaled (fig. 4.10). The calculation of a spectrogram is based on the FFT transformation.

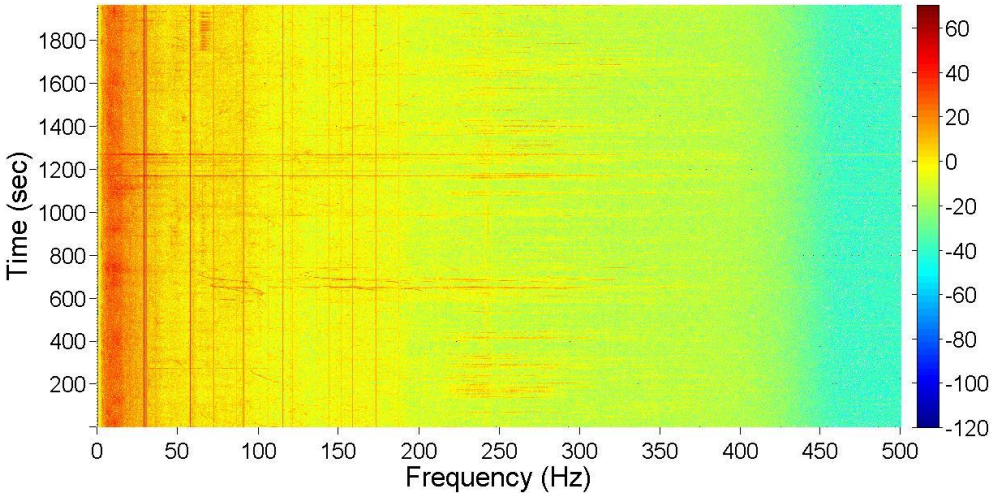

Figure 4.10: Sample Spectrogram of landslide recordings.

To begin with the calculation of a spectrogram, a seismogram is needed as an input signal. This seismogram is truncated into windows (time segments) using a window function. These windows can overlap in order to have each seismic pulse fully enclosed by a window at least once. With overlapping the possibility of a seismic pulse being divided into parts among consecutive windows is reduced (when no overlapping applies). Finally the FFT is calculated for each truncated window. The calculated FFTs are plotted parallel along the y-axis with their spectral amplitude shown in the z-axis colour scaled (fig. 4.10).

4.5 Spectral Analysis: application in this thesis

This section focuses on the effect of the input parameters used for the spectrogram and PSD calculation when applied for monitoring landslides. Artificial signals as well as recorded signals from field experiments are used in these examples. Data analysis in the frequency domain is conducted with the same parameters as chosen below to allow comparison among the different experiments.

4.5.1 Analysis in the frequency domain

The PSD calculation requires as input data the seismogram under analysis, the length of the window function, the overlapping of the windows, the NFFT length and finally the sampling rate of the signal. As mentioned previously, in this thesis the Welch method (Welch, 1967) is used to calculate the PSD curves of different signals.

When calculating the PSD of a signal the whole isolated seismogram is used to finally produce one curve that reveals the frequency characteristics of the data. For this reason, the isolated seismograms ideally contain only the seismic pulse under analysis. The length of the isolated seismogram has to be small enough to contain only the pulse under investigation and large enough to allow good frequency resolution. It is not always possible to isolate seismic pulses to calculate their PSD either because their true starting and ending point are lost in the background noise or/and because their small time duration will lead to poor accuracy in the frequency domain. This is why background noise recordings are sometimes included before and after the seismic pulse under investigation.

Since frequency resolution is the most important parameter in plotting PSD curves, the length of the window function is determined first. From the theory presented at section 4.3 the length of the window function is chosen to be 4048 samples (~4sec). This allows for a very good frequency resolution. In addition, it is found that all recorded seismic pulses are smaller than this length meaning that the window would not trim them.

The length of the isolated seismogram can be as long as the length of the window function. Optimum case scenario for the PSD calculation would be for the seismic pulse under investigation to be at the centre of the isolated seismogram to avoid any edge effects of the window function. It is a very time consuming process to trim the seismogram in windows having the pulse under investigation in their middle and difficult when the true first onset of the signal cannot be determined accurately. For this reason the isolated seismogram is chosen to be slightly larger than the optimum length of the window function. The overlapping of the windows is chosen to be set at

99% meaning that windows move along the trimmed signal every one sample. With this overlapping, the window function can start from the beginning of the trimmed seismogram and scan it till the end. This way the frequency content will still be determined with the wanted accuracy for each window and having at least one of the overlapping windows embracing the seismic pulse under investigation at their centre.

For example, there is a signal with 1000 samples and the length of the window used is 100 samples. The first window will start from Sample No1 till sample No100 of the signal, the second from Sample No2 till sample No101 and so on. The PSD will be calculated for each window separately and averaged in the end to produce the final PSD plot. The seismic pulse is present in all windows since it is almost centred to the total length of the trimmed signal with background noise before its true onset and after its end. For one window though it is perfectly centred. Any effects due to trimming the seismogram are averaged during the calculation process.

The NFFT is chosen to be equal to the length of the window function (see section 4.4). Finally the sampling rate is chosen during acquisition to be equal to 1000Hz.

Taking into account all the above the final parameters chosen for the spectrogram calculation are:

- Sampling Rate: 1000Hz
- Signal length > 4100 samples (~4sec)
- Window Length: 4096 samples (~4sec)
- Window overlap: 4095 samples (99% or every 1 sample)
- NFFT: 4096 samples

During two experiments the same source mechanism was recreated multiple times. It was necessary to account for all recorded pulses in order to find the spectral characteristics of this source. The PSD analysis conducted at those signals involved the same parameters presented above. The initial isolation of the seismogram under analysis was more complicated though.

If the recordings contain multiple signals of the same type, the isolated seismogram under analysis can contain more than one seismic pulse when calculating the PSD. The seismic pulses have to share similar signal characteristics. In such cases, PSD comparison of different PSD curves has to be made carefully. Firstly the background noise recorded by the signals under comparison must have the same characteristics. The characteristics of background noise can be identified through noise analysis (calculating PSD for only noise recordings). Secondly, the ratio between noise and seismic pulses in terms of time duration must be similar among the compared signals. The latter is because the final PSD curve is the average product of the PSD calculation of all overlapping window functions.

To understand the above concept better consider the following example. Two trimmed signals have the same type of pulses (a sinusoidal wave) with Signal1 having 3 pulses and Signal2 6 pulses (fig. 4.11). Both signals have exactly the same type of background noise (artificial random noise) recorded for the same time duration before and after the pulses were recorded (fig. 4.11). Calculation of the PSD curves of both signals takes place with the same window type, window length and overlapping parameter. The power displayed over the frequency content of the pulse for Signal2 will be twice as large as for Signal1. The final PSD plots for both signals is presented in Figure 4.12. The difference between the curves though does not seem to be large. This is because on the final step of plotting a PSD curve the y-axis is at a logarithmic scale. Figure 4.13 shows the same curves as in Figure 4.12 without though the y-axis being at a logarithmic scale. The effect of having more pulses in Signal2 than in Signal1 in the calculations is now clear. The PSD of Signal2 is slightly larger than double the PSD of Signal1 due to the background noise having different length (the three additional sin waves of Signal2 contain background noise).

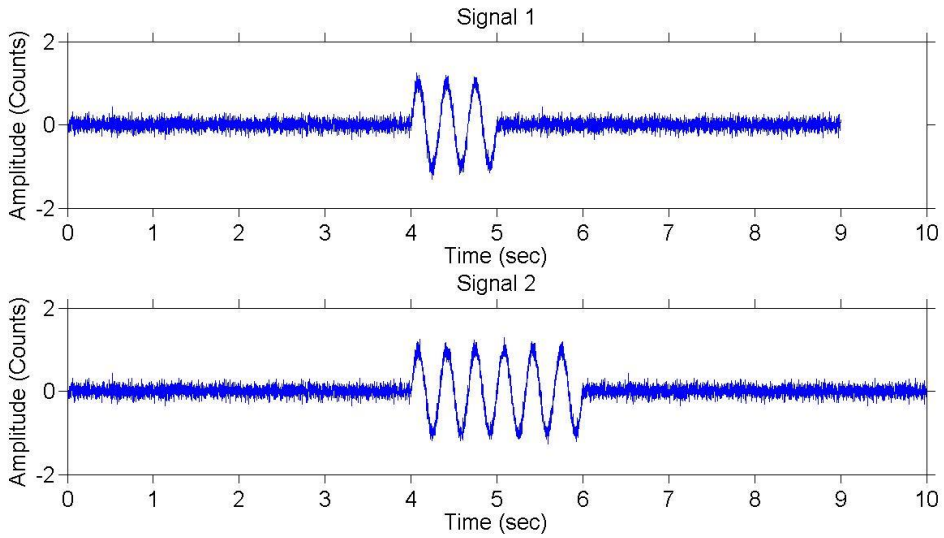

Figure 4.11: Seismograms of 2 Signals containing the same sinusoidal wave. Artificial random noise was added to both seismograms, with noise having the same time duration before and after the pulses in both signals. The only difference between the two is that Signal1 contains 3 pulses of the sinusoidal wave, while Signal2 contains 6 pulses.

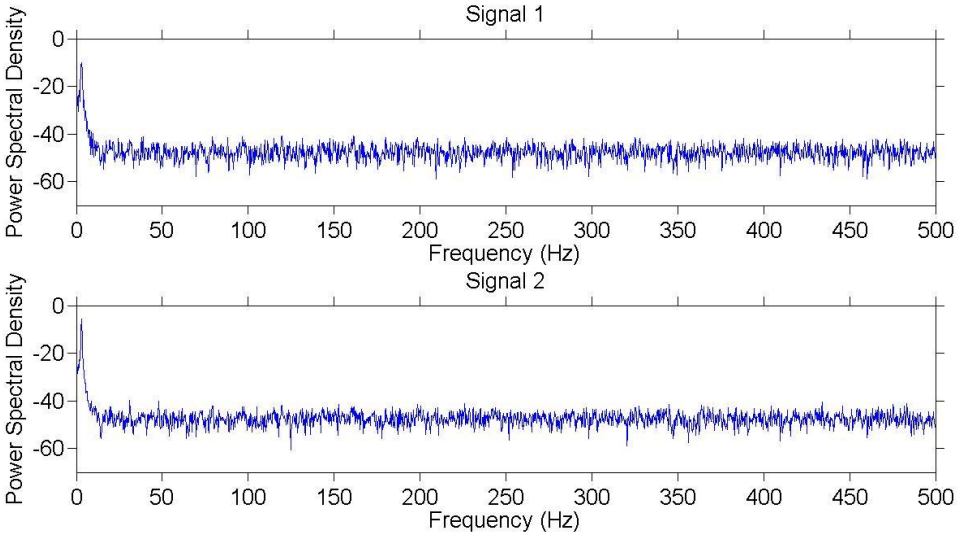

Figure 4.12: Plots of power spectral density for both seismograms. The difference between the signals in the y axis is very small. This is because the y axis is in logarithmic scale.

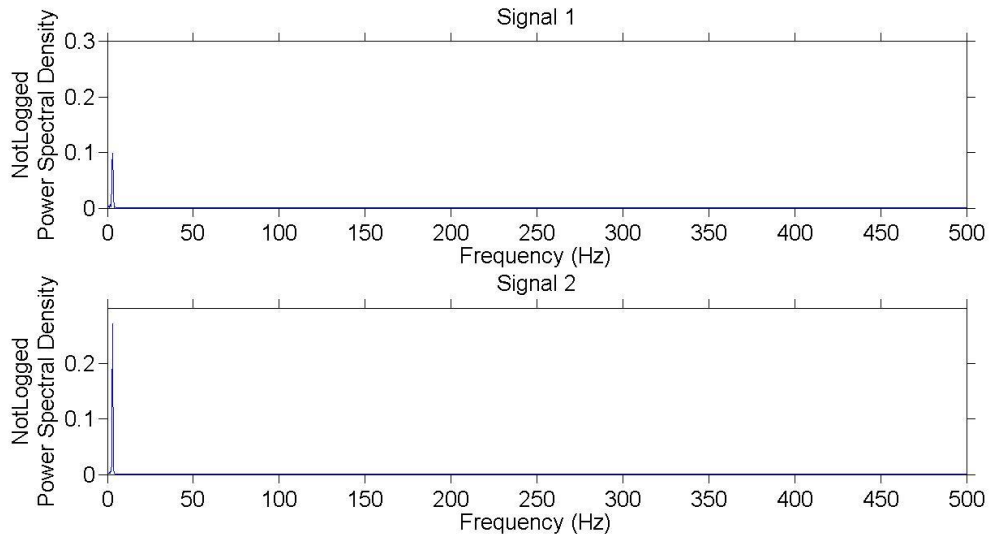

Figure 4.13: Plots of power spectral density for both seismograms without having the logarithmic scale in the y axis. The effect of having double the sinusoidal pulses in Signal2 on the calculations is now clear. The PSD of Signal2 is slightly larger than double the PSD of Signal1 due to the background noise different length of the background noise.

Figure 4.14 shows two signals with Signal1 having recordings of random noise 8sec in total with 3 sinusoidal pulses and Signal3 having 16sec of random noise recordings in total with 6 sinusoidal pulses. Signal 1 and Signal2 have the same ratio between seismic pulses and background noise recordings in terms of time duration. The PSD curves of both pulses, with the y-axes not logged, can be seen in Figure 4.15. It can be seen that PSD curves of both signals are similar. Their small difference lies in the fact that noise in both signals is random and not exactly the same. This means two signals having a similar noise-to-signal ratio can be directly compared.

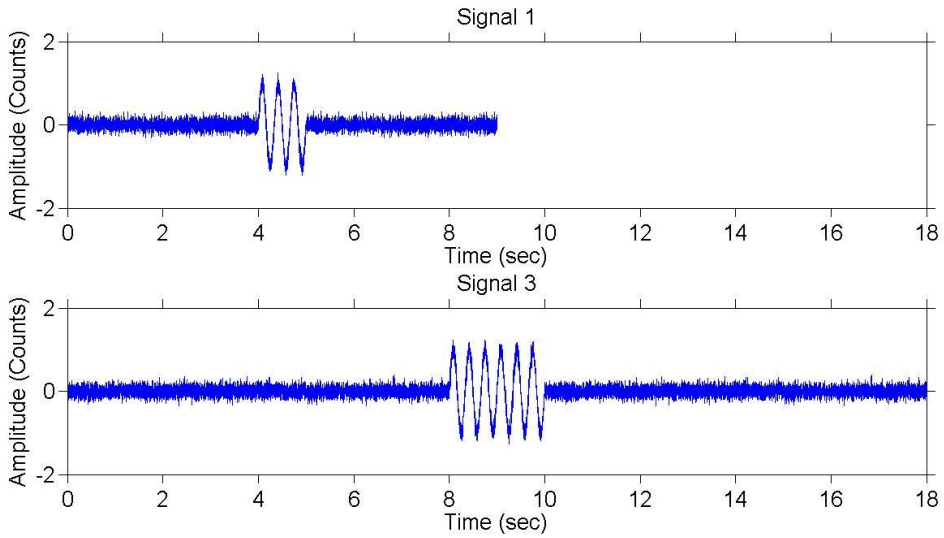

Figure 4.14 Seismogram of Signal1 with 8sec in total of background noise recordings and 3 sinusoidal pulses and Signal2 with 16sec in total of background noise recordings and 6 sinusoidal pulses. Signal1 and Signal3 have the same ratio between pulses and noise in terms of duration.

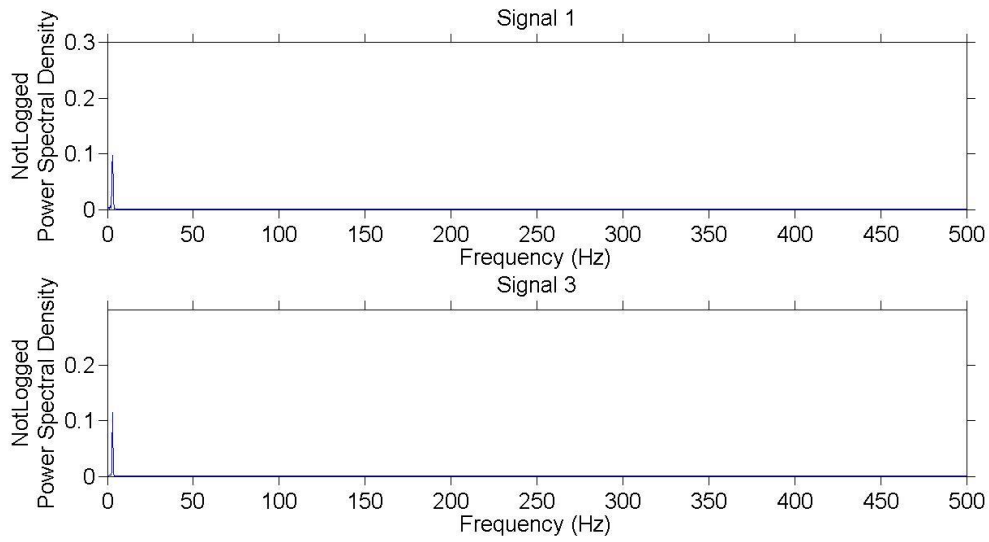

Figure 4.15: PSD curves of Signal1 and Signal3 that have the same ratio between pulses and noise in terms of duration. Curves are almost identical with the small difference in the fact that background in both signals is random and not exactly the same.

For real life seismograms containing multiple seismic pulses of the same type that their spectral characteristic need to be compared with others, must share similar noise to signal time duration ratio. The time duration of noise and signal can be calculated following the next steps:

1) Record pure background noise for a long period of time that is able of characterising the noise conditions during the monitoring period.

2) Find the amplitude threshold in the recorded seismogram above which only noise bursts exist among the recordings of Step 1. This can be done by using statistical analysis with a 97% tolerance, meaning that the amplitude threshold should be such that 97% of the noise samples have amplitude smaller than the threshold.

3) Know that the isolated seismograms under comparison share the same noise characteristics with the background noise used at Step1.

4) Use the threshold calculated in Step 2 in the trimmed signal. Samples below the threshold amplitude can be characterized as noise, samples above the noise threshold can be characterized as signal.

5) Divide the number of samples of noise to the number of samples of signal and find the ratio. This procedure should be followed for all trimmed signals that are going to be compared. If the ratio explained above is not the same among the trimmed signals, by additional trimming their ratio between noise and signal can change in order to be similar to the rest. Great care must be given during trimming the pulses in order for them to stay whole, so their frequency characteristics to be calculated correctly.

4.5.2 Analysis in the time-frequency domain

In summary, the calculation of a spectrogram needs the seismogram under analysis, the length of the window function, the overlapping of the windows, the NFFT length and finally the sampling rate of the signal.

To begin with, the seismogram under analysis can be of any length. In this thesis the length of the input seismograms if as long as the continuous recordings obtained during the experiments. In some cases smaller lengths were used in order to visualize an event better and achieve a “zoom in” effect.

The length of the window used has to be chosen next. As it was presented in section 4.3 this parameter affects the frequency resolution (width of the main lobe). To understand how the length of the window affects the calculated frequencies an example is given. Figure 4.16a is a spectrogram of landslide data recorded at 1000Hz (sampling rate) with a window length of 4096 samples (~4sec long). Figure 4.16b is a spectrogram using the same dataset and parameters as Figure 4.16a, only with a window length of 1024 samples (~1sec long). It can be seen that frequency resolution in the first spectrogram (fig. 4.16a) is better than the second (fig. 4.16b). This is easier to distinguish by comparing the monochromatic frequencies that remain constant through time (annotated in both spectrograms by black arrows). In Figure 4.16a they are presented to have thinner frequency content because frequency resolution is high compared to Figure 4.16b. Colour scale in both spectrograms was the same. Note that the window length could not be larger than the length of the total length of the signal under analysis.

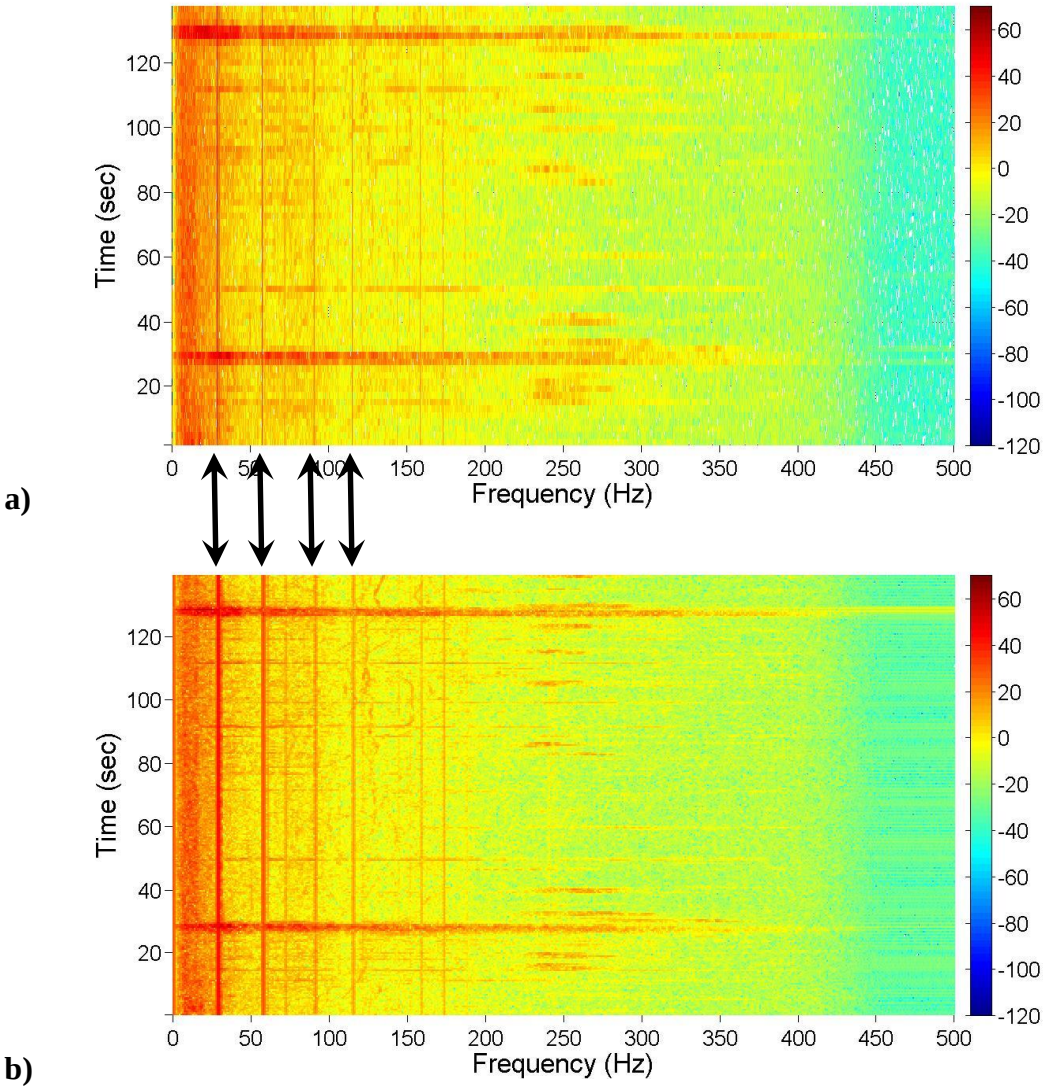

Figure 4.16: Spectrograms of landslide data recorded at 1000Hz (sampling rate) and a 50% overlap. The window length was **a)** 4096 samples (~4sec long) and **b)**. 1024 samples (~1sec long). Frequency resolution is higher at the spectrogram (a) compared to (b). This can be seen from the monochromatic frequencies annotated by the black arrows that remain constant in time. Their frequency content is visualized to be much thinner in spectrogram (a) than in (b).

Once the time length of the window function is chosen, the user has to decide about the window overlapping. In nature seismic pulses are not emitted following a certain time pattern but are distributed unevenly in time. This means that if the seismogram is

divided into windows, it is high likely that some pulses are going to be trimmed and divided among two or more consecutive windows (fig. 4.17a). The latter is against the need for having signals inside a time window, so their frequency content can be calculated accurately though the FFT transformation. For this reason windows are preferred to overlap. This is because even if a signal is trimmed in one window it will be fully enclosed from the next one (fig. 4.17b).

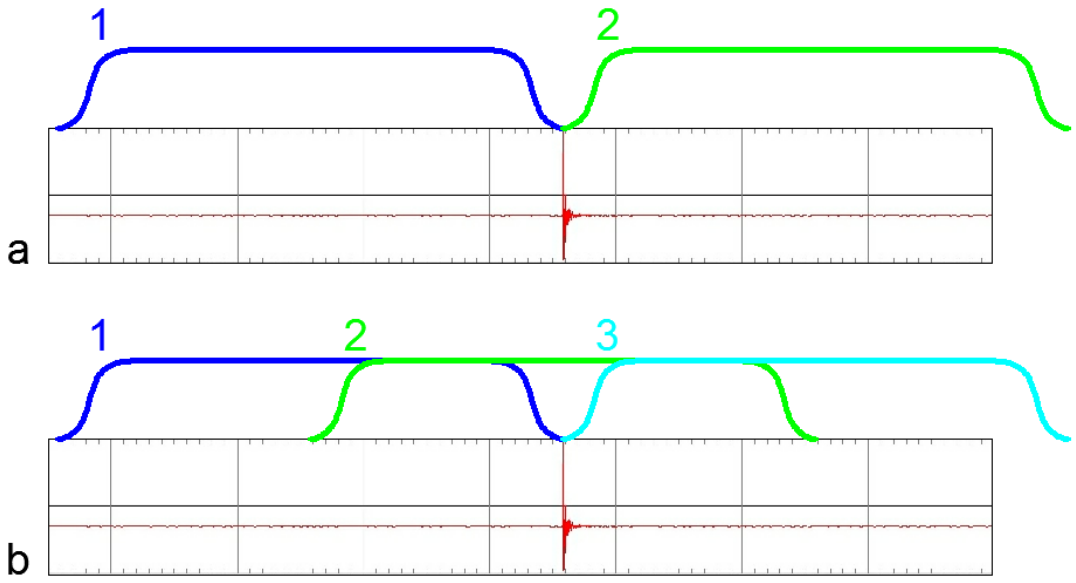

Figure 4.17: Seismic traces (a)&(b) are the same seismic recordings of a hammer hit. In trace (a) a window function 4sec long has been applied with 0% overlapping. This results resulted in trimming the seismic pulse in two segments. In trace (b) the same 4sec window function has been applied but having 50% overlapping. The first window trims the signal, but the second window fully encloses the pulse.

Typical overlapping values ranges between 25% to 50% (Smith, 2007). Overlapping needs to be large enough, allowing signals to be placed at least once intact inside a window but small enough to allow time representation of the events in the final spectrogram to be realistic. Let's say that one chooses an overlapping of 99%. This will ensure that signals are enclosed at least once intact inside windows. The later, along with the fact that the time length of windows are chosen to be larger than the

expected seismic signals, will lead to signals being included in many windows, both intact and trimmed. This means that their spectral energy will be present either in full or partly within all of these windows. Since each window occupies a certain time segment along the time axis, the time scale of the event will be stretched and presented longer in duration than it actually is. In recordings with sequences of distinct pulses closely spaced in time, e.g. at a debris flow, this smoothed effect can lead to visualizing pulses as one long event.

Finally the last parameter the user has to choose is the NFFT (length of the FFT) that controls the number of bins the frequency axis is divided to, thus the frequency resolution (see section 4.3). If the NFFT is larger than the window length, the isolated data segment will be padded with zeroes to the point the patched window and the NFFT are equal in length. This though adds to the mathematical manipulation of data and so NFFT is chosen to be equal to the window length. For this reason the window length is chosen according to the specifications presented above and in order to allow for a good frequency resolution.

In summary the length (duration) of the window function needs to be able to enclose the seismic pulses under investigation, small enough to contain optimally only one pulse at a time and finally large enough to produce the desired frequency resolution.

The sampling rate was set at 1000Hz. This is done to allow spectral estimation up to 500Hz based on the sampling theorem. The seismometers used are short period with a flat frequency response between 2Hz to 100Hz. This means that energy at frequencies higher than 100Hz will be recorded with different amplification (smaller) compared to frequencies below 100Hz (with lower sensitivity resulting at recording them with a smaller amplitude compared to their true one) since the instrumentation response is not flat. For this reason, quantitative comparison of energy between frequencies 200Hz and 300Hz or 200Hz and 50Hz for example cannot be made. However, having information above 100Hz validates whether or not high frequency seismicity exists, allowing to conclude at the optimum seismometer type for future measurements.

Taking into account all the above, the final parameters chosen for the spectrogram calculation are:

- Sampling Rate: 1000Hz
- Signal length > 10,000 samples (>10sec)
- Window Length: 4096 samples (~4sec)
- Window overlap: 2048 samples (50% or every ~2sec)
- NFFT: 4096 samples

4.6 Summary

The optimum methodology of recording signals was presented, along with the Fourier transformation. Using this knowledge, signal analysis in the time-frequency and the frequency domain was presented. Finally explanation of how these techniques were used for analysing the recorded experimental data, along with simple examples was given.

Chapter 5

Optimizing of the microseismic monitoring system

5.1 Introduction:

The aim of this chapter is to investigate how to best deploy short period seismometers in order to deploy a microseismic monitoring network able to achieve the optimal location precision for small microseismic events that could be precursors to a major landslide. Within the frame of seismology, tectonic earthquakes happen at several kilometres depth, therefore acceptable location errors can range up to a few kilometres. For engineering purposes, the location error should be a few meters or less.

As discussed in Chapter 2 the type of seismometers used, their deployment geometry and the representation of the geology of the area under investigation are factors that affect the detection and location capability of the monitoring system.

One of the main characteristics of soil deformation/displacement is that as a seismic source the total emitted energy of the seismic source is relatively small when compared to similar events in rocks for example. This is due both to the non-brittle behaviour of soils and their highly attenuating nature. In this chapter I investigate the optimum deployment of small surface microseismic arrays in order to acquire accurate locations for weak sources typical of landslides in sediments. Furthermore, the effect that different geological formations and geotechnical parameters have on the velocity model used for seismic location analysis is studied. In order to provide answers to the above a series of experiments was designed and carried out.

5.2 Experimental Set-Up:

Microseismic monitoring as an investigation tool for landslide monitoring has to combine high location accuracy of the recorded events along with low cost and easy sensor deployment. The location problem has four unknowns; the spatial coordinate (x, y, z) and the origin time of the event (see Chapter 3). For this reason the chosen microseismic array type consists of four seismic sensors deployed on the surface.

Three parameters are investigated: location accuracy, deployment geometry and source-to-sensor distance. The experiments took place in Natal between 3/10/2011 to 16/11/2011, during my time as a Marie Curie fellow in the framework of the IRSES project Geo-Excel (PIRSES-GA-2008-230860).

5.2.1 Components of the experimental set-up

1. Two surface microseismic arrays, each consisting of 3 1D and 1 3D short period seismometers (Lennartz). All sensors have a flat response between 1Hz and 100Hz.
2. Each array is connected to a datalogger set to record at 2000Hz sampling rate continuously. Seismic data of the sensors were synchronized by GPS clocks. Data loggers and GPS clocks were manufactured by DMT.
3. As a power source for the data loggers and seismometers, two common 40Amp, 12Volt car batteries were used.
4. Hand held GPS for the determination of the sensors location.
5. 2 different types of explosives (firecrackers) differing in size (fig. 5.4a) having ~1g and ~7-9g of explosive powder (g: gram).
6. A metallic cover used to cover the explosives and ensure the presence of oxygen needed to ignite the explosive's fuse (fig. 5.4d).
7. Copper cables and a car battery used to ignite the explosives.

5.2.2 Description of Experimental Set-Up

The two seismic arrays were deployed approximately 20 km South from Natal (NE Brazil), (fig. 5.1) on a site consisting of a sand and clay layer, 69m thick (top layer). The sand and clay mix is a highly attenuating material. Below the top layer lies a limestone layer 500m thick over bedrock (personal communication with prof. A.F.Nascimento). The nanoseismic equilateral triangle geometry was used (Walter et.al., 2011): The 3D sensors were placed at the triangle's centroid while the 1D sensors were placed at the vertices at radial distances 25m (1^{rst} array size (aperture) = 25m) and 50m (2^{nd} array size (aperture) = 50m) from the 3D sensors (fig. 5.2). The

equilateral triangle geometry was chosen to provide good azimuthal coverage of the surrounding area. Placing the 3D sensor in the middle of the array assured the same probability of recording the horizontal components of any seismic source without focusing in a specific part of the study area. All sensors were buried at approximately 50cm below ground surface to enhance their coupling with the surrounding soil and decrease the effect of ambient noise (fig. 5.3).

Explosions were triggered at 20, 40, 60, 80, 100, 150 and 200m away from the 3D sensors (fig. 5.2). Two types of explosives were used at each position, a weak one and a strong one (fig. 5.4a) bringing the total number of explosions to 7x2 = 14. In order to trigger the explosives, their fuse was connected to two copper cables using tape (fig. 5.4b, 5.4c). Each cable was then connected to one pole of a car battery with the electrical current lighting the fuse. For better coupling, the explosives were buried at a depth of ~30cm. In order to provide enough oxygen for the fuse to light at that depth, the explosives were covered with a metallic case before they were covered with soil (fig. 5.4d, 5.4e). The time interval between explosions was approximately ~30min. The locations of all sensors and explosions were a priori determined using a hand held GPS with an accuracy of ±5m. These locations were later used as reference for the locations obtained from the analysis.

The experimental site was more than 500m away from a busy road, with a few houses spread in the general area. These conditions made it a lucrative site in terms of background noise conditions. For this reason it was not necessary to work during night and all experimental measurements took place during the morning and afternoon.

The use of weak explosions as a source mechanism to study landslides is only helpful in the characteristic of emitting small seismic energy as expected from landslide failure events. This characteristic allows the study of attenuation and difficulties involved the signal detection and location analysis. Other than that explosions emit their seismic energy in a spherical manner, while in landslide failures events are expected to involve shear.

Figure 5.1: Experimental site 20 km South from Natal (NE Brazil). The site geology consists of a top layer of sand and clay, 69m thick, followed by a limestone layer 500m thick over bedrock is reached.

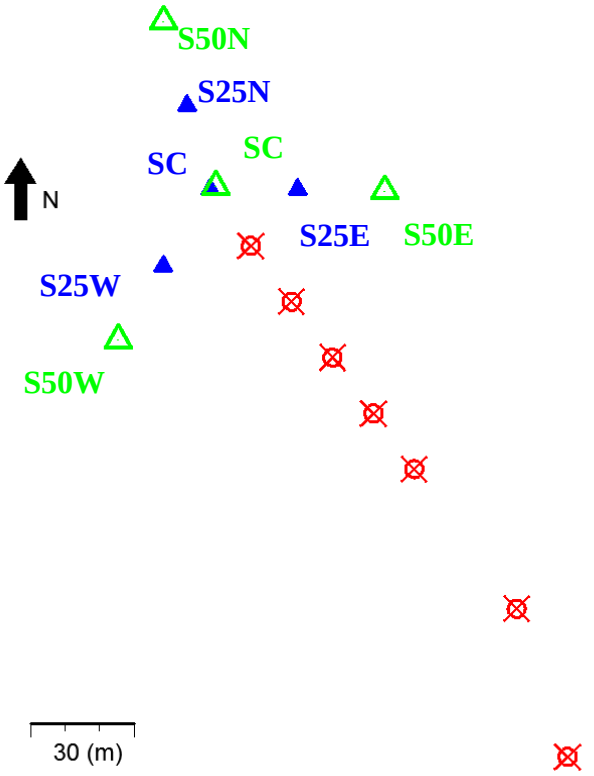

Figure 5.2: Plan view of the location of sensors and explosions. Blue Solid Triangles: microseismic array 1 (25m aperture size), Green Triangles: microseismic array 2 (50m aperture size), Red Targets: location of explosions. The 3D sensors of both arrays were placed next to each other at the triangles' centroid.

Figure 5.3: All seismometers were placed into ~50cm deep holes and were then covered with soil. This was done to increase their coupling with the surrounding soil and decrease the effect of ambient noise.

Figure 5.4: a) Explosives used during the experimental measurements. **b)** The fuse of the explosives was connected to two copper cables. **c)** The fuse and cables were taped together. **d)** The explosives were then placed inside a ~30cm deep hole and covered with a metallic case that trapped oxygen enough for lighting the fuse. **e)** The explosive and metallic case were covered with soil, with only the copper cables emerging in the surface. The cables were connected to a car battery (not shown in the figure), with the electrical current lighting the fuse.

5.2.3 Experimental Procedure:

Step 1:

Prior to each explosion, all people on site kept their positions without moving for one minute. This was done to record background noise avoiding any local noise bursts from footsteps and for making the explosion easier to distinguish in the seismic recordings.

Step 2:

The explosion was triggered with people standing still at their positions.

Step 3:

After the explosion, another minute of background noise was recorded. To ensure that the full seismic coda of the explosion was recorded without being contaminated by any movement on the site.

Step 4:

Two explosions were triggered at each location using both types of explosives. After step 3, steps 1 to 3 were repeated for the total number of explosions.

5.3 Collected Data

The seismometers were set to record data continuously. Six 1D seismograms and two 3D seismograms were produced in total from both arrays. Seismograms included all explosions and noise measurements. The seismograms were stored digitally as counts versus time, with counts being a measure of electricity (see Chapter 3) and time recorded in milliseconds. The total length of the recordings was 10 hours, with data stored in SEG2 file format requiring 1.23GB of storage space.

Detailed field notes were kept during all experimental processes. The starting and ending time of all experimental measurements, as well as the time of all explosions were noted. Time was recorded using a hand held GPS clock to ensure synchronization with seismic recordings.

5.4 Preliminary Data Analysis:

Classic seismic location procedures are based on P and S wave arrivals as discussed in Chapter 3. Seismic signals recorded at slopes have been observed to have onset times of S-waves either overlap with the P-wave coda or are hard to pick (Spillman et.al, 2007, Helmstetter and Garambois, 2010). For the needs of this location analysis only P-waves were used.

Preliminary analysis included identification of all explosions in the seismic recordings (fig. 5.5) based on the field notes. All location analysis was conducted using the "Hypoline" software (Joswig, 2008). Both the hyperbolae and the master event method (see Chapter 3) were applied. The latter was used to locate the explosions as a more accurate location technique. "Comsol Multiphysics" version 4.3 was then used to numerically simulate the experiment.

Figure 5.5: Seismogram of a large explosion recorded 50m away from a 1D sensor.

5.5 Main Analysis

5.5.1 Step 1: Preliminary P-wave velocity model for the site

The location analysis is based on P-wave arrival times. For the development of a seismic velocity model only the signals produced by the large explosives were used. This was done because they would produce clearer P-wave arrivals thus avoiding errors in phase picking.

The first 69m of the surface geology consisted of the same material, thus a half-space, single layered, isotropic velocity model could be assumed adequate. This is common practice in seismic studies. Modelling the P-wave velocities at larger depths was

considered not necessary based on a refraction seismics rule of thumb where the penetration depth of seismic waves is 1/3 to 1/5 of the distance between the seismic source used and the sensor recording (SafeLand, 2010). To be on the safe side P-wave velocities were modelled for at least the first top 50m of the geology. The influence of deeper layers though was found to have little impact on the location results.

The geology of the site was known but no seismic velocity values were available. The locations of the explosions were a priori known from GPS measurements. A single P-wave velocity (Vp) was chosen by picking the P-wave arrivals of one explosion at a time. By changing the value of the P-wave velocity, the hyperbola location in "Hypoline" result was biased to be close to the one measured. Hypocentre location was fixed using the GPS measured explosion position and the velocity was changed until the P-wave theoretical arrival times matched the picked ones. The Vp value that produced a location solution closer to the measured one through this "trial and error" procedure was chosen as the optimum velocity characterising the local geology.

As can be seen in Table 5.1, the Vp calculation led to a different P-wave velocities for different explosion events and array sizes. The first P-wave arrivals of explosions with distances larger than 80m away from the 3D sensors were not clearly recorded by all array sensors due to signal attenuation. These events could not be used for Vp estimation and this is why they are not presented in Table 5.1. Furthermore, none of the estimated Vp values could be used to minimise the differences between theoretical and manually picked P-wave onset times at all four stations of the array. These two findings suggest that the initial assumption that a single P-wave velocity model would not be adequate for this site.

Source-to-3D Sensor Distance (m)						
20	**40**	**60**	**80**	**100**	**150**	**200**
Estimated Vp (m/sec) for Array 1 using all Explosion Data						
750	850	1000	1600	-	-	-
Estimated Vp (m/sec) for Array 2 using all Explosion Data						
850	950	1100	1600	-	-	-

Table 5.1: Estimated P-wave velocities using each big explosion recordings separately. The P-wave arrival times of last 3 explosions were not recorded clearly so no velocity estimation could be made.

5.5.2 Step 2: Locations of small explosions using the Vp values determined in Step1

The representation of the site's geology by a single P-wave velocity was found to be inadequate in Step 1. Despite this, a location analysis was conducted implementing the hyperbola method for the small explosion data set using a single layer velocity model with the single P-wave velocities presented in Table 5.1. For each small explosion when located by each of the two arrays separately, a different Vp value was used (a different half spaced single layer velocity model). For example, the small explosion made 20m away from the 3D sensor was located using Array 1 & 2 separately, implementing a single P-wave velocity model of 750m/sec when Array 1 was used and a single P-wave velocity model of 850m/sec for Array 2. For the small explosion triggered 40m away from the 3D sensors the Vp value was set to 850m/sec when Array 1 was used, while the Vp value was set to 950m/sec for Array 2. This couldn't be implemented without knowing the source location, thus cannot be implemented at a real case location analysis. However, the goal was to validate the location error in cases where a single layered velocity model would be used during the location analysis.

The comparison between the calculated locations from seismic analysis locations and the GPS position of the explosions showed an error of tens and even hundreds of meters. This magnitude of error is unacceptable for civil engineering applications. The

above results only emphasized the fact that the general assumption of a single layer P-wave velocity model for shallow depths is not valid.

5.5.3 Step 3: Construction of a more accurate P-wave Velocity Model for the site

Assigning a single P-wave velocity for each geological layer is common practise in location analysis of earthquakes. Taking into account the findings of Step 1, a more geotechnical approach of the geological characterisation of material properties was considered necessary.

The information for the 69m thick layer of the same type of soil mix was combined with the expected increase in the stiffness of the soil with depth. The water level of the area was taken into account as well. During the "rainy" period it is at a depth of ~25m but since the measurements took time during the peak of the "dry" season, the water level was expected to be within 10m deeper than 25m (personal communication with prof. A.F.Nascimento). Since seismic waves travel at larger depths as the source-to-sensor distance increases these variations in the top geological layer had to be taken into account when creating the P-wave velocity model.

A number of more complex, layered, velocity models were created with various numbers of layers and thicknesses. The same trial and error procedure as in Step 1 was repeated. More than 50 different velocity models with up to five layers, and different combinations of velocity values were tried without resulting in residual times close to zero. It was noticed that with the increase in the number of layers and a gradual increase of P-wave velocity with depth, better results were produced. It was understood that abrupt changes in the velocity with depth were not favourable. Therefore, a velocity model (VM) with more layers was required to yield a smoother change in Vp. A number of models were developed. The best three are shown in Figure 5.6. The difference between theoretical and manually picked arrival times (residual times) and the hyperbola's convergence were used as an indicator of each velocity model's performance (Table 5.2, 5.3). The model that produced small location errors (<10m) compared to the measured locations of the explosions and low time residuals (Table

5.2, 5.3), was chosen as optimum. Increasing the number of model parameters generally allows lower misfit given that one introduces more degree of freedom in the solution. In our case though the geology was known and the parameters taken into account leading into a layered model are reasonable.

The third velocity model (VM3) of Figure 5.6 was found to be the optimum one. As in Step 1, the large explosives were used for this analysis step. VM3 consists of two linear parts simulating the increase in P-wave velocity due to increase in the soil's effective stress and saturation over depth. VM3 follows the trend to the empirical power law between wave velocity and effective stress in soils reported by Santamarina et.al. (2001).

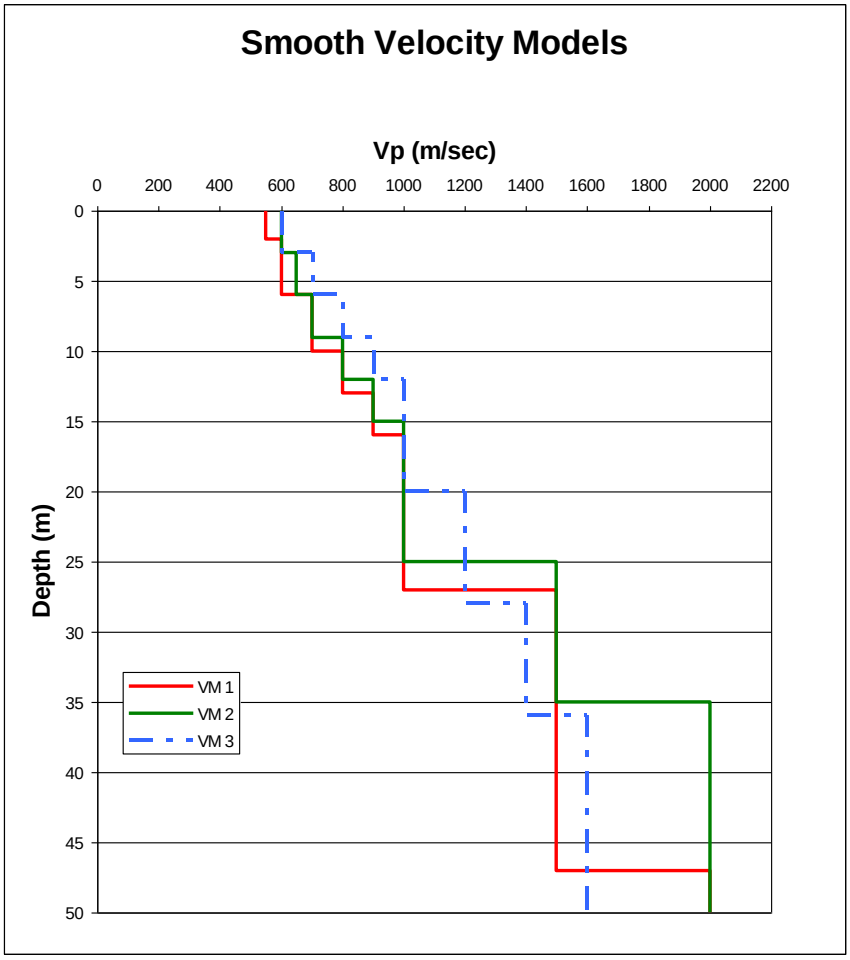

Figure 5.6: Three velocity models (VM) were developed that provided a smoother change of the P-wave velocity with depth. This was achieved by using a larger number of layers.

Residual Times for Array 1 (sec)				
Source-to-Sensor Distance (m)	**Sensors**	**VM 1**	**VM 2**	**VM 3**
20	**North**	-0.008	-0.007	**-0.001**
	West	0.000	0.000	**0.000**
	East	0.000	0.000	**0.000**
	Central	0.000	0.000	**0.000**
40	**North**	-0.002	**0.000**	**0.000**
	West	0.000	**0.000**	**0.000**
	East	0.000	**0.000**	**0.000**
	Central	0.001	**0.001**	**0.001**
60	**North**	0.000	0.000	**0.000**
	West	0.000	0.000	**0.000**
	East	0.000	0.000	**0.000**
	Central	0.004	0.005	**0.003**
Absolute Sum		0.015	0.013	0.005

Table 5.2: Residual times (sec) between theoretical and manually picked arrival times for Array 1 (25m aperture). Among the three models, Velocity Model 3 (VM 3) is the model that produces systematically the smaller error. With bold are the best values for each VM and source-to-sensor distance.

Residual Times for Array 2 (sec)				
Source-to-Sensor Distance (m)	**Sensors**	**VM 1**	**VM 2**	**VM 3**
20	**North**	-0.007	-0.005	**-0.001**
	West	-0.001	0.000	**0.000**
	East	0.000	0.000	**0.000**
	Central	0.000	0.000	**0.000**
40	**North**	-0.003	0.007	**0.001**
	West	0.000	0.000	**0.000**
	East	0.000	0.000	**0.000**
	Central	0.000	0.000	**0.000**
60	**North**	-0.010	0.000	**-0.008**
	West	0.000	0.000	**0.000**
	East	0.000	0.000	**0.000**
	Central	0.000	0.008	**0.000**
Absolute Sum		0.021	0.020	0.010

Table 5.3: Same as in Table 5.2 but for Array 2 (50m aperture). Again Velocity Model 3 (VM 3) produced the most satisfactory residual times.

5.5.4 Step 4: Location analysis using the Hyperbole method and VM1-3

Location analysis using the recordings of small explosions was conducted implementing the hyperbole method in Hypoline. Despite choosing one VM as optimum in Step 3, all three VM of Figure 5.6 were used to investigate the effect that the small differences in velocity models can have on location accuracy. The location errors for each of the three VM for array sizes 25 and 50 meters are summarized at Table 5.4. The errors represent the location difference between the measured GPS measured and those calculated from seismic analysis using the formula shown below,

$$error = \sqrt{(Y_{GPS} - Y_{Calculated})^2 + (X_{GPS} - X_{Calculated})^2 + (Z_{GPS} - Z_{Calculated})^2} \ .$$

The location results for the explosions that took place at distances larger than 60 meters from the 3D sensor were of poor accuracy (>15m), with large differences between theoretical and manually picked P-wave arrival times. Thus they were considered to be unreliable. The true P-wave arrival times of these events were considered to have been attenuated and lost below the background noise level.

Source-to-Sensor Distance (m)	**Location accuracy (m) of 25m size Array**			**Location accuracy (m) of 50m size Array**		
	VM1	**VM2**	**VM3**	**VM1**	**VM2**	**VM3**
20	<5	<5	**<5**	<5	<5	**<5**
40	<10	<10	**<5**	<5	<5	**<5**
60	<15	<15	**<5**	<20	<10	<15

Table 5.4: Errors between the calculated and measured explosion locations for the best three velocity models of Figure 5.3, for the 25m and 50m array. VM3 is proven to produce the best location results among other velocity models since it represents the local geology better than the rest.

Results presented in Table 5.4 verify the choice of velocity model 3 (VM3) of Figure 5.6 as optimum. Location results using VM3 produce the smallest difference between the known and calculated location of the small explosions. Location errors are in general below 5m (within the accuracy of the hand held GPS used to measure the coordinates of the explosion positions), a favourable result for landslide applications.

The largest source-to-sensor distance of a small explosion that was accurately located was 60m. This distance is small compared to seismometers networks locating earthquakes kilometres away. Considering the highly attenuating properties of the local geology and the very weak nature of the small explosives (firecrackers) as a seismic source, the fact that an accurate location could be calculated is a positive result. This finding gives an order of magnitude (tens of meters) improvement in the range of distances where weak events can lie away from a seismic network and be located accurately in such geological environments.

5.5.5 Step 5: Location analysis using the Master Event method

After achieving small location errors implementing the hyperbole method, the master event technique was used to see if these errors could be further reduced. The closest three small explosions to the central 3D seismometers, accurately located with the use of the hyperbola method, were set as the master events and each one was used to locate the rest. For example, the explosion located 20m away from the 3D sensors was used as a master event to locate the explosions 40m and 60m away from the 3D sensors. These events produced clear P-wave arrival times thus eliminating the possibility of picking them wrongly. This procedure focuses on the error due to poor wave correlation between the master event used each time and the other events. Only VM3 of Figure 5.6 was used during the location analysis since it was found to be the optimum. Table 5.5 shows the location error between measured and calculated source location by using the master event analysis.

Array 1			
Distance of Explosion used as Master Event from 3D sensor (m)	**Location Error of Explosion at the indicated distance away from 3D sensor**		
	20m	**40m**	**60m**
20	-	<20	<40
40	<25	-	<20
60	<35	<20	-
Array 2			
*	**20m**	**40m**	**60m**
20	-	<20	<50
40	<10	-	<25
60	<15	<35	-

Table 5.5: Location errors of the master event analysis. Each one of the first three explosions were used as master event to locate the other two.

Table 5.5 presents a much larger location error produced when the master event method is used compared to the results of the hyperbole method presented in Table 5.4. This was because the distance difference between the explosions is large compared to the distance between the explosions and the seismometers which is one of the main assumptions of the method. This means that the seismic waves of the different explosions travel though the local geology following a different path. Correlation between the wave coda is poor and so is the location accuracy using this location method. Note that the explosives used were manufactured, so their explosion mechanism, thus their emitted seismicity, is expected to be similar.

For the optimum application of the master event method for sources located close to the array (<60m), a denser "library" of known events is needed to be characterized as master events. In the analysis concluded here, the distance between the master event location and the event to be located was 20m. An optimum case scenario would be for this distance to be <10m. Such "libraries" of known seismic events could be recorded fast using hammer hits instead of explosions as a source.

5.5.6 Step 6: Optimization of the Array Aperture

A main problem in detecting and locating weak sources is to successfully record them by an adequate number of sensors that would allow for the determination of their location. There are two unfavourable cases when dealing with weak events concerning the deployment of sensors as an array; 1) having a small array size and a relative large source-to-sensor distance can result in having the array sensors recording simultaneously the event thus operating as a single seismometer making the location of the source not feasible, 2) if a large array is used, the event might not be recorded by seismometers with larger source-to-sensor distances due to dissipation of energy spreading and noise levels.

From Table 5.4 and VM3 it is shown that the array having 50m aperture size has a larger location error for the small explosion taking place 60m away from its centre compared to the array having 25m aperture size for this site and experiment. This difference in the location accuracy can be attributed to the difference between the distances of the North seismometers of both arrays from the location of the explosion. For the 50m array the North sensor was 110m away from the source and for the 25m array 85m. These sensors were the furthest apart from the source for both arrays. This difference was enough to attenuate the signal leading to erroneous phase picking and larger location error for the 50m aperture.

For the type of source used in this experiment and the surrounding local geology, locating sources using only one array is better done with small aperture sizes i.e. apertures of 25m.

5.5.7 Step 7: Time synchronization between two seismic arrays

In this experiment, two 3D sensors were deployed next to each other. The intension was to see if P-wave onset times would be recorded simultaneously from both seismometers as expected. In the literature review chapter it was reported that more

than one microseismic array might be needed to locate landslide events. For this reason it was needed to prove that two arrays are synchronised when they use different GPS devices during acquisition.

A comparison of the time recordings though shows one millisecond difference for some events. In our case the combination of the two different arrays for location determination could have led to an additional maximum error of 1.6m. This has to be taken into account at error estimation when one uses sensors from different arrays to calculate the location of a seismic event. The larger the wave's propagation velocity is, the larger the error this time difference can produce.

5.6 Chapter Summary

This experiment showed that assigning a P-wave velocity that is gradually increasing with depth to single geological layers leads to better location results compared to the results obtained when using a single layered P-wave velocity model over the whole depth. It is also shown that for our application characteristics (local geology, source-to-sensor distances and source size) small seismic arrays, i.e. arrays with apertures < 25m, can have a location error lower than 5m making them capable for use at civil engineering applications. Finally, small aperture sizes were found to be more efficient than larger ones when weak sources are under investigation. This procedure can be repeated to other geological sites using the same or different array sizes. By doing so one can investigate the issues discussed above. The procedure can be considered a necessary fast preliminary procedure if no seismic parameters are known for the site under investigation.

The geological site chosen to conduct the experiment presented in this chapter was relatively simple with one lithological layer. The geology of a landslide is expected to be more complex, with heterogeneities and consisting of layers of different materials. Nevertheless, the findings from this experiment defined a methodology to create an accurate velocity model, deploying a microseismic array in an optimum way and using suitable location techniques for the analysis of the recorded signals.

Chapter 6

Simulation of Landslide Seismic Signals at Field Scale Using an Up-Scaled Shear Box

6.1 Introduction:

Waiting for a landslide failure to occur in order to study its emitted seismicity does not address the main requirements of a landslide monitoring system: to provide a warning prior, or the least in real time, of a catastrophic landslide failure. As seen in the literature review, landslide seismicity is site specific, since parameters such as the geotechnical properties of the landslide mass and the local geology of the general area vary. There is a requirements therefore, to be able to predict the characteristics of local emitted seismic signals without having to rely on observations of failure from the landslide being monitored. This chapter presents an experimental methodology to reproduce induced soil friction events at a field scale to address this need.

The methodology is based on an easily implemented and low cost experimental set-up, and can be used for frequency pattern determination related to soil friction events and optimization of the seismic sensor deployment geometry for a specific landslide. This is the first time that landslide-like signals have been experimentally determined for use in field monitoring of landslide failure.

6.2 Experimental Set-Up:

6.2.1 Introduction

The experimental set-up was designed to induce displacement of one soil layer relative to another in order to reproduce the source mechanism of soil slip along the failure plane of a landslide. During such an event, friction between soil particles produces seismic waves that travel through the surrounding geology and are recorded by seismometers. The method uses an up-scaled shear box, a common geotechnical laboratory device, which allows control over a number of parameters presented below. The set-up is easy to implement as long as the area of interest has a road access. This is common for landslide sites close to urban areas, where their occurrence threatens

infrastructure and therefore, they are of particular interest. All parts of the experimental set up can be seen in Figures 6.1a, 6.1b and 6.2a, 6.2b.

To test the shear-box as a methodology for producing landslide like signals we chose a site in the city of Brasilia (Brazil) close to the city centre. To reduce noise from day to day activities all experiments took place early in the morning. It was important (1) to investigate whether signals generated by soil displacements can be detected above noise levels (2) to determine if recordings with high signal-to-noise ratios could be produced close to urban areas proving that seismic sensors can be realistically used as a monitoring method for landslides in such environments. A group of people facilitated these experiments: 5 Masters students, 1 PhD student and 2 technicians, all from the University of Brasilia. The group was led by the author of this thesis.

a)

b)

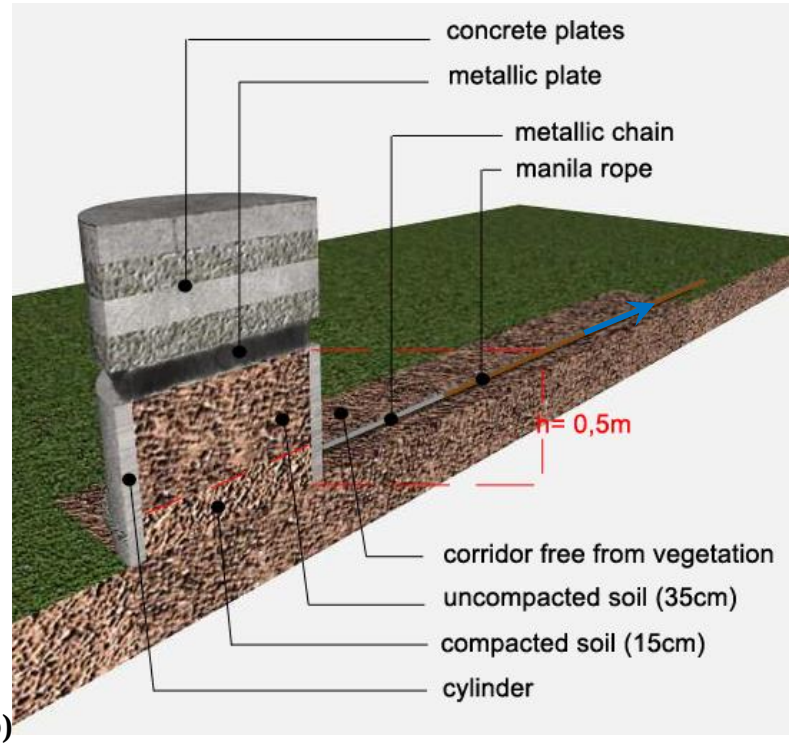

Figure 6.1: a) The concrete cylinder used for the experiment. The cylinder is filled with soil and placed on a surficial corridor free from vegetation. On top of the confined soil block, a metallic plate and up to 10 concrete plates are placed without being in direct contact with the cylinder. **b)** Drawing of a cross section of the experimental set up along the direction of movement.

a)  b) 

Figure 6.2: a) Seismometer as deployed in the field, wrapped in a plastic bag. It was placed inside a 0.5m x 0.5m square hole. **b)** Reel used for the displacement of the cylinder. Also visible is the manila rope wrapped around the reel's drum. Stabilization of the reel was made by burying its two legs into the soil at a depth of 0.5m and by fastening it onto a tree with the use of a steel chain.

Several different experiments were conducted using the concrete cylinder. These all had a common experimental set-up:

1. A concrete cylinder with external and internal diameter 0.75m and 0.65m respectively, and 0.5m high.
2. A surficial soil corridor free from vegetation, 4m long, 1.5m wide. The dimensions of the corridor were chosen such that the concrete cylinder fitted within its width. It was also desirable for the cylinder to be possible to move over a distance at least 2 times its diameter.
3. A metallic plate 0.20m thick placed on top of the cylinder (fig. 6.1), with a 0.60m diameter (smaller than the internal diameter of the cylinder), weighting ~100kg.
4. 10 circular concrete plates 0.20m thick placed on top of the metallic plate (fig. 6.1), with 0.75m as a diameter, weighting ~41-52kg each as shown in Table 6.1.

♯ Concrete Plate	Weight (kg)	♯ Concrete Plate	Weight (kg)
1	45	**6**	45
2	49	**7**	41
3	47	**8**	47
4	47	**9**	41
5	52	**10**	42

Table 6.1: Weight of all concrete plates used in the experiment.

5. A manually operated reel.
6. A high tension manila rope.
7. A high tension steel chain.
8. 7 short period 3D seismometers, with a flat frequency response from 2Hz to 100Hz, manufactured from Sercel, for the monitoring purposes of the experiments. Seismometers and all related connection cables were provided by PEG BR – Pool de Equipamentos Geofisicos do Brazil at no cost.
9. 7 dataloggers set to record continuously at 1000Hz sampling rate, synchronized with GPS clocks. Data loggers and GPS clocks were manufactured by RefTek and provided by PEG BR – Pool de Equipamentos Geofisicos do Brazil along with all connection cables at no cost.
10. A power source for the data loggers and seismometers: in this case 7 car batteries (40Amp, 12Volt).

6.2.2 Description of Experimental Set-Up:

The first step was to form a surficial soil corridor, free from vegetation without changing its natural compaction state and place a concrete, hollow, circular cylinder on top of it. The top 15m of the site's geology consisted of tropical clay, a highly porous material. This layer was above the ground water table with clay being at dry conditions.

A layer of soil, 15cm thick, was placed inside the cylinder and was compacted using the standard proctor rules (Smith, 1981) in order to match the compaction stage of the surficial soil. This created an interface between the surficial soil at the corridor and the compacted soil layer inside the cylinder. The soil placed inside the cylinder came from the top layer of the site, excavated the day of the experiment. This was important in order for the two soil layers that were in contact to share the same mechanical properties. The remaining empty space to the top of the cylinder was then filled with uncompacted clay from the site. This soil acted as an overweight, increasing the stress levels on the interface between the soil of the surficial corridor and the soil inside the cylinder.

The metallic plate was placed on top of the cylinder's soil, followed by the concrete plates. Together they controlled the stress level at the surface between the soil in the cylinder and the corridor, without being in contact with the cylinder. This ensured that the soil bore the plates' full load with no load being born by the cylinder walls (fig. 6.1a, 6.1b).

The cylinder was connected to a reel (fig. 6.2) using a steel chain and a manila rope tied together, both capable of enduring high tension levels. The chain had a stable, easily adjustable hold on the concrete cylinder (fig. 6.1a). If the chain was to be tied around the reel's drum, the small hits and friction between the chain and the drum or the chain itself could add to the seismic noise. To avoid this, a manila rope was tied around the reel's drum creating a smooth interaction surface between the two and was then tied to the chain (fig. 6.2). Stabilization of the reel was achieved by burying its two legs ~0.5m into the soil and by fastening it onto a tree (fig. 6.2).

All events were recorded by seven 3D short period seismometers. Each was wrapped in a plastic bag for protection against a sudden rise of the water level and were buried 0.5m below surface to minimize noise bursts (e.g. thunder or bell ringing), reduce local noise levels and maximise the coupling between the sensor and the soil. Each sensor had its own datalogger, GPS clock and battery to minimize data loss in case of random instrumental failures. Sensors were deployed along a line perpendicular to the

cylinder's movement direction as shown in Figure 6.3 and were all aligned to North. Source-to-sensor distances, considering the cylinder as the source, were; 4m, 5m, 7m, 9m, 11m, 13m, 15m away from the centre of the surficial corridor. This dense linear deployment geometry was designed to ensure a low detection threshold, i.e. recording of the smallest displacements of the cylinder and to allow for a detailed analysis of the emitted seismic signals as they propagated away from their source.

The seismic sensors were constantly deployed throughout the experiment and set to a continuous acquisition mode. All experiments were carried out between 05:00 and 06:45, with each experiment lasting no more than 5 minutes. This procedure ensured the same monitoring conditions for all recordings including no changes in the levelling or orientation of the seismometers.

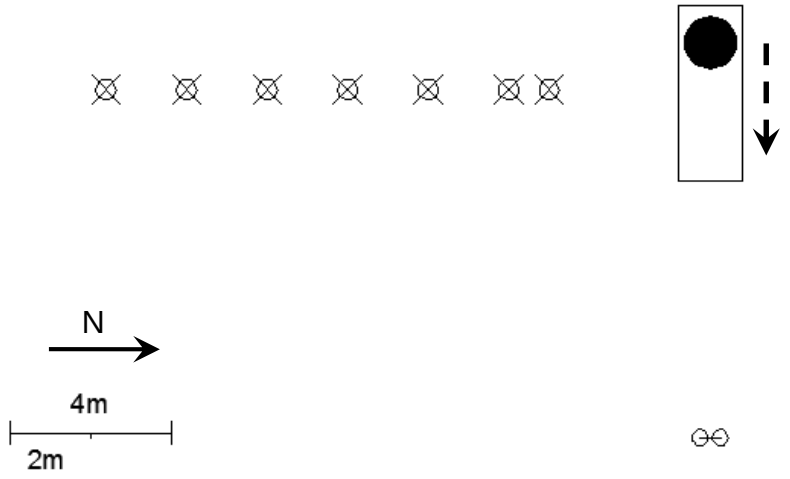

Figure 6.3: Plan view of experimental set up. Solid Black Circle; cylinder with confined soil block, Rectangle surrounding the cylinder; Surficial corridor free from vegetation, Circles marked with X; Location of seismometers, Two circles connected with a line; Position of reel. The dashed arrow shows the direction of the movement of the cylinder.

6.2.3 Experimental Procedure

Step 1:

Before moving the cylinder it was necessary to record background seismic noise. One hour of continuous noise recordings took place to collect data for the characterisation of the general background noise.

Step 2:

Three people were positioned next to the reel in order to operate it. Two people were positioned in front of the cylinder video recordings and keeping field notes.

Step 3:

Each experiment started by recording one minute of background noise measurements as additional noise recordings from Step 1.

Step 4:

The concrete cylinder filled with soil was dragged along the surficial corridor using the reel. By turning the reel's arm slowly, tension was gradually increased in the manila rope, transmitted to the steel chain and eventually the concrete cylinder. During this process the manila rope was undergoing small deformations. When this tension overcame the resistance of static friction between the compacted soil layer of the cylinder and the surficial soil of the corridor, the cylinder moved.

Step 5:

At the beginning of the cylinder's movement, the arm of the reel was kept still. As the cylinder was being displaced, the state of stress and deformation of rope was gradually restored. Meanwhile, the tension forcing the cylinder to move reduced until it was smaller than the friction resisting to the cylinder's movement. At that point the cylinder stopped moving. The displacement of the cylinder was in the range of a few centimetres at a time, with the movement lasting 1-2 seconds. The evolution of friction, force and displacement during Steps 4 and 5 are schematically shown in Figure 6.4.

Steps 4 and 5 were repeated until the cylinder was displaced more than a meter in total. This was to allow multiple cylinder slip events to occur under the same experimental conditions resulting in a large database of seismic recordings.

Step 6:
Once the cylinder was displaced more than a meter, one minute of seismic background noise was recorded.

Once Step 6 was conducted the experiment was complete. If more than a meter was left in the corridor ahead of the cylinder a new experiment could start with different parameters, e.g. a different load on top of the cylinder. If not, the cylinder was pulled back to the beginning of the corridor before the start of the next experiment.

Note that during the induced slip events of the cylinder, the concrete cylinder was in contact with the soil. The friction between concrete and soil is expected to also emit seismicity but it can be considered to be a trivial addition to the seismicity emitted due to the slip of the two soil layers. The reasons are that a) the load on the concrete was very small compared to the load on the soil surface and because b) the concrete area in touch with the soil corridor was very small compared to the soil surface area.

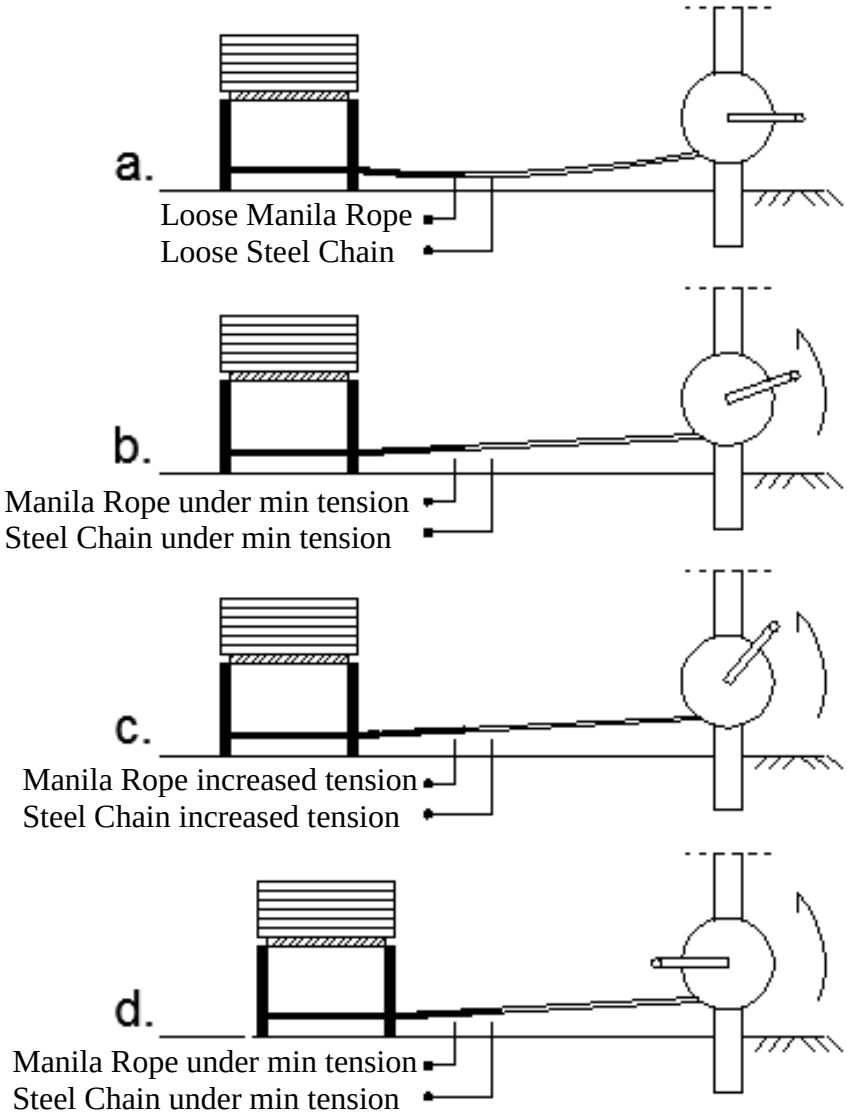

Figure 6.4: a) Cylinder filled with soil is connected to the reel with a steel chain and a manila rope that are loose; no tension is applied from the reel that is why they are curved. **b)** The arm of the reel is turned creating a tension level capable of lifting the own weight of the steel chain and manila rope and straighten them out. **c)** The arm of the reel is turned more increasing the tension of the steel chain and manila rope. The manila rope is now undergoing small deformations. The static friction developed on the slip surface between the soil of the cylinder and the surficial corridor is preventing the cylinder to move. **d)** The static friction of the slip surface between the soil of the cylinder and the surficial corridor was overcomed by the tension developed in the steel chain and manila rope allowing the cylinder to move.

During each of the cylinder's small movements, a slip surface between the surficial soil and the compacted soil layer of the cylinder was created. Great care was taken to do this without creating any additional seismic noise by the experimental process. People close to the seismic sensors remained at one place and the experimental site was 500m away from any road thus avoiding any additional anthropogenic noise.

Four different experiments were conducted using the above methodology each one with a different applied load, i.e. different stress level at the slip surface. Stress was controlled by adding or reducing load on top of the soil in the cylinder according to the relationships (1) to (3) presented below (Craig, 2004),

$$F = m \times g$$

$$\sigma_v = \gamma_{soil} \times z \qquad (1)$$

$$\sigma_v = F/S_{area} \qquad (2)$$

from (2) and (3)

$$z = (F/S_{area})/\gamma_{soil} \qquad (3)$$

where:

F: force (kN) applied on S_{area}

S_{area}*: area size of the cylindrical surface in contact with the corridor* (m^2)*g: the gravitational acceleration*

σ_v*: vertical stress* (kN/m^2) *at depth z*

γ_{soil}*: specific weight* (kN/m^3) *of soil*

z: depth (m).

The soil placed inside the cylinder also affects the loading conditions on the slip surface. This was taken into account. Load, force and stress levels on the slip surface, as well as an equivalent depth of the soil friction events if they were to occur as a landslide, are shown below in Table 6.2. The stress and equivalent depth were calculated using equations (1) to (3).

No of Experiment	Load (kg) on the slip surface ($0.33m^2$)	Force (kN)	Stress (kPa)	Equivalent Depth (m) ($\gamma_{soil}=18kN/m^3$)
1	472	4.63	14.03	0.78
2	568	5.57	16.88	0.94
3	743	7.29	22.09	1.23
4	829	8.13	24.64	1.37

Table 6.2: Load, force, stress levels and equivalent depth of landslide like soil friction events for all 4 experiments. Calculation of the equivalent depth was made using equation (3).

6.3 Data Collection

The seismometers were set to record data continuously, thus three seismograms were produced for each of the seven sensors. Seismograms included all the slip events of the four different experiments, all the noise measurements and also recorded were segments of ambient noise in-between. Seismograms were stored electronically as counts versus time, and time was recorded in milliseconds. The total length of the experimental recordings was 4 hours.

Analytical field notes were kept during all experimental processes. The starting and ending time of all experimental measurements, as well as the starting time of all slip events of the cylinder were noted. Time was kept using a hand held GPS clock to ensure synchronization with the seismic recordings.

Finally videos were taken for the duration of all four experiments using a digital photographic camera located in front of the cylinder. This was to ensure that the procedure was concluded normally and to check for errors during the analysis stage. Video recordings also allowed simultaneous sound recordings. Each time a slip event occurred the GPS time was mentioned making synchronization possible between the videos and the recorded seismic events.

6.4 Preliminary Analysis

Preliminary analysis included the conversion of the raw seismic data files (PASCAL format) into a format that could be read by Matlab (ASCII), for all sensors. This was done by running a script provided by REFTEK. All of the data analysis was conducted using Matlab and the signal processing toolbox. Data were loaded into Matlab, then the seismograms were divided into segments of different length each containing one of the four experiments. The separation was based on the field notes only.

6.5 Main Analysis

6.5.1 Step 1: Time – Frequency analysis

First task was to detect and visualise the slip events above noise levels. Using time-frequency analysis (see Chapter 4), a number of spectrograms were plotted; for each Experiment, one spectrogram was calculated per trace i.e. 7 sensors × 3 components each = 21 spectrograms per Experiment. All spectrograms plotted from all four Experiments and sensors can be seen in Appendix A.1.

The information retrieved from a representative spectrogram of the data set can be seen in Figure 6.5. The first and last part of the total duration of the recordings consist of background noise. Spikes of red colour shades represent the small movements of the cylinder, while the in between background noise segments are highlighted with yellow-cyan colour.

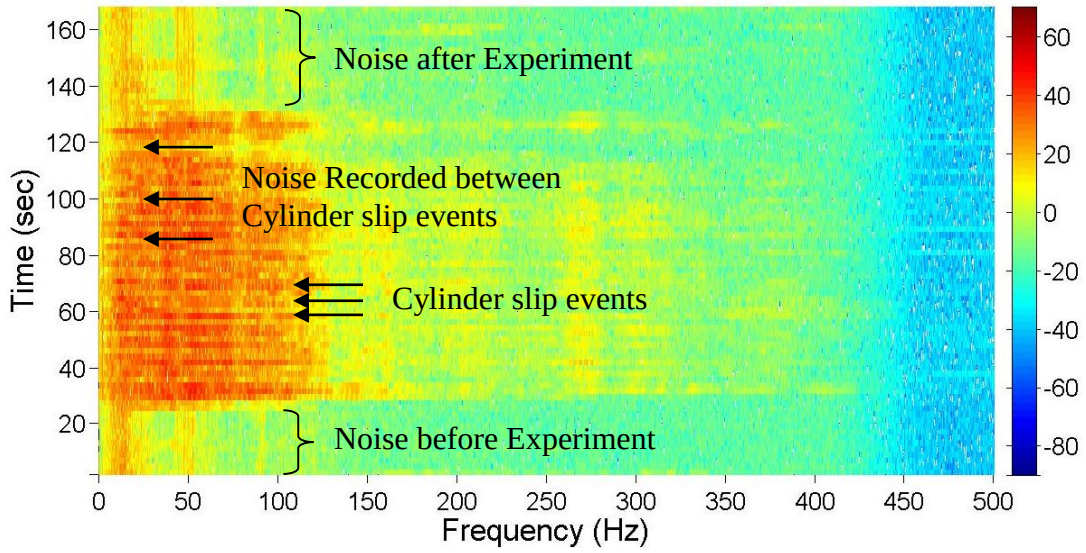

Figure 6.5: A representative spectrogram of the dataset with explanatory annotations.

All spectrograms were plotted with the same colour scale to allow for direct comparison. However if the max and min values of each graph's spectrogram amplitude defined the max and min values of the colour scale, individual events could be visualized in a more detail. As an example, two spectrograms calculated using the same dataset but different colour scale are presented in Figure 6.6.

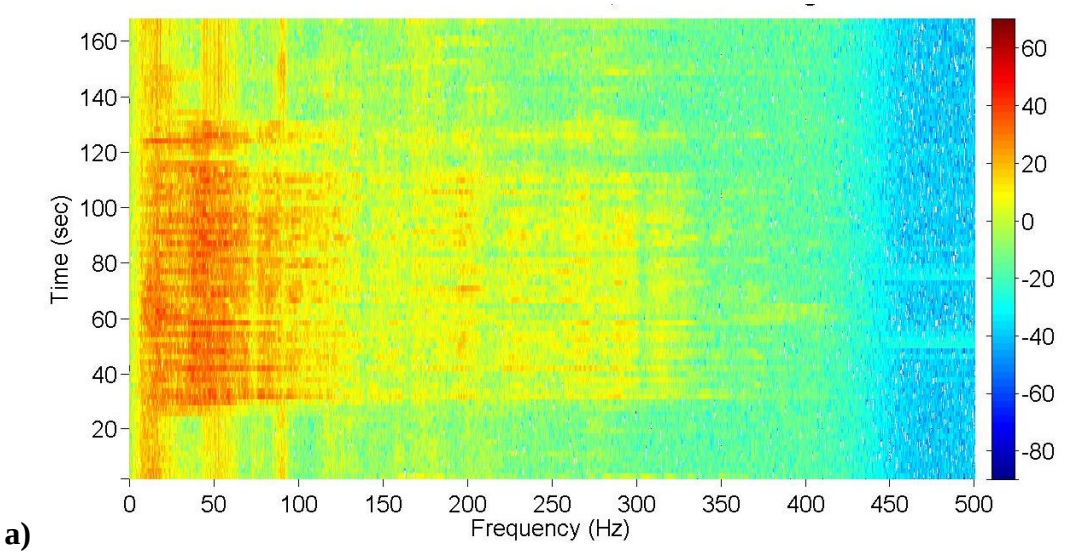

a)

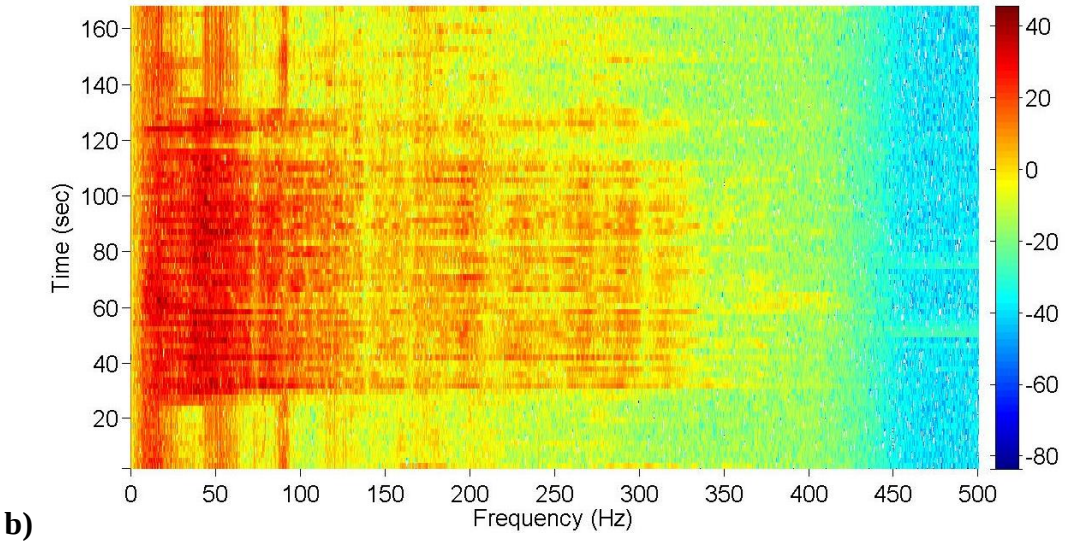

b)

Figure 6.6: Spectrograms calculated using the same dataset but different colour scale. Spectrogram (b) has its colour scale adjusted specifically for the analysed dataset compared to spectrogram (a) that has the globally chosen colour scale. It can be seen that details of the events are visualized in more detail at spectrogram (b) compare to (a). Using though specific colour scale to each spectrogram will not allow for direct comparison between them.

Figure 6.7 presents spectrograms of data recorded 4m away from the cylinder from all three components during Experiment 1 (472kg load). Comparison between spectrograms show that the slip events in each component are distinguishable from one another and that they share similar characteristics, i.e. the main spectral energy gathered is in frequencies below 150Hz, with a frequency content up to ~325Hz. Since there is no additional advantage into inspecting the spectrograms of the horizontal components, from now on only the spectrograms of the vertical component will be presented.

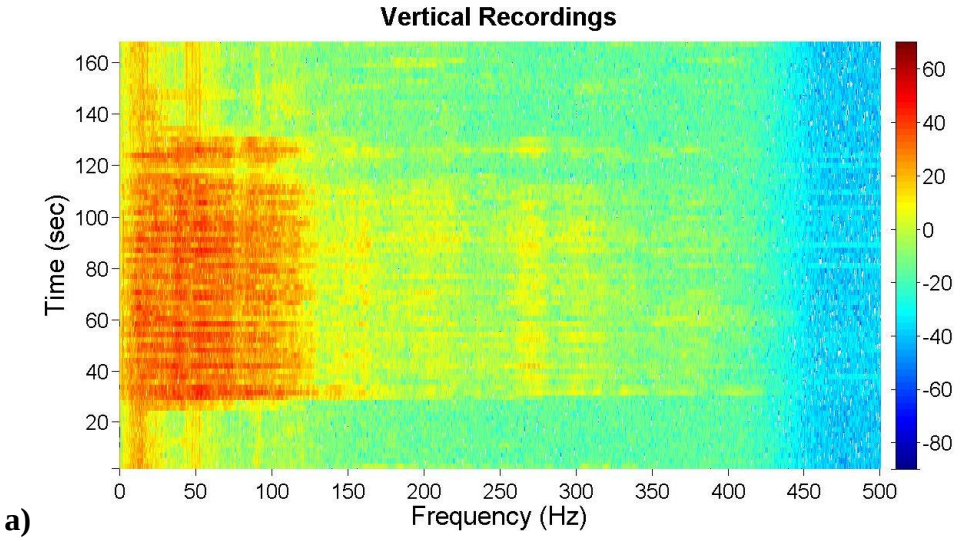

a)

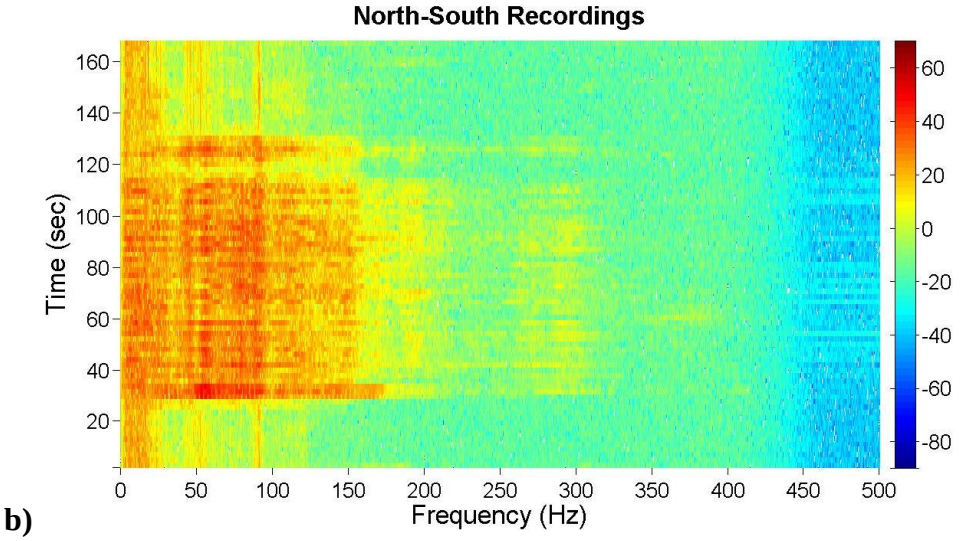

b)

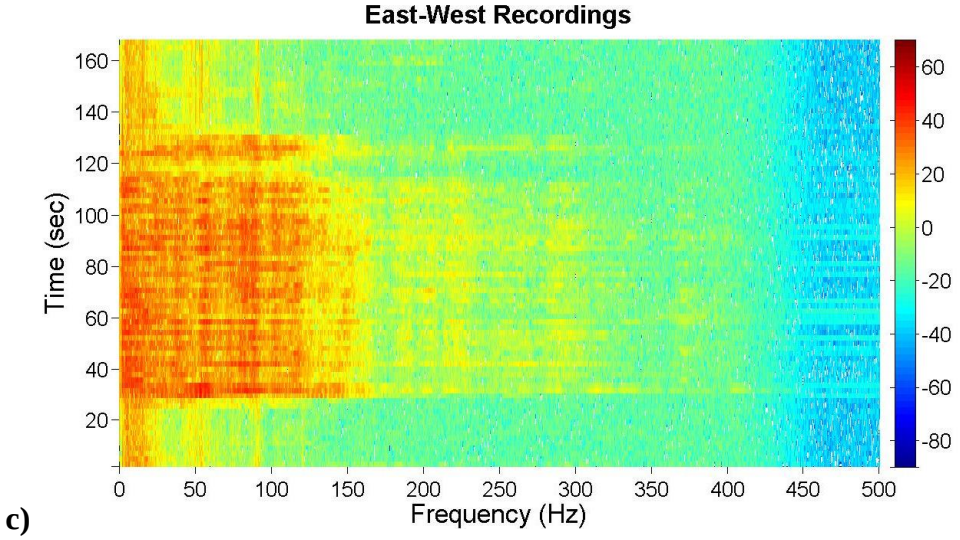

c)

Figure 6.7: Spectrograms of the data recorded during Experiment 1 from the seismometer deployed 4m away from the cylinder are presented. In-between comparison shows that retrievable information are similar.

Figure 6.8 present's spectrograms of data recorded during Experiment 1 (472kg load) 4m (fig. 6.8a) and 15m (fig. 6.8b) away from the cylinder. It can be observed that as the source-to-sensor distance increases, the spectrogram amplitude is reduced along with the detection above noise levels (displacements < 15cm). This can be attributed to attenuation during wave propagation through the soil.

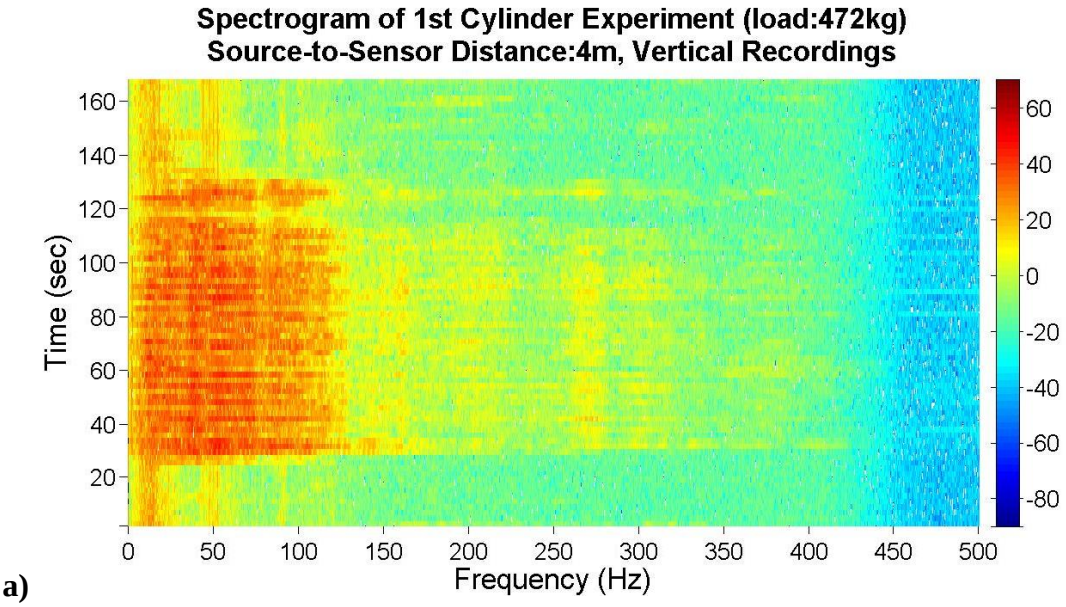

a)

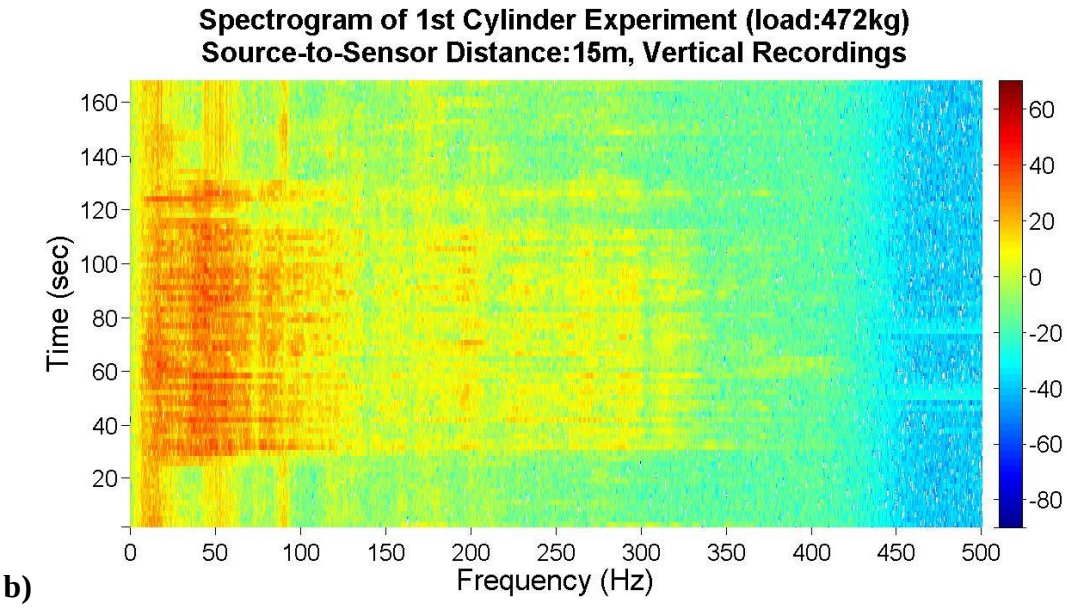

b)

Figure 6.8: Spectrograms of data recorded during Experiment 1 (472kg load), **a)** 4m and **b)** 15m away from the cylinder. It can be observed that due to the attenuation effect, as the source-to-sensor distance increases, the spectrogram amplitude is reduced along with the detection above noise levels.

Finally the spectrograms reveal a strong relationship between the loading conditions on the soil slip surface and the energy of the emitted signals. If the load applied on the soil slip surface is increased, with all other experimental parameters remaining constant, so does the calculated spectrogram amplitude. This can be seen by comparing the two sprectrograms of Figure 6.9 presenting data recorded 4m away from the cylinder during Experiment 1 (472kg load) and Experiment 2 (829kg).

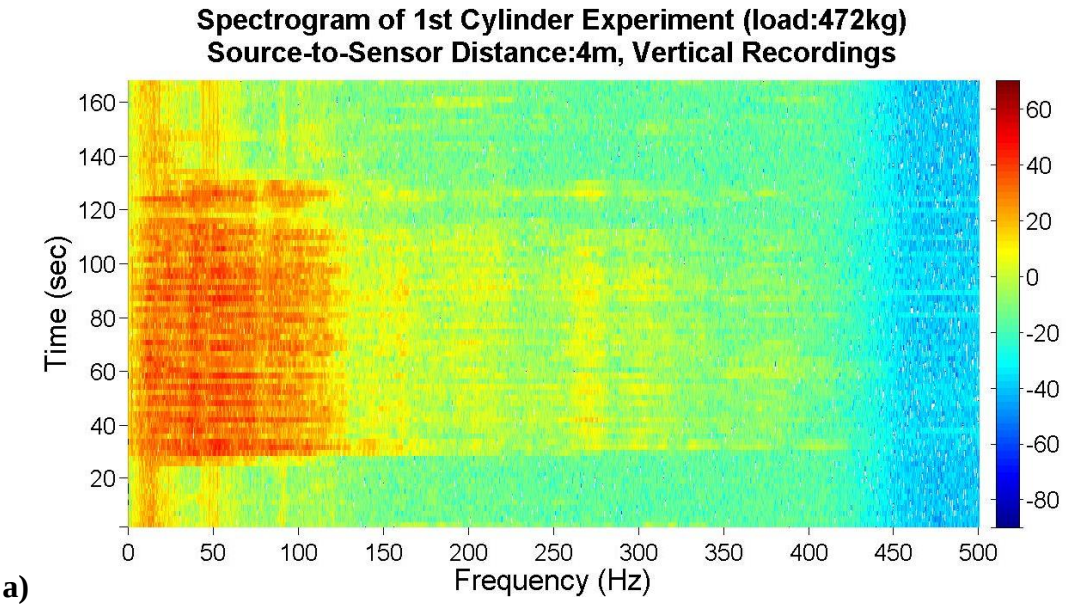

a)

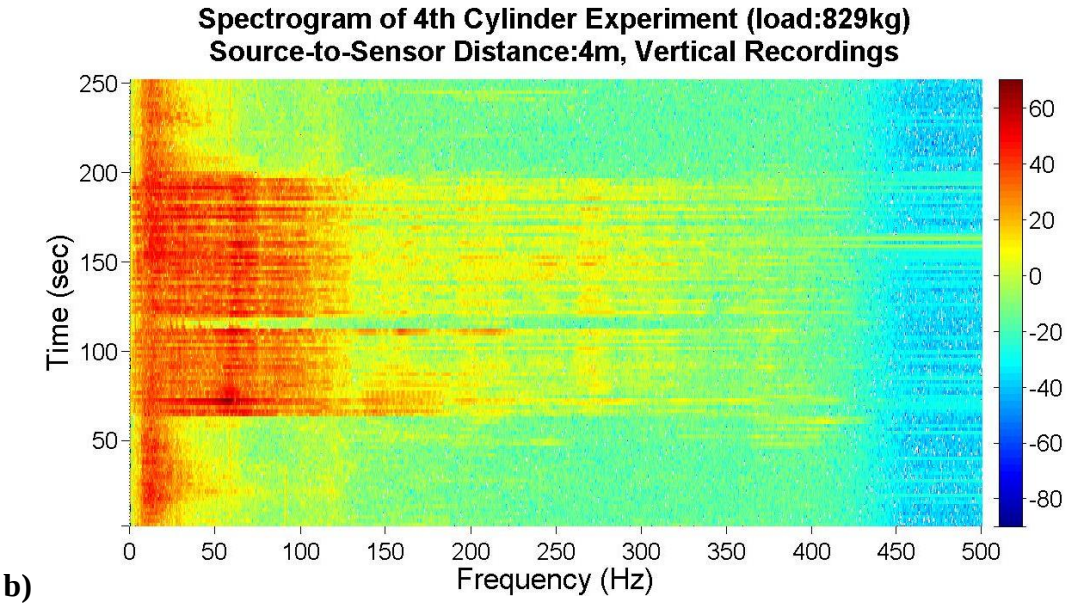

b)

Figure 6.9: Spectrograms presenting data recorded 4m away from the cylinder during **a)** Experiment 1 and **b)** Experiment 2. Comparison between them shows that if the load applied on the soil's slip surface is increased, so does the spectral amplitude.

6.5.2 Step 2: Frequency analysis

The spectrograms presented in the previous step were used to identify events from noise and to roughly mark the frequency range and spectrogram amplitude of each event. Detailed understanding of the recorded signal frequency content was achieved by applying frequency analysis. This type of analysis was carried out using Matlab and the PSD function (see Chapter 4). This analytical step also made it possible to define the relation between the amplitude of the PSD and the source-to-sensor distance, as well as between the amplitude of the PSD and the loading conditions at the soil's slip surface.

As mentioned in section 5.2, the cylinder set up produced seismic waves from soil displacement/friction/slip events by moving the concrete cylinder filled with soil along a surficial soil corridor free from vegetation in small slip events. These events were similar but not exactly identical. There was a variation in their time duration and the actual distance covered at each slip event. An assumption was made that all events were considered to emit similar seismic signals as long as the experimental conditions (i.e. loading conditions of the slip surface & degree of saturation of soil) were kept constant. This assumption allowed for the calculation of the PSD and identification of the recorded signal frequency content, using more than one slip event. All PSDs of the soil slip events induced within the same experiment were taken into account for the creation of one averaged PSD curve.

In between each slip event the cylinder was immobile. During those time segments, seismometers were recording just ambient noise. These noise recordings were of different time length. The latter along with the different number of slip events recorded at each experiment led to a different ratio between the noise and signal time duration that was recorded for each of the four different cylinder experiments. In order to be able to directly compare the frequency analysis results from the different experiments the signal-to-noise time duration ratio needed to be kept constant. The procedure that was followed to achieve this is described in Chapter 4, Section 4.5.1. This procedure led to the final seismogram segments that were used to calculate the PSD of an average

soil friction event happening under the controlled conditions of each cylinder experiment.

Figures 6.10 to 6.12 present the PSD spectra of the data recorded form all three components of the seismometers deployed at 4m and 15m away from the cylinder (source) during all four Experiments. The PSD spectra of all recorded data grouped in the same manner as Figures 6.10 to 6.12 can be found in Appendix A2.1. The dotted curve in all plots is the average PSD curve of all recorded background noise data. These plots reveal the frequency pattern of small soil slip events at different loading conditions on the slip surface for two different source-to-sensor distances. The geometrical similarities of data recorded at the same source-to-sensor distance with only the loading conditions varying as source characteristic, reveal that the frequencies present in the emitted signals are similar. Their only difference is the change in the power spectral density amplitudes due to the difference in loading conditions amongst experiments. Differences between the frequency content of the data recorded at 4m and 15m away from the cylinder can be attributed to the attenuation during wave propagation through the soil. Finally little difference in the PSD amplitude amongst the higher frequency content (>100Hz) when recorded at different source-to-sensor distances.

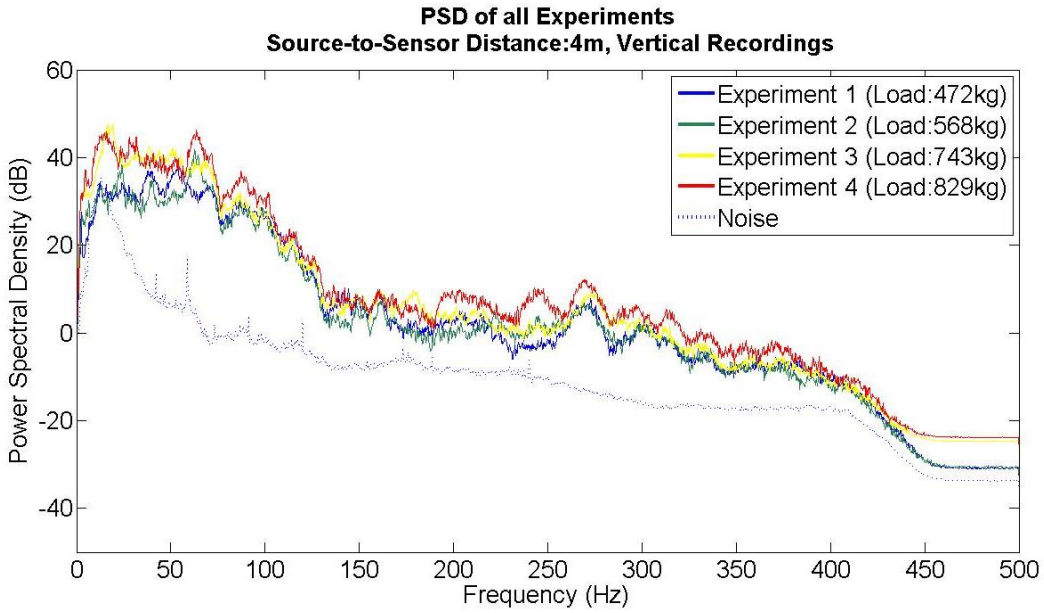

a)

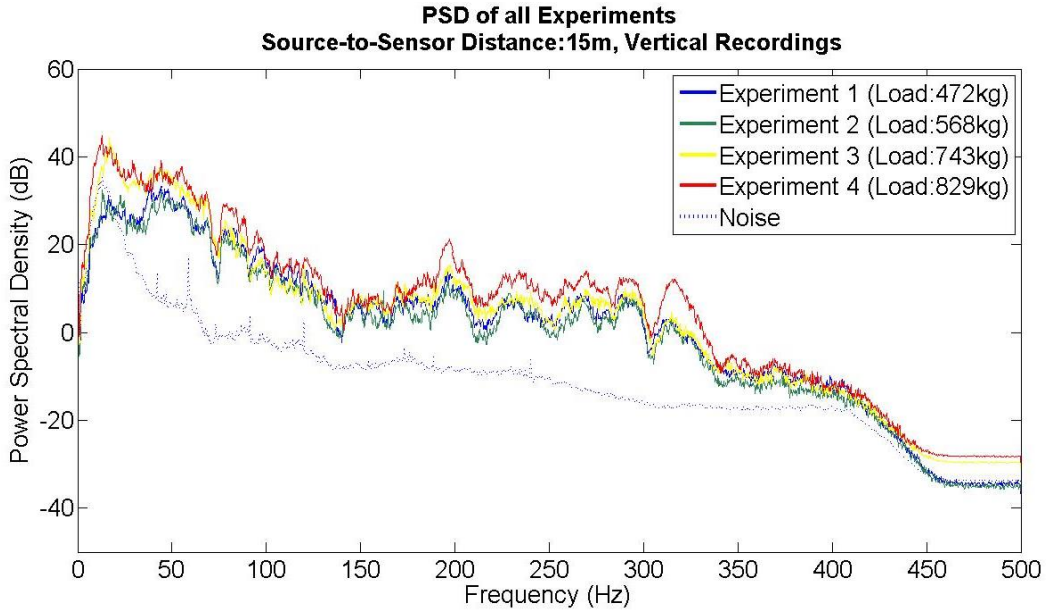

b)

Figure 6.10: PSD spectra of the vertical component of data recorded 4m away from source, from all four experiments at a) 4m and b) 15m away from the cylinder (source). The PSD spectra of noise is the average PSD product of all noise recordings as recorded by the vertical component. The geometrical similarities of the curves reveal that the frequencies present in each signal are similar. Their only difference is the change in the power spectral density amplitudes due to the difference in loading conditions. Differences between the frequency content of the data recorded at 4m and 15m away from the cylinder can be attributed to the attenuation during wave propagation through the soil.

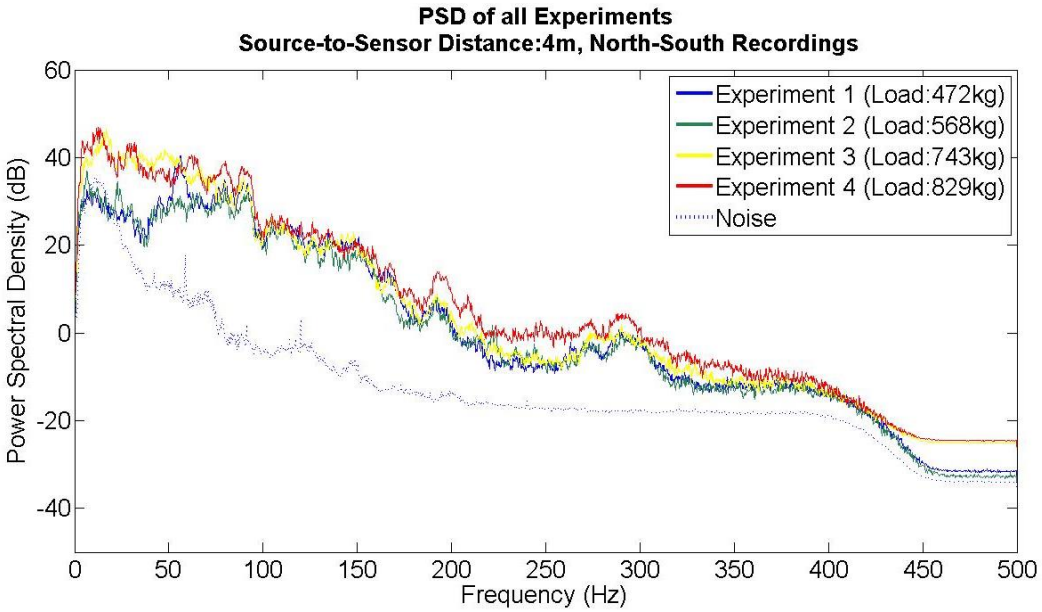

a)

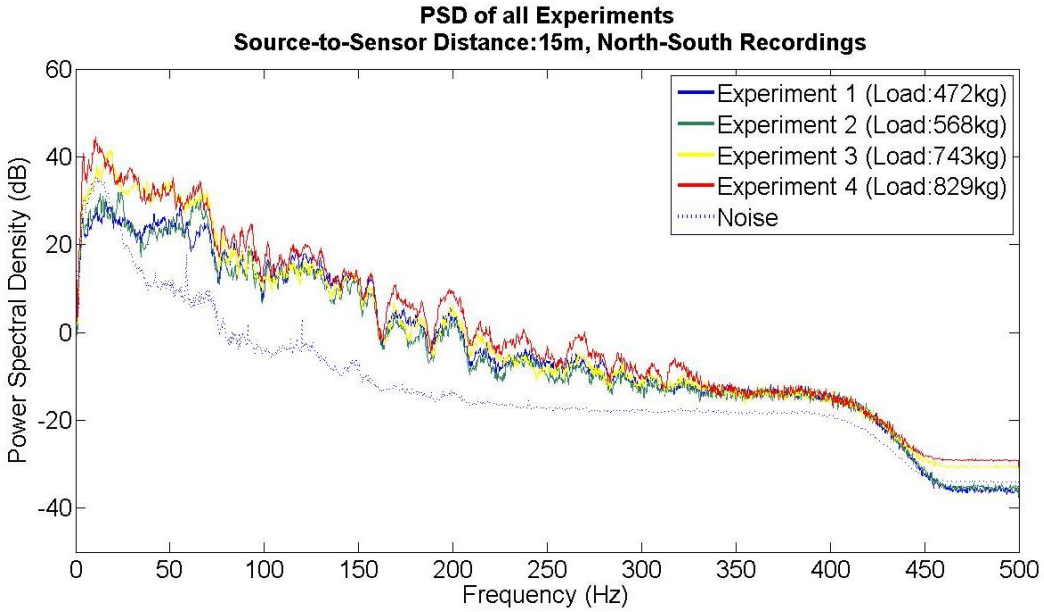

b)

Figure 6.11: As in Figure 6.8 but for the North-South horizontal component.

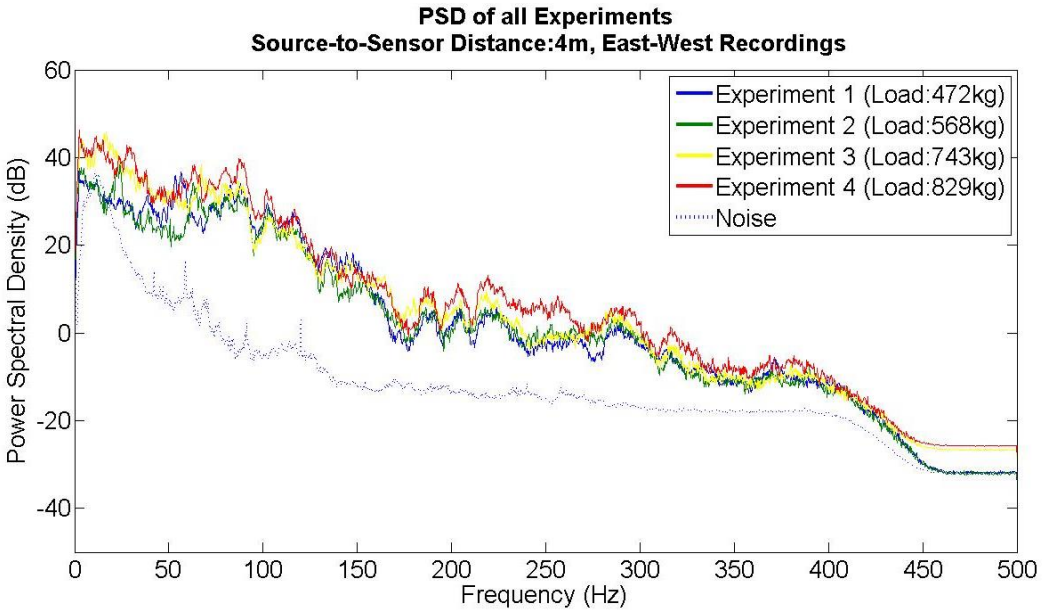

a)

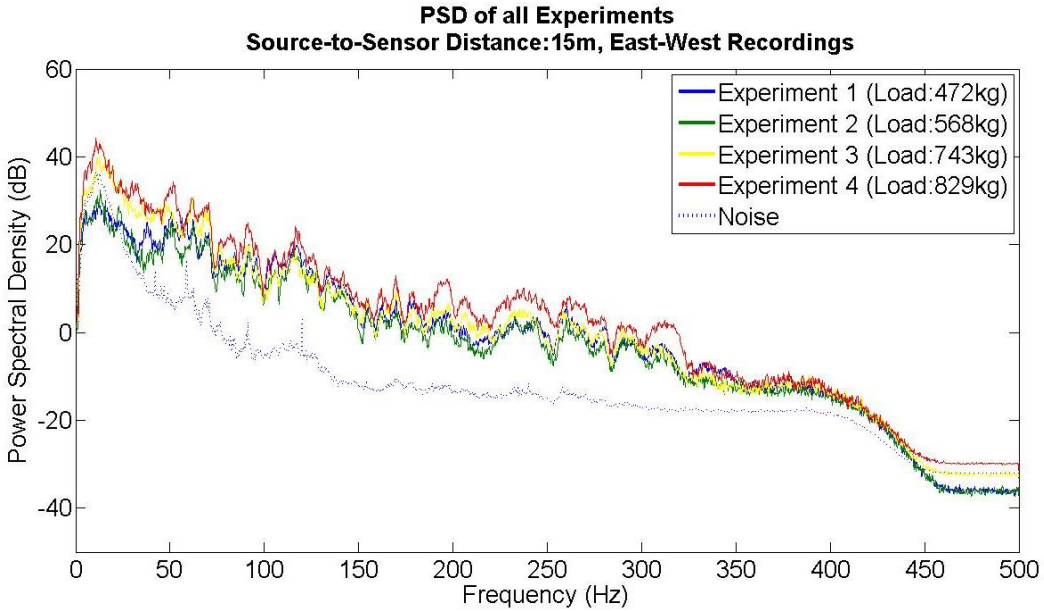

b)

Figure 6.12: As in Figure 6.8 but for the East-West component.

6.5.3 Step 3: Relationship between PSD and Loading on the soil's slip surface

Figures 6.10 to 6.12 presented previously also show that the power spectral density levels of the seismic signals emitted during soil slip events increases with increasing load on the soil slip surface in the frequency range of 0 to 500Hz. This means that the deeper the soil slip event occurs in a landslide, the larger the load applied to the slip surface and hence the larger the energy needed to create the displacement, thus more seismic energy would be emitted.

To present this trend optimally Figures 6.13 and 6.14 show a closer view of the PSD spectra of all three components of the data recorded 4m and 15m away from source during all experiments within the frequency range of 0-100Hz. Once again, all other PSD spectra can be found in Appendix A2.1. It can be seen that the higher the load the higher the PSD. At cases the PSD curves of experiments 1&2, as well as of experiments 3&4 tangle. This proves that a change of 100kg load on the slip surface, simulating a difference in depth of 0.15m, is not enough to create an absolute difference. If though the PSD curves of Exp.1&2 are compared with the PSD curves of Exp.3&4, difference of >200kg that are applied on the slip surface, then the increase of PSD with load is can be clearly seen.

Figure 6.15 allows comparison amongst the different components of the data collected during Experiment 4 (829kg load) as recorded 4 and 15m away from the source. The graphs show that the relationship between the PSD spectra and the load trend is similar amongst the components of one sensor. This means that 1D seismometers would be adequate for retrieving such information.

The same conclusions can be drawn for all other recordings following the above methodology.

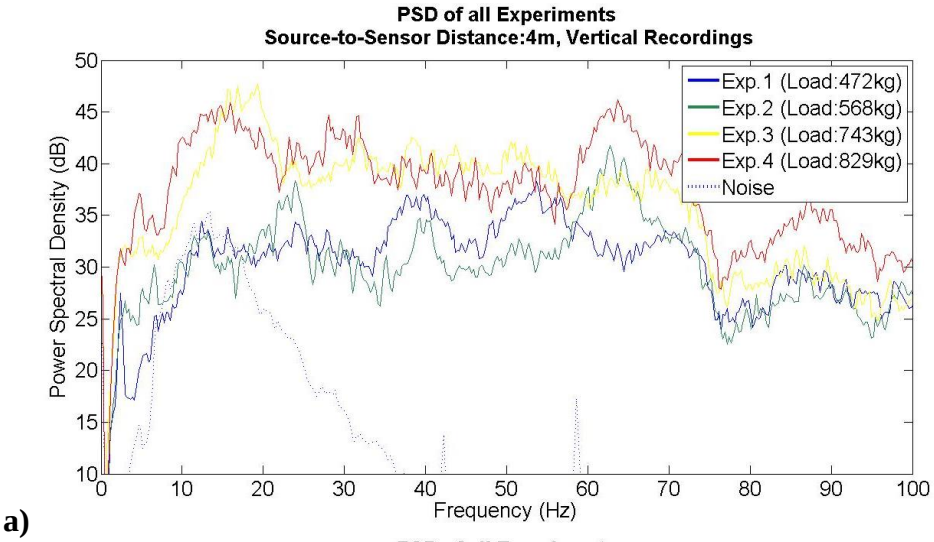

a)

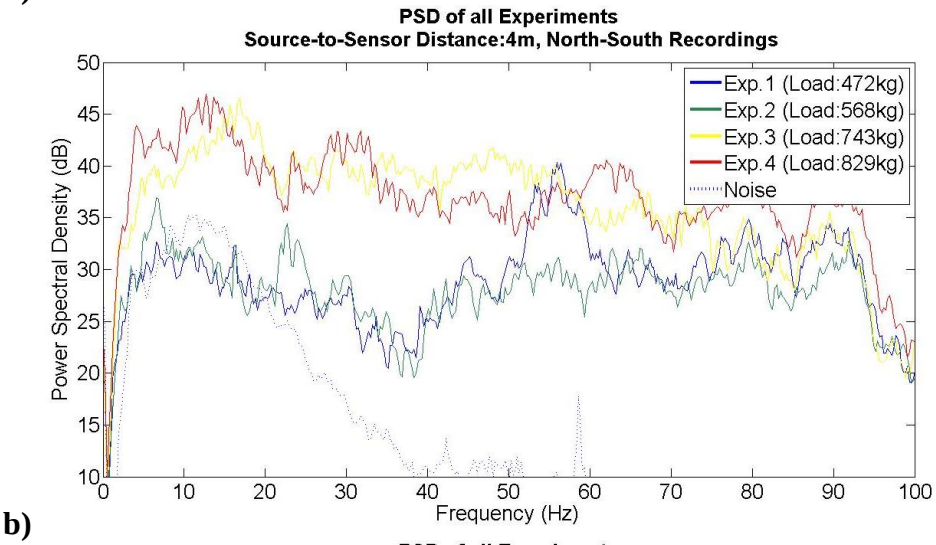

b)

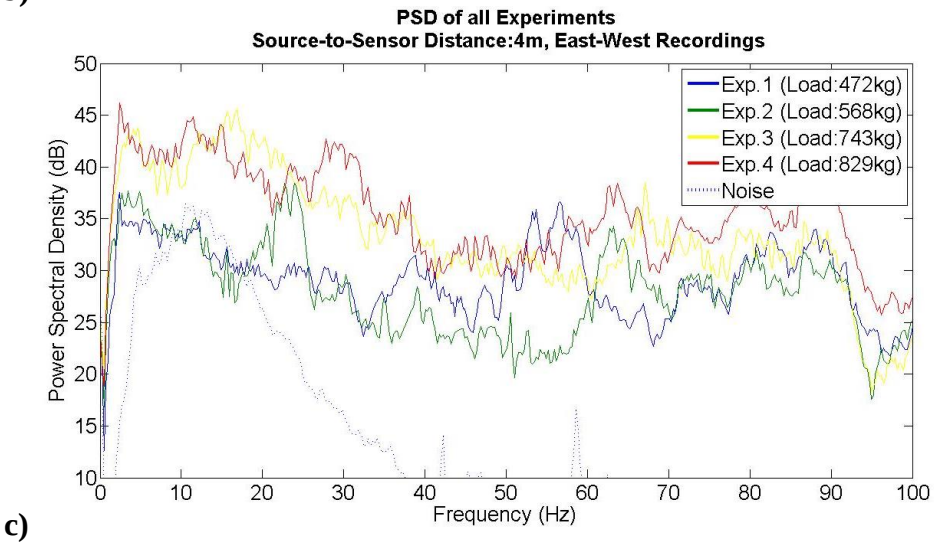

c)

Figure 6.13: Zoom of the PSD spectra of the a) vertical b) North-South and c) East-West component from the signals recorded 4m away from source emitted during all experiments within the frequency range of 0-100Hz. In general, along all different frequencies, the PSD levels increase with the increase in the load on the slip surface.

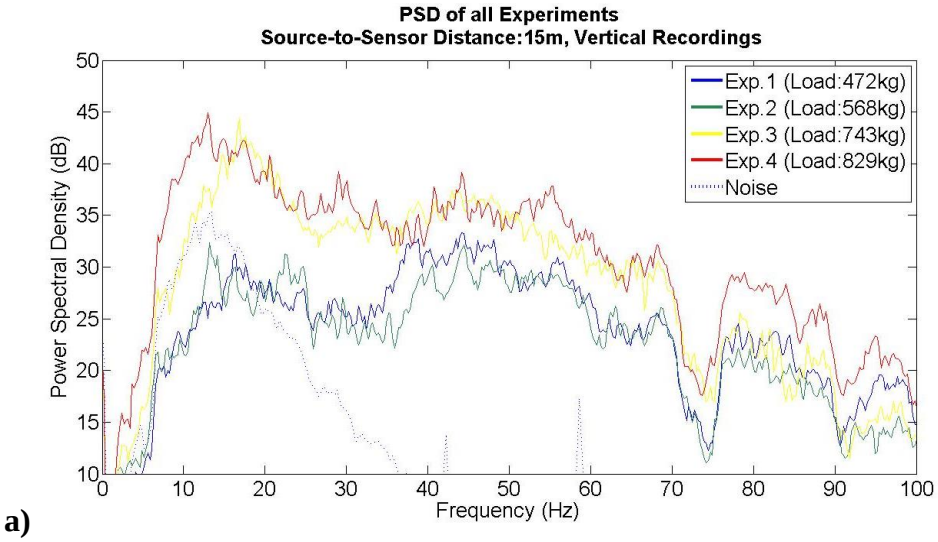

a)

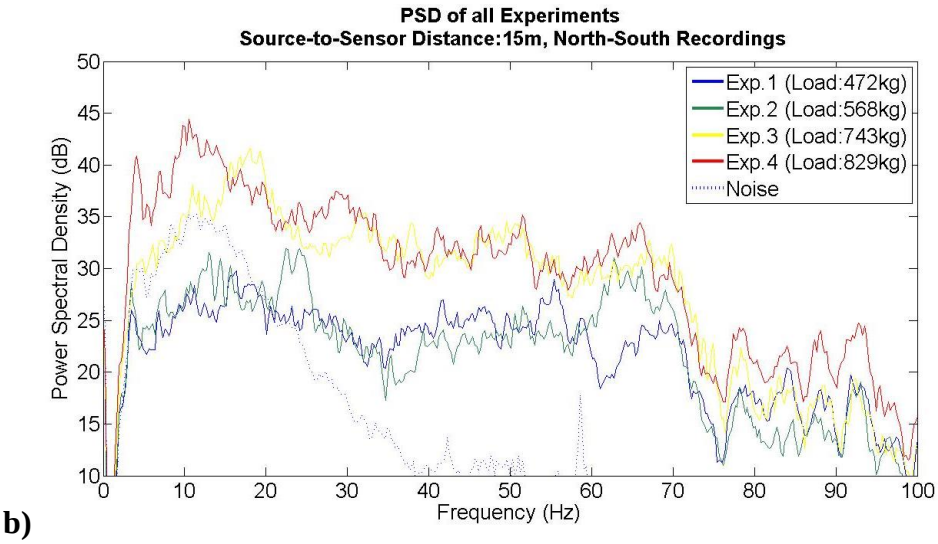

b)

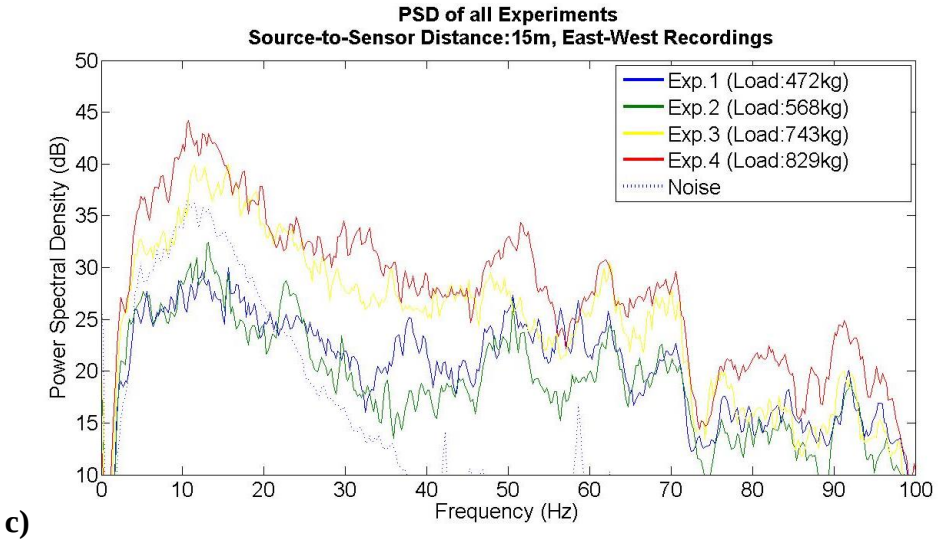

c)

Figure 6.14: As in Figure 6.13 only for signals recorded 15m away from source.

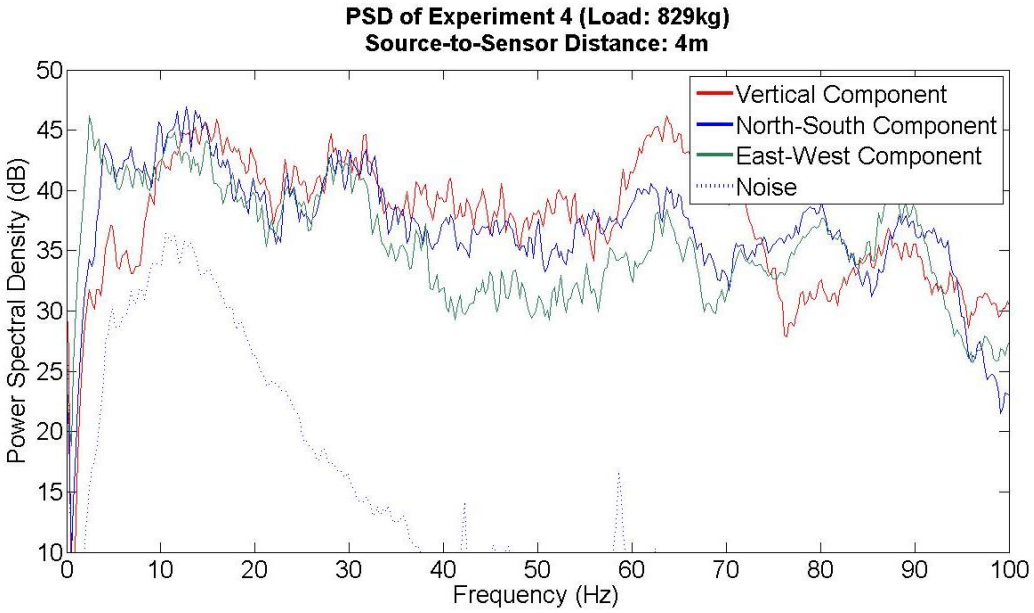

a)

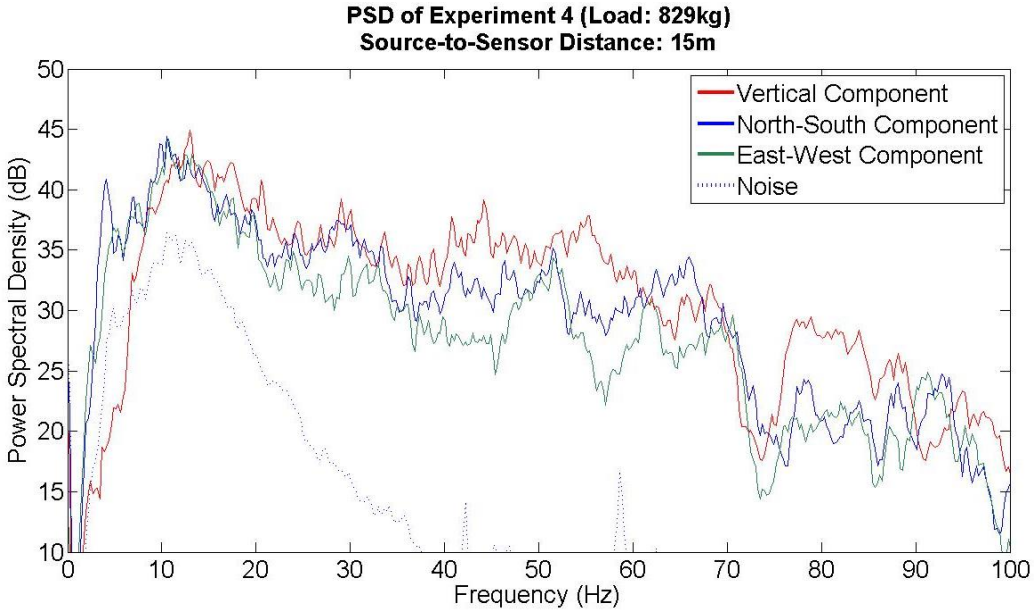

b)

Figure 6.15: Comparison amongst the different components of the data collected during Experiment 4 (829kg load) as recorded 4 and 15m away from the source. The graphs show that the relationship between the PSD spectra and the load trend is similar amongst the components of one sensor.

6.5.4 Step 4: Relationship between PSD and source-to-sensor distance

Figures 6.16 to 6.18 present the PSD spectra of soil slip events recorded from all seismometers during the cylinder experiment with 472kg load in the soil slip surface. This experiment was chosen as a representative case with results being similar for the other loads. Appendix A2.2 presents graphs of the PSD spectra of all sensor components grouped per different loading conditions similar to the graphs of Figures 6.16 to 6.18.

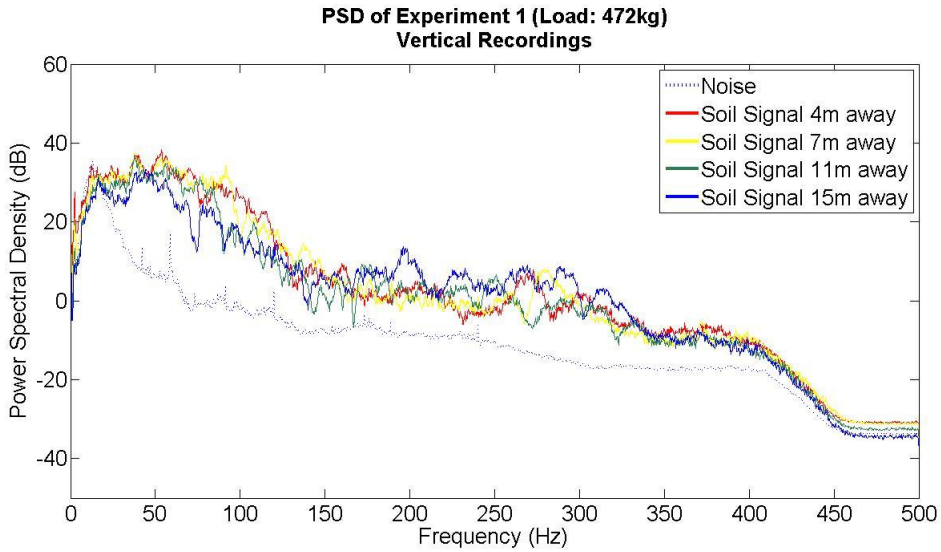

Figure 6.16: Power spectral density of all seismometer recordings during the first cylinder experiment. The dashed blue curve is an averaged PSD curve from all background noise recordings of all seismometers. All other curves are the PSD of soil friction events recorded under the same load. Each colour represents a different distance between the cylinder and the sensor. The experimental curves reveal the attenuation effect in the PSD amplitude as the source-to-sensor distance increases; PSD decreases as source-to-sensor distance increases.

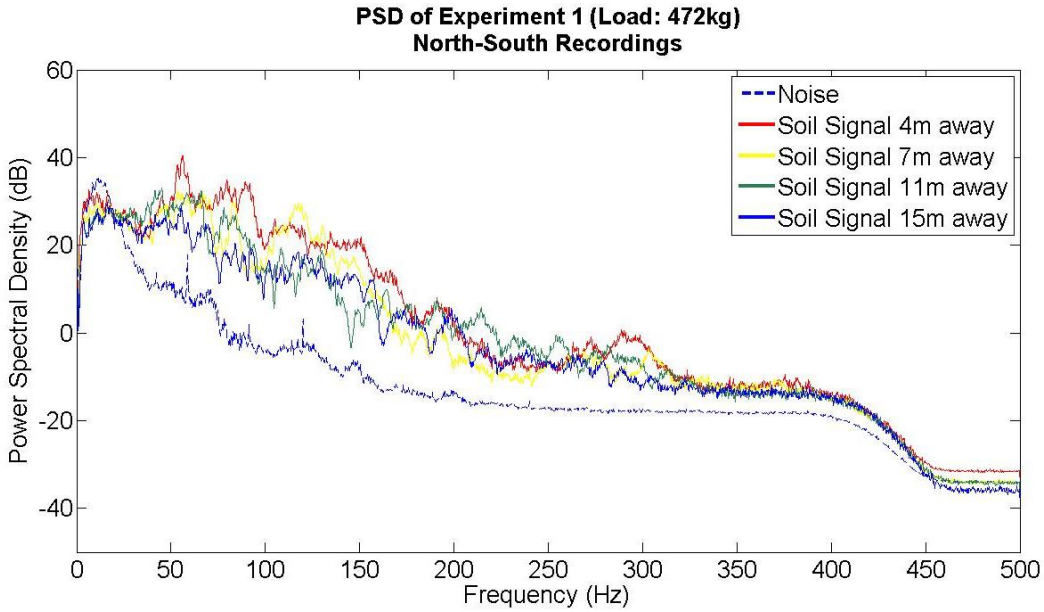

Figure 6.17: As in Figure 6.16 only for data recorded by the horizontal North-South component of the seismometers. The experimental curves reveal the attenuation effect in the PSD amplitude as the source-to-sensor distance increases; PSD decreases as source-to-sensor distance increases.

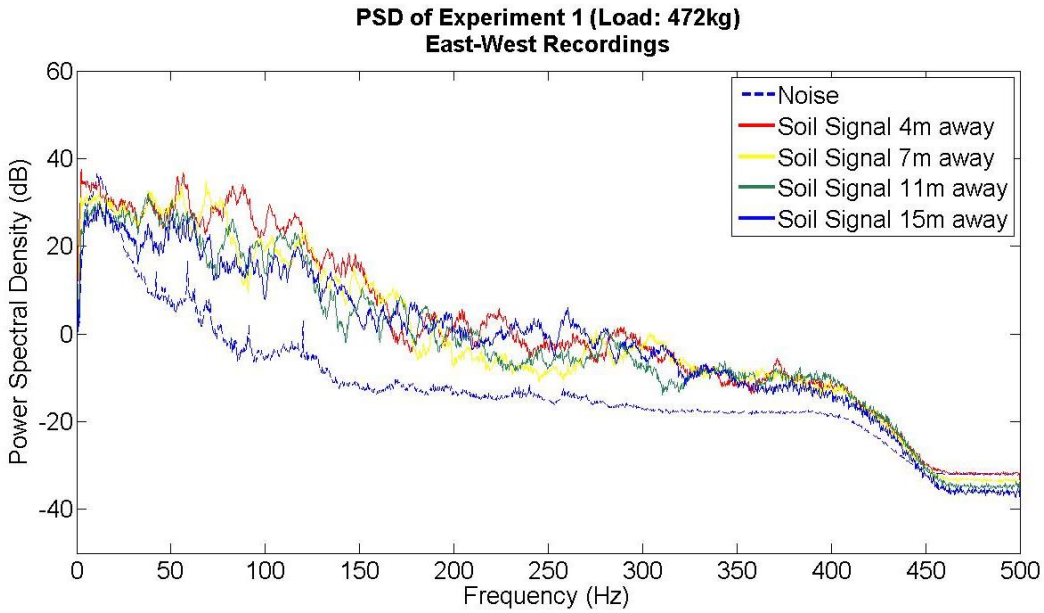

Figure 6.18: As in Figure 6.16 only for data recorded by the horizontal East-West component of the seismometers. The experimental curves reveal the attenuation effect in the PSD amplitude as the source-to-sensor distance increases; PSD decreases as source-to-sensor distance increases.

Figures 6.16 to 6.18 show that the frequency pattern of soil friction signals stays almost stable from 0-70Hz when compared among the same seismometer's components despite the different source-to-sensor distances. Differences can be attributed to the heterogeneities of the local geology and to the different travel paths seismic waves travel to reach each seismometer.

A decrease in the levels of PSD of all frequencies is also visible, as the source-to-sensor distance is increased. This is expected and can be attributed to the seismic wave attenuation as it propagates away from the source through the local geology. Figure 6.19 allows a closer look at the PSD plots between frequencies 0-100Hz of Figures 6.16 to 6.18 to observe this relationship better.

Finally Figure 6.20 allows comparison between the vertical and the two horizontal seismic traces recorded during Experiment 1 from the 3D seismometer deployed 4m and 15m from the source. The PSD plots show that there is little difference between the components and that components are affected equally by attenuation, meaning that the deployment of 1D sensors are adequate to record such events reducing the cost of similar monitoring experiments.

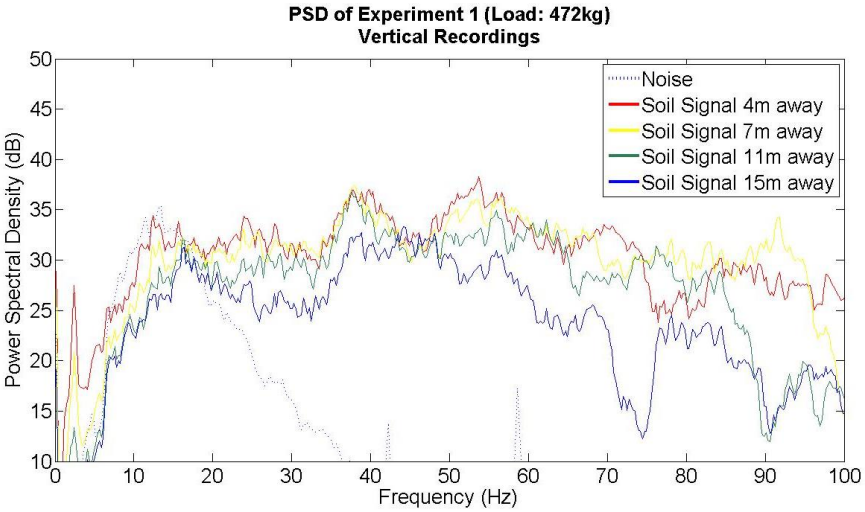

a)

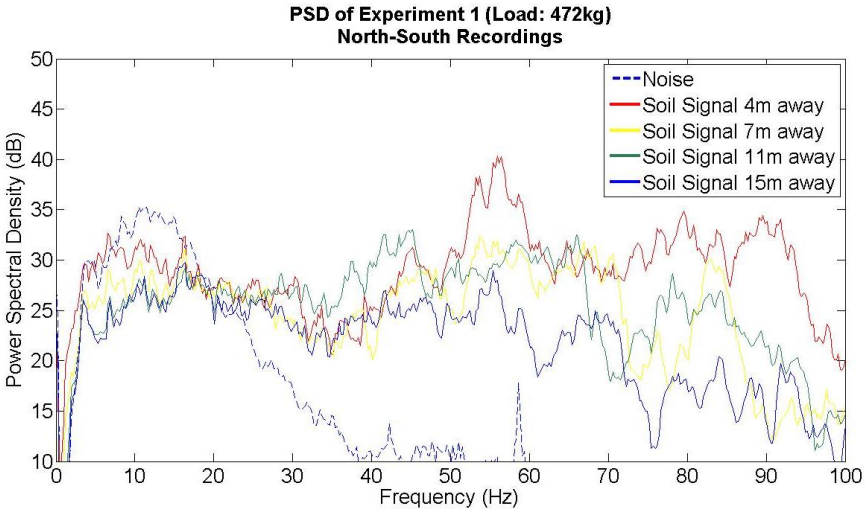

b)

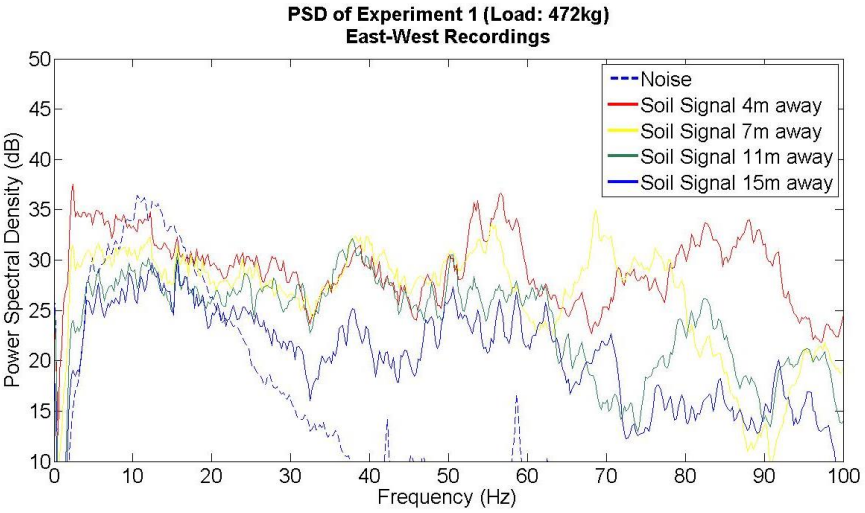

c)

Figure 6.19: Zoom of the PSD spectra of the a) Vertical b) North-South and c) East-West component for signals recorded within different distances away from the source emitted during Experiment 1 at the frequency range of 0-100Hz. PSD values decrease as the cylinder-to-sensor distance increases due to attenuation. The fluctuations in the PSD curves can be attributed to the soil heterogeneities and the different travel paths seismic waves travel to reach each seismometer.

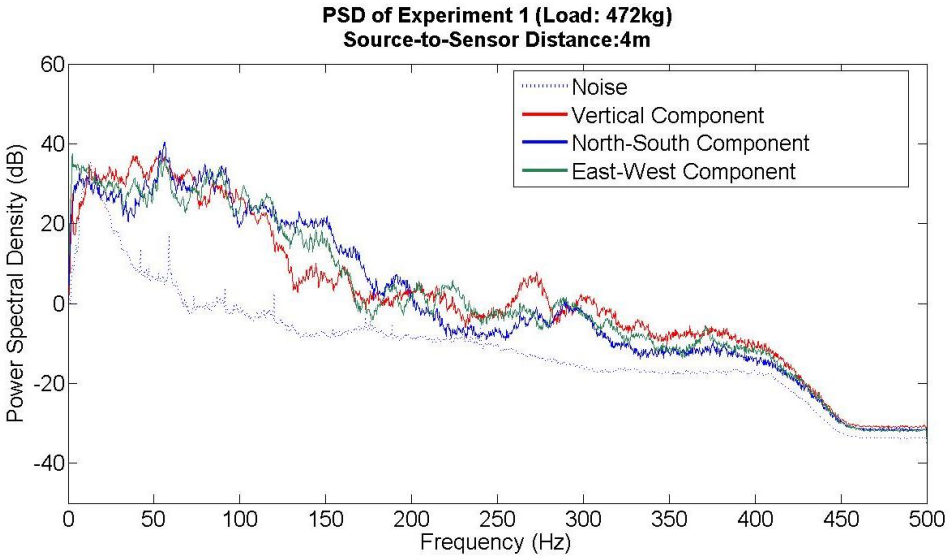

a)

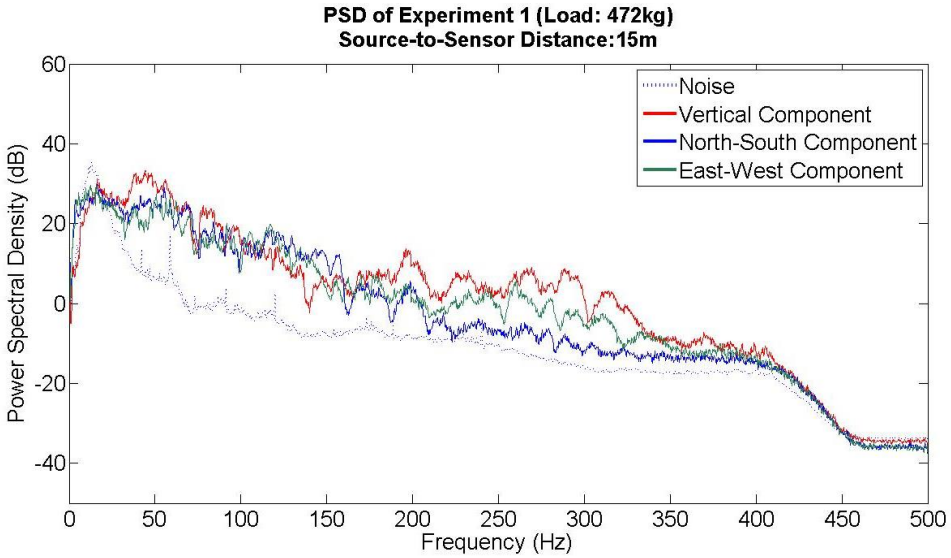

b)

Figure 6.20: PSD spectra of the data recorded during Experiment 1 by all of the seismometer's components **a)** 4m away and **b)** 15m away from the source (cylinder). The PSD plots show that there is little differences between the components and that they are affected equally by attenuation, meaning that the deployment of 1D sensors are adequate to record such events reducing the cost of similar monitoring experiments.

6.5 Chapter Summary

A methodology for simulating landslide seismic signals emitted during soil displacement/friction/slip events at the field scale was presented. The main advantages of this methodology are; a) the ability to control landslide parameters allowing simulation of different landslide scenarios, b) its low cost as it concerns both time and resources, and c) its non-destructive nature. This is the first time that seismic signals due to soil displacement have been simulated under controlled conditions. The methodology also allows a parametric study of the effects on seismic emissions due to parameters such as increasing load or attenuation, helping in the optimization of the sensor deployment geometry when monitoring soil slip events.

The main drawback of the methodology is that simulation of soil slip events at high depths requires large loads. This would be a drawback in remote areas with no road access where equipment would be carried to the site manually. Another concern in applying this methodology is that active landslides can be a dangerous environment to work in, with large slope inclinations, uneven ground and the possibility of imminent failure. In such cases the cylinder experiment should be conducted outside the active landslide area, at a near site with similar geological features.

Finally seismic monitoring is shown to be a feasible tool for monitoring centimetre long soil slip events that occur within a sliding mass. The frequency content found from these recordings is similar to landslide signals as it will be shown in Chapter 8. Seismic records of such signals could provide knowledge of the expected seismic events of real landslides and be used as an early or real time monitoring system that can trigger alerts regarding potential landslide failures. The design of such monitoring systems though should be case specific and should be taken to avoid false alarms or to avoid having results overestimating the landslide's stability.

Chapter 7

Evidence for an improved seismic monitoring system for landslides based on the use of glass shards

7.1 Introduction

The interpretation of seismic monitoring records of a landslide is challenging due to a number of factors that change over time, e.g. a complex geology that changes in time due to displacements within the soil mass and changes due to the weather conditions. Landslides are known to be heterogeneous environments meaning that failure events can involve various soil types with differing mechanical properties resulting in different microseismicity characteristics. Deploying seismometers on active slopes in order to record and study all landslide related signals, could be a very time consuming task.

A successful landslide seismic monitoring survey should address two main difficulties: First, the seismometers record both local and global seismicity, e.g. all types of earthquake signals or noise bursts, leading to complex data sets with more than one unknown seismic sources. Landslide induced seismic signals need to be distinguished among other unrelated seismic signals, e.g. tectonic earthquakes, human activities and meteorological factors (rain, wind etc.). Second, landslide induced seismic signals lack clear P and S-wave arrivals, with the coda of these two sometimes overlapping (Spillmann et.al, 2007, Helmstetter and Garambois, 2010). This can be attributed to the non-brittle nature of soils found in slopes, the attenuating nature of the weathered material that usually dominates slopes, and the energy scattering of the seismic signals. Small source-to-sensor distances can be advantageous in acquiring clear wave recordings but the problem of the overlapping coda remains. These add to the complex problem of choosing an optimum deployment geometry.

In cases where a priori knowledge of the seismicity characteristics of a landslide is absent, seismic monitoring is not always a favourable solution. If a common waveform pattern for landslide induced seismic signals existed, however, then seismic

monitoring and its interpretation would be easier. The characteristics of such a waveform pattern should be independent of the site and constant over time.

In this chapter a novel technique to produce such a waveform pattern is proposed: the use of piles filled with glass shards within a landslide. The piles of glass shards will be designed to follow the movement of the sliding mass and when they cross-cut the landslide's failure plain or at any case of the soil surrounding the glass piles being displaced, the movement of the glass shards will emit seismic signals. As a material, glass shards are angular and coarse, brittle in nature, with their mechanical properties remaining constant over time and not being affected by moisture contact. Glass shards are also a low cost recyclable material that can be easily sourced. The implementation of the proposed novel methodology requires excavation of piles inside the landslide's body. These can be excavated manually since the landslides considered in this thesis consist of soft soils. Pile excavation cannot take place at times when working on the landslide poses health and safety concerns, for example, during and after heavy rainfall.

The proposed methodology is based on two propositions: (1) friction between the glass shards will emit a unique seismic signal, easily discriminated from all other seismicity, and (2) compared to soil friction, friction between glass shards is expected to emit seismic signals larger in amplitude due to their brittle, coarse and angular nature. In order to test these propositions a field experiment was designed and carried out as described in the next sections.

7.2 Experimental Set-Up

7.2.1 Introduction

The experiment was designed to induce displacement between two surfaces consisting of soil and glass shards simultaneously without allowing any interaction between soil and glass. This way, only two types of seismic signals would be emitted at the same time during the experiment: a) signals due to soil-to-soil friction and b) signals due to glass-to-glass friction. The combination of these two seismic signals would travel through the surrounding geology and be recorded by the deployed seismic network. The basic part of the experimental set-up is the up-scaled implementation of a shear box in the form of a concrete cylinder described in Chapter 6, with the advantages that the experimental parameters is controllable.

The experiment took place at the same site during the same night as the experiments presented in Chapter 6 to allow comparison between the two data sets: a) the soil displacement events and b) the glass shard and soil displacement events both induced with the help of the cylinder methodology. A description of the site can be found in Chapter 6.

7.2.2 Components of the experimental set-up

Most of the components used in this experimental set-up were the same as presented in Chapter 6. Only three new components were introduced:

1. Glass shards were obtained by breaking unused glass panels. The glass shard size distribution is presented in Figure 7.1.
2. A wooden frame, 15cm high, 15cm wide and 65cm long (fig. 7.2b) to allow for the formation of the glass layer within the cylinder.
3. A 3m long, 15cm high and 15cm wide trench excavated in the middle of the surficial soil corridor free from vegetation filled with glass shards (fig. 7.2a).

All new components are presented in Figures 7.2a, 7.2b, 7.2c and 7.3a, 7.3b.

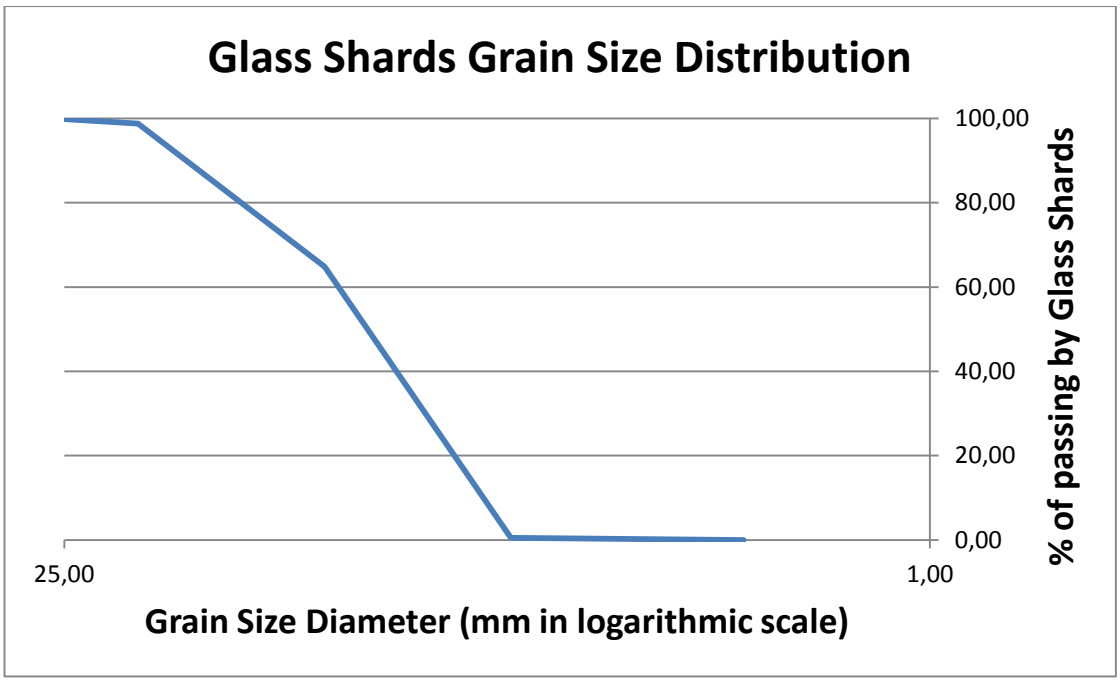

Figure 7.1: Shard size distribution of the glass used for the experiments.

7.2.3 Description of Experimental Set-Up

The experimental setup was similar to the one described in Chapter 6, modified for the needs of this study. The main objective was to induce soil-to-soil and glass shard-to-glass shard displacements simultaneously without having the two materials mixing. Finally this had to be done with a setup that allowed repetition of displacement events with low cost in time since the methodology would eventually be implemented at a real case study.

First I examine the case of a glass shard pile penetrating the soil of the cylinder and the surficial corridor. Induced displacement of the cylinder will lead to glass-to-glass slip events for a total of displacement equal to the diameter of the glass shard pile (fig. 7.2a, b). After that the glass shards pile embodied in the cylinder would not be in contact with the glass shard pile embodied in the surficial corridor (fig. 7.2c). Moving the cylinder back to its initial position in order to restart the experiment and induce more glass-to-glass slip events would lead to mixture between glass shards and soil.

This would cancel the main goal of the experiment: having glass-to-glass separately from soil-to-soil slip events. Repetition of this experimental set-up would have been very time consuming.

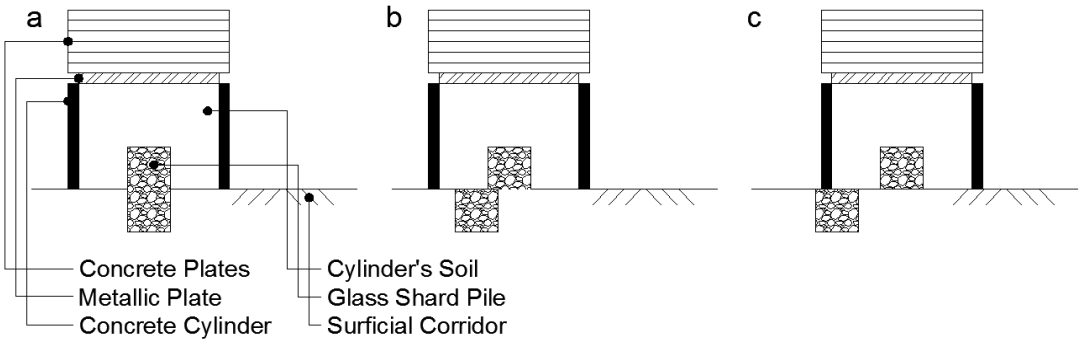

Figure 7.2: Up-scaled shear box with embedded glass shard pile. a) Experimental set-up before any displacement event, b) Experimental set-up after 1 displacement event, c) Experimental set-up after 2 displacement event. Bringing the experimental set-up from stage (c) to stage (a) would require time making the repetition of displacement events hard especially when working at a landslide. For this reason, this design was not used.

For the above reasons, a different experimental setup was designed. In the middle of the free from vegetation corridor a rectangular trench was excavated and filled with compacted glass shards (fig. 7.3a). These works were conducted without changing the natural compaction of the surficial soil.

The concrete cylinder was placed on top of the corridor with the trench of glass shards along the diameter. The wooden frame shown in Figure 7.3b was then used to divide the lower part of the cylinder in three compartments: a) an empty space inside the cylinder being exactly on top of the glass shard trench and having the same width forming a surface area equal to a 17.6cm diameter pile, b) two semi-circular sections on either side of the empty space (fig. 7.3b). The semi-circular sections were filled with dry tropical clay (same material as the top layer of the site geology) that was

compacted using the standard proctor rules (fig. 7.3b). The empty space was filled with glass shards compacted with non-destructive means and the wooden frame was then removed (fig. 7.3c). Two different types of interface between the surficial corridor and the confined materials in the cylinder were created; a soil-to-soil and a glass shards–to-glass shards surface (fig. 7.4b). Control over the simulated area and diameter of the glass shard pile can be achieved by increasing the width of the glass shard corridor formed inside the cylinder and the width of the surficial trench containing glass shards.

The remaining space within the cylinder above the glass shard layer was filled with uncompacted dry tropical clay. On top of it, a metallic plate and concrete slabs were placed as extra load (fig. 7.4a) in the same way as described in Chapter 6.

The cylinder was connected to a manually operated reel (fig. 6.2 of Ch.6) using the same methodology as presented in Chapter 6. The experimental measurements lasted for 10 minutes. Repetition of the experiment would simply require changing the direction of the cylinder movement. Different loading conditions could have been simulated, as done in the soil only cylinder experiments presented in the previous chapter. This was not considered necessary since the results of the spectral analysis using that dataset concluded that the frequency pattern remains stable under different loading conditions and it's only the spectral amplitudes that change.

The seismometers used to monitor the experiment and their deployment geometry (fig.6.3 at Chapter 6) were the same as those used in the experiment of Chapter 6 in order to minimize any changes in the conditions in which the two experiments were conducted and therefore, ensure that the results from both experiments are comparable.

a)  **b)** 

c) 

Figure 7.3: a) View of part of the surficial corridor with a trench excavated in the middle and filled with the glass shards. **b)** Concrete cylinder placed on top of the surficial corridor. A wooden frame was used to create the empty space inside the cylinder, exactly on top of the glass shard trench. The glass shards on the surficial corridor are visible. **c)** The empty space created by the wooden frame was filled with compacted glass shards. The wooden frame was removed after the glass shards were in.

a)

b)

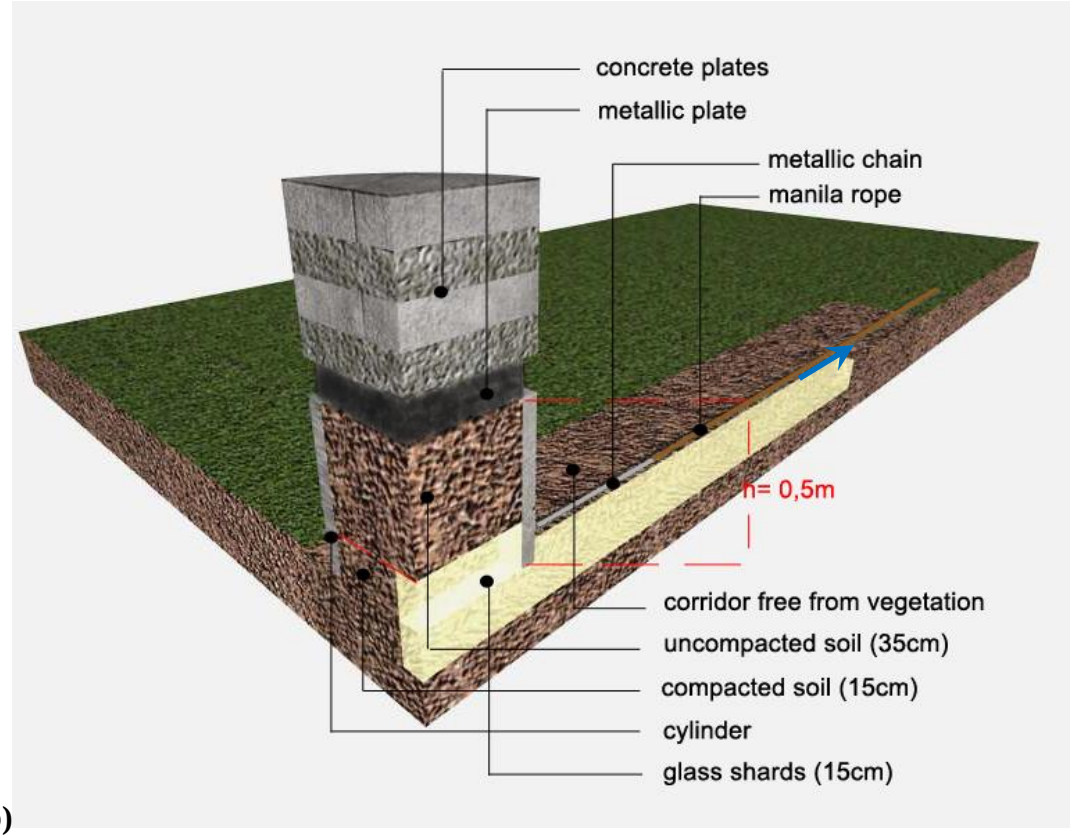

Figure 7.4: a) cylinder used with concrete slabs on top. The surficial corridor is also visible with the trench filled with glass shards in its middle. In the background, the locations of the seismometers with their dataloggers and their GPS antennas on their side can be also seen. **b)** 3D representation of a quadrant of the concrete (cross section perpendicular to and along the cylinder's movement direction). There are two interfaces; a soil-to-soil and a glass shards-to-glass shards interface

7.2.4 Experimental Procedure

The cylinder was pulled along the corridor using the same methodology as described in Chapter 6 imposing small displacements on the cylinder in the range of a few centimetres at a time. The movement took place in such a way so the glass shards of the corridor inside the cylinder and the ones inside the surficial trench were always in full contact as the cylinder never rotated around its centre. Soil friction and glass shard friction events occurred with minimal mixing of the two materials taking place. This is confirmed from Figure 7.5 where the back side of the cylinder after being displaced against the surficial corridor is shown. The glass shards of the trench are clear from soil particles.

Finally, during displacement the cylinder scraped off from the glass shard trench some glass shards that were above the ground level. These glass shards were gathered initially at the front part of the cylinder and dragged along the ground surface before they were finally positioned on the sides. This phenomenon produced interaction between the glass shards and the concrete cylinder having at a very small area compared to the glass shard interaction surface formed inside the cylinder. This is considered to have little effect on the final recordings.

Figure 7.5: View of the cylinder after it has been dragged along the corridor and the trench filled with glass shards. It is evident that the glass shards are clean, free from soil particles and the soil corridor free from glass shards. This means that during the experiment minimal mixing between glass shards and soil took place. The glass shards visible on the sides of the cylinder (at the corridor borders) are glass shards from the trench that were above the ground level and were scrapped off from the front of the cylinder during its displacement.

One experiment was conducted, with the loading parameters shown in Table 7.1. The loading conditions of the slip surface were chosen so it could be compared to the fourth cylinder experiment (simulating only soil friction events).

The difference between the loading conditions of the two different experiments was caused by the difference of the unit weight between the glass shards and the soil. As described part of the space inside the cylinder was occupied by soil in one case and by glass shards in the other. As a material, glass shards are heavier than soil leading to an increase of the total weight applied to the final slip surface. This difference is considered small to affect greatly the emitted seismicity based on the relationship between load and PSD levels during soil displacement events presented in Chapter 6. PSD plots (fig. 6.8-6.10 of Chapter 6) of soil displacement events with difference of ~100kg in the load applied on the soil slip surface show very little difference. The latter means that the 50kg load difference between the soil only cylinder experiment and the combined glass shard and soil will have an even lesser effect on the emitted seismic signals. In a real application of a glass pile within a landslide, the weight applied, and thus the stress level, at a specific depth on a glass shard surface will always be larger than the stress level applied on the surrounding soil mass found at the same depth.

Experiment	**Load (kg) on the slip surface**	**Force (kN) ($0.33m^2$)**	**Stress (kPa)**	**Simulated Depth (m) ($\gamma_{soil}=18kN/m^3$)**
4th Soil Cylinder Experiment	829	8.13	24.64	1.37
Glass Shard and Soil Cylinder Experiment	878	8.61	26.10	1.45

Table 7.1: Load, force, stress levels and simulated depth of landslide like soil friction events during the cylinder experiment with the glass shards – soil interface. For comparison, the values of the same parameters for the 4th experiment of soil-soil interface in Chapter 6 are also provided.

7.3 Data Analysis

7.3.1 Step 1: Time – frequency analysis

Figure 7.6 presents spectrogram plots of data recorded during the experiment with vertical load of 878kg applied to the slip surface between the material within the cylinder and the surficial corridor. Data presented were recorded from the vertical component of the seismometers deployed 4m and 15m away from the cylinder (source). The horizontal components are not presented here since as in the previous chapter they were found not to add information. All spectrograms presented in this chapter also share the same colour scale with the spectrograms presented in the previous chapter and are directly comparable since the experimental conditions were similar.

In all plotted spectrograms the first and last part of the total duration of the recordings consists of background noise. Spikes of reddish colour represent pulses of soil and glass shard friction signals, while in between them small background noise segments exist. Spectrograms of the rest of the sensors and experiments are presented in Appendix B1. They are not presented here because they result in the same conclusions.

Spectrograms were used to see first whether or not the combined glass shard and soil displacement events were recorded above noise levels or not, and secondly to check whether each displacement event was recorded separately from all others. Further observations such as similar frequency and spectral amplitude characteristics could also be made: A comparison between Figure 7.6a and 7.6b show the energy loss of the emitted seismic waves as they propagated away from their source (cylinder) is also notable, a phenomenon that is studied further in the next section.

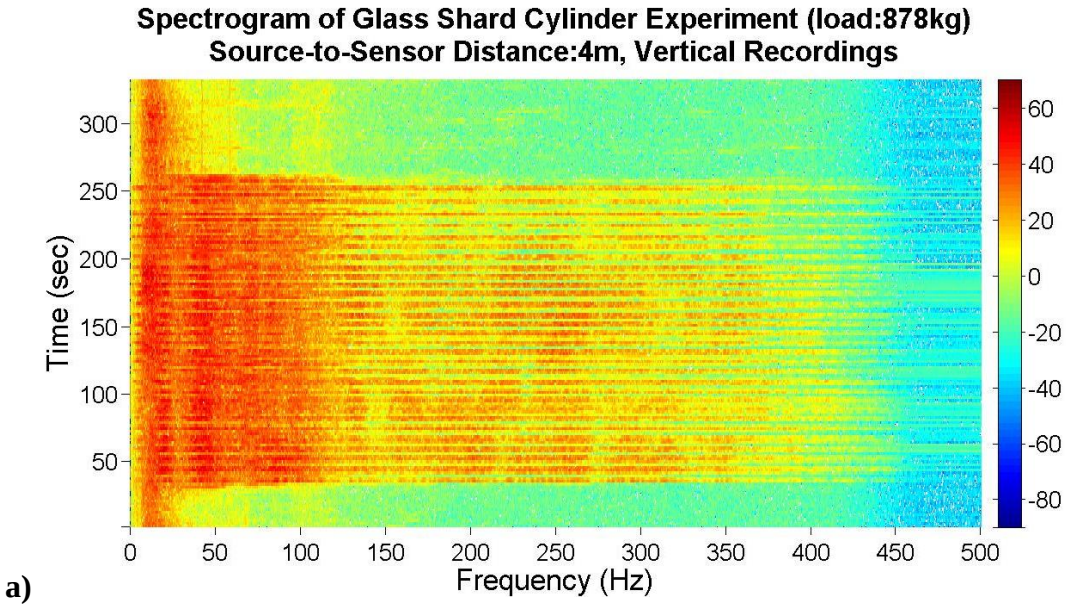

a)

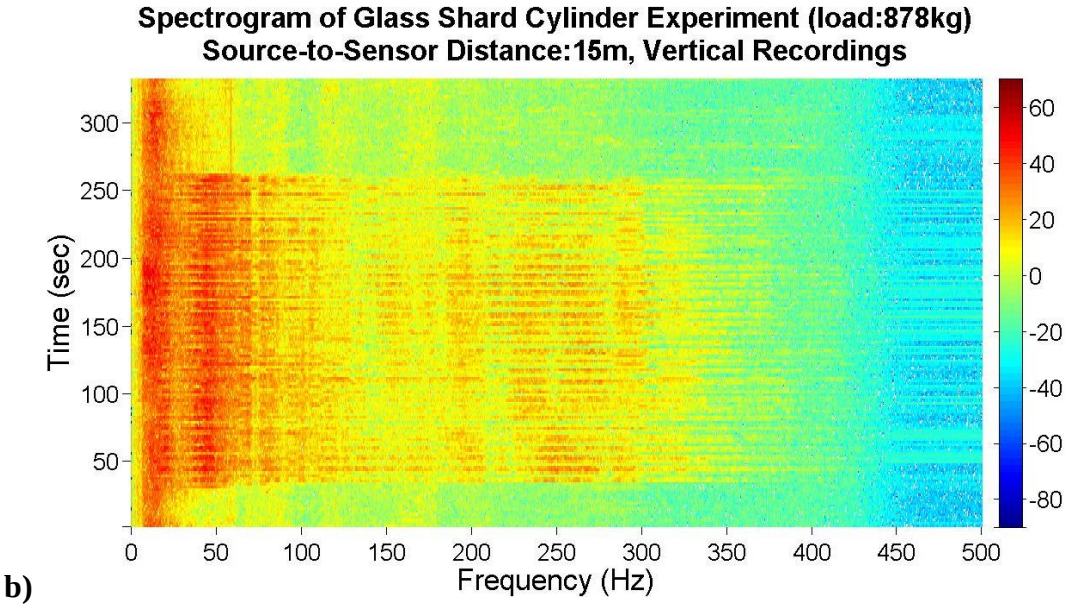

b)

Figure 7.6: Spectrograms of the glass shard and soil displacement recording with load at the soil slip surface of 878kg with data recorded (a) 4m and (b) 15m away from source from the seismometer's vertical component. The maximum frequency in the signals emitted due to glass-soil friction is up to 450Hz (fig. 7.6a). The attenuation effect as the source-to-sensor distance is increased is also visible with high frequencies (>100Hz) being attenuated more than the low frequencies.

Figure 7.7 presents the spectrograms of the data recorded during the glass shard cylinder experiment (fig. 7.7a) and of the data recorded during the soil only cylinder Experiment 4 (fig. 7.7b). Load on the slip surface during glass shard displacement was 878kg, while during the soil only cylinder Experiment 4 was 829kg. The spectrogram of the of the glass-soil slip events reveal a frequency content up to almost 450Hz while of the soil only slip events up to 350Hz. This means that slip events among glass shards produce seismic signals that have higher frequency content compared to those of only soil particles, therefore they have the potential to be easily distinguished from noise levels.

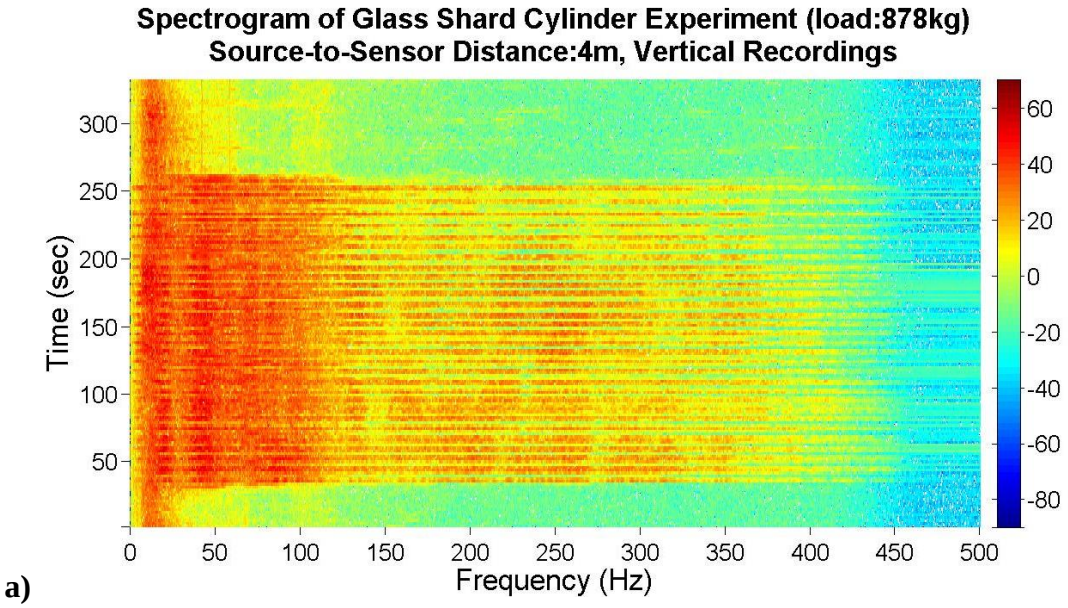

a)

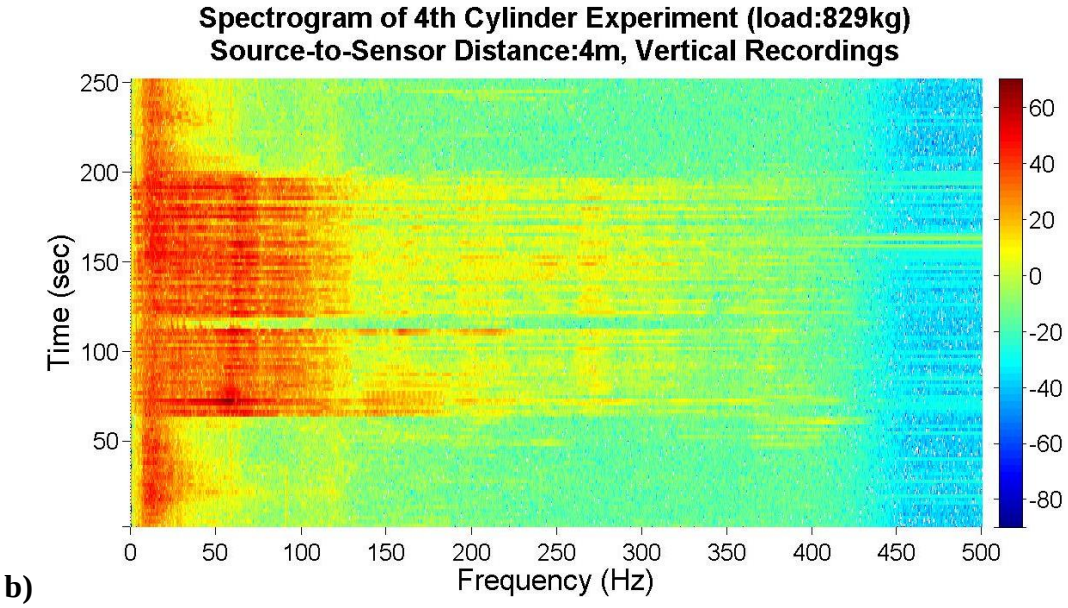

b)

Figure 7.7: Spectrograms of the data recorded during **a)** the glass shard cylinder experiment and **b)** the soil only Experiment 4 (presented in the previous chapter). Glass-soil slip events reveal a frequency content up to almost 450Hz while of the soil only slip events up to 350Hz.

7.3.2 Step 2: Frequency analysis

Detailed understanding of the recorded signals frequency content, was achieved by calculating the PSD of the recorded signals. As mentioned in section 7.2 multiple displacement events were induced between soil-to-soil and glass shards-to-glass shards material without the two interacting. These events were similar but not exactly identical. There was a variation in their time duration and the distance covered at each displacement event. However, they were induced following the same experimental procedure under the same experimental conditions, meaning that they shared the same source mechanism. For these reasons it was assumed that the emitted seismic signals had similar frequency characteristics. From the time-frequency analysis (Step 1) it was shown that this assumption is valid. This assumption allowed for the calculation of the PSD and identification of the recorded signal frequency content, using more than one displacement event.

A final goal of the spectral analysis was to compare the PSD curves produced from the data set of this experiment with the ones presented in the previous chapter to see if the seismicity emitted in the case of glass shards, is easier to record and detect than the soil displacement events. For this reason, the signal to noise ratio in the data set used for the PSD calculation had to be the same. As a result, the recordings were cropped accordingly. More details can be found at Chapter 4.

Background noise recordings were analysed in the same way as in Chapter 6. The continuous one hour noise data was merged with the one minute recordings before the start and after the end of the glass shard and soil cylinder experiment. They underwent the analysis presented in Chapter 6.

In Figure 7.8 the presented PSD curves retain the same geometry characteristics with almost no differences up until 70Hz, if the change in the spectral amplitude is not taken into account (see Appendix B2.1 for all PSD curves). Similarities in the curves exist in the remaining frequency range. Two distinct frequency maxima are visible, with one being above the noise peak at frequencies between 8-24Hz and the second being above the second lowest noise level between frequencies 35-50Hz.

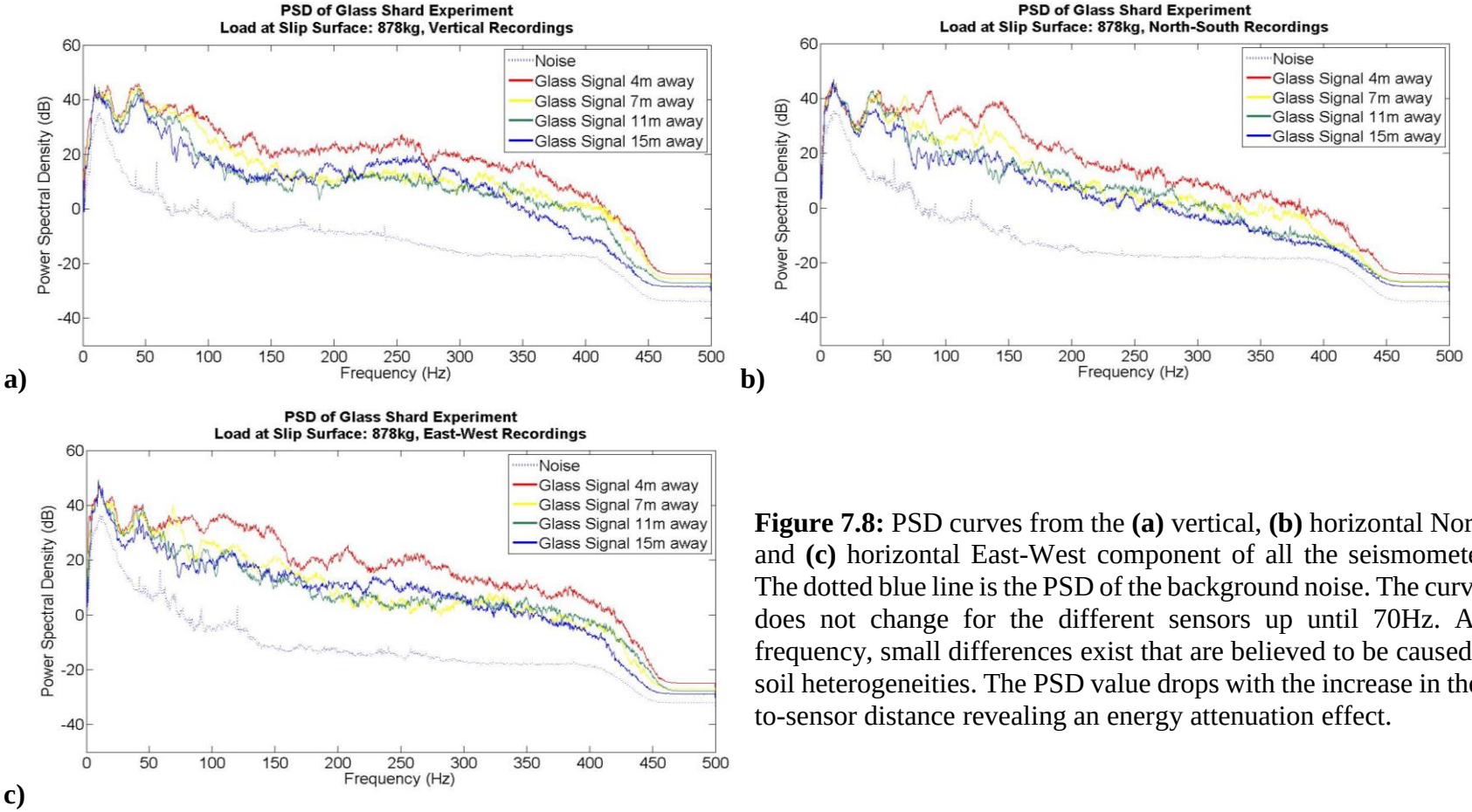

Figure 7.8: PSD curves from the **(a)** vertical, **(b)** horizontal North-South and **(c)** horizontal East-West component of all the seismometers used. The dotted blue line is the PSD of the background noise. The curve pattern does not change for the different sensors up until 70Hz. After that frequency, small differences exist that are believed to be caused by local soil heterogeneities. The PSD value drops with the increase in the source-to-sensor distance revealing an energy attenuation effect.

7.3.3 Step 3: Relationship between PSD and source-to-sensor distance

The PSD curves of Figure 7.8 present the frequency pattern of the combined glass-shard and soil slip events. In the previous analytical step these plots were used for the frequency pattern determination of glass shard and soil displacement events. In this section they will be used to reveal the loss of signal energy as it travels away from its source due to attenuation. As seen in Chapter 6, section 6.5.4, the general trend of the PSD decay as source-to-sensor distance increases remains constant and is not dependent on the frequency value. The fluctuations on some of the curves can be attributed to the effect of local soil heterogeneities and the different travel paths the seismic waves travel to be recorded on different seismometers. To visualize this better Figure 7.9 presents a closer look of the PSD curve of Figure 7.8a at the frequency range of 0-100Hz.

Finally Figure 7.10 presents the PSD curves of all components as recorded at 4m and 15m away from source (cylinder) during the glass shard experiment. There is little difference in the attenuation effect to the different components as seen in Chapter 6. Since they are affected almost equally by attenuation, the deployment of 1D sensors would be adequate to study the attenuation of the emitted seismicity.

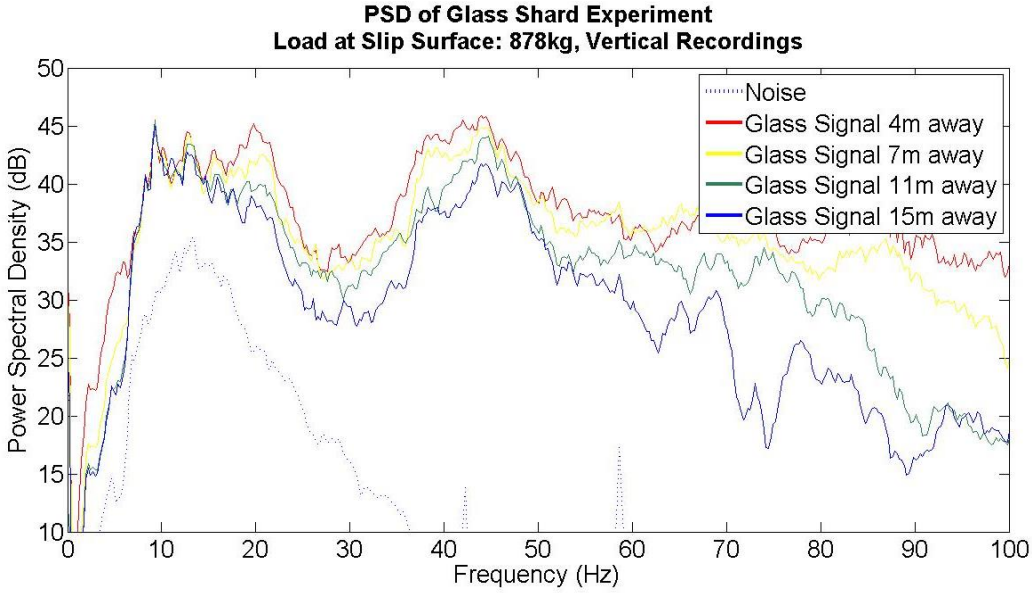

Figure 7.9: A closer look of the PSD curve of Figure 7.8a within the frequency range of 0-100Hz. The attenuation effect on the seismic signal is clearly visible as source-to-sensor distance increases.

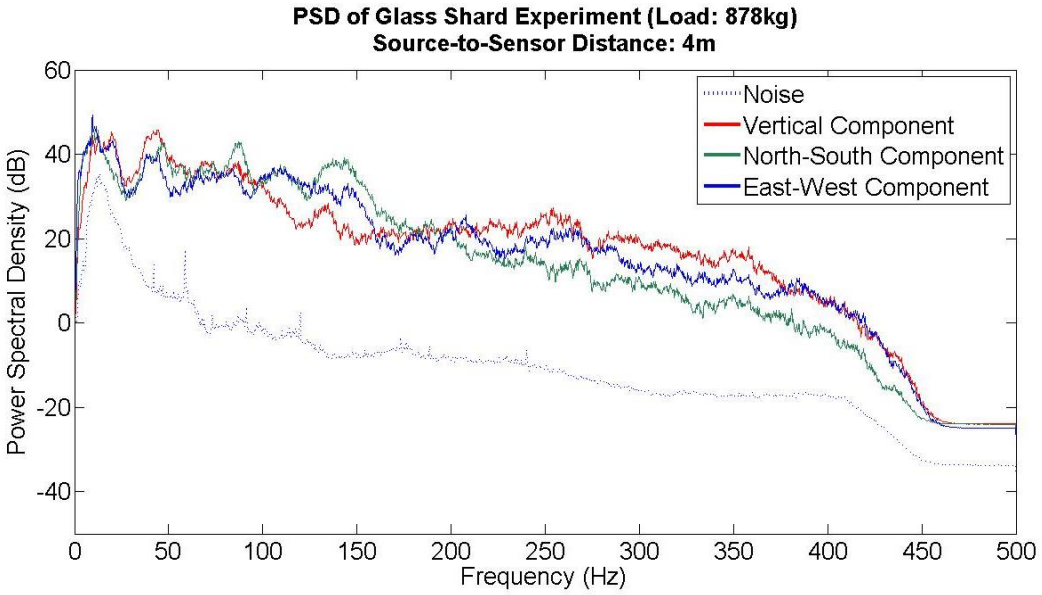

a)

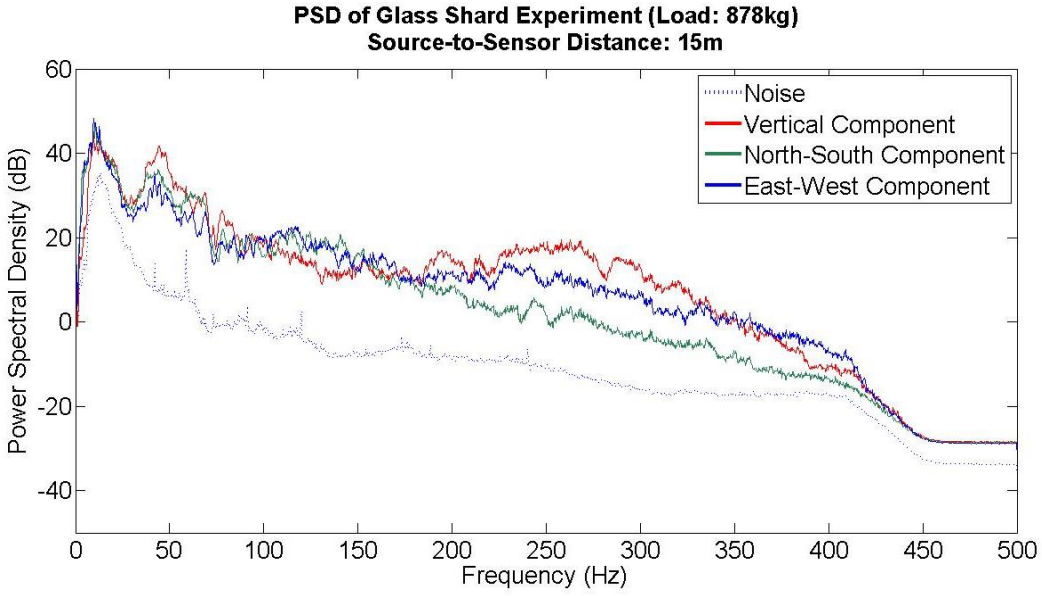

b)

Figure 7.10: PSD curves of all components as recorded at **a)** 4m and **b)** 15m away from source (cylinder) during the glass shard experiment. There is little difference in the attenuation effect to the different components meaning that the deployment of 1D sensors would be adequate to study the attenuation of the emitted seismicity.

7.3.4 Glass Shard Cylinder Exp. –VS- Soil only Cylinder Exp.

The idea of constructing piles of glass shards within the landslide mass and having combined glass shard and soil displacement events was proposed as a better solution compared to recording soil only displacements. The initial hypothesis was that slip events between glass shards can be easier detected and identified when the landslide is active compared to soil displacement events. Figures 7.11 & 7.12 present the PSD curves of noise, and the PSD curves of induced soil only slip events and the induced slip events of glass shard for all three components of the seismometers placed 4m and 15m away from the source. From these graphs one can observe three main differences in the frequency patterns of the soil-soil displacement events and the glass-soil displacement events:

Source-to-Sensor Distance: 4m

1) Peak of the PSD spectra between frequencies 8Hz to 24Hz for the glass shard slip events overlapping with the soil only slip events.

2) Decrease of the PSD spectra between the frequencies 24Hz to 35Hz for the glass shard slip events, whereas the PSD spectra of the soil only slip events continues almost flat as before.

3) There is a peak in the PSD spectra between frequencies 35Hz to 50Hz in the glass shard slip events whereas in the soil-soil events the almost flat response continues.

3) The peak at the soil only PSD spectra between 60-70Hz is considered an outlier since it is not visible at the data recorded by all other sensors.

4) In frequencies higher than 100Hz the PSD value of the glass-soil events is generally higher than the soil only slip events.

Source-to-Sensor Distance: 15m

1) As previously.

2) As previously for the glass shard slip events, while the PSD spectra of the soil only slip events is attenuated by 5dB.

3) The difference in the high frequency content (>100Hz) described previously is not visible from the recordings 15m away from source. This can be attributed to the faster attenuation of high frequencies and to the fact that the seismometers used were not designed to record accurately high frequency content.

The above suggest that the glass shard slip events are observed to be less attenuating over distance and to have a more complicated frequency pattern that allows it to be detectable over soil slip events. Observations focus on the frequency range between 8-50Hz but more research is needed to define more accurately the high frequency content (>100Hz) of the glass shard slip events and its characteristics at different source-to-sensor distances.

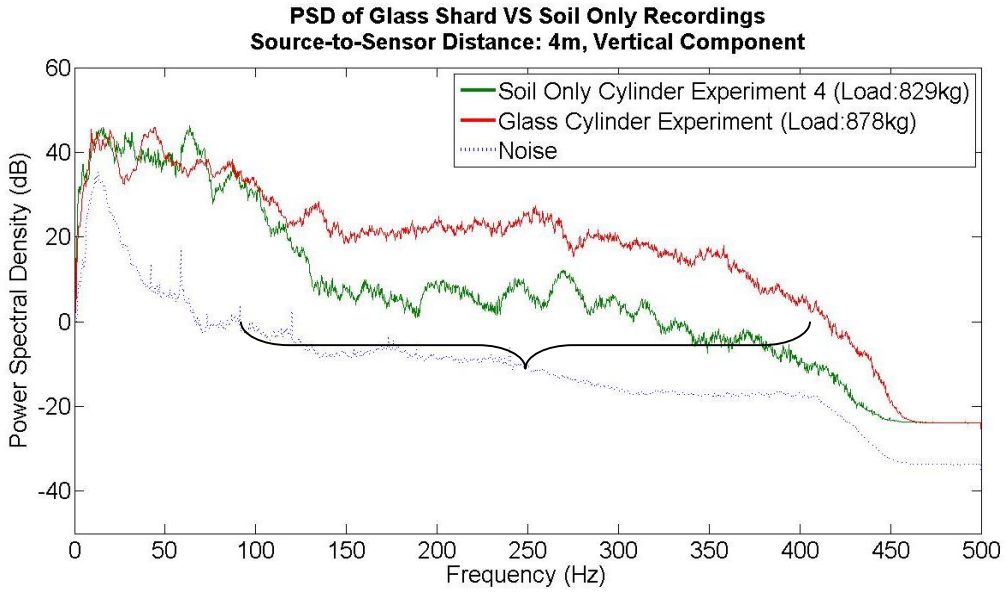

a)

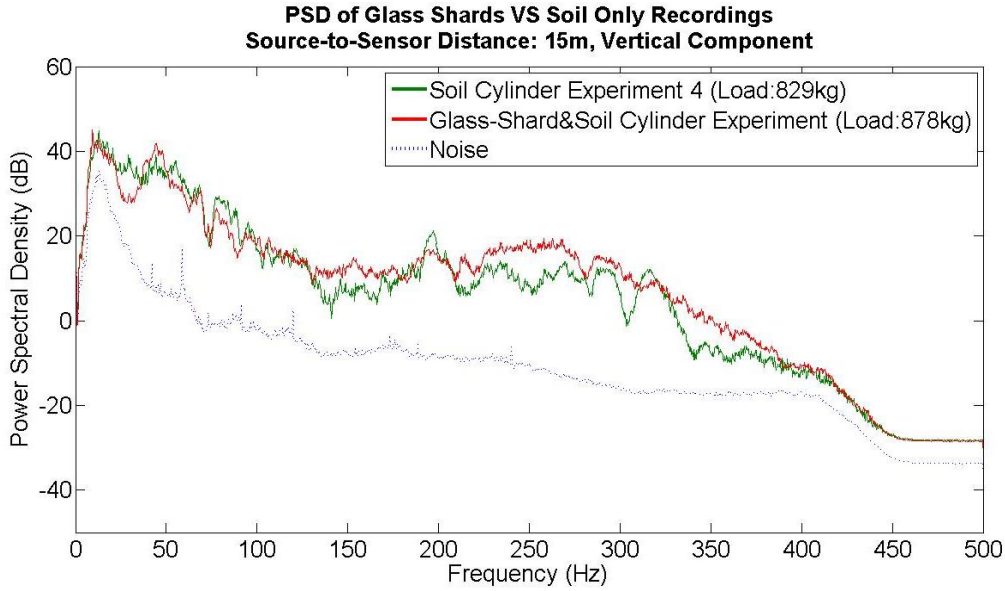

b)

Figure 7.11: PSD spectra from data recorded during the induced soil only slip events and the induced glass shard slip events by the vertical component of seismometers **a)** 4m and **b)** 15m away from source. Main difference between the two curves is the "wavy" pattern of the glass shard slip events: 1) peak between frequencies 8Hz to 24Hz, 2) drop between frequencies 24Hz to 35Hz marked with the blue and yellow line, 3) peak between 35Hz to 50Hz marked with the yellow and red line. This pattern is also clearly visible at both graphs. The peak between 60-70Hz of the soil only PSD spectra at Fig. 7.11a is considered an outlier since it is not visible at the PSD spectra of the rest of the recordings. Finally difference is the high PSD amplitude at high frequencies (>100Hz) that the glass - soil displacement events have between 100Hz and 450Hz (fig. 7.11a) compared to the soil only slip events.

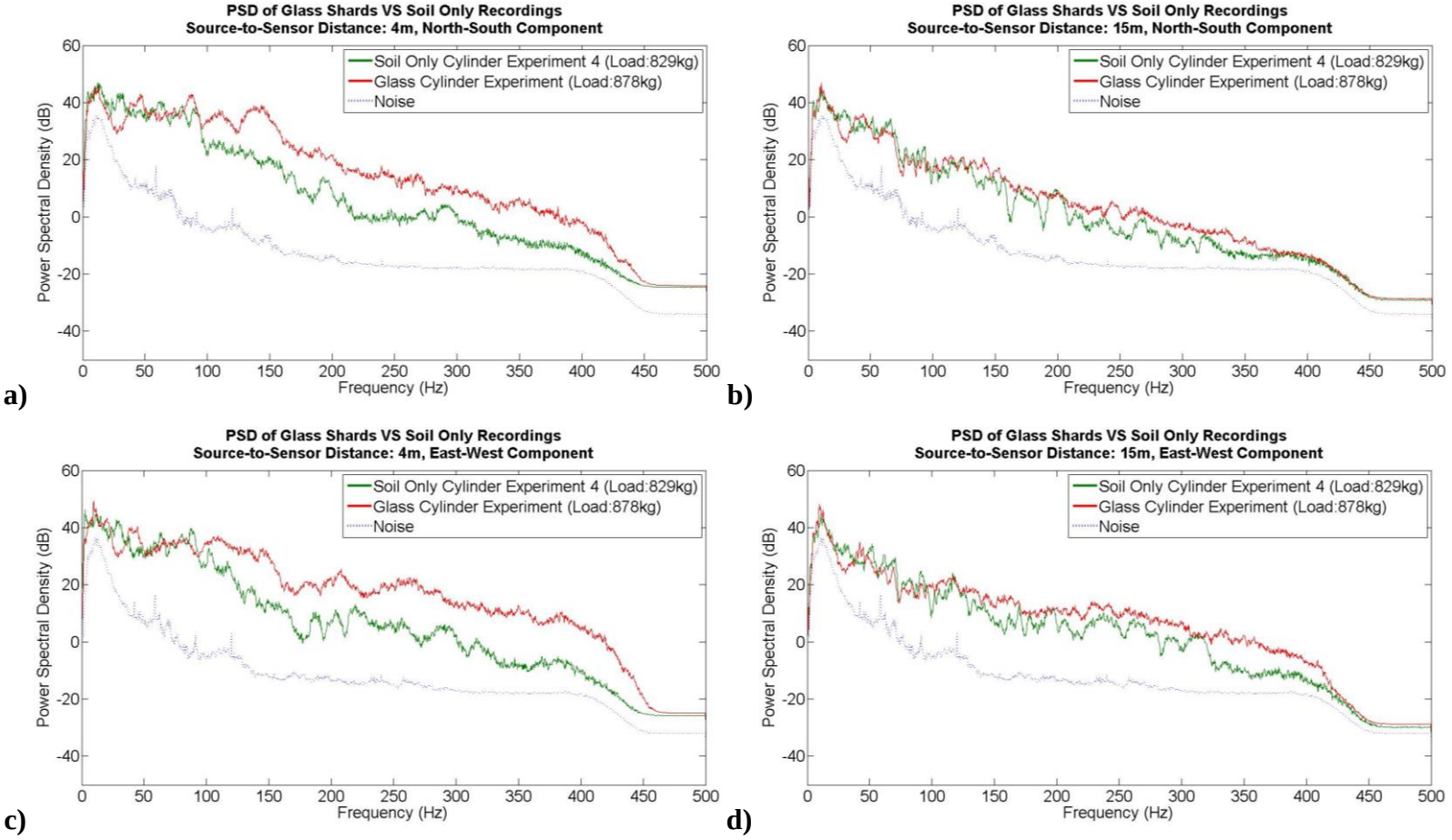

Figure 7.12: As Figure 7.11 only for data recorded by **a,b)** the horizontal North-South component and **c,d)** the horizontal East-West component of the seismometers.

There was a difference in the loading applied on the slip surface between the different experiments of 50kg. This can be considered small and still allow direct comparison. In general though, for a real case scenario where a glass shard pile would be formed inside the body of a landslide, at any given depth level, the load on the glass pile will be larger than the load on the surrounding soil. This will be caused by the difference between the unit weights of the two materials, with the unit weight of the glass shard being larger than that of the soil. The larger load on the glass shard pile will lead to larger PSD values in the recordings compared to the displacement events of the surrounding soil meaning stronger signals. The latter was proven by the relationship between load-PSD shown at Figures 6.8-6.13 in Chapter 6.

7.5 Chapter Summary

A novel methodology that utilises glass shards was presented. This methodology could enhance landslide signals and make their identification easier and more accurate. This was demonstrated by a field experiment. The initial hypothesis that the glass shard displacement events would have a distinct frequency pattern that is easier detected than soil was verified, making the idea lucrative for real seismic monitoring applications. Forming piles of glass shards inside the body of a landslide allows for immediate tracking of the slope displacements without any prior knowledge of the seismicity of the landslide or that of the general area.

Another advantage is the higher stress level that would be present at any given depth within the glass pile compared to the stress level at the same depth in the surrounding soil. This means that the energy emitted from glass friction during displacements will be higher, thus more easily distinguished from the background noise.

Finally since the location of the glass shard piles will be known a priori, locating the displacements occurring at a landslide will be easier. Even with one sensor recording the frequency pattern of the combined glass shard and soil displacement event will be

enough to attribute the event to the closest glass shard pile to the seismometer. This is important as in any other case, location analysis will require clear seismic recording of the event by four different seismometers which is not always achievable.

One disadvantage in applying glass shard piles to active landslides is the difficulty in transporting the glass shards needed for the task on the landslide and drilling the piles on unstable ground. In addition, the large inclinations found in landslides, the possible presence of rock boulders and the possibility of slope failure can complicate the application of this methodology.

Chapter 8

Seismic signature of landslides: validation based on two controlled failures

8.1 Introduction:

The experimental work presented in the previous chapters was focused on the optimisation of the detection threshold of small microseismic arrays (Chapter 5), the simulation of landslide like signals and the determination of their seismic signature (Chapter 6) and the enhancement of a microseismic monitoring system so that soil movement is easily detectable even in noisy environments (Chapter 7). This chapter is focused on three goals: 1) the identification of different types of landslide failure signals based on the controlled failure of two 2.5m vertical faces, 2) the categorisation of these events based on their failure mechanism, the soil mass involved and their frequency characteristics in order to understand which seismic recordings can be identified as catastrophic or pre-cursory events, and finally 3) the validation of the up-scaled shear box methodology presented in Chapters 6 & 7.

In the next paragraphs the methodology followed for inducing failure to the landslides is presented, as well as the findings regarding crack propagation, small displacement and failure events occurring within the failing soil mass. This is the first time a landslide failure has been induced under controlled conditions with a dense microseismic network recording the whole process.

8.2 Experimental Set-Up

8.2.1 Introduction

The design of this experiment faced two challenges: 1) the need for a slope with optimum height and gradient that would allow for an easy and uncomplicated construction and a failure within a short time, and 2) the need for the failure to be induced under controlled conditions such that no additional ambient noise would be emitted during the process, e.g. anthropogenic activities in the field.

Two methodologies were considered as potential ways to induce failure. The first was to induce slope failure by increasing the degree of saturation of the soil. Two main problems made this option unfavourable and both related to the highly porous tropical clay dominating the surficial geology of the site. First, based on preliminary numerical computations carried out by the University of Brasilia on this type of soil, a huge amount of water would be necessary to change the degree of saturation of the soil. Due to the high porosity of the soil (>55%), water would run through the soil mass to lower elevations saturating them first (Silva, 2009). Second, due to the high porosity this water would also flow in all directions. That could be a problem because of the proximity of a large construction site. The construction site was at a lower ground level and an increase in soil saturation would put their excavated slopes at risk of failure.

The second methodology was to induce failure by increasing the load on the slope's crown. This would affect only the soil at the location of the experiment and not the wider surrounding area. During the loading process, the top of the slope would be vertically displaced and should lead to small displacement events as well as formation and propagation of cracks inside the soil mass. I chose to follow this methodology.

A vertical face was chosen for the experiment as opposed to a slope for two reasons: 1) the tropical clay allowed for a stable vertical face of at least 3m in height, and 2) this geometry would lead to failure under smaller loads than any other geometry. Two "landslides", i.e. Vertical Faces, VF1 and VF2, of 2.5m height and adjacent to each other were tested, each during a separate experiment. From here onwards I refer to these experiments as Experiment L1 and L2 respectively.

All parameters i.e., local geology, the microseismic network used for the monitoring as well as the methodology used to induce failure were the same for both the L1 and L2 Experiments. The only difference between them was that inside the body of VF1, a borehole was drilled and filled with glass shards, forming a glass shard pile. This was done to provide proof of concept of the use of glass shards for landslide monitoring.

The experimental site was in the city of Brasilia (Brazil) with similar geology to the experimental site of the cylinder experiments described in Chapters 6 & 7. All experimental measurements, including noise recordings, took place between 7pm and midnight on a Saturday. No human activities were observed during that time.

8.2.2 Components of the experimental set-up

1. Hydraulic jack
2. Manually operated oil pump with mounted pressure gauge
3. Highly rigid squared metallic plate $1m^2$
4. Semi-spherical metallic plate
5. 2 highly rigid metallic cylinders
6. Highly rigid metallic beam, with an I shaped cutting, 8m long
7. 4 wooden frames capable of withstanding high vertical loads
8. 12 Π shaped construction steel beams
9. 3 foundation piles
10. Metallic measuring tape
11. Manila rope
12. Wooden sticks with a square cut 15×15cm
13. 11 short period 3D Sercel seismometers, with a flat frequency response from 2Hz to 100Hz.
14. 11 dataloggers that were set to record at 1000Hz sampling rate continuously. Seismic data of the sensors were synchronized by GPS clocks. Data loggers and GPS clocks were manufactured by RefTek.
15. 11 40Amp (12 Volt) car batteries

8.2.3 Description of Experimental Set-Up

The experimental set-up consisted of two parts:

Part 1: Three reinforced concrete piles, 0.65m diameter and 12m deep, were constructed 3m apart from each other. On the top surface of each pile, four construction steel bars were left exposed 1.5m above the ground (fig. 8.1a).

Part 2: The second part, i.e. two vertical faces, was constructed 20 days after the completion of the construction of the piles. Two reasons led to this decision: 1) the vibrations of the drilling works during the construction of the piles could have affected the stability of the vertical faces had they been constructed previously and 2) the piles should only be used 20 days after their construction to allow for the concrete to reach its full strength potential. VF1 and VF2 were formed by a vertical excavation of a 12m by 4m orthogonal area approximately 2.5m deep (fig. 8.1b). This resulted in 2 vertical faces 2.5m high and 3m wide (distance between each consecutive pile) next to each other (fig. 8.1b). The front of VF1 and VF2 was approximately 0.5m away from the three piles (fig. 8.1b).

a)  **b)**

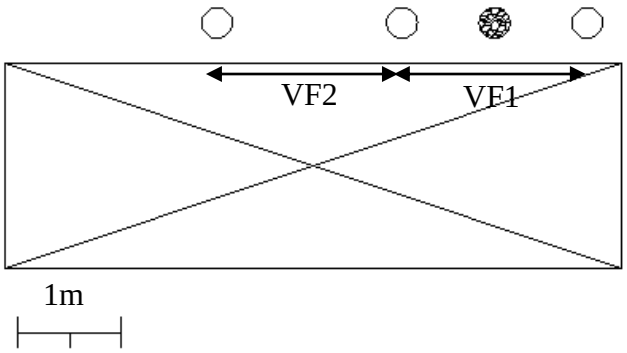

Figure 8.1: a) Three 12m deep piles with four construction steel bars exposed ~1.5m above ground level. The piles were constructed along the same line. **b)** Plane view of orthogonal excavation 12m x 4m marked by X, approximately 2.5m deep, with the three construction piles 0.5m behind the vertical face and 3m apart presented as circles. The glass shard pile is seen in line with the construction piles as a circle filled with coarse particles, 0.5m away from VF1 and in the middle of the distance between two piles.

On top of the piles a high rigid I shaped metallic beam was placed supported by wooden stands at a levelled position (fig. 8.2). A test conducted at the site showed that three of these stands were able to fully support the metallic beam. As a factor of safety, four wooden stands were used for support.

The construction steel bars within each pile were placed either side of the metallic beam as shown in Figure 8.2 and welded against it with the help of 12 Π shaped construction steel bars (fig. 8.3a, 8.3b). This way, any vertical movements of the beam were restrained.

Figure 8.2: I shaped metallic beam placed on top of the three piles at a levelled position with two construction steel bars at either side of it. The weight of the beam was supported by four wooden stands, which restrained the beam from moving downwards. The wooden sticks on the left were used to keep the beam levelled.

a)  b) 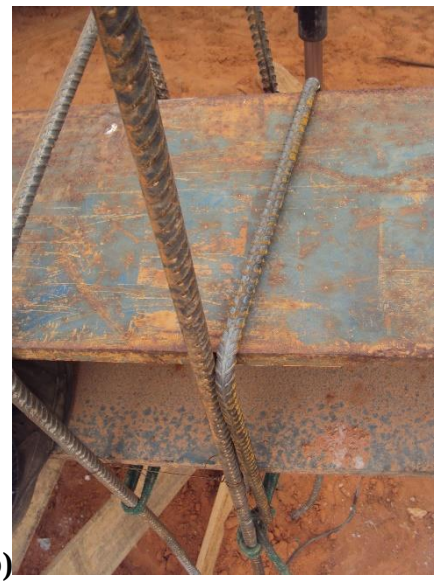

Figure 8.3: a) Π shaped construction steel bars were used for welding two of the pile's construction steel bars on either side of the metallic beam. The Π shaped bars were also welded on the beam. A total of 12 Π shaped bars were used to weld the beam on the construction steel bars of all piles. After welding no vertical movement of the beam was possible.

Below the metallic beam and in each pair of consecutive piles a soil area of $1m^2$ was levelled. On the levelled surface a rigid $1m^2$ square metallic plate was placed (fig. 8.4). This formed the base for the installation of a hydraulic jack (fig. 8.4), which was in turn connected to a manually operated oil pump. A measuring tape connected to the I shaped metallic beam and the hydraulic jack was used to provide information on the extension of the latter (fig. 8.4). This set-up was reconstructed for the needs of Experiment L2 between the second pair of piles. A photo of the experimental site with both vertical faces visible and the loading mechanism in place for Experiment L1 can be seen in Figure 8.5.

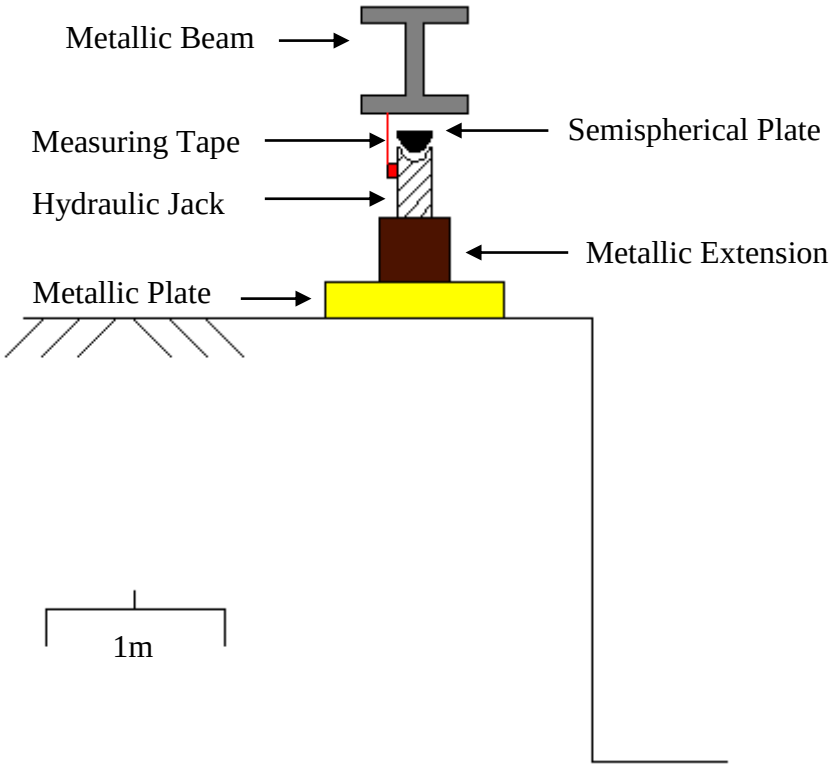

Figure 8.4: Drawing of the loading mechanism (mobile parts).

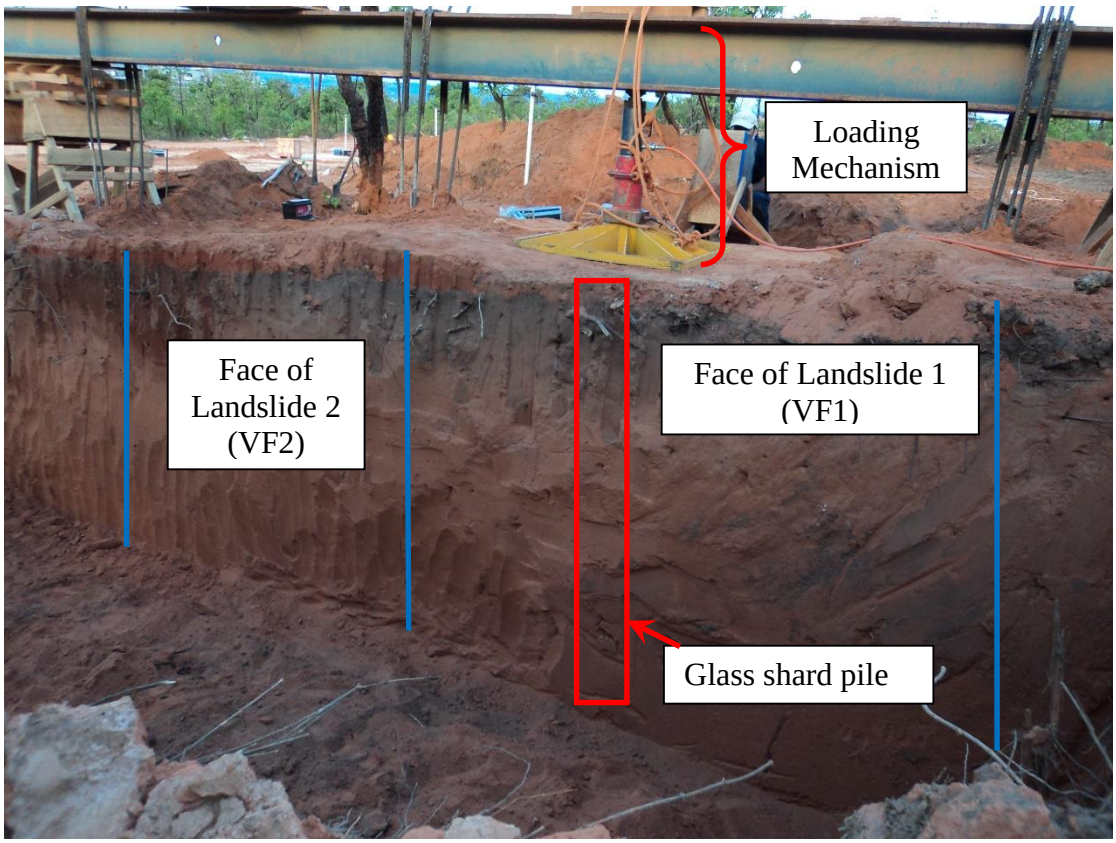

Figure 8.5: VF1 and VF2 for Experiments L1 and L2, respectively. VF1 had a glass shard pile in its mass, under the centre of the metallic plate that was in the middle of the VF1 span as shown. Failure was induced first to VF1 without though inducing failure to the glass shard pile. The loading mechanism is in place with all movable parts tied to the metallic beam with manila rope. Experiment L2 and VF2 took place afterwards with the same loading mechanism set-up, but in this case located above VF2.

Using the oil pump, the hydraulic jack was extended, pressing against the I shaped metallic beam on its top and the metallic plate at its bottom. Because all upward movements of the metallic beam were restrained, the extension of the hydraulic jack resulted in only a downwards movement. The increase in the pressure in the hydraulic jack resulted in an increase in the induced displacement on the top surface of VF1 (or VF2 for Experiment L2) and eventually led to failure. The use of a manually operated pump ensured that no additional ambient seismic noise was produced. The vertically

applied load was monitored using the gauge on the oil pump while the incurred vertical displacement was measured using the metallic measuring tape.

It was very important that all mechanical parts for the application of the load were levelled for two reasons:
1) To assure that the load would be applied vertically to the crown of VF1 and/or VF2. With this achieved, the reading at the oil pump gauge is representative and correct. In the opposite case, the load would be applied with an inclination. This would mean that the total load would be split into a vertical and a horizontal component. It would be the vertical component that would induce failure. The value of the vertical component could not be estimated.
2) For health and safety reasons. A perfectly vertical set-up minimises the chances of accidents due to misalignments. In a non-vertical setting the horizontal component would move the set-up laterally. If this horizontal force overcame the friction, part of the loading mechanism could move. Under high loads this movement could be abrupt and possibly lead to some of the parts shooting into the air and causing injuries.

All parts of the loading mechanism were tied with manila rope to the metallic beam (fig. 8.5). In the event of the soil below the metallic plate failing, the part of the loading mechanism located on the metallic plate would fall inside the excavation. This would result in undesirable signals related to the impact of the equipment as it hit the ground and not related to the soil failure.

8.2.4 Set-up for the verification of the glass shards methodology

In VF1 a 2.5m deep and 25cm diameter borehole was manually excavated exactly below the location of the metallic plate and hydraulic jack using a drill. The borehole was then filled with glass shards up to the first 2.5m from bottom (fig. 8.6&8.7a). The remaining empty space within the borehole was filled with soil (fig. 8.7a). This was done to avoid direct loading of the glass shard pile from the movement of the hydraulic jack. The glass shard pile was intended to follow the vertical and horizontal displacements of the vertical face as would happen in a real landslide. The vertical

displacement of the landslide would lead to “crushing” part of the glass shard pile at its lower point where stress would be larger and to “tilting” its upper part due to the horizontal displacement of the landslide (fig. 8.7b). If VF1 would be displaced, so would the glass shard pile, with both of them failing at the final stage of the experiment.

Figure 8.6: Manually excavated 2.5m deep, 25cm diameter borehole. The first 2m from bottom were filled with glass shards and the remaining 0.5m with soil. The glass shard pile was exactly below the hydraulic jack.

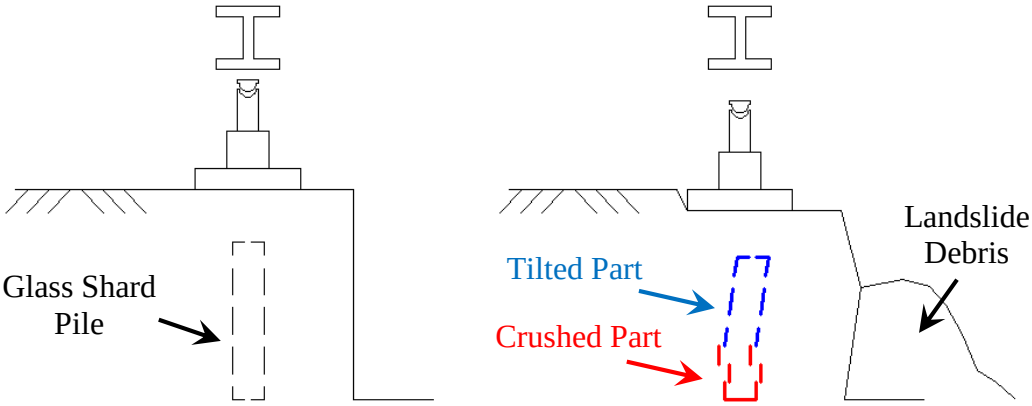

a) **b)**

Figure 8.7: Experimental design for Experiment L1. **a)** Embedded glass shard pile below the loading mechanism. No loading is applied at this stage. **b)** VF1 after loading starts. The landslide undergoes vertical and horizontal displacement and along with it so should the glass shard pile.

8.2.5 Monitoring

Eleven 3D short period seismometers were deployed following the same procedure as described in Chapter 6. Only the deployment geometry was different.

A dense deployment geometry that combined different size seismic monitoring arrays was designed to ensure recording of all types of expected events, e.g. crack formation and propagation (pre-cursory events), small or large displacements and failure events. The location of all seismometers used relative to the location of the vertical faces can be seen in Figure 8.8. The sensor numbers and their distances from the pile between the two vertical faces are presented in Table 8.1. The difference in distance between the middle point of each vertical face to any seismometer is very small (<0.5m). Only sensors No7, 10 and 11 have a +1m (or -1m) to VF1 or (VF2) compared to the values shown in Table 8.1. Such differences though can still be considered small according to the findings of Chapter 6 presenting PSD curves of the same source (shear of soil) recorded at different source-to-sensor distances.

This geometry allowed for the formation of three arrays. First, if all sensors are combined together, forming a microseismic array with approximately 5m to 10m spacing (fig. 8.8a). This technique is used to cover an area that might be of interest without knowing a priori the location of the seismic source. Second, two separate microseismic arrays, each consisting of 4 sensors, with aperture size 10m and 20m (fig. 8.8b), respectively. This deployment technique is used when a location solution is needed using the minimum number of sensors. If the source is close to this type of array (~80m away based on the findings of Chapter 5) P-wave arrivals can be used to calculate hyperbolas and locate the recorded seismic event. Third, a linear array (fig. 8.8c) consisting of sensors at distances 10m, 15m, 20m and 30m from the excavation and allowing detailed study of the emitted landslide signals, e.g. the study of the attenuation effect. One seismometer was finally placed inside the excavation at a different elevation than the rest. This was done to study any differences between deployment of sensors behind and in front of a landslide's face and to assure that the smallest failures expected to emit weaker signals would be recorded.

The deployment geometry did not change for the duration of Experiments L1 and L2 in order to avoid small differences in the orientation and levelling of the seismometers, thus allowing for direct comparison between results.

A video camera was placed inside the excavation looking at the vertical faces and was recording continuously. Unfortunately, the quality of the video recordings was sufficient only during Experiment L1. There was not enough daylight to allow for good quality video footage for Experiment L2.

Sensor No	**Distance from the pile between the two landslides (m)**	**Sensor No**	**Distance from the pile between the two landslides (m)**
1	10	7	20
2	15	8	26.5
3	20	9	43.5
4	30	10	36
5	17.5	11	10.5
6	26.5		

Table 8.1: Seismic sensors deployed in the field and their distance from the pile between the two vertical faces.

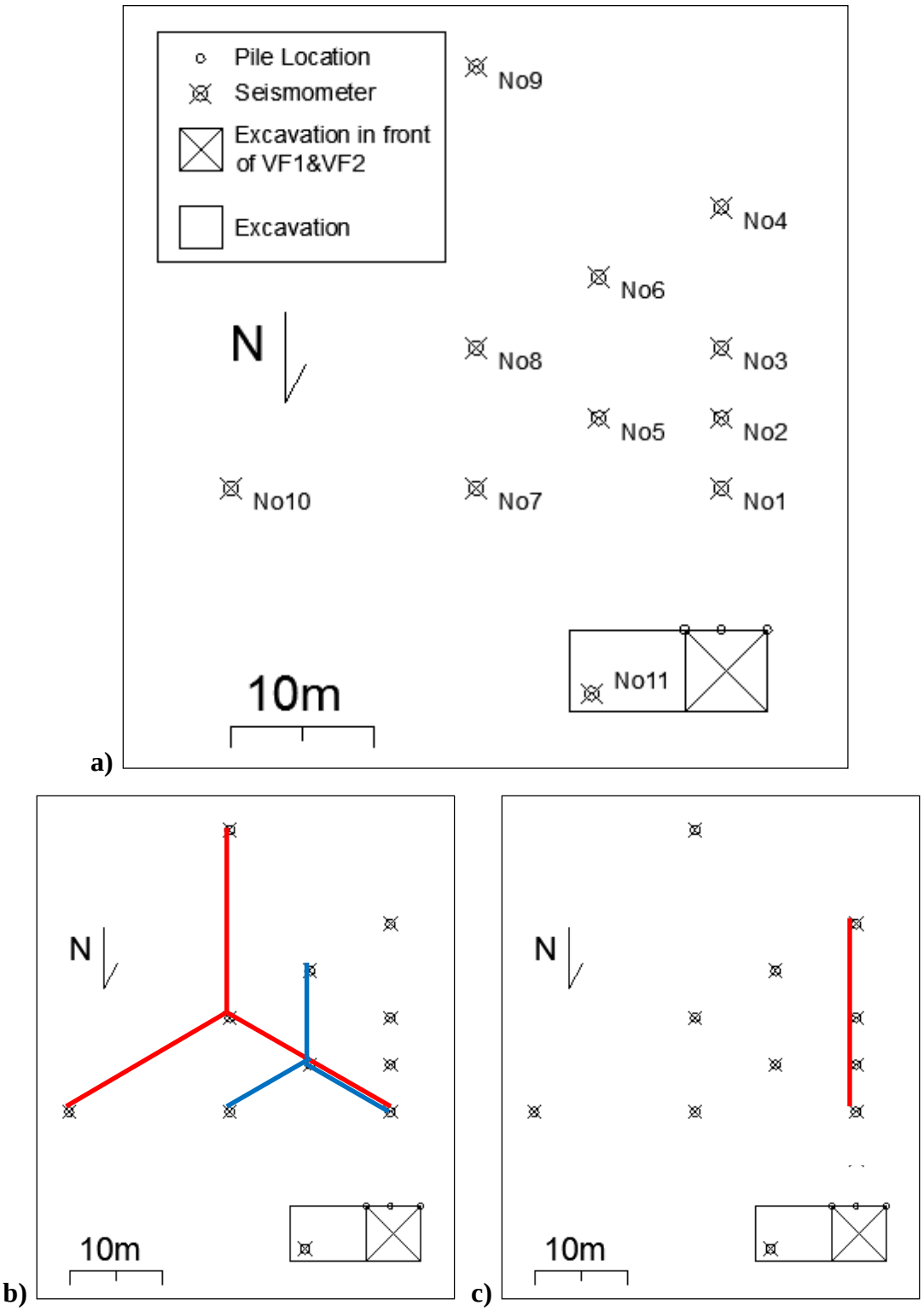

Figure 8.8: Plan view of the experimental site. **a)** Deployment geometry of seismic sensors, forming a microseismic array. **b)** Seismic sensors forming two smaller microseismic arrays with aperture sizes 10m (Blue lines) and 20m (Red lines), respectively. **c)** Linear array.

8.2.6 Experimental Procedure

The procedure followed during the application of the vertical load on the crown of the landslide was the same for both Experiments L1 and L2 and is presented below:

Step 1:

After finishing with the experimental set-up and the deployment of the seismometers, one hour of background noise measurements was conducted. These recordings took place before the start of the experiments and were used for the characterization of the site background noise.

There were no other people on site except for the 5 people conducting the experiment. The workload was distributed as follows: One person was positioned behind the loading mechanism observing the indications of the measuring tape, thus the vertical displacement of the crown of the vertical face. One person was operating the oil pump. One person was observing the vertical face from the side. One person was taking photos of the vertical face at a location exactly opposite across. Finally, one person was keeping field notes of the behaviour of the vertical face (e.g. visible crack propagation, recording the values of the vertical displacement and the load applied) and was also positioned opposite the vertical face.

Step 2:

Once everyone was at their posts, one minute of background noise was recorded. This was done to mark the start of the experiment in the seismic recordings and for additional data for noise characterization.

Step 3:

During the loading process, load increase took place in steps of 10kN starting from 0kN load. This loading step was considered small enough to allow small displacements and crack formation inside the soil.

Step 4:

After each loading step the vertical displacement reading was observed for at least one minute. If there was no displacement during this period, Step 3 was repeated. This was done to ensure that phenomena like small displacements would develop for every small loading step, without being affected by the next loading step.

Step 5:

Steps 3 and 4 were repeated until failure occurred or the hydraulic jack was fully extended. In the first case, the experiment was completed. In the second case, the experiment was stopped, the hydraulic jack was removed and a metallic cylinder was placed in its place. Then the hydraulic jack was placed on top of it. This was done to replace the length of the extended hydraulic jack and allow for the jack to be able to apply additional load and displacement to the crown of the landslide. Then the experimental procedure was repeated from Step 1.

There were a number of points at which the experiment was stopped for health and safety reasons, e.g. to check whether the mobile parts of the loading mechanism were still levelled. At these times the experiment was stopped and the experimental procedure started again from Step 1. These time segments were excluded from the data analysis.

8.3 Data Collection

The type of data collected were similar to Chapter 6. Total length of the seismic recordings was 9 hours. Analytical field notes were made during all experimental processes marking the starting and ending time of all experimental measurements and events. Data recorded manually were the loading and displacement values during the experiments and any visual observations of the behaviour of the vertical faces, e.g. crack formation/propagation or failure. Time was kept using a hand held GPS clock to ensure synchronization with seismic recordings.

Finally video recordings were made for the duration of all four experiments using a digital photographic camera looking at the cross-section of the vertical face. This was to ensure that the procedure was concluded normally and check for errors during the analysis stage. Video recordings were synchronized with the seismic recordings using the main failure events recorded in the field notes. Unfortunately the video monitoring only proved useful for Experiment L1 when natural light was still available. The artificial lighting system in place was not enough for such observations.

8.4 Data Analysis

A preliminary analysis, similar to that described in Chapter 6, was conducted as a first step in order to prepare the raw data for the main analysis.

8.4.1 Step 1: Analysis in the time-frequency domain

Figure 8.9 presents spectrograms of the first part of the dataset recorded by sensor No1 (~10m away from the middle point of both vertical faces) during Experiment L1. All three components of the seismometer are presented. The spectrograms of the remaining dataset recorded during Experiments L1 & L2 were similar to those of Figure 8.9. The spectrograms of both experiments from data recorded by sensors No1 and No11 are included in the Appendix C1. These sensors were closer to the both landslides and had the larger possibility of recording landslide related seismic events. For this reason only their data are presented in the Appendix C1. They are not presented here since spectrograms were used mainly for manual detection of seismic events and the optimum data to use were those of seismometer No1 being closer to both Vertical Faces (VF1 & VF2). As mentioned earlier the experimental measurements sometimes had to be stopped (for safety or because the hydraulic jack was fully extended). This is why the data presented in the spectrograms are divided into segments. As a result, Experiment L1 was split into 7 segments with duration ~32, ~17, ~6, ~21, ~11, ~7, ~2 minutes (fig. 8.10). Experiment L2 was split into two segments with durations ~41 and ~20mins (fig. 8.11). All spectrograms have the same colour scale that spans the spectral amplitude of events.

All spectrograms plotted (Appendix C1) reveal a very complex data set with many recorded events. It is difficult to characterize them and divide them into groups, e.g. noise, landslide failure, landslide movement etc. just by looking at the spectrograms and the waveforms. An argument for different types of recorded events could be built based on frequency content and spectral amplitude correlating them with events from previously published studies. However, in this study, visual observations were used along with the obtained loading and displacement curves to interpret the seismic data.

The results from the cylinder experiment filled only with soil (Chapter 6) were not used to interpret the events of these experiments. The results of this chapter are compared with the results of Chapter 6 later to validate the cylinder methodology.

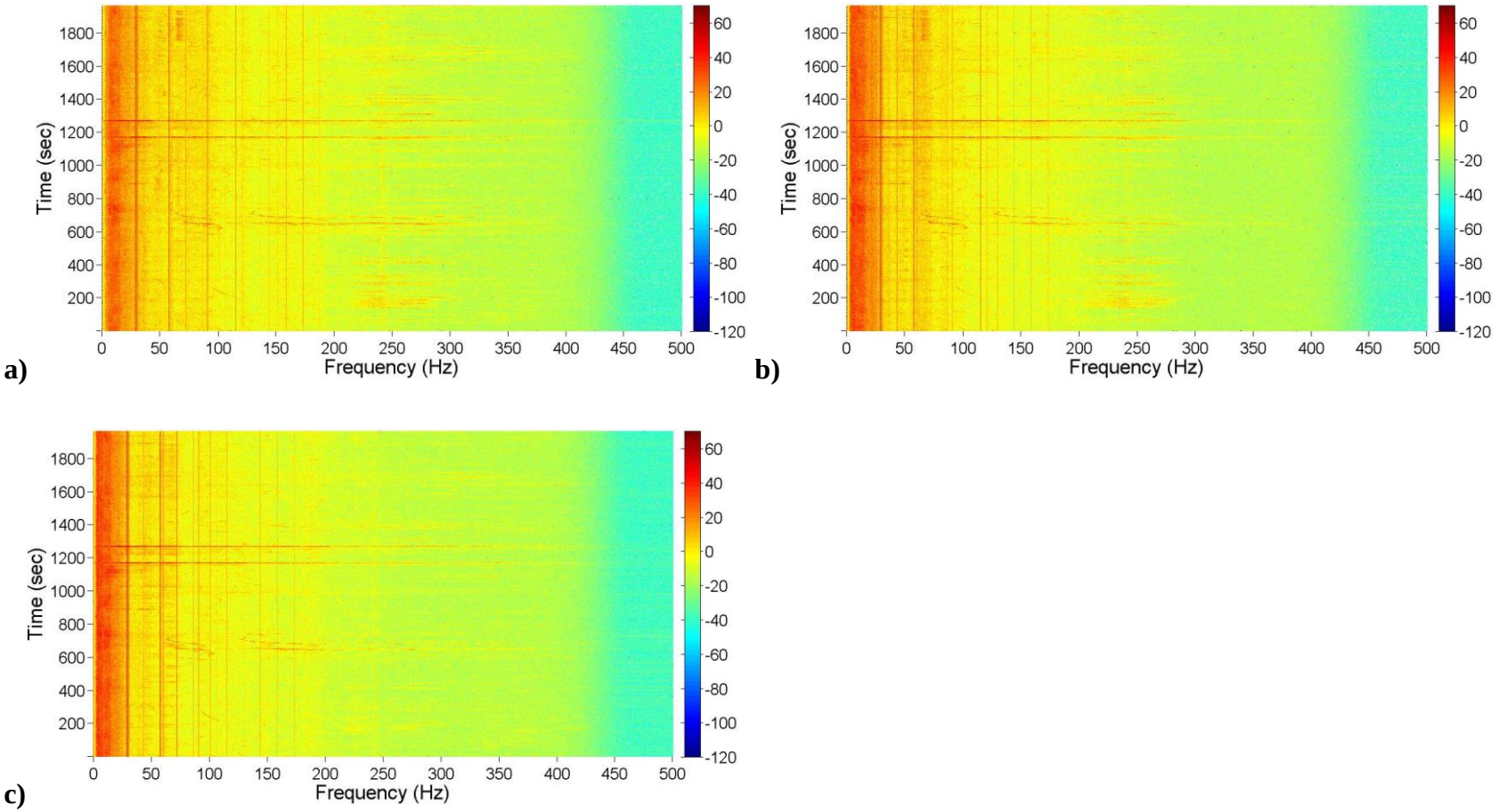

Figure 8.9: Spectrograms of the first segment of the seismic data recorded during Experiment L1 by sensor No1 (~10m away from both landslides) visualising **a)** Vertical component, **b)** North-South component, **c)** East West component. Multiple events are visible (red lines parallel to the frequency axis) but are hard to interpret using only the spectrograms.

8.4.2 Step 2: Analysis of visually observed failures

This step of the analysis aims to identify and characterise the recorded events based on visual inspection. During the conduction of both landslide experiments, landslide failure events were visually identified and recorded in the field notes. These failure events were captured by video recordings or/and photographs when light conditions allowed it. The time of origin of these events was noted with the use of a GPS clock that helped to correlate between the field notes and the seismic data and can be seen on Figures 8.10 & 8.11 for the landslide with the glass shard pile and the soil only landslide respectively. In total 3 different Failure Types (FT) were observed: a) FT1: Crack Formation/Propagation Events, b) FT2: Soil Block Topple and Fall Events, c) FT3: Soil Block Fall Events. They are all described in this section analytically.

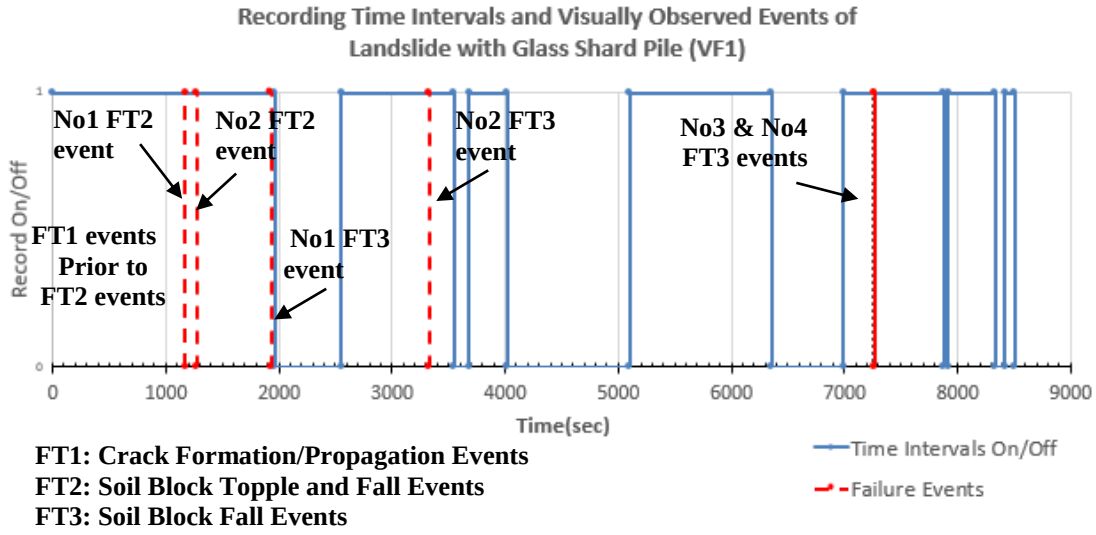

Figure 8.10: Time line of intervals when no additional background noise was present in the field during the induced failure of the landslide with the glass shard pile (Vertical Face 1, VF1). Annotated are the times when the visually observed failure events occurred.

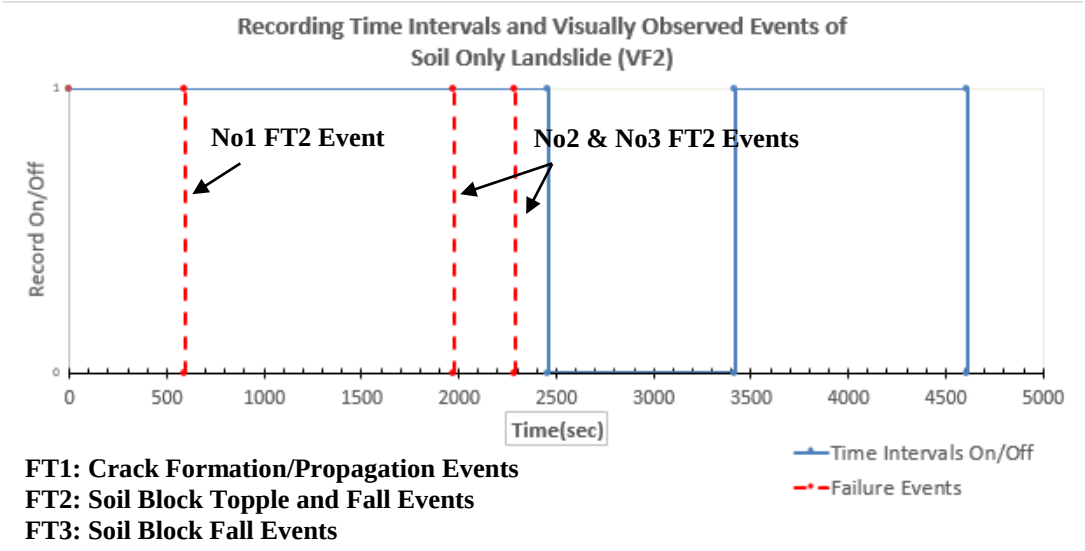

Figure 8.11: As for figure 8.10 only for the soil only landslide (Vertical Face 2, VF2).

FT1: Crack formation/propagation

As the vertical load and displacement of the landslide's crown was increased cracks started to form (fig. 8.12b, 8.13b). Initially cracks were observed at the bottom of the vertical face and they propagated up to the crown of the landslide (fig. 8.12c, 8.13c-to-8.13d). During propagation the "older" part of the cracks was getting wider and easier for the eye to see. When the cracks reached the landslide's crown they stopped propagating but continued to get wider (fig. 8.13d-to-8.13f). This process was observed only during the first part of the Experiment L1, at Vertical Face 1 (VF1), due to favourable light conditions. In the absence of natural light, the light from the available field lamp was not strong enough for such observations. Cracks are believed to have formed inside the landslide mass as well, but they were not visible. As cracks formed and propagated in VF1, there were 6 times when soil was observed bursting out of them in the form of dust (fig. 8.12b, 8.12c, 8.13b). The time these soil bursts occurred was noted and was correlated later with the seismic recordings.

a)

b)

c)

Figure 8.12: Experiment L1. **(a)** Face of VF1 without any formed cracks due to low loading/deformation. **(b, c)** Crack formation and propagation events annotated by red arrows starting from the bottom of the VF and going up. Soil bursted out of the crack in the form of dust due to the slope's displacement.

Figure 8.13: Experiment L1 **(a)** Face of VF1 without any cracks formed due to low loading/deformation. **(b, c, d, e, f)** Crack formation and propagation events starting from the bottom of the landslide's face and going up. As the crack was propagating the older parts of the crack were getting wider. During the crack formation/propagation soil bursted out at times due to the slope displacement.

FT2: Soil block topple and fall

Failure Type 2 (FT2) involves soil block toppling and falling as well as shear between the soil mass involved, occurring immediately after cracks were fully formed in Vertical Face 1 (VF1). The cracks had marked the area on VF1, where a FT2 event was about to take place. As vertical displacement was increasing FT2 occurred (fig. 8.14a, 8.15d&e). The cohesion of the soil was retained after the detachment of the soil volume from VF1 with the soil mass forming soil blocks that initially toppled before reaching the ground (fig. 8.15f). This failure type occurred only twice during Experiment L1 and were the only two failures that included such large soil volumes.

a)

b)

Figure 8.14: The FT2 No1 failure event (FT2: soil block topple and fall), Experiment L1. After cracks surrounded a volume of soil, it was detached from the vertical face of the landslide. The FT2 No2 involved **a)** soil blocks toppling and **b)** falling on ground surface and was the most complex one observed in both landslide experiments. FT2 No1 was one of the two largest failure events that occurred during both Experiments L1 & L2.

Figure 8.15: The FT2 No2 failure event (FT2: soil block topple and fall), L1 Experiment. **(a)** VF1 after Failure 1, **(b)** Crack just before FT2 No2 took place, **(c)** Soil blocks 1&2 detached from VF1, that toppled and fell on the ground surface milliseconds before the main landslide failure event occurred. These events were considered part of the main Failure 2 event. **(d, e)** Main part of soil mass consisting FT2 No2, involving soil block topples and falls. FT2 No2 failure event along with FT2 No1 were the two largest failure event that occurred during Experiments L1 and L2.

FT3: Soil block fall (without toppling)

This was the most common failure mechanism observed in both landslide experiments. It involved having parts of both Vertical Faces (VF1 & VF2) falling on the ground surface (fig. 8.16, 8.17). Failure No.1 of VF1 was the largest soil block fall observed (fig. 8.17).

a)

b)

Figure 8.16: Photos of FT3 No4 failure event during Experiment L1 before (a) and after (b) with the soil block that fell inside the excavation indicated with a red box.

a)

b)

Figure 8.17: Photo before (a) and after (b) FT3 No.1 failure event of Experiment L2 (FT3: soil block fall). This was the biggest failure event occurring in this slope and the biggest failure event of FT3.

8.4.3 Step 3: Interpretation of Spectrograms based on visual observations

For the failure events that were detected visually, the recorded GPS time of origin was correlated with the seismic recordings. Figures 8.18 to 8.20 present spectrograms from different parts of the recordings with the failure events annotated. Data visualised belong to sensor No1, the closest one to both slopes (~10m away). This was chosen because it was the sensor that recorded all Failure Types (FT) clearly thus allowing comparison of the spectral characteristics between events.

FT1: Crack Formation/Propagation

The time of the observed crack formation/propagation incidents was correlated with the seismic recordings. At both times when FT1 events were observed they led to an FT2 event (FT2: soil block topple and fall). These FT2 events were the first big events to be observed on Vertical Face 1 (VF1) and will be named FT2 No.1&No.2 failure events. Figure 8.18 present the spectrograms of all three components of sensor No1. Black arrows annotate the FT2 No.1&No2 failure events. The red spikes before those events belong to FT1 events. The duration of the FT1 type events is smaller in duration and weaker in spectral amplitude compare to the FT2 No.1&No2 failure events. Their frequency content (analysed in section 8.4.4) is also smaller (mostly <150Hz).

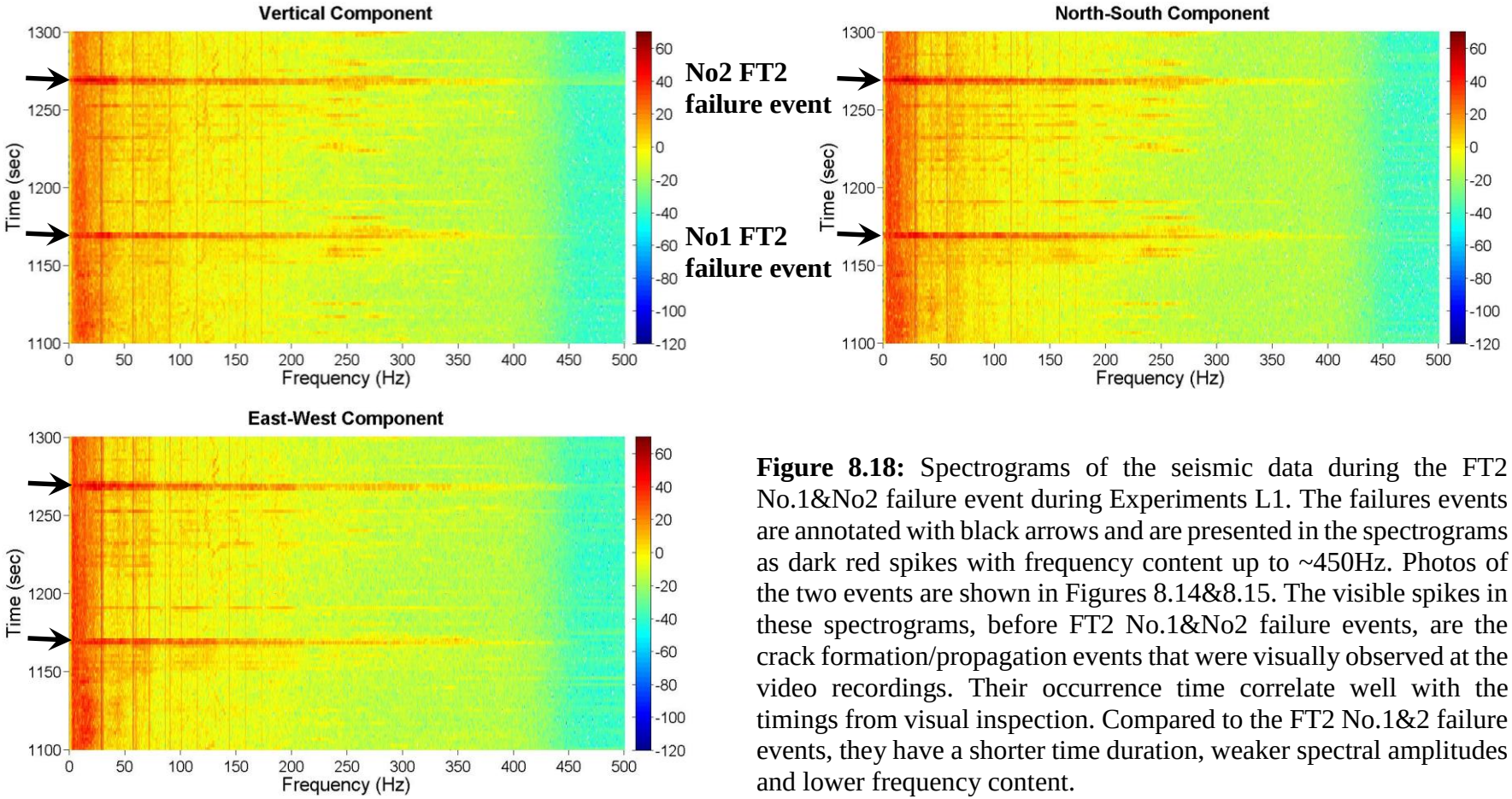

Figure 8.18: Spectrograms of the seismic data during the FT2 No.1&No2 failure event during Experiments L1. The failures events are annotated with black arrows and are presented in the spectrograms as dark red spikes with frequency content up to ~450Hz. Photos of the two events are shown in Figures 8.14&8.15. The visible spikes in these spectrograms, before FT2 No.1&No2 failure events, are the crack formation/propagation events that were visually observed at the video recordings. Their occurrence time correlate well with the timings from visual inspection. Compared to the FT2 No.1&2 failure events, they have a shorter time duration, weaker spectral amplitudes and lower frequency content.

FT2: Soil block topple and fall

The FT2 No.1&No2 failure events of Experiment L1 were the largest ones observed during both landslide experiments. They were also the more complex ones regarding their failure mechanism involving soil block toppling and falling at the bottom of the excavation. Their visual observed time of incident was correlated with the seismic recordings and the failures are annotated with black arrows in the spectrograms presented in Figure 8.18. They are visualized as dark red spikes with frequency content up to ~450Hz.

FT3: Soil block fall

This Failure Type was the most commonly observed. Figures 8.19 & 8.20 present spectrograms only of the vertical component of the seismic data since there are no significant differences in the horizontal components. The spectrograms of the horizontal components can be seen in Appendix C2. The FT3 events are annotated with black arrows. The spectrograms reveal that FT3 events have differences in their frequency content with frequency content ranging up to 60Hz (fig. 8.19a), 160Hz (fig. 8.19b), 260Hz (fig. 8.19c), 350Hz (fig. 8.20a), 125 (fig. 8.20b), 250Hz (fig. 8.20c). This seems to be correlated with:

1) The volume of soil involved in the failure event: The larger the volume of soil involved in the failure event the larger the frequency content recorded.
2) The distance from the initial position of the soil block to the ground surface: The initial height of the VF1&2 was ~2.5m. As failures occurred and soil fell on the ground surface this height was gradually reduced. The Failures occurring towards the end had smaller travelling distance to the ground meaning that their impact was weaker, leading to lower frequencies in the spectra.

The above can be verified by comparing FT3 No.4 failure event of Experiment L1 and failure FT3 No.1 of Experiment L2. Photos of the two events revealing the soil volume involved in the failure and the distance covered during the fall can be seen at Figures 8.16 and 8.17 while their spectrograms at Figures 8.19c and 8.20a respectively. Failure

FT3 No.4 of Exp.L1 has lower frequencies in the spectra, compared to the failure FT3 No1 of Exp L2, due to the smaller volume of soil involved in the failure and the smaller distance of the fall. Further analysis of these differences is presented in the next section.

The spectrograms of Figures 8.19a and 8.20c reveal spikes that look similar to the annotated failure events (annotated with blue arrows). These events were not visually observed during the Experiments L1 and L2. This was in part due to the large amount of field data needed to be kept manually, the low visibility conditions and the fatigue. Another reason might be that these were internal failure events that were not observed on the landslide face. The latter is unlikely since the energy emitted during such failures is larger compared to FT1 events that could occur internally.

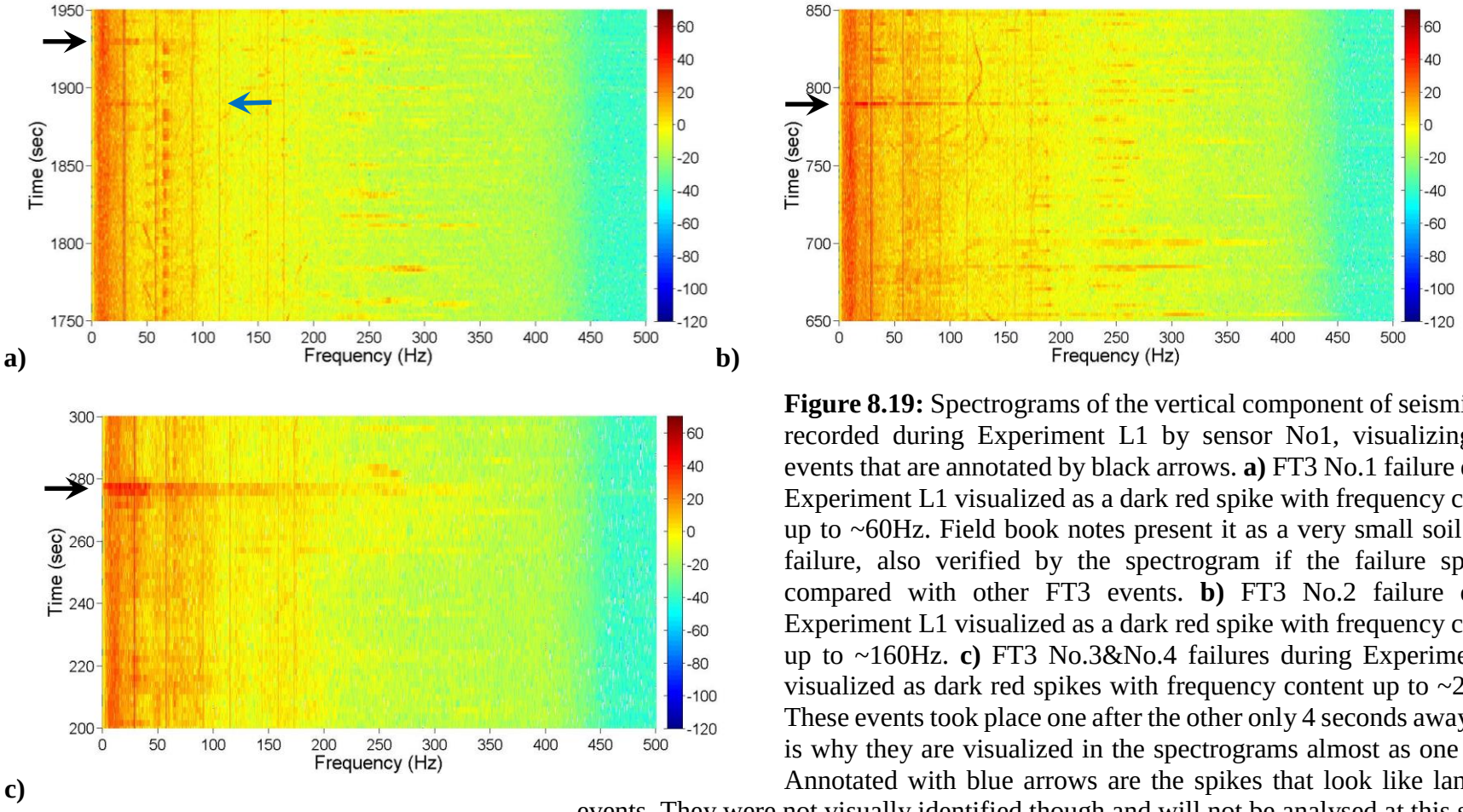

Figure 8.19: Spectrograms of the vertical component of seismic data recorded during Experiment L1 by sensor No1, visualizing FT3 events that are annotated by black arrows. **a)** FT3 No.1 failure during Experiment L1 visualized as a dark red spike with frequency content up to ~60Hz. Field book notes present it as a very small soil block failure, also verified by the spectrogram if the failure spike is compared with other FT3 events. **b)** FT3 No.2 failure during Experiment L1 visualized as a dark red spike with frequency content up to ~160Hz. **c)** FT3 No.3&No.4 failures during Experiment L1 visualized as dark red spikes with frequency content up to ~260Hz. These events took place one after the other only 4 seconds away. This is why they are visualized in the spectrograms almost as one spike. Annotated with blue arrows are the spikes that look like landslide events. They were not visually identified though and will not be analysed at this stage.

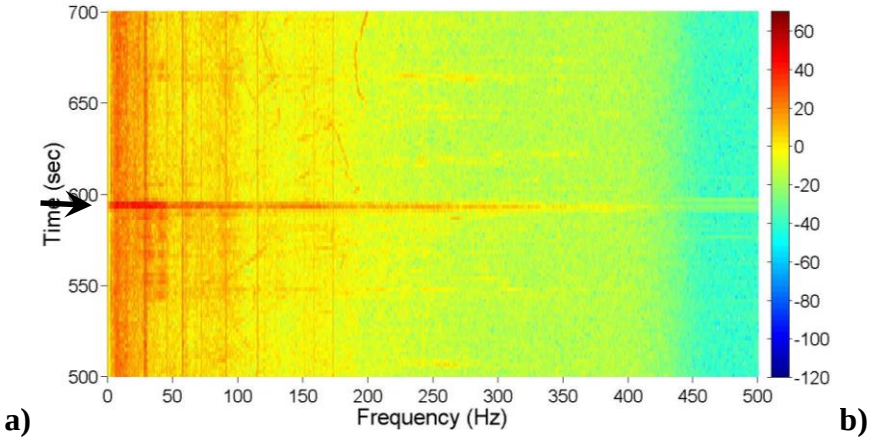

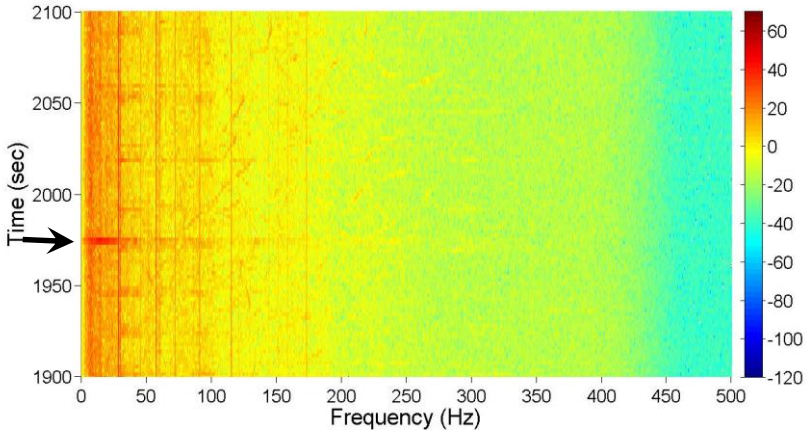

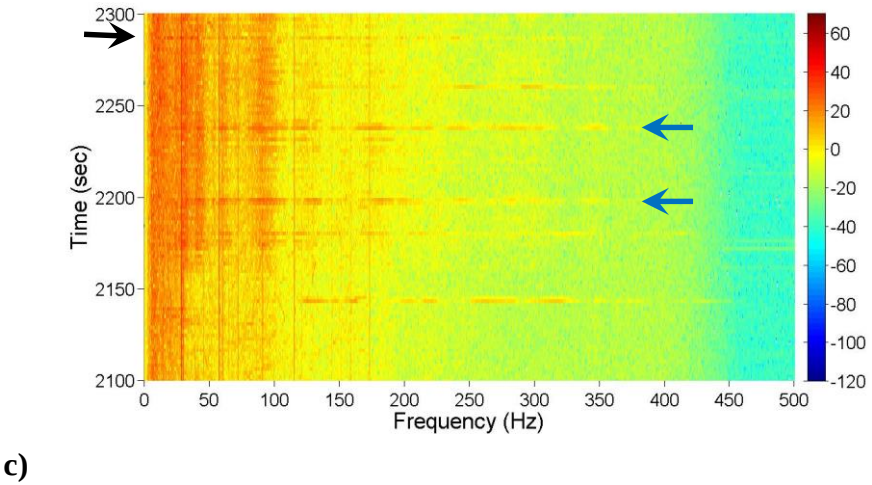

Figure 8.20 As in Figure 8.19 only for data recorded during Experiment L2. **a)** FT3 No.1 failure during Experiment L2 visualized as a dark red spike with frequency content up to ~350Hz. This failure event is the biggest FT3 event that took place during Experiment L2 and the third biggest amongst all failure events. Photos before and after this failure are shown in Figure 8.17.a,b respectively. **b)** Failure No.2 of Experiment L2 visualized as a dark red spike with frequency content up to ~125Hz. **c)** Failure event 3 during L2 visualized as a dark red spike with frequency content up to ~250Hz. Annotated with blue arrows are the spikes that look like landslide events. They were not visually identified though and will not be analysed at this stage.

8.4.4 Step 4: Spectral analysis of the visually observed landslide failures

The failures that were visually observed in Step 2, detected in the seismic recordings with the use of spectrograms in Step 3, are analysed in Step 4 in the frequency domain. This was done in order to understand the energy distribution over their frequency content. Data recorded from sensor No1 were used because the failure signals recorded by this sensor were of the best quality.

Background noise was also analysed using spectral analysis. The PSD of long duration noise recordings (~1 hour) and the PSD of short duration noise recordings (5 minutes) were calculated for each sensor separately and presented along with the PSD of the failures. This was done because it was found that short duration noise recordings had slightly larger values of the PSD compared to long duration. This is probably as a consequence of small noise variations that occurred during the field trials.

FT1: Crack Formation/Propagation

Figures 8.21 & 8.22 present the PSD spectra of two FT1 events of Experiment L1, for all three components of sensor No1. The rest of the visually observed FT1 events that were detected above background noise levels in the seismic recordings of other sensors are presented in Appendix C3.1. Since crack formation/propagation was observed as a continuous phenomenon in the field, the focus was on detecting the soil bursts in the seismic data as separate events. As shown in the photos of Step 2 (fig. 8.12b&c, 8.13d), these are very small events occurring at a specific point along the crack. These events can be considered as precursory events to the larger failures, e.g. the FT2 No.1&No2 failure events of Experiment L1. Their source-to-sensor distance detection threshold was found to be 15m (fig. 8.21d, 8.22d).

FT1 events were very weak, with the first visually observed soil burst being below background noise levels. Their weak nature makes them very hard to detect and to determine their frequency pattern (characteristic geometry of the PSD curve). Between frequencies 20Hz and 100Hz higher energy from noise exists in all components and all events (fig. 8.21a, b, c & 8.22a, b, c). There are additional differences between

signal and noise between frequencies 100Hz and 325Hz but these are not consistent either between the components of the sensor nor between individual FT1 events. Differences between the spectra of FT1 events may be due to differences in the physics involved; the active slip surface was not displaced in the same manner thus leading to different FT1 events. Small soil heterogeneities along the different travel path of the recorded seismic waves may also be part of the explanation. Finally the horizontal components of these events seem to record FT1 events with slightly larger energy by comparison to the vertical component of the sensor.

This small energy variation is important for events that are barely visible above noise levels giving the use of 3D sensors an advantage over 1D. Note that cracks were formed at an almost vertical plane. The mechanism involved is that of shearing between two soil layers. Thus, P-waves would form perpendicular to the shearing plane (being in almost vertical orientation). Having the latter in mind, it makes sense that the horizontal components recorded FT1 events clearer than the vertical component. At a real case scenario, with the failure plane being below the seismic sensors the vertical component is expected to record clearly the emitted seismicity.

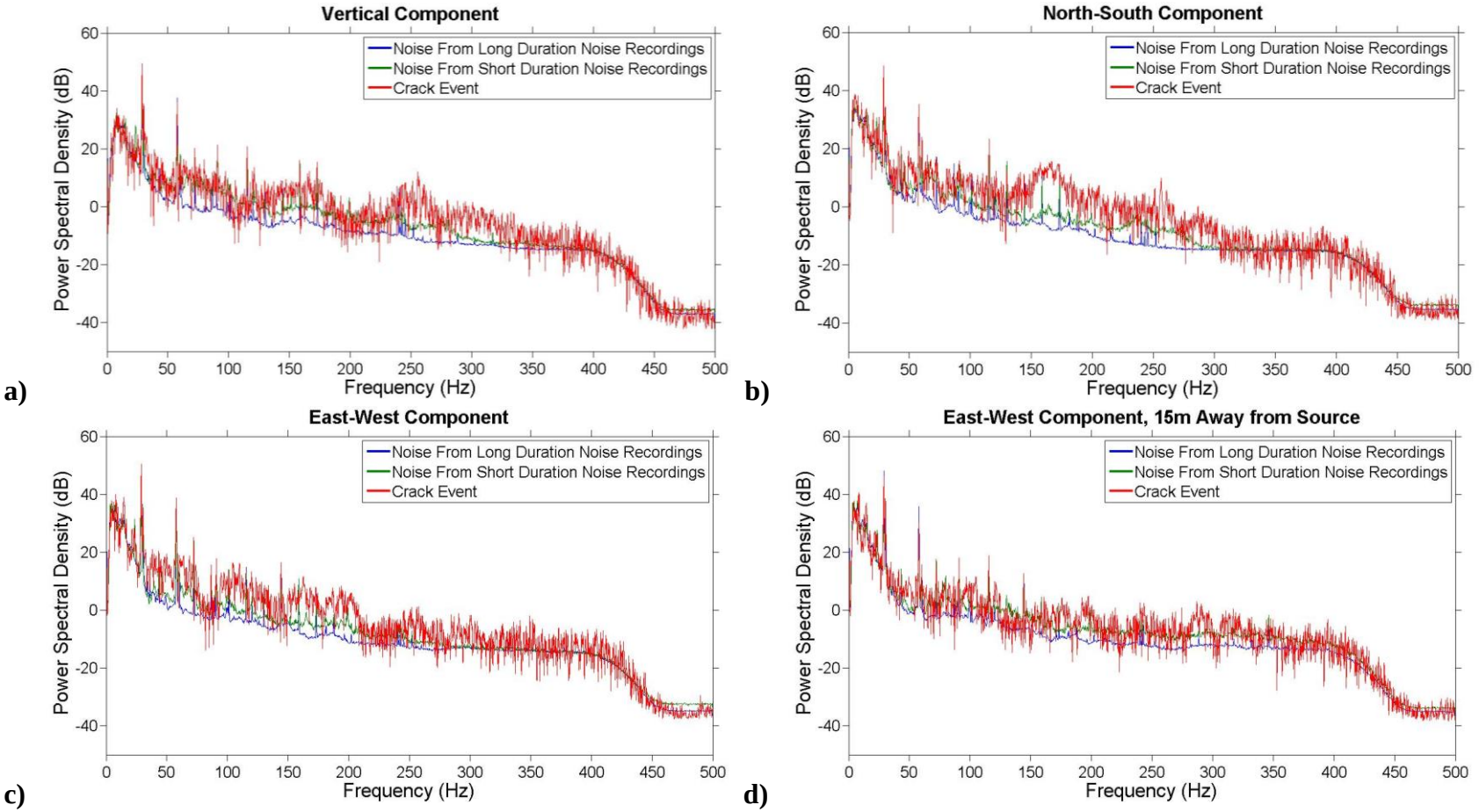

Figure 8.21: a,b,c) PSD of No.2 soil burst that was visually observed before Failure No.1 of Experiment L1 and recorded by sensor No1. Between frequencies 20Hz to 100Hz higher energy from noise exists in all components. There are additional differences between signal and noise between frequencies 100Hz and 325Hz without though being consistent among the components of the sensor. Soil bursts are easier detected from the horizontal component of the recordings. **d)** Event last detected by East-West Component at 15m away from source.

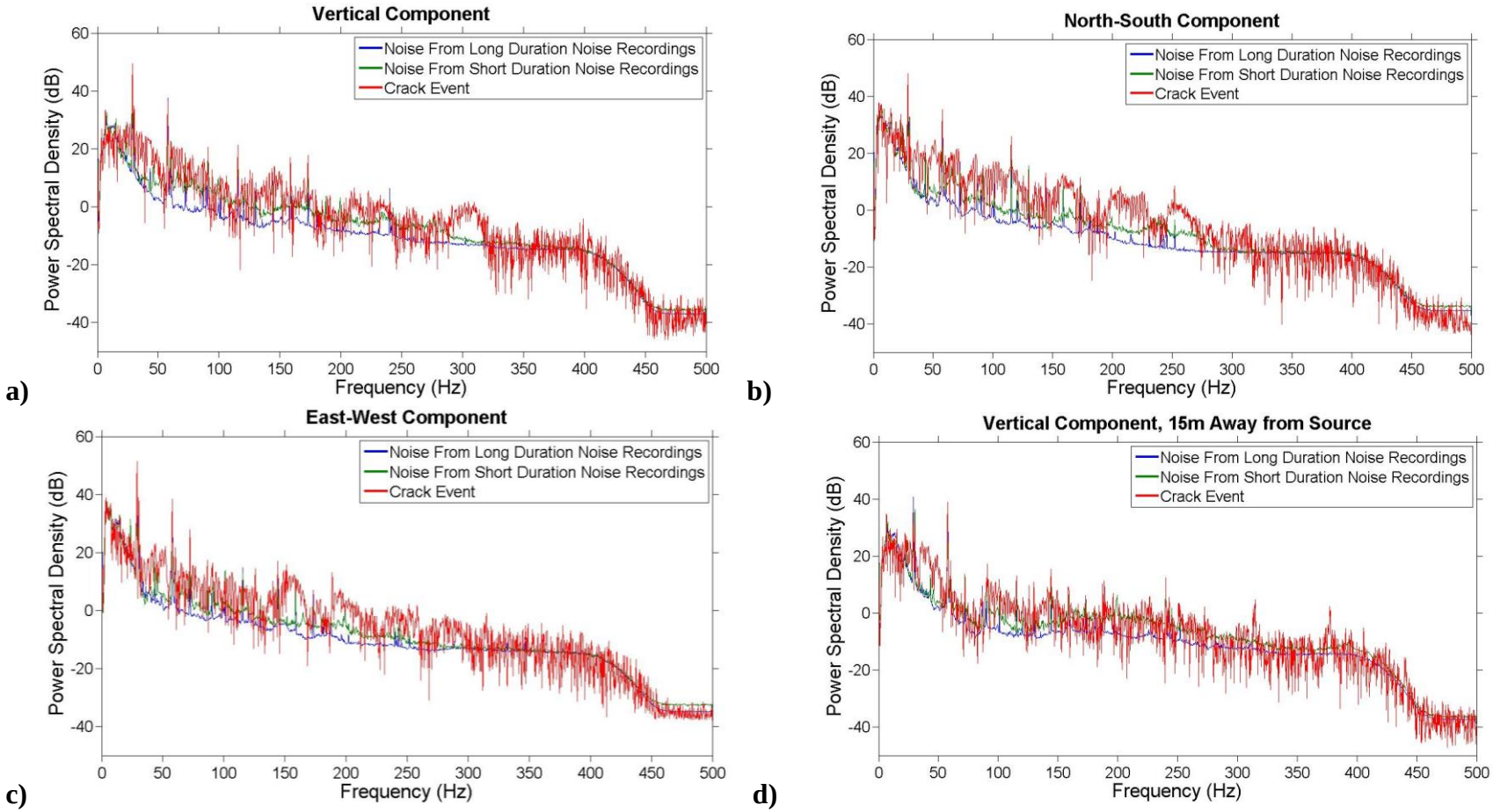

Figure 8.22: a,b,c)PSD curves of No.2 soil burst event that was visually observed before Failure No.2 of Experiment L1 and recorded by sensor No1. This is the strongest burst event that was visually observed. PSD levels of the signal start differentiating from noise at 25Hz up to 275Hz in all components. The event is easier to detect in the horizontal components. **d)** Event last detected by all component at 15m away from source (only vertical component is shown as the rest are in Appendix C3.1.4)

FT2: Soil block topple and fall

Figures 8.23 & 8.24 present the PSD spectra of the FT2 No1&No2 failure events recorded during Experiment L1 by the vertical component of sensor No1. The horizontal traces produced similar results. All deployed sensors recorded clearly these two events. All their PSD spectra can be found at Appendix C3.2 These two events were the largest ones observed. For this reason their PSD spectra reveal increased energy content throughout the whole frequency range examined. All components have similar frequency characteristics: high seismic energy between 10Hz and 30Hz with a gentle and almost linear reduction of energy with increasing frequency. The largest differences between the PSD amplitudes of the noise and the landslide signal are in the range from 30Hz to 80Hz. Their source-to-sensor distance detection threshold wasn't reached from the dense deployed microseismic array and was proven to be larger than 50m.

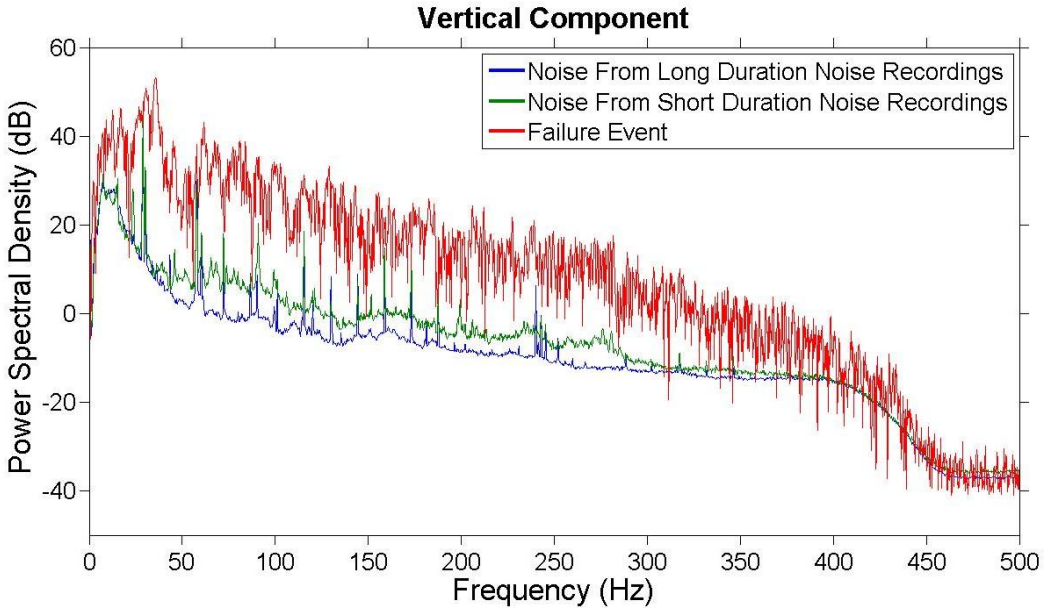

Figure 8.23: PSD spectra of FT2 No.1 failure event categorized as a soil block topple and fall event (FT2) recorded during Experiment L1 by the vertical component of sensor No1. It can be seen that this event emitted energy at all recorded frequencies: Largest PSD amplitudes are between 10Hz and 30Hz, with largest difference between PSD amplitudes of noise and signal in the range of 30Hz and 80Hz. Horizontal components have similar frequency characteristics. The spectrogram and photos of this Failure can be seen in Figure 8.18 and 8.14 respectively.

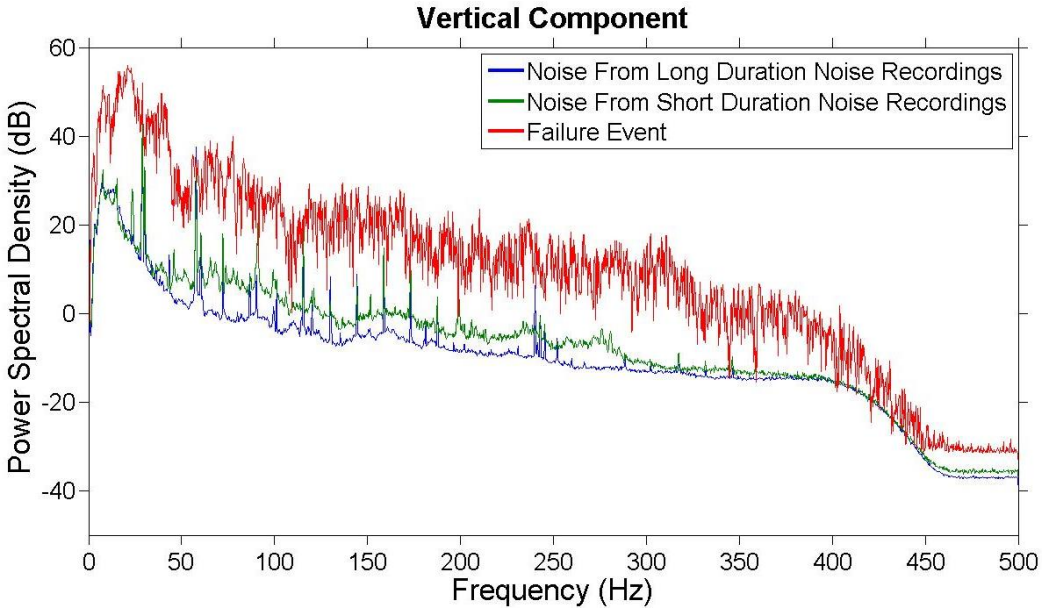

Figure 8.24: PSD spectra of FT2 No.2 failure event categorized as a soil block topple and fall event (FT2), recorded during Experiment L1 by the vertical component of sensor No1. This combined failure events emitted energy at all recorded frequencies almost evenly distributed above noise levels: Largest PSD amplitudes are between 10Hz and 30Hz, with largest difference between PSD amplitudes of noise and signal in the range of 30Hz and 80Hz. Horizontal components have similar frequency characteristics. Spectrogram and photos of the Failure can be seen at Figure 8.18 and 8.15 respectively.

FT3: Soil block fall

The PSD spectra of different FT3 events are presented in Figures 8.25 to 8.27. Additional PSD spectra can be found in Appendix C3.3 As mentioned in Step 3, the size of the soil block that was detached from the face of the slope and finally fell inside the excavation, as well as the height of the fall, affected the PSD levels and the frequency range of the emitted energy.

This FT can be divided into three subcategories: (1) Small FT3 events with their spectral energy mainly between 25Hz and 50Hz being at maximum 10dB larger than background noise. These events might have higher spectral energy than noise at other frequencies with differences up to 5dB that do not seem to be constant along different events. Such events are the FT3 No1 event (fig. 8.23, see also Appendix C3.3.1) and

FT3 No3 event (see Appendix C3.3.2) observed during Experiment L1. This type of event was found to have a 15m maximum distance away from source that acts as detection threshold. (2) Medium FT3 events with their spectral energy mainly between 25Hz and 100Hz being 20dB to 30dB larger than background noise. These events also contained spectral energy at frequencies 100Hz to 200Hz being 5dB to 10dB larger than background noise. Such events are the FT3 No2 event of L1 (fig. 8.24, see also Appendix C3.3.3) and the FT3 No2 & No3 events of L2 (see Appendix C3.3.4 & C3.3.5). This type of event was recorded by all deployed sensors and the source-to-sensor distance detection threshold was not reached. From results, the event detection threshold is estimated to be around 50m (source-to-sensor distance needed for event to be recorded). (3) Large FT3 events with their spectral energy mainly between 25Hz and 100Hz being 20dB to 30dB larger than background noise. These events also contained spectral energy at frequencies 100Hz to 400Hz being 5dB to 10dB larger than background noise. Such events are the FT3 No1 event of L2 (fig. 8.25, see Appendix C3.3.6) and the FT3 No4 event of L1 (see Appendix C3.3.7). As before, this type of event was recorded by all deployed sensors. Results show that the source-to-sensor distance detection threshold is larger than 50m. The spectral differences between the spectral characteristics of FT3 events and background noise are summarized in Table 8.2. These differences are site specific.

The comparison between the vertical and horizontal seismic traces is more complicated for FT3 events. For large and medium FT3 events (fig. 8.26, 8.27) the horizontal components do not seem to add any significant value to the detection process. For weak FT3 events though (fig. 8.25) where the spectral energy is barely above noise levels the horizontal components make the identification process easier. Adding the fact that the FT1 events were easier to identify in the horizontal traces compared to the vertical, if the goal of the monitoring campaign is to detect weak events barely visible above noise levels the use of 3D seismometers can be considered advantageous.

<table>
<tr><th>Frequency Range
(Hz)</th><th>Small
FT3 Events</th><th>Medium
FT3 Events</th><th>Large
FT3 Events</th></tr>
<tr><td>- / -</td><td colspan="3">dB difference from Noise levels</td></tr>
<tr><td>0 - 25</td><td>0</td><td><10</td><td><20</td></tr>
<tr><td>25 - 50</td><td><10</td><td rowspan="2"><20-30</td><td rowspan="2"><20-30</td></tr>
<tr><td>50 - 100</td><td rowspan="3"><5dB without having a constant frequency range where spectral differences appear</td></tr>
<tr><td>100 - 200</td><td><5</td><td rowspan="2"><5-10</td></tr>
<tr><td>200 - 400</td><td>0</td></tr>
<tr><td>Detection Distance Threshold From Source</td><td>20m</td><td>around 50m</td><td>>50m</td></tr>
</table>

Table 8.2: Summary of the spectral differences of FT3 events from noise levels, as well as of the maximum distance away from the source that acts as detection threshold. These differences are site specific.

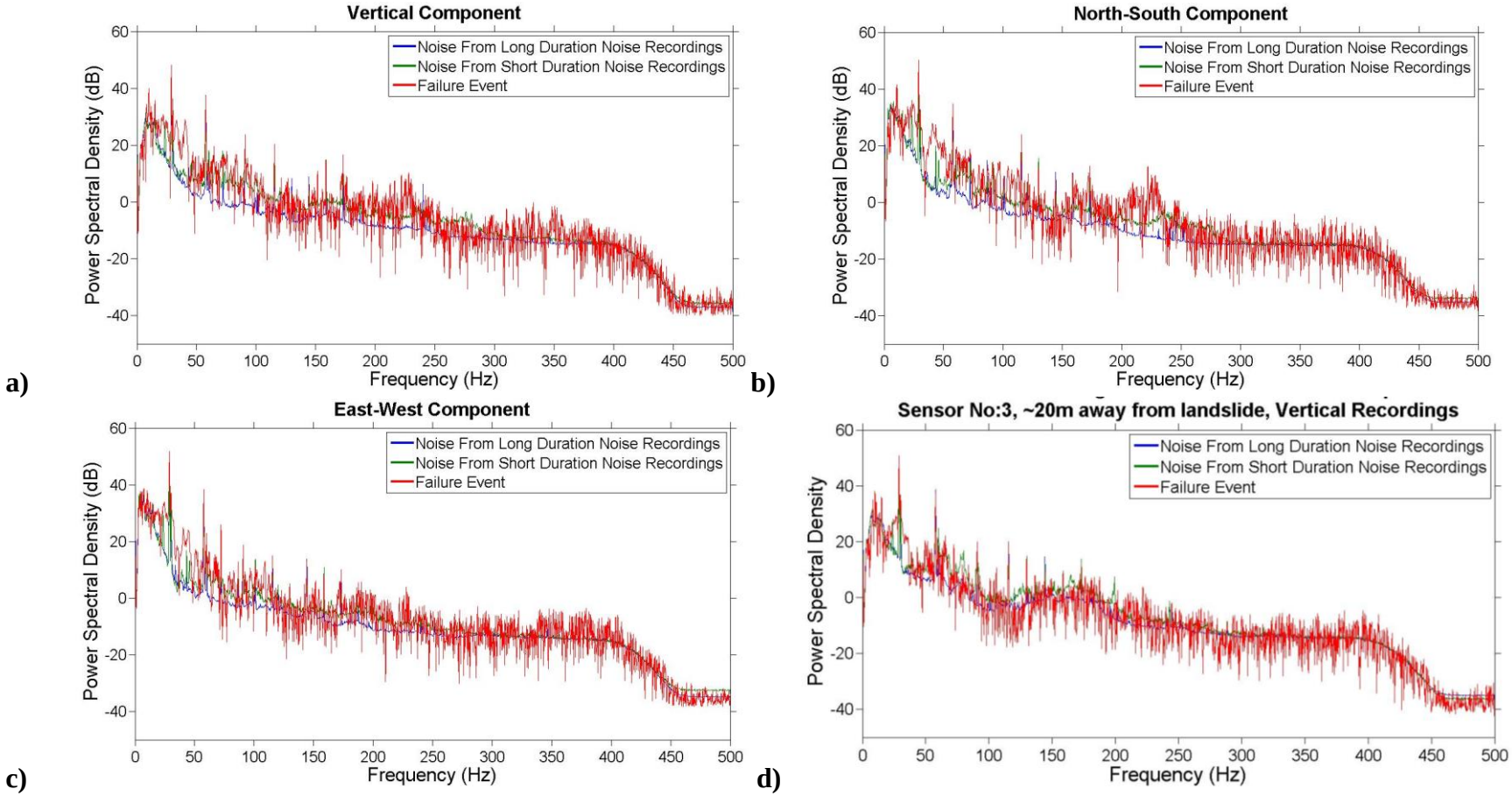

Figure 8.25: a,b,c) PSD of FT3 No1 event during Experiment L1 recorded by sensor No1. This failure is a small FT3 event and was barely recorded above noise levels. The frequency range that the event can be observed above noise are between 20Hz to 50Hz, the same frequency range where the noise level has a steep fall in PSD amplitude. The spectrogram of this Failure can be seen in Figure 8.19a. **d)** The event was last detected by all components 20m away from source (only the Vertical Component is visible here as all PSD spectra are in Appendix C3.3.1.

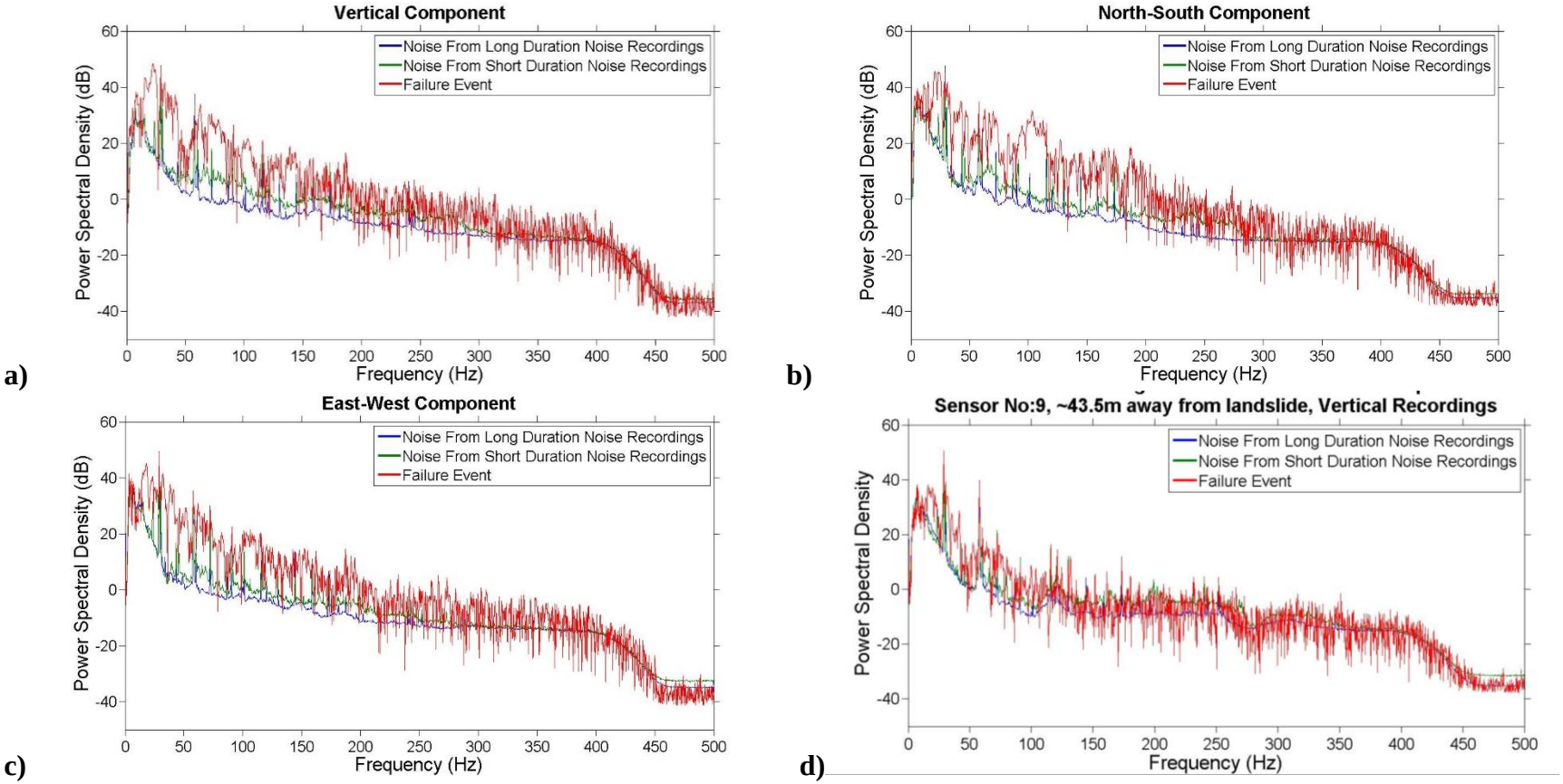

Figure 8.26:a,b,c)PSD of FT3 No2 event during Experiment L1 recorded by sensor No1 (~10m away from L1). This is a medium FT3 event with its seismic energy above noise levels mainly between 20Hz to 200Hz. Largest difference of PSD amplitude between signal and noise levels can be found between 20Hz and 50Hz, where PSD noise levels have a steep fall. The spectrogram of this Failure can be seen in Figure 8.19b. **d)** The event was recorded by all sensors, but it is almost lost below the background noise levels at 43.5m away from the source, so the detection threshold must be around 50m (Vertical Component is visible here, all PSD spectra are in Appendix C3.3.3).

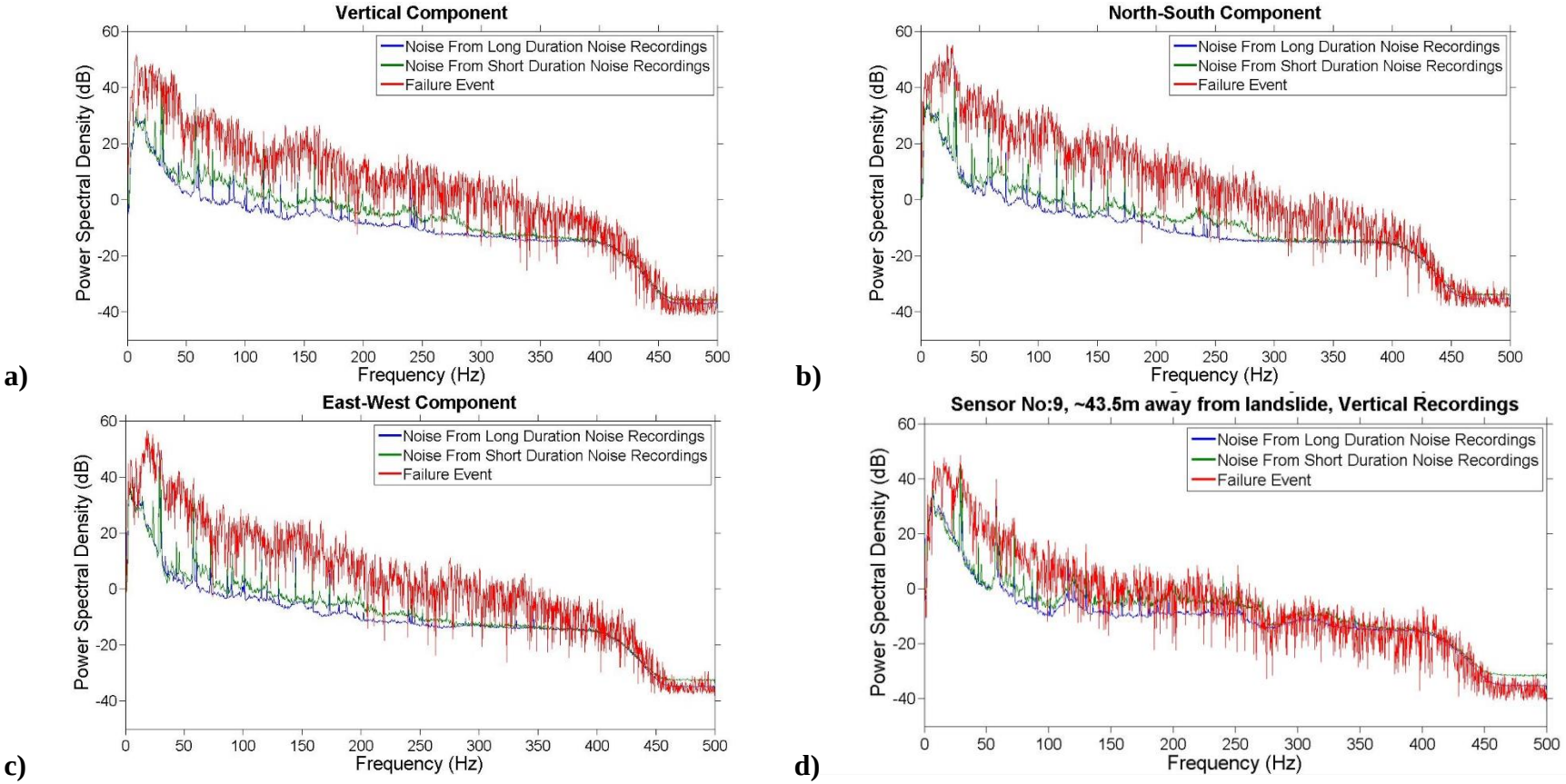

Figure 8.27: a,b,c) PSD of FT3 No1 event during Experiment L2 recorded by sensor No1. This event is categorized as a large FT3 event with its emitted seismic energy above noise levels mainly between 20Hz to 350Hz almost evenly distributed above noise levels. Note that this was the biggest failure event observed during the Experiment L2 and the third biggest in both landslide experiments. The spectrogram and photos of this Failure can be seen in Figure 8.20a and 8.17 respectively. **d)** This type of event was recorded by all deployed sensors and no distance detection threshold was reached. The PSD spectra indicate that it is greater than 50m (also see Appendix C3.3.6).

8.4.5 Step 5: Identification of failures or displacements based on the load and displacement curves only

All visually observed landslide events have been analysed in Steps 2 and 4. In this Step the data collected regarding the vertical load applied on the crown of the VF 1&2 and the subsequent monitored vertical displacements are exploited. Figures 8.28&8.29 show the time histories for both L1 and L2 Experiments, respectively.

In these figures, the origin time of the visually observed landslide failures have been marked with dashed green lines. These events have been analysed in Steps 2 to 4. From the figures it can be seen that the failure events can be divided into two categories. (1) The failure events that occurred at a time when a sudden fall in the applied load occurred (FT2 No1 & No2 events and FT3 No3, FT3 No4 and FT3 No5 events during Exp.L1 and FT3 No1 event during Exp.L2) and (2) the failure events that occurred at a period of high vertical displacement rate (FT3 No2 event during Exp.L1 and FT3 No3 event during Exp.L2). The FT3 No1 event of Experiment L1 and FT3 No2 event of Experiment L2 took place just after a period of high displacement rate, so they can be categorized in the second group.

The graphs presented in Figures 8.28 and 8.29 are used for the identification of time periods that can be categorized in the previously discussed two groups (1) sudden load drops and (2) periods of high displacement rates. From the analysis so far these conditions indicate that failure events might have occurred during these time periods. The seismic recordings of the time segments highlighted with yellow ellipses in Figures 8.28&8.29 were analysed further in order to detect possible failure events.

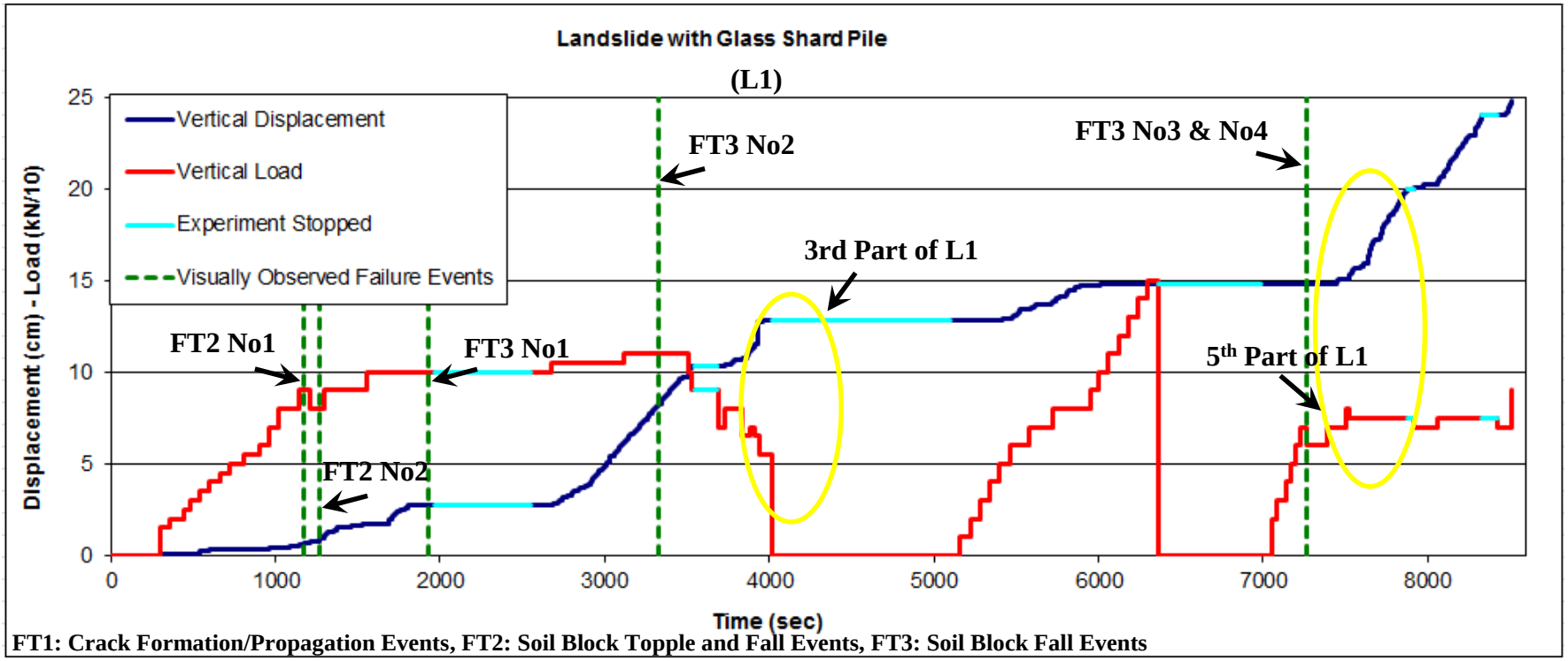

Figure 8.28: Experiment L1. Applied vertical load (red line) and recorded vertical displacement (dark blue line). Cyan plotted lines mark the time periods when the experiment was stopped. The time of the visually observed failure events has been marked as green dashed lines. Also marked are the time segments when sudden load drops occurred during high displacement rate (yellow ellipses). During these periods failure events might have occurred, a possibility that is examined with the help of the seismic recordings.

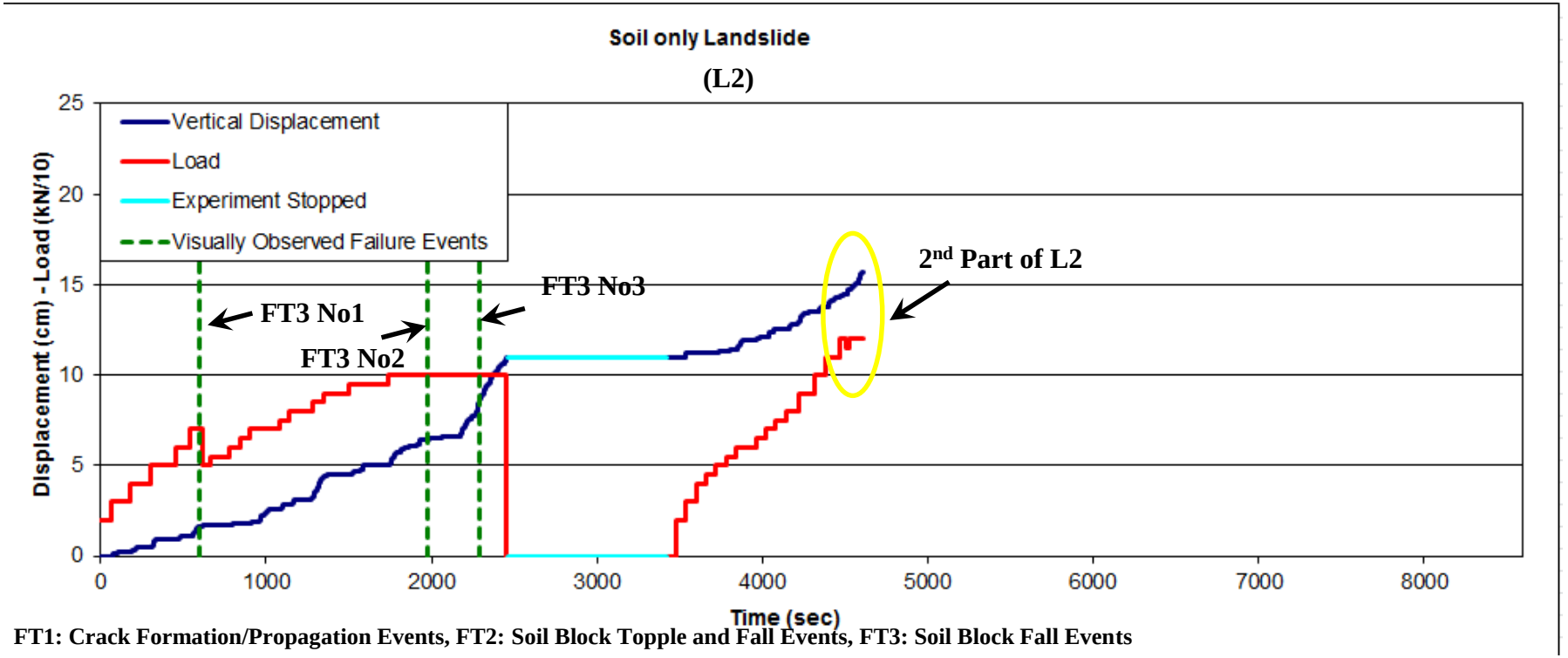

Figure 8.29: As Figure 8.28 only for the Experiment L2.

8.4.6 Step 6: Combining Steps 3&4 (Spectrograms & PSD) along with Step 5 (Loading and displacement curves) to detect landslide failure or displacement events

In Step 5 three time periods where possible failures (PF) occurred were identified. For each of these time periods a spectrogram was calculated in order to visualize the seismic recordings in the time-frequency domain. In the spectrograms, possible failures have been identified based on the findings of Step 3. The latter meant that peaks in the spectrograms with frequency content above 60Hz and up to 450Hz were candidates for possible failures. Each of these possible failures were isolated from the rest of the recordings in order to calculate their PSD. Their categorization to Failure Type categories occurred based on their PSD plots and the findings of Step 4.

Many failures were identified in this Step but only one example of each Failure Type is presented. This was done to validate the characterization criteria concluded in the previous Steps. Background noise conditions were found to be stable throughout the seismic recordings with an absence of noise bursts due to human activity and the spectral energy mainly below 30Hz.

Figures 8.30 to 8.32 present spectrograms of the time periods where possible failures occurred. Data were recorded by sensor No1. Annotated on the spectrograms are either possible failures or time periods containing multiple possible failures. The latter was done when such events were closely spaced in time and shared similar frequency characteristics.

Figures 8.33 to 8.39 present PSD plots of sensor No1 for some of the detected possible failures annotated on the spectrograms of Figure 8.30 to 8.32 respectively. Not all annotated failures are presented in this section because they were similar and categorized in the same Failure Type. Additional PSD spectra of these identified possible failure events can be found in Appendix C4.

Categorization of the Possible Failures to Failure Types

To begin with the categorization process, the properties of the potential failure events were correlated with the properties of the complex soil block topple and fall events (FT2), the strongest observed events. None of the marked events of this Step can be categorised as FT2 events for two reasons: a) they would involve a large volume of soil, too big to miss in the field even with poor light conditions and fatigue or being preoccupied in keeping notes of other collected data, b) the calculated PSD of the possible failure events does not match the characteristics of FT2 events as described in Step 4.

The second strongest failure type that was visually verified and analysed at Steps 2 to 5 was the soil block falls (FT3). This category was divided into three subcategories based on their spectral characteristics a) small, b) medium, c) large (see Step 4, Table 8.2). The Possible Failures identified and presented in the PSD curves of this Step and were not visually observed during the experiments were categorized as: (1) small FT3 event occurring at 3915sec of L1 (fig. 8.33), (2) two medium FT3 events occurring at 3789sec of L1 (fig. 8.34) and at 4482sec of L2 (see Appendix C4.1), and (3) three large FT3 events occurring at 3948sec (see Appendix C4.2), 7587sec (fig. 8.35) and 7633sec of L1 (see Appendix C4.3).

Finally the last failure type that was visually verified and analysed at Steps 2 to 5 was the crack formation/propagation (FT1). These failures have very little spectral energy above background noise levels. They differentiated from noise by 5dB to 10dB, usually at frequencies above 40Hz. What they have in common is that they are easier to identify on the horizontal components of the seismometers. Five FT1 events were identified occurring at 3844sec (fig. 8.36), 3846sec (see Appendix C4.4), 7605sec (see Appendix C4.5), 7610sec (see Appendix C4.6) and 7619sec (see Appendix C4.7) during L1.

The data set is too large to isolate each possible failure separately and analyse it in the frequency domain. For this reason, the frequency characteristics (PSD) of multiple possible failure events with small time difference in between them and a similar

frequency content were analysed jointly. It was found that their spectral characteristics were a combination of the characteristics of FT1 and FT3 events. This was expected since the time segments can contain distinct events of either FT. The spectral characteristics of the time segments 3849sec-3914sec (fig. 8.37), 3924sec-3946sec (see Appendix C4.8), 3950sec-4005sec (see Appendix C4.9) and 7641sec-7877sec (see Appendix C4.10) of L1 seem to be closer to FT1 events meaning that there probably are some FT3 events, but there are either too few or too weak to affect the total spectrum of the time segment more. On the other hand, the spectral characteristics of the time segments 4320sec-4360sec (fig. 8.38), and 4435sec-4480sec (see Appendix C4.11) of L2 seem to be closer to FT3 events.

Uncertainties of Categorization process

The categorization of the events in this analysis step is not free from uncertainties. It was shown that weak signals can be emitted by soil block falls (FT3) and during crack formation/propagation (FT1).It was also shown that failure events of the same category do not always share the same frequency characteristics. In addition FT1 and FT3 events were recorded just above noise levels, making them very difficult to identify. All these can lead to uncertainty in categorizing an event found in the seismic data.

The event in Figure 8.33 for example, could be a small FT3 event or a strong FT1. This was finally categorized as a small FT3 event due to the fact that only once a FT1 event was visually observed with similar spectral characteristics. What can be said for certain is that it was related to the failure process of VF1.

Another example is the event presented at Figure 8.39. This could also be either a FT1 or a small FT3 event. The event contained high spectral energy at high frequencies above 100Hz. Such frequency content was found in Chapter 7 during the glass shard displacements using the cylinder methodology. The event presented at Figure 8.39 though has very little or no energy above background noise levels at frequencies below 100Hz that does not allow categorizing it as a glass shard slip event. This high frequency energy might be an indication of the signal being an unexpected

anthropogenic noise source. Extra care though was given in excluding anthropogenic noise sources during experimental measurements so the real source of the event cannot be determined and the event cannot be categorized as a landslide failure event. Despite having visual observations of many events, it was never believed that all recorded signals could have been characterized.

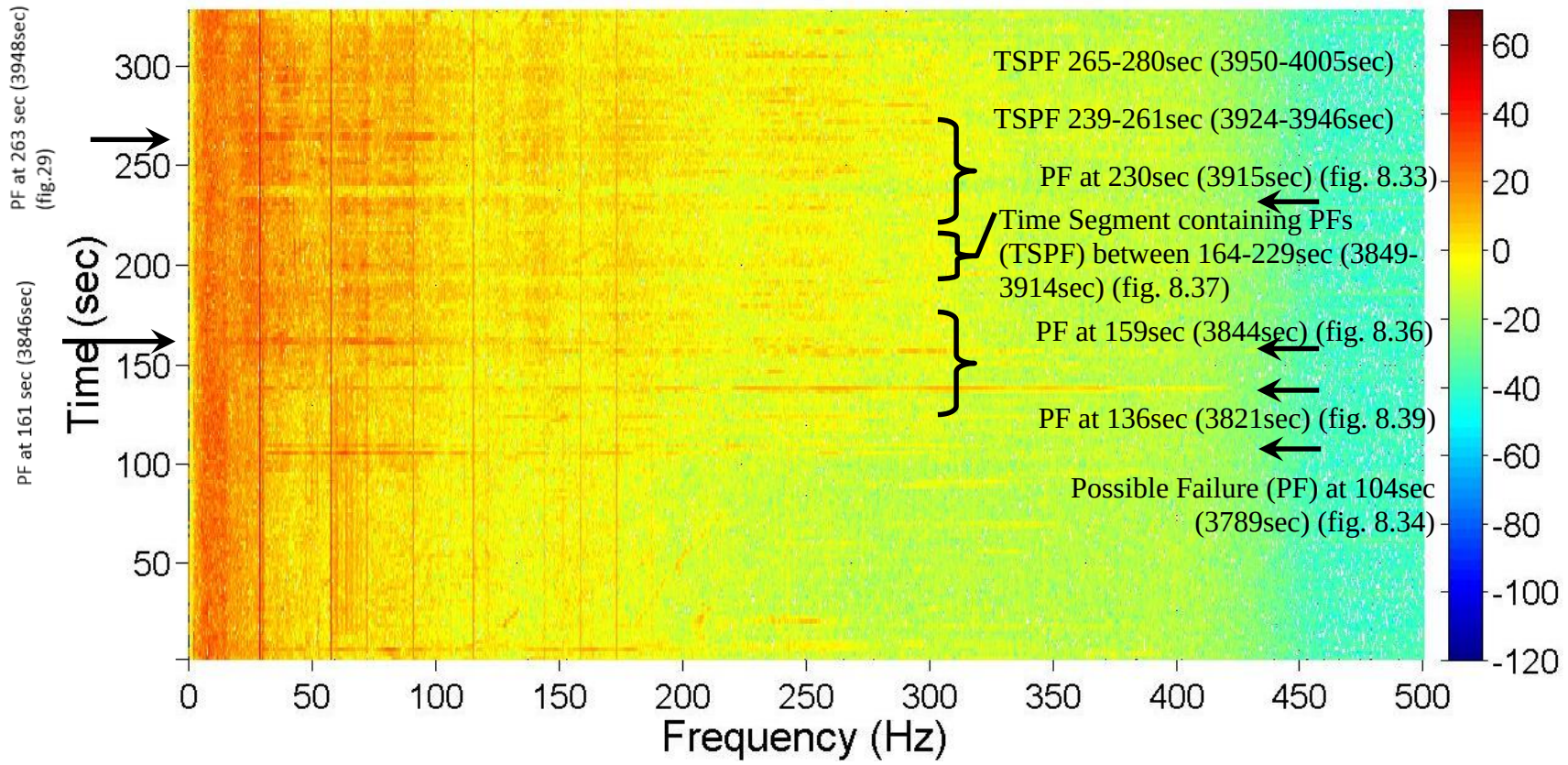

Figure 8.30: Spectrogram of the third part of L1 (marked in fig. 8.28) with monitored high vertical displacement rate and sudden drops in the vertical load applied on the crown of the landslide. On the figure the possible failures (PF) are marked with arrows. The time when PF are seen in the spectrogram and their origin time from the beginning of data acquisition of L1 (in brackets) can be seen next to the arrows. Also marked on the spectrogram are the Time Segments containing multiple PFs (TSPF). Data of the spectrogram belong to the vertical component of the sensor No1.

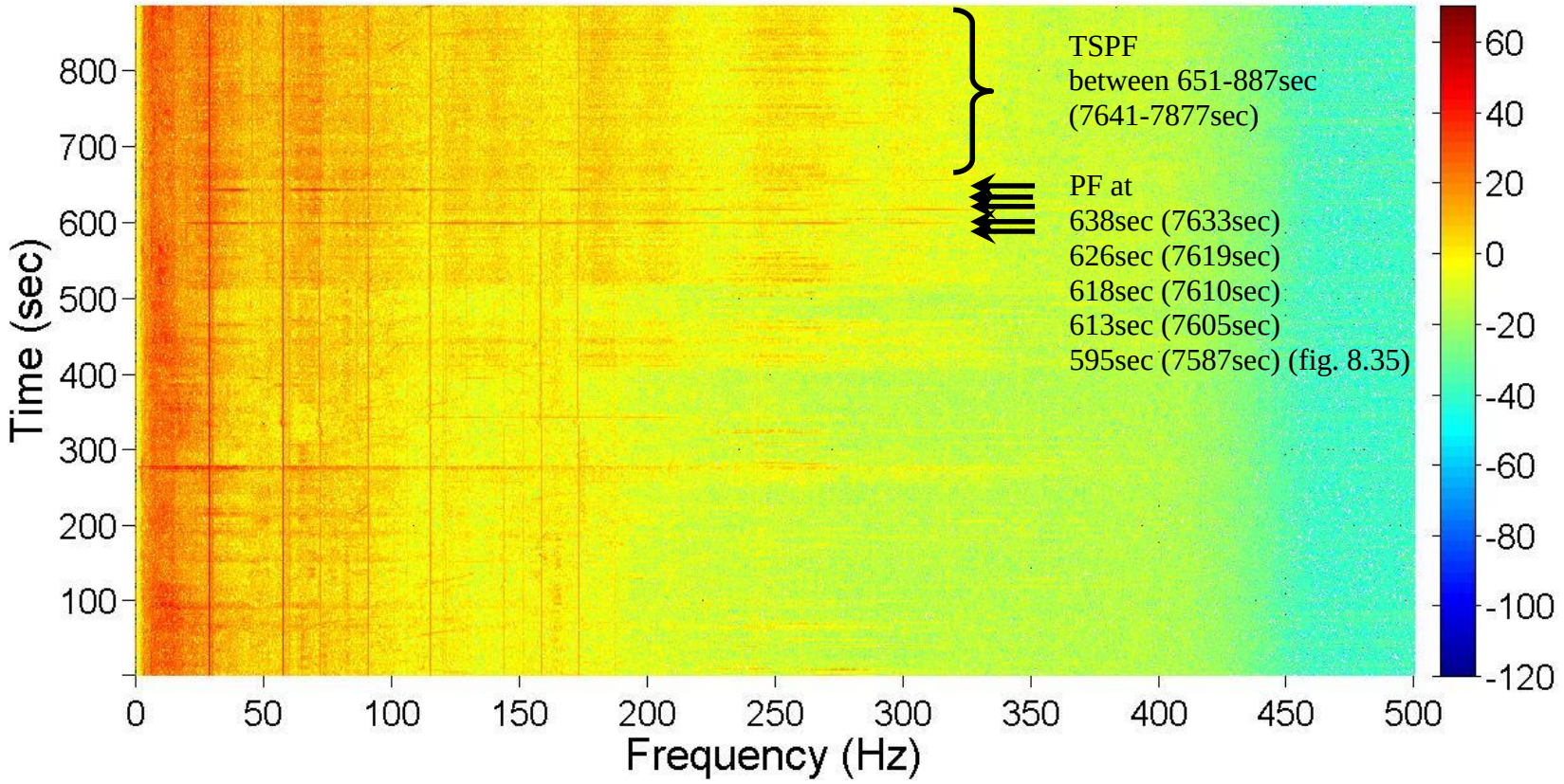

Figure 8.31: As in Figure 8.30 only for the fifth part (marked in fig. 8.28).

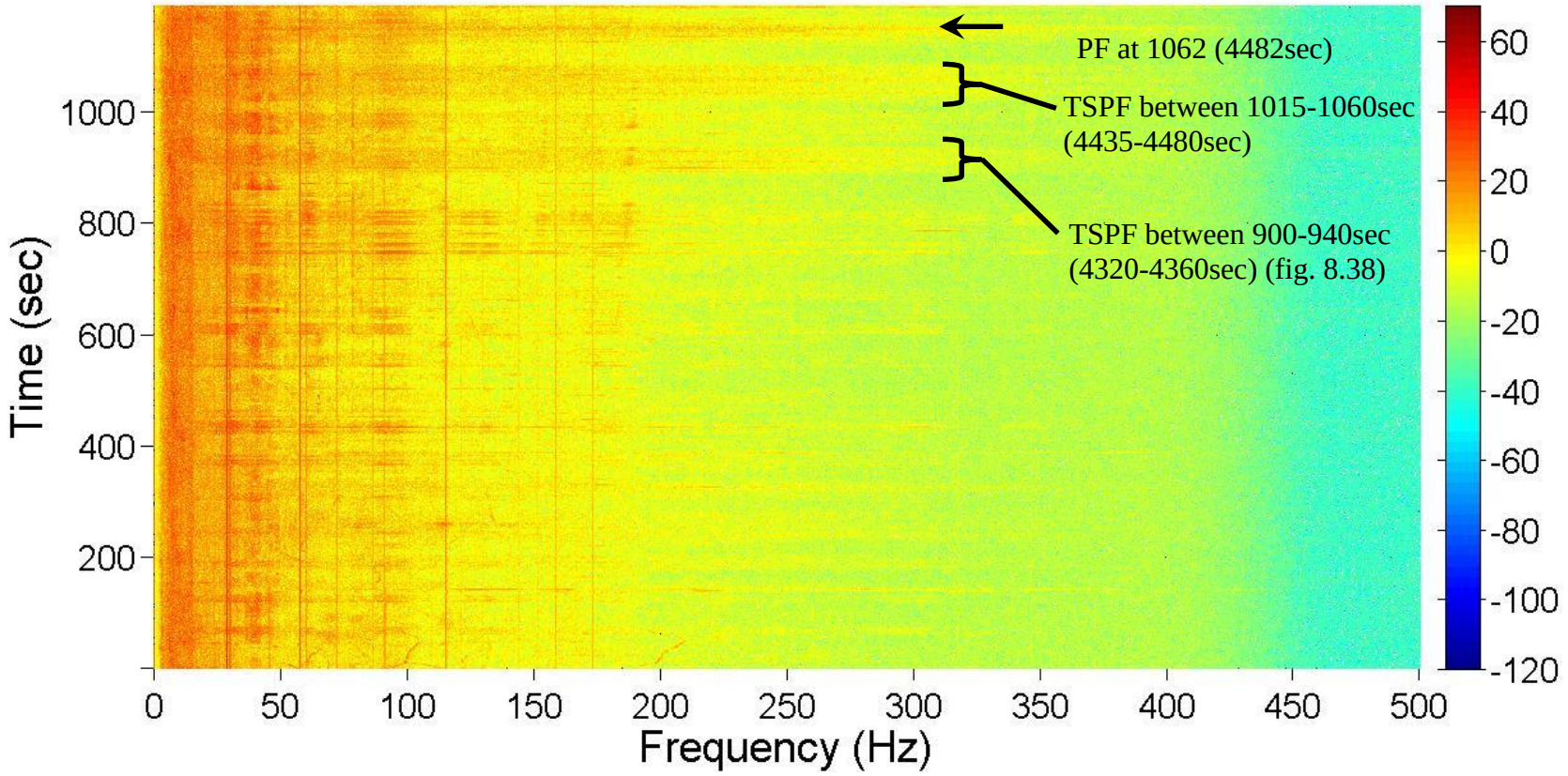

Figure 8.32: As in Figure 8.30 only for the second part of L2 marked on Figure 8.29.

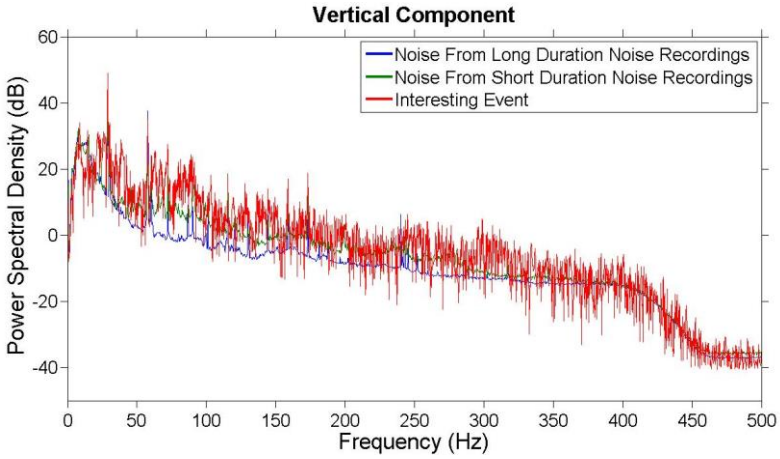

a)

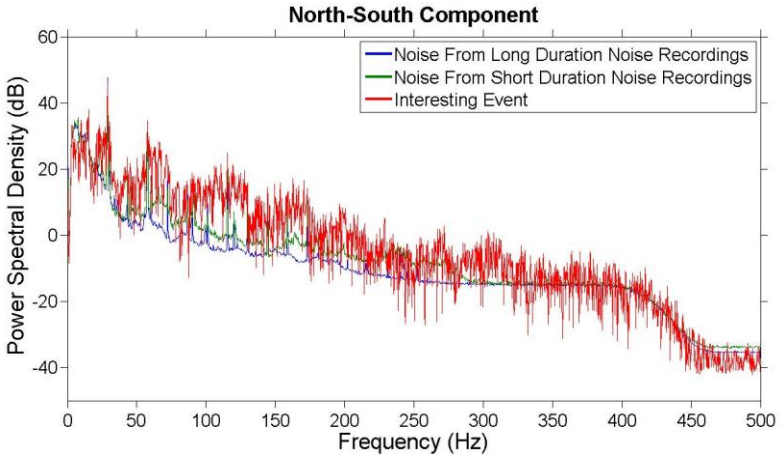

b)

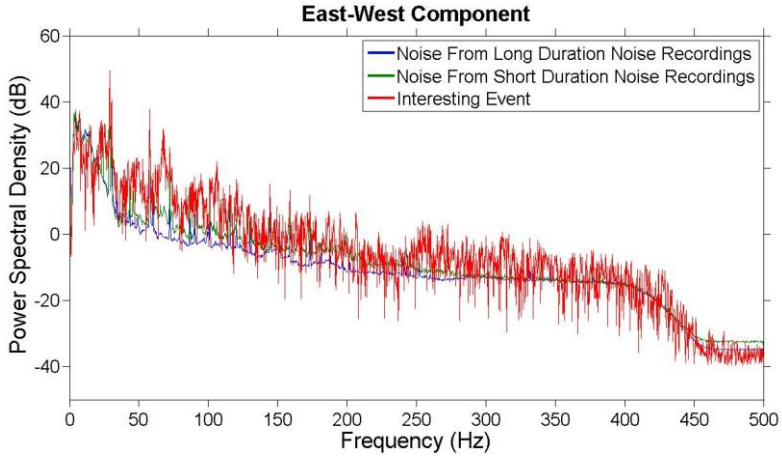

c)

Figure 8.33: PSD of possible failure event detected at the 230sec of the 3rd part of L1 (or at the 3915sec from the beginning of acquisition) among the seismic recordings. Data were recorded by sensor No1. Based on the knowledge obtained in Step 4 the event was categorised a small FT3 event. This event could also be a FT1 event based on the PSD curves presented in Figure 8.22. This was considered unlikely because from the FT1 events that were visually observed only once such a strong FT1 event occurred.

a)

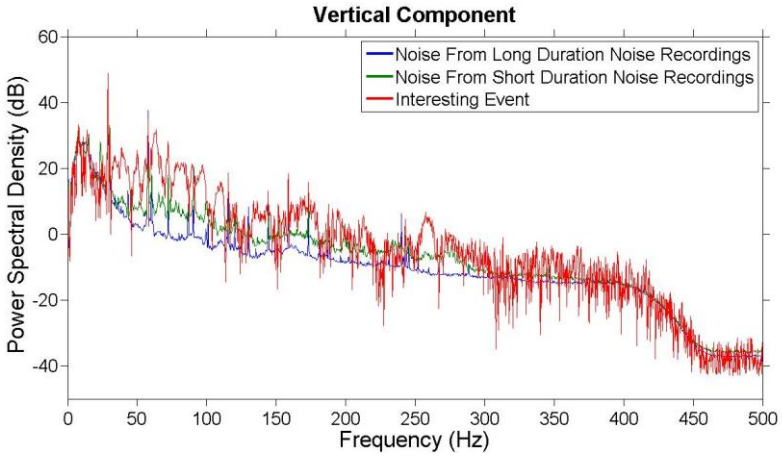

b)

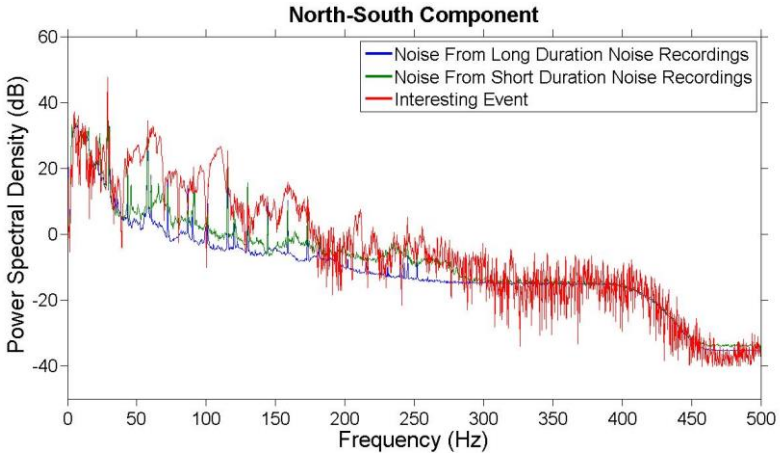

c)

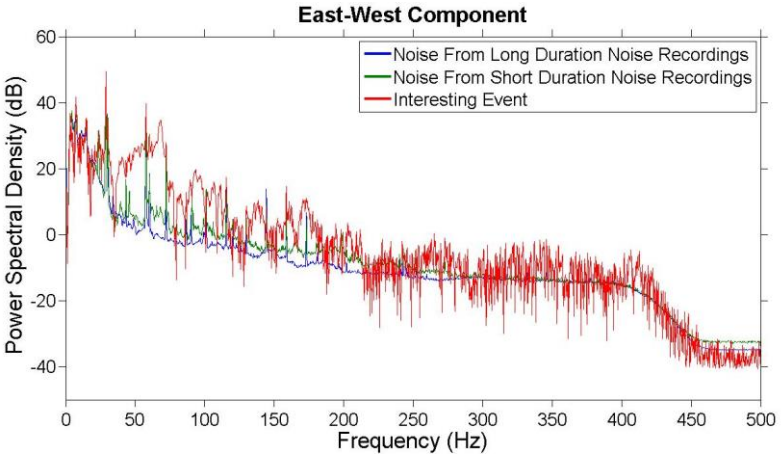

Figure 8.34: PSD of possible failure event detected at the 104sec of the 3rd part of L1 (or at the 3789sec from the beginning of acquisition) among the seismic recordings. Data were recorded by sensor No1. Based on the knowledge obtained in Step 4 (see Table 8.2) the event was categorised as a medium FT3 event.

a)

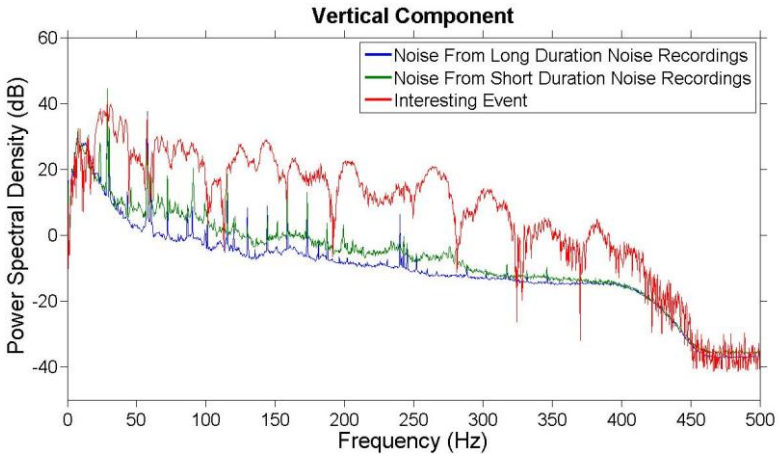

b)

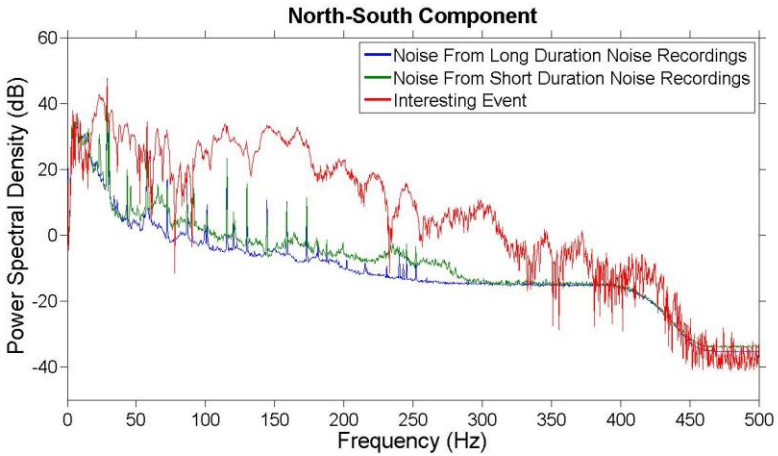

c)

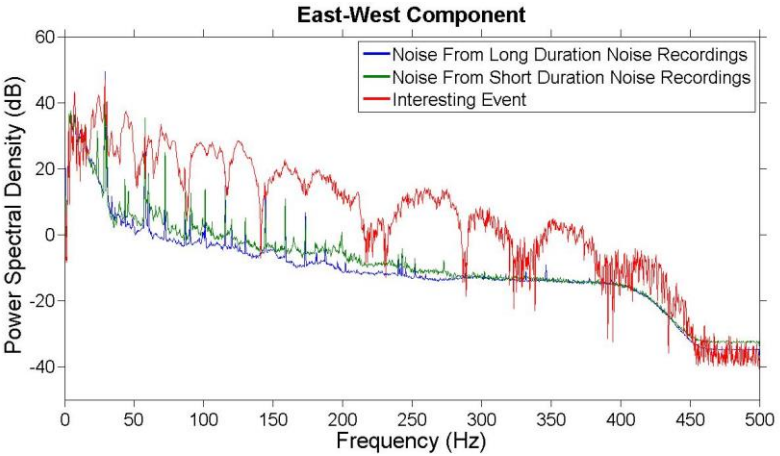

Figure 8.35: PSD of possible failure event detected at the 595sec of the 3rd part of L1 (or at the 7587sec from the beginning of acquisition) among the seismic recordings. Data were recorded by sensor No1. Based on the knowledge obtained in Step 4 the event is categorized as a large FT3 event.

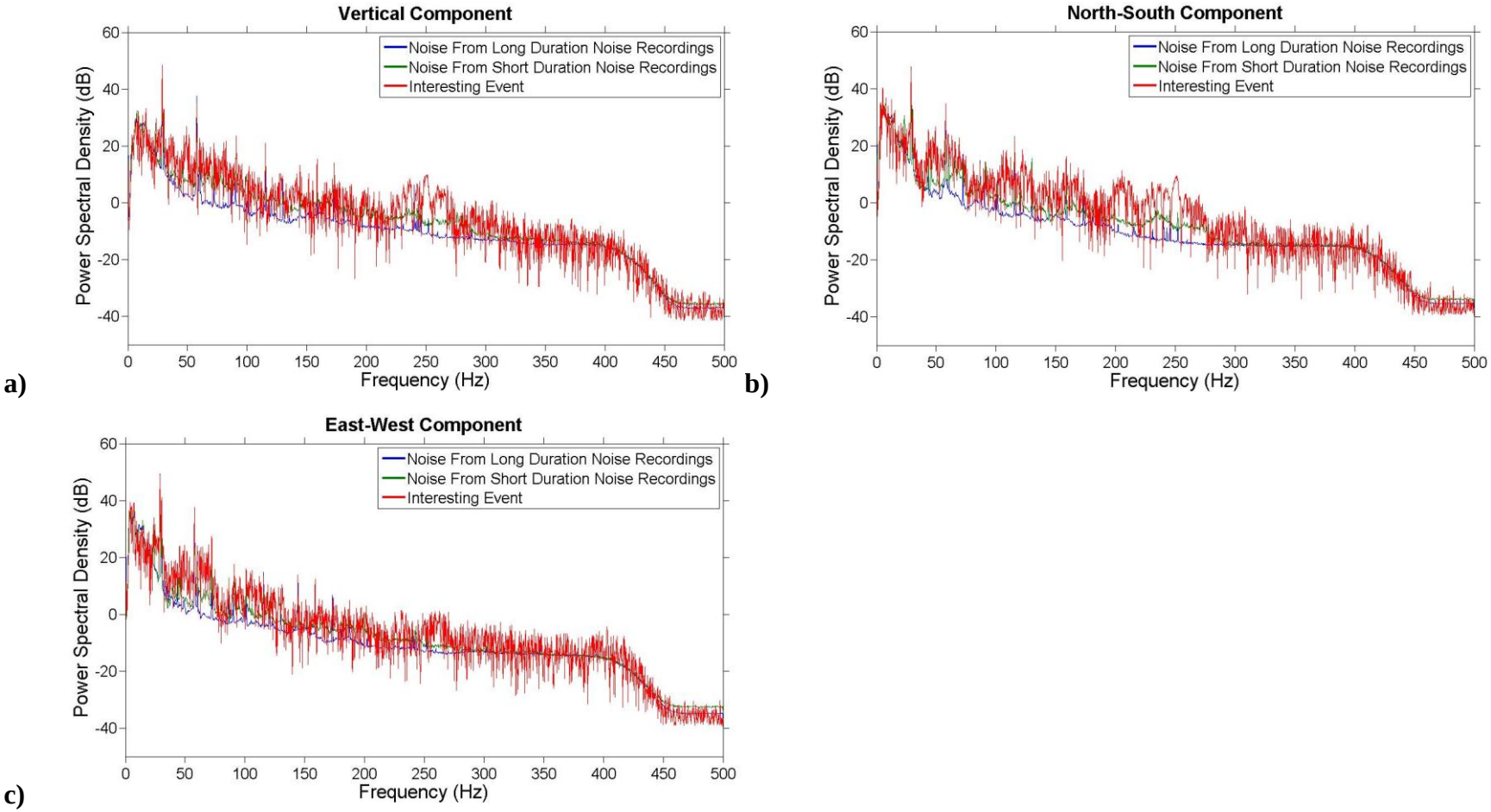

Figure 8.36: PSD of possible failure event detected at the 159sec of the 3rd part of L1 (or at the 3844sec from the beginning of acquisition) among the seismic recordings. Data were recorded by sensor No1. Based on the knowledge obtained in Step 4 the event was categorised as a FT1 event.

a)

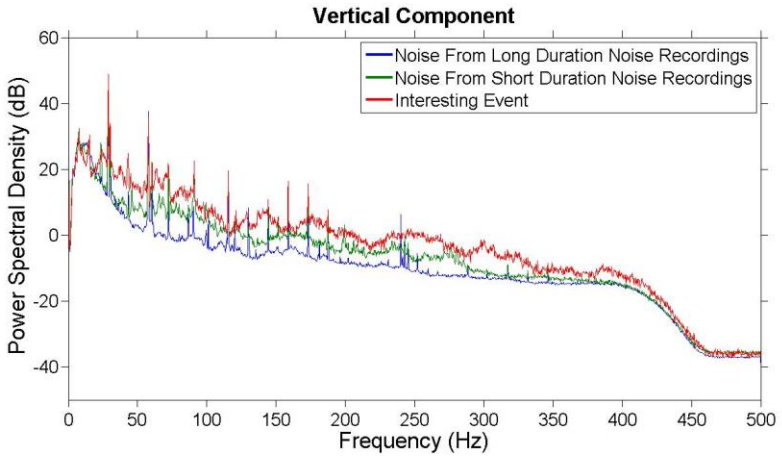

b)

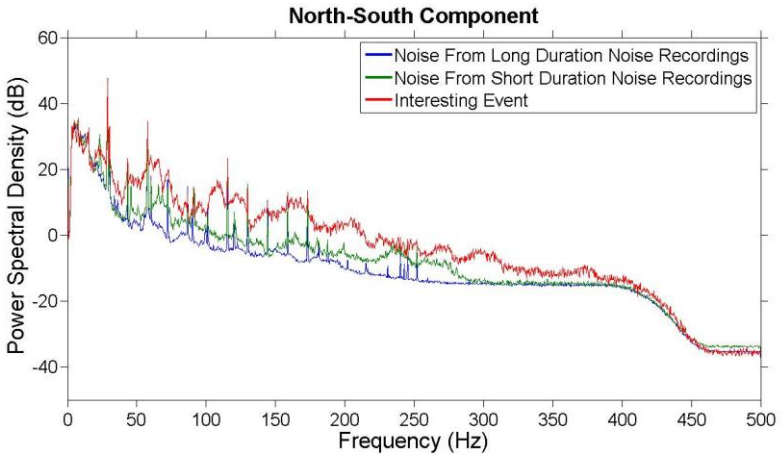

c)

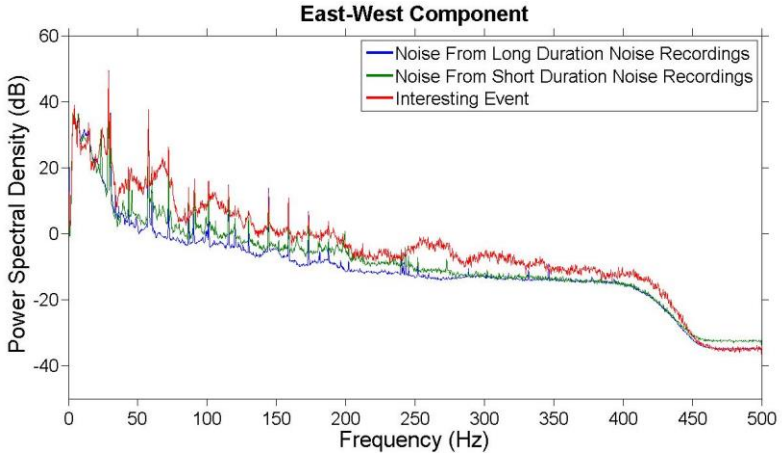

Figure 8.37: PSD of time segment detected between 164sec and 229sec of the 3rd part of L1 (or between 3849sec and 3914sec from the beginning of acquisition) containing possible failure events. The spectral characteristics of these events was analysed together because of their similarity when visualised in the spectrogram of Figure 28. Data were recorded by sensor No1. From the knowledge obtained at Step 4 the events could be either FT1 events or weak FT3 events.

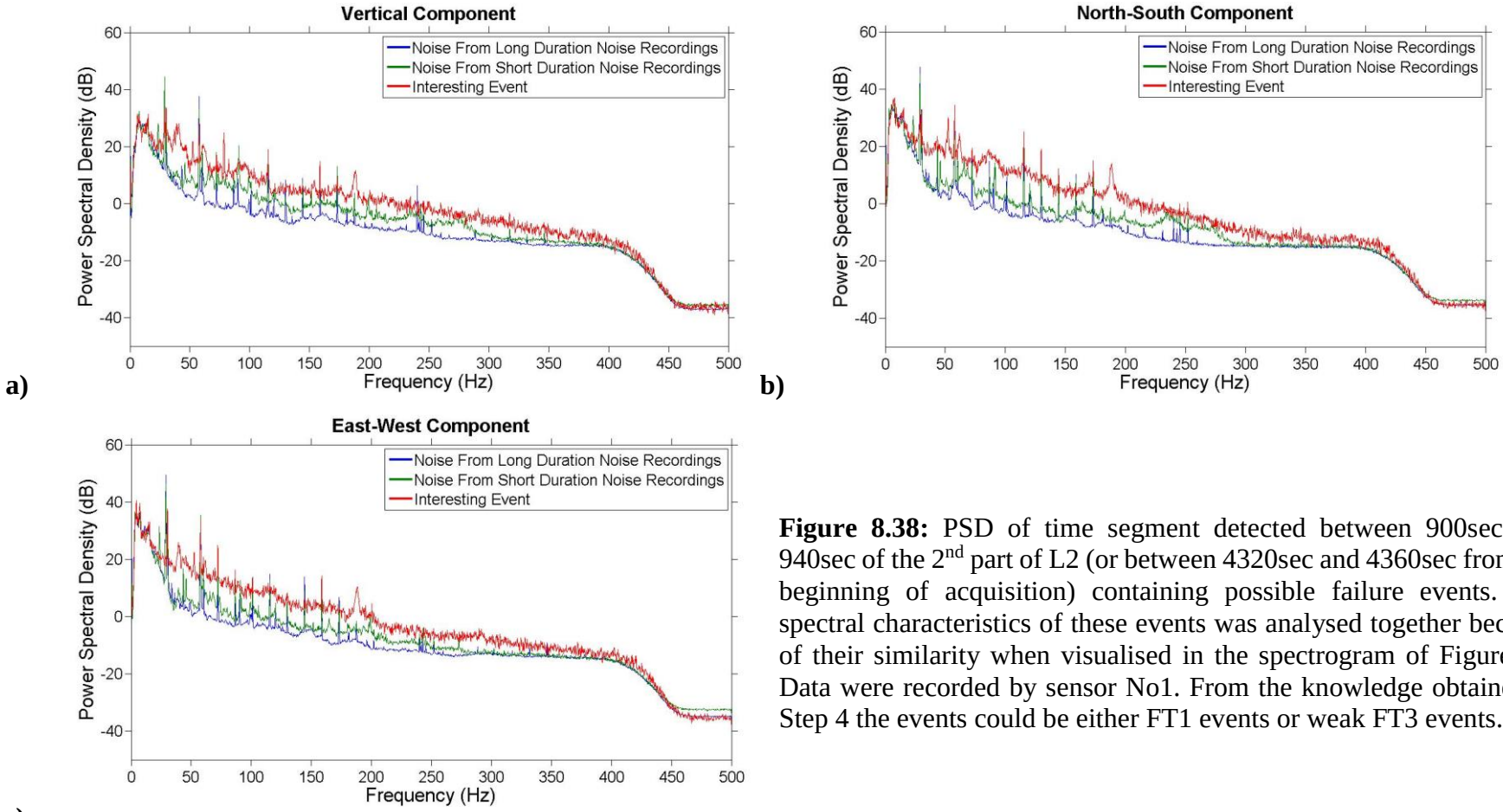

Figure 8.38: PSD of time segment detected between 900sec and 940sec of the 2nd part of L2 (or between 4320sec and 4360sec from the beginning of acquisition) containing possible failure events. The spectral characteristics of these events was analysed together because of their similarity when visualised in the spectrogram of Figure 28. Data were recorded by sensor No1. From the knowledge obtained at Step 4 the events could be either FT1 events or weak FT3 events.

a)

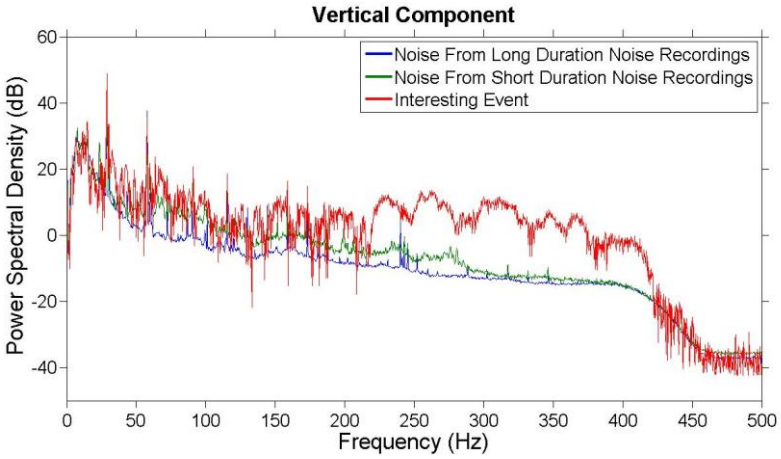

b)

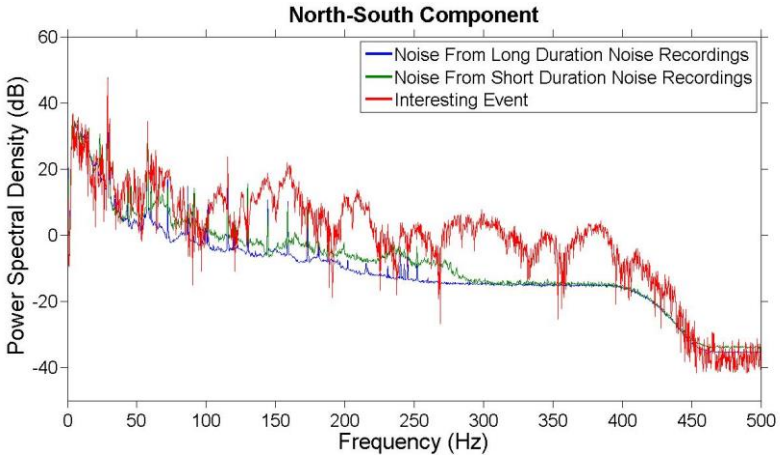

c)

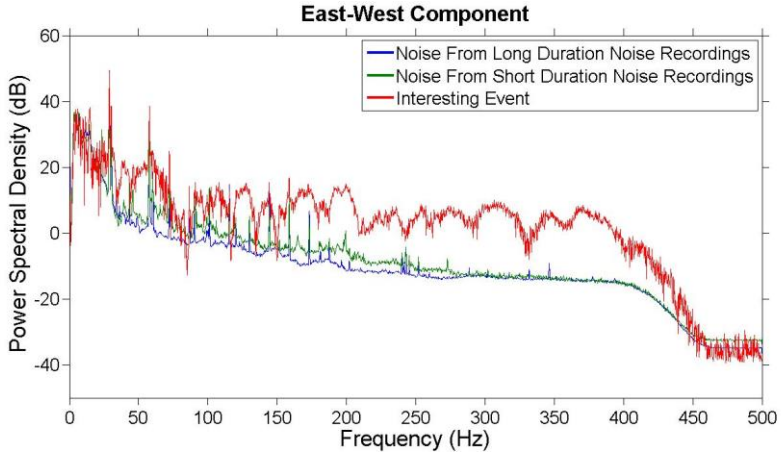

Figure 8.39: PSD of possible failure event detected at the 136sec of the 3rd part of L1 (or at the 3821sec from the beginning of acquisition) among the seismic recordings. Data were recorded by sensor No1. Based on the knowledge obtained in Step 4 the event could be either a FT1 or small FT3 event. It has though an unusual high frequency content of high spectral energy that was not found in the visually observed FT1 events. This might be due to a high frequency noise burst that was not expected. For this reason the event cannot be categorized as a landslide failure event.

8.5 Validation of the Cylinder Experiments (Ch.6 & Ch.7)

8.5.1 Introduction

Since landslide failure events were successfully recorded and analysed they were compared in the frequency domain to the displacement events induced with the cylinder methodology presented at Chapters 6&7. Both the soil only displacement events of Chapter 6, as well as the combined displacement events of soil and glass shards of Chapter 7 were compared to recordings from the two landslide experiments presented in this chapter. This frequency pattern comparison allows validation of the cylinder methodology using real landslide data.

8.5.2 Validation of the Soil Only Cylinder Experiment using Landslide Data

In this section, landslide failure events were correlated with the soil only displacement events recorded during the soil only cylinder experiments of Chapter 6. The soil only displacement events were induced under different loading conditions with the two extremes, 472kg and 829kg load, being easily distinguishable amongst all of them. For this reason those two were compared with different landslide failure events: a) the induced soil only displacement events under the smallest load (472kg) were compared with one of the soil block fall events (FT3) (fig. 8.40), b) the induced soil only displacement events under the largest load (829kg) were compared with one of the complex soil block topple (FT2) events (fig. 8.41). Note that the soil block fall events (FT3) were the most commonly observed failure during both landslide experiments, while the complex failures of soil block topples and falls (FT2) were the stronger failure events recorded.

The good correlation between the PSD spectra compared in Figures 8.40&8.41 prove that the cylinder methodology is capable of emitting landslide like signals due to soil displacement events. Differences between the curves can be attributed to the different conditions between the landslide and cylinder experiments. Such differences can be in the geology conditions (same soil type but different soil heterogeneity), loading conditions and differences in the deployment geometry (e.g. similar but not exactly the

same source-to-sensor distance, differences in the levelling and orientation of the sensors).

The failure mechanisms of the events compared were different. The soil displacement events induced from the cylinder involved only friction between soil. The FT2 event though involved friction between soil during the face detachment as well as during the movement of the failed soil volume. It also involved toppling of soil blocks (small in-between impacts) and soil impact on the ground surface. The FT3 event on the other hand involved soil friction during the detachment of the soil block from the landslide face as well as impact with the ground surface.

Comparison of the soil displacement events induced with the cylinder and FT1 events did not result in good correlation. That was because FT1 events were too weak compared to the induced soil displacement events. If the load used during the cylinder experiments had been lower then maybe correlation of the two was better.

a)

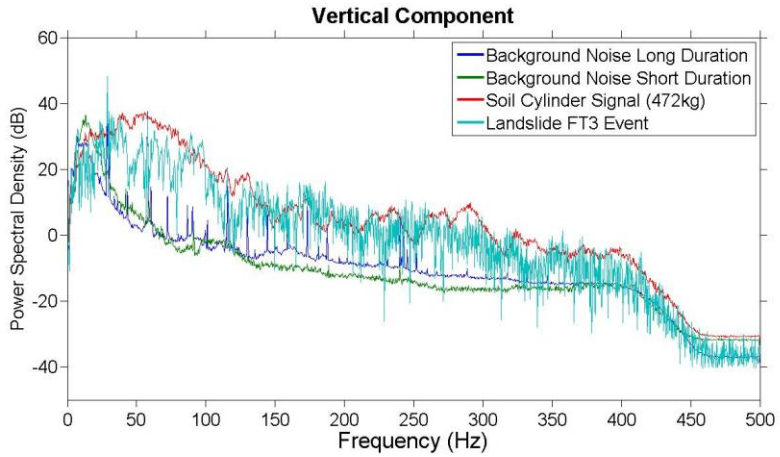

b)

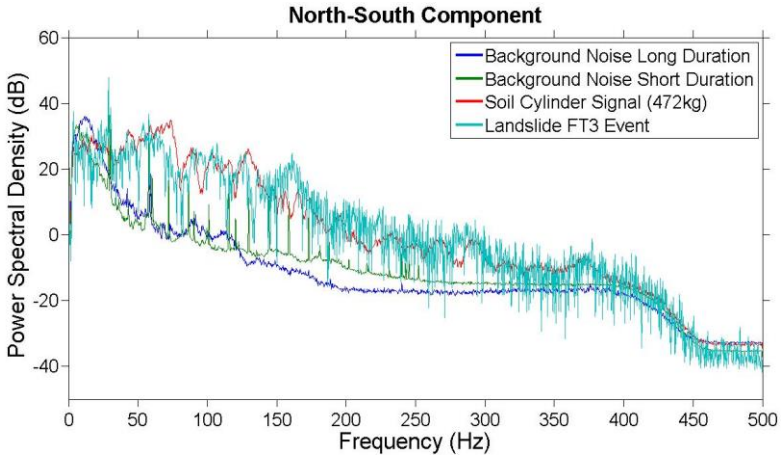

c)

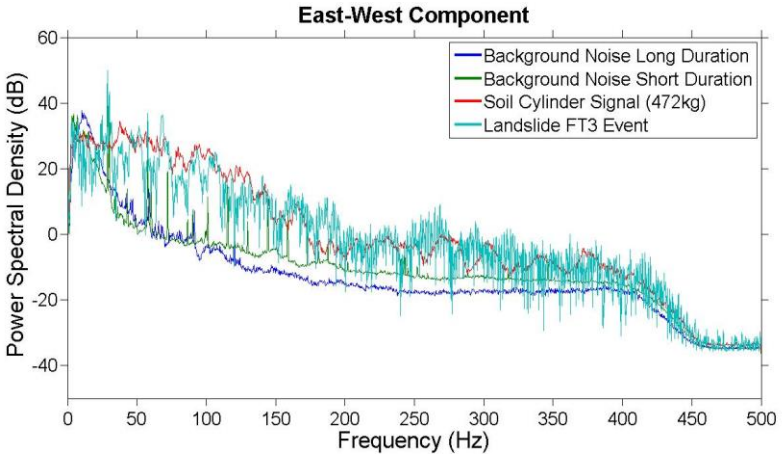

Figure 8.40: PSD curve of an FT3 event plotted against the PSD curve of induced soil displacement events using the cylinder methodology. Data were recorded ~10m away from the source for both experiments. The PSD curves of the two different sources correlate well. The latter means that the cylinder methodology is able to simulate seismic signals of landslide failure events.

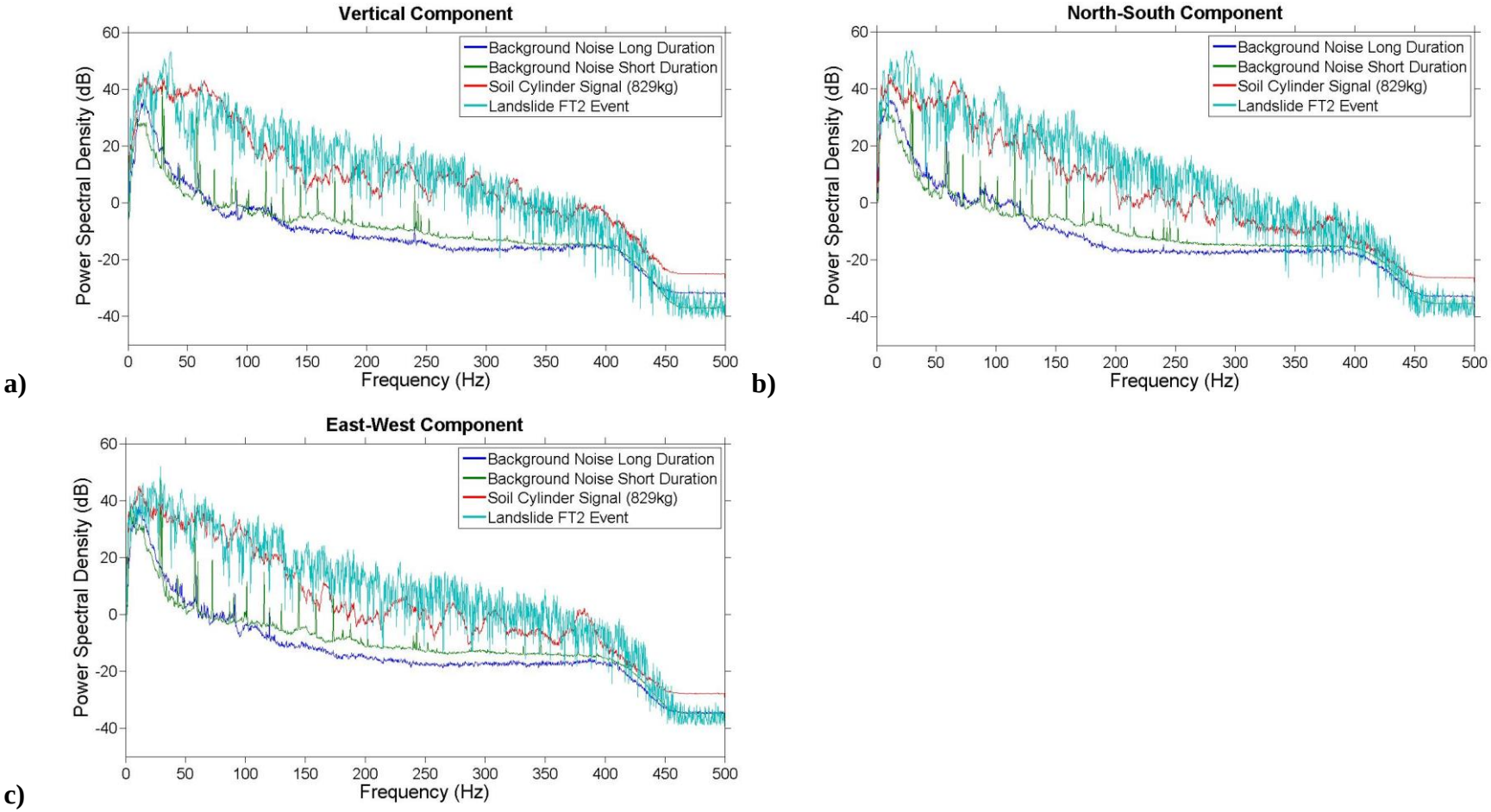

Figure 8.41: PSD curve of an FT2 event plotted against the PSD curve of induced soil displacement events using the cylinder methodology. Data were recorded ~10m away from the source for both experiments. The PSD curves of the two different sources correlate well. The latter means that the cylinder methodology is able to simulate seismic signals of landslide failure events.

8.5.3 Validation of the Glass Shard Cylinder Experiment using Landslide Data

The pile of glass shards that was embedded in the Vertical Face (VF1) of Experiment L1 did not fail during the loading of the landslide's crown and it was impossible to visually observe its state. The VF1 underwent vertical displacements that were verified visually and by measurements. It was also visually observed that it under went some horizontal displacement. The latter are believed to have led to vertical displacements of the glass shard pile causing the pile to "crush" and to horizontal displacement causing the pile to tilt (fig. 8.7). The lower part of the glass shard pile was more likely to "crush" because stress levels were higher at that part (induced load transported from the landslide crown and self-weight of glass shard pile). If the above behaviour of the glass shard pile is true, then the small displacements amongst the glass shards taking place during the deformation of the pile, might have emitted seismic signals strong enough to be recorded by the deployed seismometers.

In order to validate the above hypothesis a PSD plot was calculated every 5 seconds using all seismic recordings. These PSD plots had 50% overlapping meaning that the first plot was between the time increment of 0sec to 5sec, the second plot between 2.5sec to 7.5sec, etc. In all of these plots the PSD curve of the background noise, as well as the PSD curve of the induced glass shard displacement events of Chapter 7 were plotted. This was done to allow direct comparison between noise, glass shard frequency pattern and the landslide recordings in order to identify horizontal displacements of the glass shard pile. Data recorded from sensor No.11 (inside the excavation, ~10.5m away from VF1) were used it was the closest sensor to the lower part of the glass shard pile(the "crushing" part), deployed on soil similar to that area (2.5m deeper than all other seismometers). The latter were expected to lead to smaller travel paths for the emitted seismic waves with less attenuation.

Figures 8.42 to 8.45 present the PSD curves of the soil only induced slip events under 829kg of load (Chapter 6), the induced glass shard slip events under 878kg of (Chapter 7) and of the best PSD match from the landslide data analysed as stated on the previous paragraph. All data were recorded approximately 10m away from source. The comparison of the PSD spectra is done below:

Vertical Component (fig. 8.42)

It is clear that the PSD curve of the induced soil only slip events does not match the other two. On the other hand, the induced glass shard slip events correlate very well with the landslide event, both exhibiting a wavy pattern between the frequencies 8Hz and 50Hz (details on Table 8.3). This indicates that the landslide event could be caused by the displacement of the glass shard pile placed inside the landslide mass.

	Vertical Component		
	First Peak between	**Decrease between**	**Second Peak between**
Induced Glass Shard Slip Events	8Hz-24Hz	24Hz-35Hz	35Hz-50Hz
Landslide Event	5Hz-20Hz	20Hz-30Hz	30Hz-44Hz

Table 8.3: Details of wavy frequency pattern of the induced glass shard slip events and the landslide event for the Vertical Component.

North-South Component (fig. 8.43)

As before the PSD curve of the induced soil only slip events does not correlate with the other two. The landslide event exhibits a wavy pattern between frequencies 8-50Hz, but the horizontal components correlate less well (details on Table 8.4). This is to be expected since the North-South components of the different sensors recording the events were aligned differently to the position of the source.

	North-South Component		
	First Peak between	**Decrease between**	**Second Peak between**
Induced Glass Shard Slip Events	5Hz-24Hz	24Hz-35Hz	35Hz-50Hz
Landslide Event	5Hz-15Hz	15Hz-25Hz	25Hz-50Hz

Table 8.4: Details of wavy frequency pattern of the induced glass shard slip events and the landslide event for the North-South Component.

East-West Component (fig. 8.44)

This time there is very little correlation in the frequency range of 8-50Hz, the range were the glass shard events exhibit their wavy frequency pattern. This can be also attributed to the difference between the alignment of the sensors recording compared to the movement of the slip events.

The induced glass shard slip events and the landslide event that is compared to them have a different source characteristic: the total displacement of the cylinder was more than 1m and each event of induced glass shard displacement was larger than 10cm, while the total horizontal displacement of the vertical face VF1 was smaller than 50cm and occurred during the total duration of the experiment. In addition, the geology where both experiments were conducted was similar but differences are to be expected. Finally as said before the alignment of the horizontal components of the sensors to the movement of the source was different. Under this scope the comparison of the two events is not bad and can be accepted as possible evidence that the landslide event was caused by the displacement of the glass shard pile of the landslide.

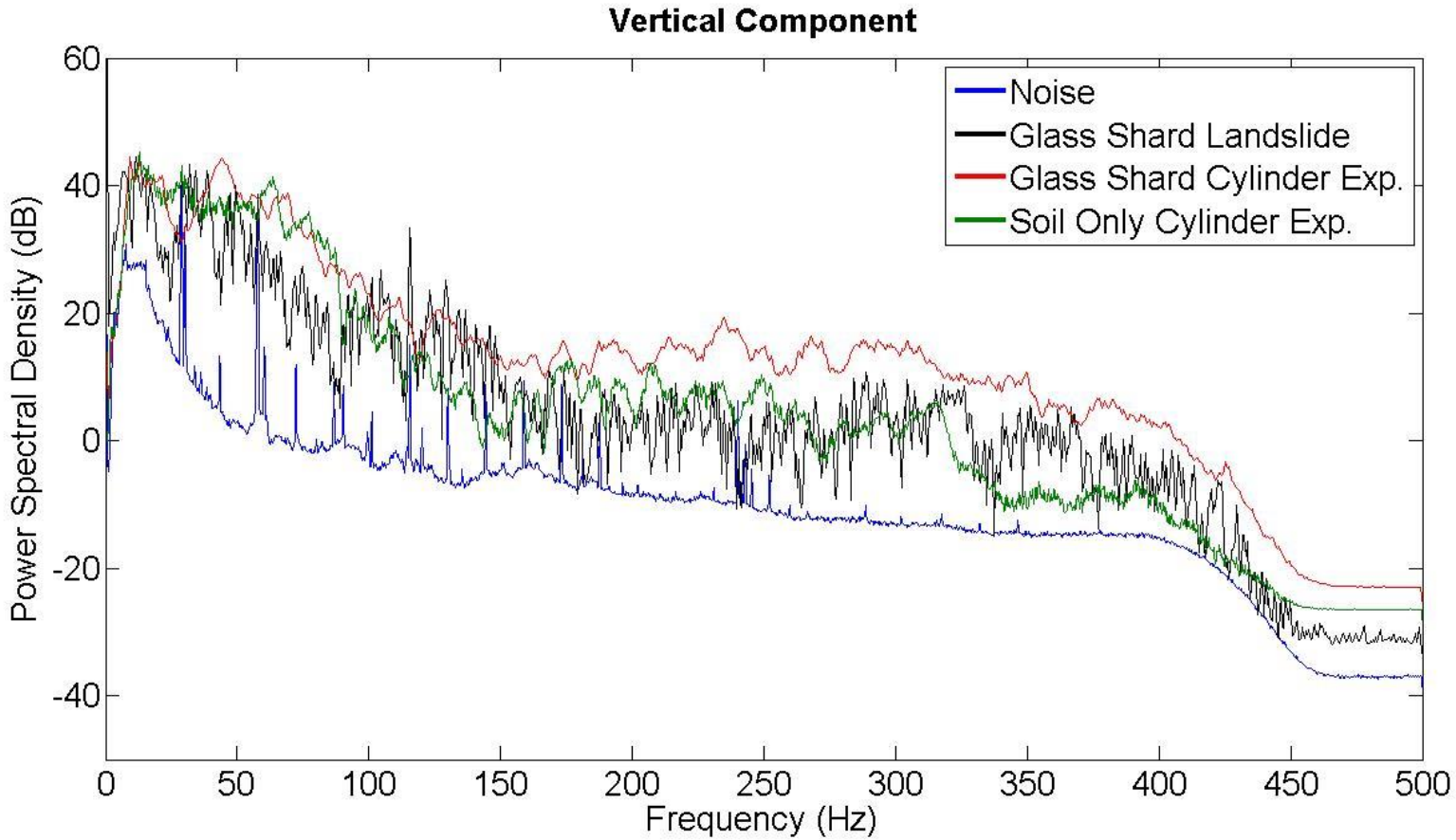

Figure 8.42: Comparison between the induced soil only slip events (Chapter 6), the induced glass shard slip events (Chapter 7) and of event recorded during the landslide Experiment L1 all recorded ~10m away from source by the Vertical component of a seismometer. The PSD spectra of the induced soil only events do not match any of the curves. The other two PSD spectra correlate quite well, both exhibiting a wavy frequency pattern between frequencies 8Hz-50Hz. This correlation provides possible evidence that the recorded landslide event is caused by the displacement of the glass shard pile placed inside the landslide mass.

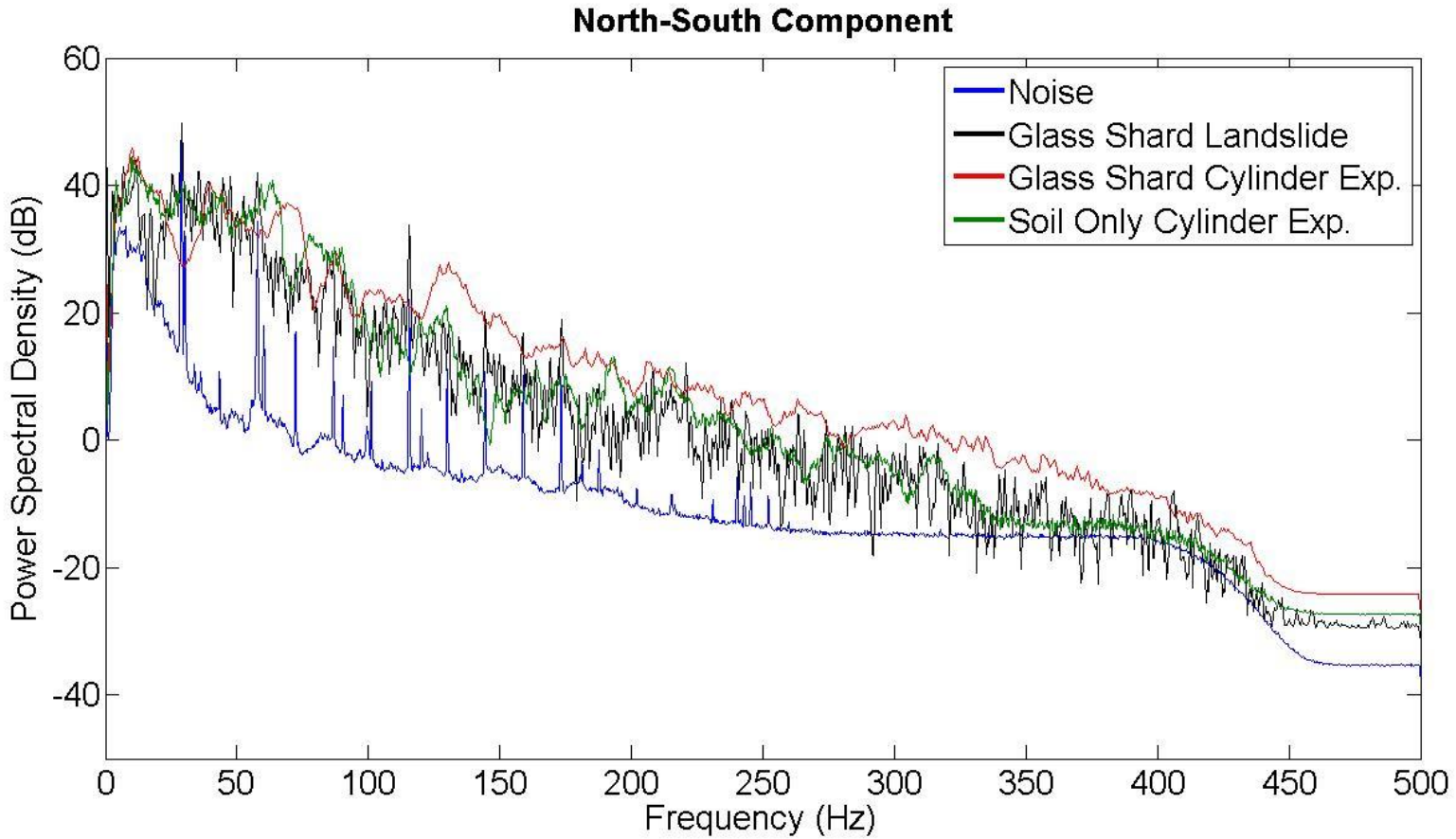

Figure 8.43: As for Figure 8.44 only for data recorded by the North-South component of a seismometer. The PSD spectra of the induced soil only events do not match any curves. Both of the other two curves still exhibiting a wavy frequency pattern between frequencies 8Hz-50Hz, but this time they do not correlate that well. The different orientation of the sensor to the movement of the glass shards is believed to be responsible for this result. The wavy pattern of the landslide data though still adds evidence to the fact that it is an event possibly caused by the displacement of the glass shard pile placed inside the landslide mass.

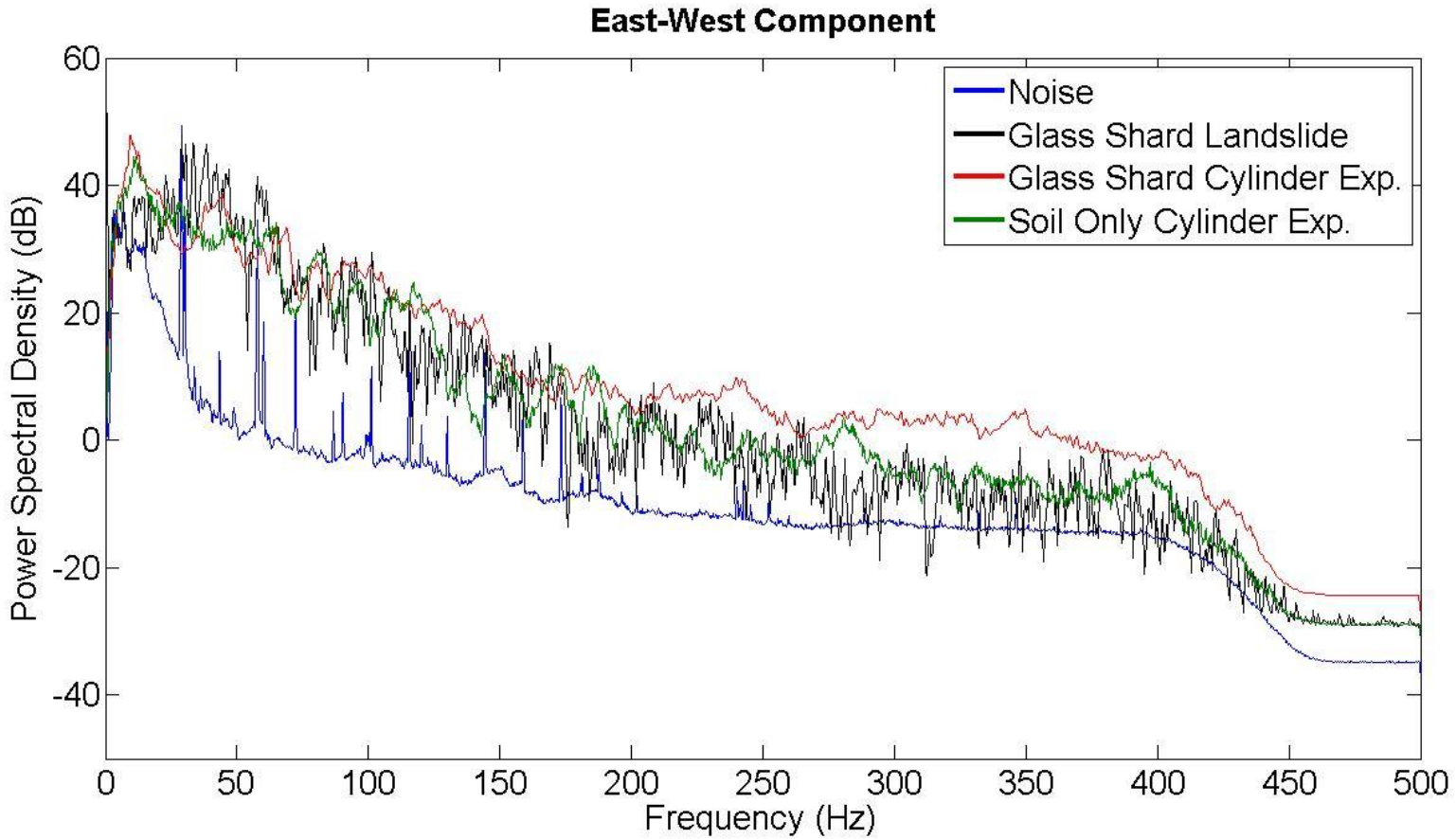

Figure 8.44: As for Figure 8.44 only for data recorded by the East-West component of a seismometer. The PSD spectra of the induced soil only events do not match any curves. Correlation between the other two curves is not optimum in this case. The PSD spectra of the landslide event does not exhibit the first peak between frequencies 8-24. The different orientation of the sensor to the movement of the glass shards is believed to be responsible for this result.

8.6 Chapter Summary

In this chapter the experimental set-up, procedure and findings of the induced failure of two 2.5m high landslides was presented. Failure in both landslides was induced by increasing the vertical load applied on the landslide's crown. Three types of failure events were visually observed; 1) crack formation/propagation forming from bottom-to-top which can be considered as precursory events of larger failures, 2) soil block topple and fall which were the largest failure events observed, 3) soil block fall which were divided into three categories of small, medium and large. The most commonly observed failure was the latter.

The visually observed events were the first seismic signals that were analysed using spectrograms and power spectral density curves. Using the results obtained from these events, other seismic signals were analysed and categorized. It was shown that similarities among the same type of events do exist but one cannot expect two events to be identical since a large number of parameters affect the final recorded signals e.g. soil heterogeneity and volume of soil mass undergoing failure.

The recorded landslide failure events were also compared with the induced soil displacement events recorded using the cylinder methodology (Chapter 6). A good correlation was found between the frequency patterns of signals recorded on both experiments. This result validated the cylinder methodology making it a good tool for researching expected landslide seismicity prior to landslide failure events.

Finally, it was hypothesised that the horizontal displacements observed at the first vertical face (VF1), lead to displacement of the glass shard pile that was inside the landslide body. In order to validate this claim the landslide data were correlated with the induced displacement events of glass shards by using the cylinder methodology (Chapter 7). After comparing the frequency patterns between different time segments of the landslide data and the induced events of Chapter 7 a good correlation was found. This first validation of using glass shards as a landslide monitoring technology looks very promising for three reasons: 1) seismicity due to glass shard displacement was recorded in the landslide without having total failure of the glass shard pile. 2) During

the induced glass shard displacement events the cylinder was displaced more than 1m with each displacement event being more than 10cm while the total horizontal displacement of the landslide was smaller than 50cm. 3) The frequency pattern of glass shard displacement events is easier identified over soil failure events mainly due to its high frequent content (>100Hz).

Chapter 9
Discussion

9.1 Introduction

In this chapter the main outcomes and impact of the experiments conducted within the work of this thesis is going to be given. In addition, the novel ideas presented along this thesis are going to be extended in the possible application of a real case scenario.

9.2 Optimisation of the microseismic monitoring system (Chapter 5)

In this experimental campaign two microseismic arrays were deployed with an equilateral triangle geometry, sharing the same centre but having different aperture sizes. They were deployed on a highly attenuating geological material (dry mixture of sand and clay) for recording weak seismic sources (firecrackers). The main goal for this experiment was to identify the location accuracy of microseismicity and optimize the aperture size.

A key factor for high location accuracy (<5m) was the use of a velocity model that represented accurately the local geology. It was found that the velocity model should not only model different geological layers with different seismic velocities, but also the change of geotechnical properties within these layers. Increasing stress and compaction due to the materials own weight, as well as increasing in saturation were found to be important. By modelling these parameters through the velocity model used, the location accuracy increased, with errors being smaller than 5m. The need for modelling such parameters might come from the small monitoring area of the experiment (<100x100m) compared to earthquake monitoring that is at a kilometre scale. Achieving such accurate results makes microseismic monitoring a strong tool that can be used for engineering applications such as landslide monitoring.

An important outcome of this experiment was also the fact that the small aperture array (25m) was found to produced better location results compared to the larger one (50m). This was because the source-to-sensor distances of the 25m array was always smaller

compared to the source-to-sensor distance of the 50m array. The 50m array reduced the attenuation effect of the local geology, leading to clearer seismic recordings for the seismometers of the small array. This finding goes against the general rule of maximizing the area covered within the deployment geometry of seismometers. Large arrays are used to increase chances of having the seismic source within the seismometers allowing for better constraint of the location solution. In such cases though the signal has to travel longer distances increasing the effect of attenuation and making it hard to record clear phase onsets of weak sources.

It would be useful for this experiment to be repeated at a real landslide environment. This way the effect of the expected spatial heterogeneities of soil can be studied. Two or more arrays can be deployed on site with small explosions used as a source. The up-scaled shear box methodology could alternatively be used as a source if simulation of landslide like seismic signals are considered to be useful. In order to study the heterogeneity of the landslide's body trigger points of the source must include different radial directions having as a start the centre of the deployed arrays.

9.3 Simulation of Landslide Seismic Signals at Field Scale Using an Up-Scaled Shear Box (Chapter 6)

In this chapter a novel methodology was presented for inducing soil displacement events in the field using an up-scaled shear box (cylinder). These displacement events were simulating possible displacements along a failure plane of a landslide emitting similar seismicity.

The main merit of the methodology presented is its low cost and its non-destructive nature. The materials needed for conducting the experiment are easy to obtain and transport to a landslide site, as long as an access road exists. Furthermore, the methodology can provide information regarding the expected landslide seismicity prior to any landslide failure, such as the frequency content of soil displacement events and the expected attenuation of the emitted seismic energy during wave propagation. The user can deploy seismic sensors at different locations and compare the changes of

the signal characteristics as recorded by the different sensors. Such information can be used for the optimisation of the deployment geometry, leading to a successful monitoring campaign.

Finally by using the proposed methodology, the user can control a large number of parameters seen below:

(a) the soil type used inside the cylinder and for the corridor

Soil material matching any geological layer involved in the landslide mass can be used inside the cylinder, as well as to form the surficial corridor on which the cylinder can be displaced. If the soil material used are identical to one geological layer, the up-scaled shear box methodology will simulate seismic signals emitted during shear within that layer. Use of different soil types in the cylinder and the corridor will simulate the seismicity emitted during shear between two different geological layers. The needed soil material can either be bought or obtained through on site excavation.

(b) compaction of the soil

In the complex geological environment of a landslide, soil compaction can take multiple values with depth. Simulation of this parameter can take place by using standard soil compaction techniques to the soil placed inside the cylinder and to the soil of the surficial corridor.

(c) stress level on the slippage surface

Controlling the force applied on the slippage surface (stress) allows simulation of soil slip events at different depths. Stress levels on the slip surface can be controlled by either increasing the load placed on top of the cylinder according to the presented methodology or by changing the area size of the slip surface (change of the cylinder's diameter). A small slip area needs smaller load compared to a large slip area to achieve the same stress levels

(d) the degree of saturation of the soil

Rain is be one of the main triggering mechanisms of landslides. Soil saturation can be controlled by adding water to the soil that will fill the concrete cylinder. The water content of the ground soil corridor can also be controlled by either spraying water on it, or by laying a new soil layer that has the needed water content on the ground surface

(e) the area of slippage surface

Soil displacement can occur at the whole area of the active slope or at smaller ones. By using cylinders with different diameters it is possible to study how the area size of the slippage surface affects the emitted seismic signals. Since the experiment is at field scale, the slippage surface of the experiment is related to a same size failure plane in a landslide.

Control over the above parameters allows for simulation of different landslide failure scenarios, such as strong precipitation events (control over soil saturation) or soil displacement events occurring at different depths (control over stress levels). The obtained information from such experimental measurements can lead to a seismic dataset of events that has the potential to allow identification not only of landslide failure events, but also of their failure mechanism. Such a dataset could allow the real time characterisation of a landslide failure event, without further need for validating the analysis using other monitoring techniques or data.

In future this experimental methodology should be repeated in order to study different landslide failure scenarios. As presented previously, the methodology allows control of different geotechnical parameters simulating different conditions during soil slip. It is of great importance to use the proposed methodology in order to create a library of landslide seismic signals that could potentially be recorded at real case monitoring campaigns. For example, a very important parameter that should be changed in future experiments is the soil saturation, since water content is one of the main landslide triggers. Such a library would be helpful during the design of the seismometer's deployment geometry and signal characterisation analysis. Finally, different

broadband and high frequency seismometers should be deployed along with short period in order to record all frequency bands, allowing for a detailed frequency spectrum characterisation. It would be adequate for these sensors should be deployed at 5m to 10m intervals compared to the very dense sensor spacing introduced in this chapter.

9.4 Evidence for an improved seismic monitoring system for landslides based on the use of glass shards (Chapter 7)

In the literature review it was understood that landslides can occur under different geological and geotechnical conditions. In addition, landslides are not a point failure phenomenon but have a 3D failure mechanism. The possible combinations of conditions that can lead to failure along with the geological heterogeneities create a complex problem. For the above reasons successful monitoring and behavioural understanding of landslides needs extensive study.

Landslide monitoring would be easier if a common parameter was present to all seismic monitored slopes. This parameter should lead to recordings of unique seismicity that is easy to detect and remains unaffected by time or naturally occurring events such as precipitation. For these reasons it was hypothesised that piles of glass shards could be the common parameter in seismically monitored landslides. Glass shards are a manmade recyclable material, easy to find around the world, with angular/coarse shape and brittle behaviour. Piles of this material could be embedded inside the landslide mass and deform along the landslide, tracking its displacements.
Glass shard displacement events were induced using the methodology of the up-scaled shear box (cylinder) presented in Chapter 6. It was found that their emitted seismicity had a higher frequency content compared to soil displacement events. In addition glass shard displacement events have a wavy frequency pattern in the first 60Hz with two distinct peaks compared to a rather flat response during purely soil displacement events. This difference can be attributed to the differences between the material properties of glass shards and soil.

In a real landslide monitoring case, glass shard piles could be created as shown in the plane view of a landslide site in Figure 9.1. The landslide area with the greatest failure risk should have equally spread glass shard piles with seismometers in between them. Such a geometry leads to a dense monitoring system able to detect both soil and glass shard displacements. The geometry of the seismometers used in Figure 9.1 is optimally designed to reduce the number of seismometers needed, thus reducing the high cost of acquiring and operating them compared to building glass shard piles. Such a system could implement the simple technique of zonal location (see Chapter 3) to determine the active landslide area without the need of clear on-set wave arrivals. By assessing the number of events and the seismic energy released the engineers in charge of the monitoring campaign can determine measures such as a closer engineering inspection or even the evacuation of the area affected by a possible landslide failure.

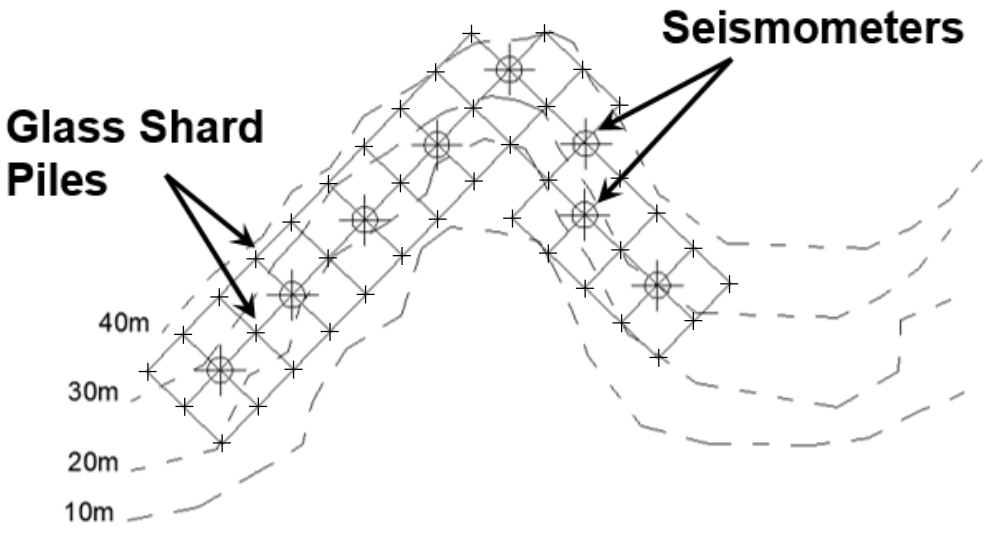

Figure 9.1: Plane of a landslide site where glass shard piles and seismometers could be deployed for detecting and locating landslide displacements. The area prominent to failure has been identified and glass shard piles have been built at constant increments. Seismometers could be positioned in the centre of the area surrounded by such piles. This design minimizes the need for seismometers that have a higher cost in obtaining and operating them compared to building glass shard piles.

Glass shard piles could also act to increase the strength of landslides. Glass shards are angular material compared to soil particles, thus have a higher shear strength resulting in slope stabilization. The design of the piles (diameter and length) will be case specific based on the geotechnical parameters of the area prone to failure. In addition, such piles will have high permeability compared to soil due to the angularity of the glass shards. The latter means that glass shard piles could be used as part of a landslide drainage system leading to increased slope stability.

Further research needs to be done in the novel technique of using glass shards to track landslide displacements. Optimization of parameters such as the glass shard particle size, as well as the diameter and length of the piles used in the field needs to be conducted in order to apply it effectively in a real case. In addition research in the emitted seismicity of other angular materials should be made, e.g. gravel, that has similar properties as glass shards in terms of its angularity and brittle behaviour. Finally glass shard seismicity should be compared to landslide seismicity triggered due to increases in soil saturation, e.g. by a precipitation event. Saturated soil loses its brittle behaviour meaning that the expected emitted seismic energy during soil displacement would be smaller. On the other hand glass shards remain unaffected by water giving them a strong advantage in emitting detectable seismic energy when displaced.

As the discussion of the previous section, this experiment should also be repeated using different values of the parameters the user has control on. Soil saturation and different size of the effective slip surface should be put into test. In addition different coarse and brittle material with unaltered parameters through time should be tested as an alternative to using glass shards, e.g. gravel. Their emitted seismicity might be proven more advantageous and possibly having a higher cost-benefit return. Different seismic sensors should also be used to determine accurately the frequency spectrum of the emitted seismicity. In this case emphasis should be given to high frequent seismometers since it was shown that there is spectral energy emitted above 100Hz. This would allow the detailed study of the attenuation of the emitted high frequency energy that could not be made in this work due to the type of seismometers used.

9.5 Seismic signature of landslides: validation based on two controlled failures (Chapter 8)

This chapter described the methodology and findings of inducing failure to two 2.5m high landslides by increasing the vertical load to their crown. This was the first controlled landslide experiment designed to allow the validation of the emitted seismicity. The controlled conditions of the experiment and the ability to have visual observation of failure events allowed the characterization of seismic signatures during landslide failure. The only difference between the two landslides was that in one of them a glass shard pile was constructed. Unfortunately the glass shard pile was not seen to fail, but it is believed to have deformed vertically and horizontally, along with the landslide, as it was originally designed to do so.

Three failure types were visually identified: 1) crack formation/propagation, 2) combination of soil block topple and fall and 3) soil block fall. The frequency characteristics of these failure types was characterized and found that each category had a distinct pattern allowing grouping in similar events. The induced failure events were relatively small compared to cases were thousands of cubic meters of soil are involved in landslides. They are of great importance though because they can be considered as precursory events of larger landslide failure events. If the monitoring system is able to detect such events in real time, then risk mitigation actions can be made to avoid human casualties. For such an application, microseismic monitoring can be considered as an early warning monitoring system.

This dataset can be used in similar landslide cases in order to characterize the recorded seismicity but also in order to plan the deployment geometry of seismic sensors. It was shown that small failures like the one recorded emit little seismic energy that is attenuated rapidly. The latter means that a dense microseismic array is needed to detect such events. In the conducted experiments 3D short period seismometers were used for the monitoring purposes. It was found out that horizontal components are advantageous when it comes to detecting crack formation/propagation events. In addition landslide seismicity was found to be mostly above 10Hz with background noise being higher at frequencies below 20Hz. This means that the use of geophones

with flat response above 10Hz or 20Hz can be used at landslide monitoring campaigns reducing greatly the cost of the system.

Both landslides consisted of tropical clay, the same soil material used in Chapter 6. This allowed correlation between data sets and validation of the up-scaled shear box (cylinder) methodology with real landslide data. Comparison showed that landslide failure events and induced soil displacements using the cylinder methodology share similar frequency characteristics. This means that the up-scale shear box methodology can be used predictively to study the expected seismicity emitted during a future soft soil landslide failure. Such data can allow the optimisation of the seismic sensors needed for the monitoring campaign, as well as the optimisation of their deployment geometry.

Finally, the seismic recordings of the landslide with the embedded glass shard pile were correlated with the data collected during the induced glass shard displacement events (Chapter 7). Their good correlation suggests that even small displacements in the glass shard pile emit easily detectable seismicity. Along with the glass shards having stable characteristics as a material over time and are not affected by changes in saturation, it is additional evidence that the having piles of glass shards in landslide might be a good methodology in optimising the seismic detection of landslide displacements. More research is needed on this matter, but current results are optimistic that the use of glass shard piles can be advantageous as part of an early or real time warning system of landslide failures.

Amongst all experiments presented in this thesis, this is the hardest to repeat. There is interest in doing so to record additional data regarding the observed soil failures. It would be advantageous to record video footage of failures at better light conditions or with a technology that is not affected by light. Video footage should also be done in a way that will allow volume calculation of the soil mass being involved in the observed failure events. This should be relatively easy since one or two additional cameras recording at different angles would be adequate. In addition, a monitoring technology able to record the vertical as well as the horizontal displacements of the face of the

landslide undergoing failure would add to the understanding of the landslide's behaviour. Finally, failure should be induced at a glass shard pile that is located inside the body of a landslide. This way the effect of horizontal displacements as well as that of the total failure could be studied in the recordings. To do so more analytical, an inclinometer could be positions at the centre of the glass shard pile. Doing so will allow the comparison between the displacement of the glass shard pile with those the landslide undergoes.

Chapter 10
Conclusions

This thesis investigated the kinematic behaviour and the emitted seismicity of soft soil landslides with the help of microseismic monitoring. Landslides are of particular engineering interest since they still are proven to be greatly catastrophic around the globe, claiming numerous human lives. Microseismic monitoring was chosen as the optimum tool for such research since it is proven to detect and locate extremely weak geological processes. The seismic sensors used for such studies are also easily deployed and can provide continuous data remotely. Specific focus was given on soft soil landslides as it was found that there has been little research done on such cases compared to landslides dominated by rock. Finally soft soils are a highly attenuating geological material compare to rock formations adding an additional challenge in recording and analysing weak seismic signals coming from small soil deformations.

The first experimental work of this thesis (Chapter 5) was focused on the location capabilities of two microseismic arrays with different apertures (25m and 50m), each consisting of four short period seismometers deployed at an equilateral geometry: three 1D sensors on the corners and one 3D sensor at the centre of the triangle. The local geology consisted of a surface layer of sand and clay mixture overlying a 500m thick limestone layer and bedrock. Firecrackers were used as a weak active seismic source. The results of this experiment showed that geological information alone are not enough to produce a seismic velocity model that represents realistically the geological medium seismic waves travel: geotechnical parameters such as increase of compaction and increase in water saturation need to be taken into account. Using a realistic seismic velocity model and microseismic data the recordings of weak seismic events can be accurately located, making microseismic monitoring a powerful tool for engineering purposes such as landslide monitoring. Finally it was shown that small microseismic arrays provide more accurate location results compared to larger ones. This is due to the fact that the seismic sensors of a small microseismic array are more likely to record clearly weak seismic events, before seismic waves are lost below background noise levels due to attenuation.

The second experimental work (Chapter 6) was focused on creating a methodology able to simulate landslide like seismic signals by inducing soil slip events. The methodology included using an up-scaled shear box (a concrete cylinder) on the field containing soil under different loading conditions. By displacing the up-scaled shear box on a soil surface at the field, soil slip events were induced emitting seismic signals. The followed methodology was proven easy to apply, allowing simulation of different geotechnical soil conditions, such as stress. Using signal analysis techniques, information regarding the frequency pattern of the emitted seismicity, as well as the effect that different stress conditions and attenuation have on it were retrieved.

From the literature review it was understood that landslide seismicity is complex and can take the form of seismic signals with different characteristics. For this reason the third experimental work of this thesis (Chapter 7) was focused on creating a methodology that would allow the presence of a common seismic source on soft soil landslide and be triggered from landslide displacements. This source, when triggered, would emit seismic signals with a priory seismic characteristics, easily detectable amongst other seismic recordings. Glass shards were chosen as such a seismic source that in the form of glass shard piles inside the landslide mass would be triggered upon landslide displacement. The signal characteristics were firstly studied with the use of the up-scaled shear box methodology and were found to be different from those of the simulated slip events. The emitted glass shard seismicity was proven to be advantageous over the induced soil slip events since it had a wavy frequency pattern below 50Hz and a high frequency content, above 100Hz, making it easy to detect and distinguish amongst other seismic signals.

The final experimental chapter (Chapter 8) was focused on the signal analysis of landslide failures recorded during the induced failures of two vertical soft soil landslide faces. A glass shard pile was placed inside one of them that was not seen to fail but is believed to have been vertically and horizontally displaced due to the landslide's displacement. Three failure types were observed that had different frequency characteristics: a) crack formation/propagation, b) soil block topple and fall and c) soil block fall. The weakest recordings were observed during the crack

formation/propagation events and can be considered as early warning signals. The ability to record such events proves that microseismic monitoring can be used as an early warning monitoring system of landsides. The strongest during the soil block topple and fall. The weakest events were only recorded at a source-to-sensor distance of ~15m, while the strongest could be recorded at a distance of ~43.5m and results allowed the assumption that they could be recorded further than 50m. Findings also showed that the observed seismicity was generally above 10Hz and that horizontal components were proven advantageous over the vertical only in recording very weak events (crack formation/propagation). The above result suggests that 1D geophones with a flat response above 10Hz, deployed at a 40m intervals, can be successfully used for monitoring most landslide failure events. Finally, the frequency characteristics of two landslide failure events were found to correlate well with the frequency characteristics of the recorded seismicity during the two up-scaled shear box experiments separately: 1) the soil only induced slip events and 2) the glass shard induced events. The first showed that the up-scaled shear box methodology can be used for emitting landslide like seismic signals in the field. The second suggest that even the small displacements of a glass shard pile inside a landslide can be recorded and identified. The main outcome though is that the data obtained with the up-scaled shear box methodology can be used proactively to characterise the expected seismicity of landslide failures. Such information can allow real time analysis of the collected data and the deployed microseismic monitoring system to act as an early warning system of large landslide failures.

Bibliography

Alonso, E.E., Pinyol, N.M. & Puzrin, A.M. (2010) *Geomechanics of Failures. Advanced Topics*, Dordrecht: Springer Netherlands.

Amitrano, D., Gaffet, S., Malet, J.-P., Maquaire, O. (2007) "Understanding mudslides through micro-seismic monitoring: the Super-Sauze (South-East French Alps) case study", *Bulletin de la Société Géologique de France,* vol.178, No. 2, pp. 149–157.

Amitrano, D., Arattano, M., Chiarle, M., Mortara, G., Occhiena, C., and Pirulli, M., Scavia, C. (2010) "Microseismic activity analysis for the study of the rupture mechanisms in unstable rock masses", *Nat. Hazards Earth Syst. Sci*., vol.10, pp. 831-841.

Amitrano, D., Grasso, J.R., Senfaute, G. (2005) "Seismic precursory patterns before a cliff collapse and critical point phenomena", *Geophysical Research Letters*, vol.32, Issue 8.

Barta, J., Dostal, D., Benes, V., Tesar, M. (2005) "Application of geophysical methods in the study of landslide movements, taking into account geological conditions in the Sudety mountains", *Acta Geodynamica Et Geomaterialia*, vol 2, No 3 (139), pp. 121-129.

Bormann, P. (ed.) (2002) *New manual of seismological observatory practice (NMSOP)*, GeoForchungsZentrum Potsdam.

Brückl, E., and Mertl, S. (2006) "Seismic monitoring of deep-seated mass movements", *Disaster Mitigation of Debris Flows, Slope Failures and Landslides – Conference Proceedings*, INTERPRAEVENT International Symposium, pp. 571–580.

Burtin, A., Bollinger, L., Cattin, R., Vergne, J. and Nábělek, J.L. (2009) "Spatiotemporal sequence of Himalayan debris flow from analysis of high-frequency seismic noise", *Journal of Geophysical Research,* vol. 114. Issue F4.

Calder, E.S., Luckett, R., Sparks, R.S.J. and Voight, B. (2002) 'Mechanisms of lava dome instability and generation of rockfalls and pyroclastic flows at Soufrére Hills volcano', in Druitt, T. H. and Kokelaar, B. P. (eds) (2002) *The Eruption of the Southfriere Hills Volcano, Montserrat, from 1995 to 1999,* Geological Society, London Memoir , vol.21, pp.173-190.

Caplan-Auerbach, J. and Huggel, C. (2007) 'Precursory seismicity associated with frequent, large ice avalanches on Iliamna volcano, Alaska, USA', *Journal of Glaciology*, vol. 53, Issue 180, pp. 128–140.

Chen, Z., Stewart, R.R., and Bland, H.C. (2005) 'Analysis of microseismicity at a mountain site', *CREWES Research Report*, vol. 5, University of Calgary.

Cheon, D.-S., Jung, Y.-B., Park, E.-S., Song, W.-K. and Jang, H.-I. (2011) 'Evaluation of damage level for rock slopes using acoustic emission technique with waveguides', *Engineering Geology*, vol.121, Issues 1-2, pp. 75–88.

Craig, R.F. (2004) '*Craig's soil mechanics'*, Seventh edition, Spon Press, London; New York.

Dammeier, F., Moore, J.R., Haslinger, F. and Loew, S. (2011) 'Characterization of alpine rockslides using statistical analysis of seismic signals', *Journal of Geophysical Research,* vol.116, Issue F4.

Del Gaudio V.,Wasowski J., Pierri P., Mascia U. and Calcagnile G. (2000) 'Gravimetric study of a retrogressive landslide in Southern Italy', *Surveys in Geophys.*, vol. 21, Issue 4, pp. 391-399.

Deparis, J., Jongmans, D., Cotton, F., Baillet, L., Thouvenot, F. and Hantz, D. (2008) 'Analysis of Rock-Fall and Rock-Fall Avalanche Seismograms in the French Alps', *Bulletin of the Seismological Society of America*, vol. 98, no. 4, pp. 1781–1796.

Dixon, N., Hill, R. and Kavanagh, J. (2003) 'Acoustic emission monitoring of slope instability: development of an active wave guide system', *Geotechnical. Engineering*, vol. 156, Issue 2, pp. 83–95.

Dixon, N. and Spriggs, M. (2007) 'Quantification of slope displacement rates using acoustic emission monitoring', *Canadian Geotechnical Journal,* vol. 44(8), pp. 966–976.

Ekström, G. and Stark, C.P. (2013) 'Simple scaling of catastrophic landslide dynamics', *Science*, vol. 339, no. 6126, pp. 1416–1419.

Feng, Z. (2011) 'The seismic signatures of the 2009 Shiaolin landslide in Taiwan', *Natural Hazards and Earth System Science,* vol. 11, pp.1559–1569.

Fujisawa, K., Highuchi, K., Koda, A. and Harada, T. (2007) 'Landslide detection, monitoring, prediction, emergency measures and technical instruction in a busy city, Atami, Japan', *Conference Proceedings, First North American Landslide Conference, Vail, Colorado*. pp. 65–73.

Galitzin, P. B. (1915) 'Sur le tremblement de terre du 18 de f´evrier 1911', *Comptes Rendus Acad. Sc. de Paris*, vol. 160, pp. 810–813.

Ge M. (2003) 'Analysis of source location algorithms: Part I. Overview and non-iterative methods', *J Acoust Emission*, vol. 21, pp. 14–28.

Ge M. (2003) 'Analysis of source location algorithms: Part II. Iterative methods', *J Acoust Emission*, vol. 21, pp.29–5.

Geiger, L. (1912) ‘Probability method for the determination of earthquake epicentres from the arrival time only’, *Bull. St. Louis. Univ.* vol.8, pp.60-71.

Gendzwill, D. and Prugger, A. (1989) ‘Algorithms for micro-earthquake location’, in *Proc. 4th Conf. Acoustic emission/Microseismic Activity in Geologic Structures*, Trans Tech. Publications, Clausthal-Zellerfeld, Germany, pp.601-605.

Gomberg, J., Bodin, P., Savage, W. and Jackson, M.E. (1995) ‘Landslide faults and tectonic faults, analogs?: The Slumgullion earthflow, Colorado’, *Geology,* vol. 23, no. 1, pp. 41.

Gomberg, J., Schulz, W., Bodin, P. and Kean, J. (2011) ‘Seismic and geodetic signatures of fault slip at the Slumgullion Landslide Natural Laboratory’, *Journal of Geophysical Research*, vol.116, Issue B9.

Got, J.-L., Mourot, P. and Grangeon, J. (2010) ‘Pre-failure behaviour of an unstable limestone cliff from displacement and seismic data’, *Natural Hazards & Earth System Sciences,* vol. 10, pp. 819-829

Häge, M. and Joswig, M. (2009) ‘Mapping local microseismicity using short-term tripartite small array installations–Case study: Coy region (SE Spain)’, *Tectonophysics*, vol.471, Issues3-4, pp. 225–231.

Harris, F.J. (1978) ‘On the use of windows for harmonic analysis with the discrete Fourier transform’, *Proceedings of the IEEE,* vol. 66, pp. 51–83.

Havskov, J. and Alguacil, G. (2010) *‘Instrumentation in earthquake seismology’*, Springer Netherlands.

Helmstetter, A., and S. Garambois (2010) ‘Seismic monitoring of Séchilienne rockslide (French Alps): Analysis of seismic signals and their correlation with rainfalls’, *J. Geophys. Res*., vol. 115, Issue F3.

Hibert, C., Mangeney, A., Grandjean, G. and Shapiro, N.M. (2011) 'Slope instabilities in Dolomieu crater, Réunion Island: From seismic signals to rockfall characteristics', *Journal of Geophysical Research*, vol.116, Issue F04032.

Highland, L. M. and Bobrowsky, P. (2008) The Landslide Handbook – A Guide to Understanding Landslides: Reston, Virginia, U.S. Geological Survey Circular 1325, 125p.

Horiuchi, S., Negishi, H., Abe, K., Kamimura,A. and Fujinawa, Y. (2005) 'An automatic processing system for broadcasting earthquake alarms', *Bulletin of the Seismological Society of America*, vol. 95, no. 2, pp. 708-718.

Huang, C.-J., Yin, H.-Y., Chen, C.-Y., Yeh, C.-H. and Wang, C.-L. (2007) 'Ground vibrations produced by rock motions and debris flows', *Journal of Geophysical Research*, vol. 112, Issue F2.

Jeffreys, H. (1923) 'The Pamir earthquake of 18 February 1911, in relation to the depths of earthquake foci', *Geophysical Journal International*, vol. 1, Issue Supplement 2, pp. 22–31.

Jongmans, D., Bièvre, G., Renalier, F., Schwartz, S., Beaurez, N. and Orengo, Y. (2009) 'Geophysical investigation of a large landslide in glaciolacustrine clays in the Trièves area (French Alps)', *Engineering Geology*, vol. 109, Issues 1-2, pp. 45–56.

Jongmans, D., and Garambois, S. (2007) 'Geophysical investigation of landslides: A review', *Bulletin Société Géologique de France* ,vol.178, no. 2. pp.101-112.

Joswig, M. (2008) 'Nanoseismic Monitoring fills the gap between microseismic networks and passive seismic', *First Break*, vol. 26, pp. 121-128.

Kandawasvika, A. and Reinhardt, W. (2005) 'Concept for interoperable usage of multi-sensors within a landslide monitoring application scenario', In *Submitted paper for 8th AGILE Conference on GIScience*.

Kane, W.F. and Beck, T.J. (2000) 'Instrumentation Practice for Slope Monitoring', *Engineering Geology Practice in Northern California, Association of Engineering Geologists Sacramento and Sun Francisco Sections*, 13.

Kao, H., Kan, C.-W., Chen, R.-Y., Chang, C.-H., Rosenberger, A., Shin, T.-C., Leu, P.-L., Kuo, K.-W., and Liang, W.-T. (2012) 'Locating, monitoring, and characterizing typhoon-linduced landslides with real-time seismic signals', *Landslides*, vol. 9, pp. 557–563.

Kayal, J.R. (2008) '*Microearthquake Seismology and Seismotectonics of South Asia*', Springer Netherlands.

Kearey, P., Brooks, M. and Hill, I. (2002) *An introduction to geophysical exploration*, Blackwell Science, Malden, MA.

Kennett, B. N. L. and Engdahl, E. R. (1991), 'Travel times for global earthquake location and phase identification', *Geophys. J. Int.*, 105 (2), pp. 429–465.

Kishimura, K., Izumi, K. (1997) 'Seismic signals induced by snow avalanche flow', *Natural Hazards*, vol. 15, Issue 1, pp. 89–100.

Konagai, K., Johansson, J., Mayorca, P.,vYamamoto, T., Miyajima, M., Uzuoka, R.,. Pulido, N.E., Duran, F.C., Sassa, K., and Fukuoka,H. (2002) 'Las Colinas landslide caused by the January 13, 2001 off the coast of El Salvador earthquake', Journal of Japan Association for Earthquake Engineering, Vol. 2, No.1.

Lee, W.H.K. and Stewart, S.W. (1981) *Principles and applications of microearthquake networks*, Academic Press, New York.

Levy, C., Jongmans, D. and Baillet, L. (2011) ‘Analysis of seismic signals recorded on a prone-to-fall rock column (Vercors massif, French Alps)’, *Geophysical Journal International*, vol. 186, Issue 1, pp. 296–310.

Lin, C.H., Kumagai, H., Ando, M. and Shin, T.C. (2010) ‘Detection of landslides and submarine slumps using broadband seismic networks: LANDSLIDES DETECTED BY SEISMIC NETWORKS’, *Geophysical Research Letters*, vol. 37, Issue 22.

Lyons, R.G. (2011) *Understanding digital signal processing*, Prentice Hall, Upper Saddle River, NJ.

Mainsant, G., Larose, E., Brönnimann, C., Jongmans, D., Michoud, C. and Jaboyedoff, M. (2012) ‘Ambient seismic noise monitoring of a clay landslide: Toward failure prediction’, *Journal of Geophysical Research*, vol. 117, Issue F1.

Maurer, H., Spillmann, T., Heincke, B., Hauck, C., Loew, S., Spingman, M. and Green, A. (2010) ‘Geophysical characterization of slope instabilities’, *First Break*, vol. 28, no. 8, pp. 53-61.

Meric, O., Garambois, S., Malet, J.-P., Cadet, H., Gueguen, P. and Jongmans, D. (2007) ‘Seismic noise-based methods for soft-rock landslide characterization’, *Bulletin de la Societe Geologique de France*, vol. 178, no. 2, pp. 137–148.

Méric, O., Garambois, S., Jongmans, D., Wathelet, M., Chatelain., J.L. and Vengeon, J.M. (2005) ‘Application of geophysical methods for the investigation of the large gravitational mass movement of Séchilienne, France’, *Canadian Geotechnical Journal.*, vol. 42(4), pp. 1105-1115.

Mohorovieid, A. (1915) ‘Die bestimmung des epizentrum eines nahbebens’, *Gerl. Beitr. z. Geophys.* Vol.14, pp.199-205.

Moran, S. C., R. S. Matoza, M. A. Garce´s, M. A. H. Hedlin, D. Bowers, W. E. Scott, D. R. Sherrod, and J. W. Vallance (2008), 'Seismic and acoustic recordings of an unusually large rockfall at Mount St. Helens, Washington', *Geophys. Res. Lett*., vol. 35, Issue 19.

Myers, S.C. (2000). '*Feasibility of Monitoring Rock Fall in Yosemite Valley Using Seismic Methods*', U.S. Department of Commerce National Technical Information Service.

Okada, H. (2006) 'Theory of efficient array observations of microtremors with special reference to the SPAC method', *Exploration Geophysics,* Vol. 37(1), pp.73–85.

Petley, D. (2012) 'Global patterns of loss of life from landslides' *Geology, October 2012, v. 40, p. 927-930, first published on August 1, 2012, doi:10.1130/G33217.1*

Pujol, J. (2004) 'Earthquake Location Tutorial: Graphical Approach and Approximate Epicentral Location Techniques', *Seismological Research Letters*, Vol.75, No.1, pp.63-74

Press, W.H., Flannery, B. P., Teukolsky, S. A. and Vetterling, W. T. (1992) *Numerical recipes in C: the art of scientific computing*, 2nd edition, Cambridge Univ. Pr., Cambridge.

Prugger, A. and Gendzwill, D. (1989) 'Microearthquake location: a non-linear approach that makes use of a Simplex stepping procedure', *Bull. Seism. Soc. Am.* Vol.78, pp.799-815.

Pugin, A.J.M., Larson, T.H., Sargent, S.L., McBride, J.H. and Bexfield, C.E. (2004) 'Near surface mapping using SH-wave and P-wave seismic landslide streamer data acquisition in Illinois, U.S.', *The Leading Edge*, vol.23, pp. 667-682.

Rawlinson, N., Hauser, J. and Sambridge, M. (2007) 'Seismic ray tracing and wavefront tracking in laterally heterogeneous media', *Advances in geophysics*, vol. 49, pp. 203-267.

Renalier, F., Bièvre, G., Jongmans, D., Campillo, M. and Bard, P.Y. (2010) 'Clayey landslide investigations using active and passive Vs measurements', in Miller, R. D., Bradford, J. H. and Holliger, K. (eds.) *Advances in Near-Surface Seismology and Ground-Penetrating Radar*, Geophysical Developments Series No. 15, pp.397–414.

Riedel, B. and Walther, A. (2008) 'InSAR processing for the recognition of landslides', *Advances in Geosciences*, vol. 14, pp.189-194.

Rost, S. and Thomas, C. (2002) 'Array seismology: Methods and applications', *Reviews of Geophysics*, vol. 40, Issue 3, pp. 2-1-2-27.

Rothmund, S. and Joswig, M. (2012) 'Investigating Brittle Fracture during Viscous Creep at the Super-Sauze Mudslide by a Comprehensive Field Laboratory', *Near Surface Geoscience 2012 – poster paper*, 18th European Meeting of Environmental and Engineering Geophysics.

Rotman, H. (2011) 'Seismic Wave Attenuation in Cracks and Pores of Partially Saturated Rock', New Mexico Tech, Outside Courses, GEOP 523, available: http://www.ees.nmt.edu/outside/courses/GEOP523/Docs/Rotman.pdf

Rouse, C., Styles, P. and Wilson, S.A. (1991) 'Microseismic emissions from flowslide-type movements in South Wales', *Engineering Geology*, vol. 31, Issue 1, pp. 91-110.

Roux, P.-F., Marsan, D., Métaxian, J.-P., O'Brien, G. and Moreau, L. (2008) 'Microseismic activity within a serac zone in an alpine glacier (Glacier d'Argentière, Mont Blanc, France)', *Journal of glaciology*, vol. 54, Issue 184, pp. 157–168.

Rydelek, P. and Pujol, J. (2004) 'Real-Time Seismic Warning with a Two-Station Subarray', *Bulletin of the Seismological Society of America*, Vol. 94, No. 4, pp. 1546–1550.

Michoud C., Abellán A., Derron M.-H. and Jaboyedoff M., (2010). '*Review of Techniques for Landslide Detection, Fast Characterization, Rapid Mapping and Lond-Term Monitoring.'* SafeLand European project, Available at *http://www.safeland-fp7.eu*

Santamarina, J. C., K. A. Klein, and M. A. Fam (2001) *Soils and Waves*, John Wiley & Sons, Ltd, Chichester, UK.

Schneider, D., Bartelt, P., Caplan-Auerbach, J., Christen, M., Huggel, C. and McArdell, B.W. (2010) 'Insights into rock-ice avalanche dynamics by combined analysis of seismic recordings and a numerical avalanche model', *Journal of Geophysical Research*, vol. 115, Issue F4.

Schulz, W.H. (2007) 'Landslide susceptibility revealed by LIDAR imagery and historical records, Seattle, Washington', *Engineering Geology*, vol.89, Issues 1-2, pp.67–87.

Schweitzer, J., Fyen, J., Mykkeltveit, S., Kvaerna, T. (2002) '*Manual of Seismological Observatory Practice'*, Chapter 9, available: ftp://ftp.ingv.it/pub/elisabetta.danastasio/grot/manual_seismological_observatory-2002.pdf

Senfaute, G., Duperret, A. and Lawrence, J.A. (2009) 'Micro-seismic precursory cracks prior to rock-fall on coastal chalk cliffs: a case study at Mesnil-Val, Normandie, NW France', *Natural Hazards & Earth System Sciences*, vol. 9, pp. 1625-1641.

Shiotani, T. (2006) Evaluation of long-term stability for rock slope by means of acoustic emission technique', *NDT & E International*, vol. 39, Issue 3, pp. 217–228.

Silva, M.T.M.G. (2009) '*Metodologia para determinação de parâmetros para solos não saturados utilizando ensaios com umidade conhecida'*, MSc. dissertation, Universidade de Brasília, Brasília, Brazil.

Smith, M.J. (1981) *Soil Mechanics*, 4rth edition, Edinburg: George Godwin.

Spillmann, T., Maurer, *H.*, Green, *A. G.*, Heincke, *B.*, Willenberg, *H. and* S. Husen *(*2007*)* 'Microseismic investigation of an unstable mountain slope in the Swiss Alps', *J. Geophys. Res., vol.* 112, *Issue B7.*

Stamps, D. S. and Smalley, R. (2006) '*Strings and Things for Locating Earthquakes',* Seismological Research Letters, Vol.77, No.6, pp.677-683.

Stoica, P. and Moses, R.L. (2005) Spectral analysis of signals, Pearson/Prentice Hall, Upper Saddle River, N.J.

Stuart, G., Murray, T., Brisbourne, A., Styles, P. and Toon, S. (2005) 'Seismic emissions from a surging glacier: Bakaninbreen, Svalbard', *Annals of Glaciology*, vol. 42, no. 1, pp. 151–157.

Suriñach, E., Sabot, F., Furdada, G. and Vilaplana, J.M. (2000) 'Study of seismic signals of artificially released snow avalanches for monitoring purposes', *Physics and Chemistry of the Earth, Part B: Hydrology, Oceans and Atmosphere*, vol. 25, Issue 9, pp. 721–727.

Suriñach, E., Vilajosana, I., Khazaradze, G., Biescas, B., Furdada, G. and Vilaplana, J.M. (2005) 'Seismic detection and characterization of landslides and other mass movements', *Natural Hazards & Earth System Sciences*, vol. 5, pp. 791-798.

Suwa, H., Mizuno, T., Suzuki, S., Yamamoto, Y. and Ito, K. (2008) 'Sequential processes in a landslide hazard at a slate quarry in Okayama, Japan', *Natural Hazards*, vol. 45, Issue 2, pp.321–331.

Thurber, C. H. (1985) 'Nonlinear earthquake location: theory and examples', *Bull. Seism. Soc. Am.* Vol.75, pp.779-790.

Tonnellier, A., Helmstetter, A., Malet, J.-P., Schmittbuhl, J., Corsini, A. and Joswig, M. (2013) 'Seismic monitoring of soft-rock landslides: the Super-Sauze and Valoria case studies', *Geophysical Journal International*, vol. 193 (3), pp. 1515–1536.

Trnkoczy, A., Havskov, J., Ottemöller, L. (2012) 'New Manual of Seismological Observatory Practice 2', (NMSOP), GeoForchungsZentrum Potsdam, available at http://nmsop.gfz-potsdam.de

Varnes, D.J. (1978) *'Slope movement types and processes in landslides'*, Analysis Control, Special Report 176, Transportation Research Board, Washington, pp. 11-13.

Vaseghi, S.V. (2000) 'Power Spectrum and Correlation' in *Advanced Digital Signal Processing and Noise Reduction*, 2nd Edition, John Wiley & Sons Ltd.

Vilajosana, I., Suriñach, E., Abellán, A., Khazaradze, G., Garcia, D. and Llosa, J. (2008) 'Rockfall induced seismic signals: case study in Montserrat, Catalonia', *Natural Hazards and Earth System Sciences*, Vol. 8, pp. 805- 812.

Walter, M., Niethammer, U., Rothmund, S. And Joswig, M. (2009) 'Joint analysis of the Super-Sauze (French Alps) mudslide by Nanoseismic Monitoring and UAV-based remote sensing', *first break*, vol. 27.

Walter, M. and Joswig, M. (2009) 'Seismic characterization of slope dynamics caused by softrock-landslides: The Super-Sauze case study', *Proceedings of the International Conference on Landslide Processes: from geomorpholgic mapping to dynamic modelling*, Strasbourg, CERG Editions, pp. 215-220.

Walter, M. and Joswig, M. (2008) 'Seismic monitoring of fracture processes generated by a creeping landslide in the Vorarlberg Alps', *First Break,* vol. 26.

Walter, M., Arnhardt, C. and Joswig, M. (2012) 'Seismic monitoring of rockfalls, slide quakes, and fissure development at the Super-Sauze mudslide, French Alps', *Engineering Geology*, vol. 128, pp. 12–22.

Walter, M., Schwaderer, U. and Joswig, M. (2012) 'Seismic monitoring of precursory fracture signals from a destructive rockfall in the Vorarlberg Alps, Austria', *Natural Hazards and Earth System Science*, vol. 12, pp. 3545–3555.

Walter, M., Walser, M. and Joswig, M. (2011) 'Mapping Rainfall-Triggered Slidequakes and Seismic Landslide-Volume Estimation at Heumoes Slope', *Vadose Zone Journal*, vol.10,no. 2, pp. 487-495.

Welch, P.D. (1967) 'The use of fast Fourier transform for the estimation of power spectra: a method based on time averaging over short, modified periodograms', *IEEE Transactions on audio and electroacoustics*, vol. 15, Issue2, pp. 70–73.

Wielandt, E. (2009) 'Seismic Sensors and their Calibration', *New Manual of Seismological Observatory Practice (NMSOP)*, Potsdam: Deutsches GeoForschungsZentrum GFZ, p. 1-46.

Wieczorek, G.F. and Snyder, J.B. (2009) 'Monitoring slope movements', *in* Young, R., and Norby, L., Geological Monitoring: Boulder, Colorado, Geological Society of America, p. 245–271, doi: 10.1130/2009.monitoring(11).

Wust-Bloch, H.G. (2010) 'Characterizing and Locating Very Weak ($-2.2 \geq M_L \geq -3.4$) Induced Seismicity in Unstable Sandstone Cliffs by Nanoseismic Monitoring', *Pure and Applied Geophysics*, vol. 167, Issue 1-2, pp. 153–167.

Zimmer, V.L., Collins, B.D., Stock, G.M. and Sitar, N. (2012) ‘Rock fall dynamics and deposition: an integrated analysis of the 2009 Ahwiyah Point rock fall, Yosemite National Park, USA: ROCK FALL DYNAMICS AND DEPOSITION: AN ANALYSIS OF A YOSEMITE ROCK FALL’, *Earth Surface Processes and Landforms,* vol. 37, Issue 6, pp. 680–691.

Zobin, V.M., Plascencia, I., Reyes, G. and Navarro, C. (2009) ‘The characteristics of seismic signals produced by lahars and pyroclastic flows: Volcán de Colima, México’, *Journal of Volcanology and Geothermal Research,* vol. 179, Issues 1-2, pp. 157–167.

Appendix A

Simulation of Landslide Seismic Signals at Field Scale Using an Up-Scaled Shear Box

In this appendix all additional graphs of Chapter 6 will be presented. The deployment geometry of the seismometers is presented first, as well as a table summarizing the parameters of the experiments conducted as a reminder to the reader so he or she doesn't have to search for this information back to the original chapter.

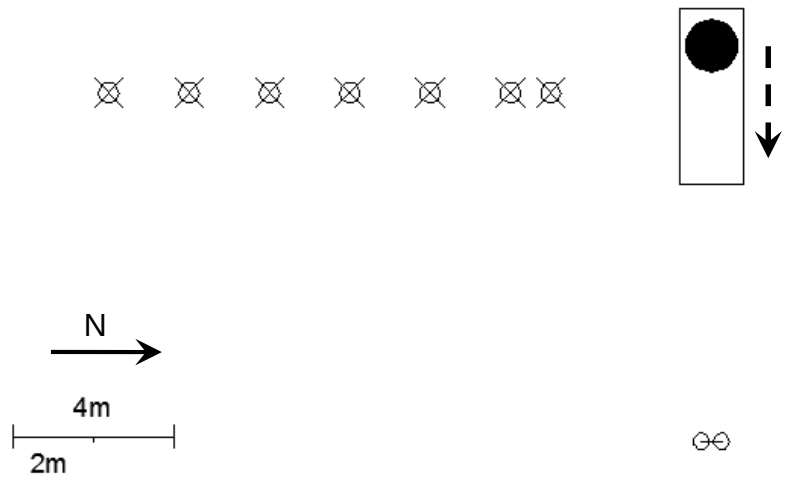

Plan view of experimental set up. Solid Black Circle: cylinder with confined soil block, Rectangle surrounding the cylinder: Surficial corridor free from vegetation, Circles marked with X: Location of seismometers, Two circles connected with a line: Position of reel. The dashed arrow shows the direction of the movement of the cylinder.

No of Experiment	Load (kg) on the slip surface ($0.33m^2$)	Force (kN)	Stress (kPa)	Equivalent Depth (m) ($\gamma_{soil}=18kN/m^3$)
1	472	4.63	14.03	0.78
2	568	5.57	16.88	0.94
3	743	7.29	22.09	1.23
4	829	8.13	24.64	1.37

Load, force, stress levels and equivalent depth of landslide like soil friction events for all 4 experiments.

A.1 Spectrograms from Section 6.5.1 *"Step 1: Time – Frequency analysis"*

Section 6.5.1 presented the use of spectrograms for detection and visualisation of the slip events above noise levels. Here all spectrograms of all three components of the seismometers are presented for each experiment separately.

A.1.1 Spectrograms of 1st Cylinder Experiment

a) Vertical Component

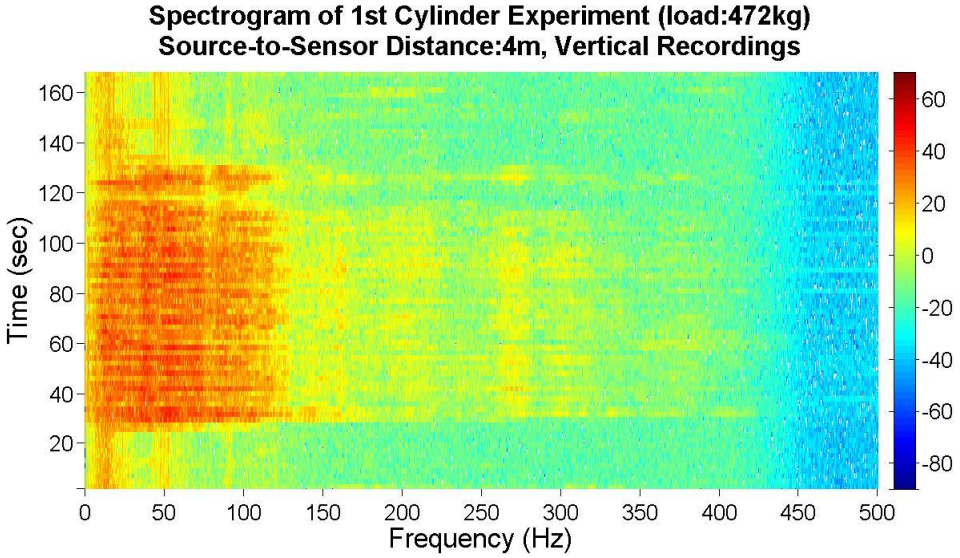

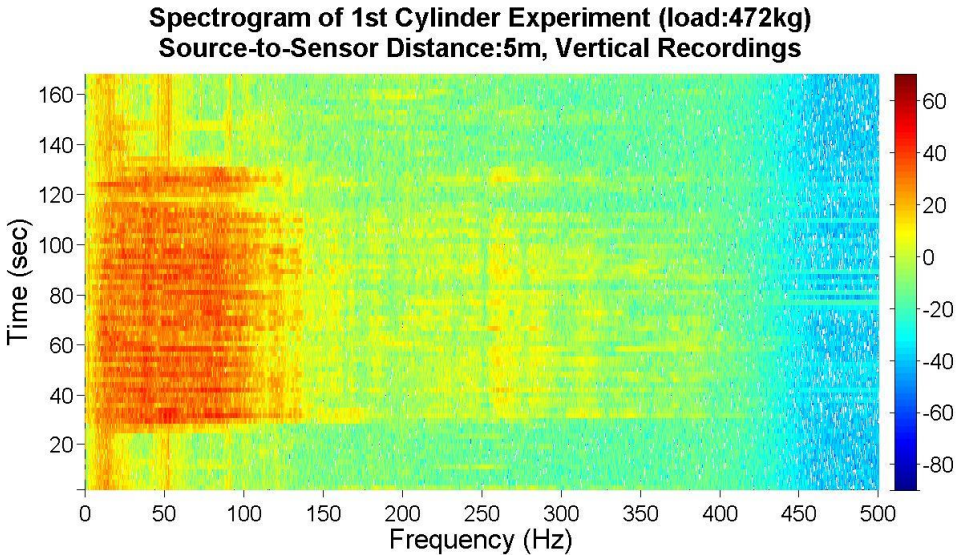

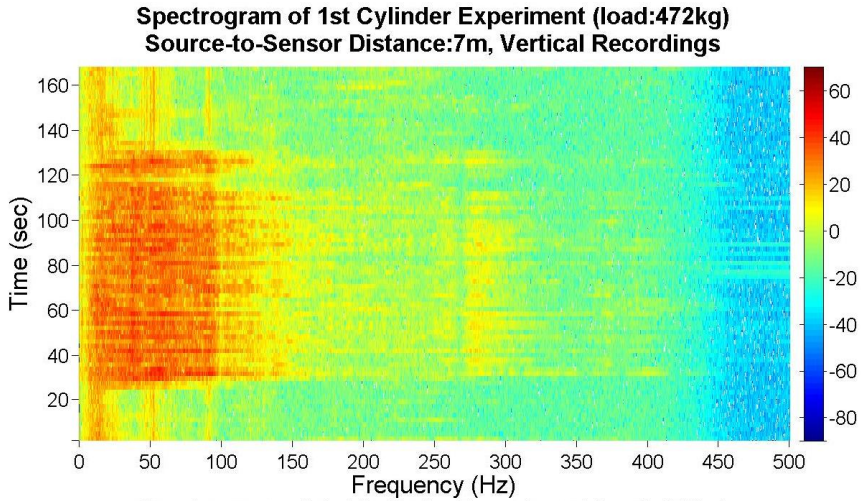
Spectrogram of 1st Cylinder Experiment (load:472kg)
Source-to-Sensor Distance:7m, Vertical Recordings
Time (sec)
Frequency (Hz)

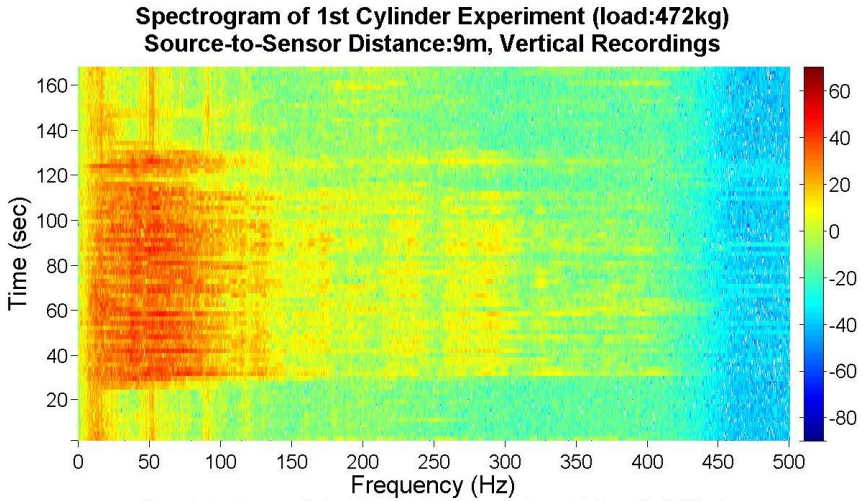
Spectrogram of 1st Cylinder Experiment (load:472kg)
Source-to-Sensor Distance:9m, Vertical Recordings
Time (sec)
Frequency (Hz)

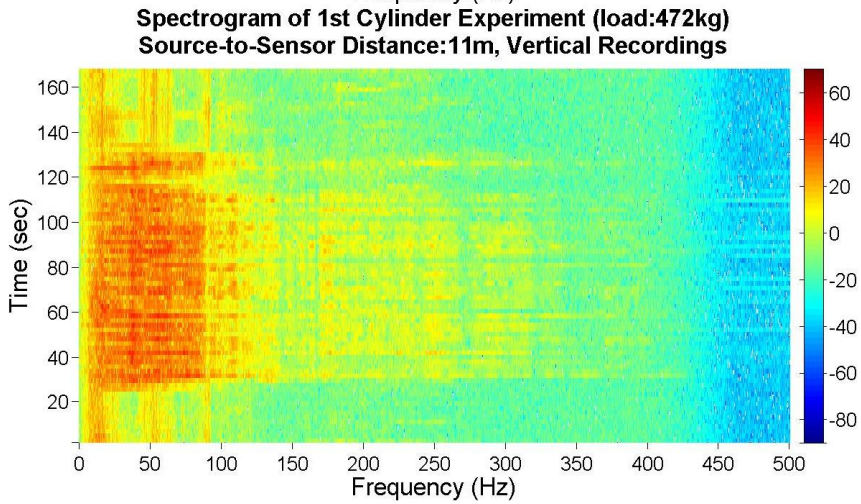
Spectrogram of 1st Cylinder Experiment (load:472kg)
Source-to-Sensor Distance:11m, Vertical Recordings
Time (sec)
Frequency (Hz)

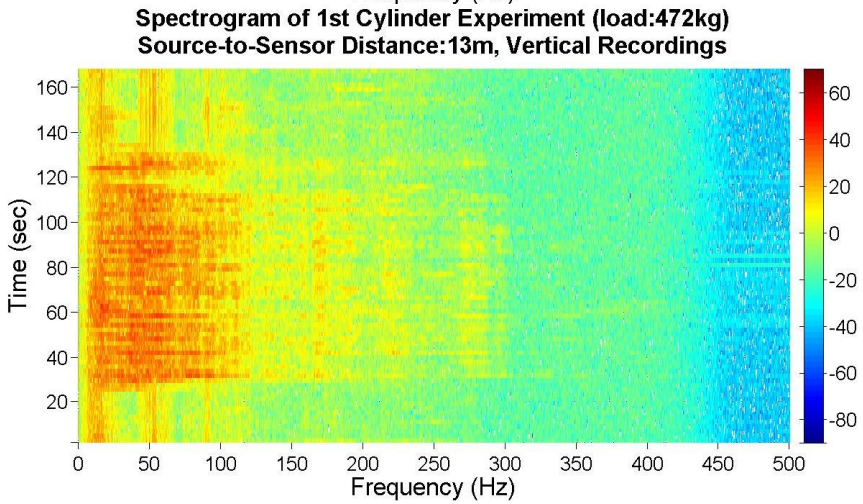
Spectrogram of 1st Cylinder Experiment (load:472kg)
Source-to-Sensor Distance:13m, Vertical Recordings
Time (sec)
Frequency (Hz)

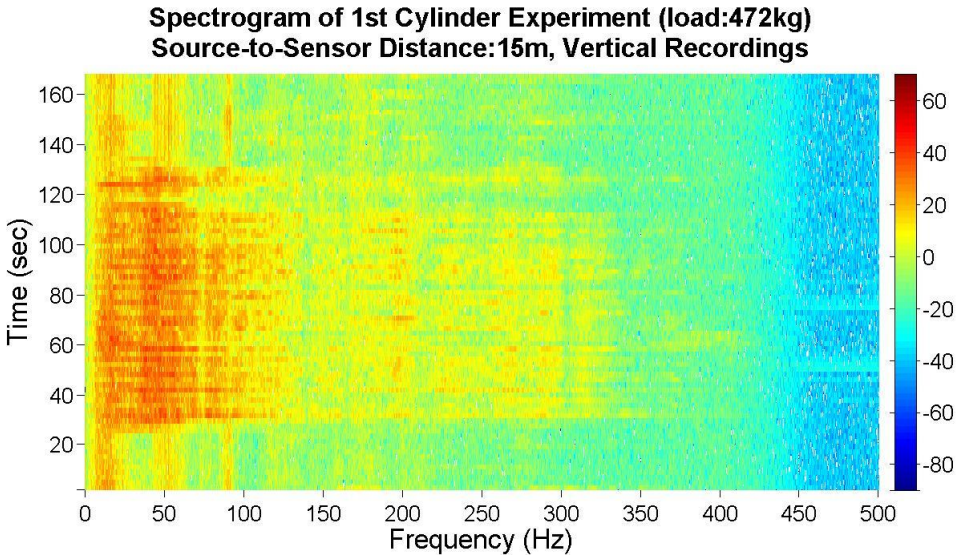
Spectrogram of 1st Cylinder Experiment (load:472kg)
Source-to-Sensor Distance:15m, Vertical Recordings
Time (sec)
160
140
120
100
80
60
40
20
0
50
100
150
200
250
300
350
400
450
500
Frequency (Hz)
60
40
20
0
-20
-40
-60
-80

b) North-South Component

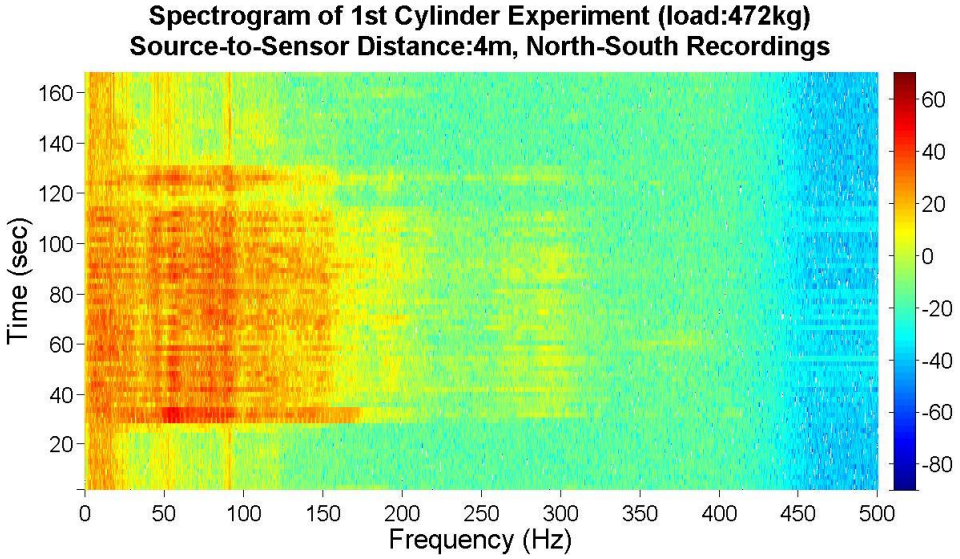

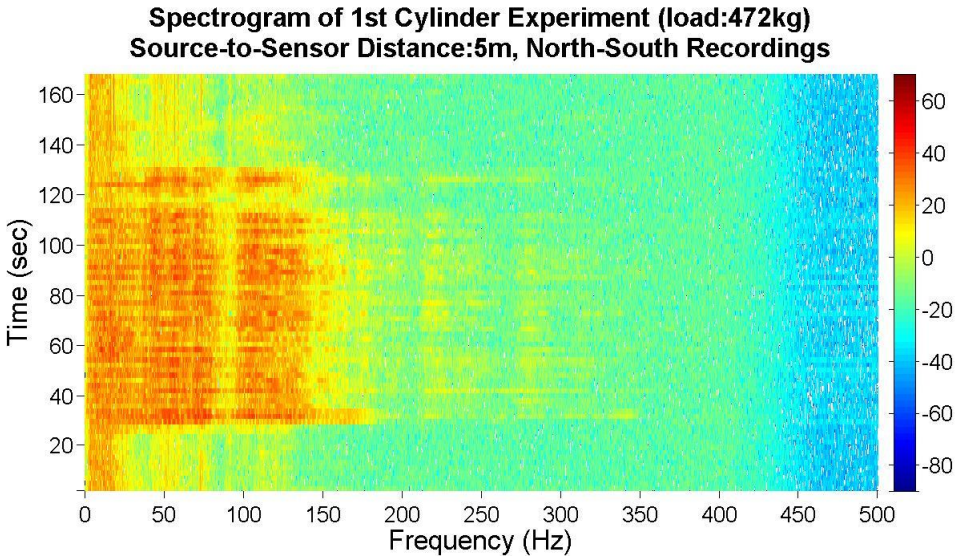

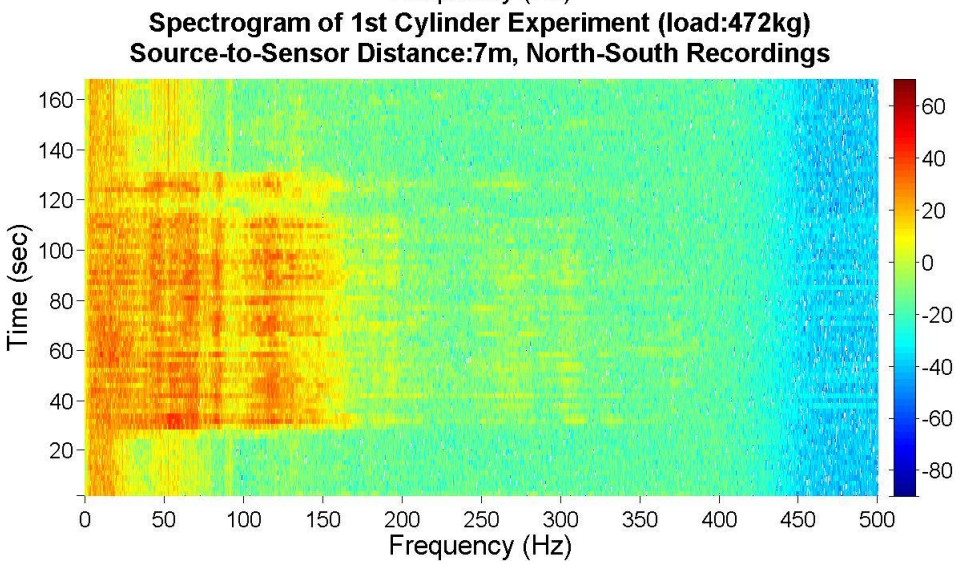

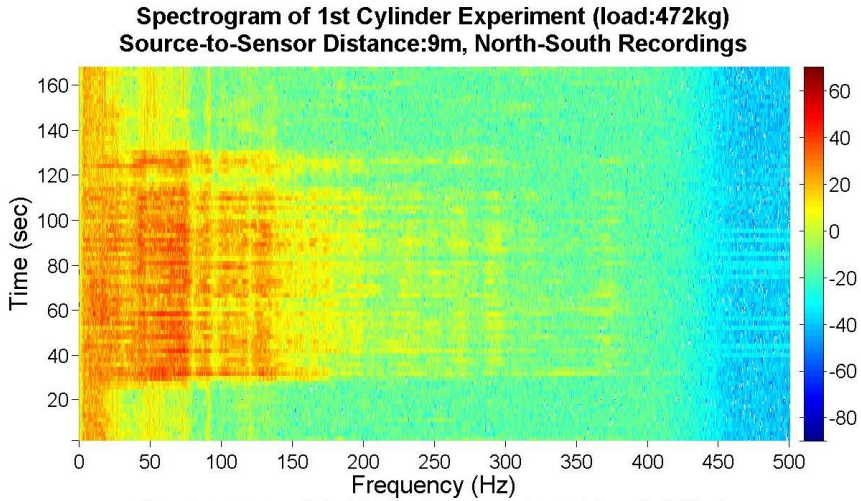
Spectrogram of 1st Cylinder Experiment (load:472kg)
Source-to-Sensor Distance:9m, North-South Recordings
Time (sec)
Frequency (Hz)

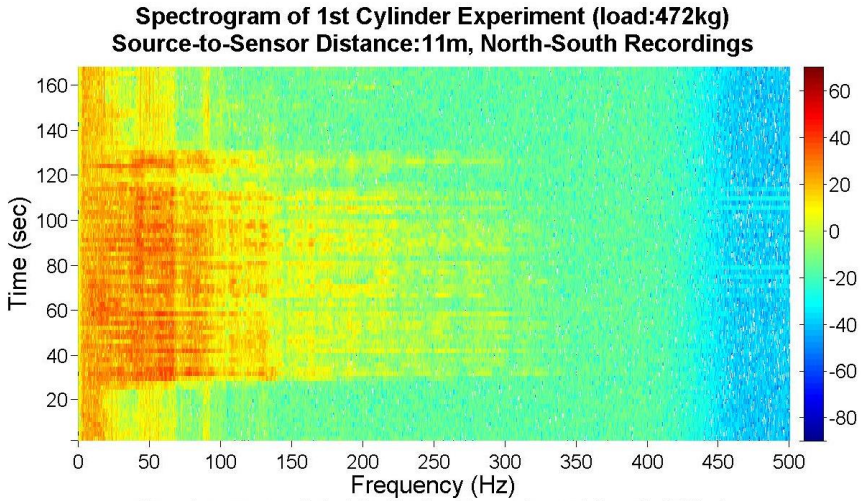
Spectrogram of 1st Cylinder Experiment (load:472kg)
Source-to-Sensor Distance:11m, North-South Recordings
Time (sec)
Frequency (Hz)

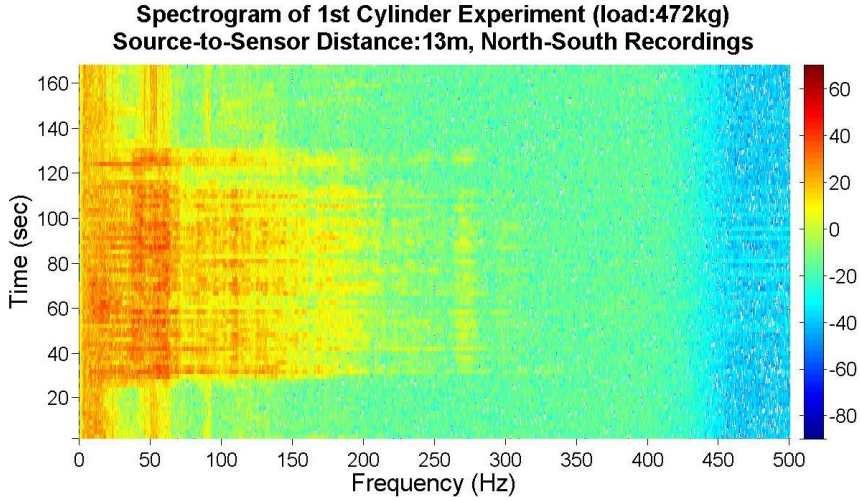
Spectrogram of 1st Cylinder Experiment (load:472kg)
Source-to-Sensor Distance:13m, North-South Recordings
Time (sec)
Frequency (Hz)

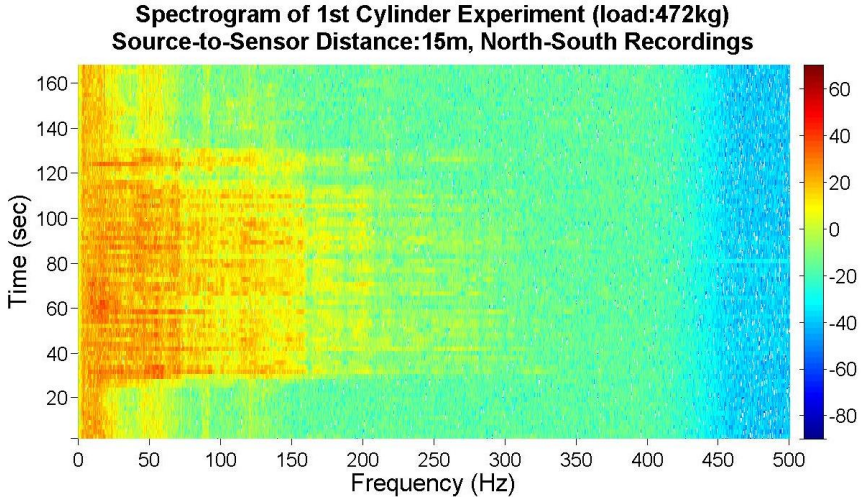
Spectrogram of 1st Cylinder Experiment (load:472kg)
Source-to-Sensor Distance:15m, North-South Recordings
Time (sec)
Frequency (Hz)

c) East-West Component

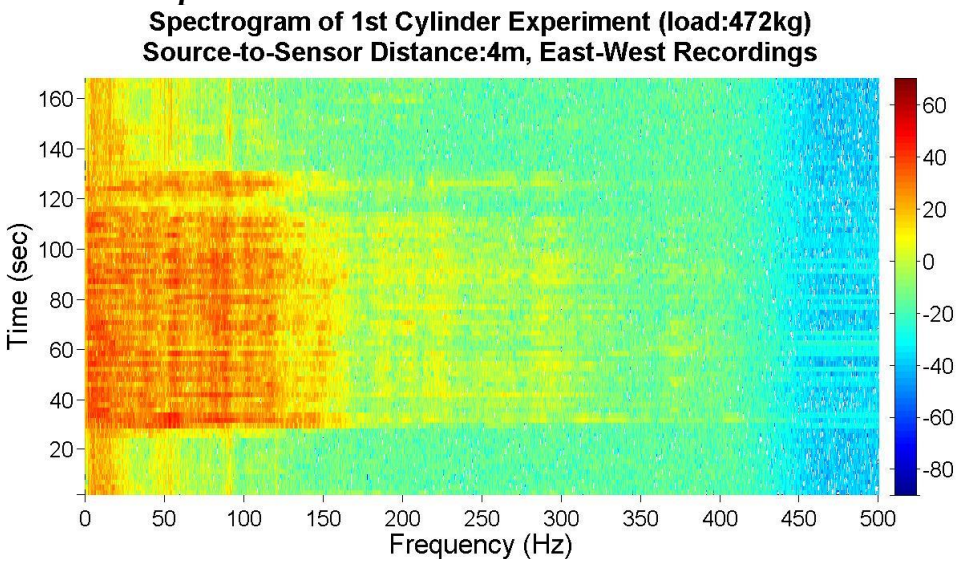

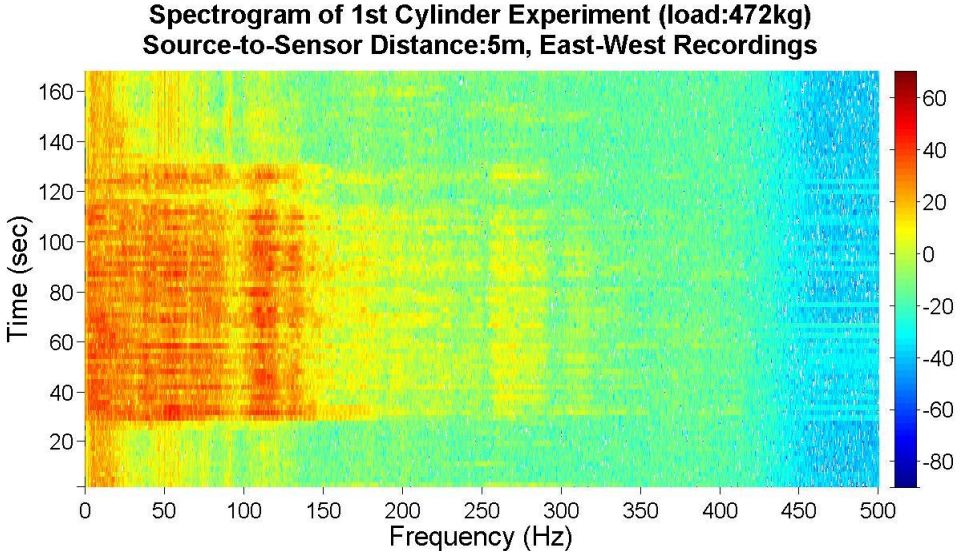

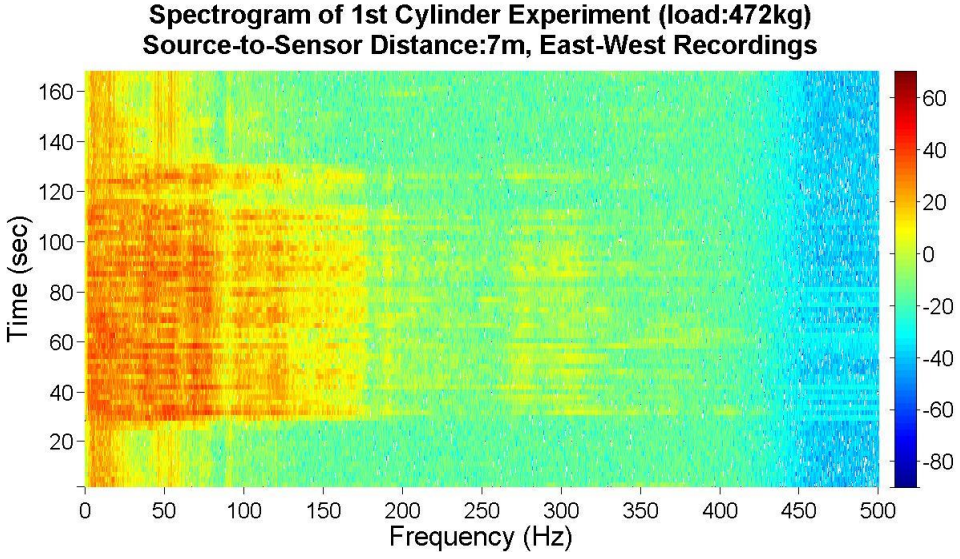

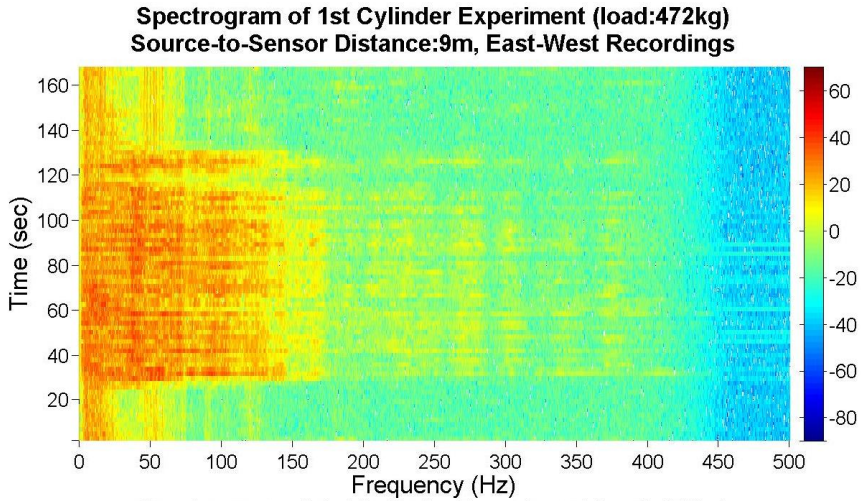
Spectrogram of 1st Cylinder Experiment (load:472kg)
Source-to-Sensor Distance:9m, East-West Recordings
Time (sec)
Frequency (Hz)

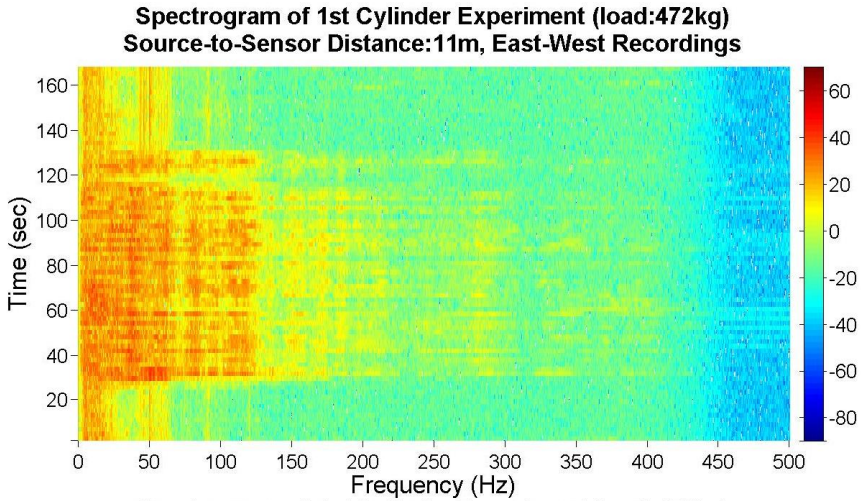
Spectrogram of 1st Cylinder Experiment (load:472kg)
Source-to-Sensor Distance:11m, East-West Recordings
Time (sec)
Frequency (Hz)

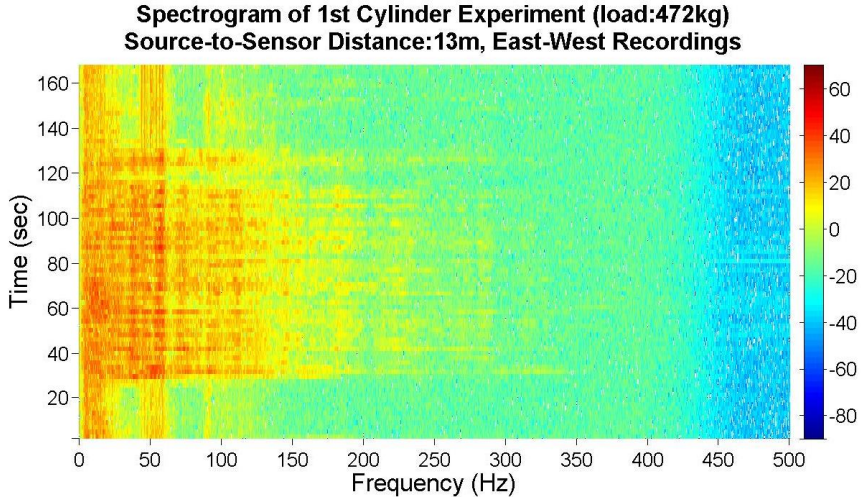
Spectrogram of 1st Cylinder Experiment (load:472kg)
Source-to-Sensor Distance:13m, East-West Recordings
Time (sec)
Frequency (Hz)

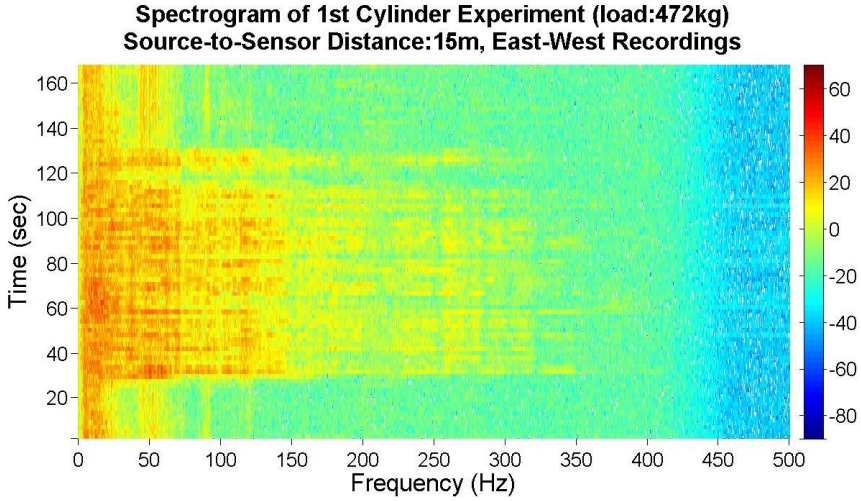
Spectrogram of 1st Cylinder Experiment (load:472kg)
Source-to-Sensor Distance:15m, East-West Recordings
Time (sec)
Frequency (Hz)

A.1.2 Spectrograms of 2nd Cylinder Experiment

a) Vertical Component

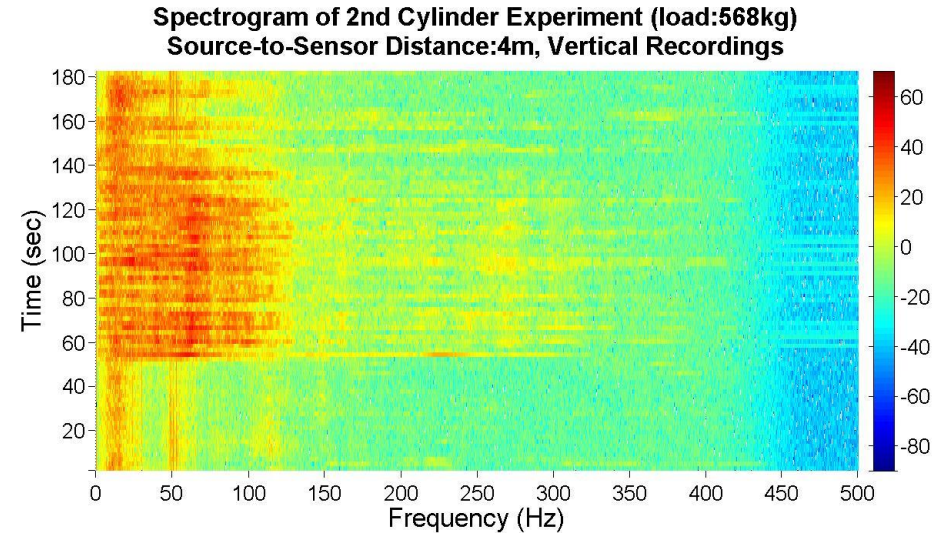

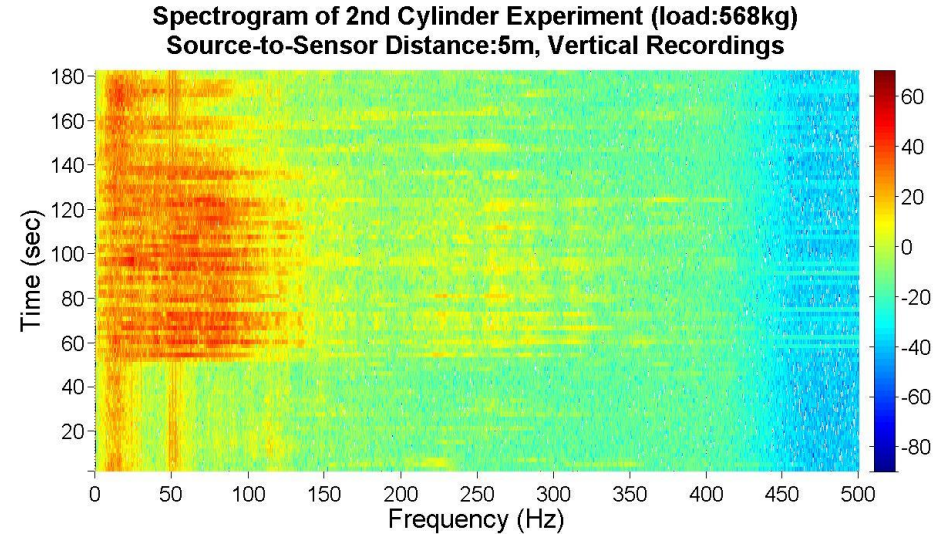

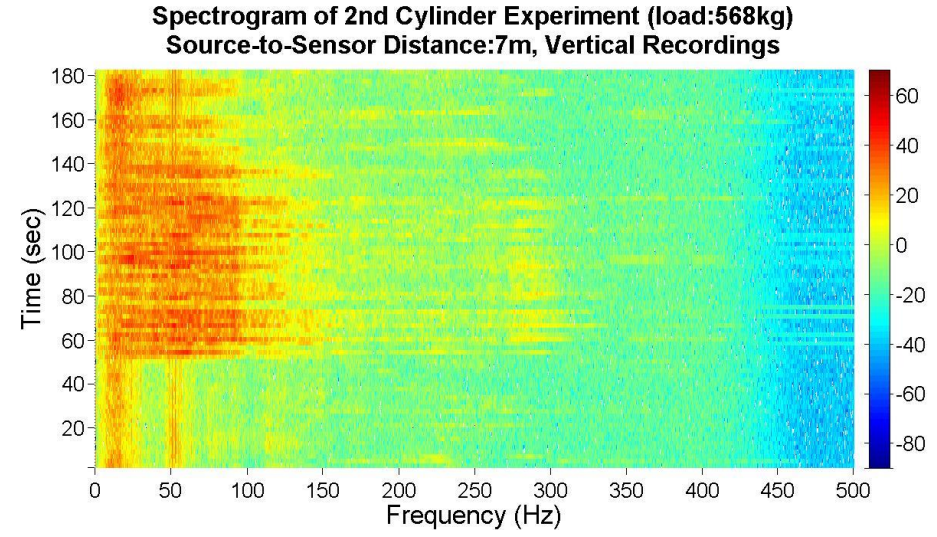

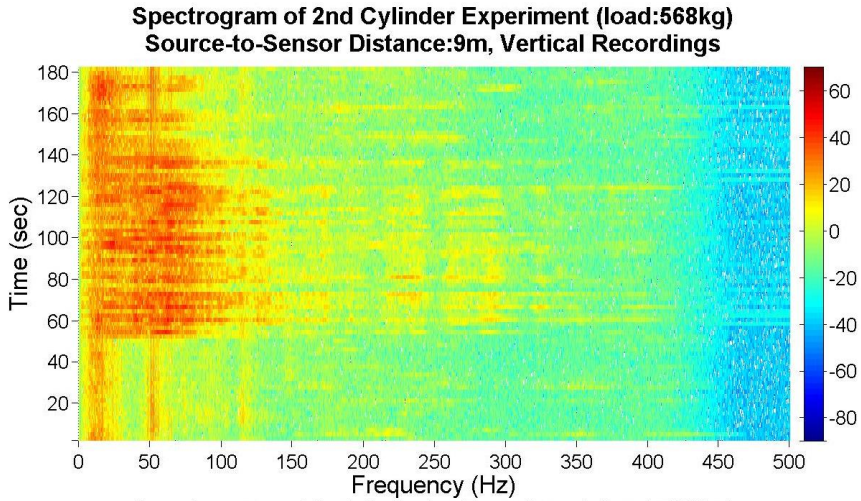
Spectrogram of 2nd Cylinder Experiment (load:568kg)
Source-to-Sensor Distance:9m, Vertical Recordings
Time (sec)
Frequency (Hz)

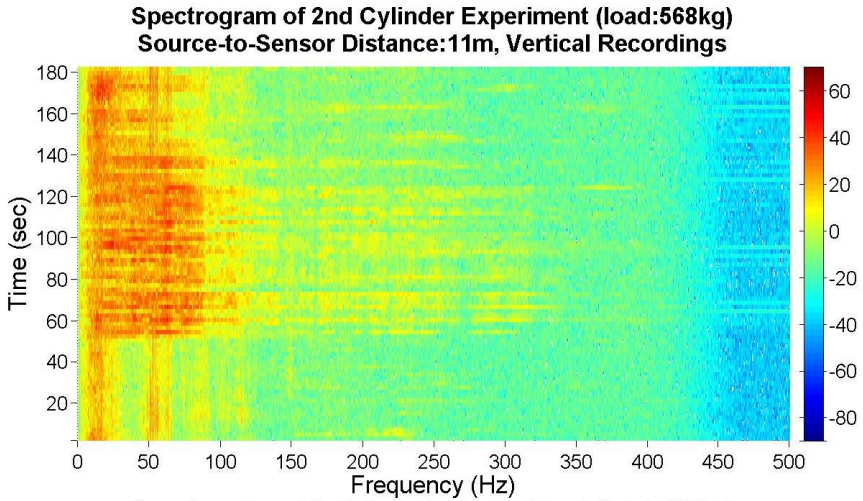
Spectrogram of 2nd Cylinder Experiment (load:568kg)
Source-to-Sensor Distance:11m, Vertical Recordings
Time (sec)
Frequency (Hz)

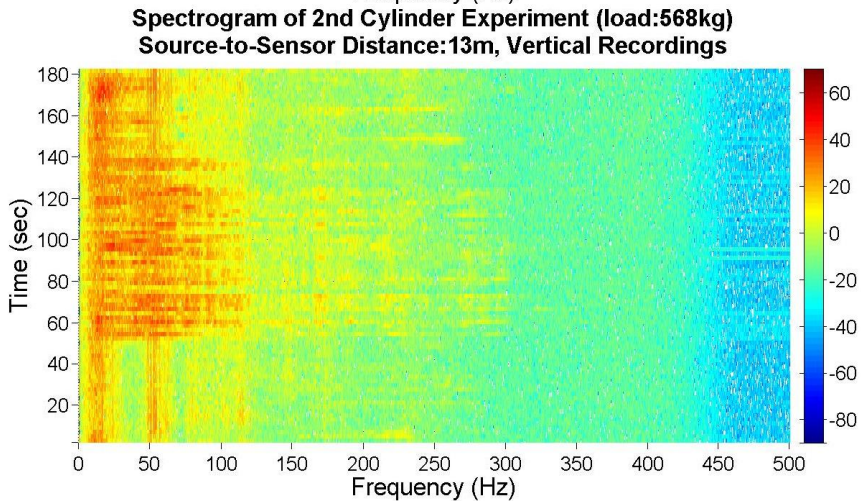
Spectrogram of 2nd Cylinder Experiment (load:568kg)
Source-to-Sensor Distance:13m, Vertical Recordings
Time (sec)
Frequency (Hz)

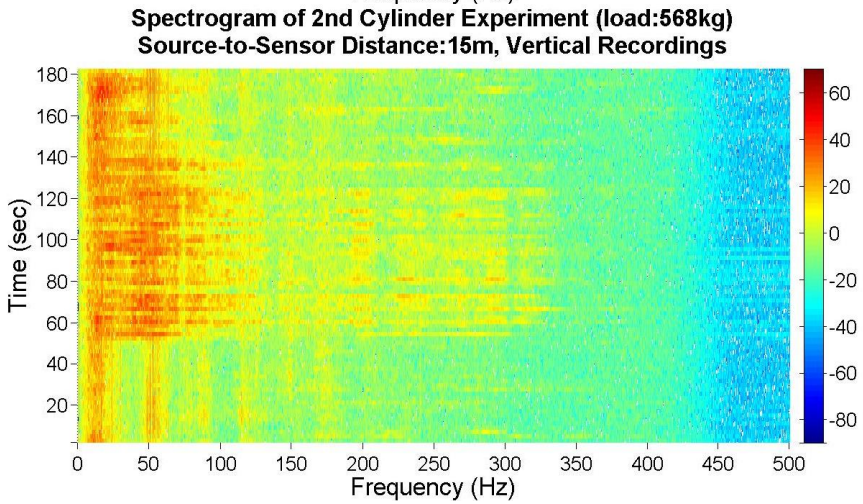
Spectrogram of 2nd Cylinder Experiment (load:568kg)
Source-to-Sensor Distance:15m, Vertical Recordings
Time (sec)
Frequency (Hz)

b) North-South Component

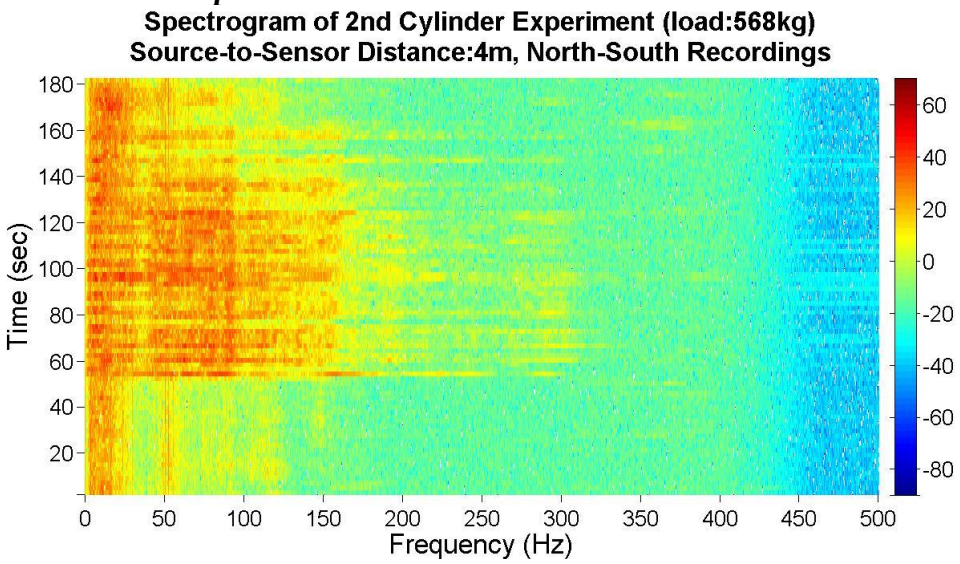

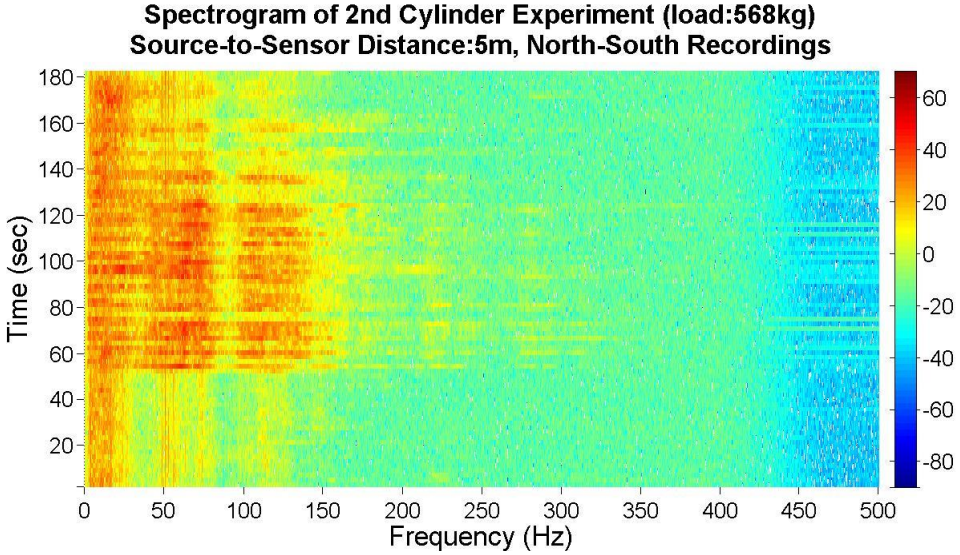

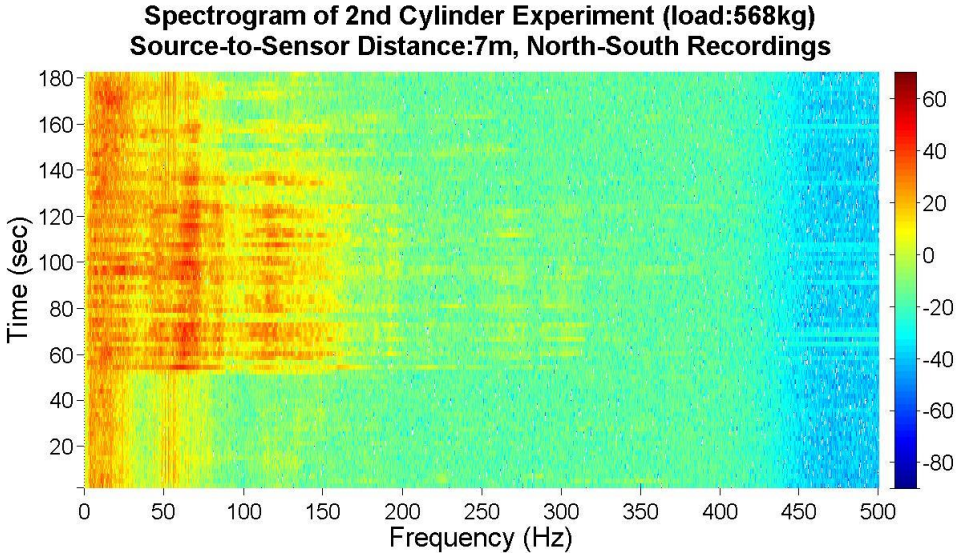

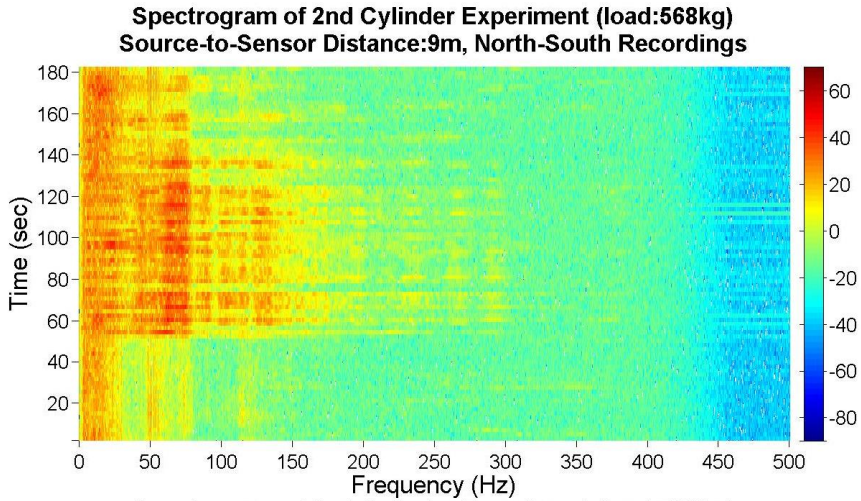
Spectrogram of 2nd Cylinder Experiment (load:568kg)
Source-to-Sensor Distance:9m, North-South Recordings
Time (sec)
Frequency (Hz)

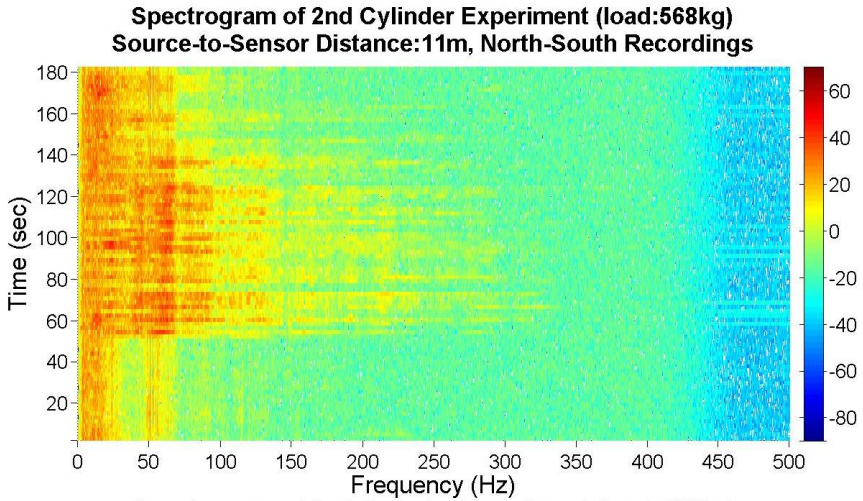
Spectrogram of 2nd Cylinder Experiment (load:568kg)
Source-to-Sensor Distance:11m, North-South Recordings
Time (sec)
Frequency (Hz)

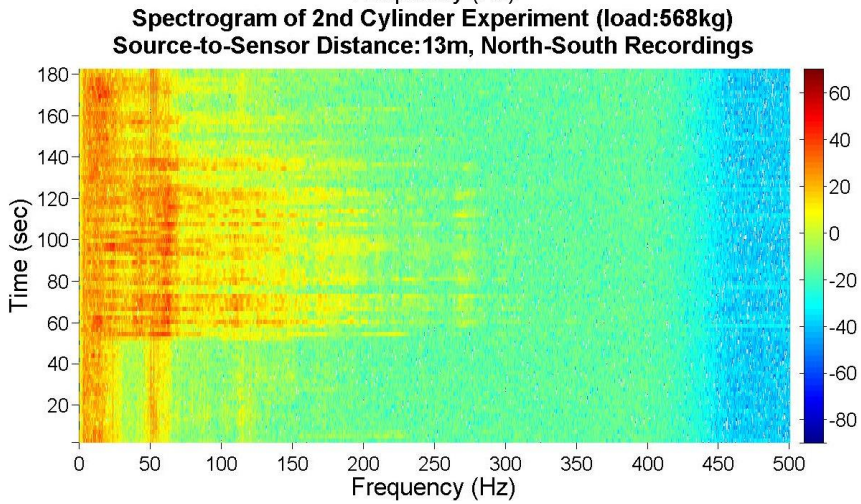
Spectrogram of 2nd Cylinder Experiment (load:568kg)
Source-to-Sensor Distance:13m, North-South Recordings
Time (sec)
Frequency (Hz)

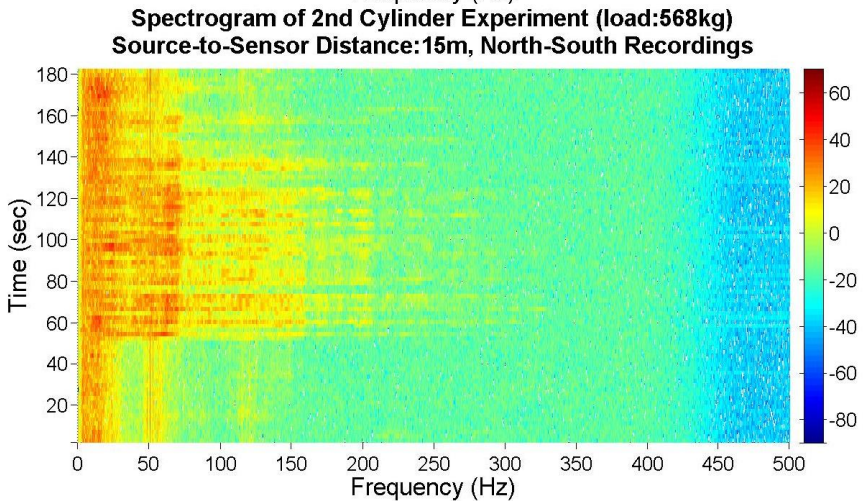
Spectrogram of 2nd Cylinder Experiment (load:568kg)
Source-to-Sensor Distance:15m, North-South Recordings
Time (sec)
Frequency (Hz)

c) East-West Component

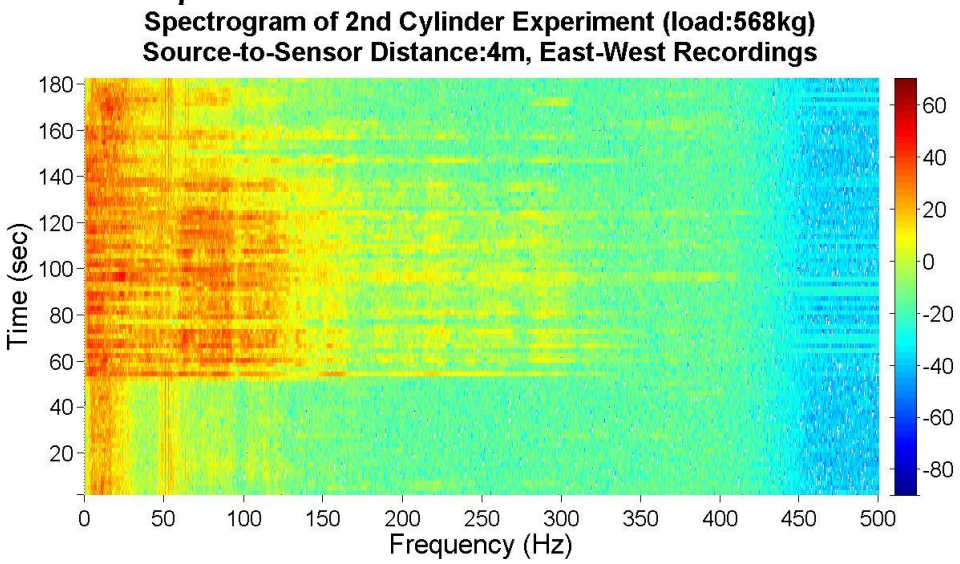

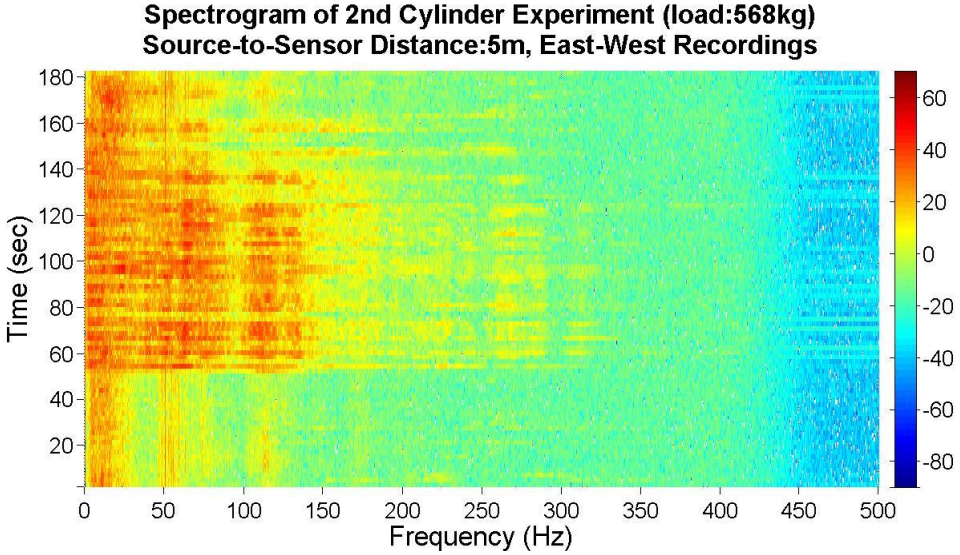

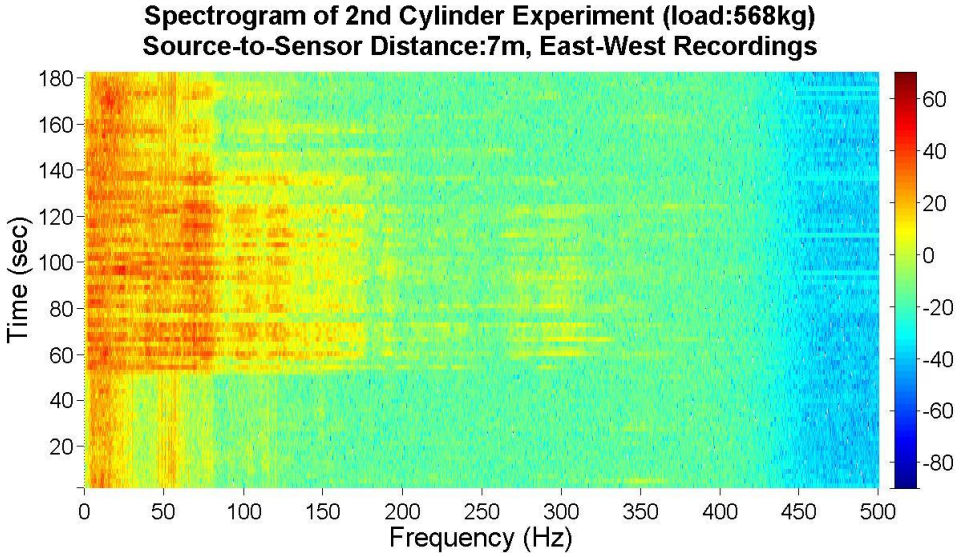

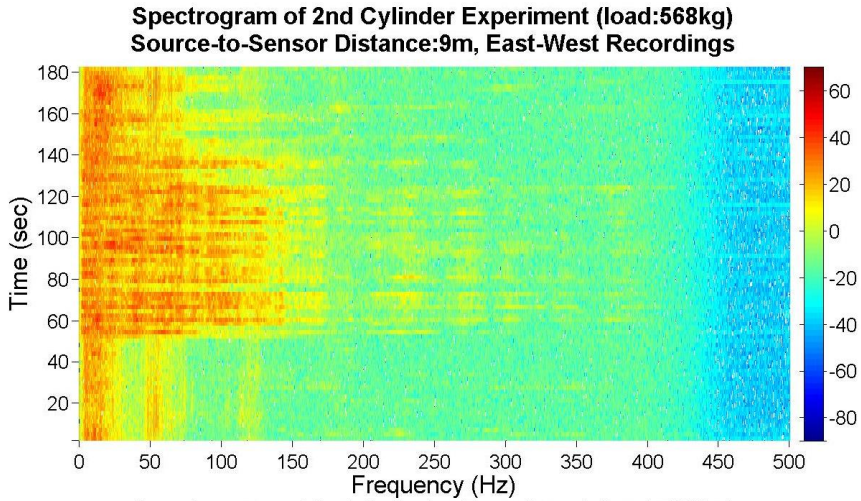
Spectrogram of 2nd Cylinder Experiment (load:568kg)
Source-to-Sensor Distance:9m, East-West Recordings
Time (sec)
Frequency (Hz)

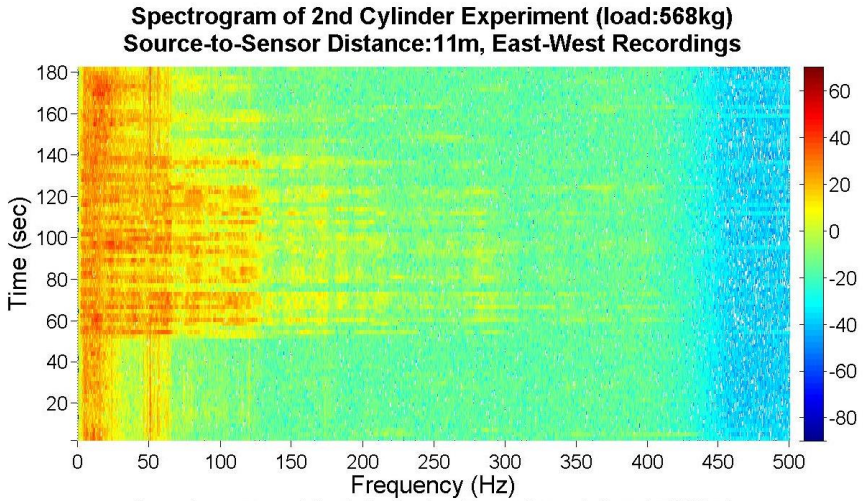
Spectrogram of 2nd Cylinder Experiment (load:568kg)
Source-to-Sensor Distance:11m, East-West Recordings
Time (sec)
Frequency (Hz)

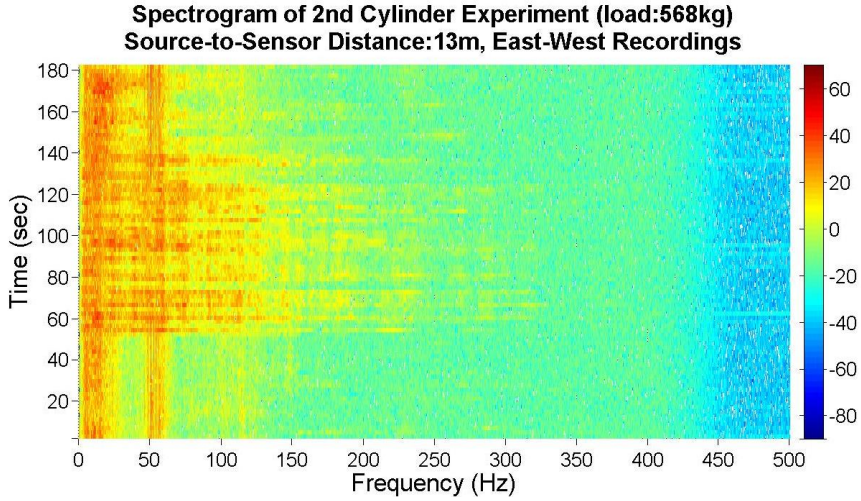
Spectrogram of 2nd Cylinder Experiment (load:568kg)
Source-to-Sensor Distance:13m, East-West Recordings
Time (sec)
Frequency (Hz)

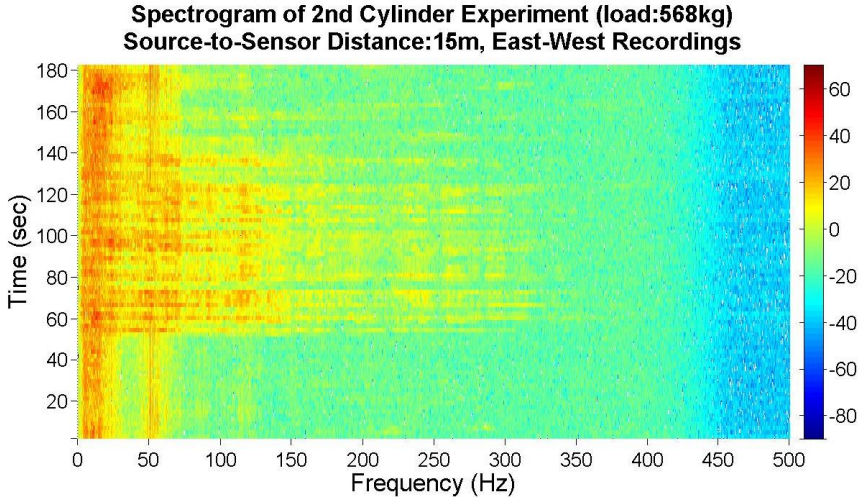
Spectrogram of 2nd Cylinder Experiment (load:568kg)
Source-to-Sensor Distance:15m, East-West Recordings
Time (sec)
Frequency (Hz)

A.1.3 Spectrograms of 3rd Cylinder Experiment

a) Vertical Component

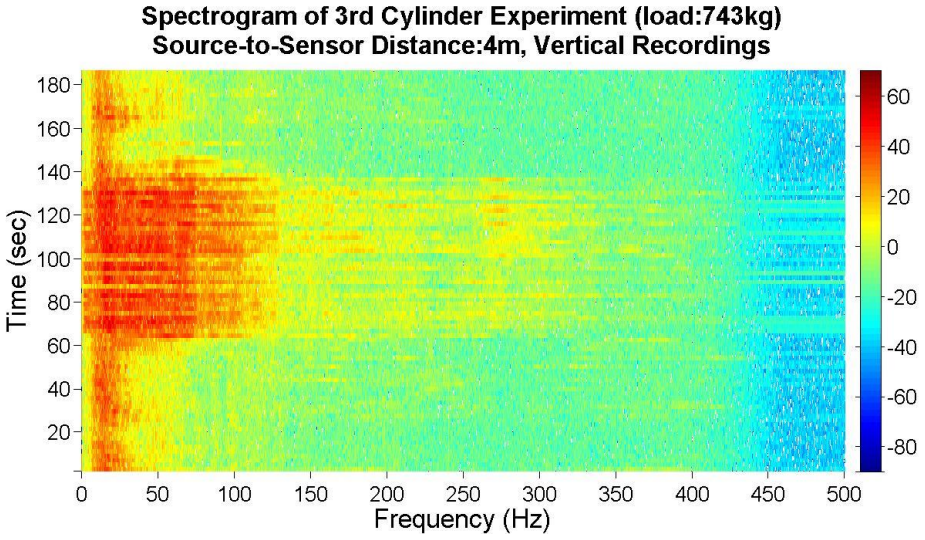

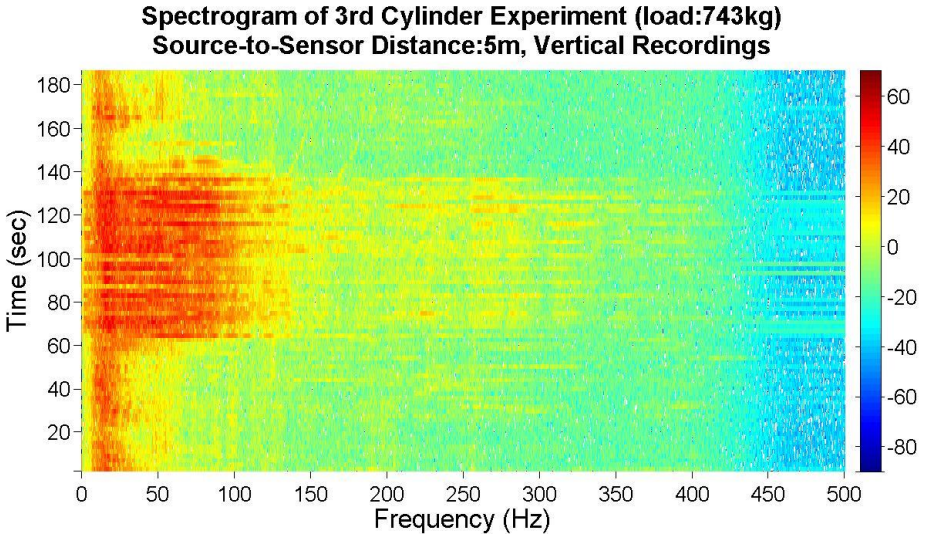

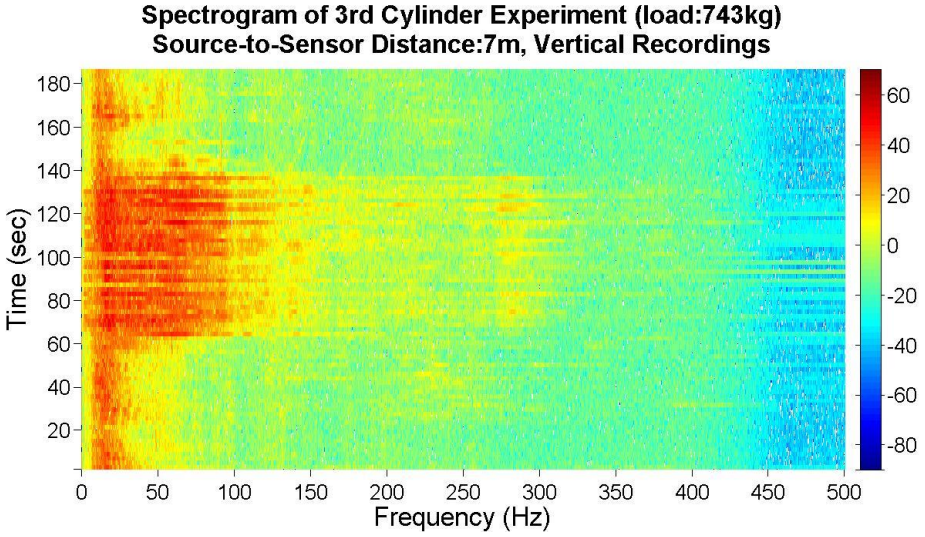

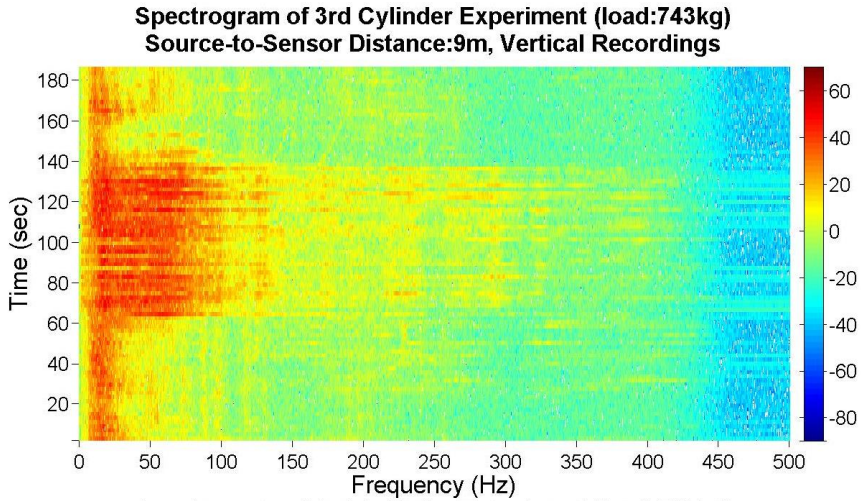
Spectrogram of 3rd Cylinder Experiment (load:743kg)
Source-to-Sensor Distance:9m, Vertical Recordings
Time (sec)
Frequency (Hz)

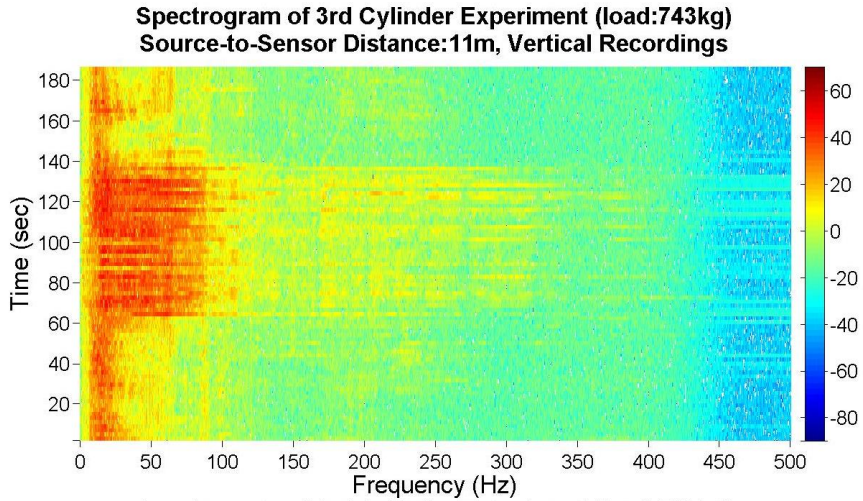
Spectrogram of 3rd Cylinder Experiment (load:743kg)
Source-to-Sensor Distance:11m, Vertical Recordings
Time (sec)
Frequency (Hz)

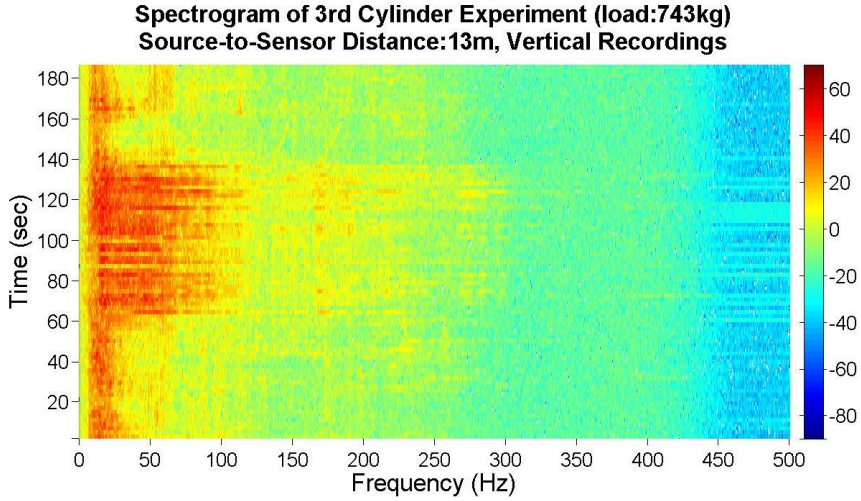
Spectrogram of 3rd Cylinder Experiment (load:743kg)
Source-to-Sensor Distance:13m, Vertical Recordings
Time (sec)
Frequency (Hz)

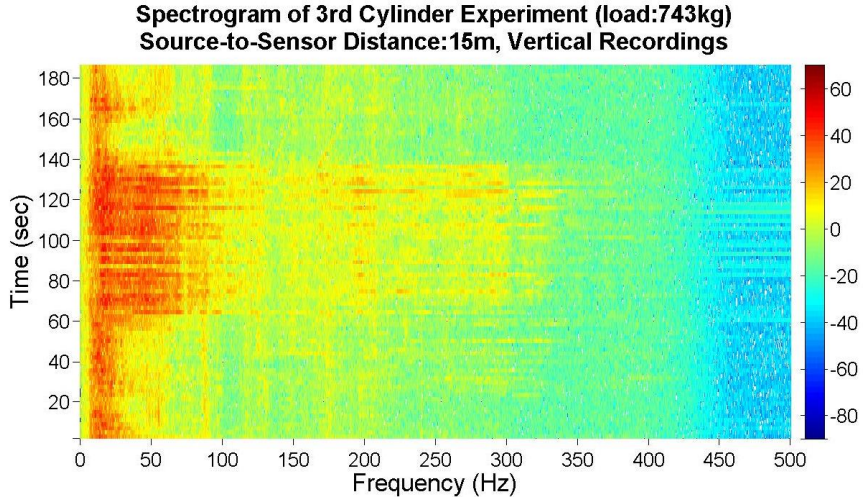
Spectrogram of 3rd Cylinder Experiment (load:743kg)
Source-to-Sensor Distance:15m, Vertical Recordings
Time (sec)
Frequency (Hz)

d

a) North-South Component

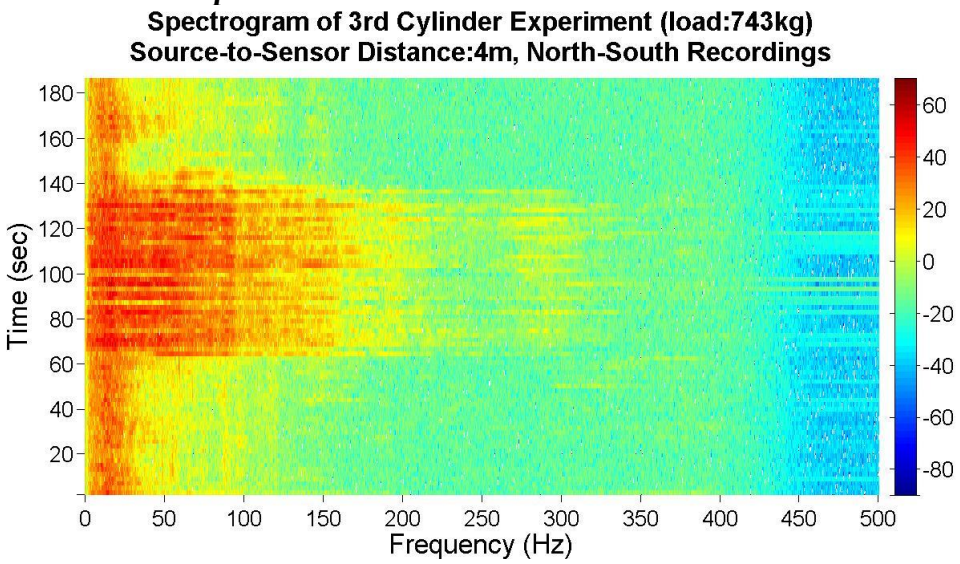

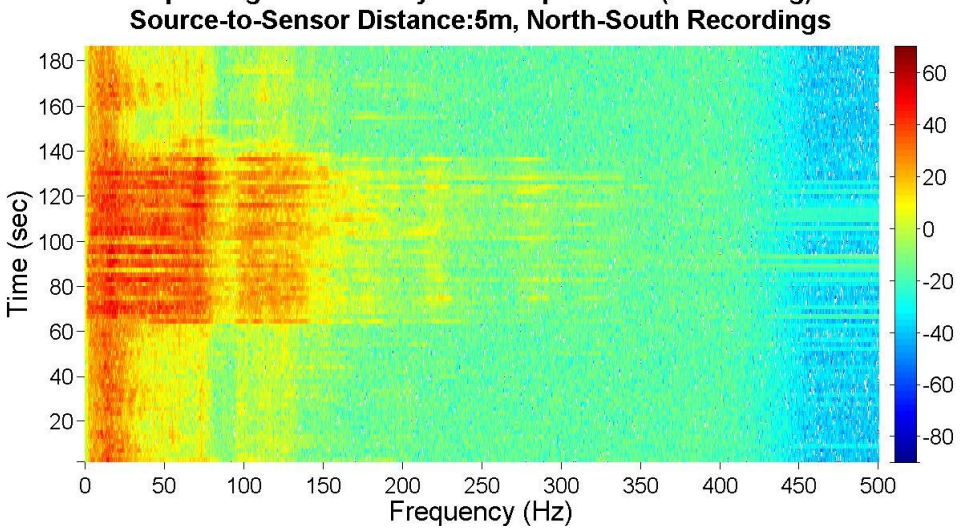

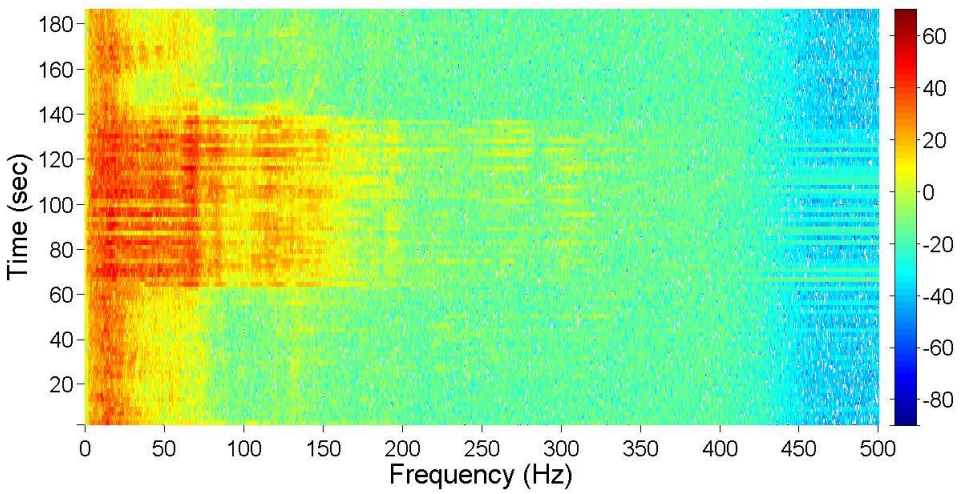

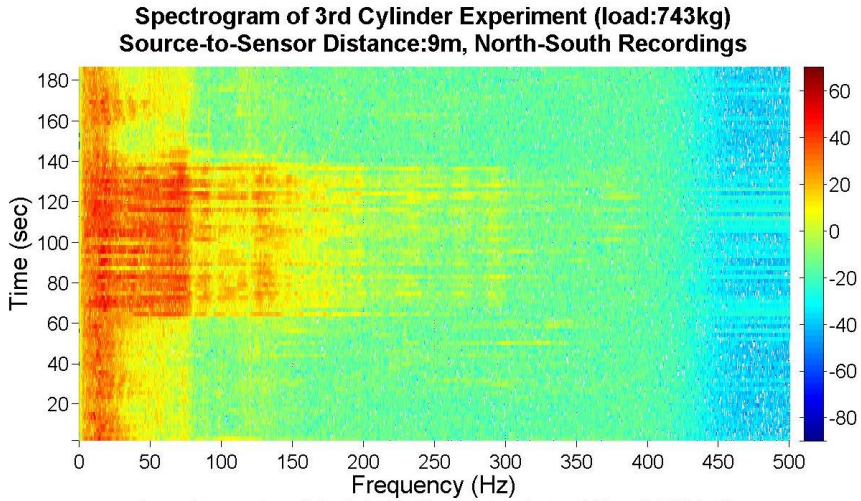
Spectrogram of 3rd Cylinder Experiment (load:743kg)
Source-to-Sensor Distance:9m, North-South Recordings
Time (sec)
Frequency (Hz)

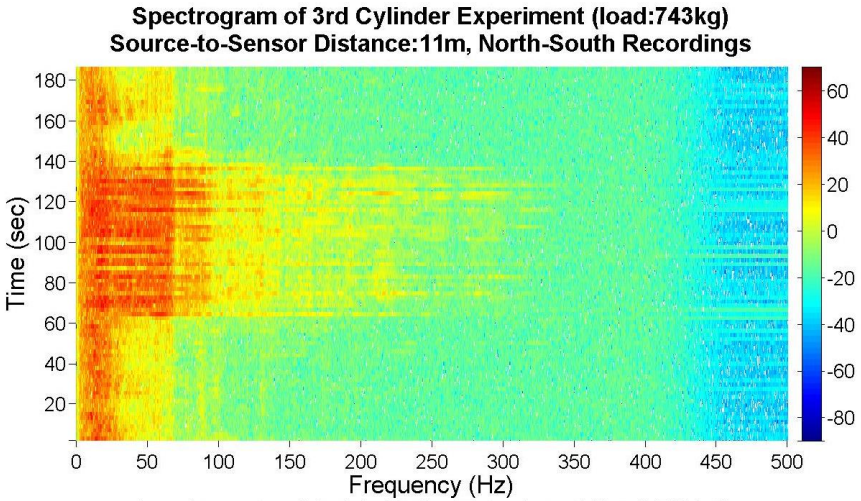
Spectrogram of 3rd Cylinder Experiment (load:743kg)
Source-to-Sensor Distance:11m, North-South Recordings
Time (sec)
Frequency (Hz)

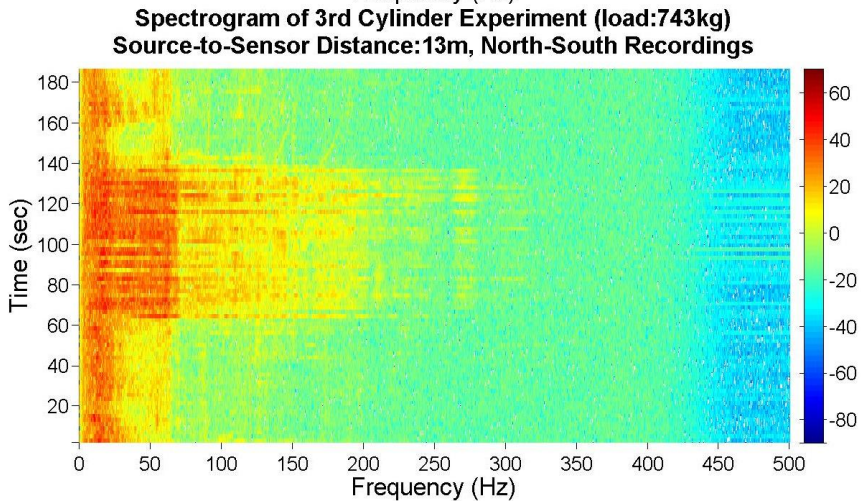
Spectrogram of 3rd Cylinder Experiment (load:743kg)
Source-to-Sensor Distance:13m, North-South Recordings
Time (sec)
Frequency (Hz)

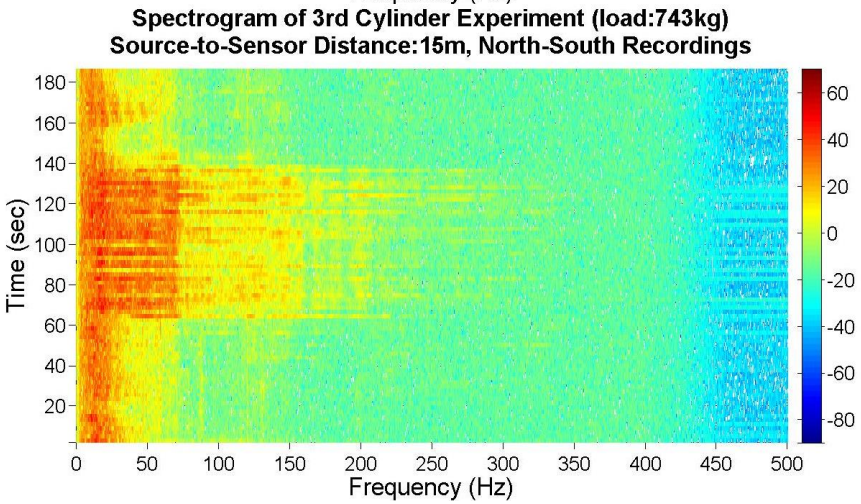
Spectrogram of 3rd Cylinder Experiment (load:743kg)
Source-to-Sensor Distance:15m, North-South Recordings
Time (sec)
Frequency (Hz)

c) East-West Component

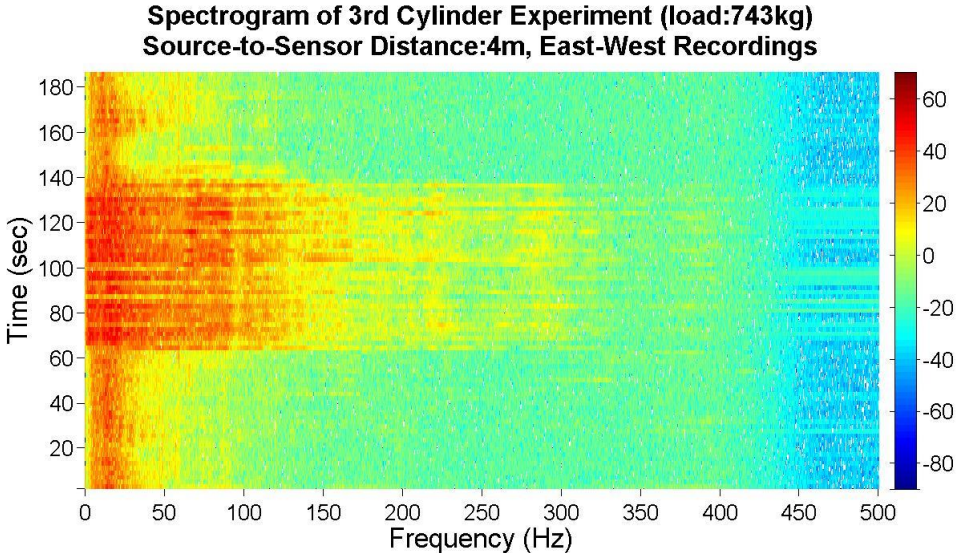

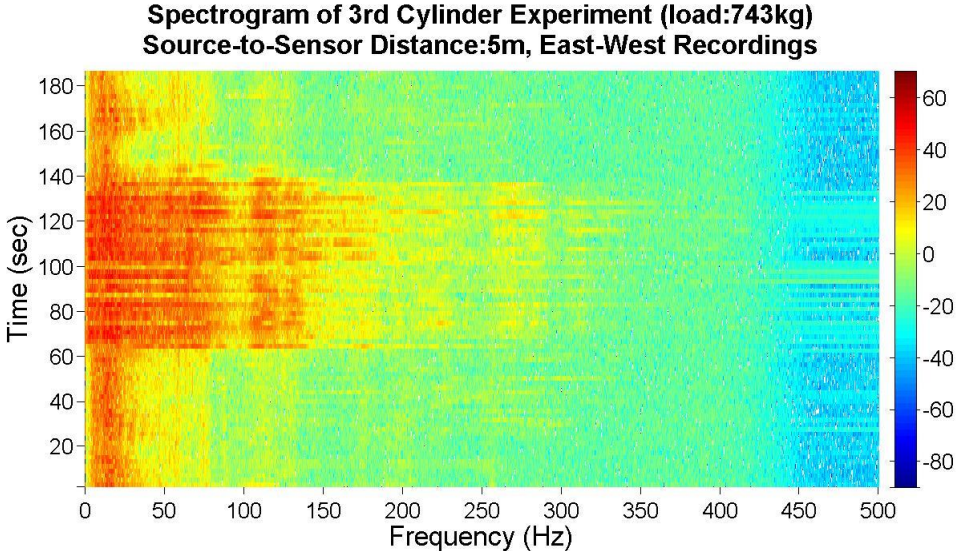

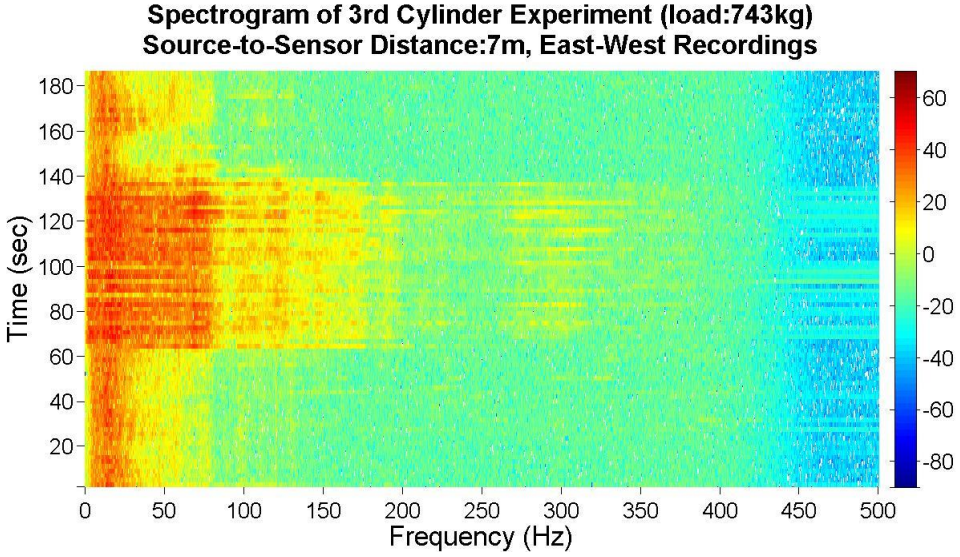

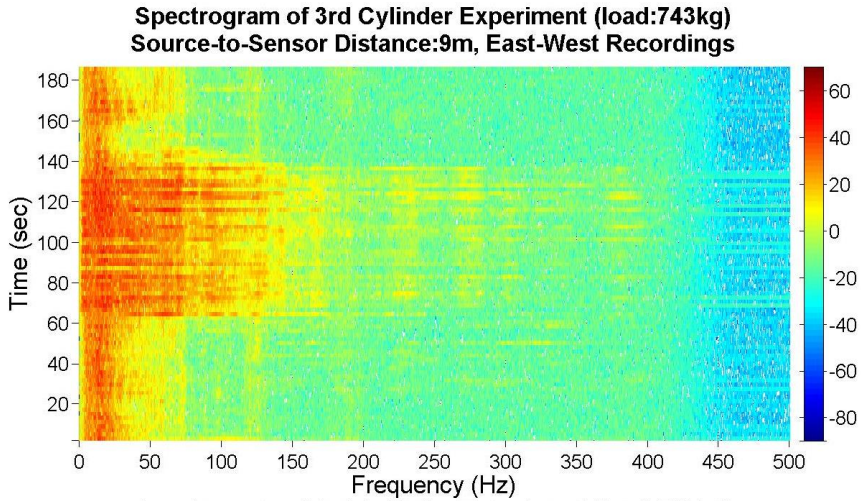
Spectrogram of 3rd Cylinder Experiment (load:743kg)
Source-to-Sensor Distance:9m, East-West Recordings
Time (sec)
Frequency (Hz)

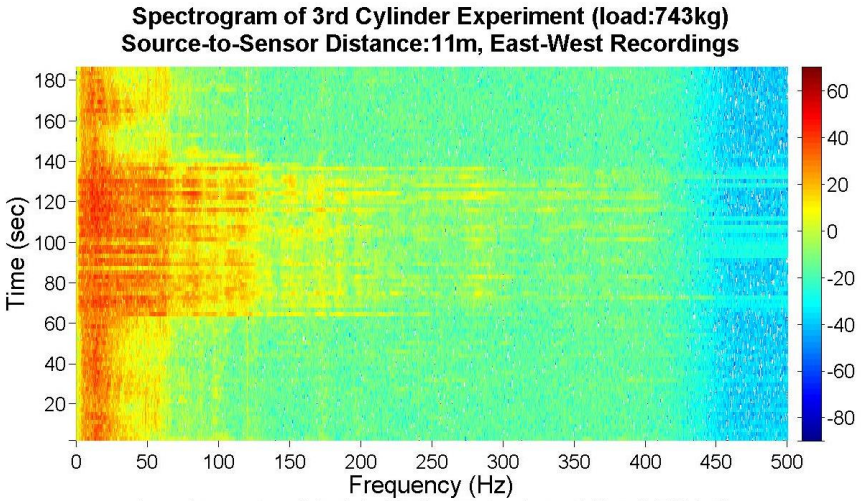
Spectrogram of 3rd Cylinder Experiment (load:743kg)
Source-to-Sensor Distance:11m, East-West Recordings
Time (sec)
Frequency (Hz)

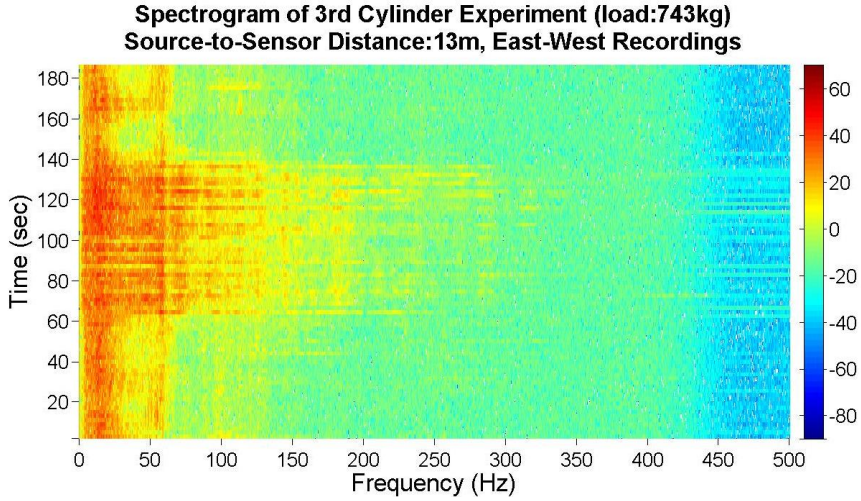
Spectrogram of 3rd Cylinder Experiment (load:743kg)
Source-to-Sensor Distance:13m, East-West Recordings
Time (sec)
Frequency (Hz)

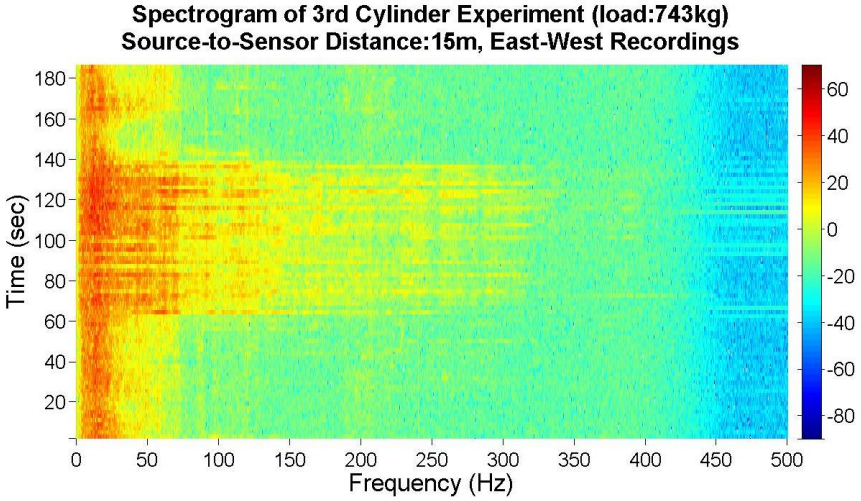
Spectrogram of 3rd Cylinder Experiment (load:743kg)
Source-to-Sensor Distance:15m, East-West Recordings
Time (sec)
Frequency (Hz)

A.1.4 Spectrograms of 4th Cylinder Experiment

a) Vertical Component

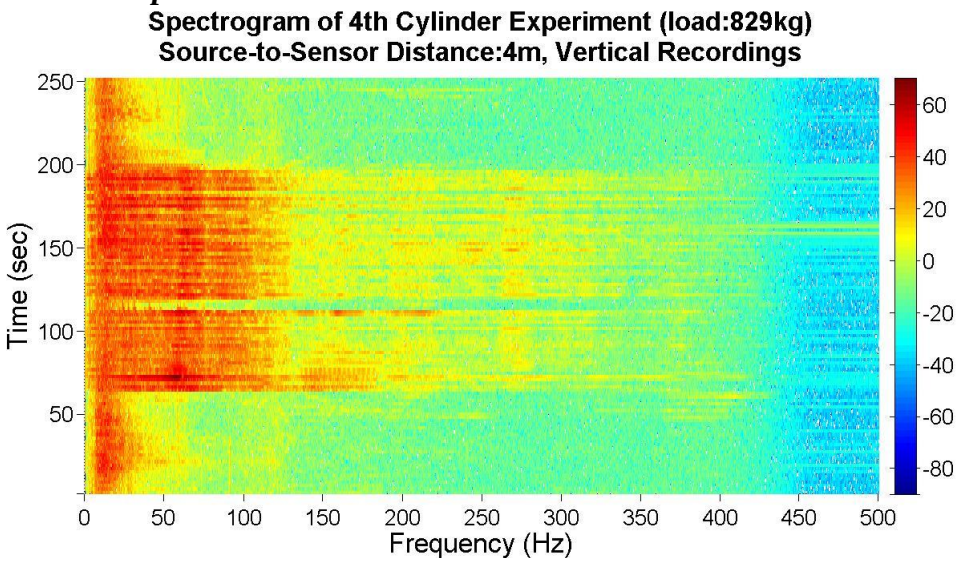

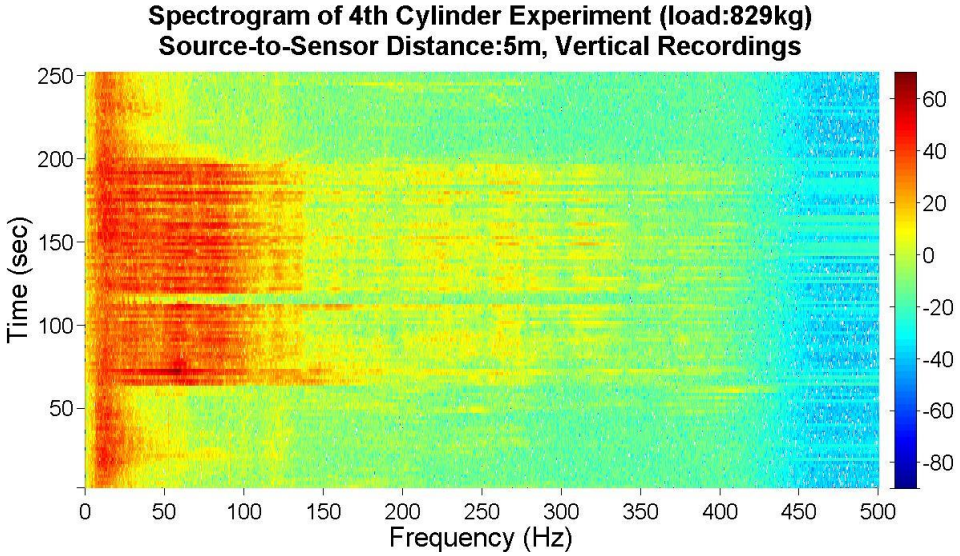

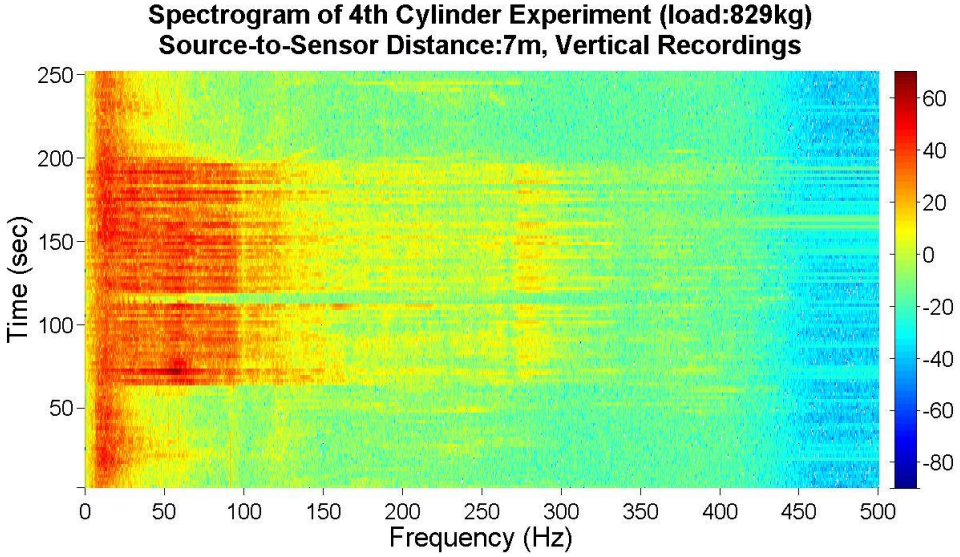

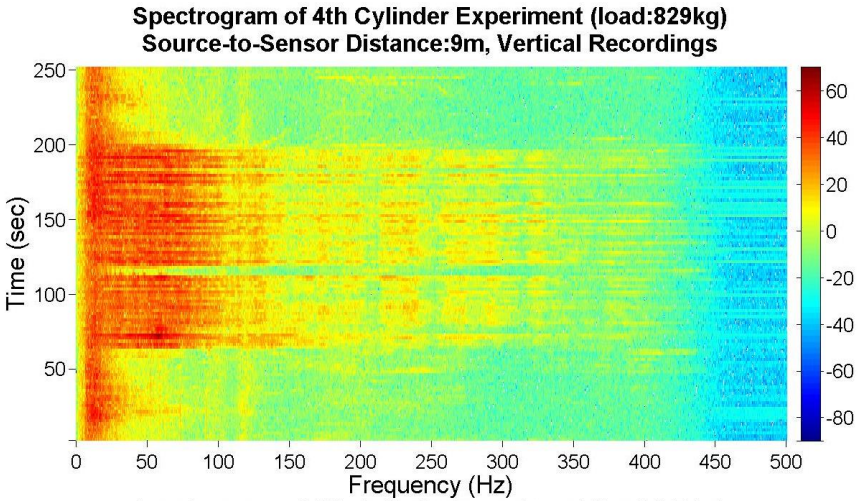
Spectrogram of 4th Cylinder Experiment (load:829kg)
Source-to-Sensor Distance:9m, Vertical Recordings
Time (sec)
Frequency (Hz)

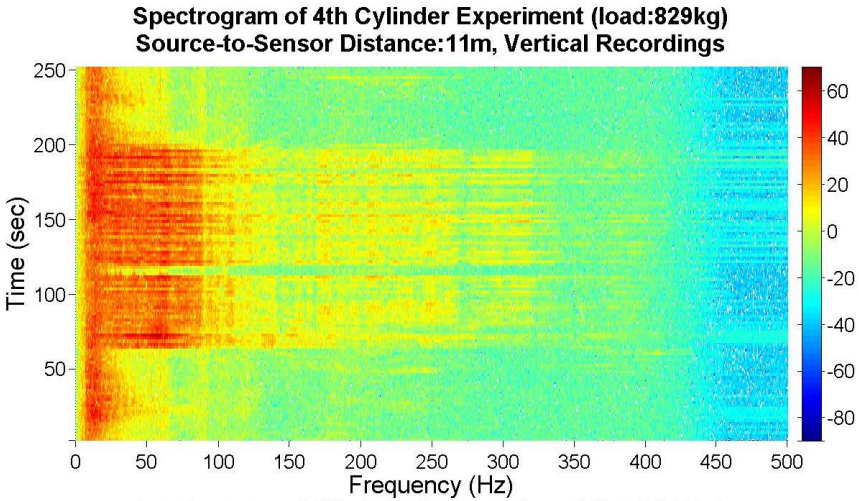
Spectrogram of 4th Cylinder Experiment (load:829kg)
Source-to-Sensor Distance:11m, Vertical Recordings
Time (sec)
Frequency (Hz)

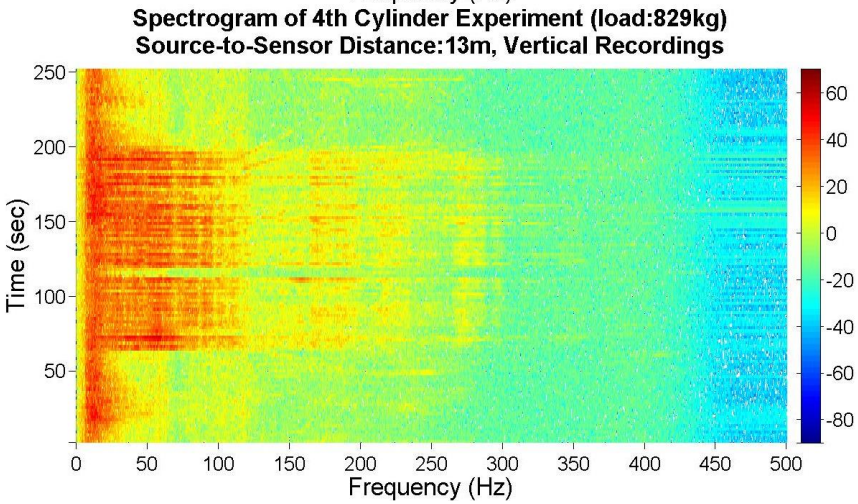
Spectrogram of 4th Cylinder Experiment (load:829kg)
Source-to-Sensor Distance:13m, Vertical Recordings
Time (sec)
Frequency (Hz)

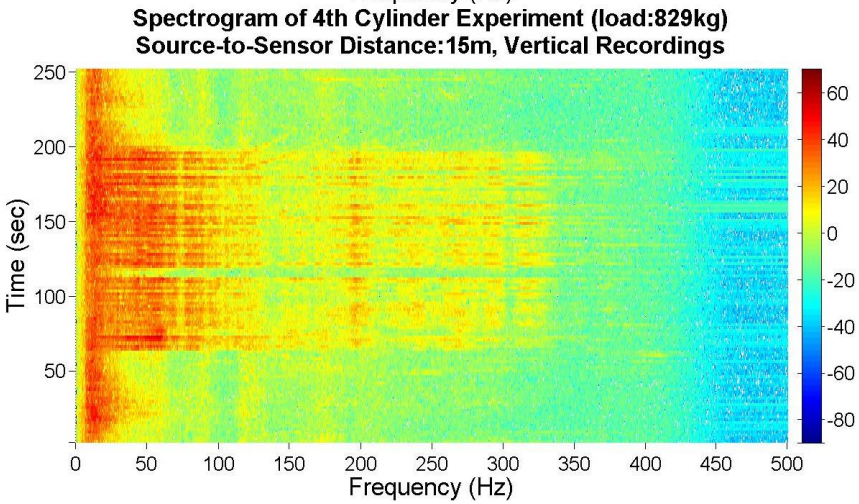
Spectrogram of 4th Cylinder Experiment (load:829kg)
Source-to-Sensor Distance:15m, Vertical Recordings
Time (sec)
Frequency (Hz)

b) North-South Component

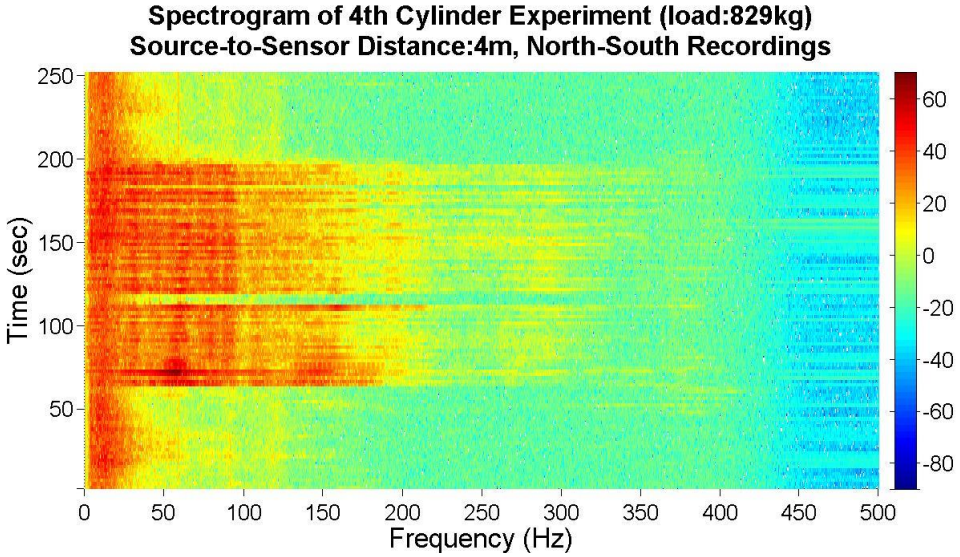

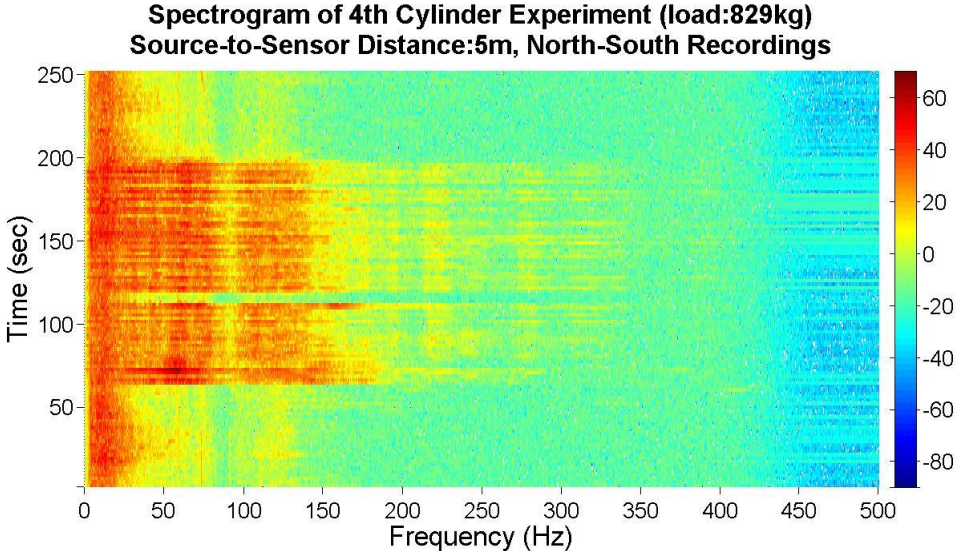

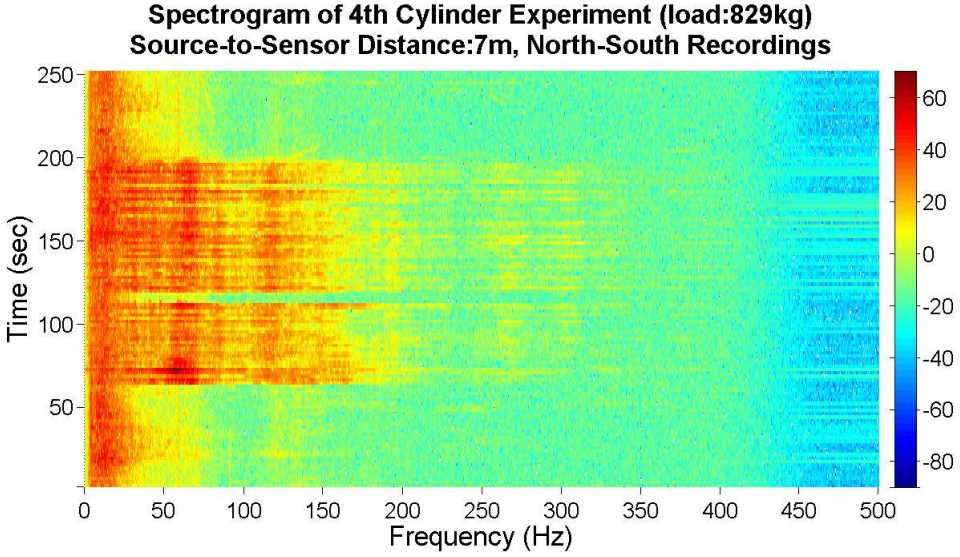

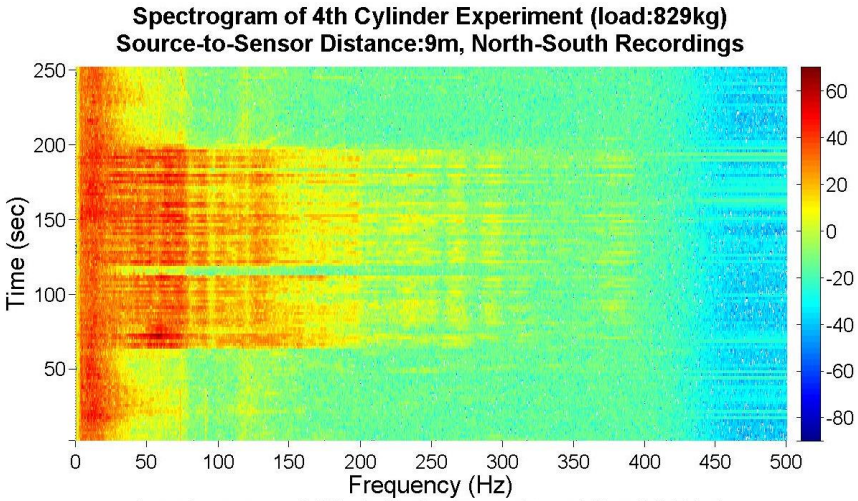
Spectrogram of 4th Cylinder Experiment (load:829kg)
Source-to-Sensor Distance:9m, North-South Recordings
Time (sec)
Frequency (Hz)

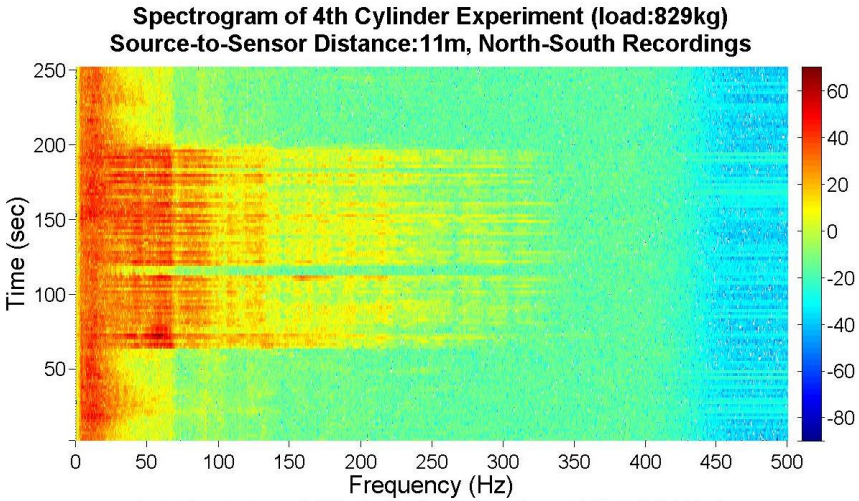
Spectrogram of 4th Cylinder Experiment (load:829kg)
Source-to-Sensor Distance:11m, North-South Recordings
Time (sec)
Frequency (Hz)

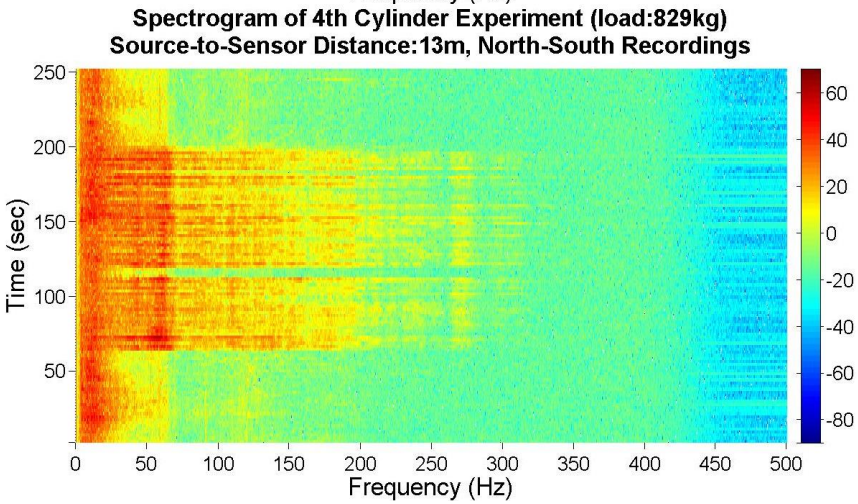
Spectrogram of 4th Cylinder Experiment (load:829kg)
Source-to-Sensor Distance:13m, North-South Recordings
Time (sec)
Frequency (Hz)

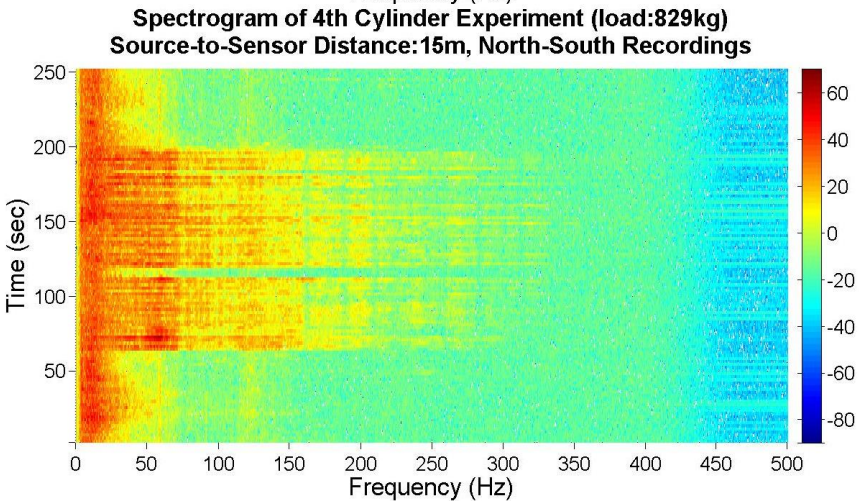
Spectrogram of 4th Cylinder Experiment (load:829kg)
Source-to-Sensor Distance:15m, North-South Recordings
Time (sec)
Frequency (Hz)

c) East-West Component

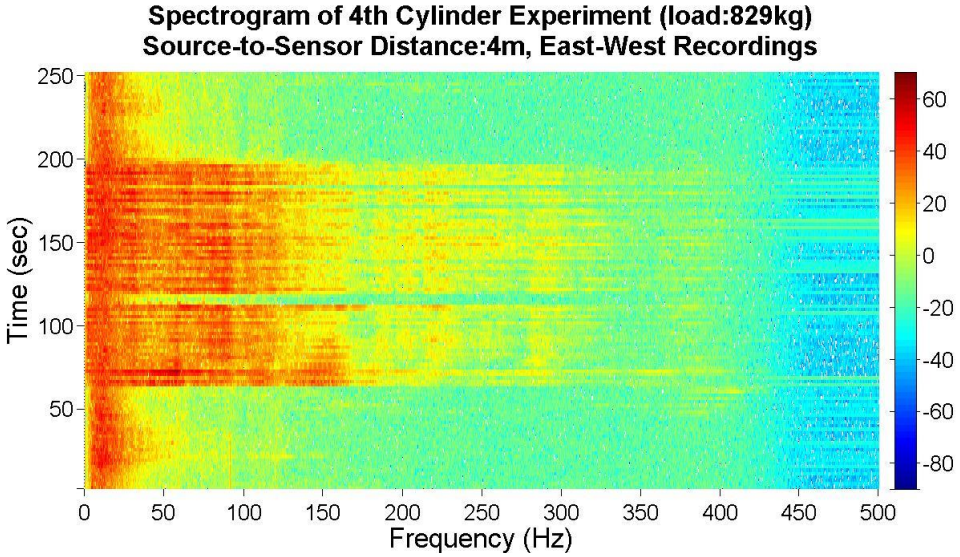

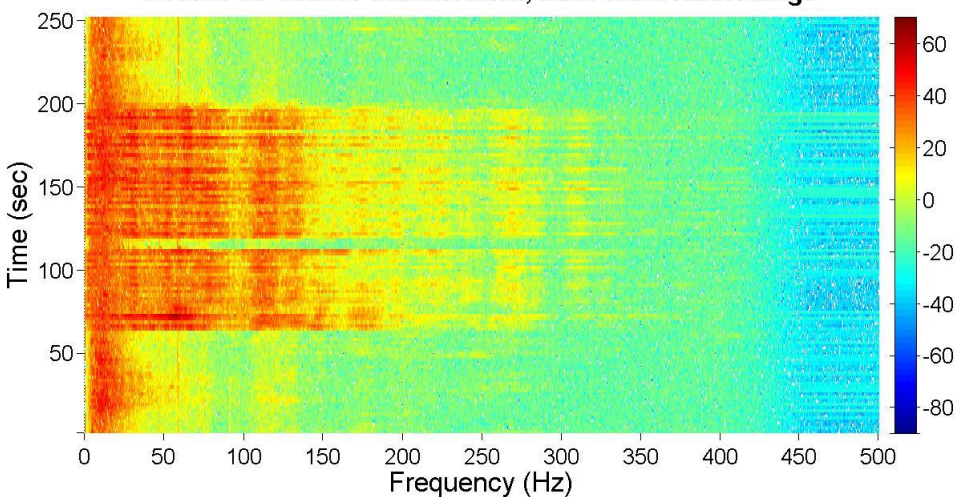

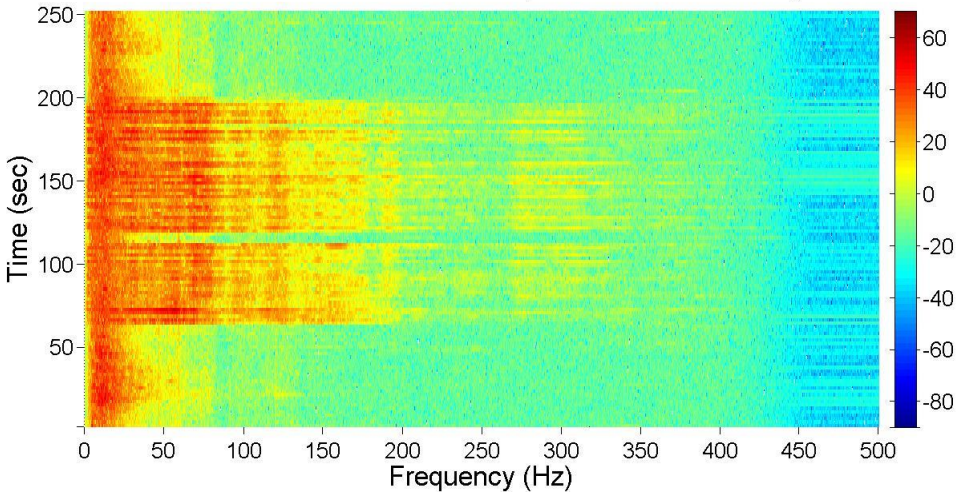

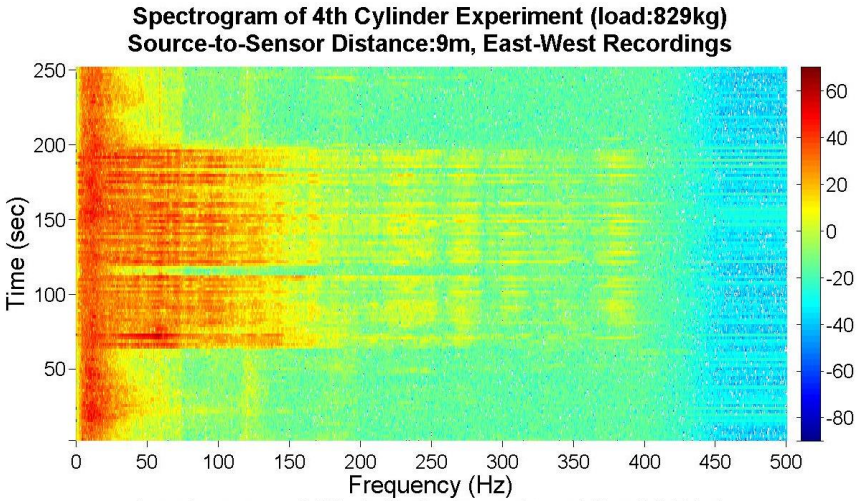
Spectrogram of 4th Cylinder Experiment (load:829kg)
Source-to-Sensor Distance:9m, East-West Recordings
Time (sec)
Frequency (Hz)

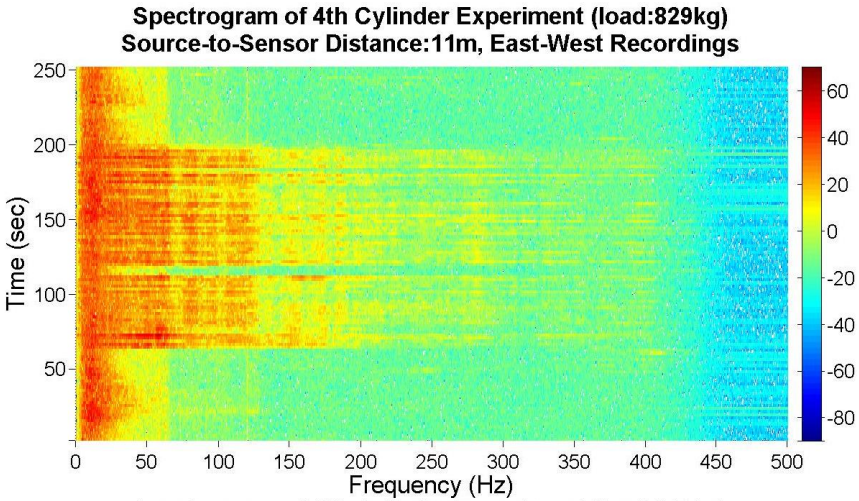
Spectrogram of 4th Cylinder Experiment (load:829kg)
Source-to-Sensor Distance:11m, East-West Recordings
Time (sec)
Frequency (Hz)

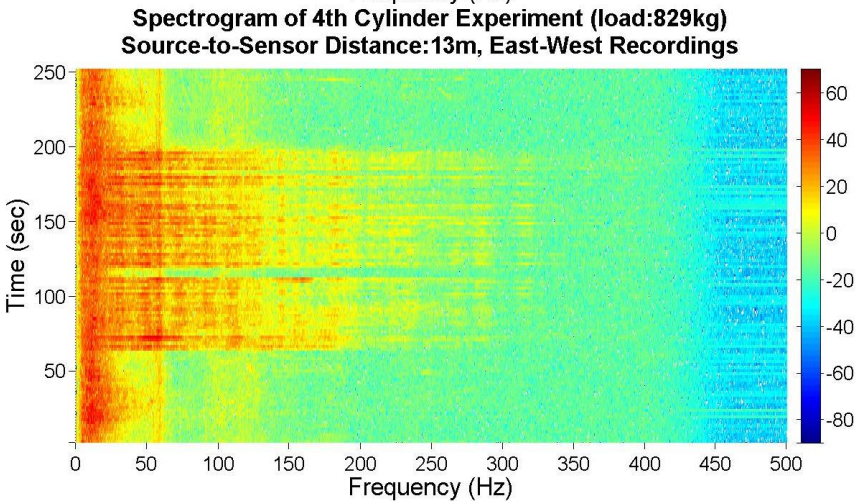
Spectrogram of 4th Cylinder Experiment (load:829kg)
Source-to-Sensor Distance:13m, East-West Recordings
Time (sec)
Frequency (Hz)

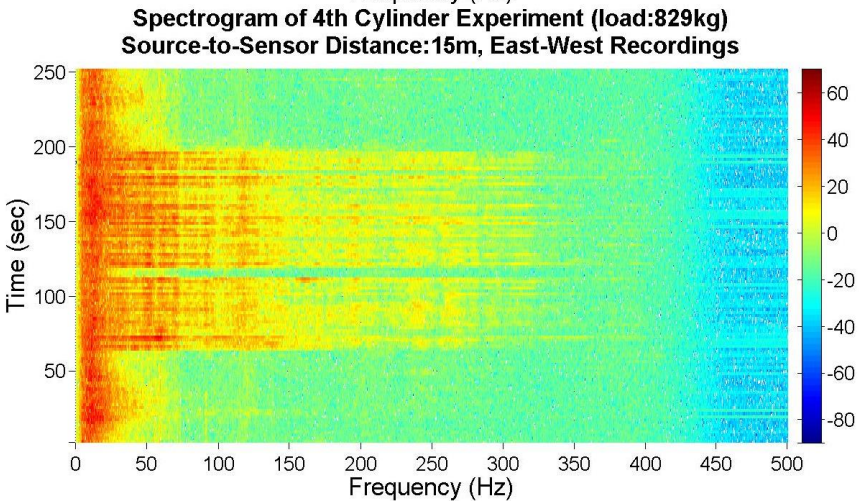
Spectrogram of 4th Cylinder Experiment (load:829kg)
Source-to-Sensor Distance:15m, East-West Recordings
Time (sec)
Frequency (Hz)

A.2 Power Spectral Density graphs (PSD)

Section 6.5.2 to 6.5.4 presented the use of power spectral density graphs (PSD) to deeply understand frequency content of the recorded signals. The same PSD spectra were used to understand the frequency characteristics of the recorded signals emitted during the up-scaled shear box methodology, to understand the changes in the frequency characteristics as the load on the soil slip surface was increasing, and finally to understand the changes in the frequency characteristics as source-to-sensor distance increases.

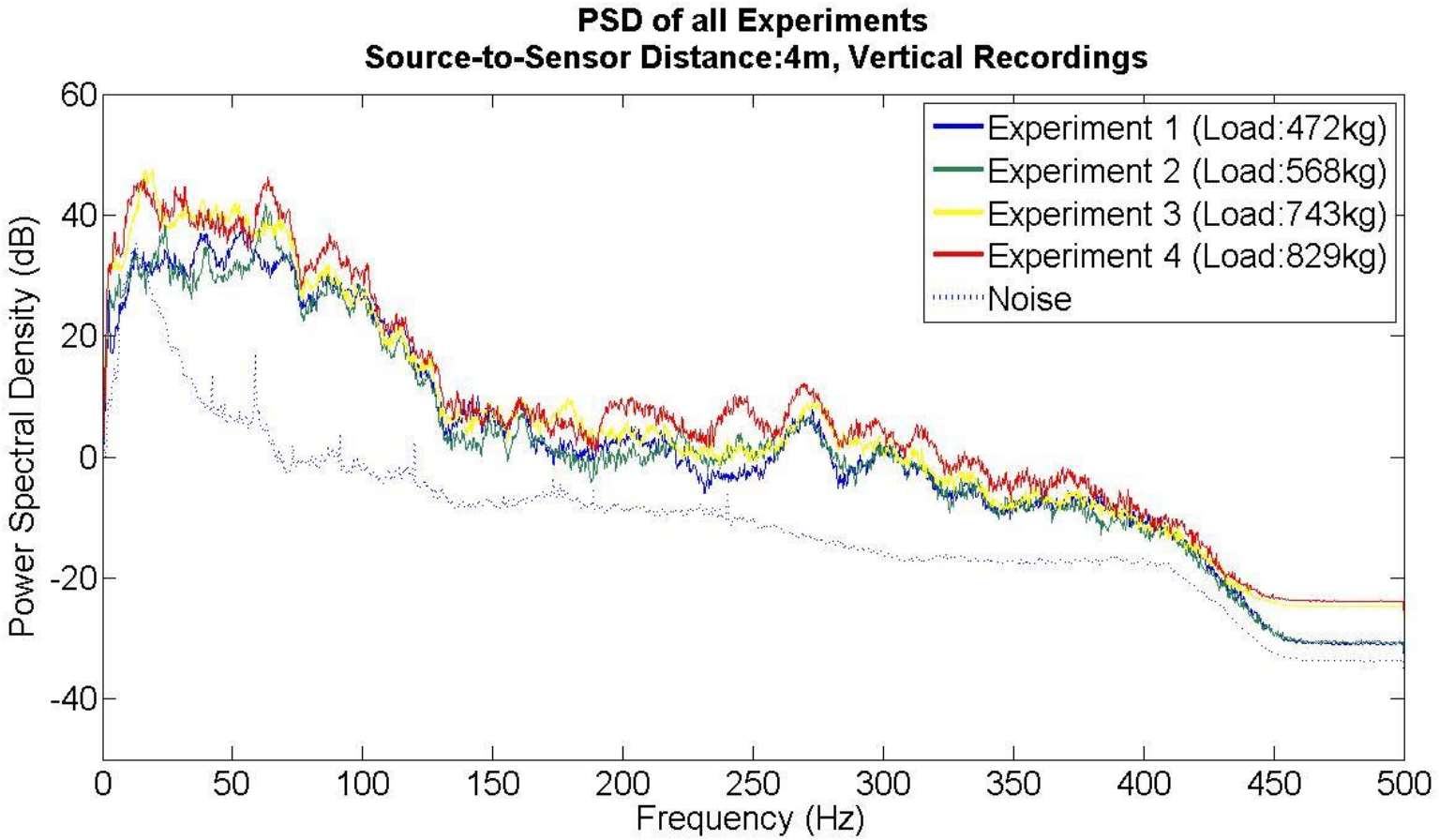
PSD of all Experiments
Source-to-Sensor Distance:4m, Vertical Recordings
Power Spectral Density (dB)
Frequency (Hz)
Experiment 1 (Load:472kg)
Experiment 2 (Load:568kg)
Experiment 3 (Load:743kg)
Experiment 4 (Load:829kg)
Noise
60
40
20
0
-20
-40
0
50
100
150
200
250
300
350
400
450
500

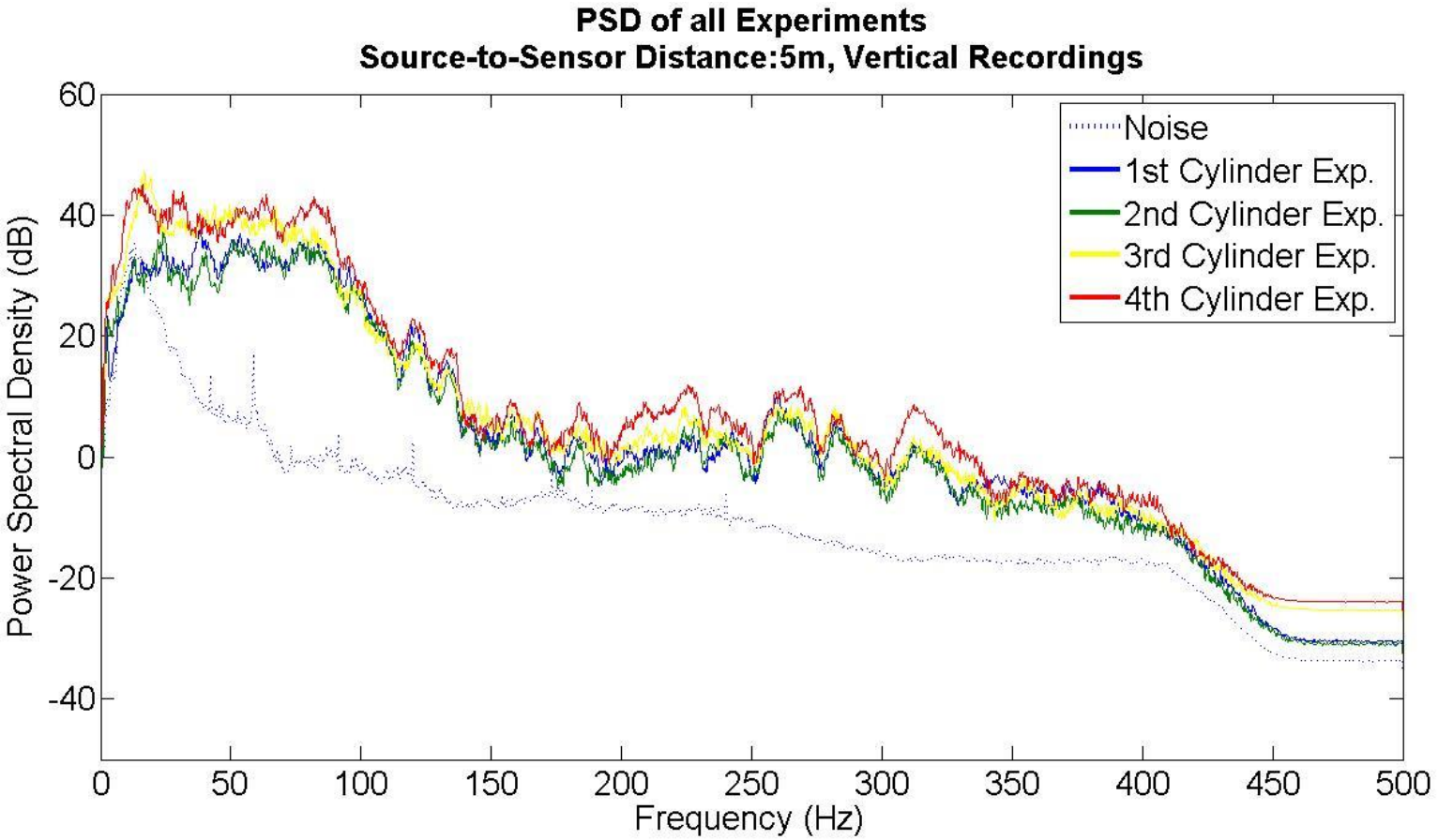
PSD of all Experiments
Source-to-Sensor Distance:5m, Vertical Recordings
Power Spectral Density (dB)
Frequency (Hz)
Noise
1st Cylinder Exp.
2nd Cylinder Exp.
3rd Cylinder Exp.
4th Cylinder Exp.
60
40
20
0
-20
-40
0
50
100
150
200
250
300
350
400
450
500

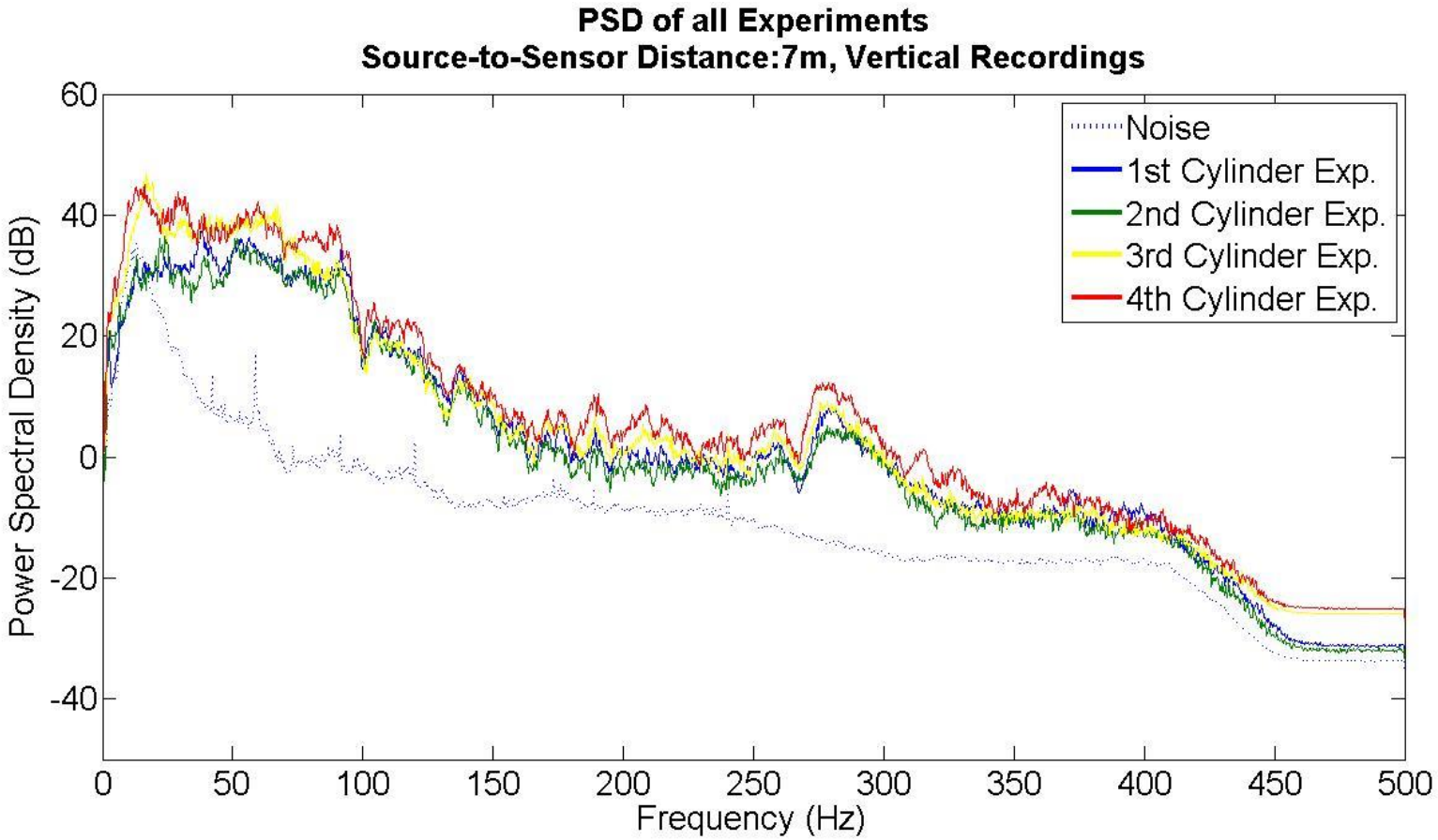
PSD of all Experiments
Source-to-Sensor Distance:7m, Vertical Recordings
Power Spectral Density (dB)
Frequency (Hz)
Noise
1st Cylinder Exp.
2nd Cylinder Exp.
3rd Cylinder Exp.
4th Cylinder Exp.
60
40
20
0
-20
-40
0
50
100
150
200
250
300
350
400
450
500

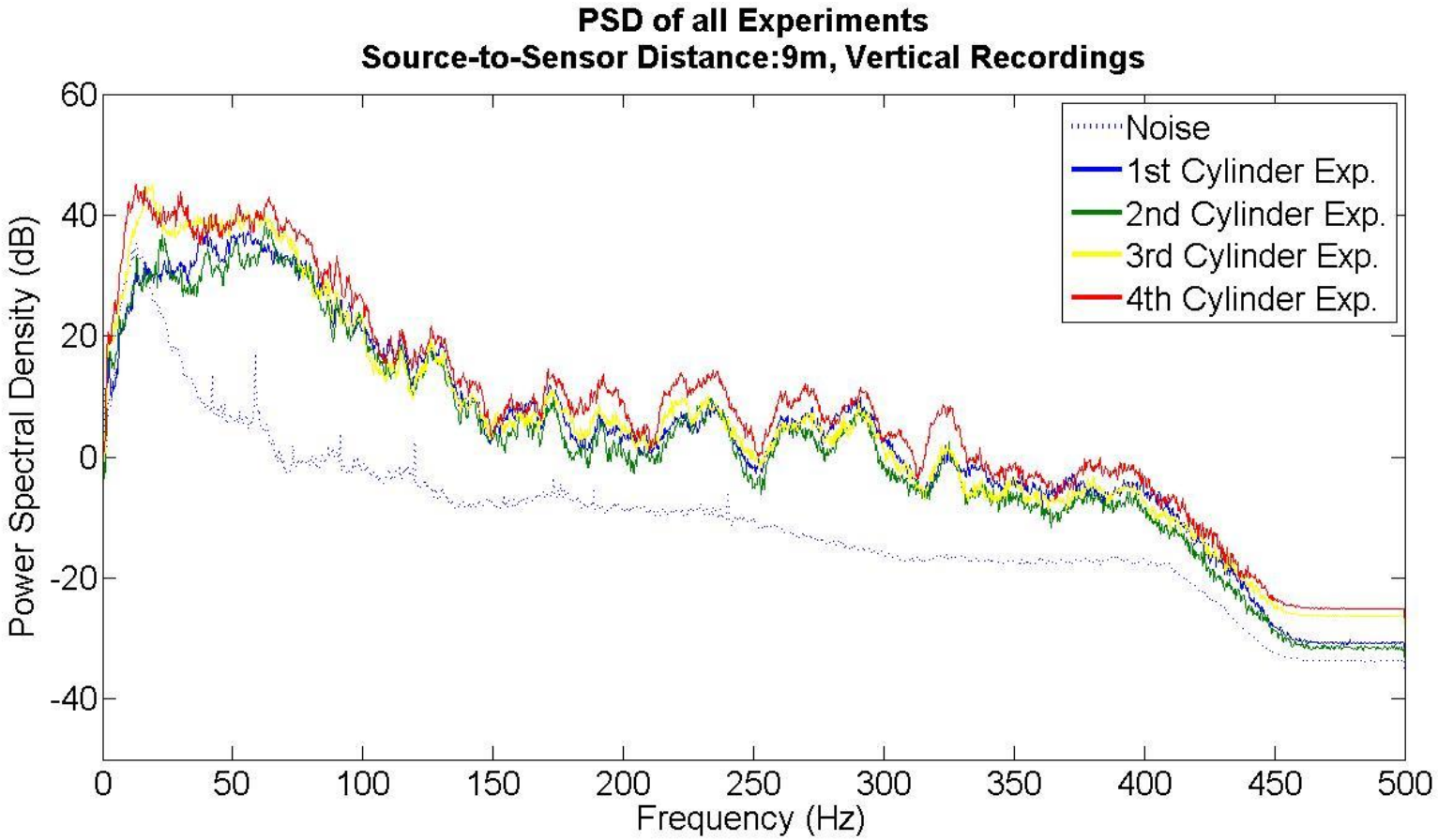
PSD of all Experiments
Source-to-Sensor Distance:9m, Vertical Recordings
Power Spectral Density (dB)
Frequency (Hz)
Noise
1st Cylinder Exp.
2nd Cylinder Exp.
3rd Cylinder Exp.
4th Cylinder Exp.
60
40
20
0
-20
-40
0
50
100
150
200
250
300
350
400
450
500

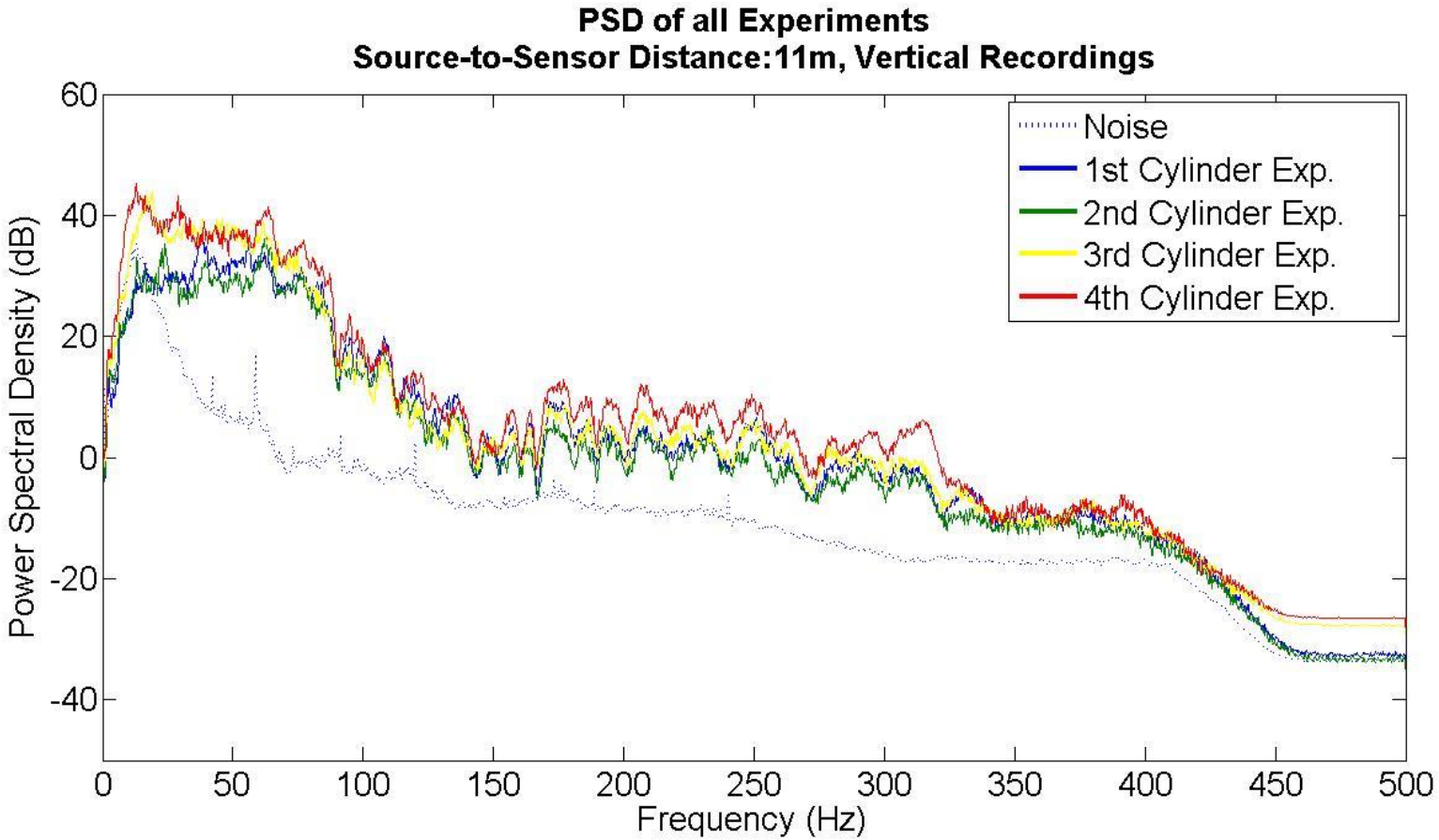
PSD of all Experiments
Source-to-Sensor Distance:11m, Vertical Recordings
Power Spectral Density (dB)
Frequency (Hz)
Noise
1st Cylinder Exp.
2nd Cylinder Exp.
3rd Cylinder Exp.
4th Cylinder Exp.
60
40
20
0
-20
-40
0
50
100
150
200
250
300
350
400
450
500

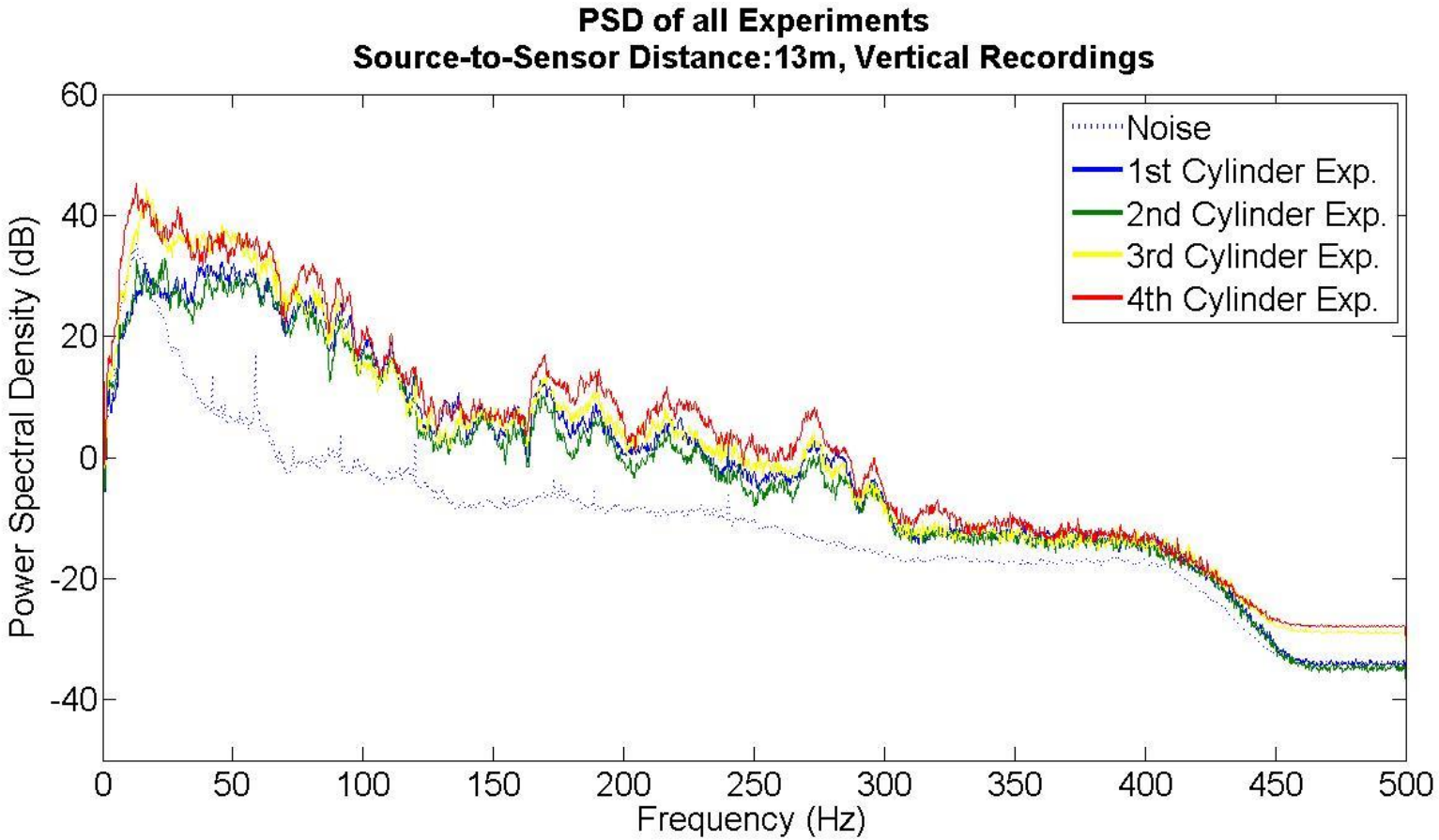
PSD of all Experiments
Source-to-Sensor Distance:13m, Vertical Recordings
Noise
1st Cylinder Exp.
2nd Cylinder Exp.
3rd Cylinder Exp.
4th Cylinder Exp.
Power Spectral Density (dB)
Frequency (Hz)
60
40
20
0
-20
-40
0
50
100
150
200
250
300
350
400
450
500

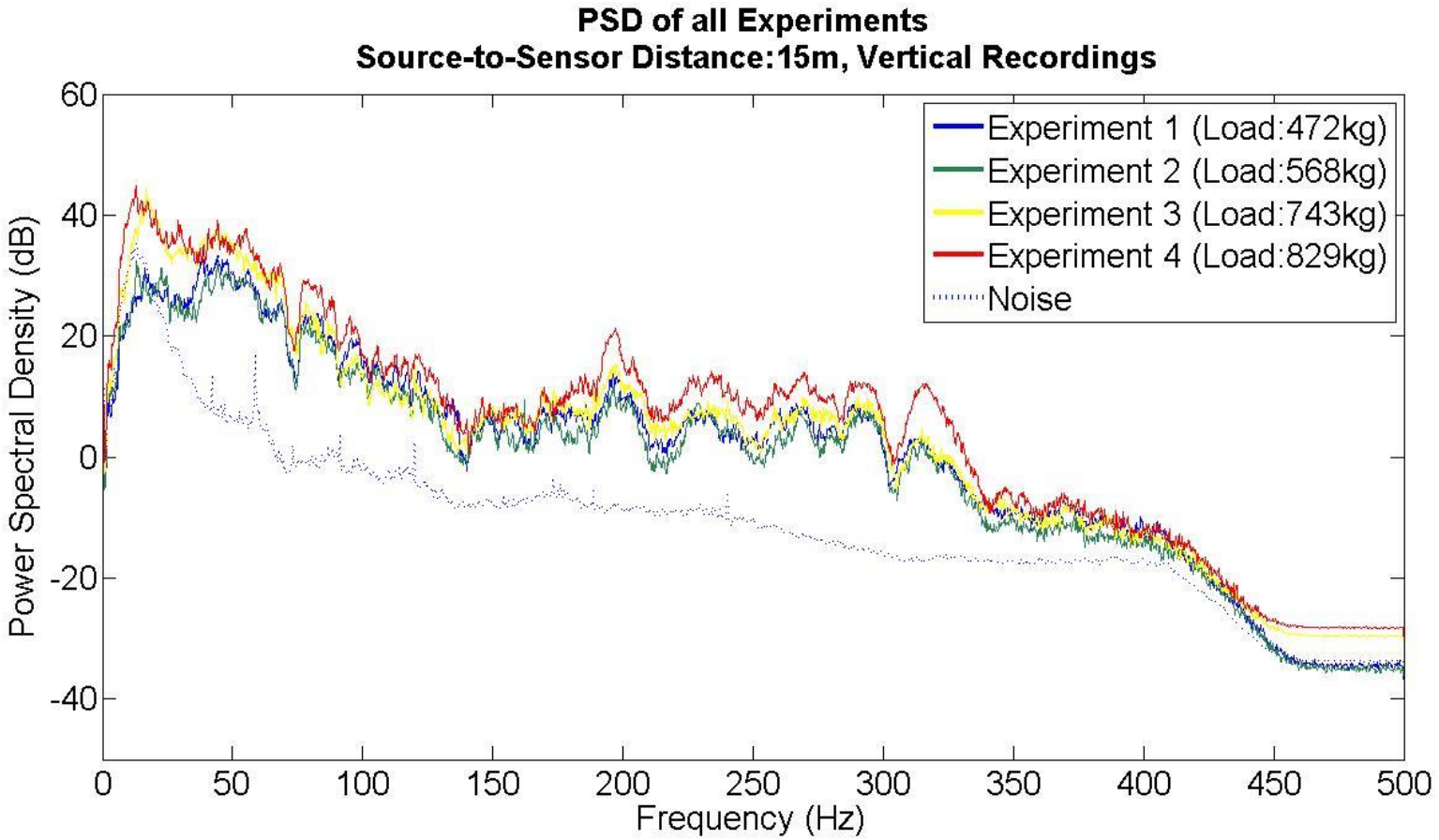
PSD of all Experiments
Source-to-Sensor Distance:15m, Vertical Recordings
Power Spectral Density (dB)
Frequency (Hz)
60
40
20
0
-20
-40
0
50
100
150
200
250
300
350
400
450
500
Experiment 1 (Load:472kg)
Experiment 2 (Load:568kg)
Experiment 3 (Load:743kg)
Experiment 4 (Load:829kg)
Noise

b) North-South Component

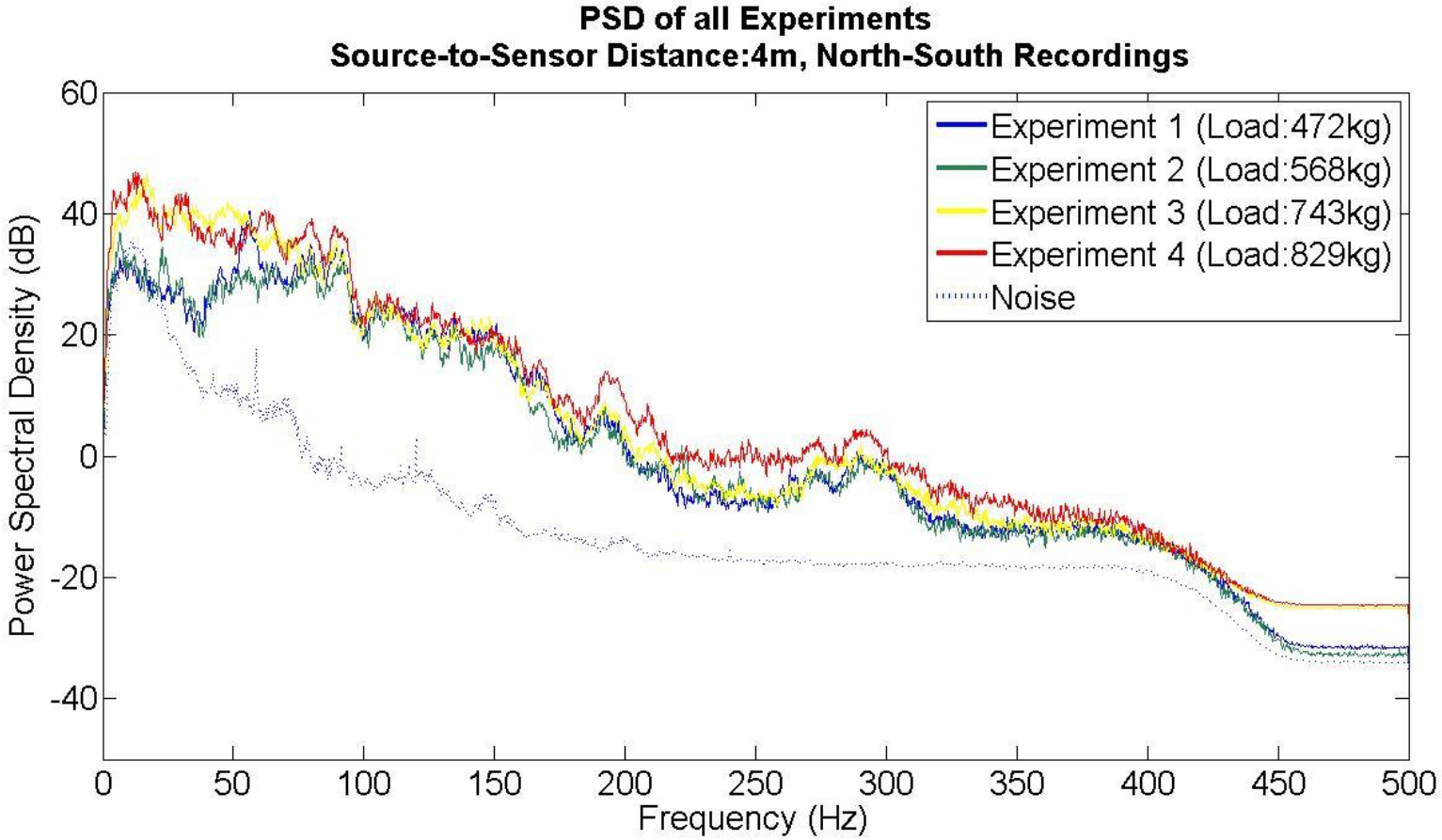

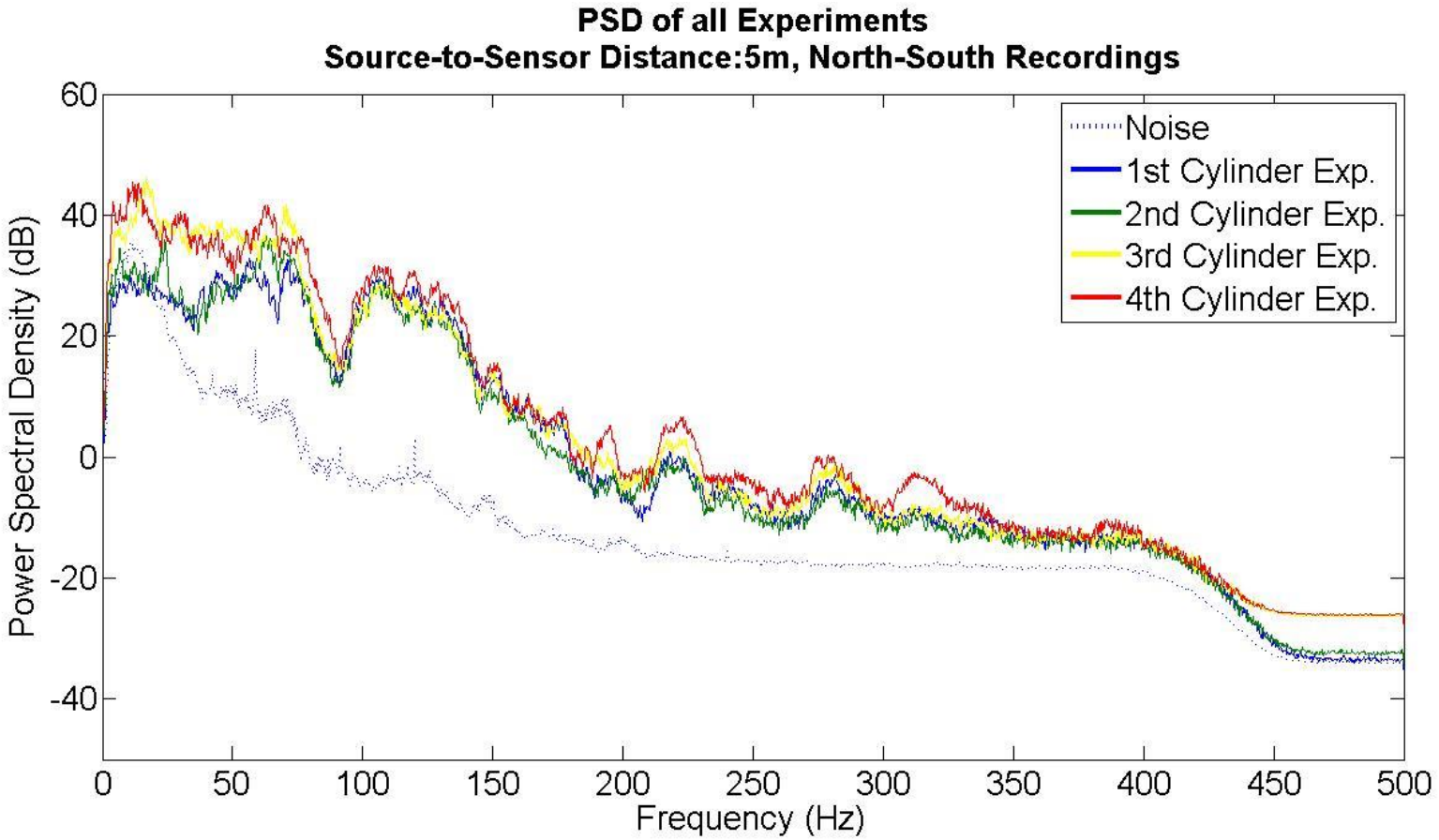
PSD of all Experiments
Source-to-Sensor Distance:5m, North-South Recordings
Noise
1st Cylinder Exp.
2nd Cylinder Exp.
3rd Cylinder Exp.
4th Cylinder Exp.
Power Spectral Density (dB)
Frequency (Hz)
60
40
20
0
-20
-40
0
50
100
150
200
250
300
350
400
450
500

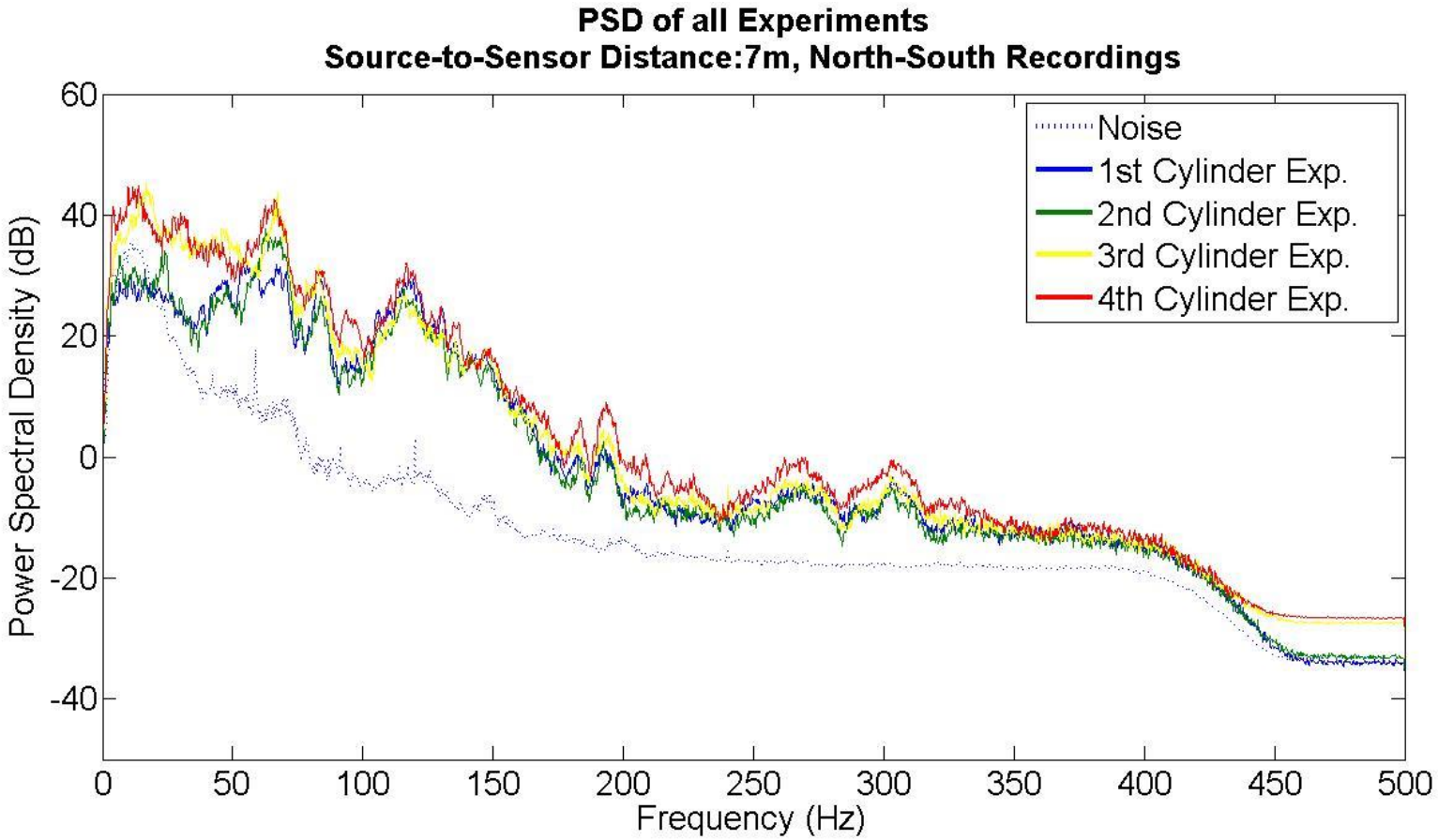
PSD of all Experiments
Source-to-Sensor Distance:7m, North-South Recordings
Power Spectral Density (dB)
Frequency (Hz)
Noise
1st Cylinder Exp.
2nd Cylinder Exp.
3rd Cylinder Exp.
4th Cylinder Exp.
60
40
20
0
-20
-40
0
50
100
150
200
250
300
350
400
450
500

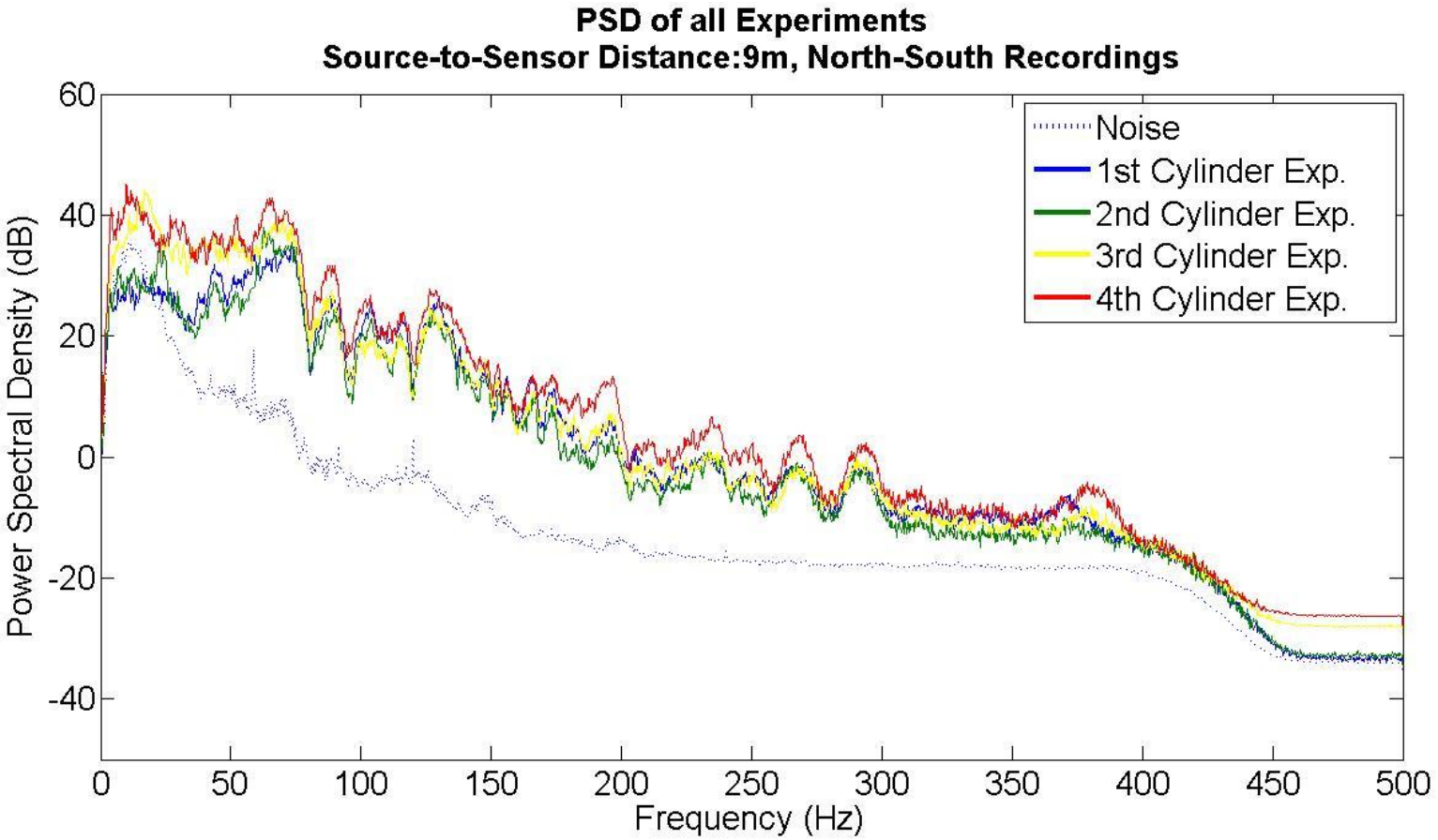
PSD of all Experiments
Source-to-Sensor Distance:9m, North-South Recordings
Power Spectral Density (dB)
Frequency (Hz)
Noise
1st Cylinder Exp.
2nd Cylinder Exp.
3rd Cylinder Exp.
4th Cylinder Exp.
60
40
20
0
-20
-40
0
50
100
150
200
250
300
350
400
450
500

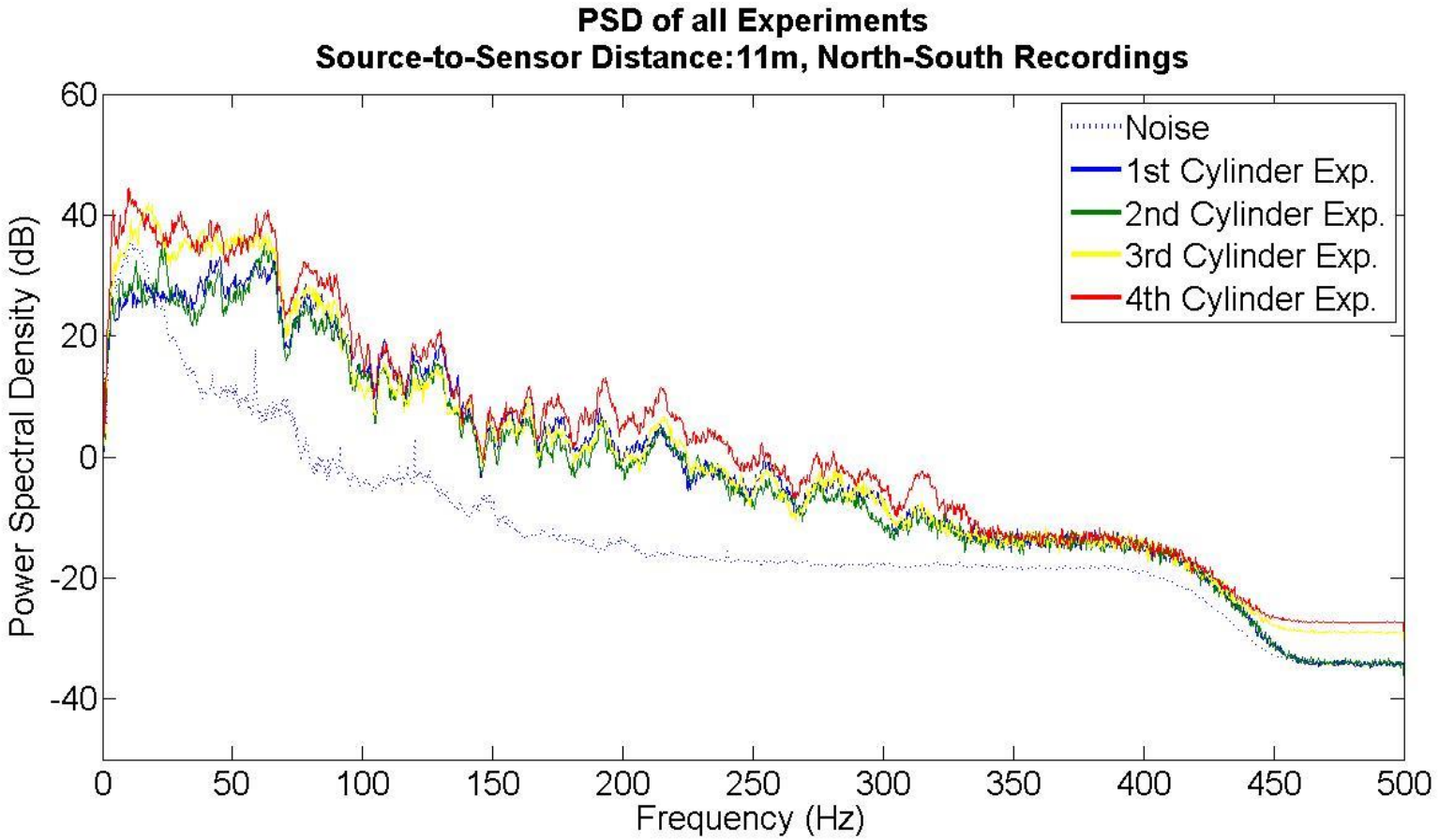
PSD of all Experiments
Source-to-Sensor Distance:11m, North-South Recordings
Noise
1st Cylinder Exp.
2nd Cylinder Exp.
3rd Cylinder Exp.
4th Cylinder Exp.
Power Spectral Density (dB)
Frequency (Hz)
60
40
20
0
-20
-40
0
50
100
150
200
250
300
350
400
450
500

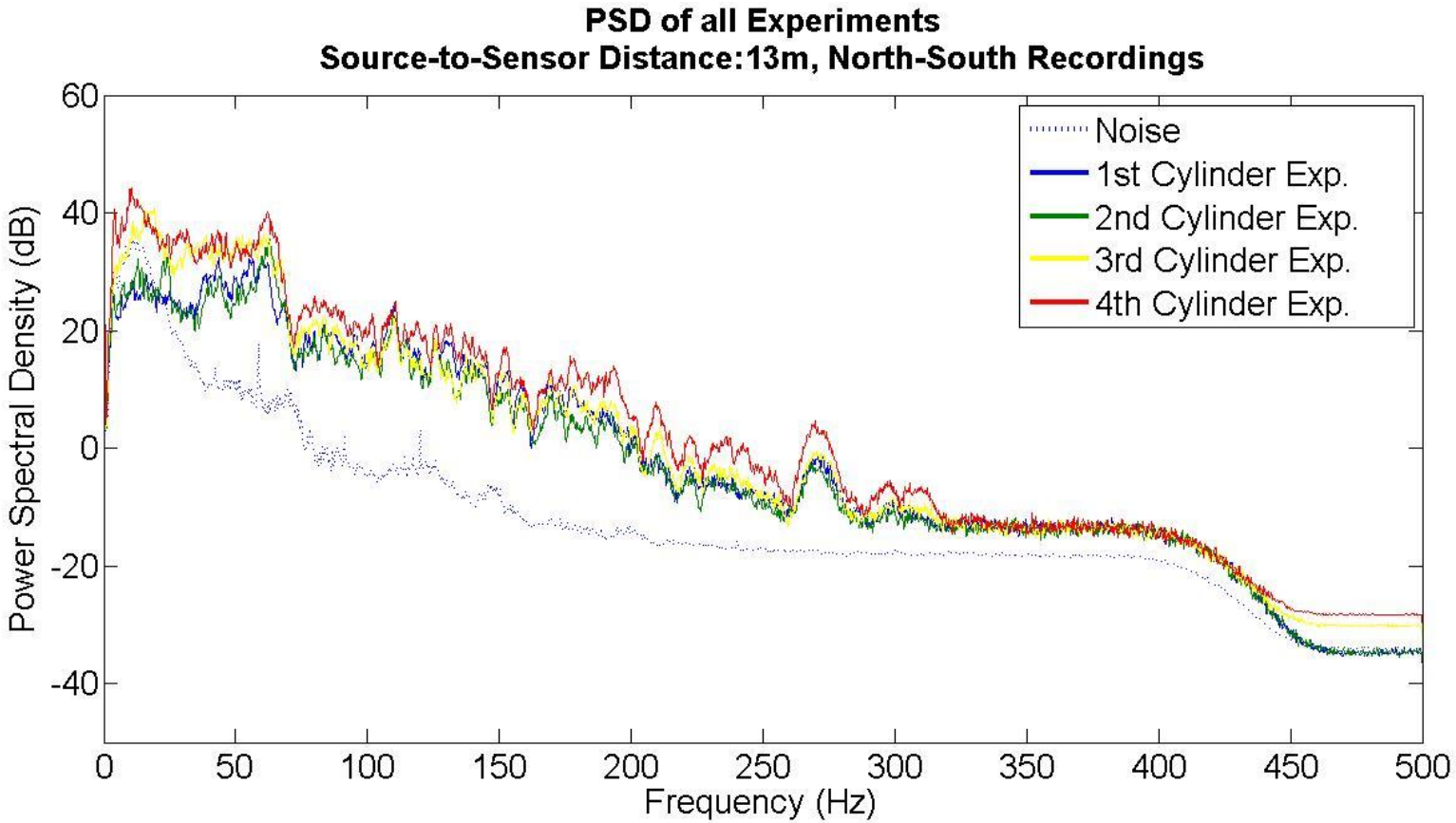
PSD of all Experiments
Source-to-Sensor Distance:13m, North-South Recordings
Noise
1st Cylinder Exp.
2nd Cylinder Exp.
3rd Cylinder Exp.
4th Cylinder Exp.
Power Spectral Density (dB)
60
40
20
0
-20
-40
0
50
100
150
200
250
300
350
400
450
500
Frequency (Hz)

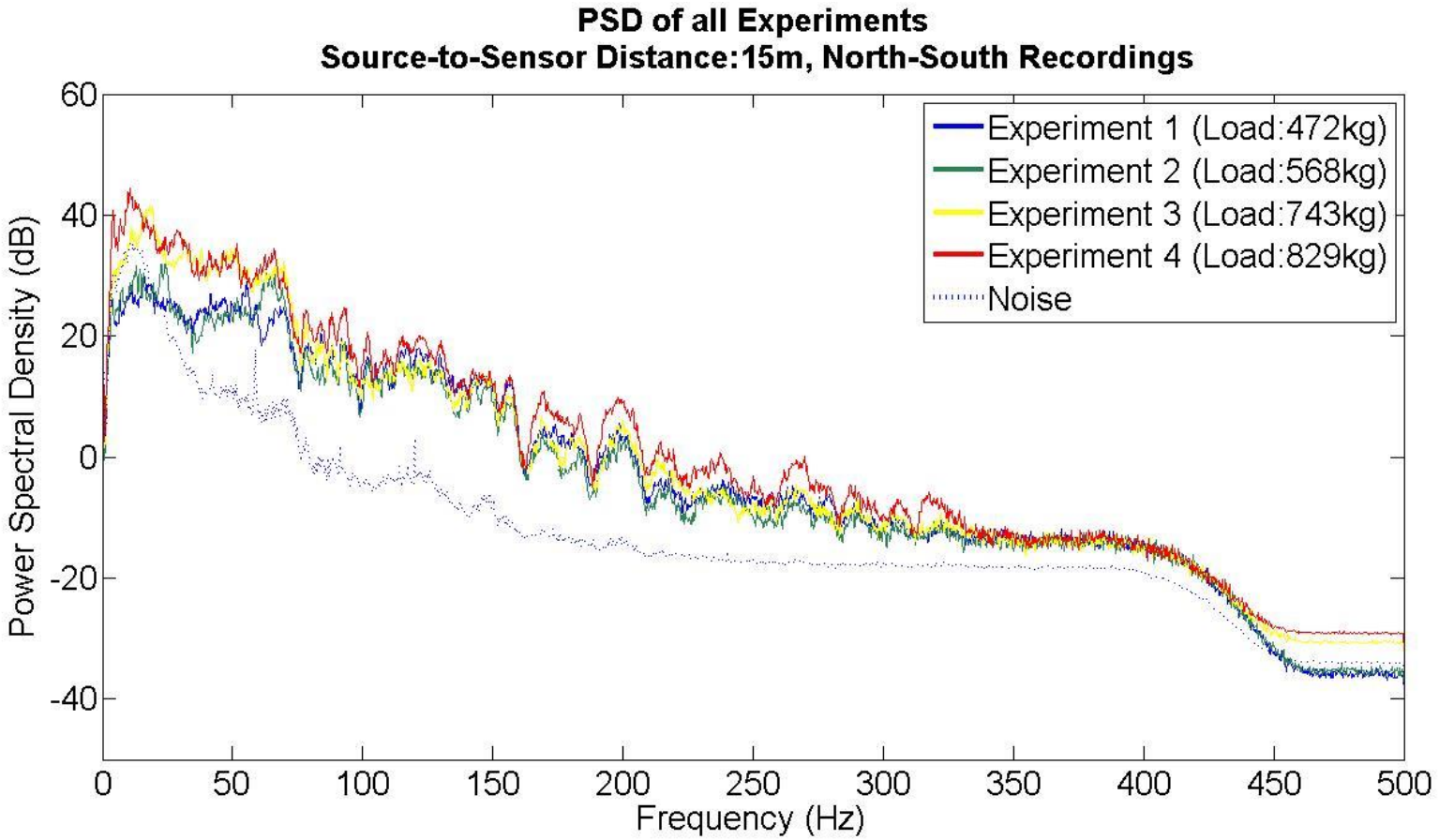
PSD of all Experiments
Source-to-Sensor Distance:15m, North-South Recordings
Power Spectral Density (dB)
Frequency (Hz)
60
40
20
0
-20
-40
0
50
100
150
200
250
300
350
400
450
500
Experiment 1 (Load:472kg)
Experiment 2 (Load:568kg)
Experiment 3 (Load:743kg)
Experiment 4 (Load:829kg)
Noise

c) East-West Component

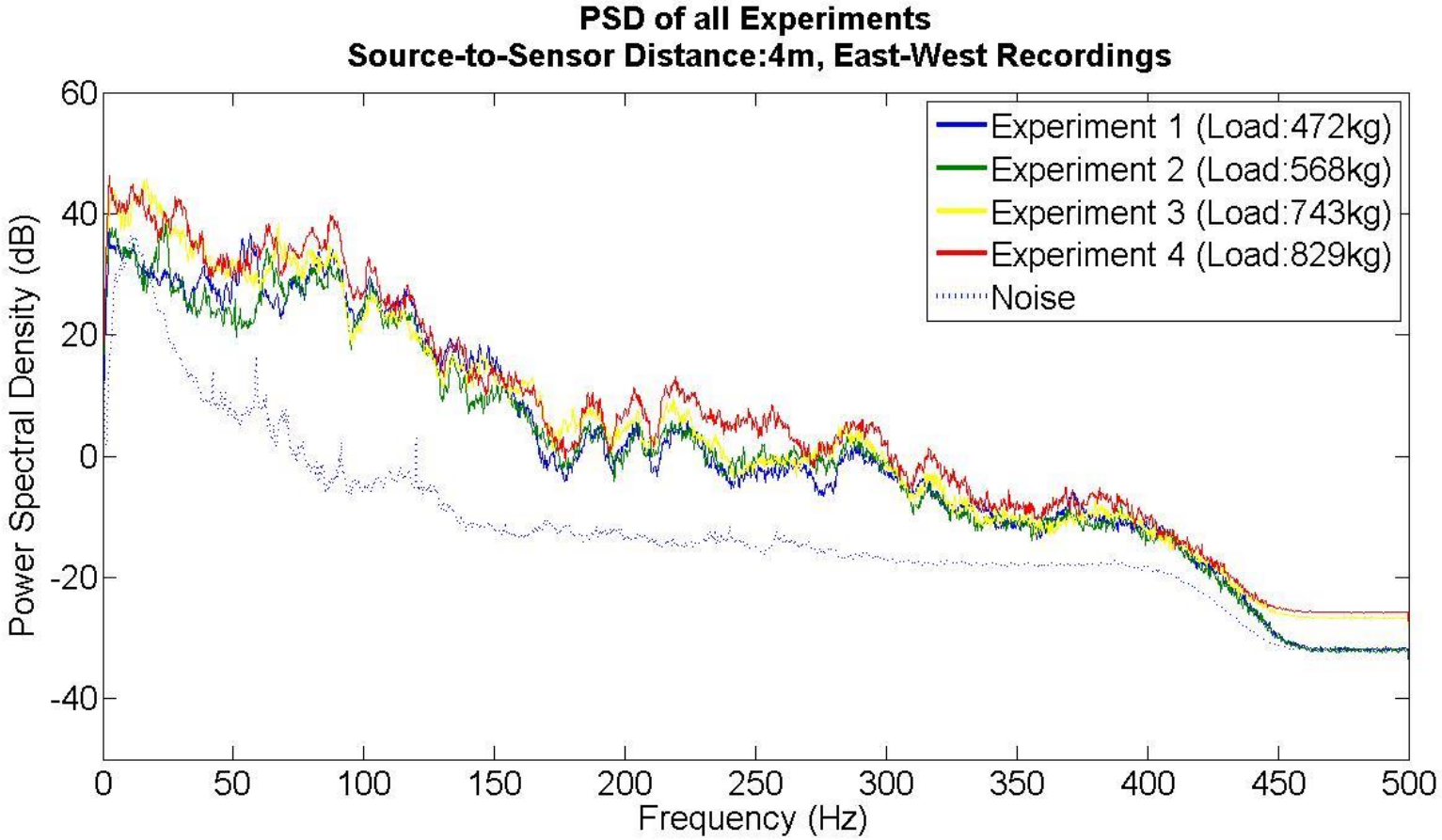

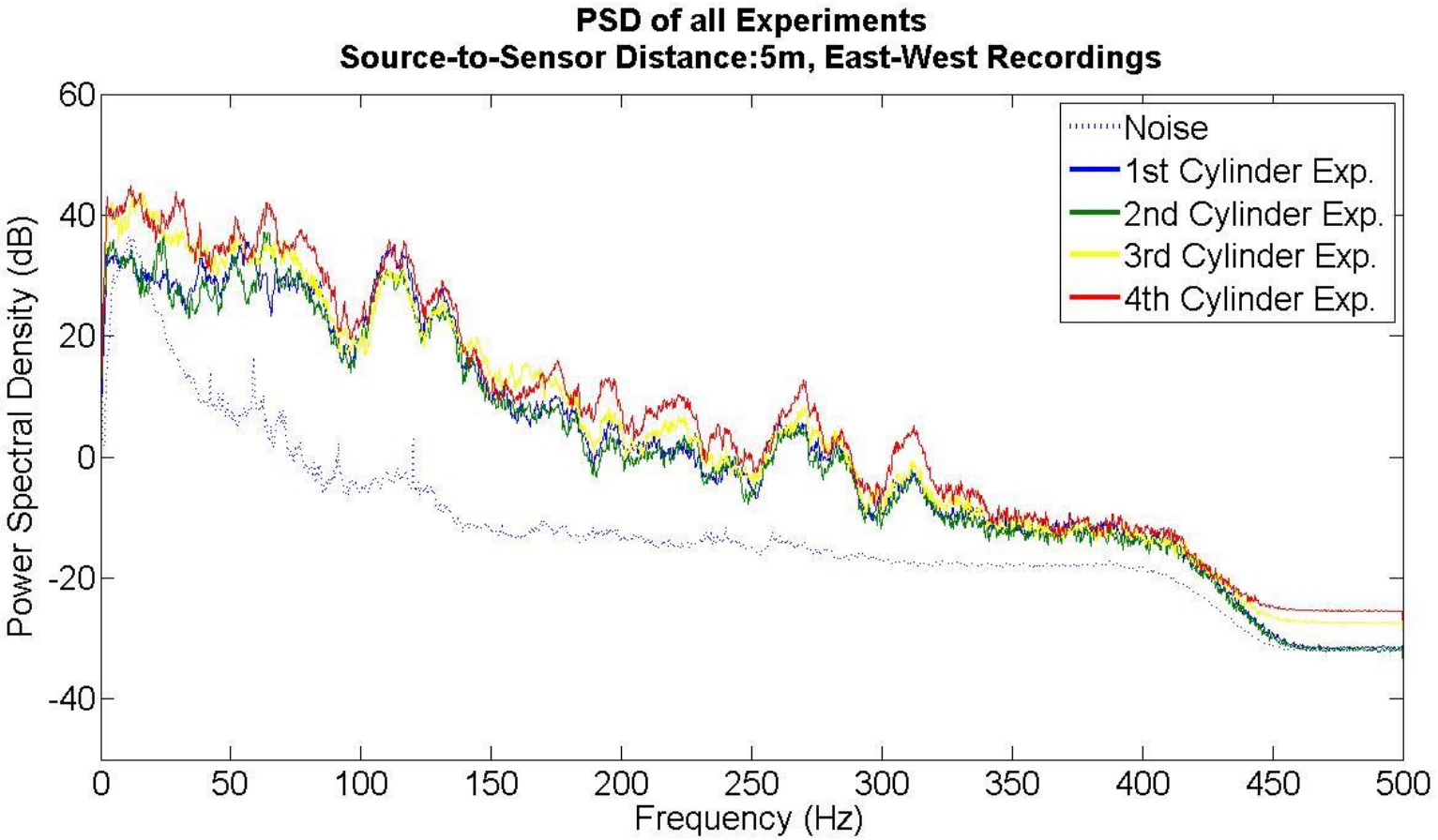
PSD of all Experiments
Source-to-Sensor Distance:5m, East-West Recordings
Power Spectral Density (dB)
Frequency (Hz)
60
40
20
0
-20
-40
0
50
100
150
200
250
300
350
400
450
500
Noise
1st Cylinder Exp.
2nd Cylinder Exp.
3rd Cylinder Exp.
4th Cylinder Exp.

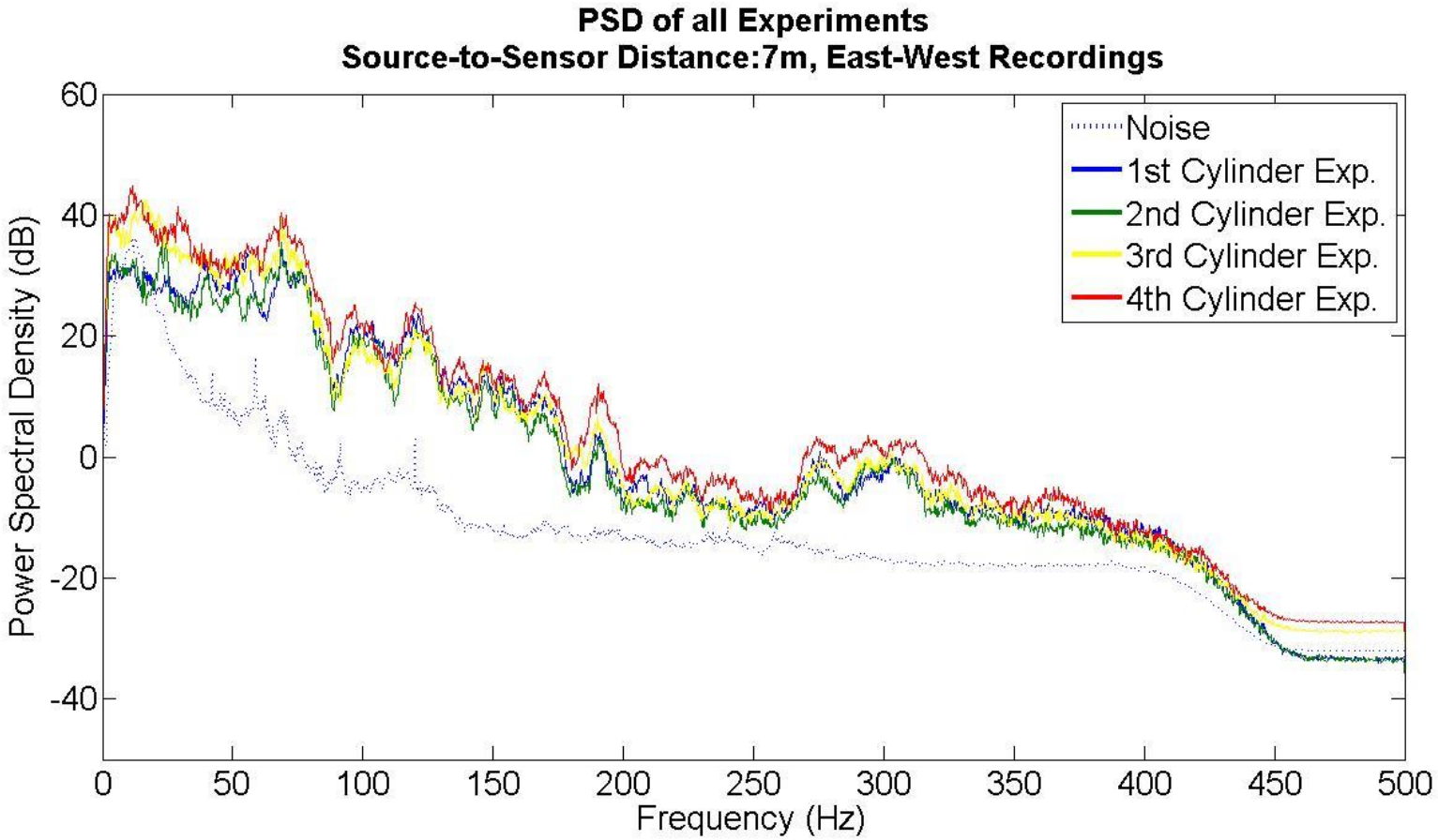
PSD of all Experiments
Source-to-Sensor Distance:7m, East-West Recordings
Noise
1st Cylinder Exp.
2nd Cylinder Exp.
3rd Cylinder Exp.
4th Cylinder Exp.
Power Spectral Density (dB)
Frequency (Hz)
60
40
20
0
-20
-40
0
50
100
150
200
250
300
350
400
450
500

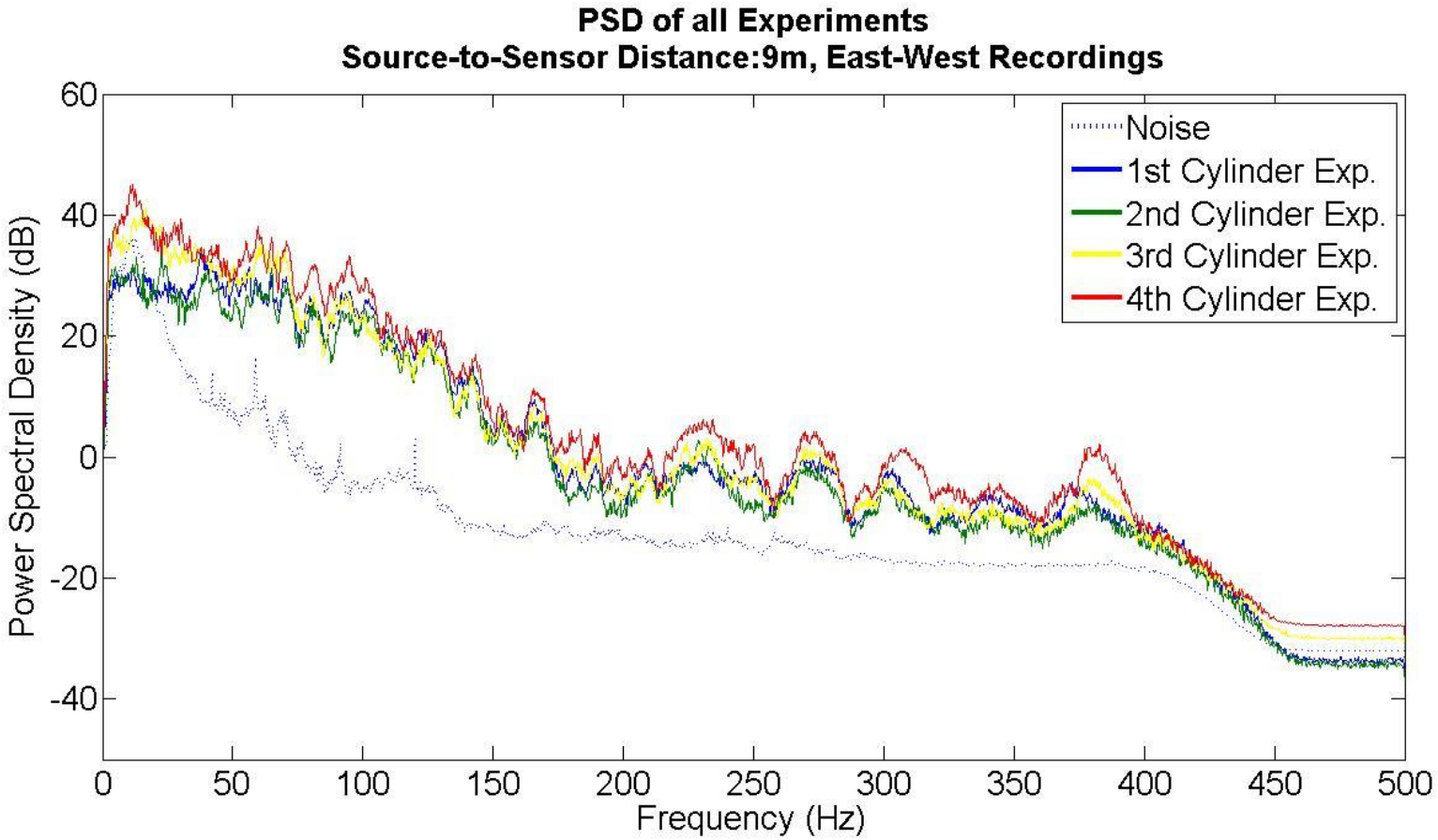
PSD of all Experiments
Source-to-Sensor Distance:9m, East-West Recordings
Power Spectral Density (dB)
Frequency (Hz)
Noise
1st Cylinder Exp.
2nd Cylinder Exp.
3rd Cylinder Exp.
4th Cylinder Exp.
60
40
20
0
-20
-40
0
50
100
150
200
250
300
350
400
450
500

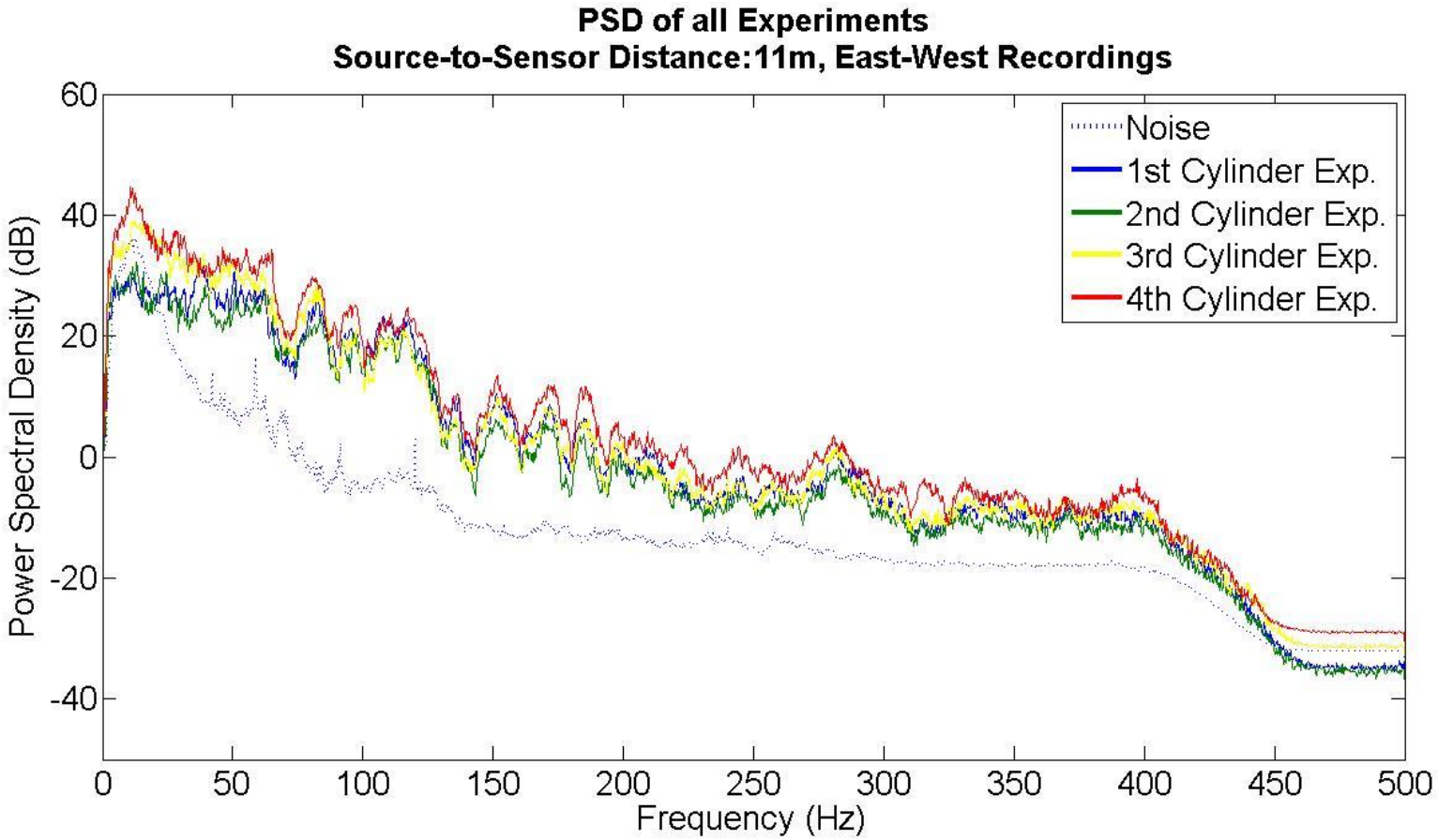
PSD of all Experiments
Source-to-Sensor Distance:11m, East-West Recordings
Noise
1st Cylinder Exp.
2nd Cylinder Exp.
3rd Cylinder Exp.
4th Cylinder Exp.
Power Spectral Density (dB)
Frequency (Hz)
60
40
20
0
-20
-40
0
50
100
150
200
250
300
350
400
450
500

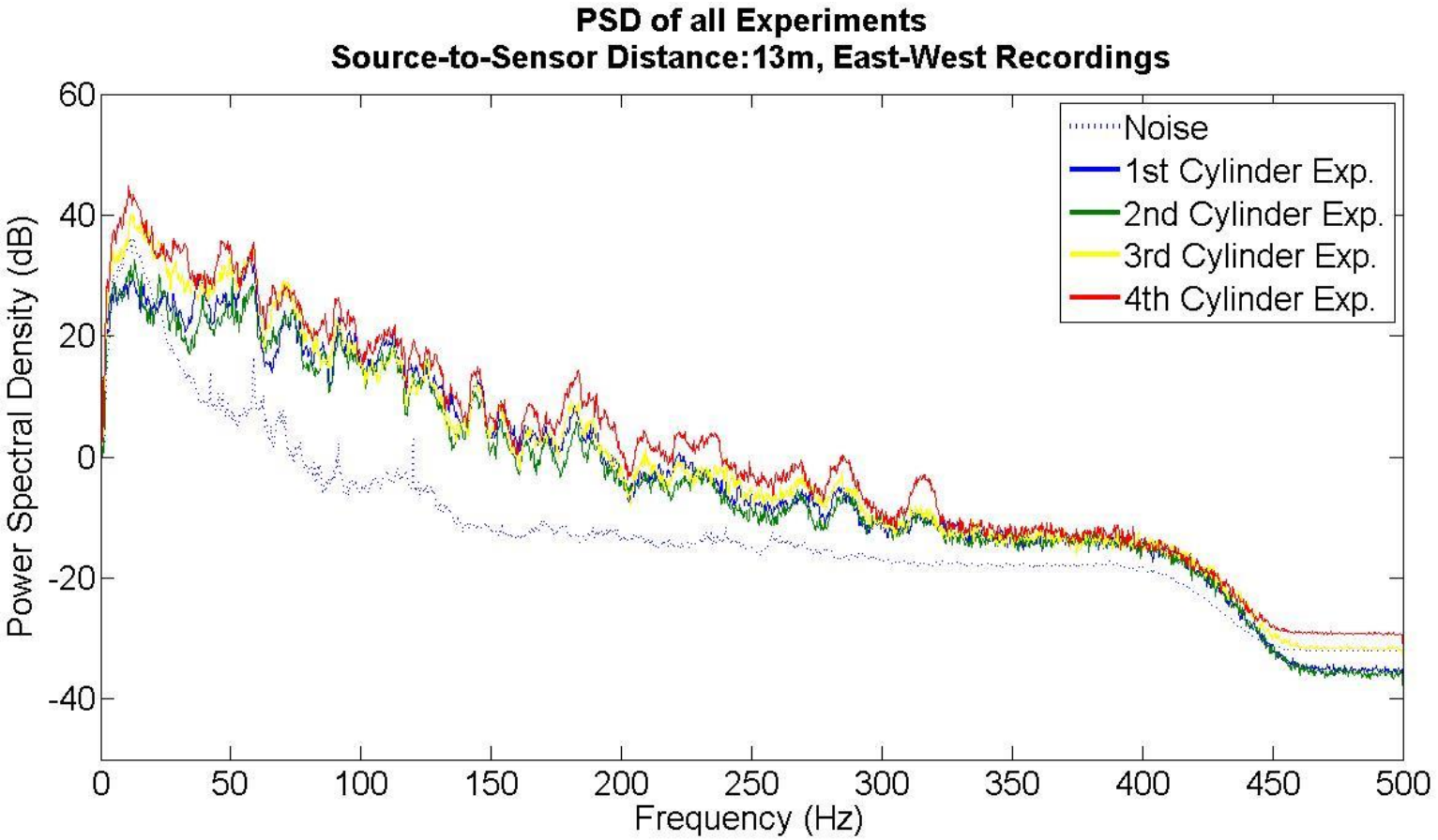
PSD of all Experiments
Source-to-Sensor Distance:13m, East-West Recordings
Power Spectral Density (dB)
Frequency (Hz)
Noise
1st Cylinder Exp.
2nd Cylinder Exp.
3rd Cylinder Exp.
4th Cylinder Exp.
60
40
20
0
-20
-40
0
50
100
150
200
250
300
350
400
450
500

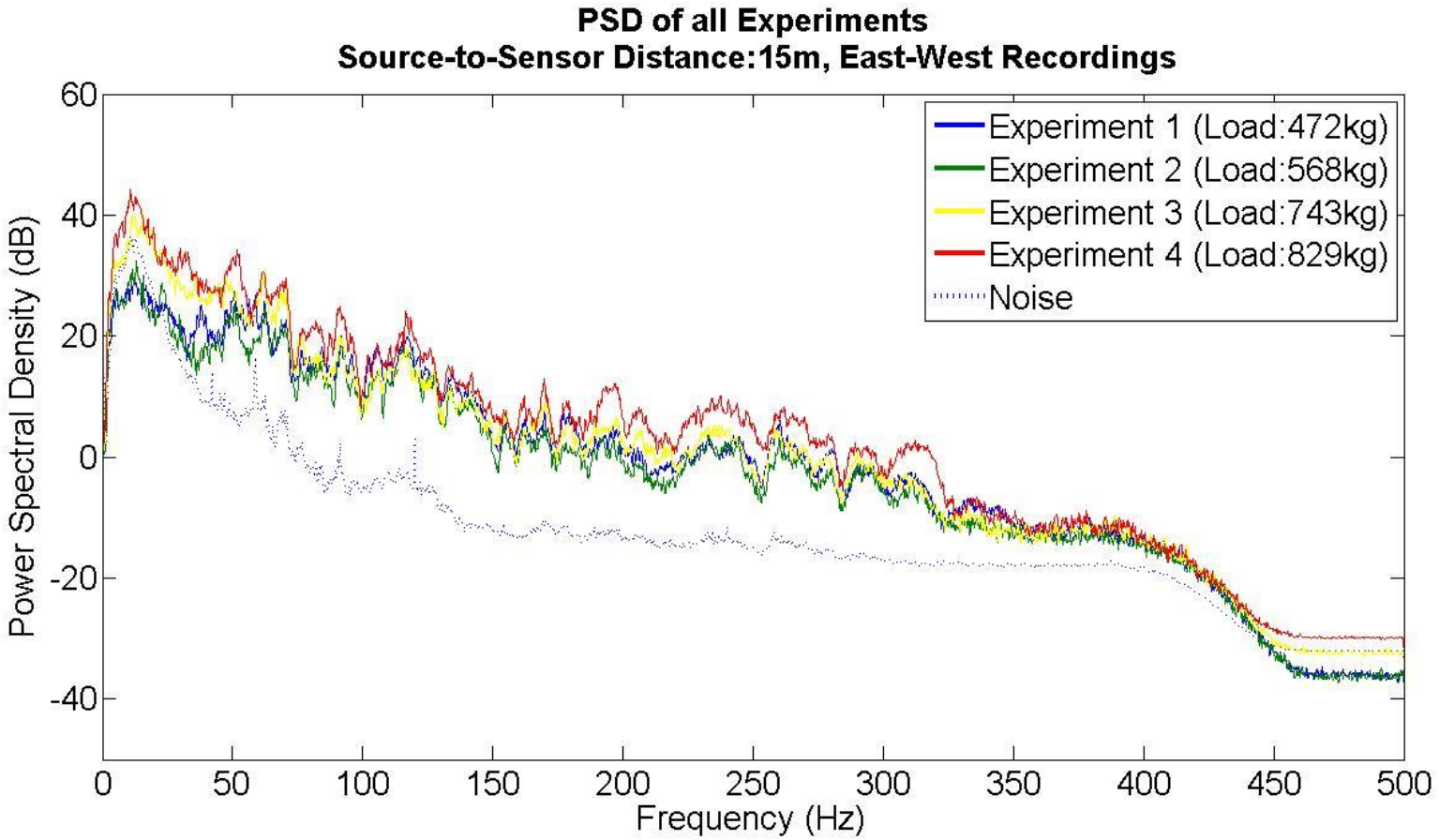
PSD of all Experiments
Source-to-Sensor Distance:15m, East-West Recordings
Power Spectral Density (dB)
Frequency (Hz)
60
40
20
0
-20
-40
0
50
100
150
200
250
300
350
400
450
500
Experiment 1 (Load:472kg)
Experiment 2 (Load:568kg)
Experiment 3 (Load:743kg)
Experiment 4 (Load:829kg)
Noise

A.2.2 PSD graphs of Section 6.5.4 "Step 4: Relationship between PSD and source-to-sensor distance"

a) Vertical Component

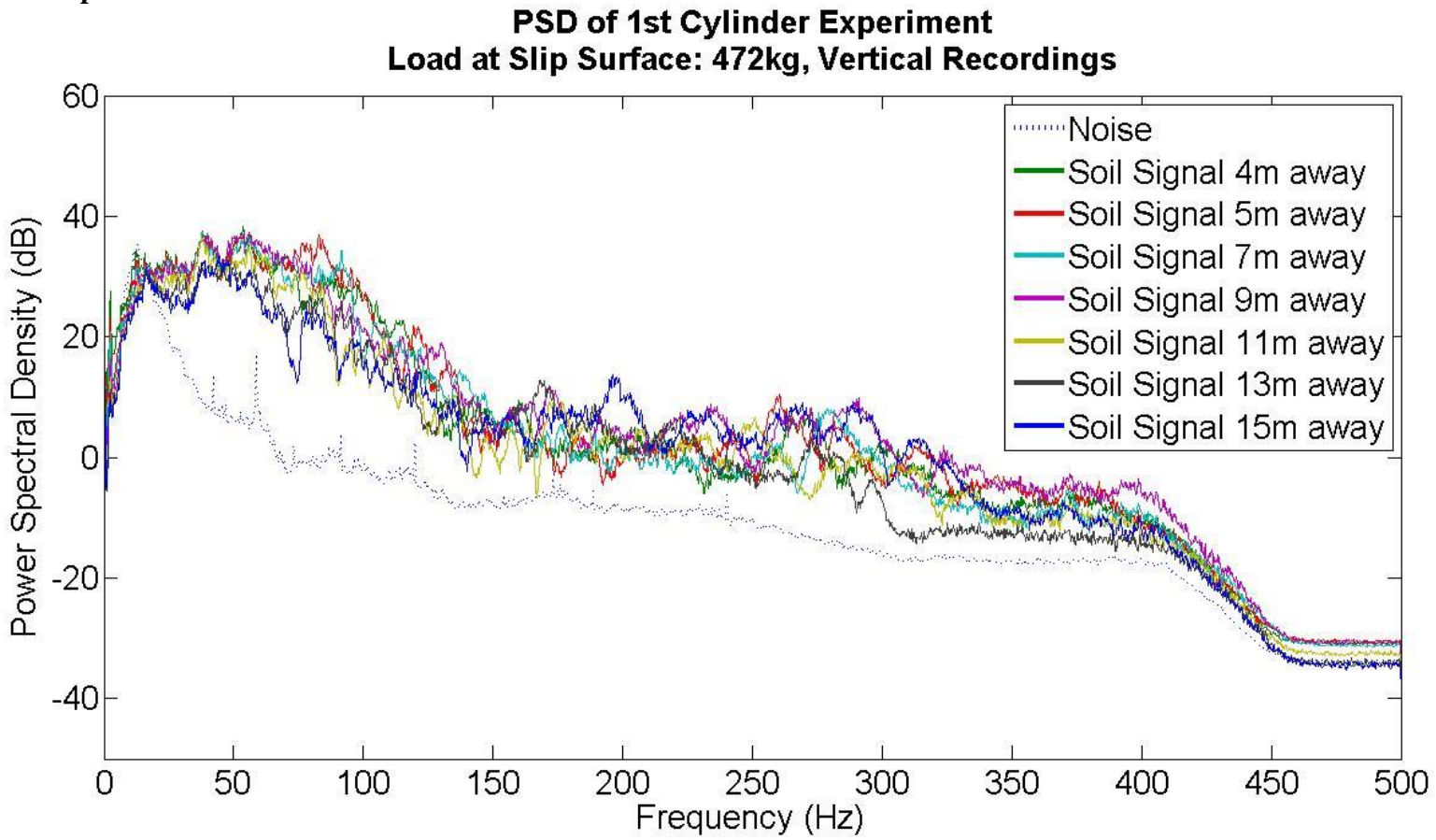

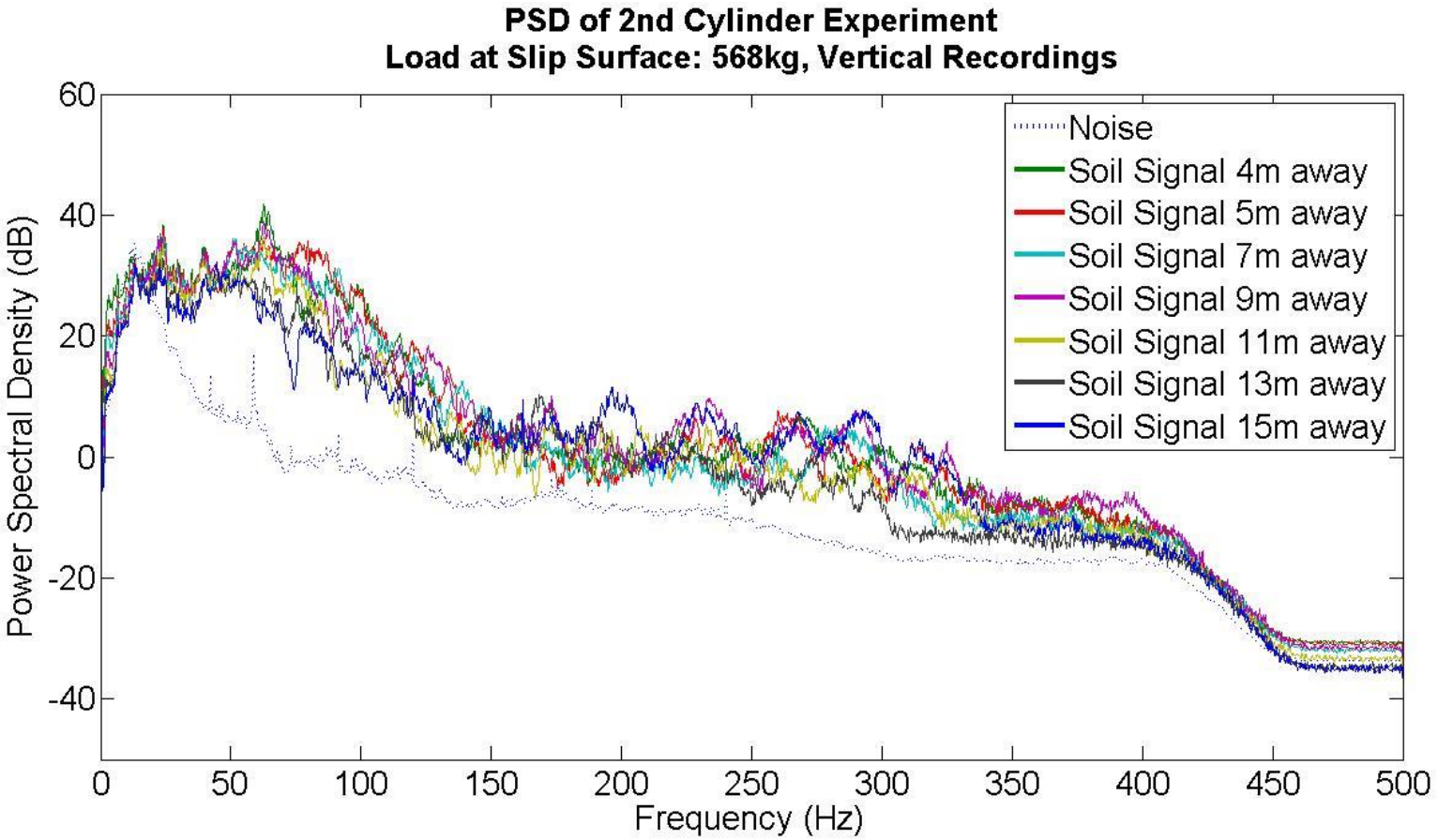
PSD of 2nd Cylinder Experiment
Load at Slip Surface: 568kg, Vertical Recordings
Power Spectral Density (dB)
Frequency (Hz)
60
40
20
0
-20
-40
0
50
100
150
200
250
300
350
400
450
500
Noise
Soil Signal 4m away
Soil Signal 5m away
Soil Signal 7m away
Soil Signal 9m away
Soil Signal 11m away
Soil Signal 13m away
Soil Signal 15m away

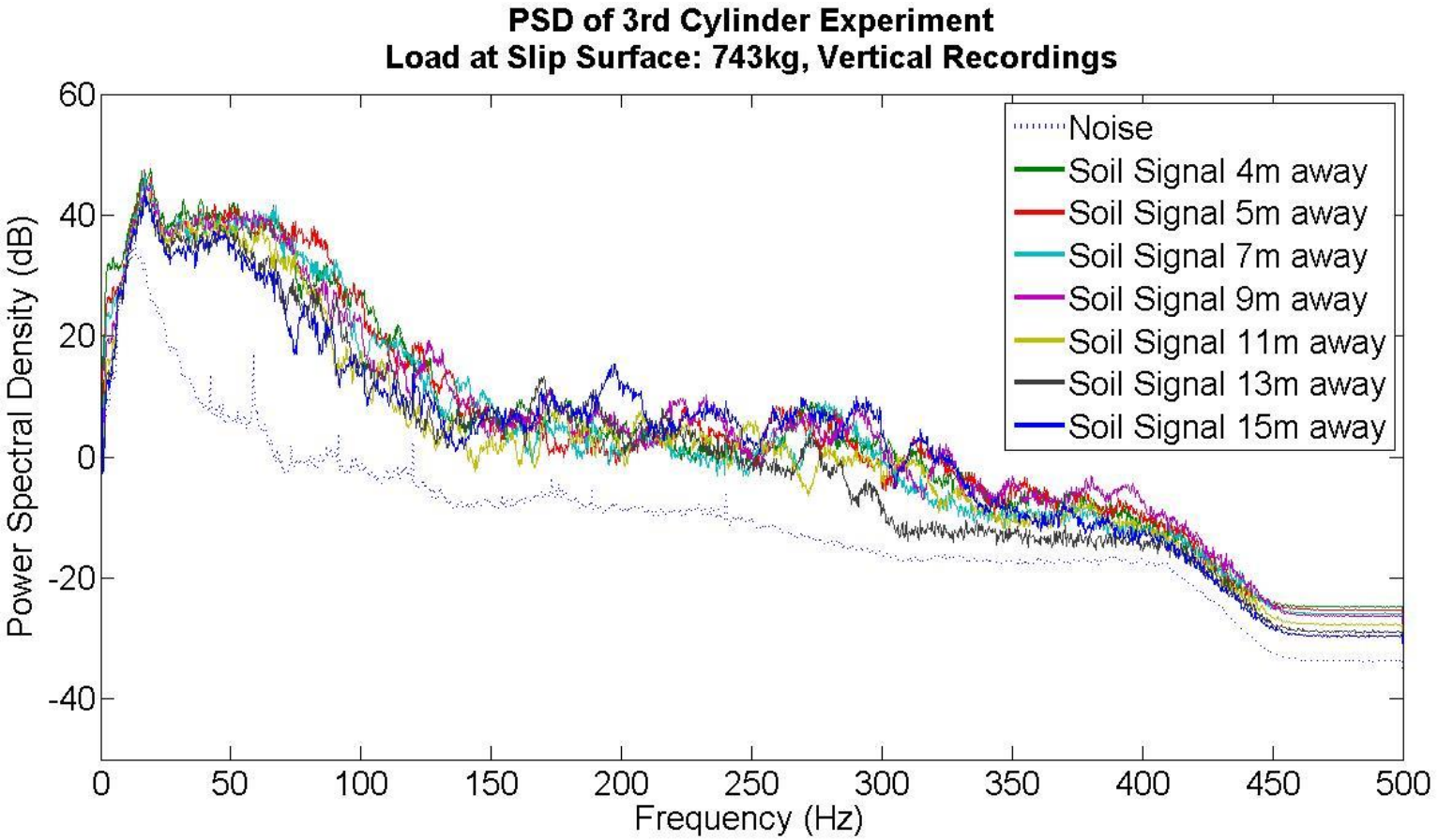
PSD of 3rd Cylinder Experiment
Load at Slip Surface: 743kg, Vertical Recordings
Power Spectral Density (dB)
Frequency (Hz)
60
40
20
0
-20
-40
0
50
100
150
200
250
300
350
400
450
500
Noise
Soil Signal 4m away
Soil Signal 5m away
Soil Signal 7m away
Soil Signal 9m away
Soil Signal 11m away
Soil Signal 13m away
Soil Signal 15m away

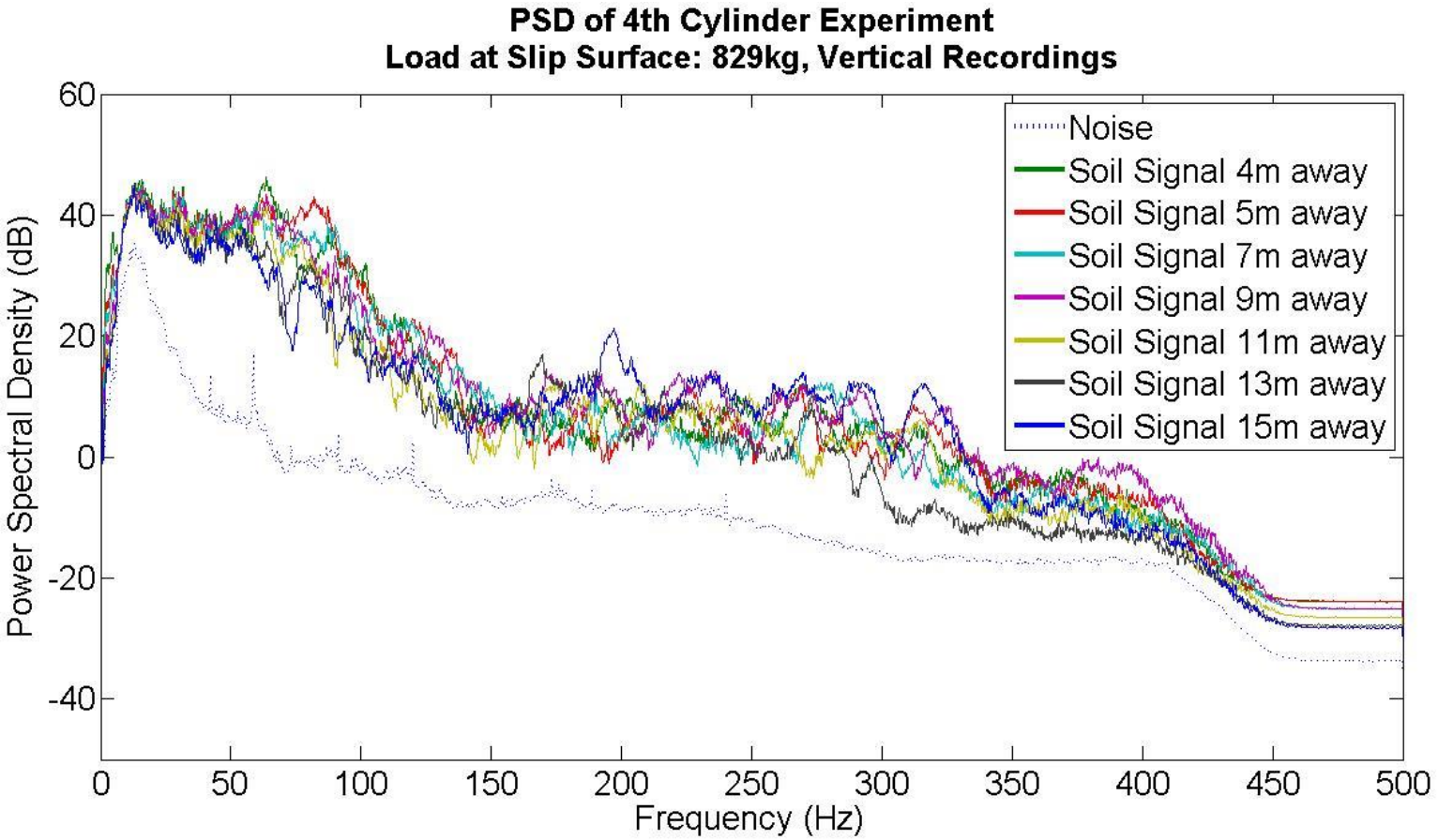
PSD of 4th Cylinder Experiment
Load at Slip Surface: 829kg, Vertical Recordings
Power Spectral Density (dB)
Frequency (Hz)
60
40
20
0
-20
-40
0
50
100
150
200
250
300
350
400
450
500
Noise
Soil Signal 4m away
Soil Signal 5m away
Soil Signal 7m away
Soil Signal 9m away
Soil Signal 11m away
Soil Signal 13m away
Soil Signal 15m away

b) North-South Component

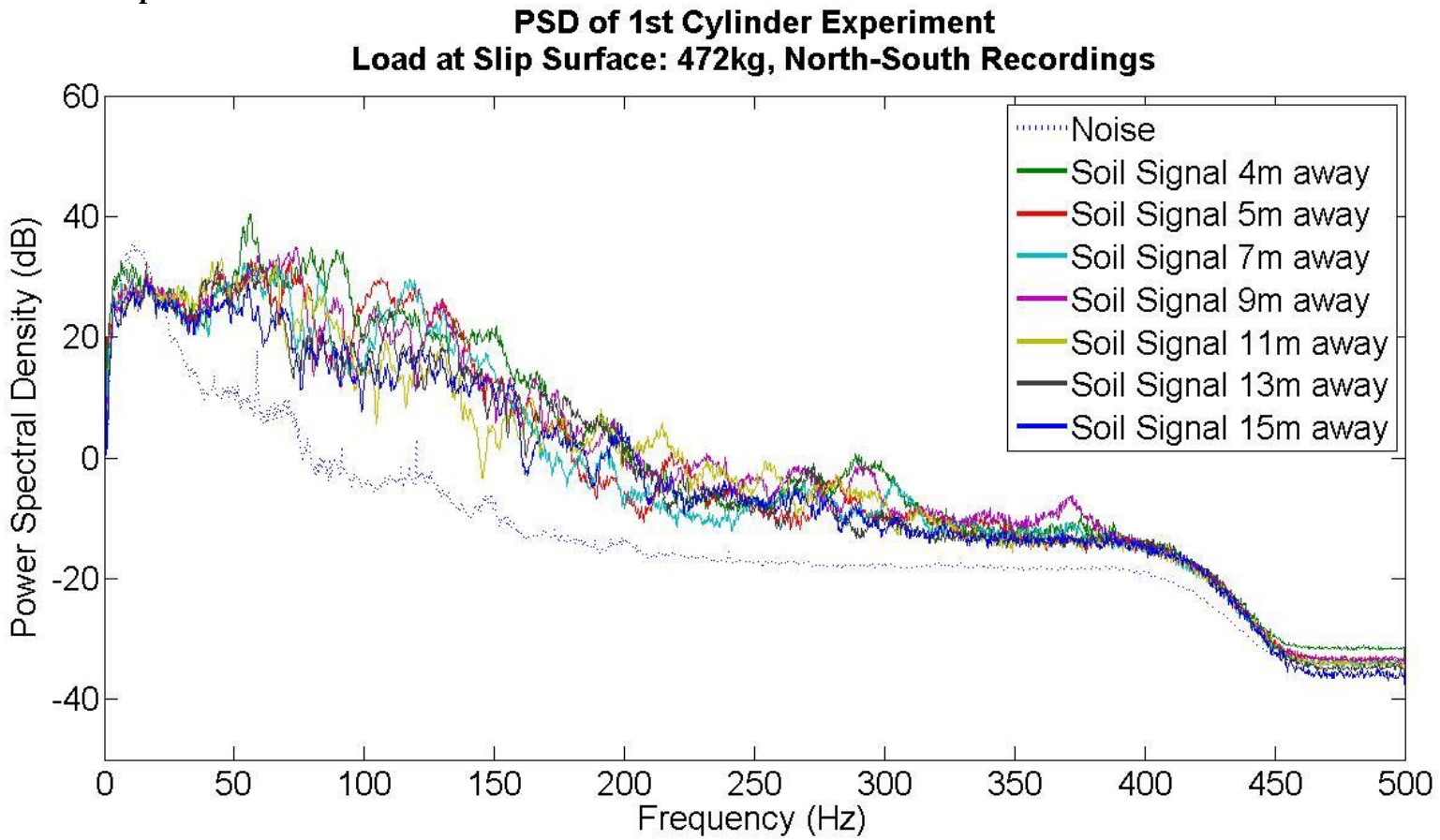

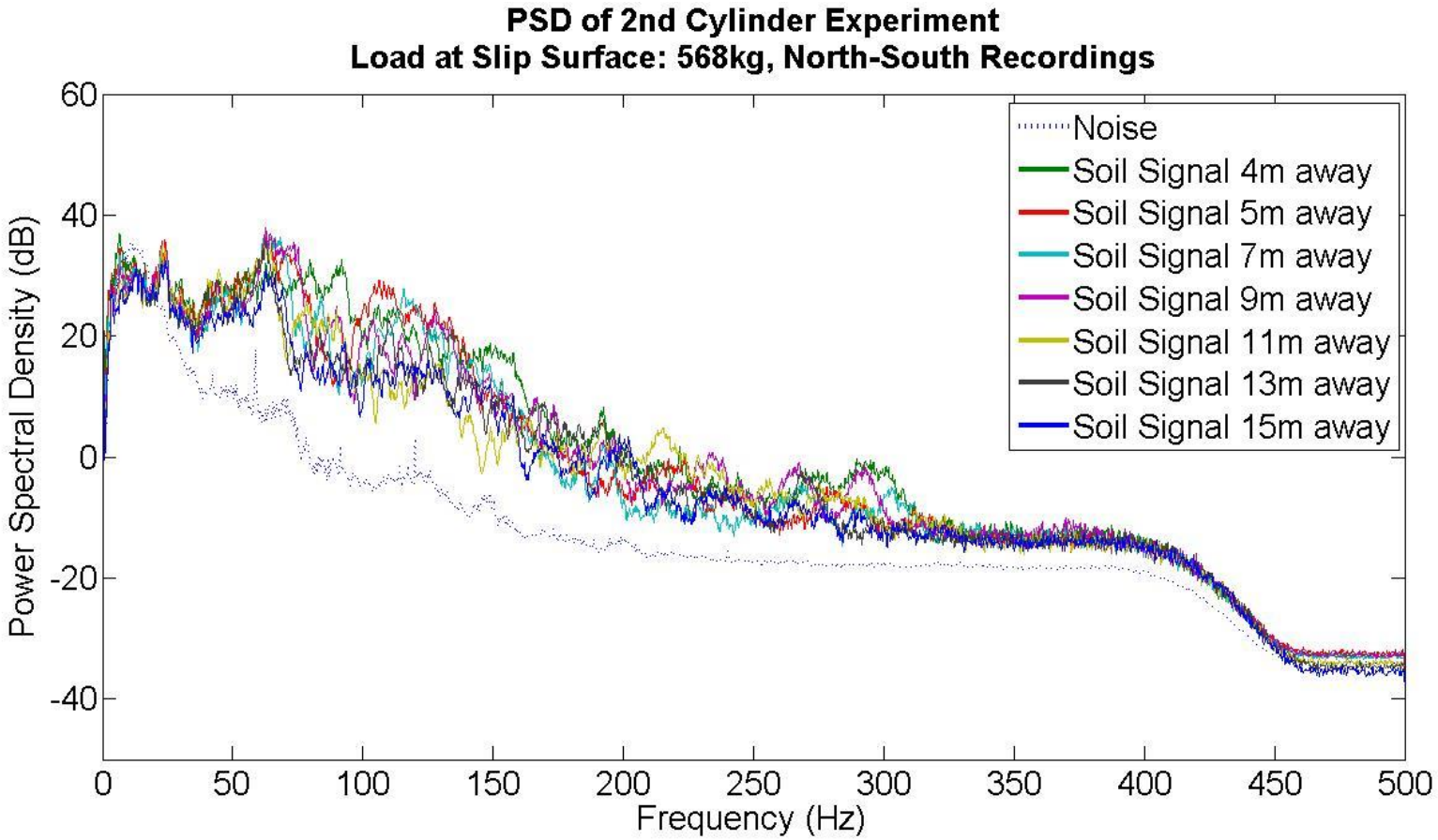
PSD of 2nd Cylinder Experiment
Load at Slip Surface: 568kg, North-South Recordings
Power Spectral Density (dB)
Frequency (Hz)
60
40
20
0
-20
-40
0
50
100
150
200
250
300
350
400
450
500
Noise
Soil Signal 4m away
Soil Signal 5m away
Soil Signal 7m away
Soil Signal 9m away
Soil Signal 11m away
Soil Signal 13m away
Soil Signal 15m away

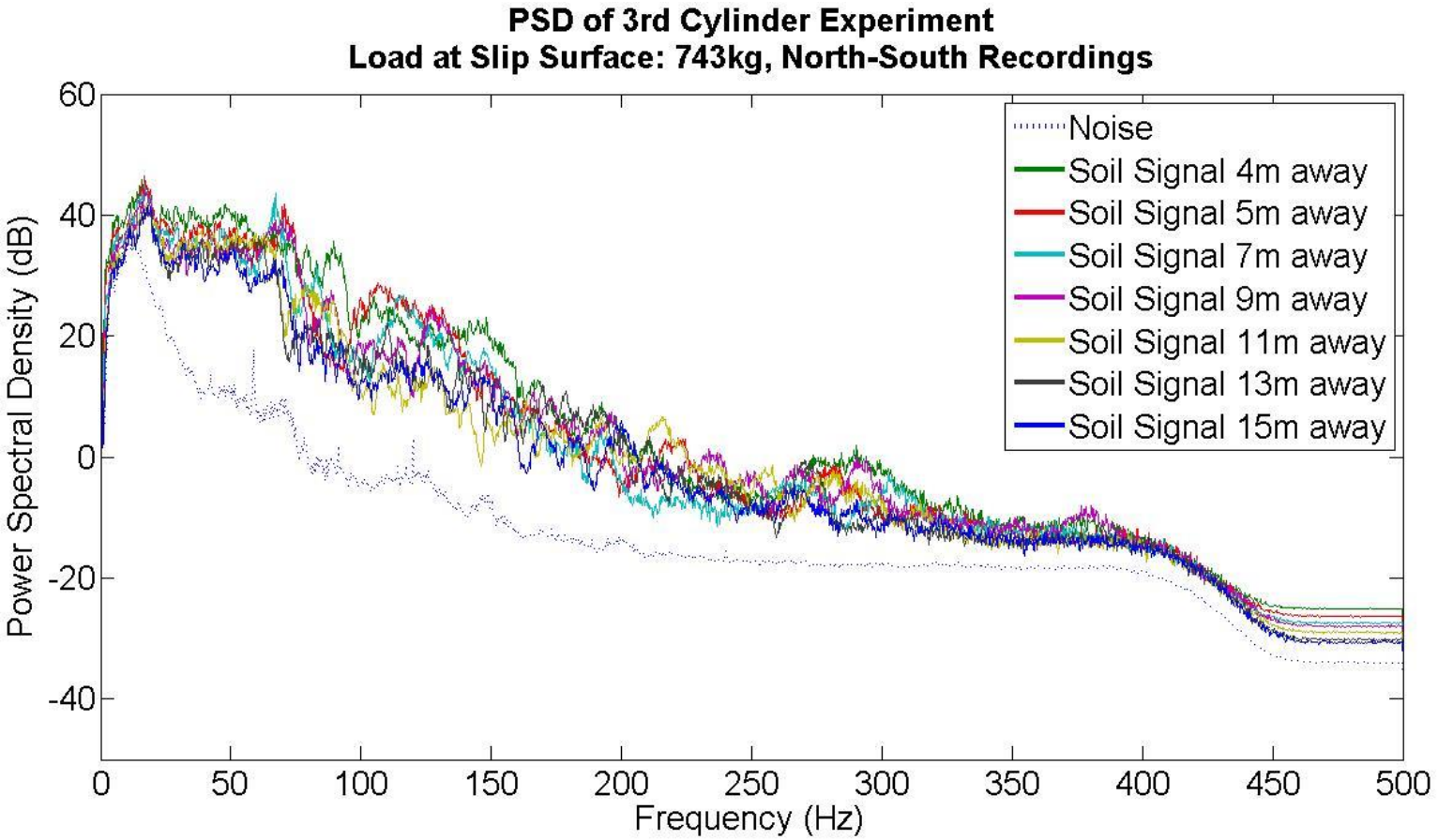
PSD of 3rd Cylinder Experiment
Load at Slip Surface: 743kg, North-South Recordings
Power Spectral Density (dB)
Frequency (Hz)
60
40
20
0
-20
-40
0
50
100
150
200
250
300
350
400
450
500
Noise
Soil Signal 4m away
Soil Signal 5m away
Soil Signal 7m away
Soil Signal 9m away
Soil Signal 11m away
Soil Signal 13m away
Soil Signal 15m away

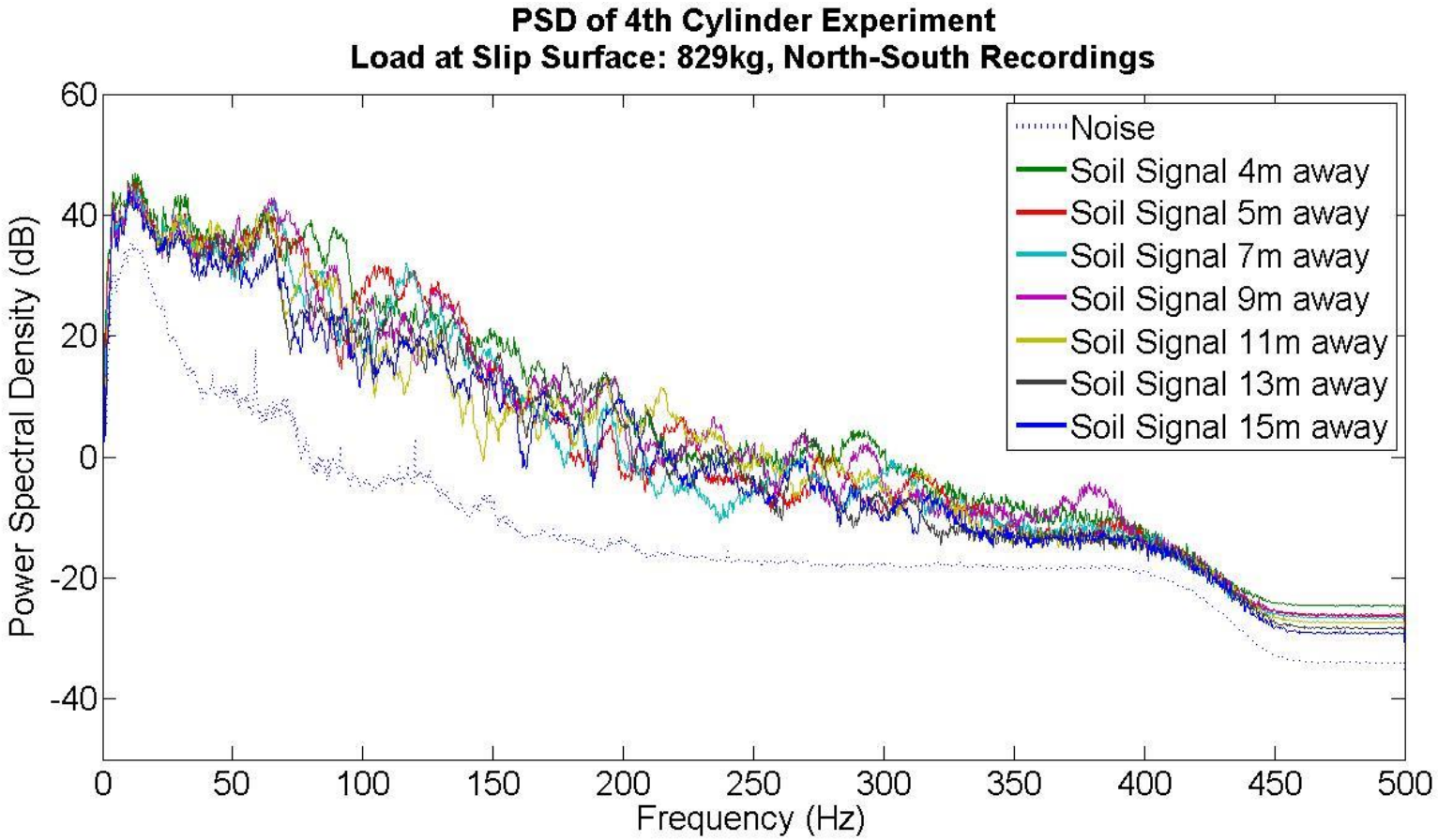
PSD of 4th Cylinder Experiment
Load at Slip Surface: 829kg, North-South Recordings
Power Spectral Density (dB)
Frequency (Hz)
60
40
20
0
-20
-40
0
50
100
150
200
250
300
350
400
450
500
Noise
Soil Signal 4m away
Soil Signal 5m away
Soil Signal 7m away
Soil Signal 9m away
Soil Signal 11m away
Soil Signal 13m away
Soil Signal 15m away

c) East-West Component

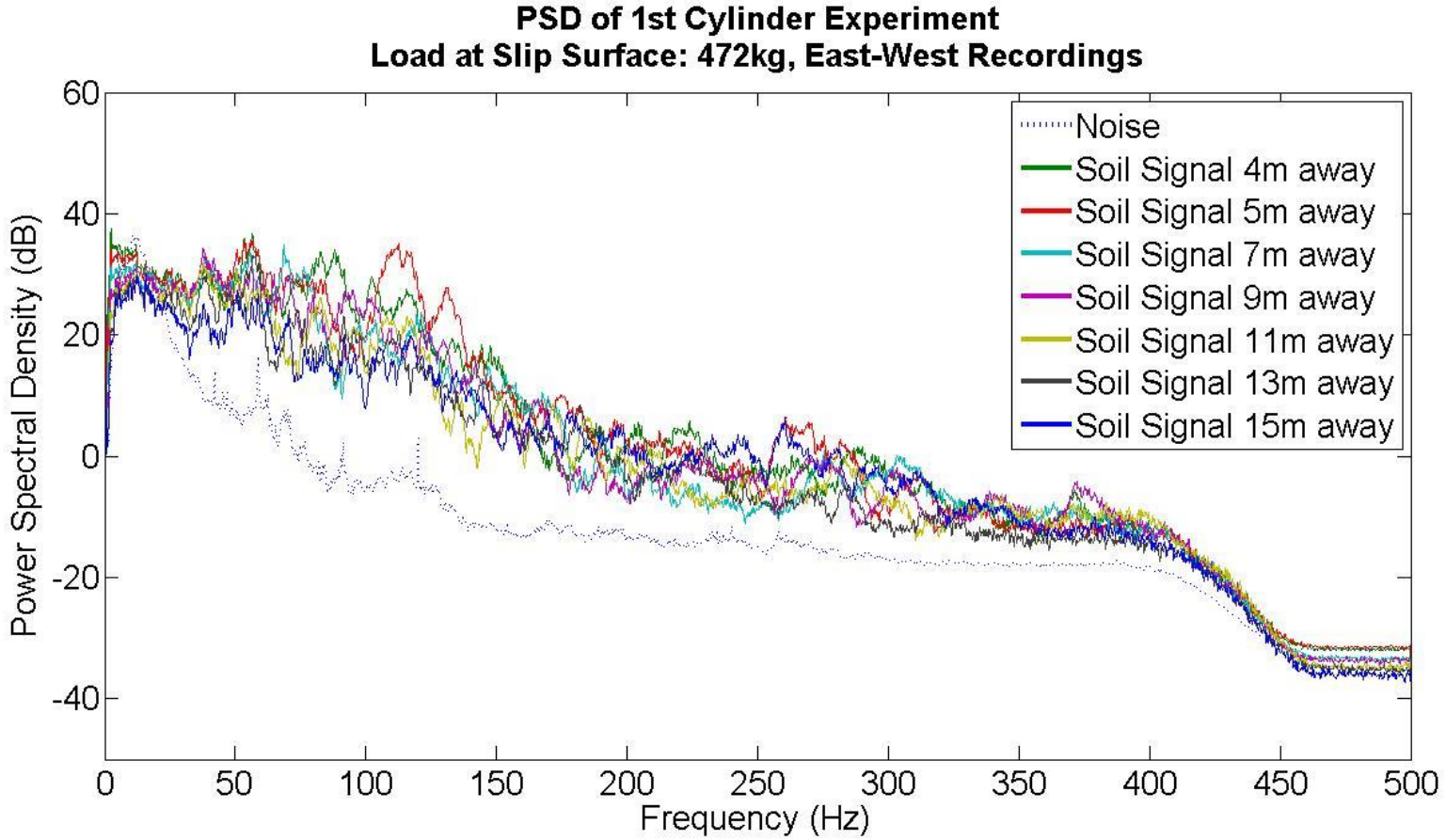

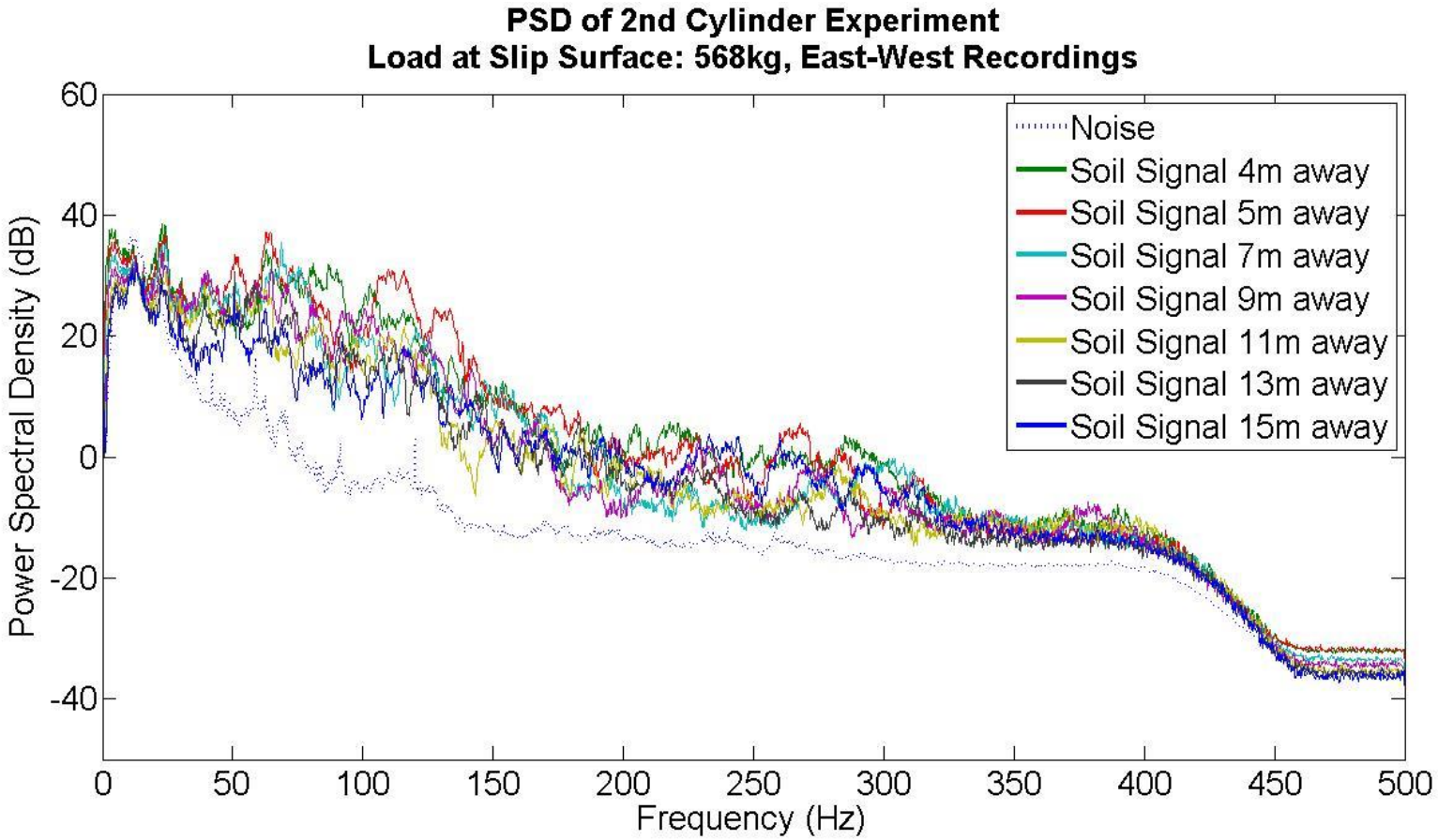
PSD of 2nd Cylinder Experiment
Load at Slip Surface: 568kg, East-West Recordings
Power Spectral Density (dB)
Frequency (Hz)
60
40
20
0
-20
-40
0
50
100
150
200
250
300
350
400
450
500
Noise
Soil Signal 4m away
Soil Signal 5m away
Soil Signal 7m away
Soil Signal 9m away
Soil Signal 11m away
Soil Signal 13m away
Soil Signal 15m away

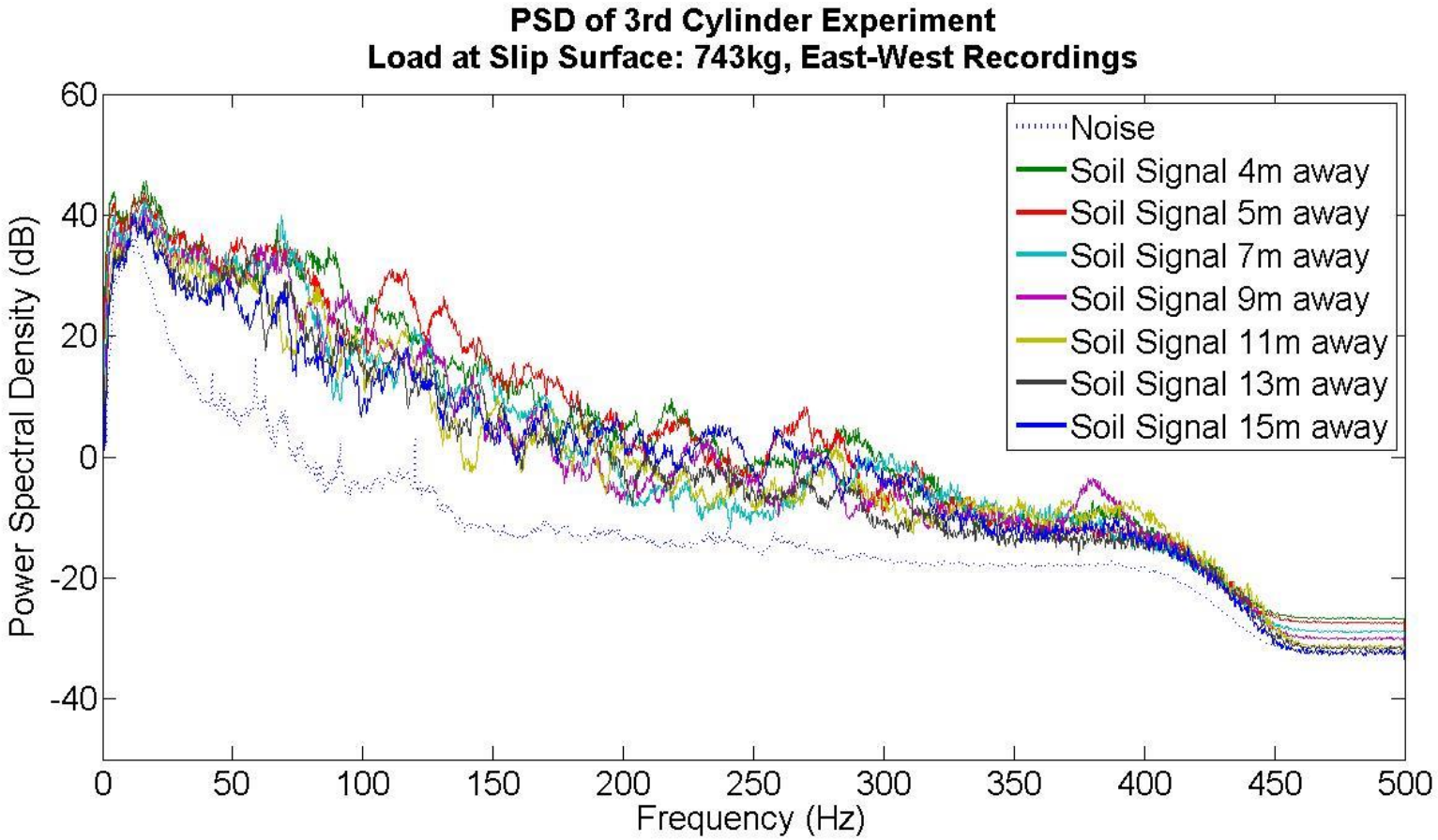
PSD of 3rd Cylinder Experiment
Load at Slip Surface: 743kg, East-West Recordings
Power Spectral Density (dB)
Frequency (Hz)
60
40
20
0
-20
-40
0
50
100
150
200
250
300
350
400
450
500
Noise
Soil Signal 4m away
Soil Signal 5m away
Soil Signal 7m away
Soil Signal 9m away
Soil Signal 11m away
Soil Signal 13m away
Soil Signal 15m away

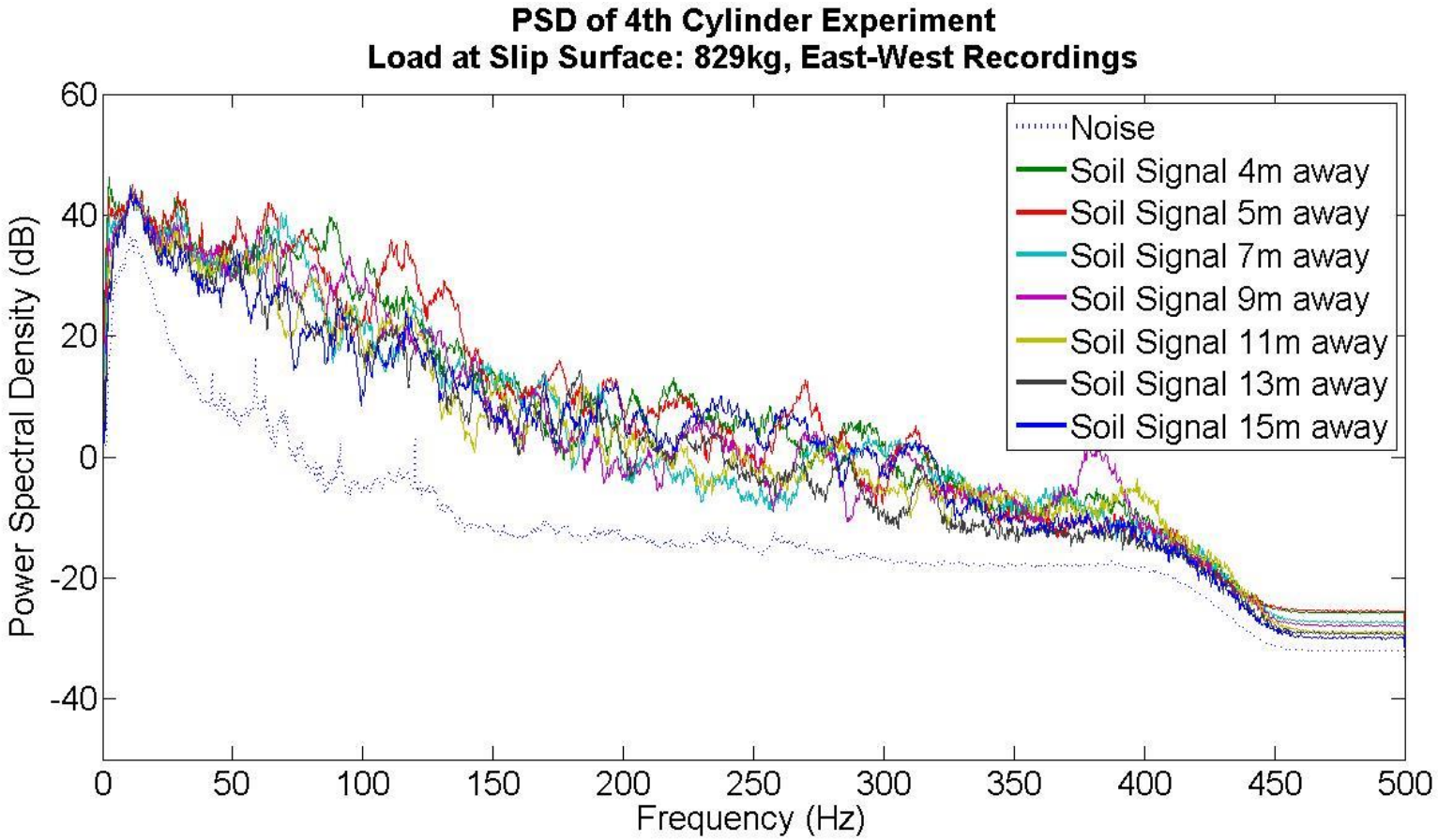
PSD of 4th Cylinder Experiment
Load at Slip Surface: 829kg, East-West Recordings
Power Spectral Density (dB)
Frequency (Hz)
60
40
20
0
-20
-40
0
50
100
150
200
250
300
350
400
450
500
Noise
Soil Signal 4m away
Soil Signal 5m away
Soil Signal 7m away
Soil Signal 9m away
Soil Signal 11m away
Soil Signal 13m away
Soil Signal 15m away

Appendix B

Evidence for an improved seismic monitoring system for landslides based on the use of glass shards

In this appendix all additional graphs of Chapter 7 will be presented. The deployment geometry of the seismometers is presented first, as well as a table summarizing the parameters of the experiment conducted as a reminder to the reader so he or she doesn't have to search for this information back to the original chapter.

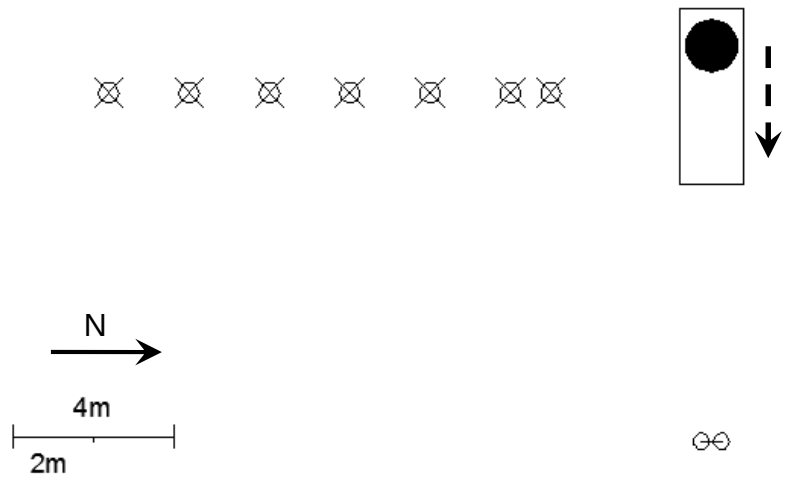

Plan view of experimental set up. Solid Black Circle: cylinder with confined soil block, Rectangle surrounding the cylinder: Surficial corridor free from vegetation, Circles marked with X: Location of seismometers, Two circles connected with a line: Position of reel. The dashed arrow shows the direction of the movement of the cylinder.

Experiment	Load (kg) on the slip surface ($0.33m^2$)	Force (kN)	Stress (kPa)	Simulated Depth (m) ($\gamma_{soil}=18kN/m^3$)
Glass Shard and Soil Cylinder Experiment	878	8.61	26.10	1.45

Load, force, stress levels and simulated depth during the cylinder experiment with the glass shards – soil interface.

B1 Spectrograms from Section 7.3.1 "Step 1: Time – frequency analysis"

Section 7.3.1 presented the use of spectrograms for detecting and visualising the glass shard slip events above noise levels. Here all spectrograms of all three components of the seismometers are presented for each experiment separately.

a)Vertical Component

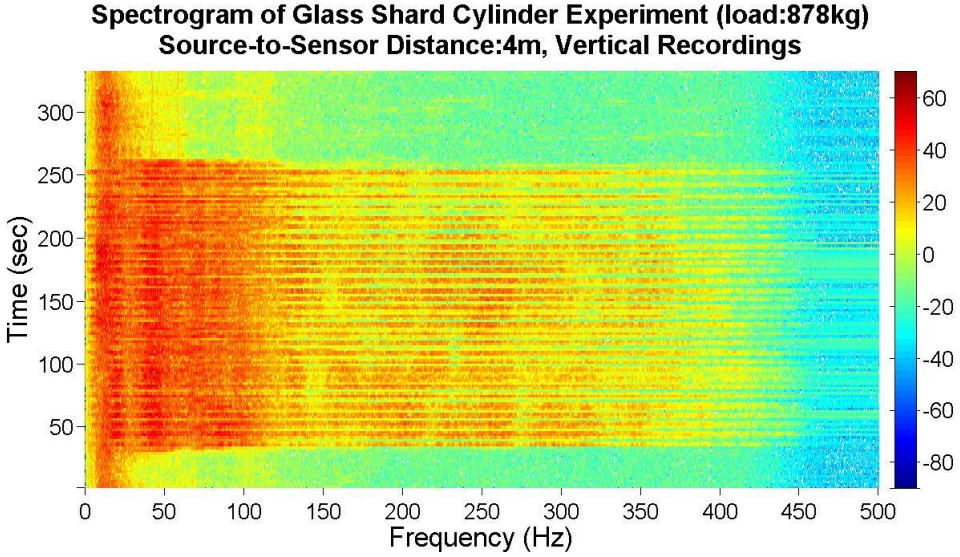

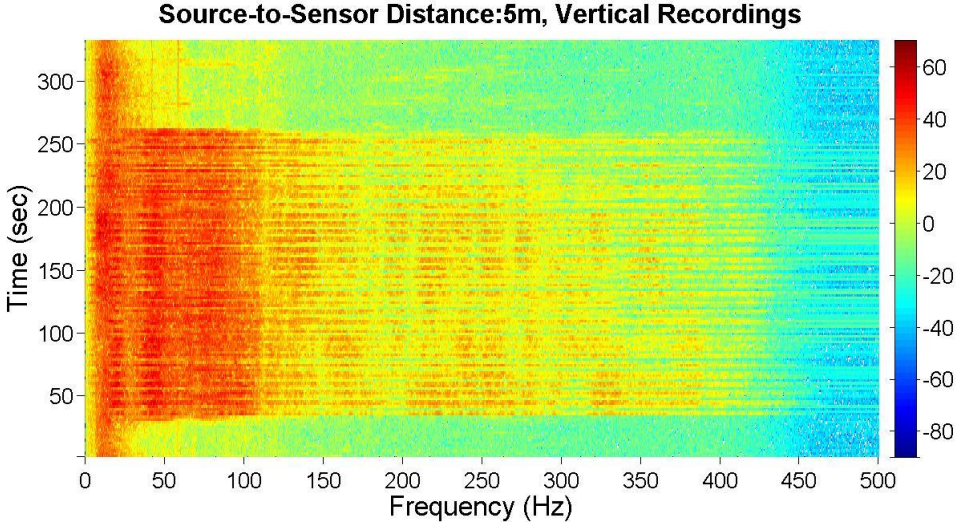

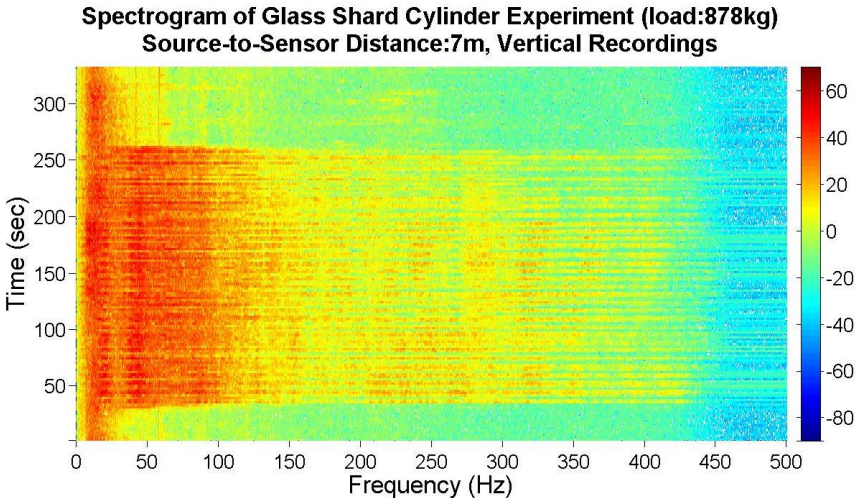
Spectrogram of Glass Shard Cylinder Experiment (load:878kg)
Source-to-Sensor Distance:7m, Vertical Recordings
Time (sec)
Frequency (Hz)

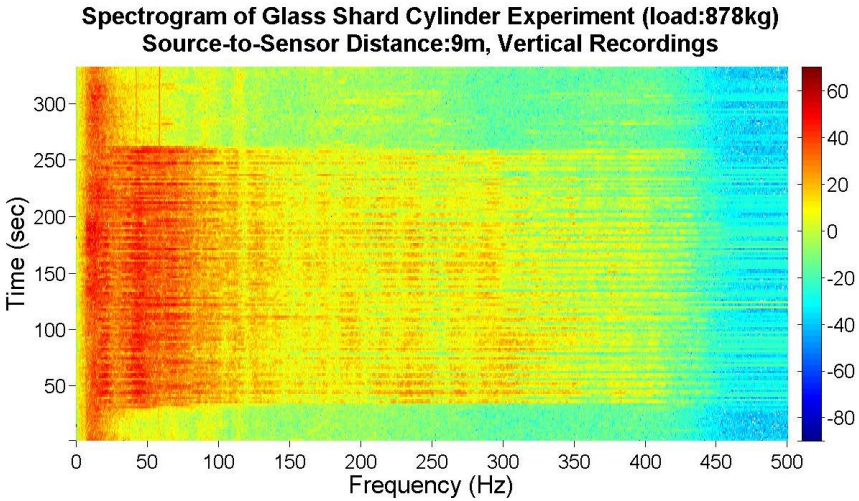
Spectrogram of Glass Shard Cylinder Experiment (load:878kg)
Source-to-Sensor Distance:9m, Vertical Recordings
Time (sec)
Frequency (Hz)

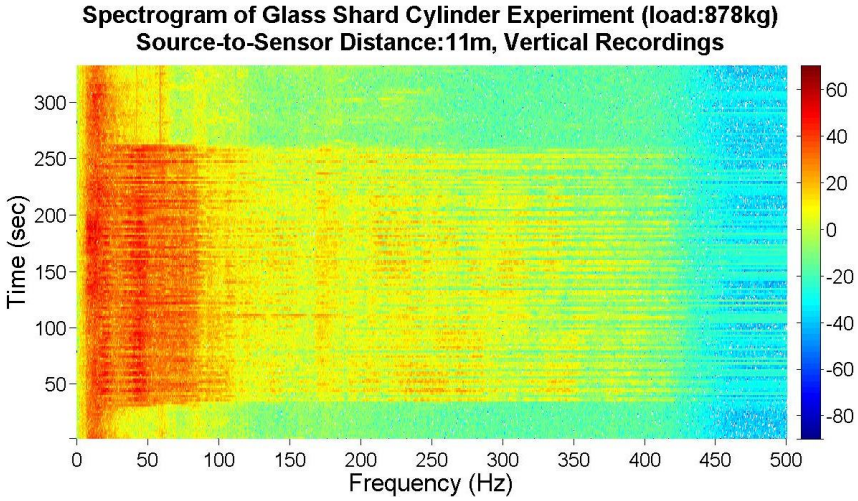
Spectrogram of Glass Shard Cylinder Experiment (load:878kg)
Source-to-Sensor Distance:11m, Vertical Recordings
Time (sec)
Frequency (Hz)

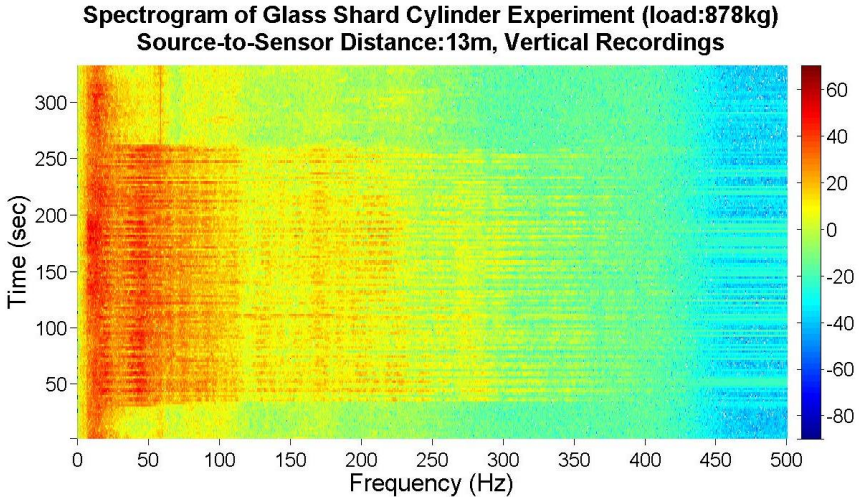
Spectrogram of Glass Shard Cylinder Experiment (load:878kg)
Source-to-Sensor Distance:13m, Vertical Recordings
Time (sec)
Frequency (Hz)

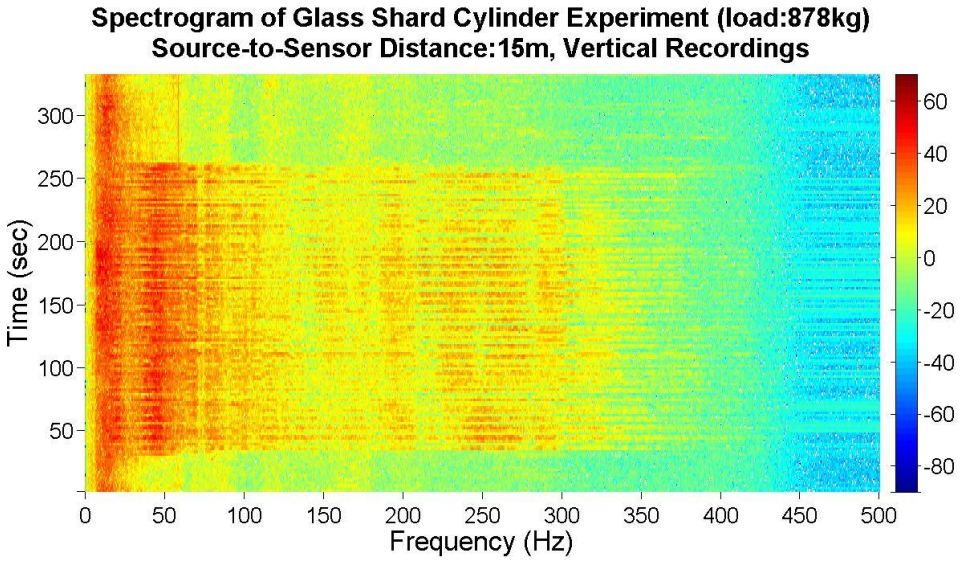

b) North South Component

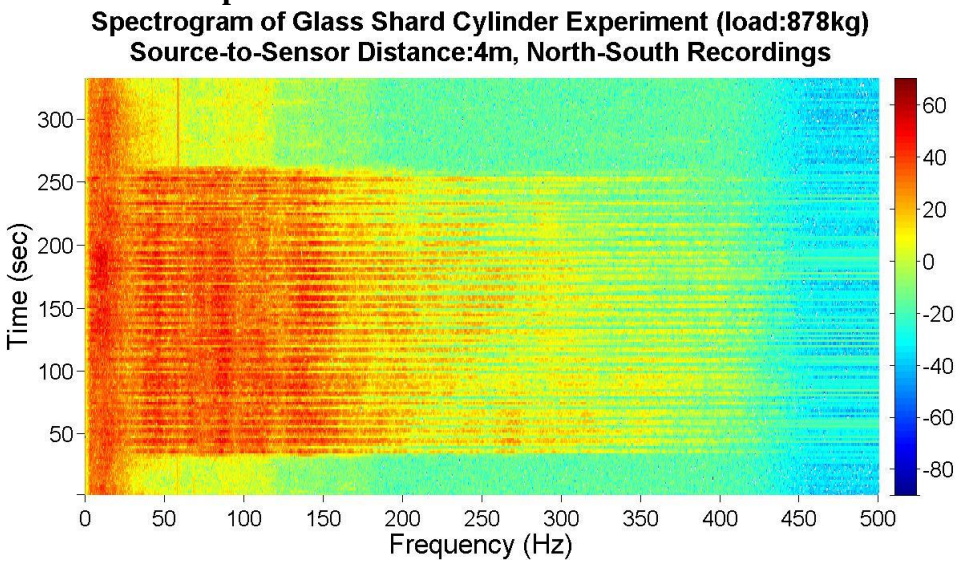

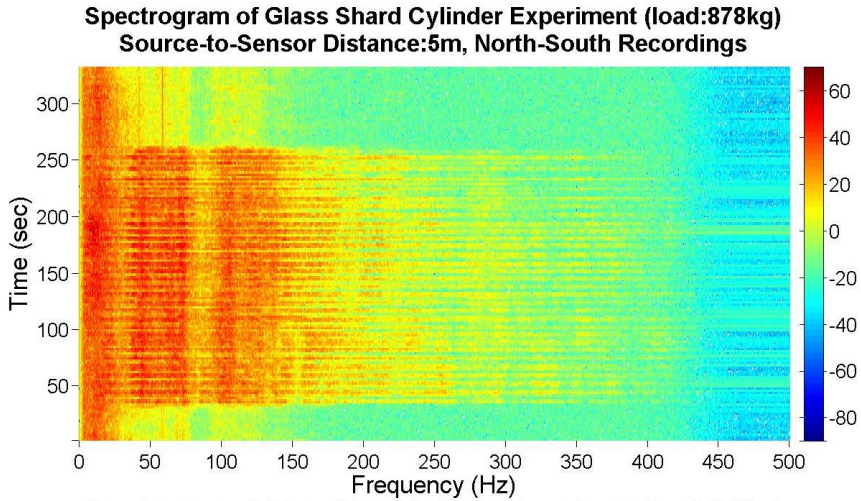
Spectrogram of Glass Shard Cylinder Experiment (load:878kg)
Source-to-Sensor Distance:5m, North-South Recordings
Time (sec)
Frequency (Hz)

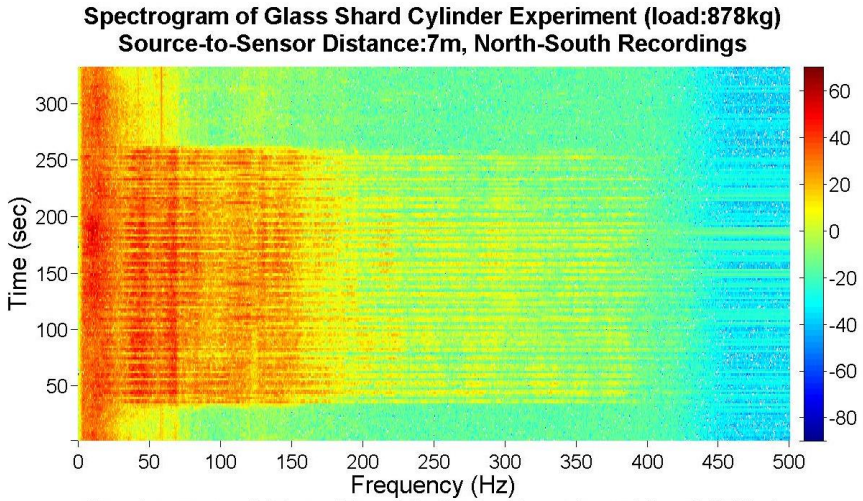
Spectrogram of Glass Shard Cylinder Experiment (load:878kg)
Source-to-Sensor Distance:7m, North-South Recordings
Time (sec)
Frequency (Hz)

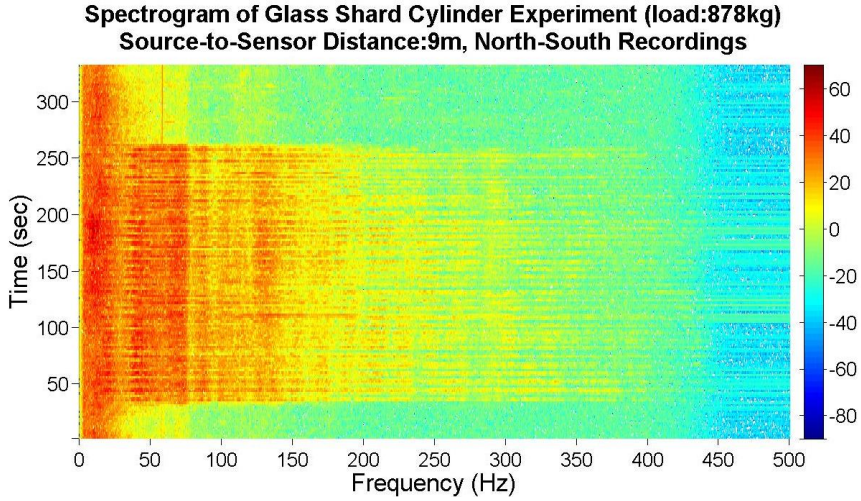
Spectrogram of Glass Shard Cylinder Experiment (load:878kg)
Source-to-Sensor Distance:9m, North-South Recordings
Time (sec)
Frequency (Hz)

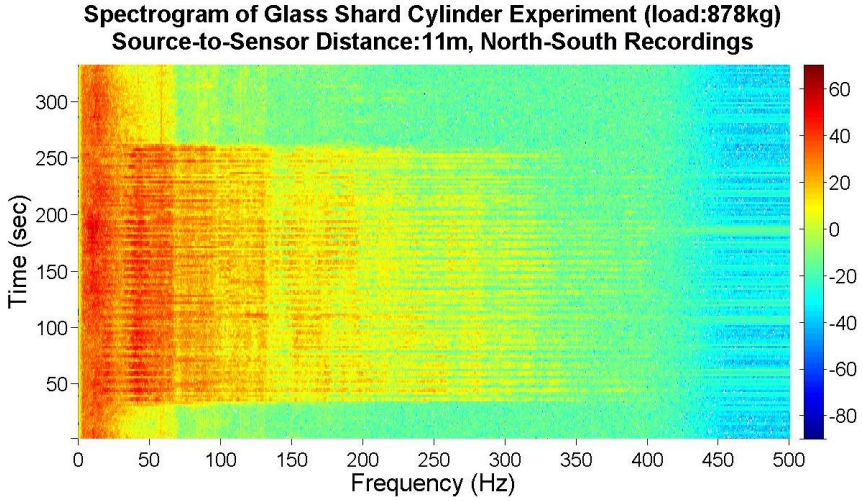
Spectrogram of Glass Shard Cylinder Experiment (load:878kg)
Source-to-Sensor Distance:11m, North-South Recordings
Time (sec)
Frequency (Hz)

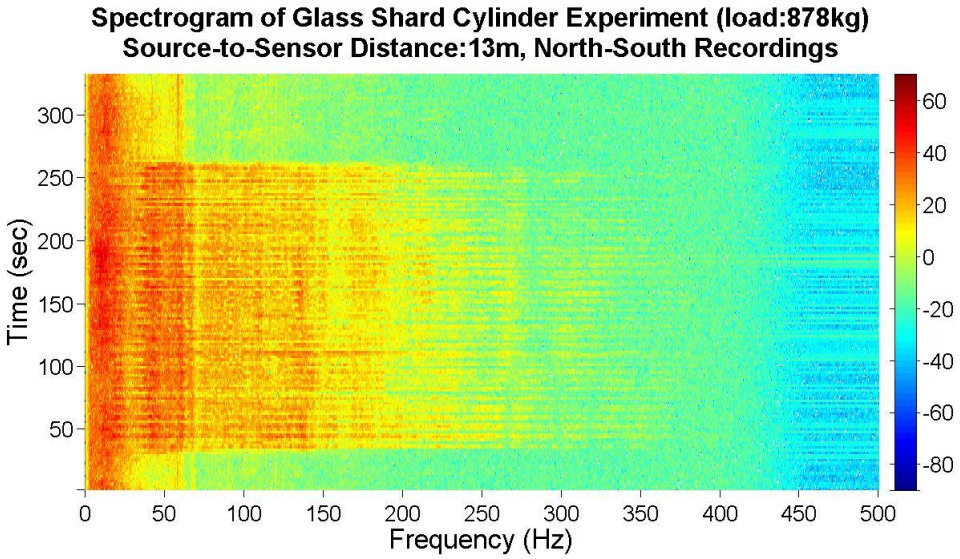
Spectrogram of Glass Shard Cylinder Experiment (load:878kg)
Source-to-Sensor Distance:13m, North-South Recordings
Time (sec)
300
250
200
150
100
50
0
50
100
150
200
250
300
350
400
450
500
Frequency (Hz)
60
40
20
0
-20
-40
-60
-80

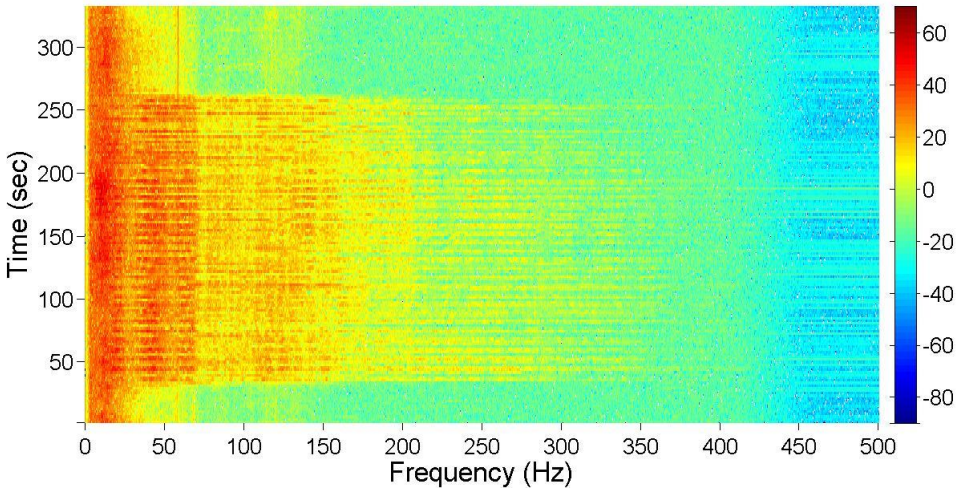
Spectrogram of Glass Shard Cylinder Experiment (load:878kg)
Source-to-Sensor Distance:15m, North-South Recordings
Time (sec)
300
250
200
150
100
50
0
50
100
150
200
250
300
350
400
450
500
Frequency (Hz)
60
40
20
0
-20
-40
-60
-80

c) East-West Component

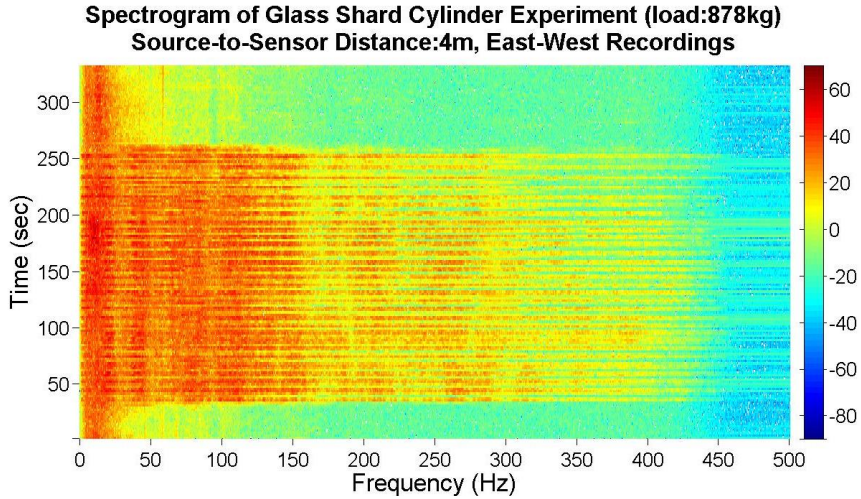

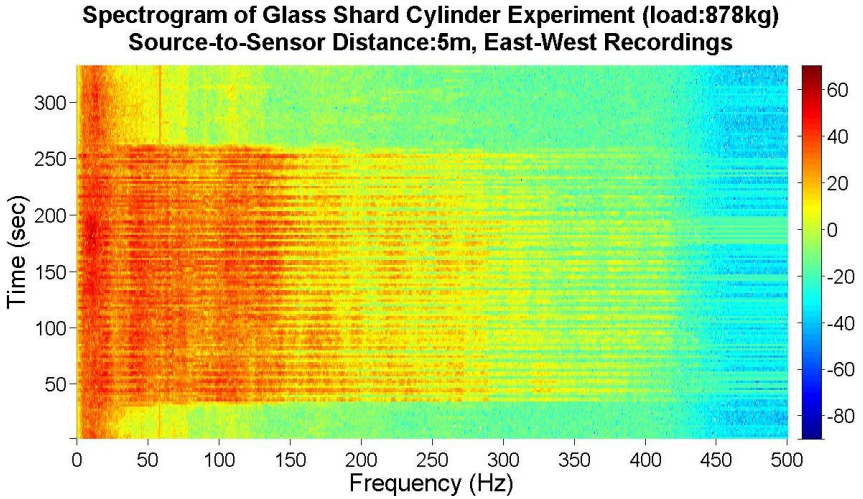

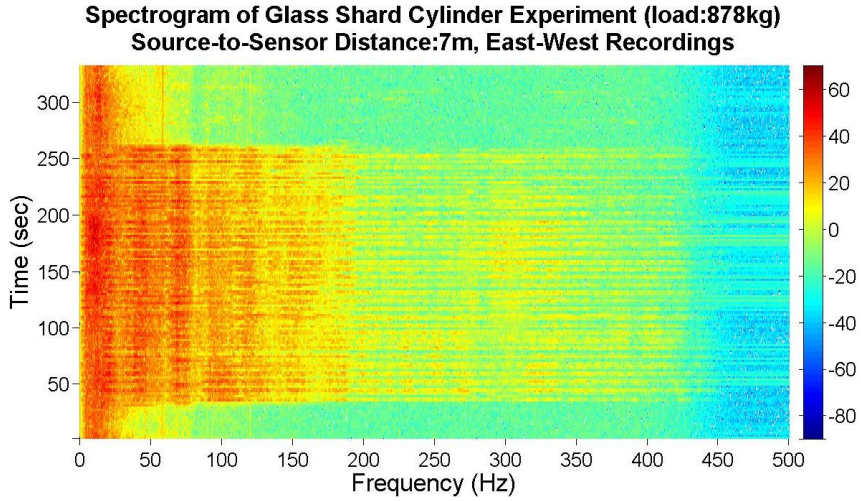

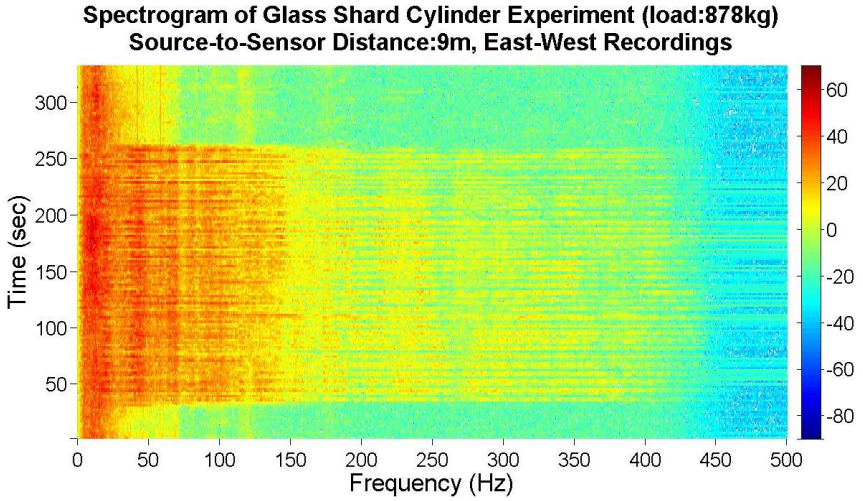

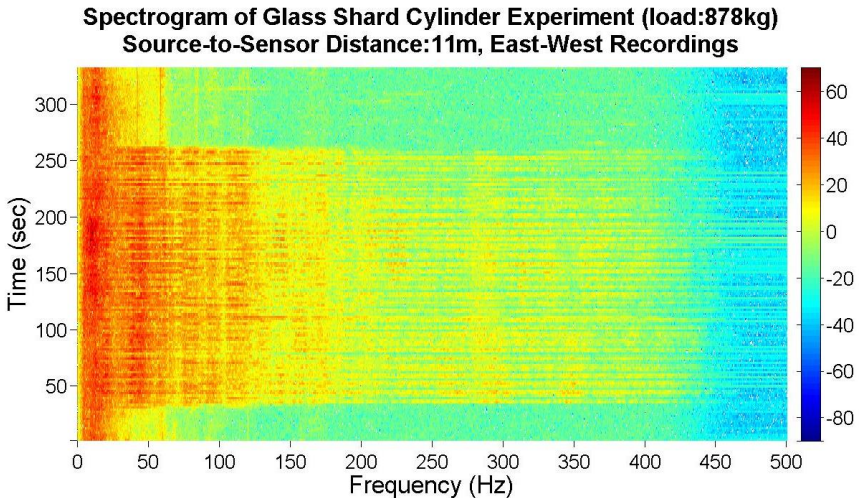
Spectrogram of Glass Shard Cylinder Experiment (load:878kg)
Source-to-Sensor Distance:11m, East-West Recordings
Time (sec)
Frequency (Hz)
300
250
200
150
100
50
0
50
100
150
200
250
300
350
400
450
500
60
40
20
0
-20
-40
-60
-80

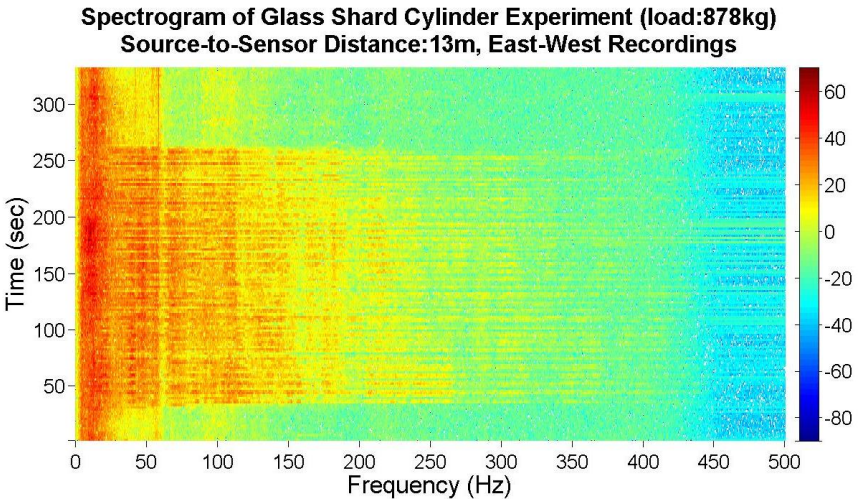
Spectrogram of Glass Shard Cylinder Experiment (load:878kg)
Source-to-Sensor Distance:13m, East-West Recordings
Time (sec)
Frequency (Hz)
300
250
200
150
100
50
0
50
100
150
200
250
300
350
400
450
500
60
40
20
0
-20
-40
-60
-80

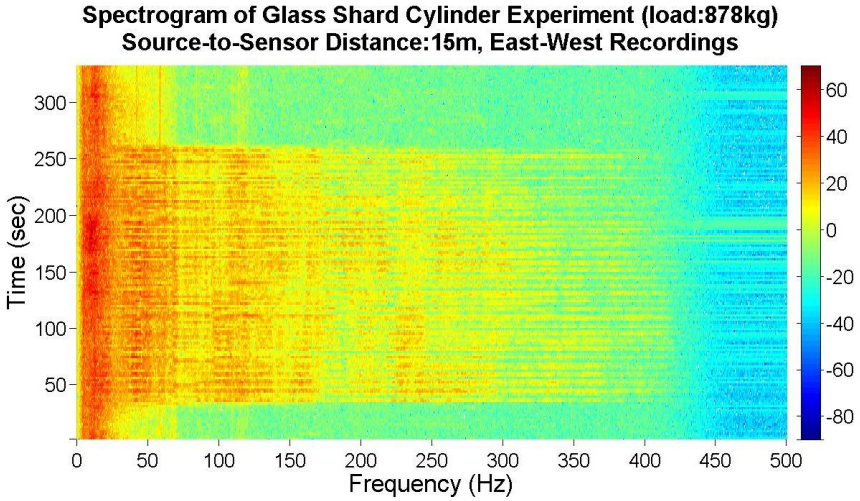
Spectrogram of Glass Shard Cylinder Experiment (load:878kg)
Source-to-Sensor Distance:15m, East-West Recordings
Time (sec)
Frequency (Hz)
300
250
200
150
100
50
0
50
100
150
200
250
300
350
400
450
500
60
40
20
0
-20
-40
-60
-80

B2 Power Spectral Density graphs (PSD)

Section 7.3.2 to 7.3.4 presented the use of power spectral density graphs (PSD) to deeply understand frequency content of the recorded signals. The same PSD spectra were used to understand the frequency characteristics of the recorded signals emitted during glass shard slip events (B2.1), to understand the changes in the frequency characteristics as the source-to-sensor distance increases (B2.1) and finally to compare the frequency characteristics of the glass shard slip events with the soil only slip events (B2.2).

B2.1 All PSD spectra of Section 7.3.2 "Step 2: Frequency analysis" and Section 7.3.3 "Step 3: Relationship between PSD and source-to-sensor distance"

a) Vertical Component

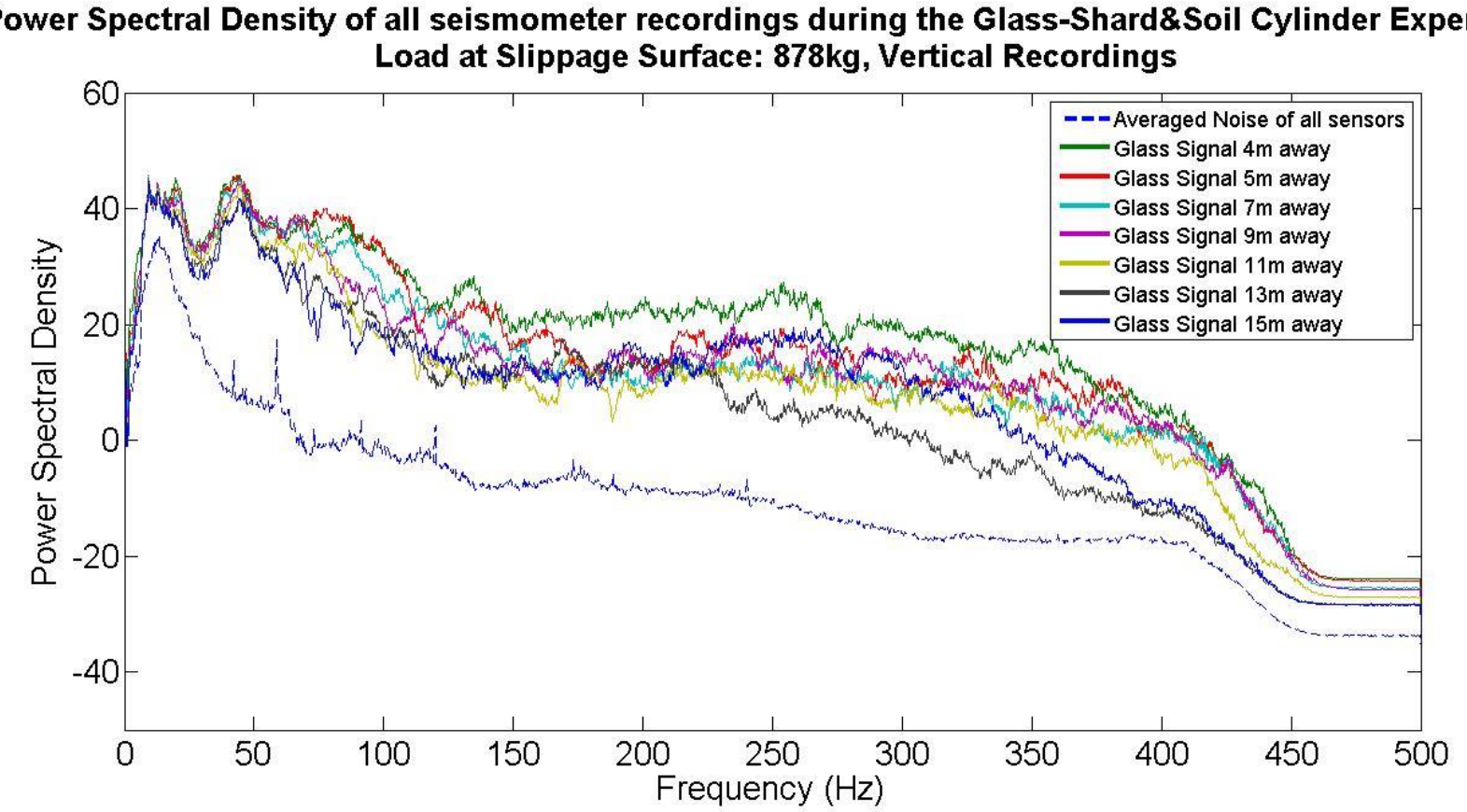

b) North-South Component

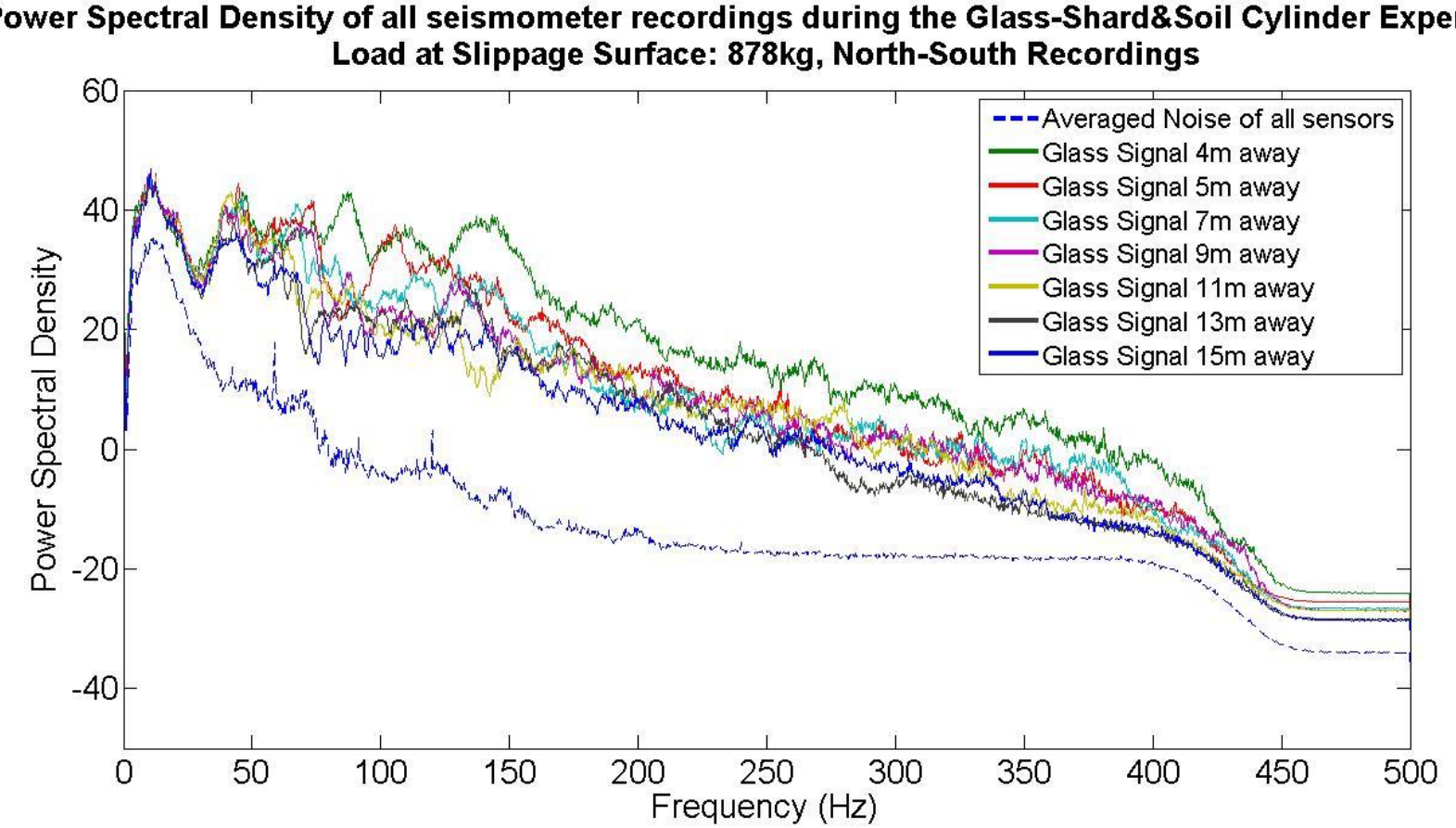

c) East-West Component

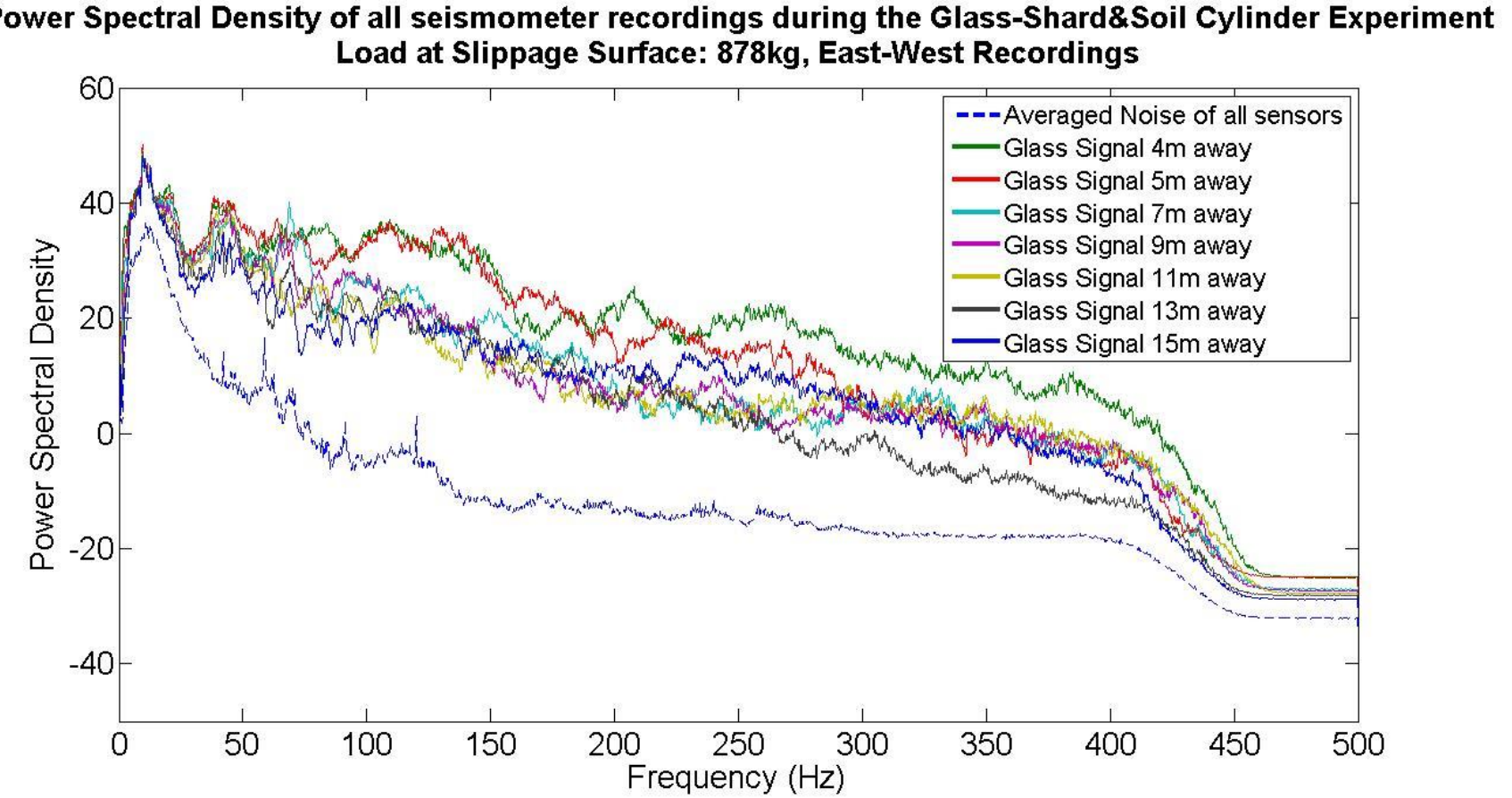

B2.2 All PSD spectra of Section 7.3.4 "Glass Shard Cylinder Exp. –VS- Soil only Cylinder Exp."

a) Vertical Component

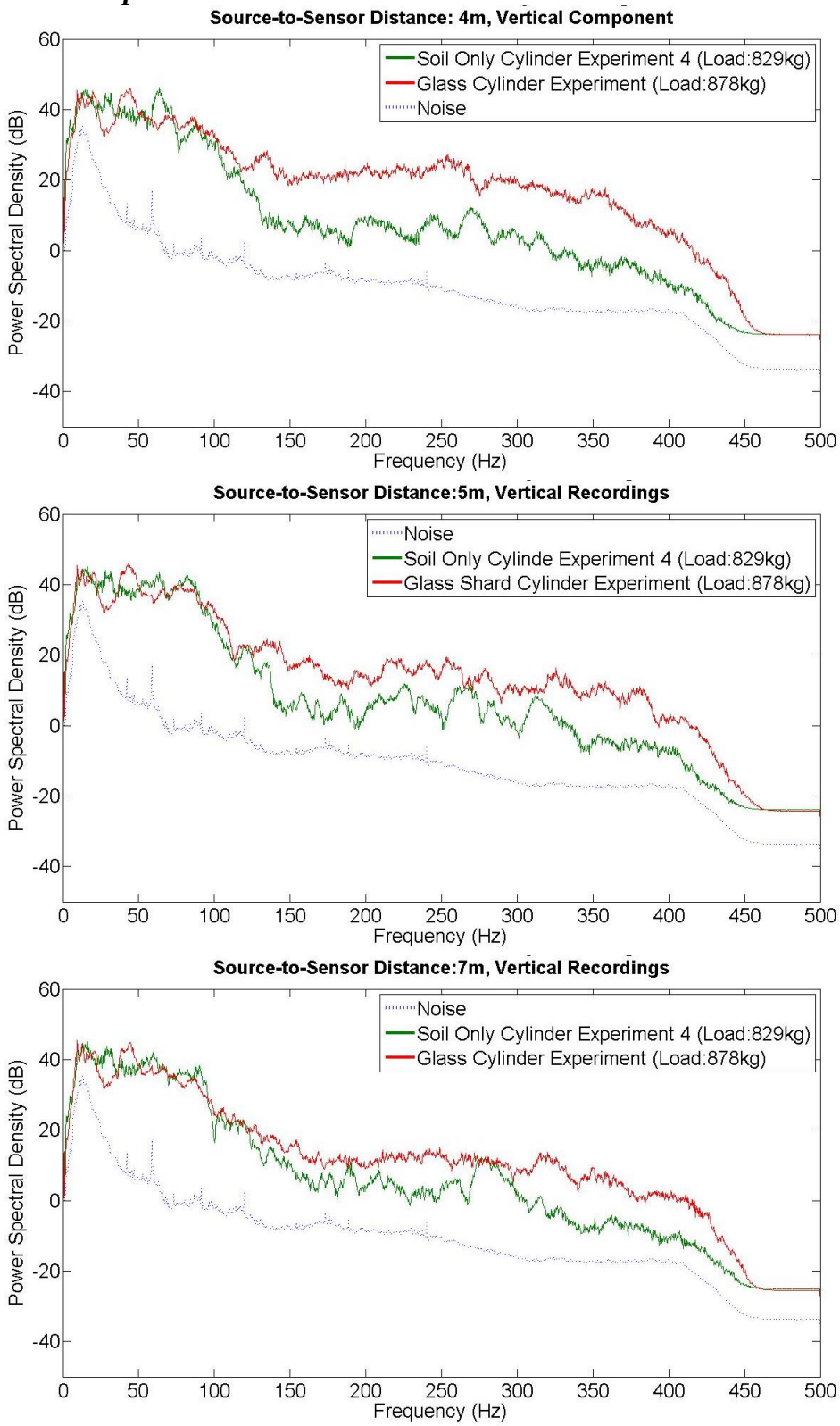

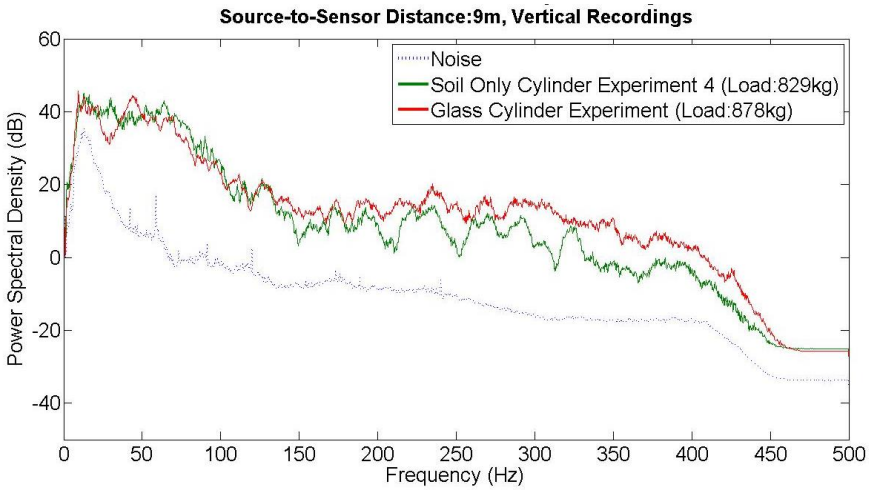
Source-to-Sensor Distance:9m, Vertical Recordings
Noise
Soil Only Cylinder Experiment 4 (Load:829kg)
Glass Cylinder Experiment (Load:878kg)
Power Spectral Density (dB)
Frequency (Hz)

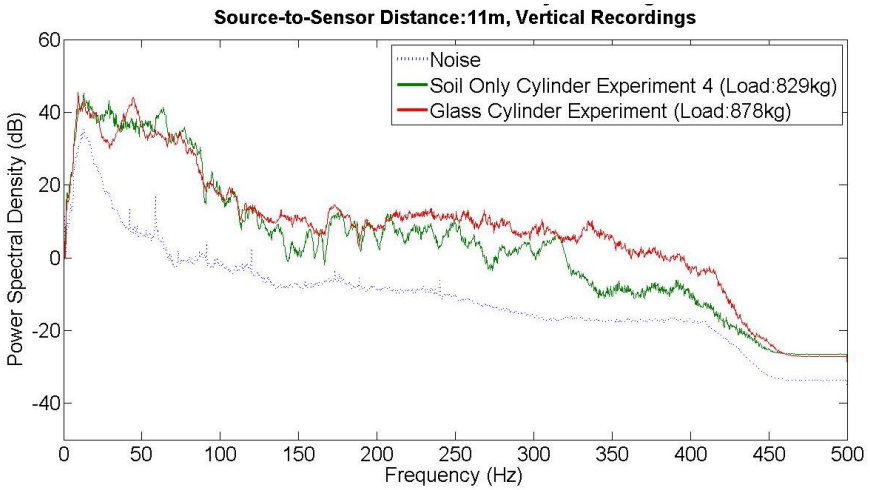
Source-to-Sensor Distance:11m, Vertical Recordings
Noise
Soil Only Cylinder Experiment 4 (Load:829kg)
Glass Cylinder Experiment (Load:878kg)
Power Spectral Density (dB)
Frequency (Hz)

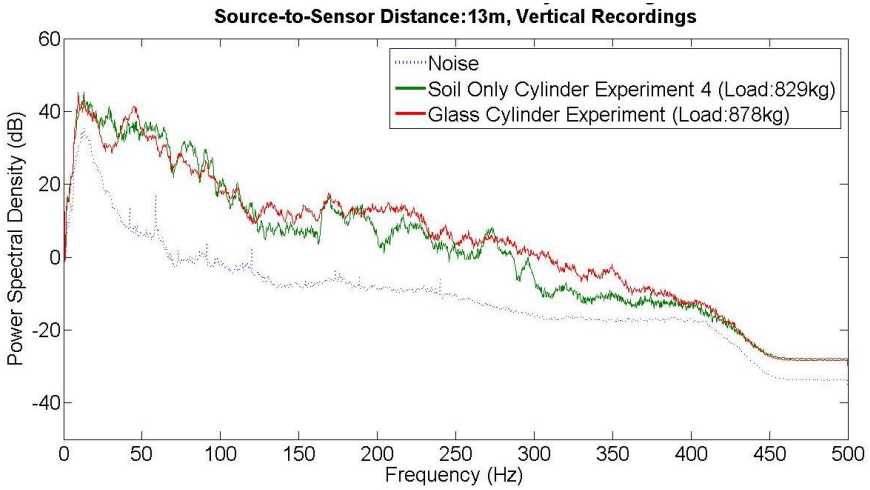
Source-to-Sensor Distance:13m, Vertical Recordings
Noise
Soil Only Cylinder Experiment 4 (Load:829kg)
Glass Cylinder Experiment (Load:878kg)
Power Spectral Density (dB)
Frequency (Hz)

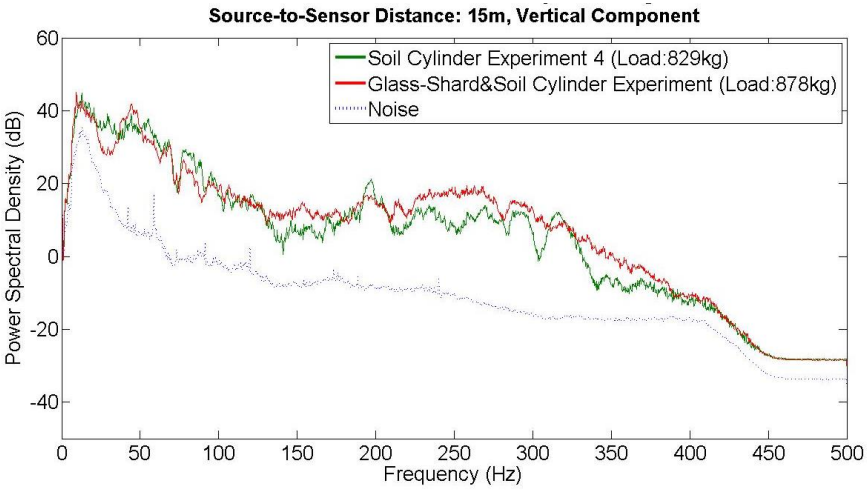
Source-to-Sensor Distance: 15m, Vertical Component
Soil Cylinder Experiment 4 (Load:829kg)
Glass-Shard&Soil Cylinder Experiment (Load:878kg)
Noise
Power Spectral Density (dB)
Frequency (Hz)

b) North-South Component

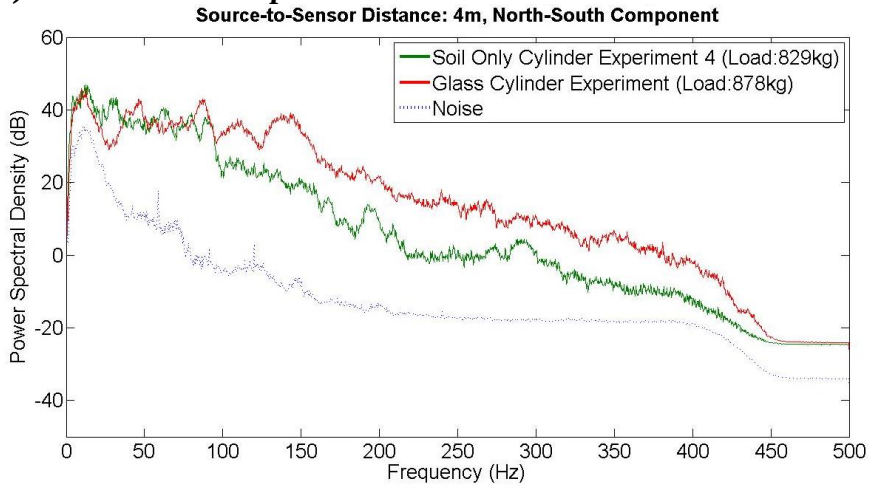

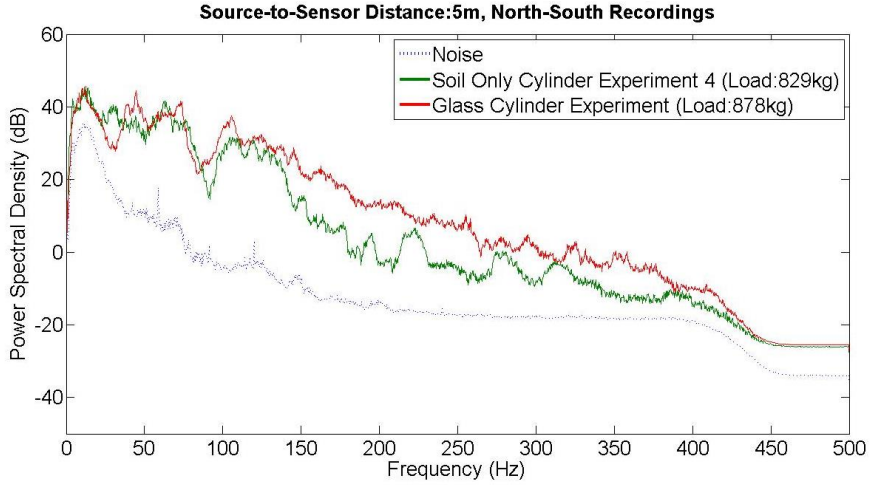

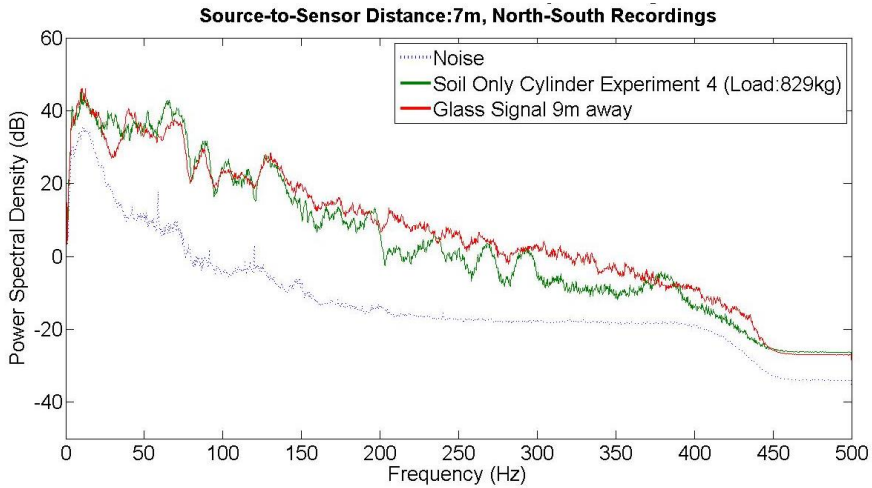

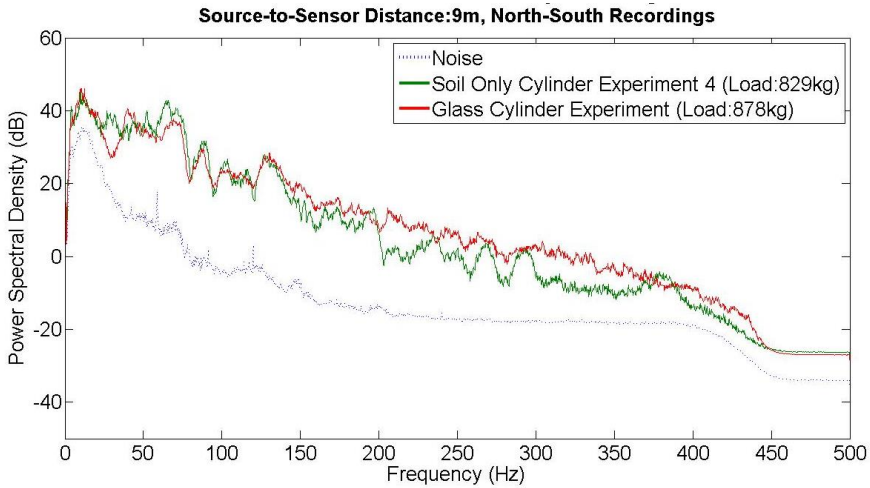

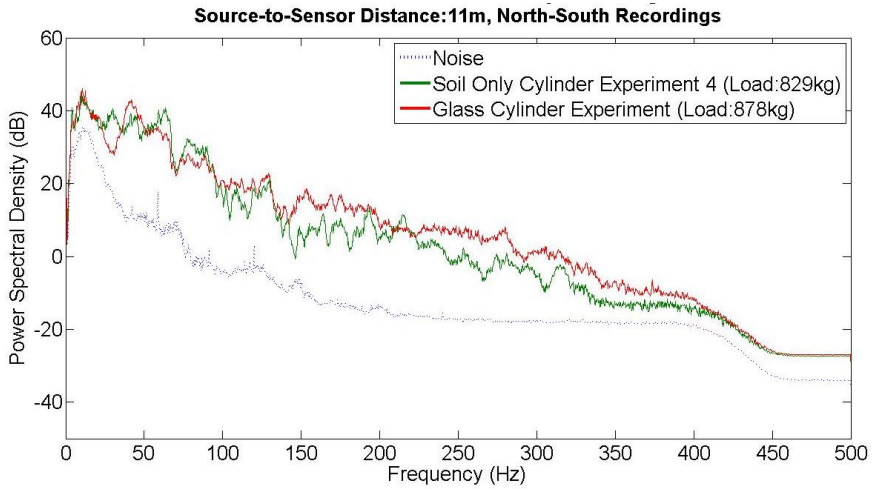
Source-to-Sensor Distance:11m, North-South Recordings
Noise
Soil Only Cylinder Experiment 4 (Load:829kg)
Glass Cylinder Experiment (Load:878kg)
Power Spectral Density (dB)
Frequency (Hz)
60
40
20
0
-20
-40
0
50
100
150
200
250
300
350
400
450
500

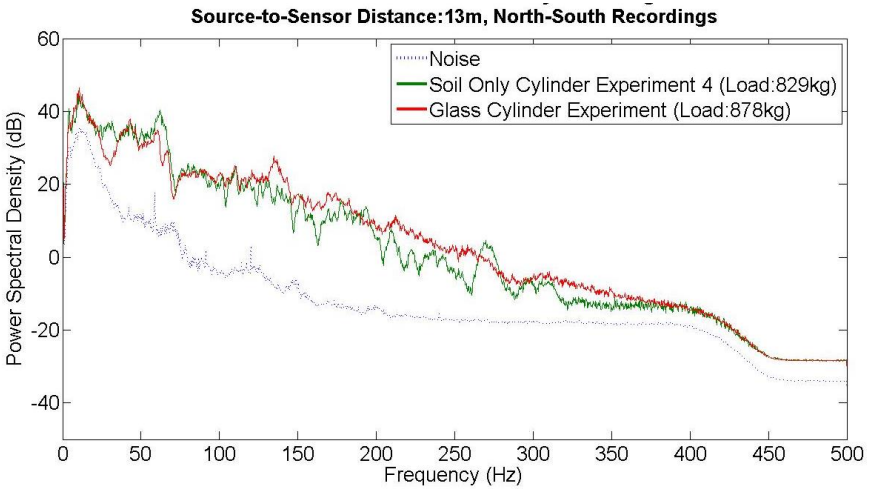
Source-to-Sensor Distance:13m, North-South Recordings
Noise
Soil Only Cylinder Experiment 4 (Load:829kg)
Glass Cylinder Experiment (Load:878kg)
Power Spectral Density (dB)
Frequency (Hz)
60
40
20
0
-20
-40
0
50
100
150
200
250
300
350
400
450
500

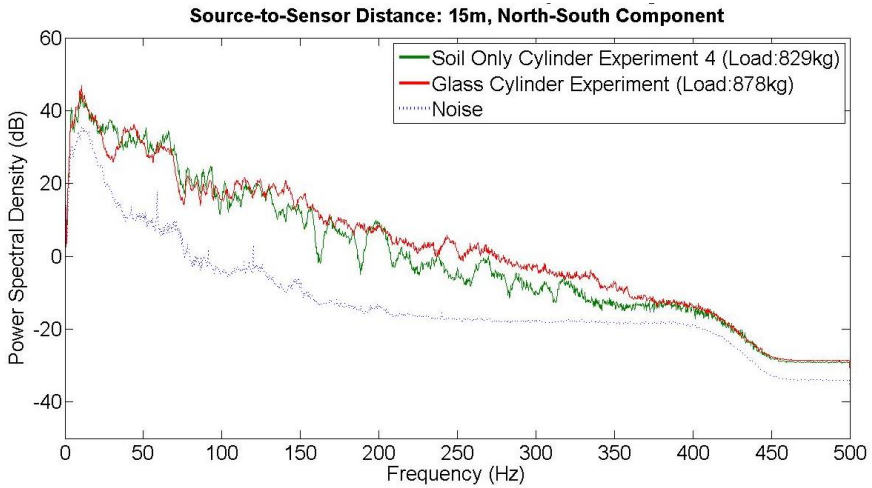
Source-to-Sensor Distance: 15m, North-South Component
Soil Only Cylinder Experiment 4 (Load:829kg)
Glass Cylinder Experiment (Load:878kg)
Noise
Power Spectral Density (dB)
Frequency (Hz)
60
40
20
0
-20
-40
0
50
100
150
200
250
300
350
400
450
500

c) East-West Component

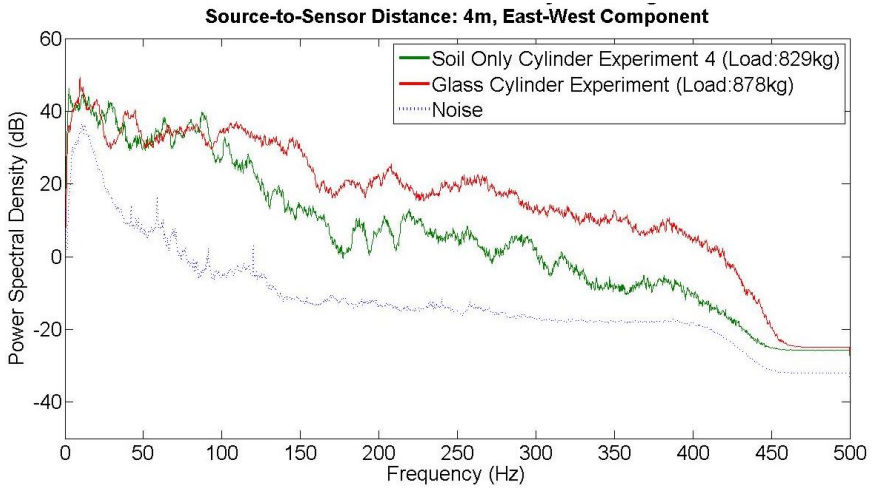

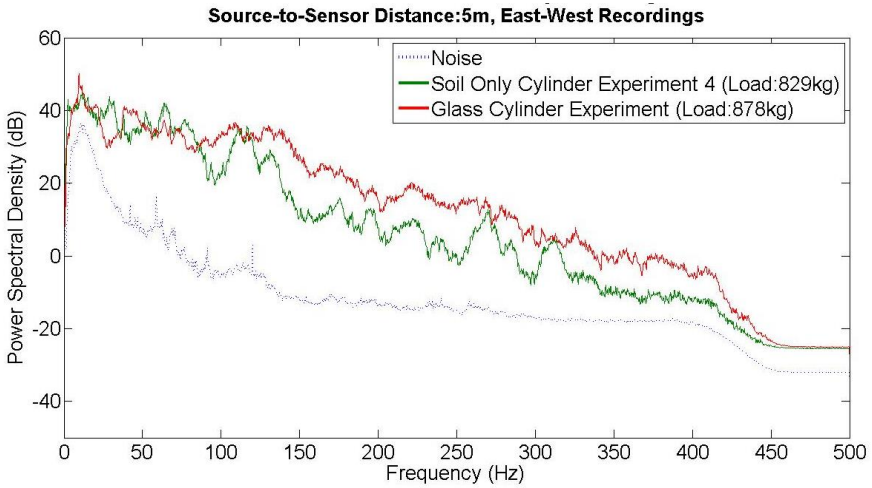

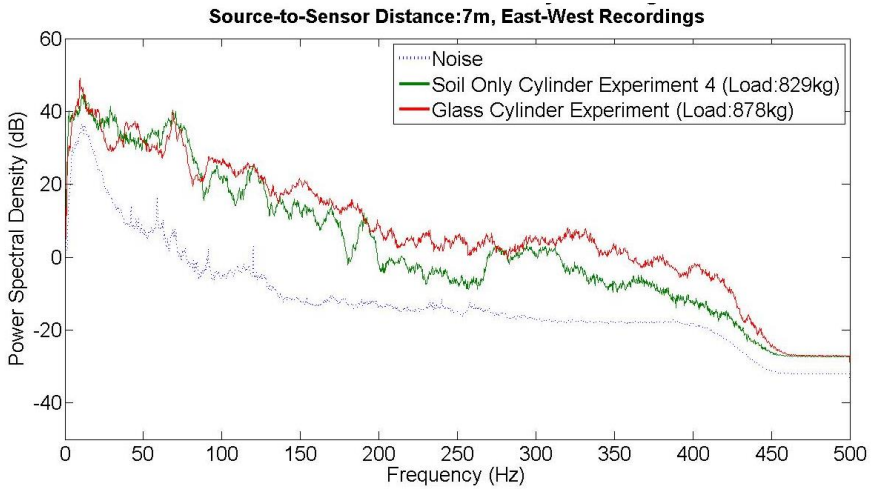

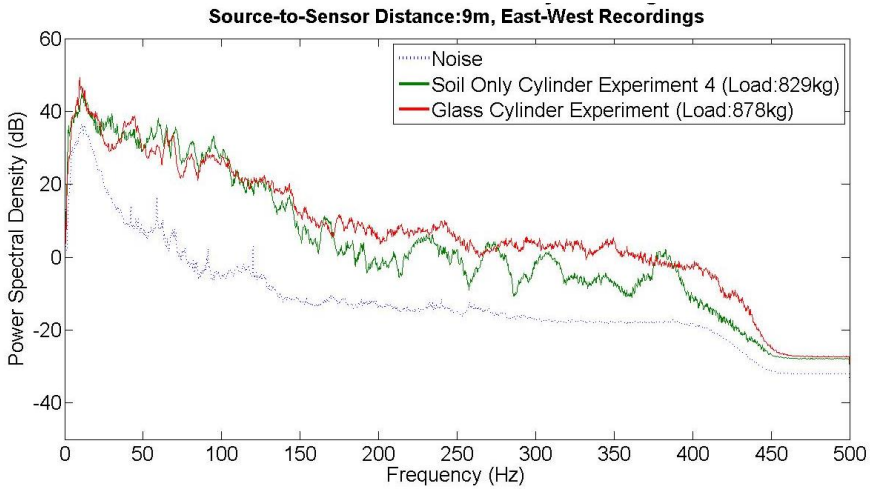

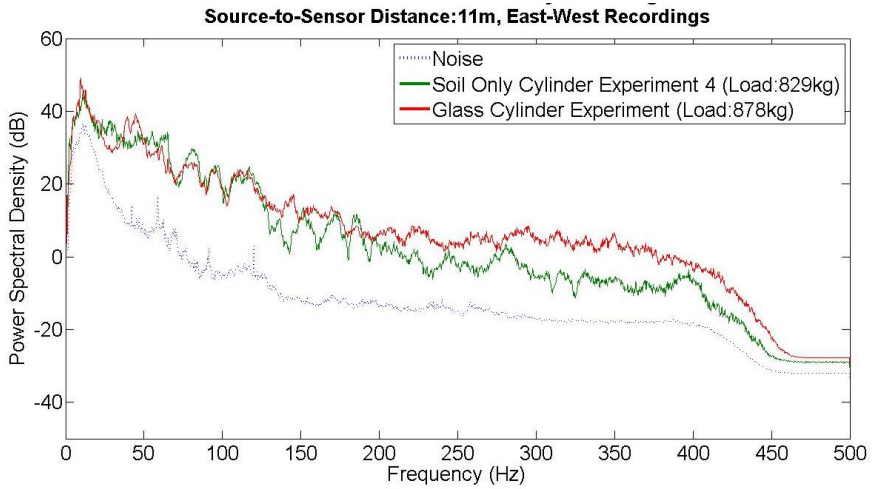
Source-to-Sensor Distance:11m, East-West Recordings
Noise
Soil Only Cylinder Experiment 4 (Load:829kg)
Glass Cylinder Experiment (Load:878kg)
Power Spectral Density (dB)
Frequency (Hz)

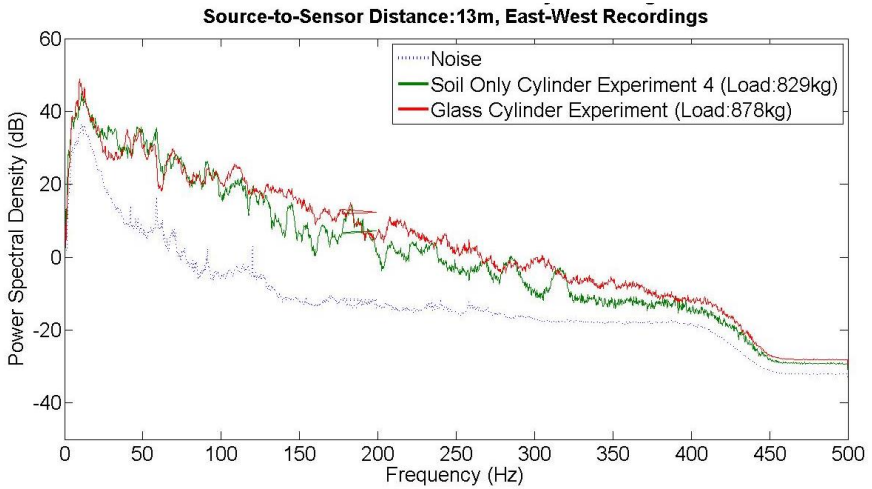
Source-to-Sensor Distance:13m, East-West Recordings
Noise
Soil Only Cylinder Experiment 4 (Load:829kg)
Glass Cylinder Experiment (Load:878kg)
Power Spectral Density (dB)
Frequency (Hz)

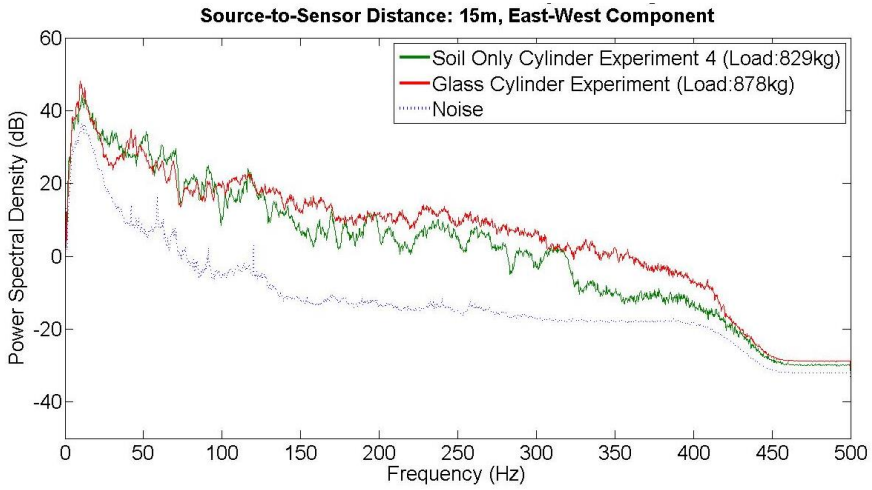
Source-to-Sensor Distance: 15m, East-West Component
Soil Only Cylinder Experiment 4 (Load:829kg)
Glass Cylinder Experiment (Load:878kg)
Noise
Power Spectral Density (dB)
Frequency (Hz)

Appendix C

Seismic signature of landslides: validation based on two controlled failures

In this appendix all additional graphs of Chapter 7 will be presented. Note that only the sensors that recorded events above background noise levels are presented. The deployment geometry of the seismometers is also presented first as a reminder to the reader so he or she doesn't have to search for this information back to the original chapter.

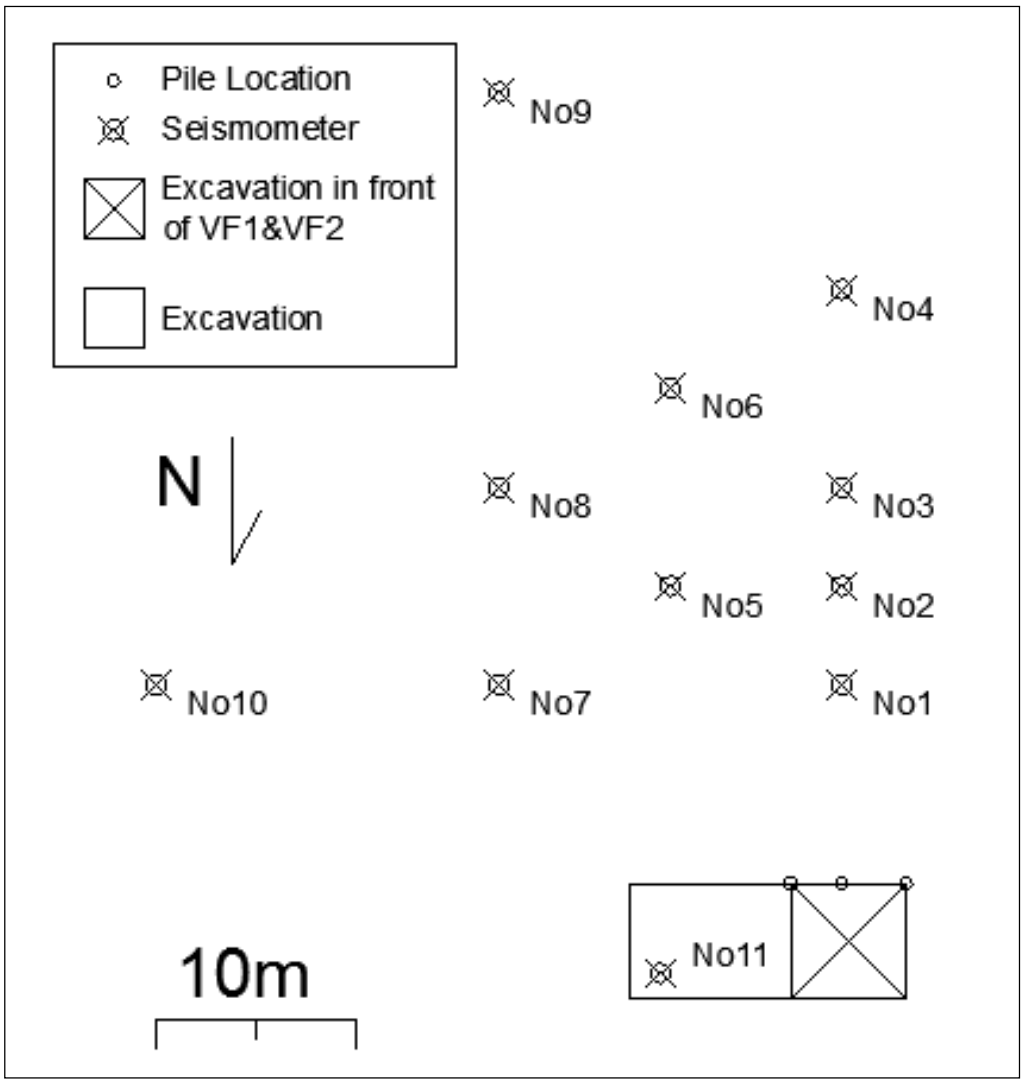

Plan view of the experimental site. **a)** Deployment geometry of seismic sensors, forming a microseismic array.

C1. Spectrograms from Section 8.4.1 "Step 1: Analysis in the time-frequency domain"

C1.1 Spectrograms from data recorded during the induced failure of the Landslide with the Glass Shard Pile

C1.1.1 Spectrograms from data recorded by sensor No1

a) Vertical Component

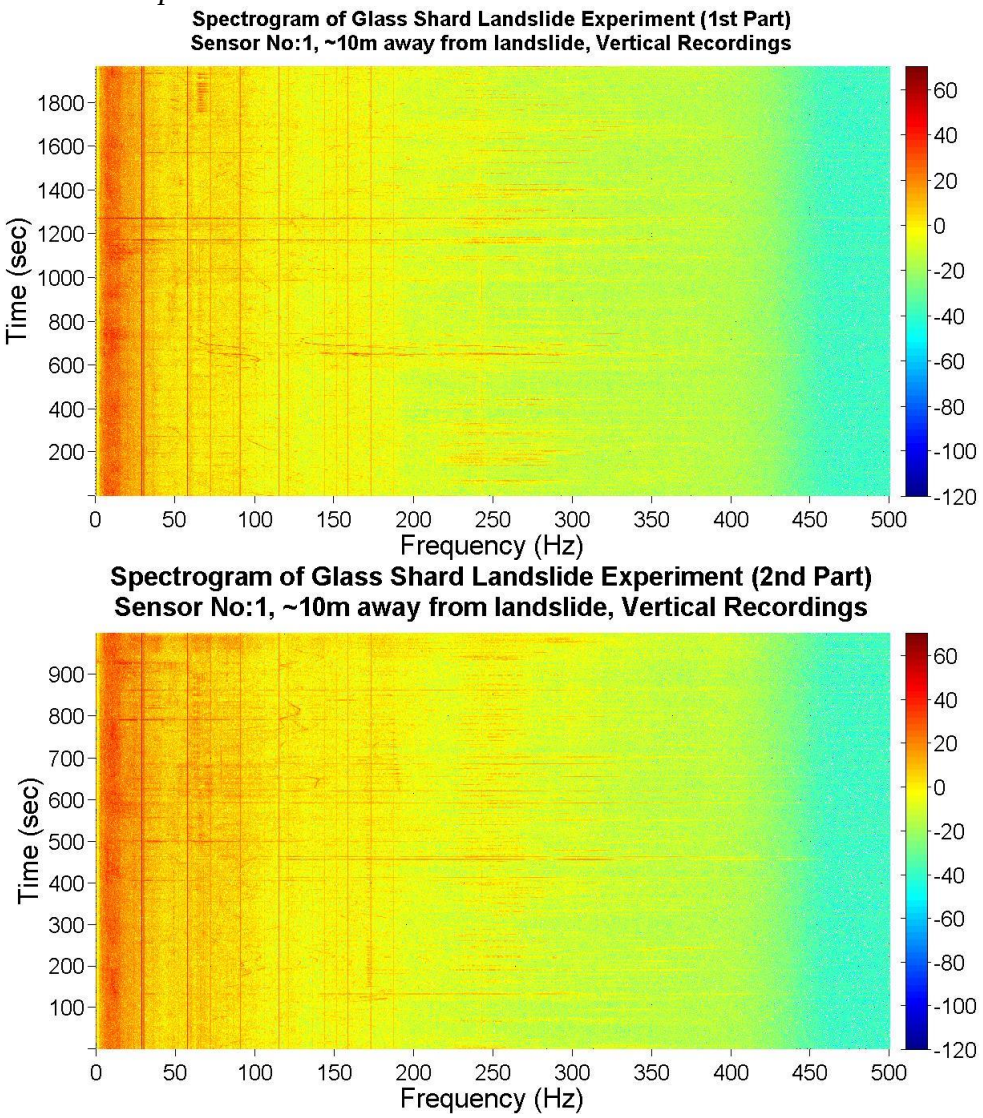

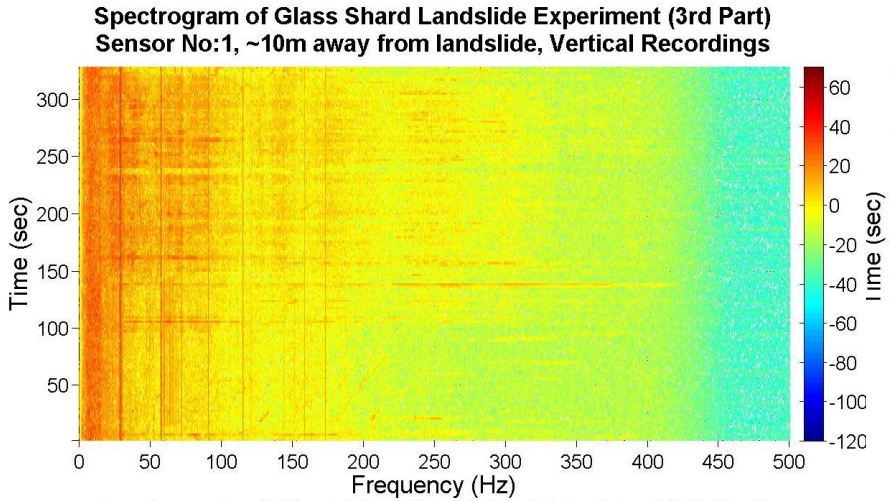
Spectrogram of Glass Shard Landslide Experiment (3rd Part)
Sensor No:1, ~10m away from landslide, Vertical Recordings
Time (sec)
Frequency (Hz)

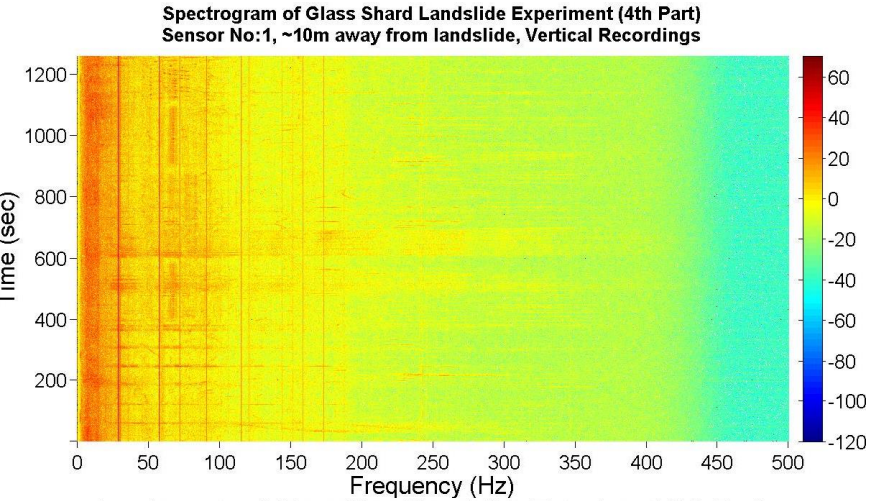
Spectrogram of Glass Shard Landslide Experiment (4th Part)
Sensor No:1, ~10m away from landslide, Vertical Recordings
Time (sec)
Frequency (Hz)

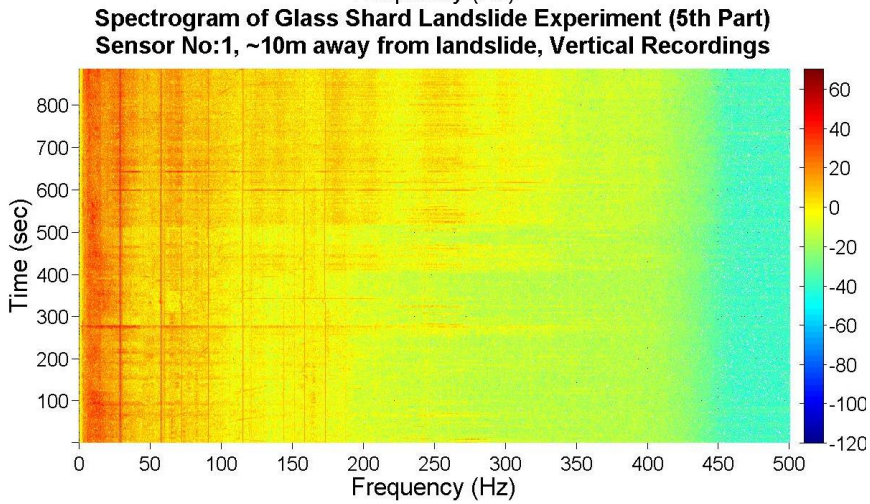
Spectrogram of Glass Shard Landslide Experiment (5th Part)
Sensor No:1, ~10m away from landslide, Vertical Recordings
Time (sec)
Frequency (Hz)

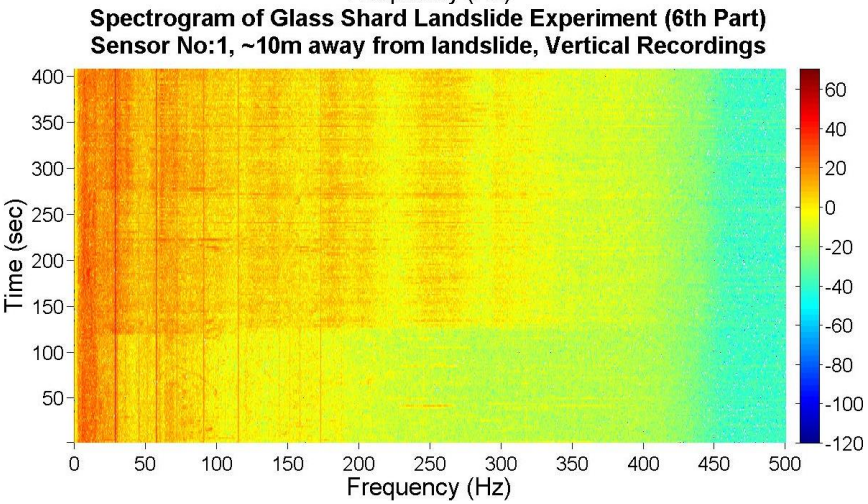
Spectrogram of Glass Shard Landslide Experiment (6th Part)
Sensor No:1, ~10m away from landslide, Vertical Recordings
Time (sec)
Frequency (Hz)

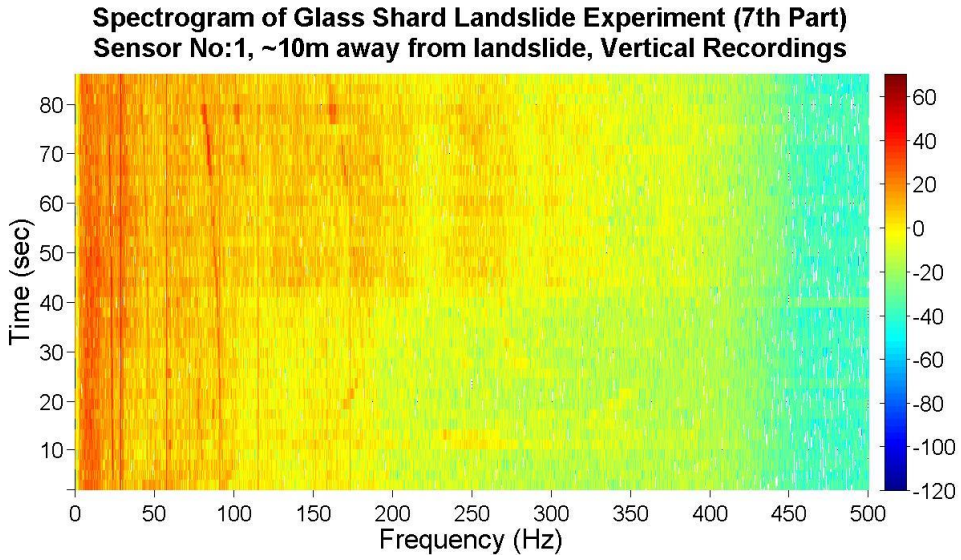

b) North-South Recordings

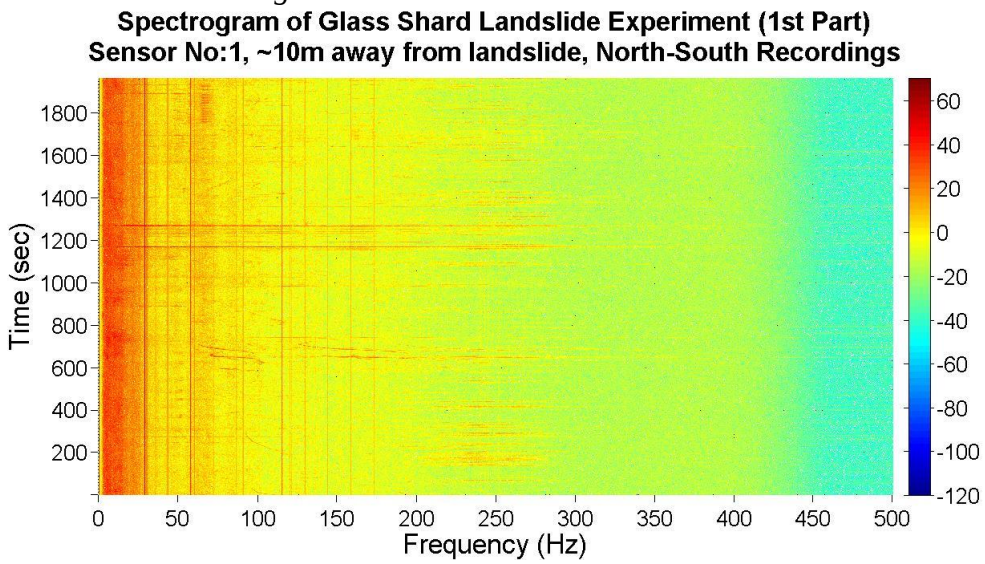

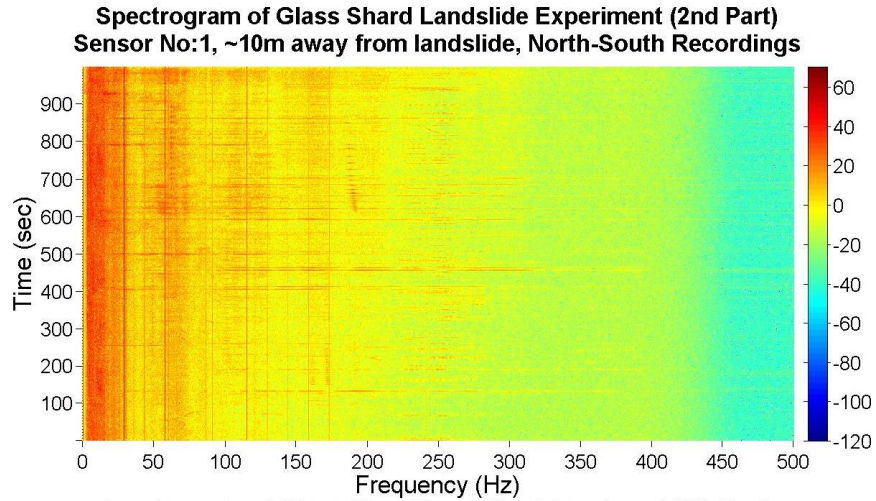
Spectrogram of Glass Shard Landslide Experiment (2nd Part)
Sensor No:1, ~10m away from landslide, North-South Recordings
Time (sec)
Frequency (Hz)

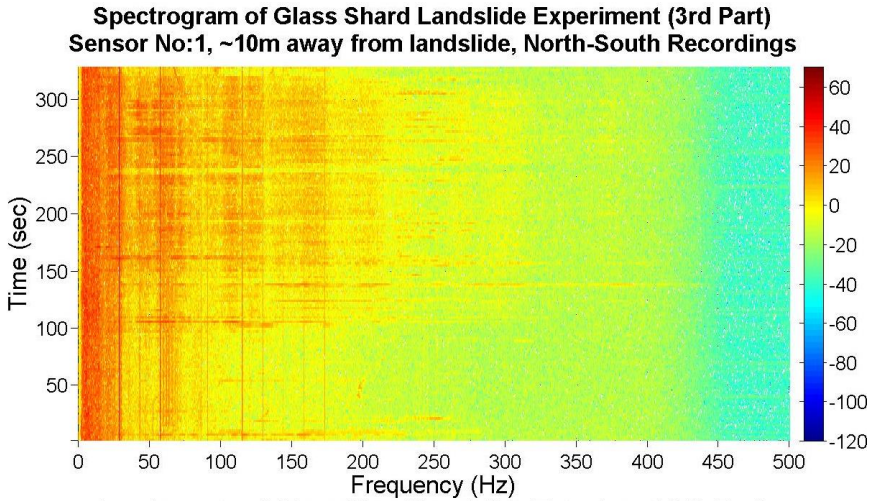
Spectrogram of Glass Shard Landslide Experiment (3rd Part)
Sensor No:1, ~10m away from landslide, North-South Recordings
Time (sec)
Frequency (Hz)

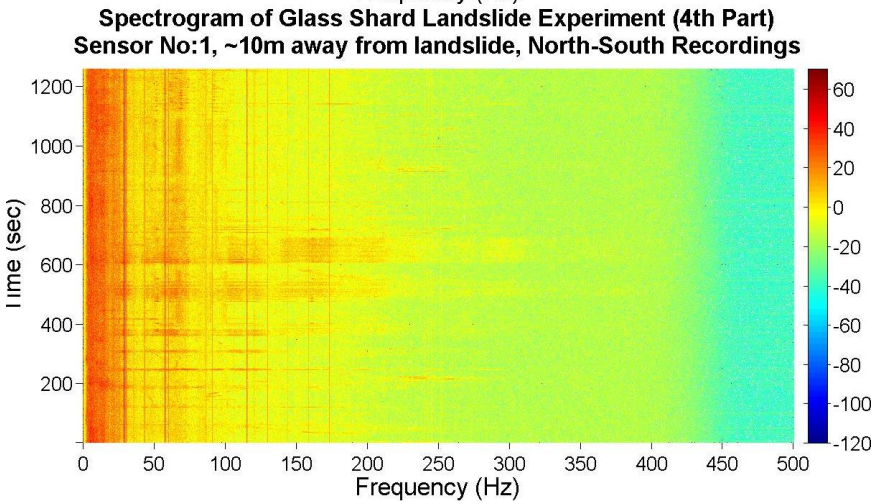
Spectrogram of Glass Shard Landslide Experiment (4th Part)
Sensor No:1, ~10m away from landslide, North-South Recordings
Time (sec)
Frequency (Hz)

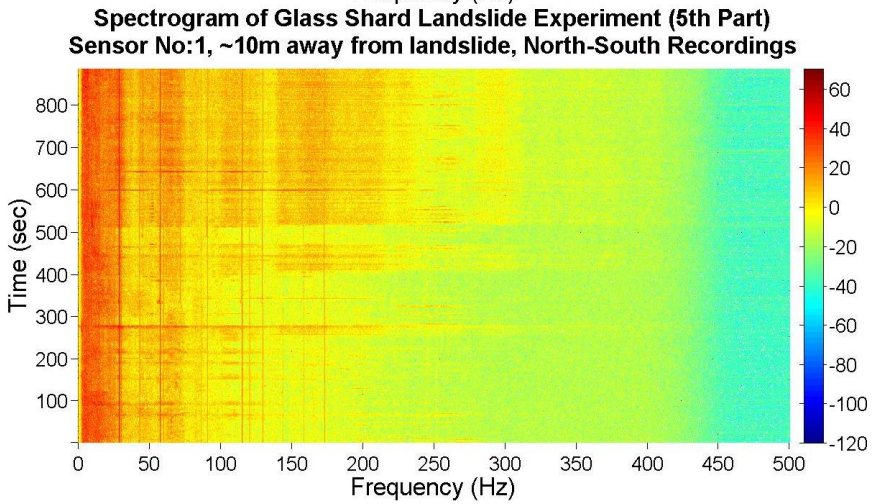
Spectrogram of Glass Shard Landslide Experiment (5th Part)
Sensor No:1, ~10m away from landslide, North-South Recordings
Time (sec)
Frequency (Hz)

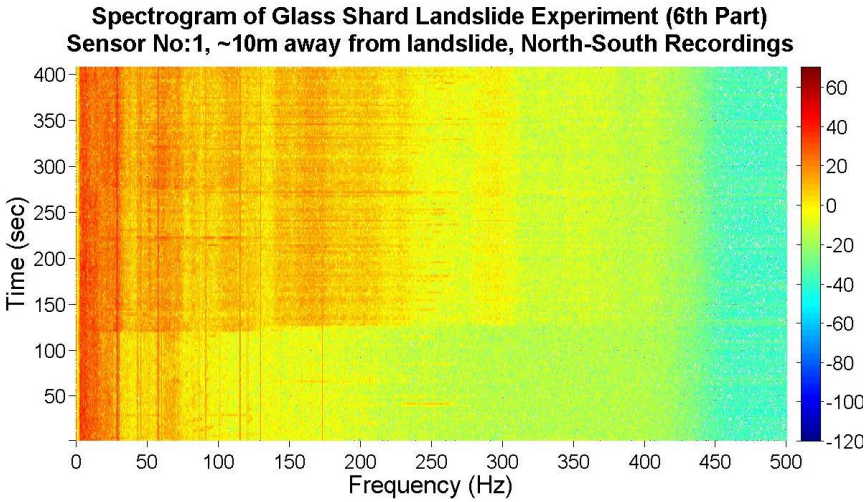
Spectrogram of Glass Shard Landslide Experiment (6th Part)
Sensor No:1, ~10m away from landslide, North-South Recordings
Time (sec)
Frequency (Hz)
400
350
300
250
200
150
100
50
0
50
100
150
200
250
300
350
400
450
500
60
40
20
0
-20
-40
-60
-80
-100
-120

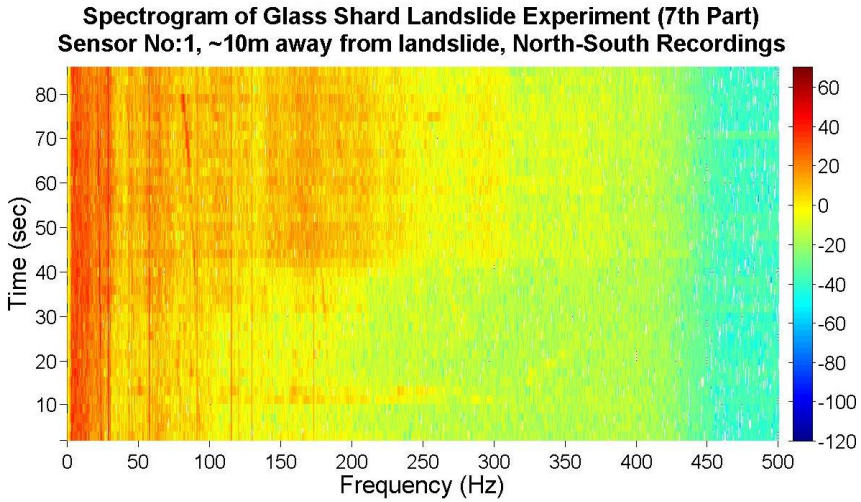
Spectrogram of Glass Shard Landslide Experiment (7th Part)
Sensor No:1, ~10m away from landslide, North-South Recordings
Time (sec)
Frequency (Hz)
80
70
60
50
40
30
20
10
0
50
100
150
200
250
300
350
400
450
500
60
40
20
0
-20
-40
-60
-80
-100
-120

c) East-West Component

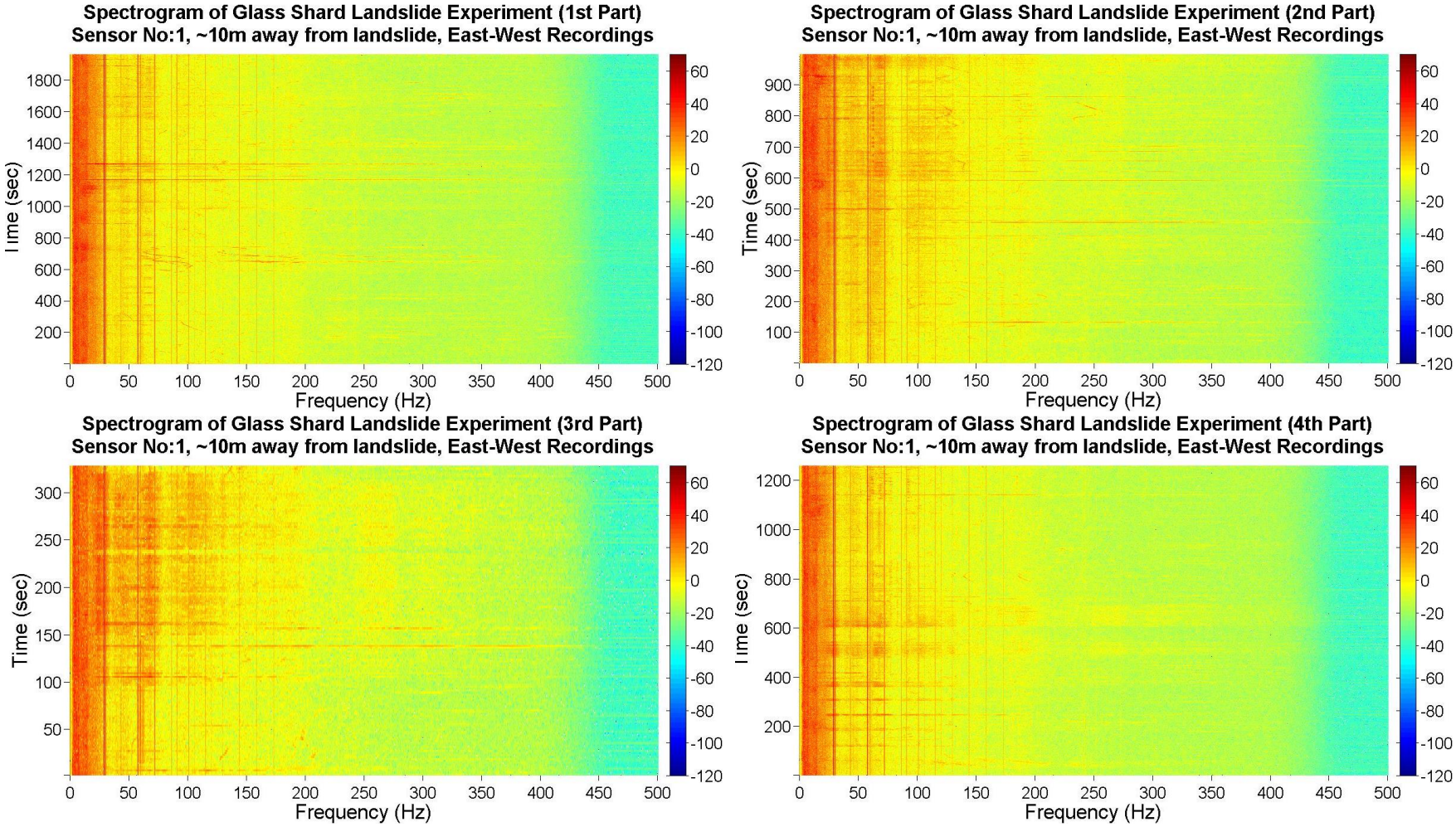

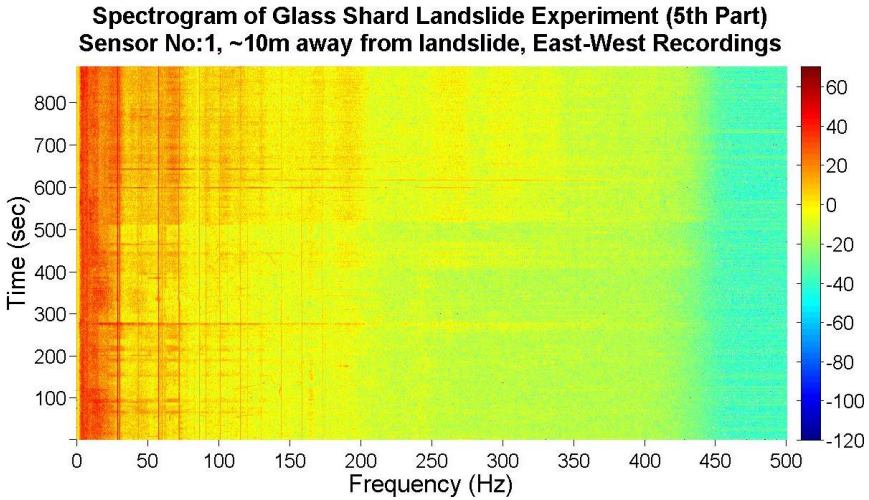
Spectrogram of Glass Shard Landslide Experiment (5th Part)
Sensor No:1, ~10m away from landslide, East-West Recordings
Time (sec)
Frequency (Hz)

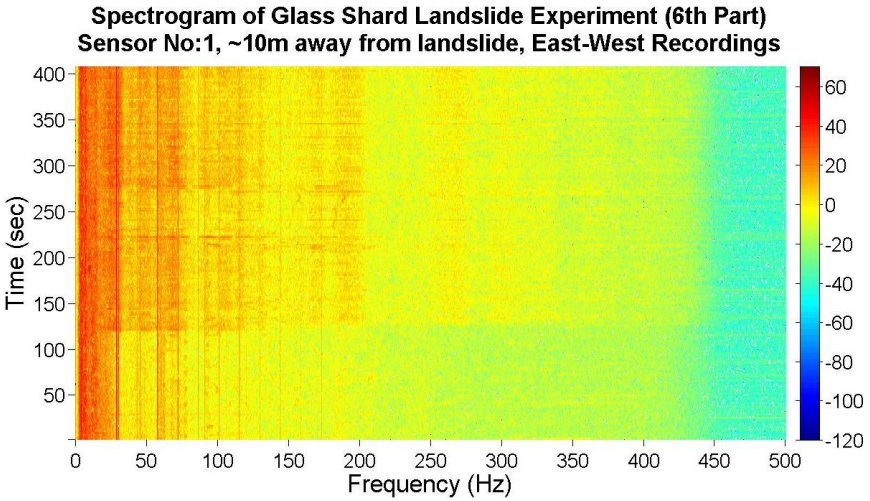
Spectrogram of Glass Shard Landslide Experiment (6th Part)
Sensor No:1, ~10m away from landslide, East-West Recordings
Time (sec)
Frequency (Hz)

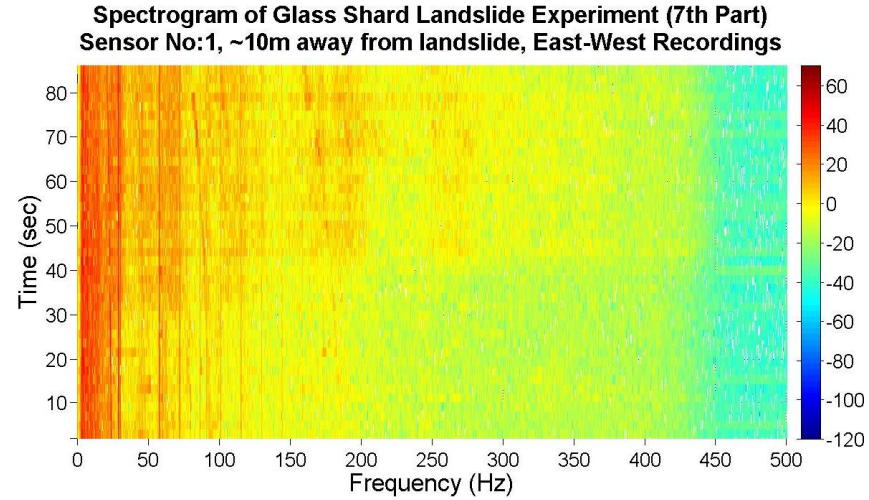
Spectrogram of Glass Shard Landslide Experiment (7th Part)
Sensor No:1, ~10m away from landslide, East-West Recordings
Time (sec)
Frequency (Hz)

C1.1.2 Spectrograms from data recorded by sensor No11

a) Vertical Component

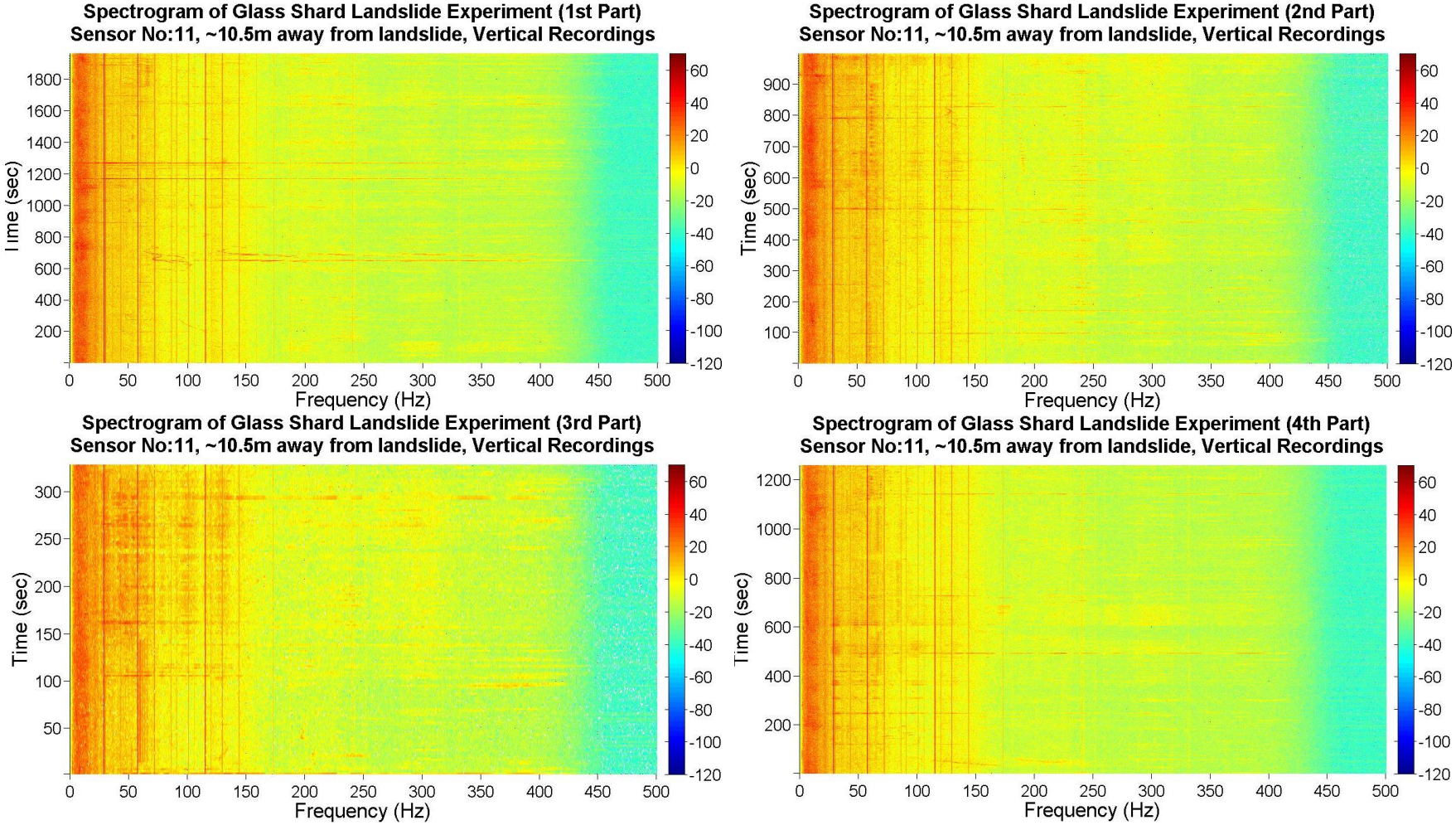

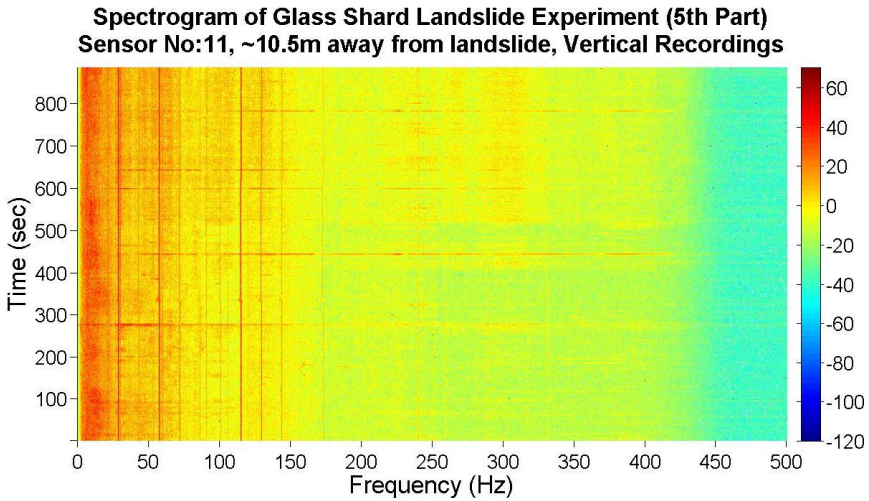
Spectrogram of Glass Shard Landslide Experiment (5th Part)
Sensor No:11, ~10.5m away from landslide, Vertical Recordings
Time (sec)
Frequency (Hz)

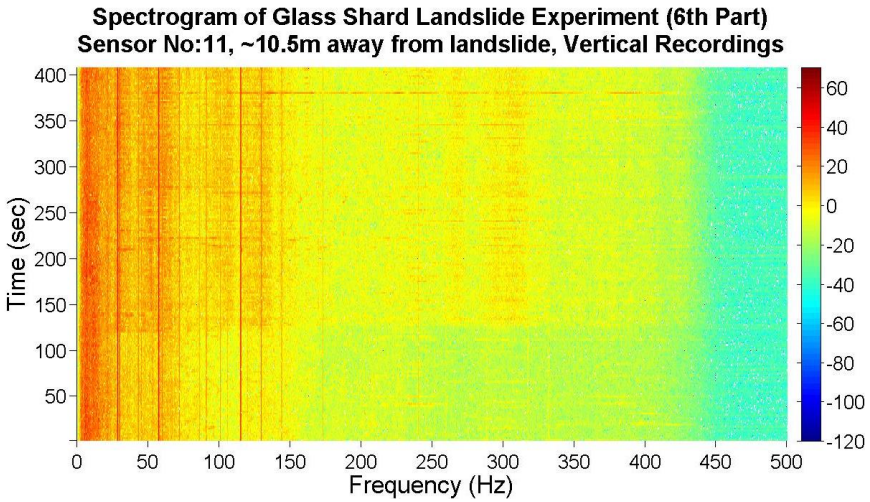
Spectrogram of Glass Shard Landslide Experiment (6th Part)
Sensor No:11, ~10.5m away from landslide, Vertical Recordings
Time (sec)
Frequency (Hz)

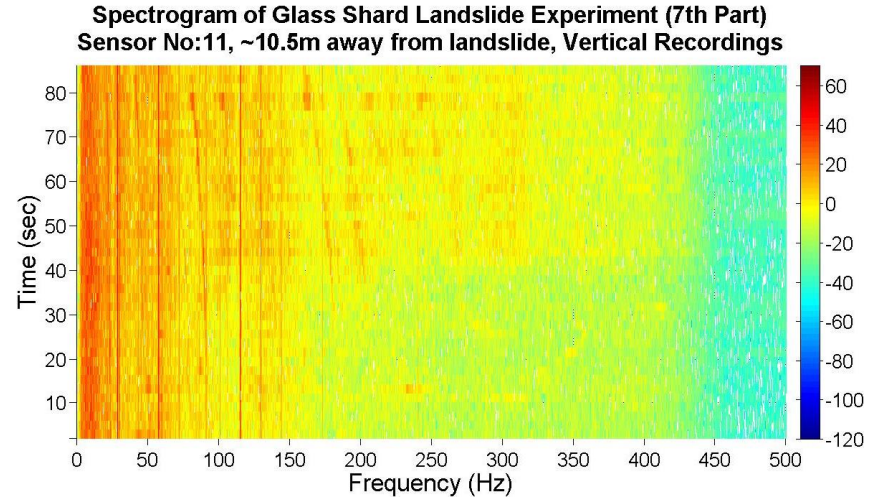
Spectrogram of Glass Shard Landslide Experiment (7th Part)
Sensor No:11, ~10.5m away from landslide, Vertical Recordings
Time (sec)
Frequency (Hz)

b) North-South Component

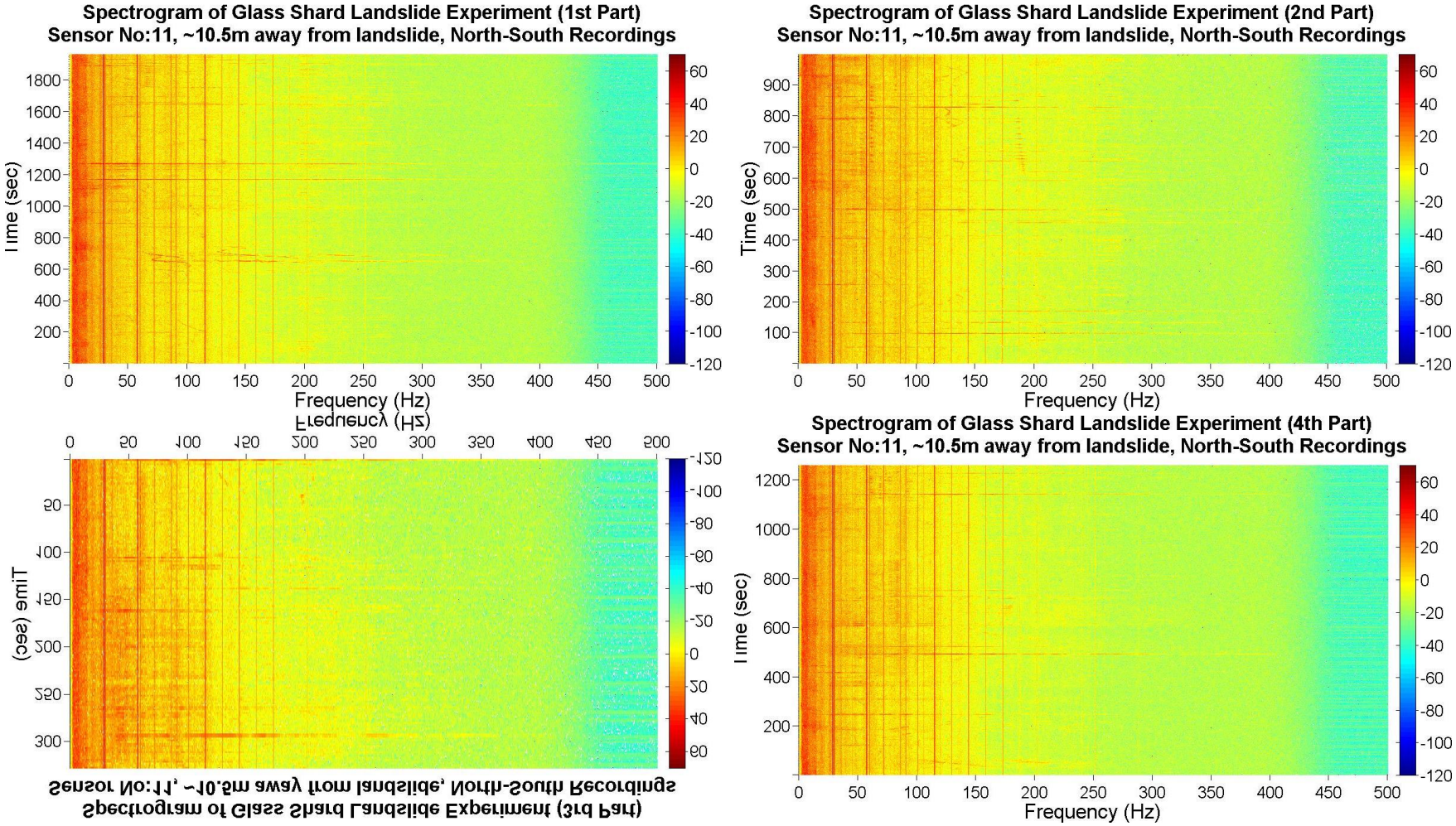

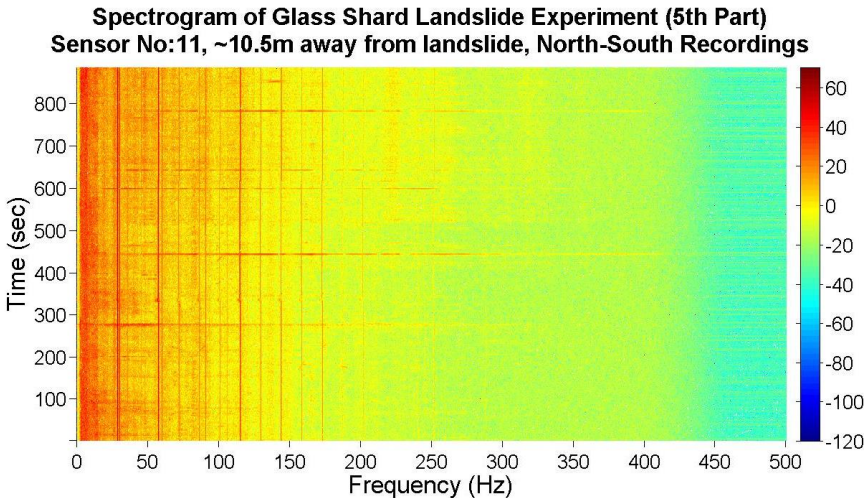
Spectrogram of Glass Shard Landslide Experiment (5th Part)
Sensor No:11, ~10.5m away from landslide, North-South Recordings
Time (sec)
Frequency (Hz)

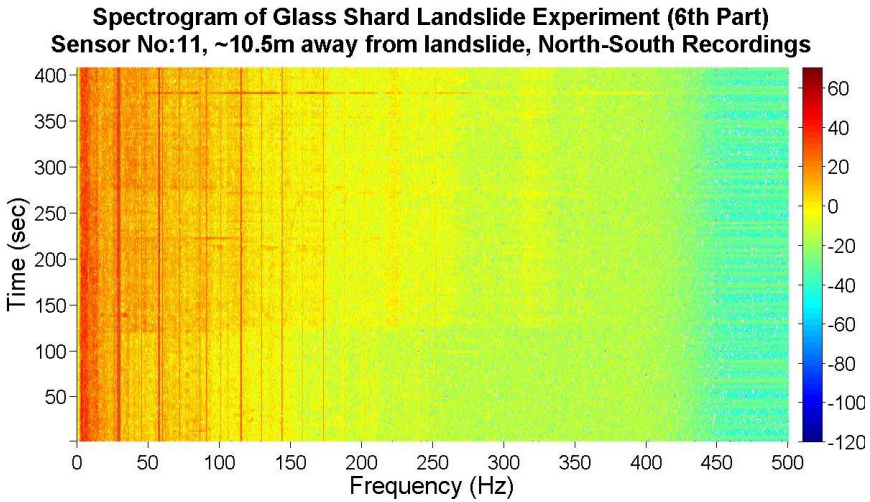
Spectrogram of Glass Shard Landslide Experiment (6th Part)
Sensor No:11, ~10.5m away from landslide, North-South Recordings
Time (sec)
Frequency (Hz)

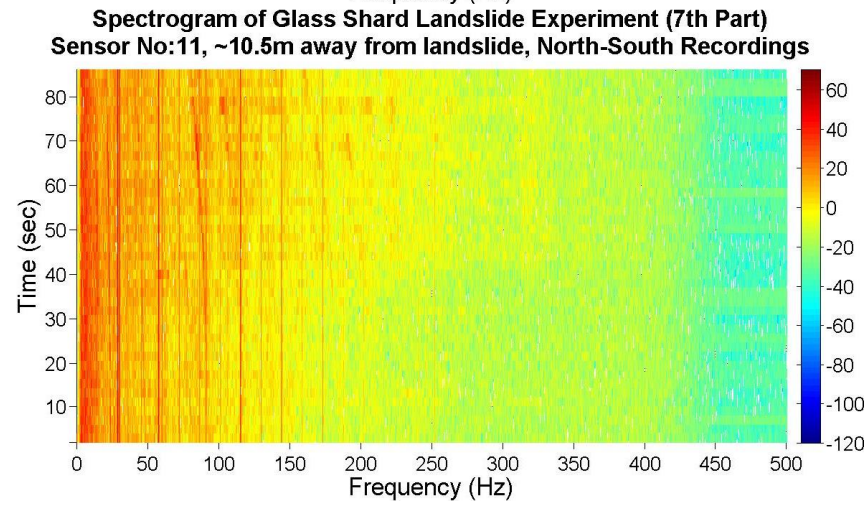
Spectrogram of Glass Shard Landslide Experiment (7th Part)
Sensor No:11, ~10.5m away from landslide, North-South Recordings
Time (sec)
Frequency (Hz)

c) East-West Component

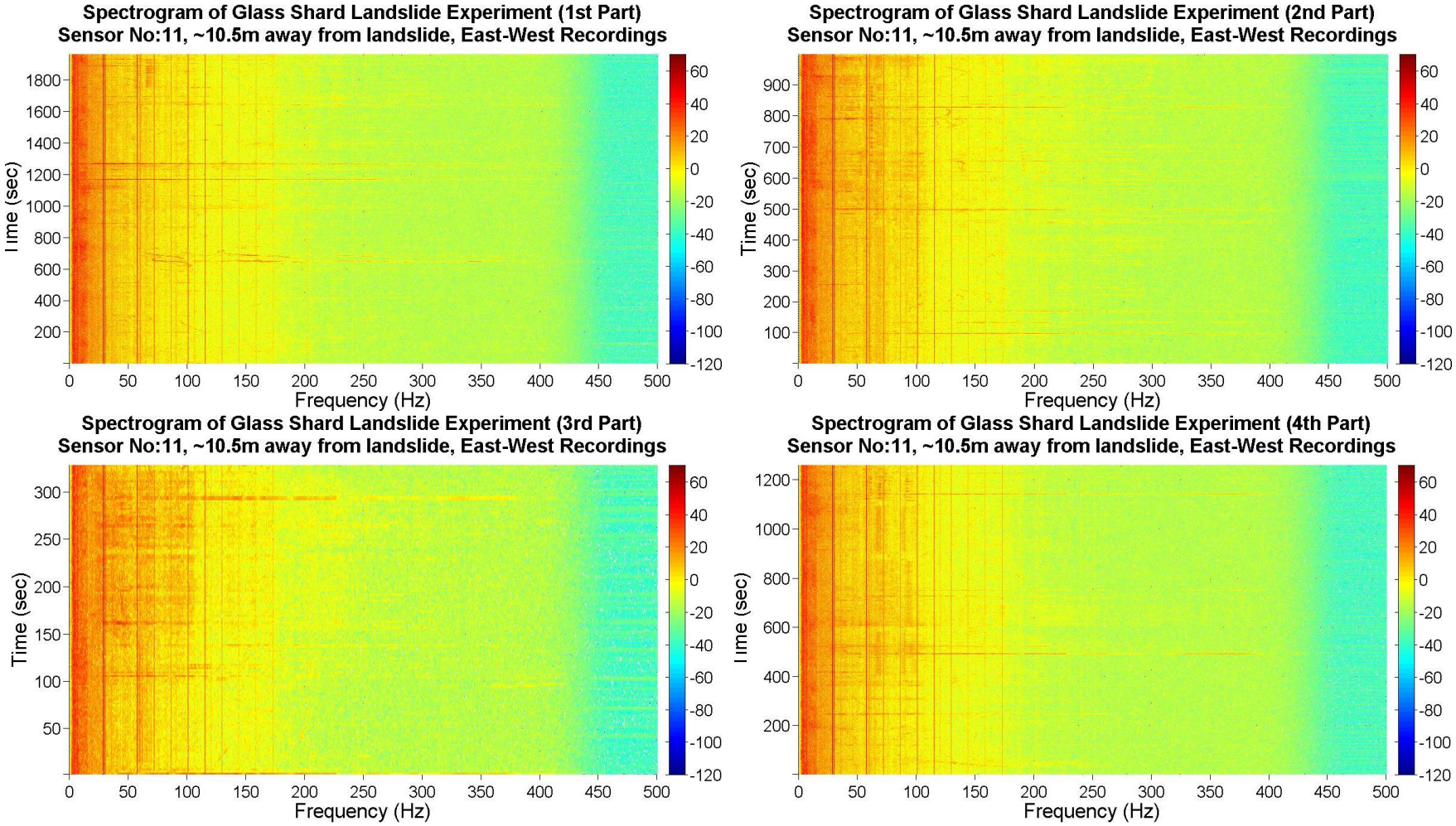

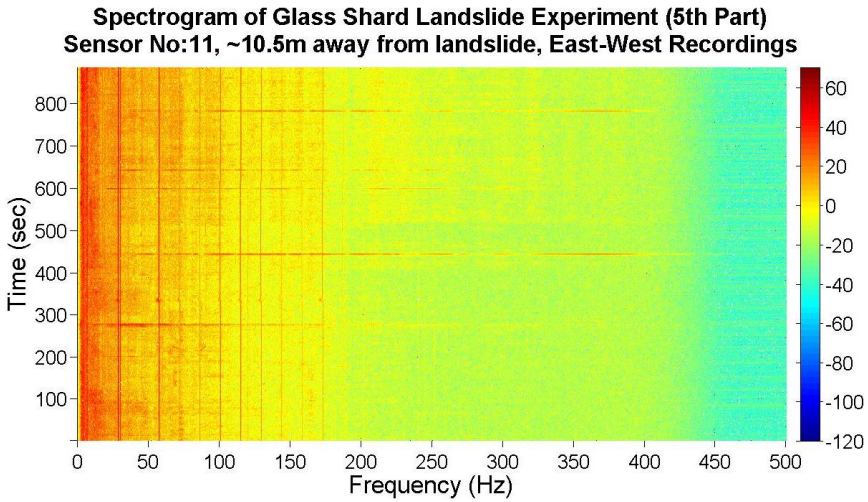
Spectrogram of Glass Shard Landslide Experiment (5th Part)
Sensor No:11, ~10.5m away from landslide, East-West Recordings
Time (sec)
Frequency (Hz)

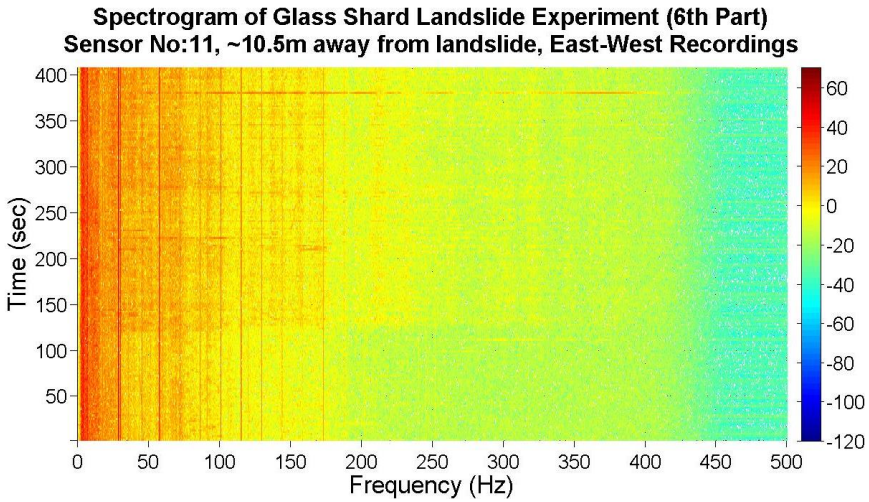
Spectrogram of Glass Shard Landslide Experiment (6th Part)
Sensor No:11, ~10.5m away from landslide, East-West Recordings
Time (sec)
Frequency (Hz)

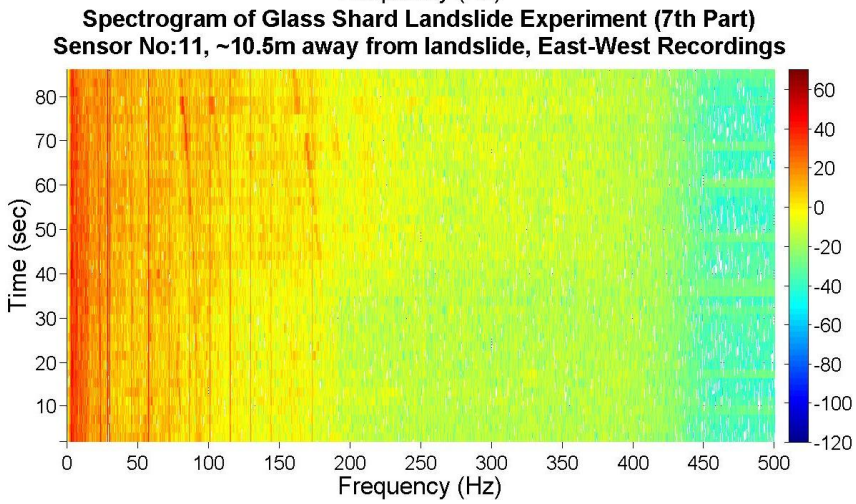
Spectrogram of Glass Shard Landslide Experiment (7th Part)
Sensor No:11, ~10.5m away from landslide, East-West Recordings
Time (sec)
Frequency (Hz)

C1.2 Spectrograms from data recorded during the induced failure of the Soil Only Landslide

C1.2.1 Spectrograms from data recorded by sensor No1

a) Vertical Component

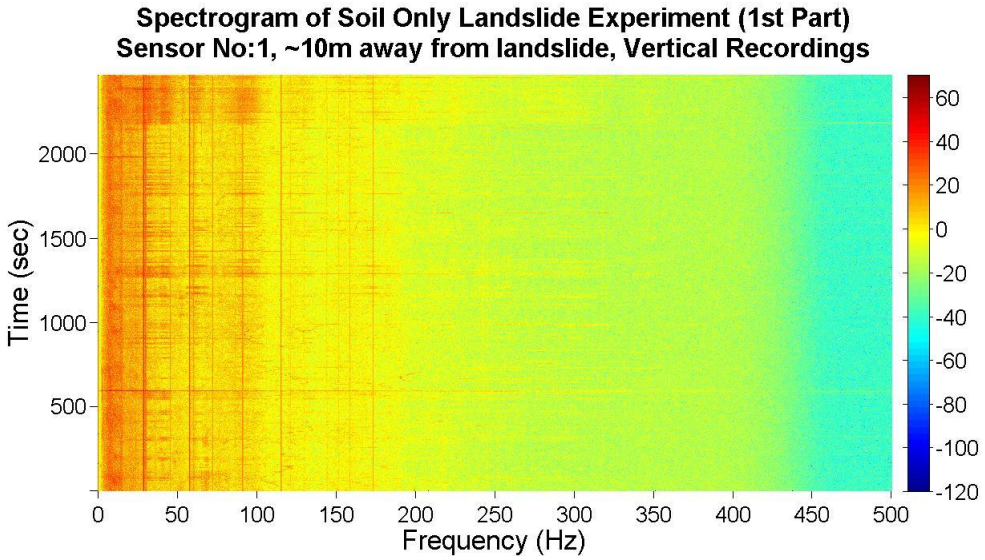

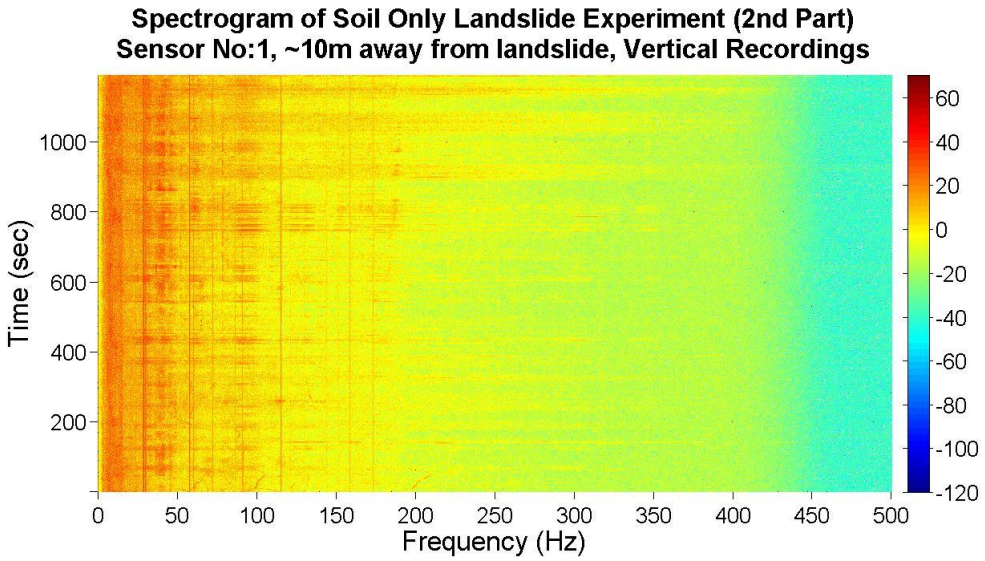

b) North-South Component

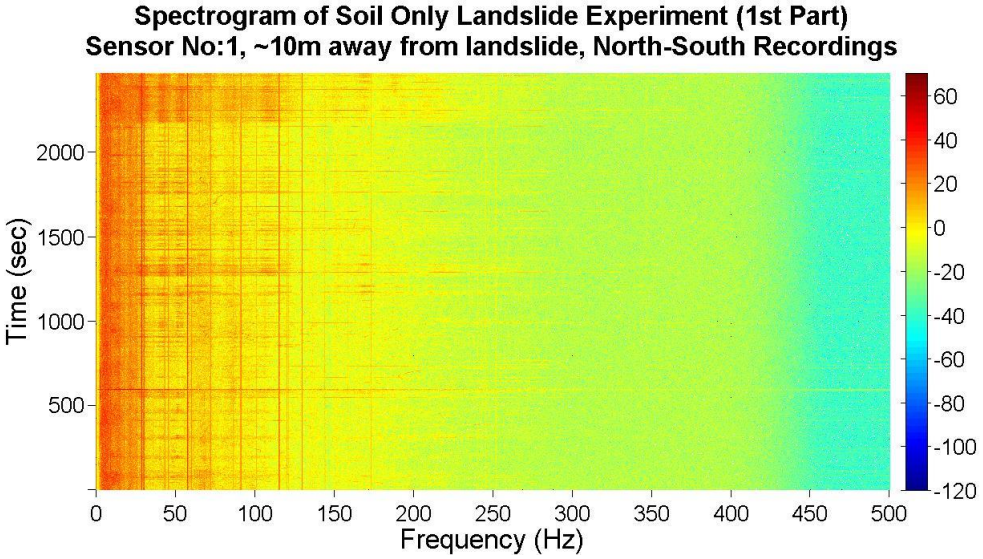

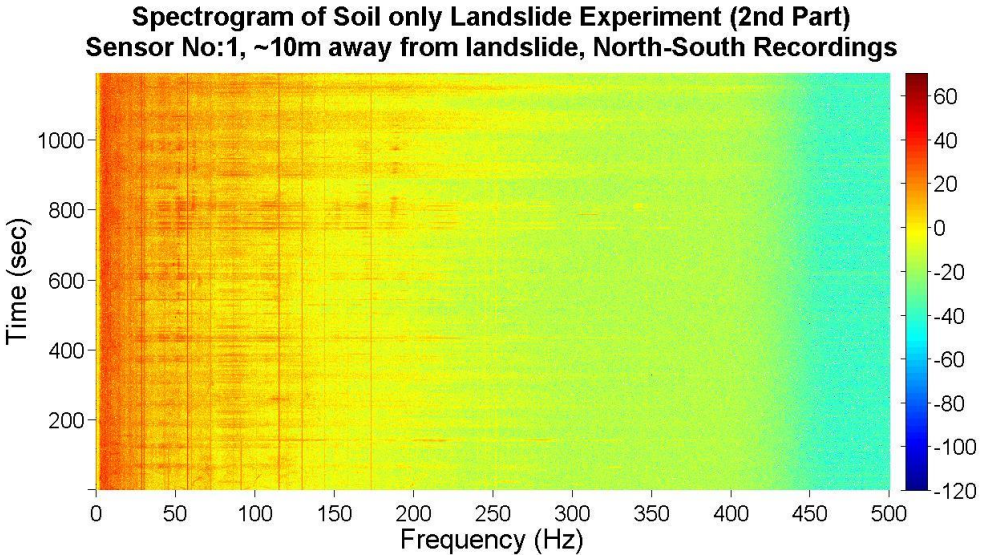

c) East-West Component

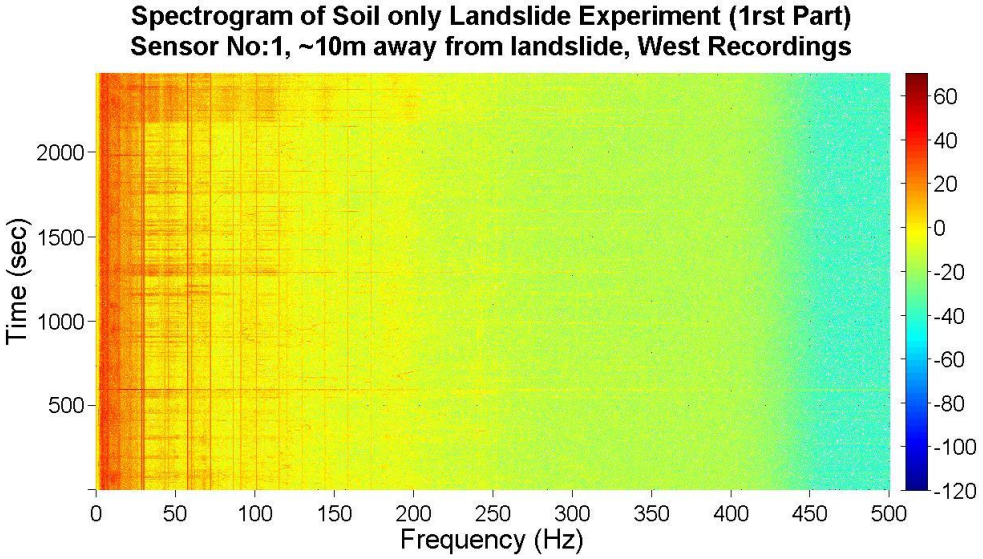

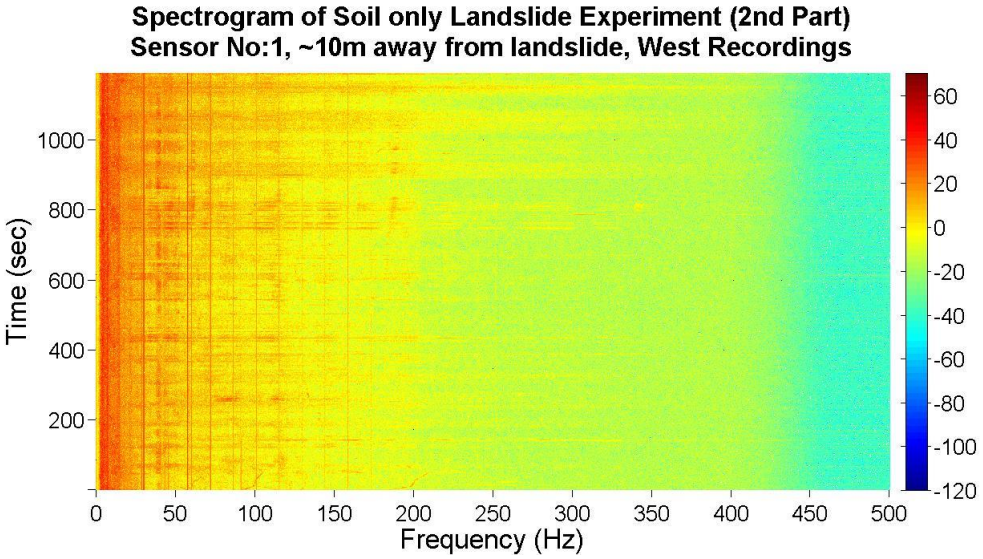

C1.2.2 Spectrograms from data recorded by sensor No11

a) Vertical Component

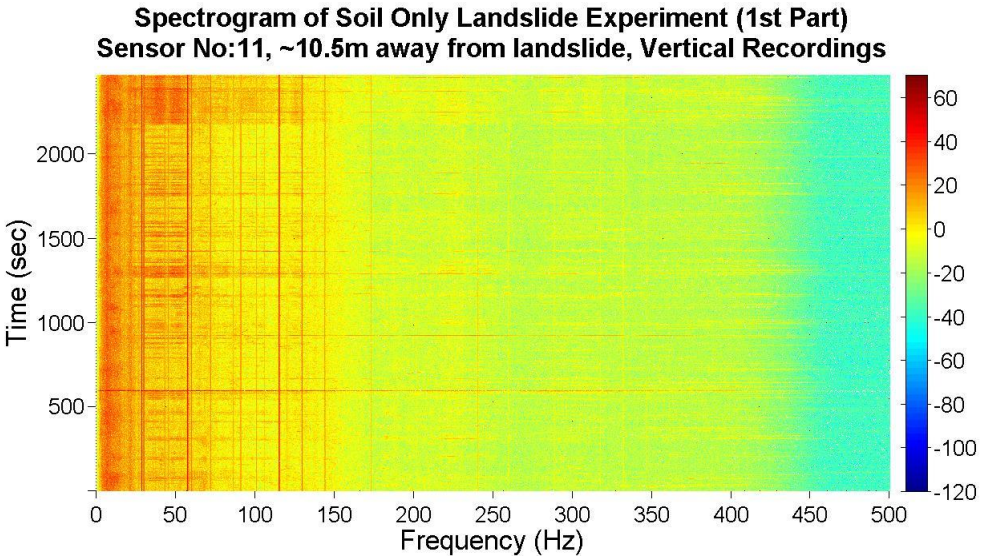

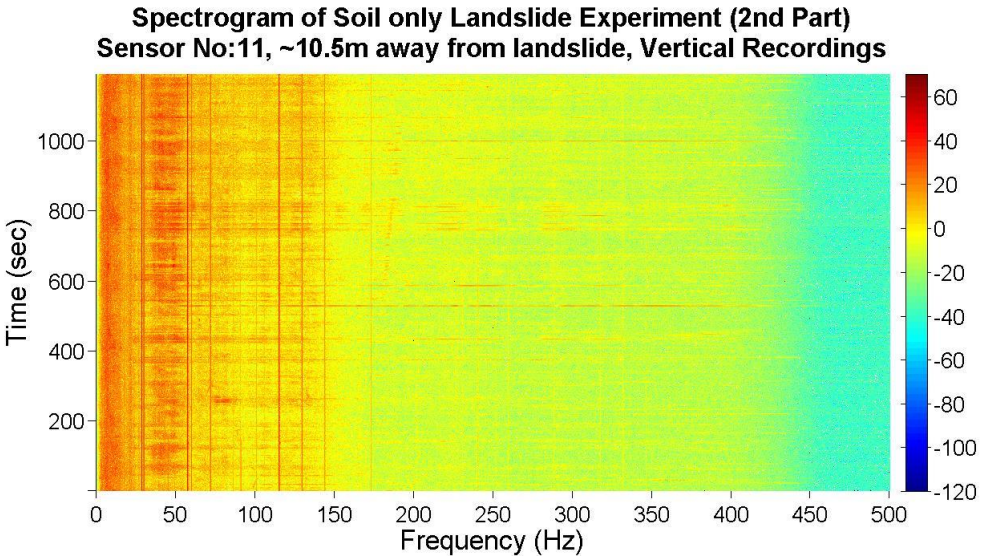

b) North-South Component

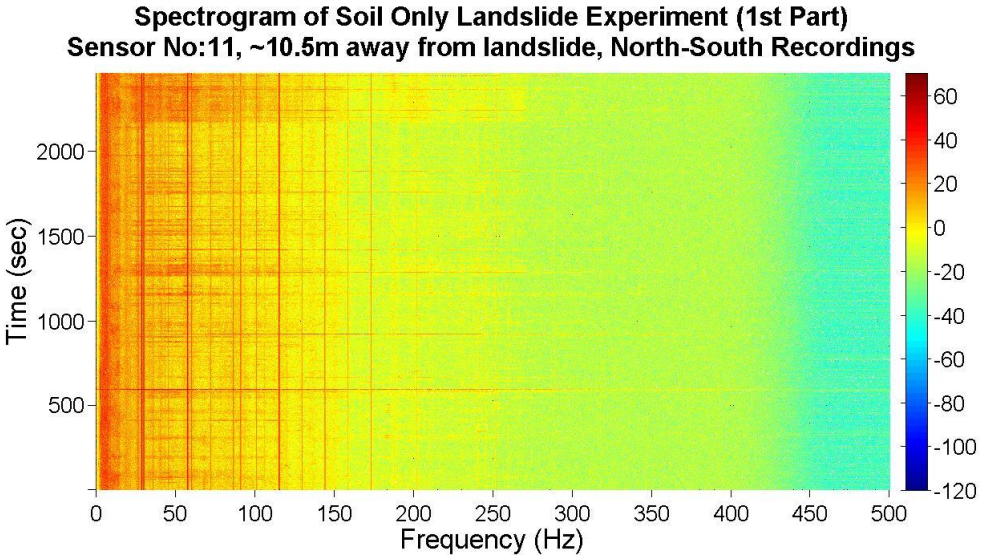

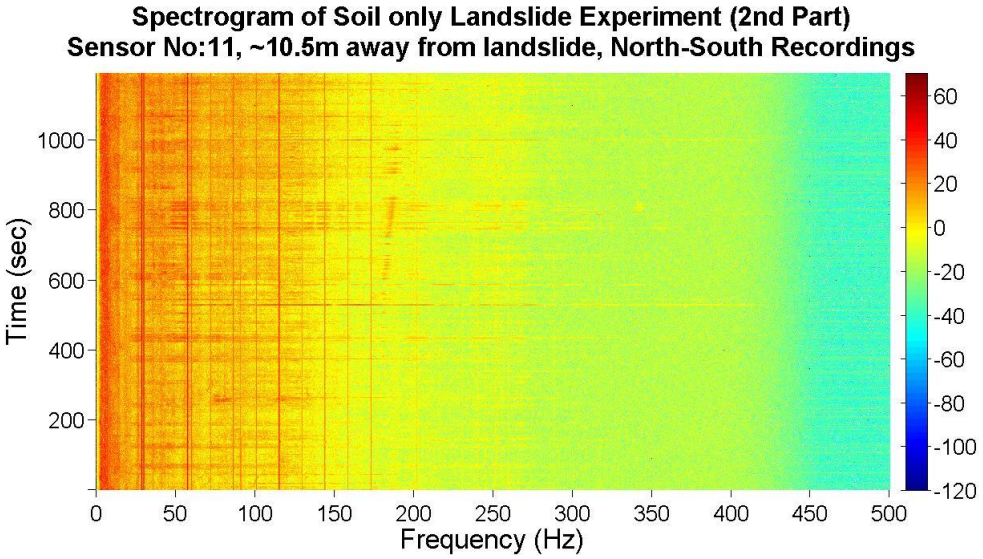

c) East-West Component

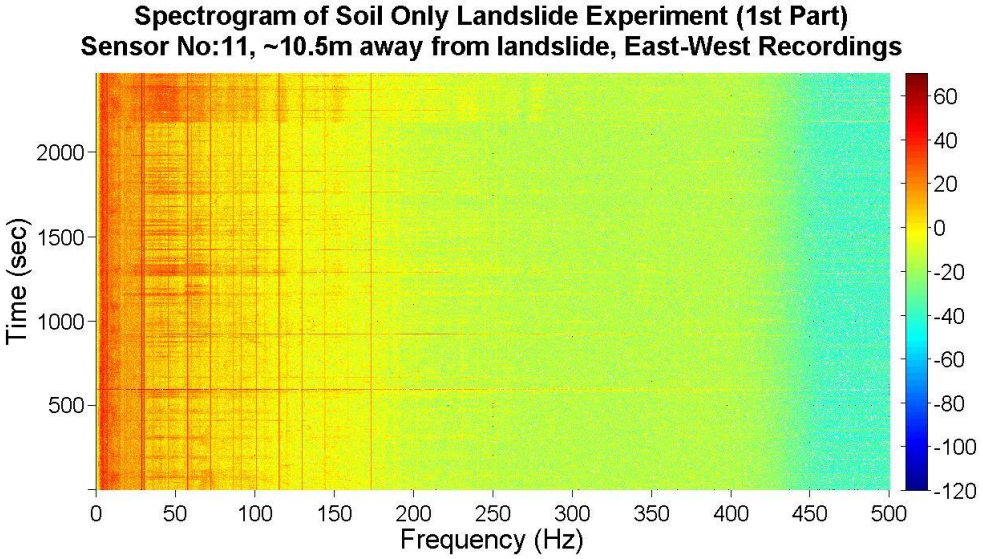

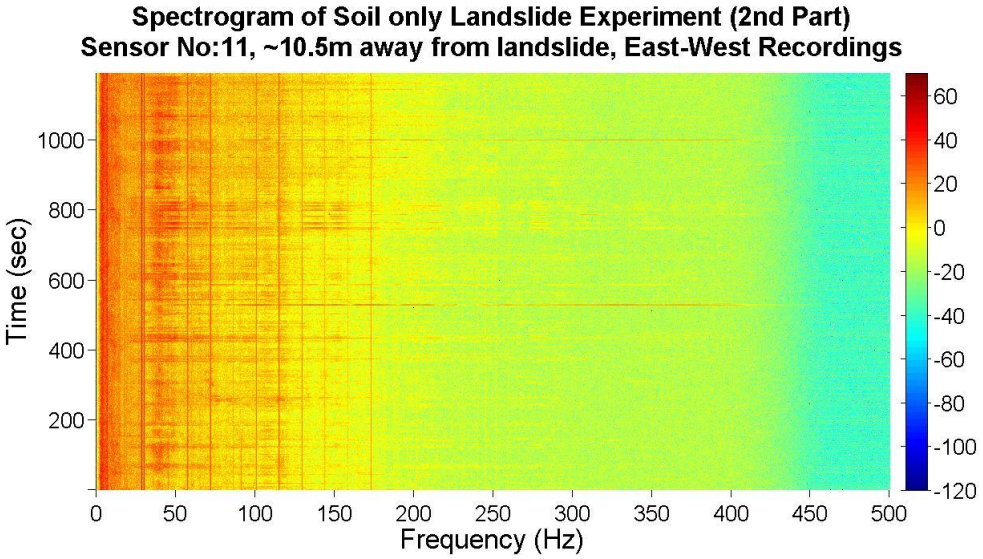

C2 Spectrograms from Section 8.4.3 "Step 3: Interpretation of Spectrograms based on visual observations"

C2.1 Spectrograms of FT3 No.1 failure during Experiment L1 (additional graphs for Figure 8.19a)

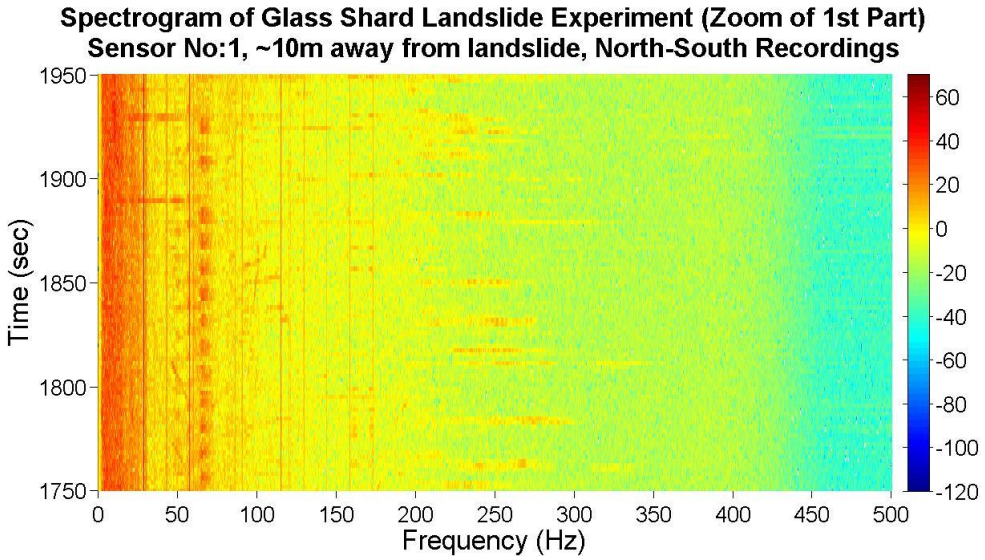

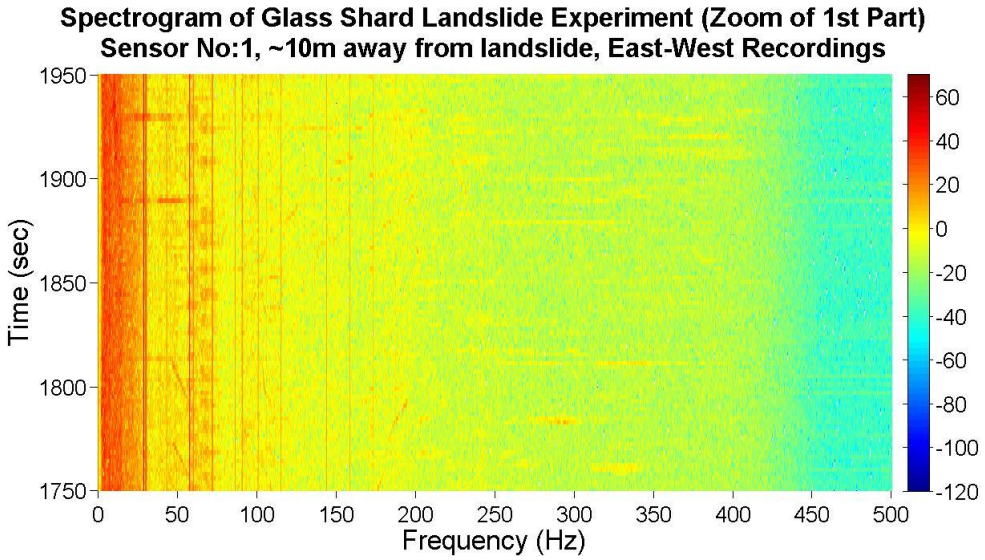

C2.2 Spectrograms of FT3 No.1 failure during Experiment L1 (additional graphs for Figure 8.19b)

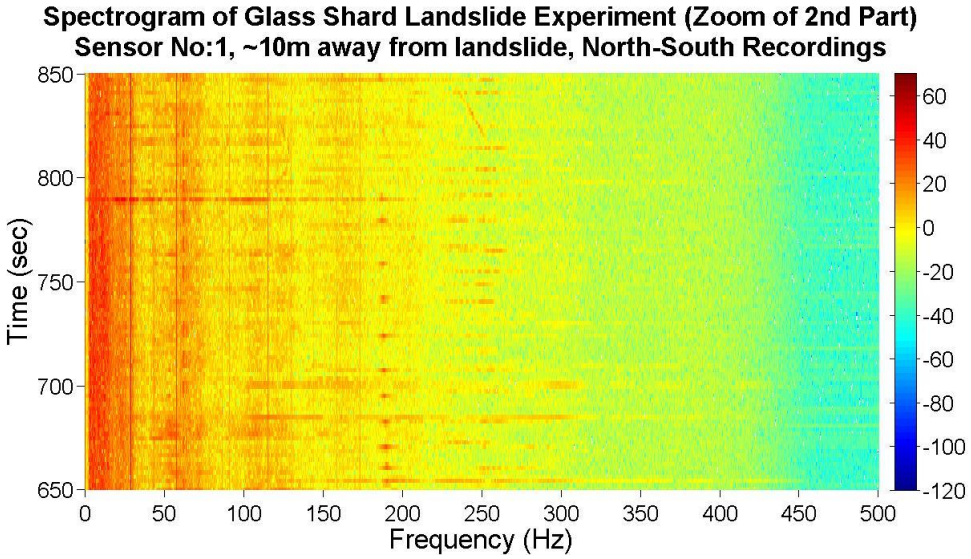

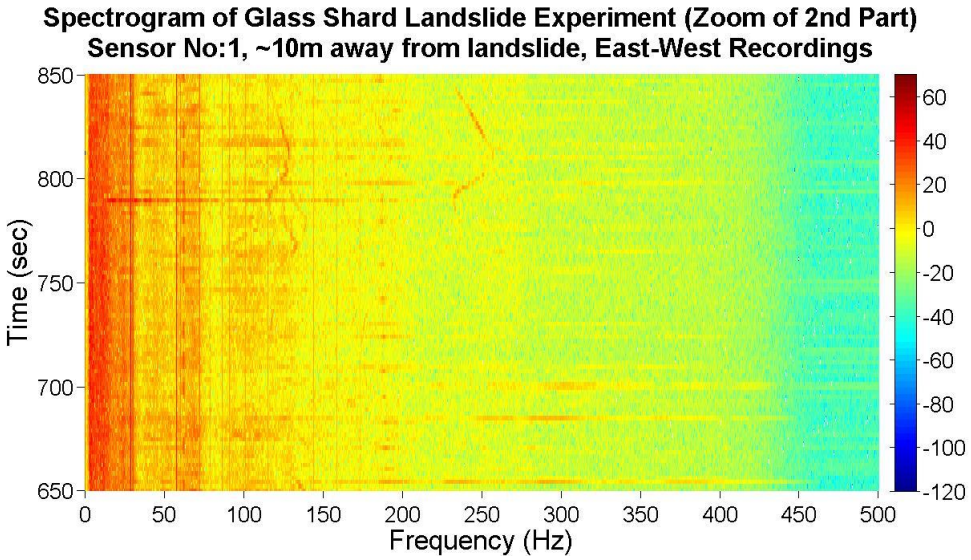

C2.3 Spectrograms of FT3 No.1 failure during Experiment L1 (additional graphs for Figure 8.19c)

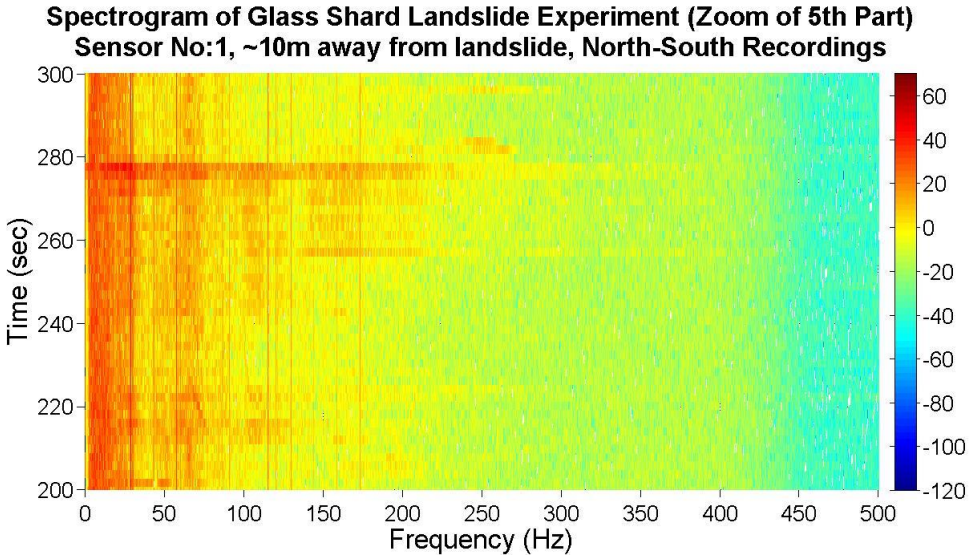

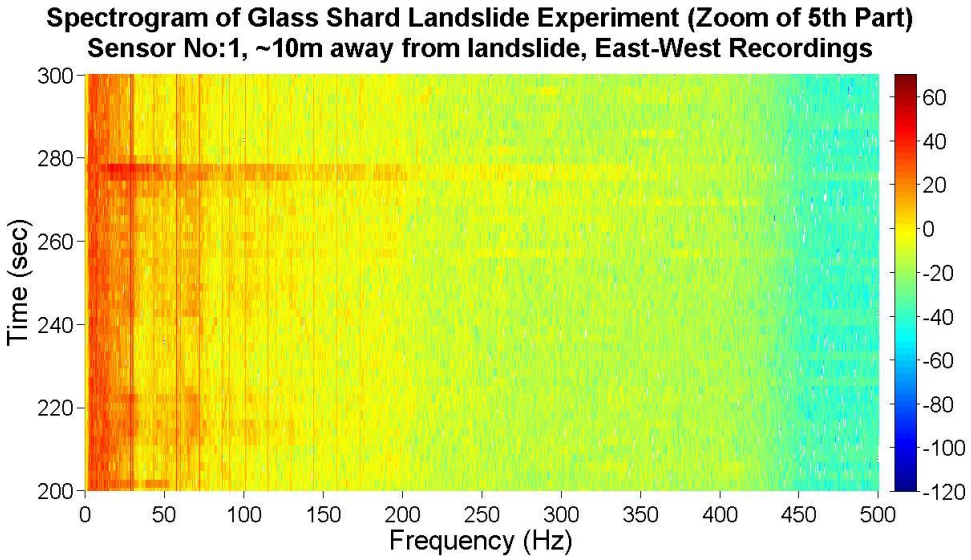

C2.4 Spectrograms of FT3 No.1 failure during Experiment L1 (additional graphs for Figure 8.20a)

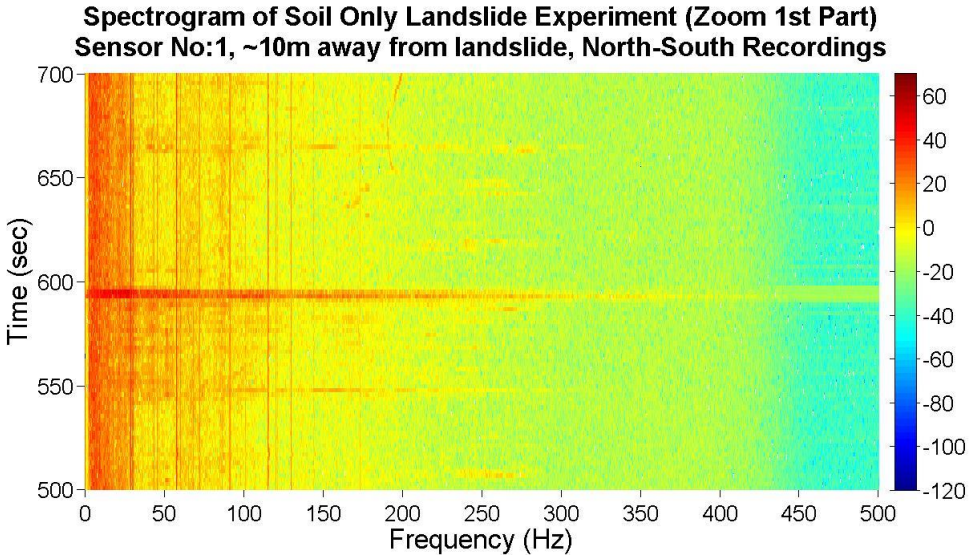

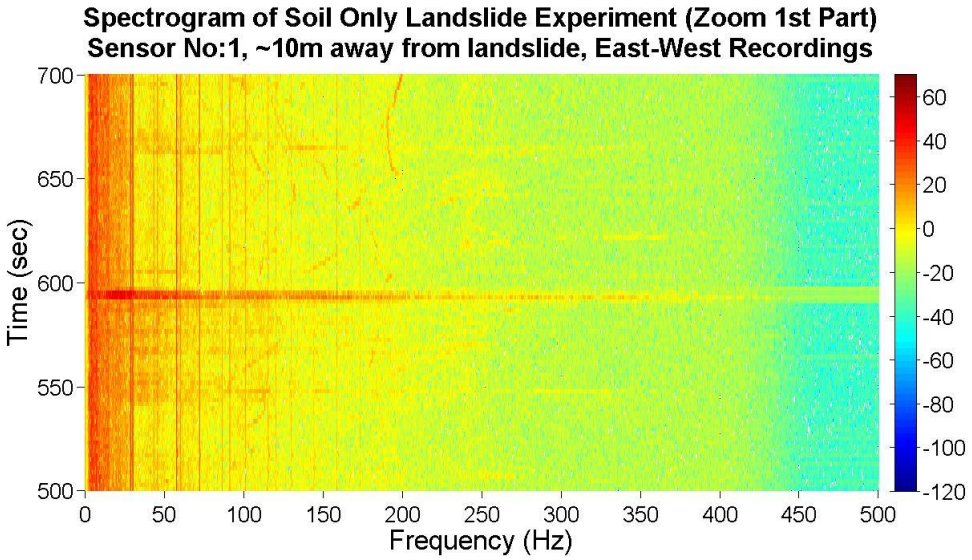

C2.5 Spectrograms of FT3 No.1 failure during Experiment L1 (additional graphs for Figure 8.20b)

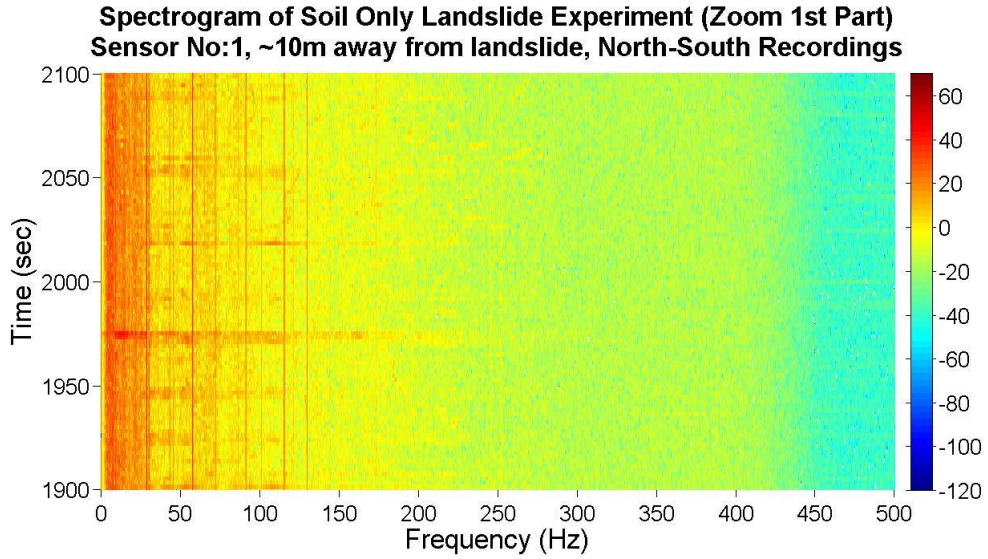

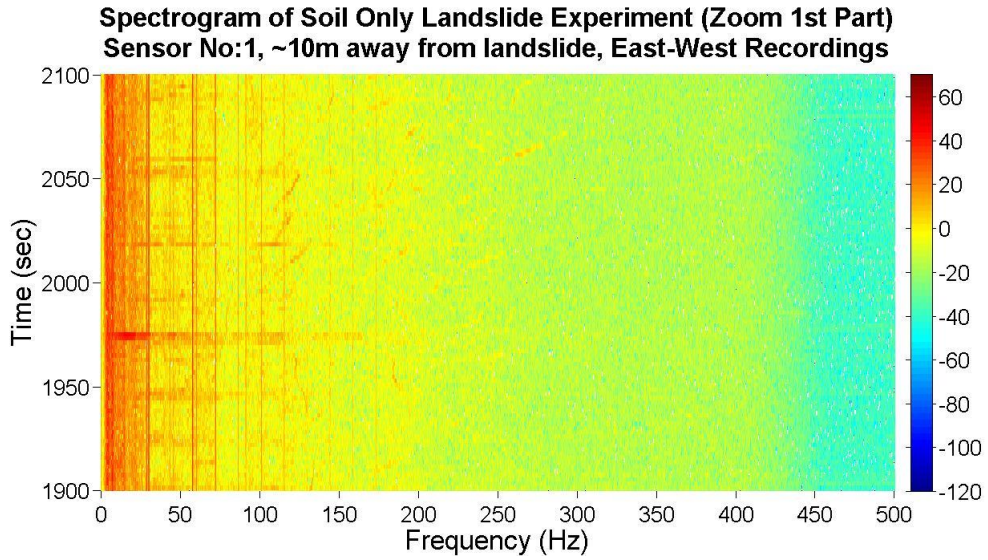

C2.5 Spectrograms of FT3 No.1 failure during Experiment L1 (additional graphs for Figure 8.20c)

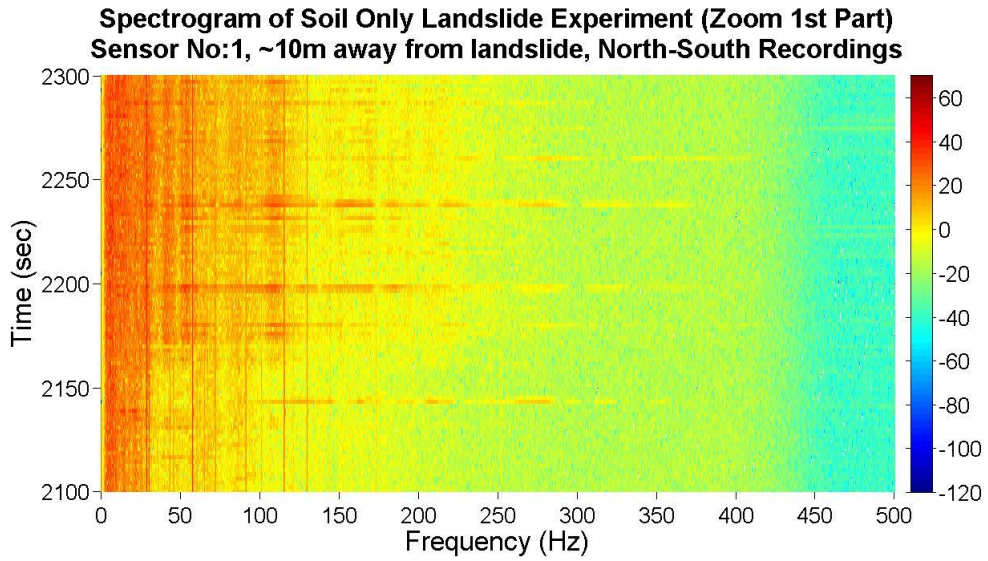

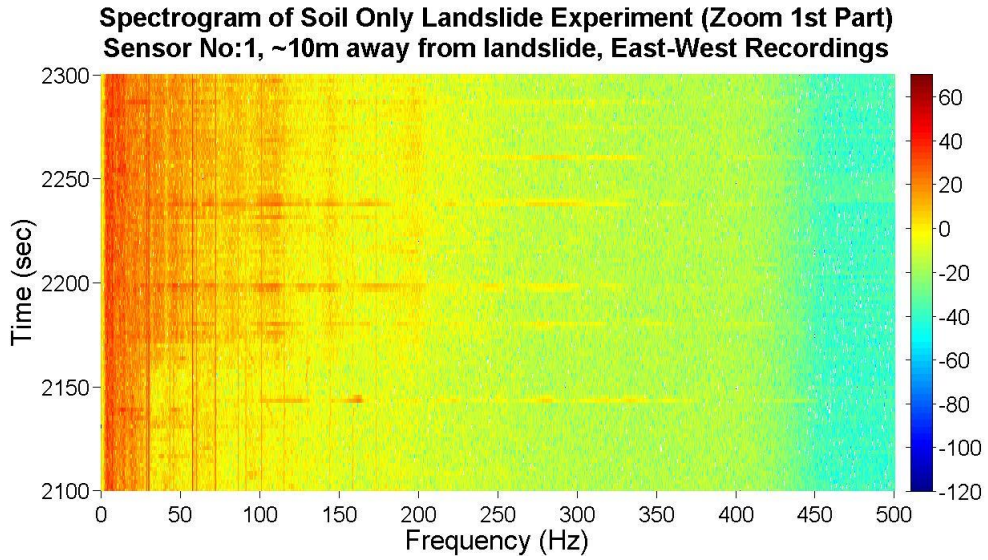

C3 PSD graphs for Section 8.4.4 "Step 4: Spectral analysis of the visually observed landslide failures"

C3.1 Additional PSD graphs for FT1: Crack Formation/Propagation

C3.1.1 Additional PSD graphs of FT1 No2 event of L1 detected before FT2 No1 failure presented at Figure 8.21

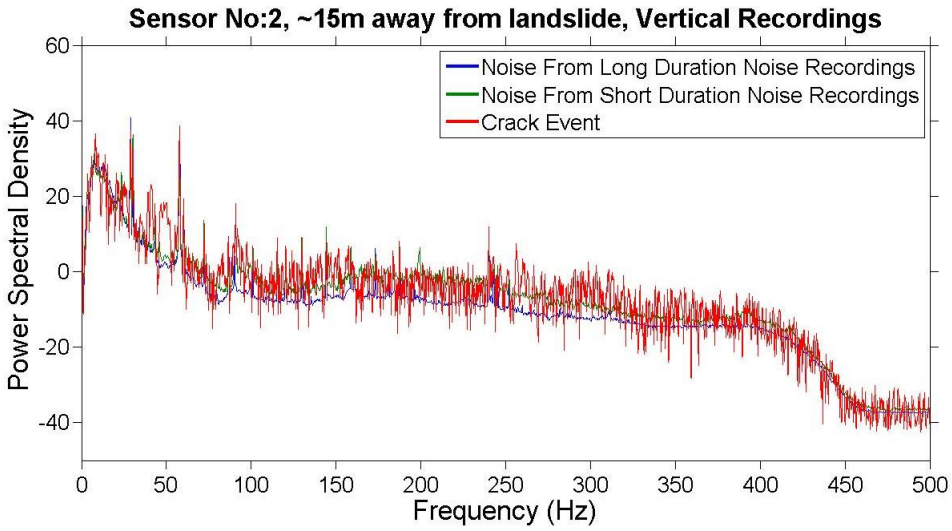

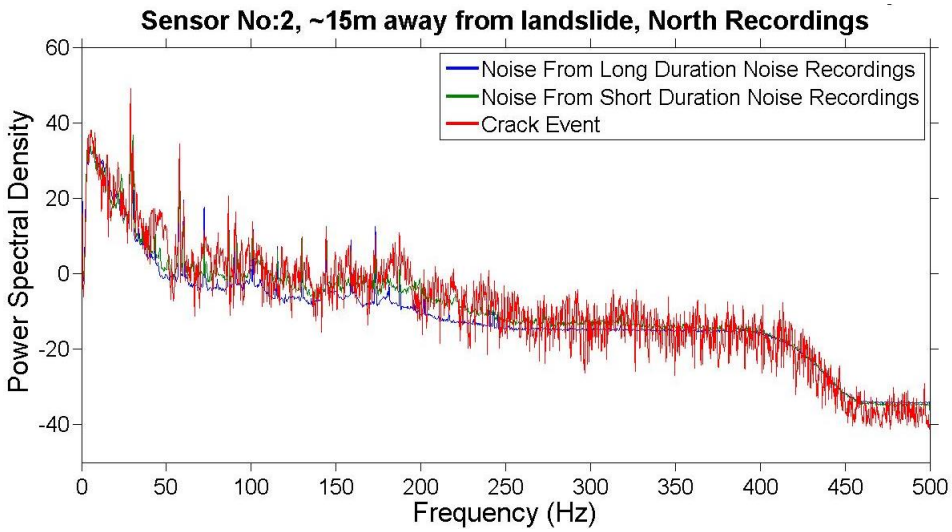

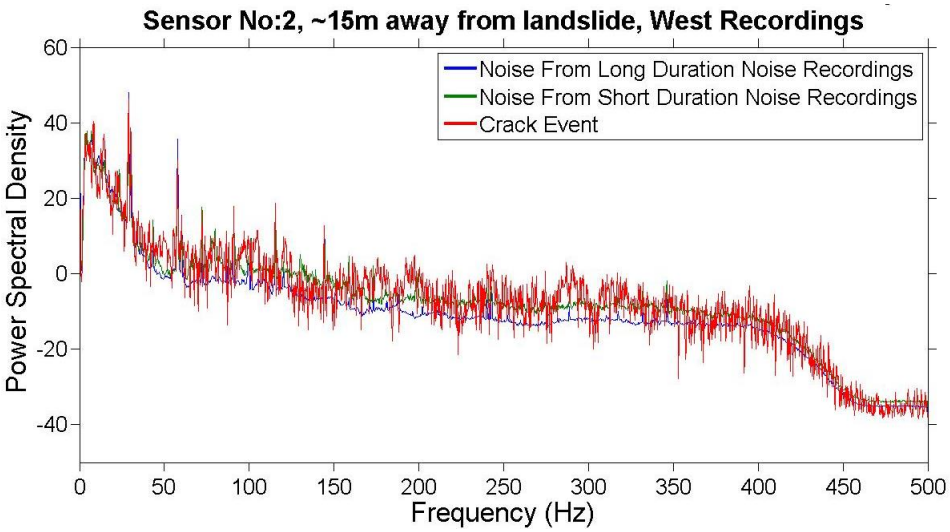

C3.1.2 Additional PSD graphs of FT1 No3 event of L1 detected before FT2 No1 failure presented at Figure 8.21

a) Sensor No1

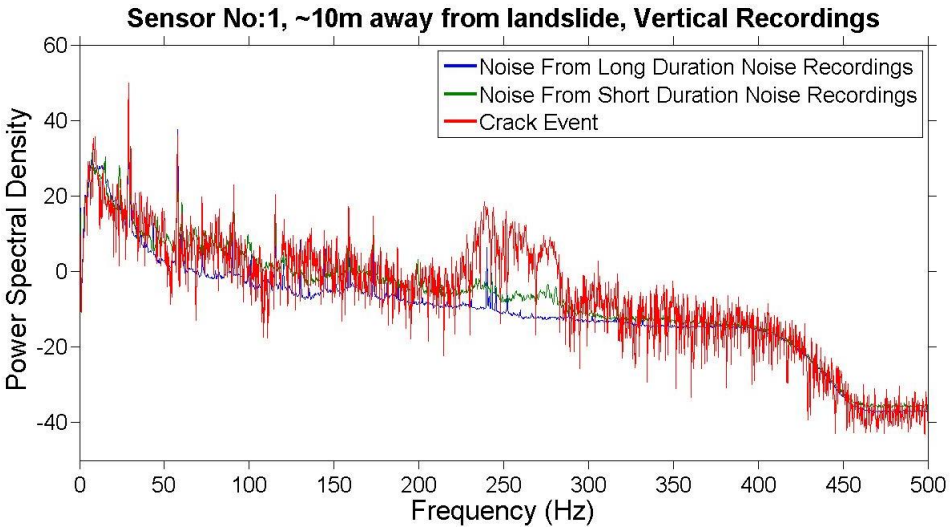

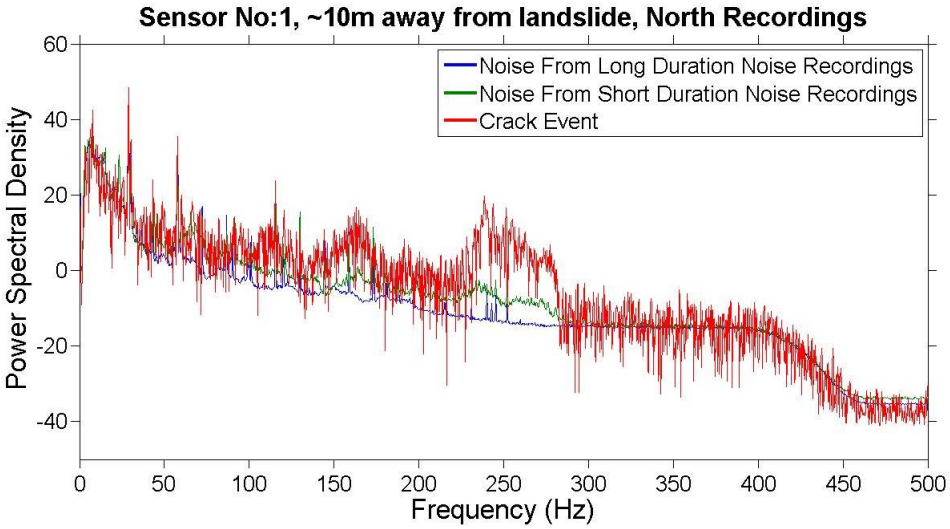
Sensor No:1, ~10m away from landslide, North Recordings
Noise From Long Duration Noise Recordings
Noise From Short Duration Noise Recordings
Crack Event
Power Spectral Density
Frequency (Hz)
60
40
20
0
-20
-40
0
50
100
150
200
250
300
350
400
450
500

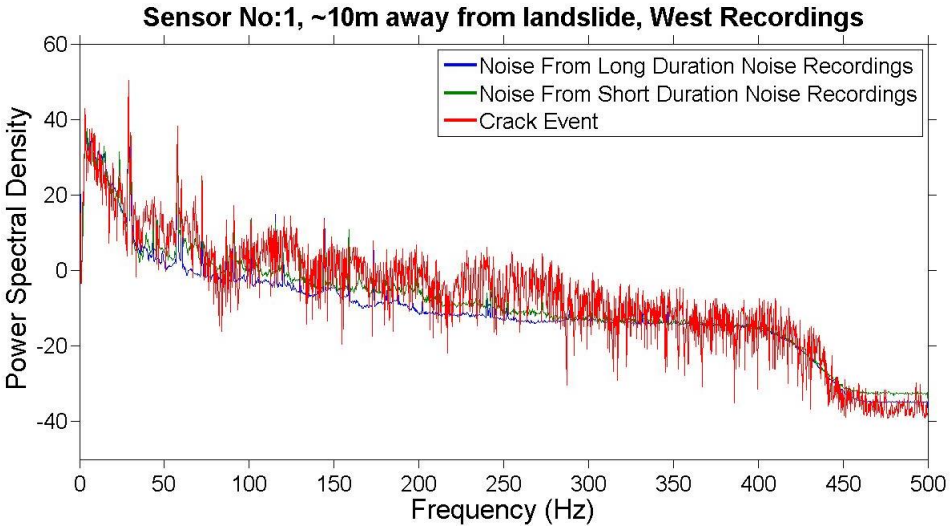
Sensor No:1, ~10m away from landslide, West Recordings
Noise From Long Duration Noise Recordings
Noise From Short Duration Noise Recordings
Crack Event
Power Spectral Density
Frequency (Hz)
60
40
20
0
-20
-40
0
50
100
150
200
250
300
350
400
450
500

b) Sensor No2

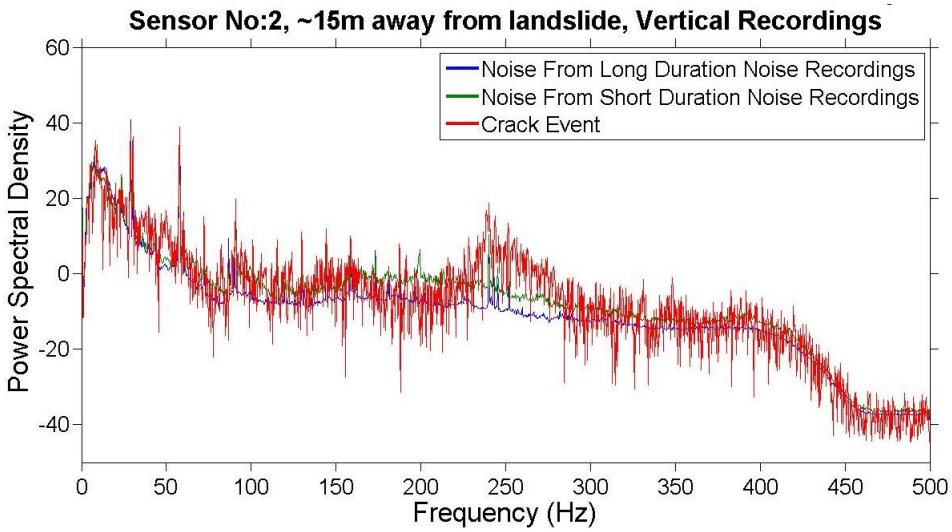
Sensor No:2, ~15m away from landslide, Vertical Recordings
Noise From Long Duration Noise Recordings
Noise From Short Duration Noise Recordings
Crack Event
Power Spectral Density
Frequency (Hz)

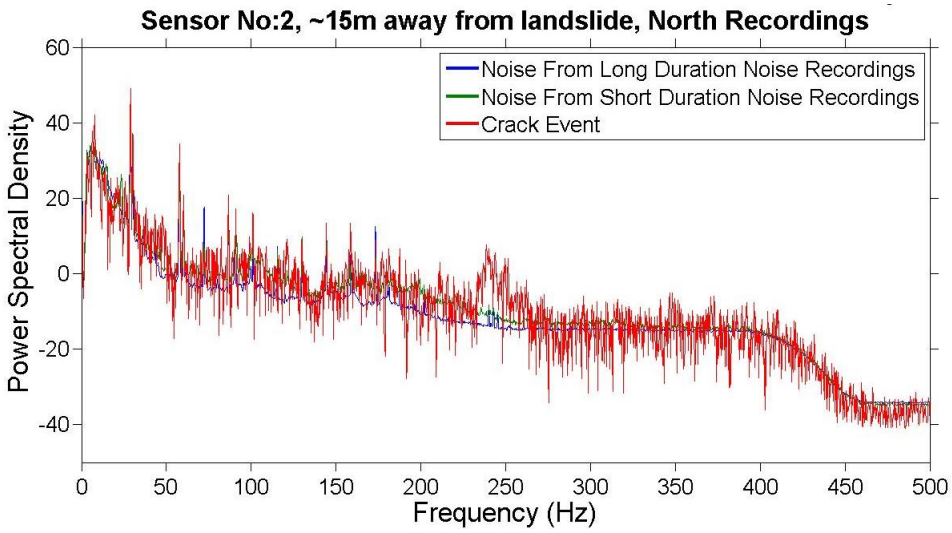
Sensor No:2, ~15m away from landslide, North Recordings
Noise From Long Duration Noise Recordings
Noise From Short Duration Noise Recordings
Crack Event
Power Spectral Density
Frequency (Hz)

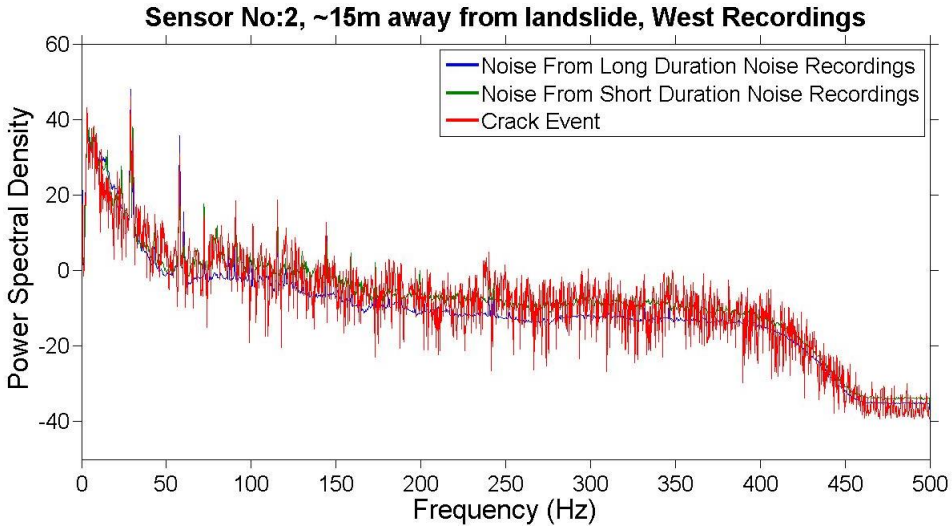
Sensor No:2, ~15m away from landslide, West Recordings
Noise From Long Duration Noise Recordings
Noise From Short Duration Noise Recordings
Crack Event
Power Spectral Density
Frequency (Hz)

C3.1.3 Additional PSD graphs of FT1 No1 event of L1 detected before FT2 No2 failure

a) Sensor No1

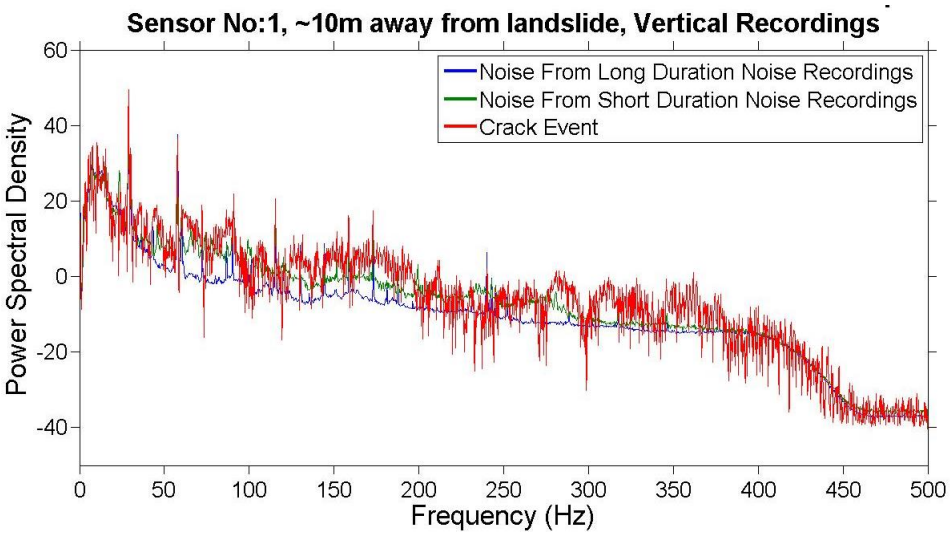

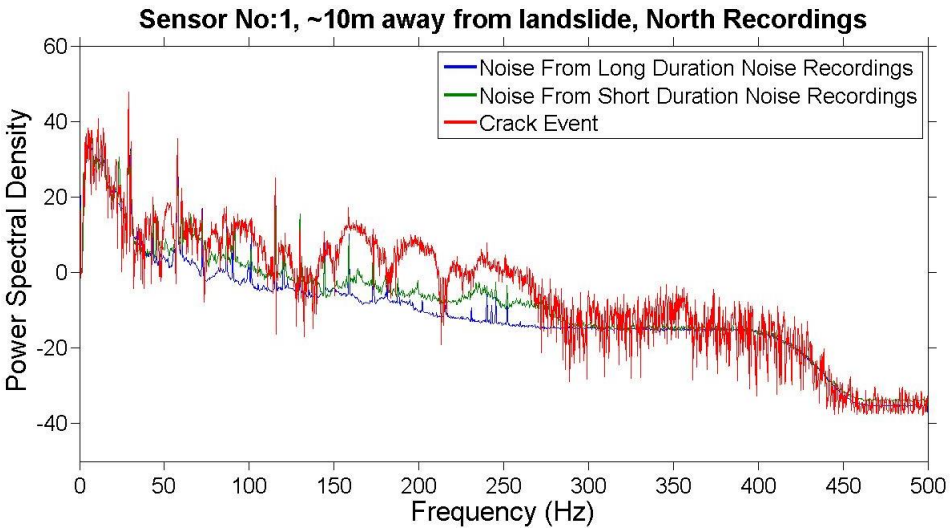

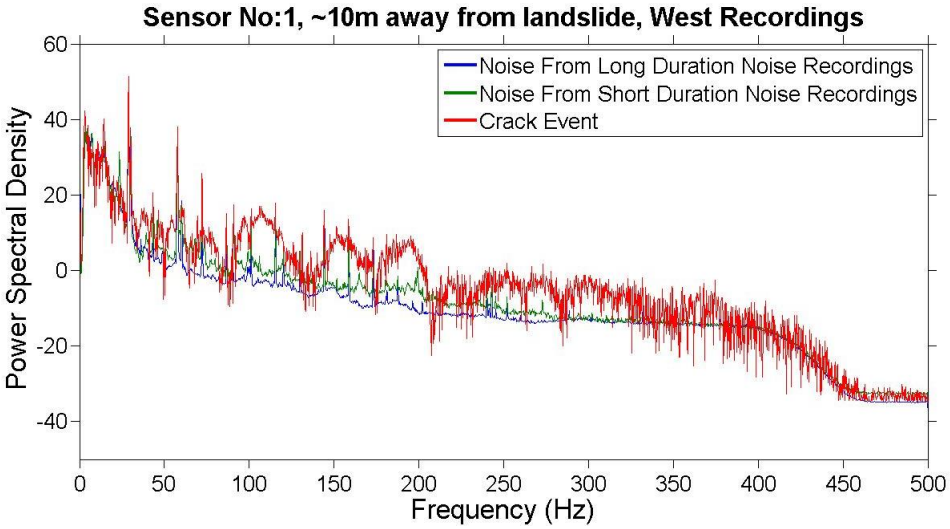
Sensor No:1, ~10m away from landslide, West Recordings
Noise From Long Duration Noise Recordings
Noise From Short Duration Noise Recordings
Crack Event
Power Spectral Density
Frequency (Hz)
60
40
20
0
-20
-40
0
50
100
150
200
250
300
350
400
450
500

b) Sensor No2

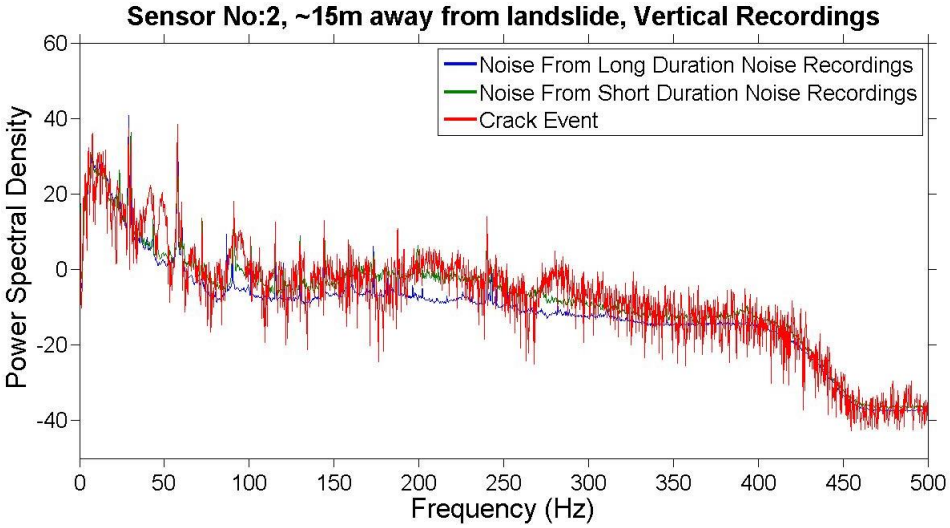
Sensor No:2, ~15m away from landslide, Vertical Recordings
Noise From Long Duration Noise Recordings
Noise From Short Duration Noise Recordings
Crack Event
Power Spectral Density
Frequency (Hz)
60
40
20
0
-20
-40
0
50
100
150
200
250
300
350
400
450
500

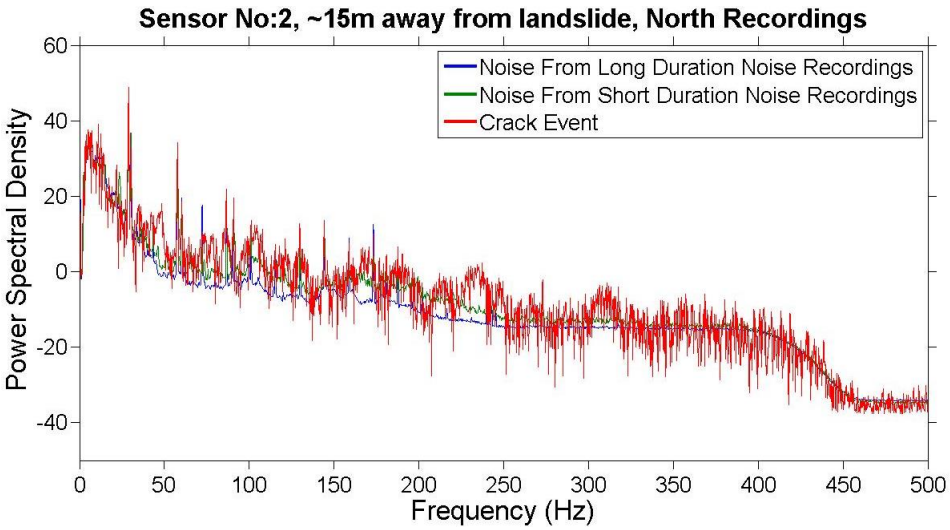
Sensor No:2, ~15m away from landslide, North Recordings
Noise From Long Duration Noise Recordings
Noise From Short Duration Noise Recordings
Crack Event
Power Spectral Density
Frequency (Hz)
60
40
20
0
-20
-40
0
50
100
150
200
250
300
350
400
450
500

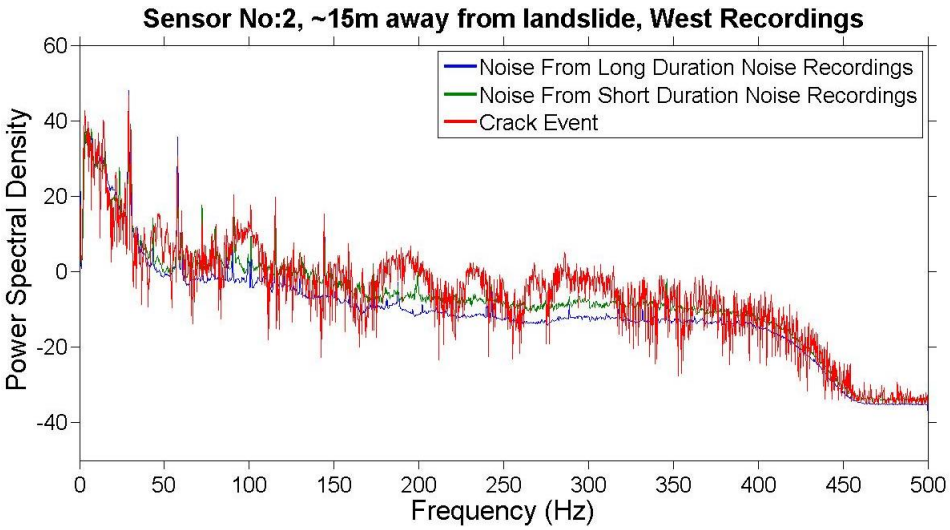
Sensor No:2, ~15m away from landslide, West Recordings
Noise From Long Duration Noise Recordings
Noise From Short Duration Noise Recordings
Crack Event
Power Spectral Density
60
40
20
0
-20
-40
0
50
100
150
200
250
300
350
400
450
500
Frequency (Hz)

C3.1.4 Additional PSD graphs of FT1 No2 event of L1 detected before FT2 No2 failure presented at Figure 8.22

a) Sensor No2

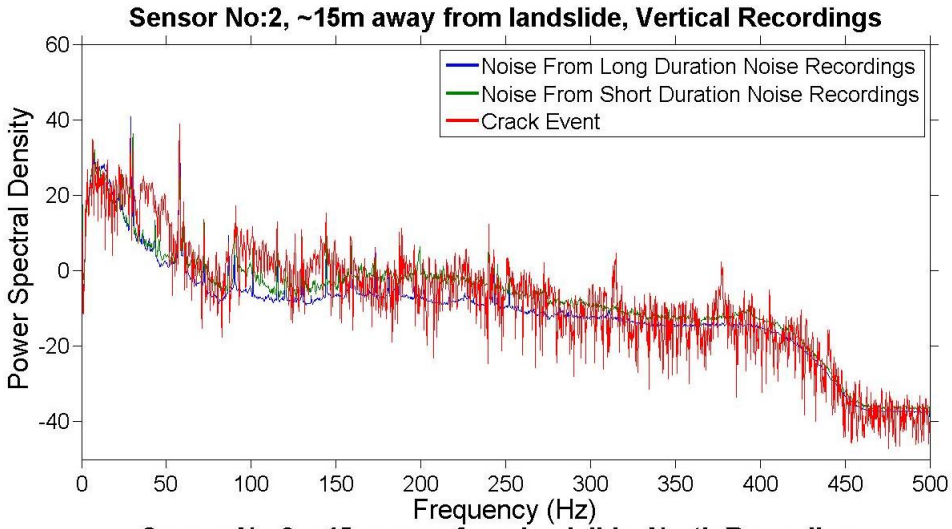

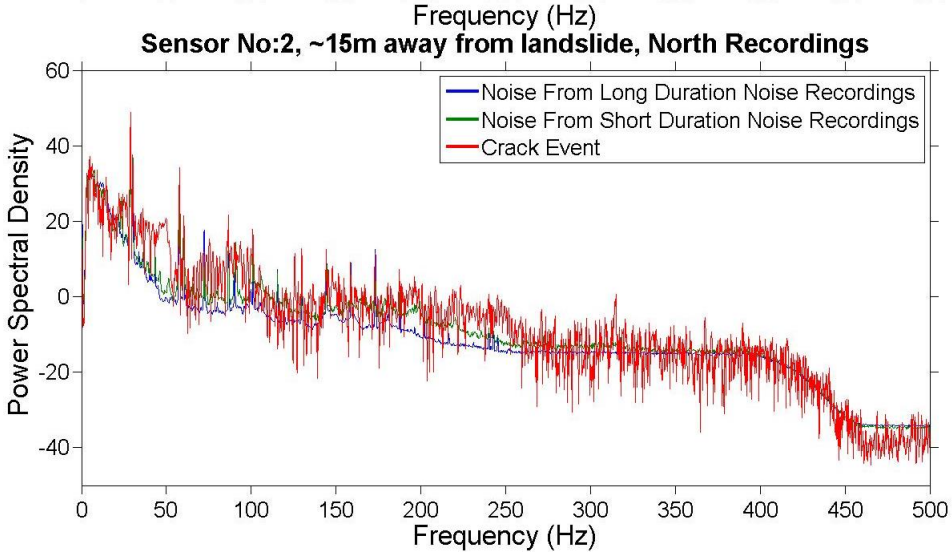

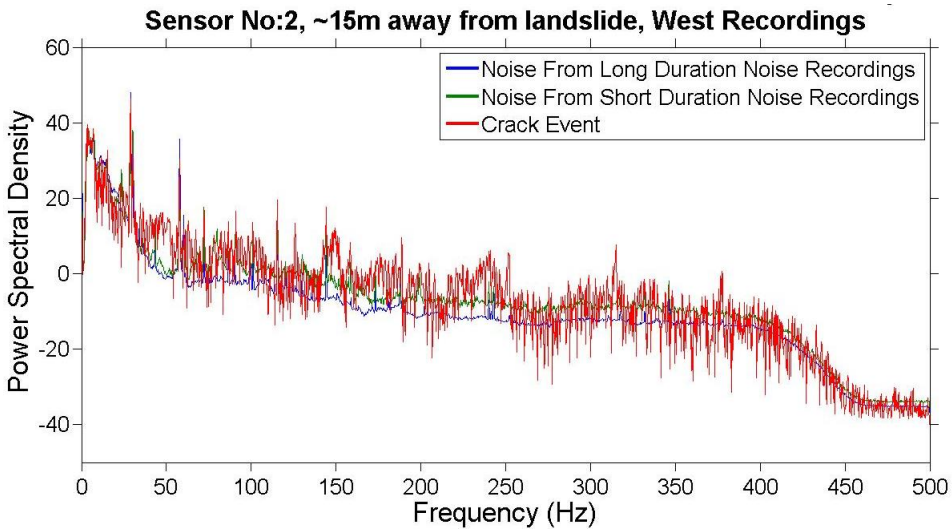

b) Sensor No 4

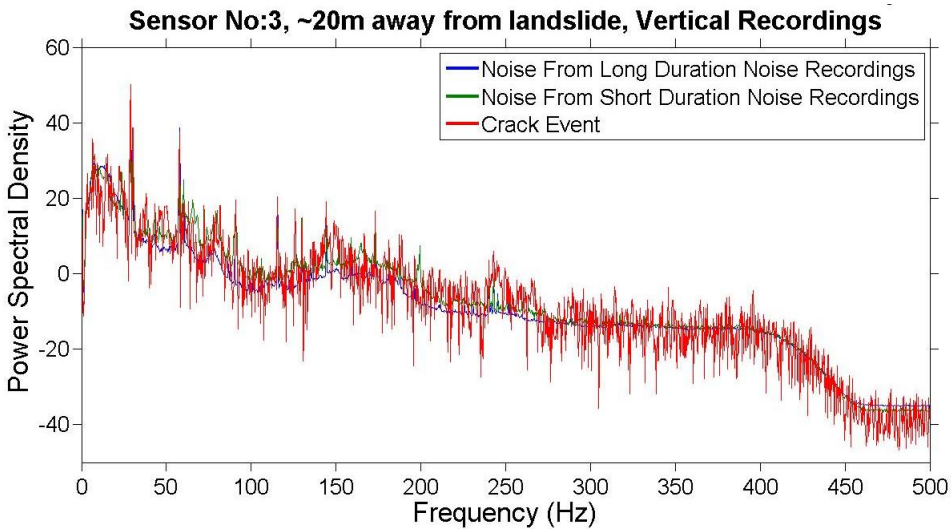
Sensor No:3, ~20m away from landslide, Vertical Recordings
Noise From Long Duration Noise Recordings
Noise From Short Duration Noise Recordings
Crack Event
Power Spectral Density
Frequency (Hz)

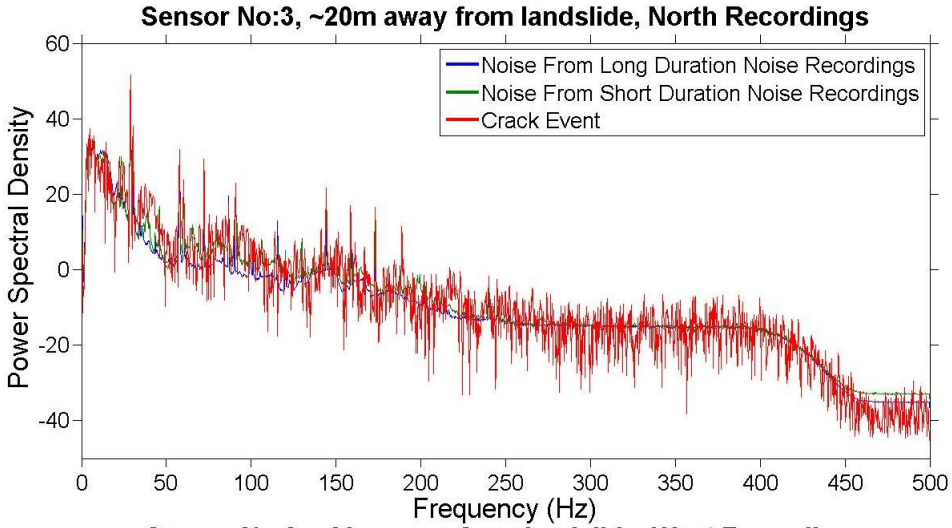
Sensor No:3, ~20m away from landslide, North Recordings
Noise From Long Duration Noise Recordings
Noise From Short Duration Noise Recordings
Crack Event
Power Spectral Density
Frequency (Hz)

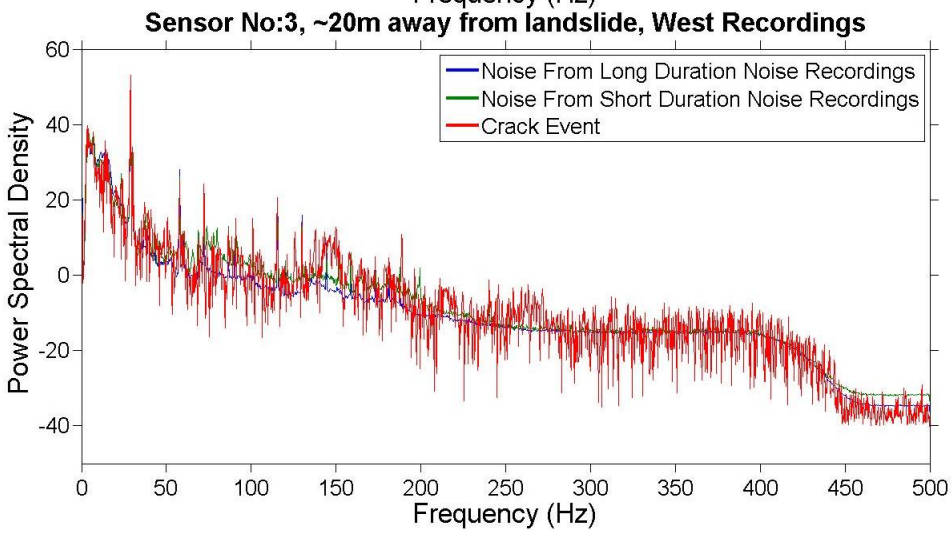
Sensor No:3, ~20m away from landslide, West Recordings
Noise From Long Duration Noise Recordings
Noise From Short Duration Noise Recordings
Crack Event
Power Spectral Density
Frequency (Hz)

c) Sensor No11

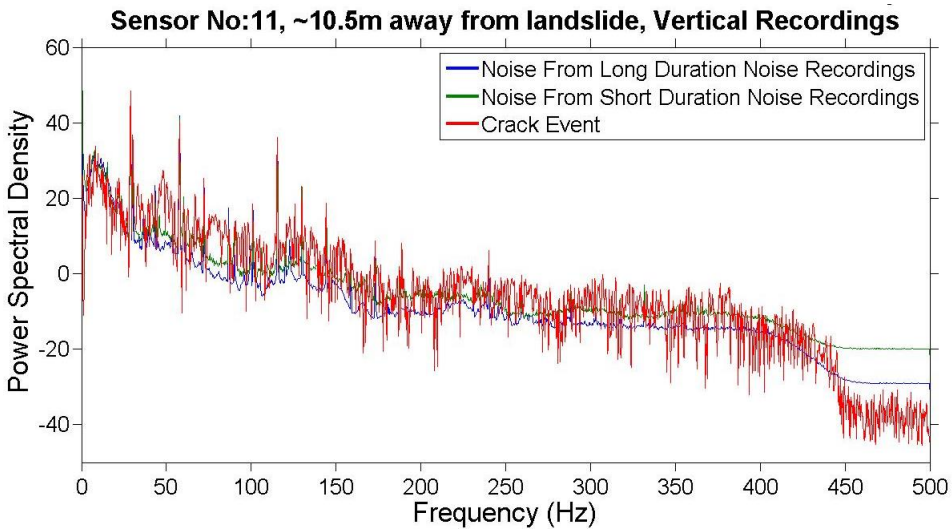

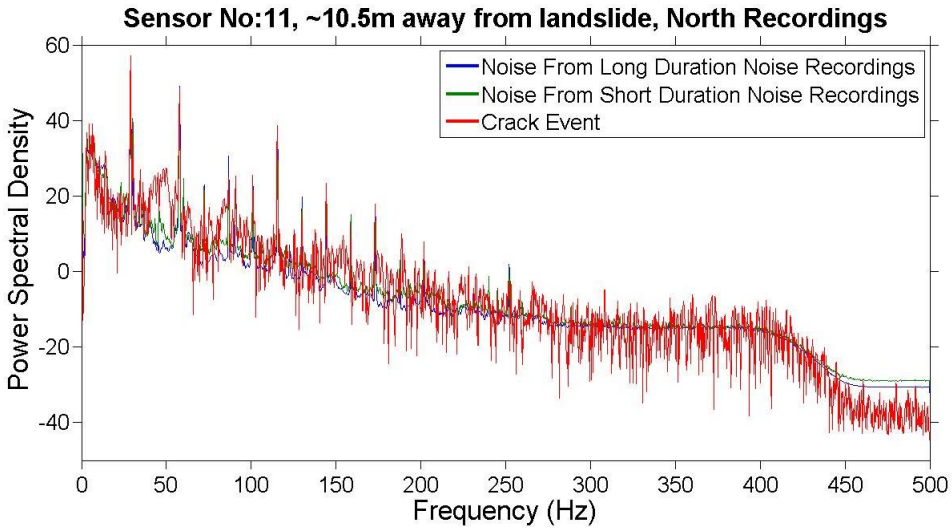

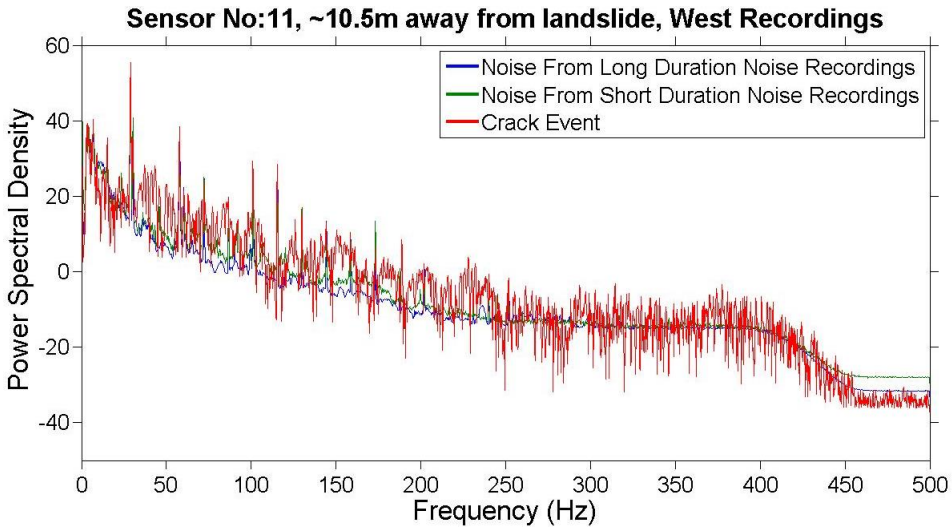

C3.1.5 Additional PSD graphs of FT1 No3 event of L1 detected before FT2 No2 failure

a) Sensor No1

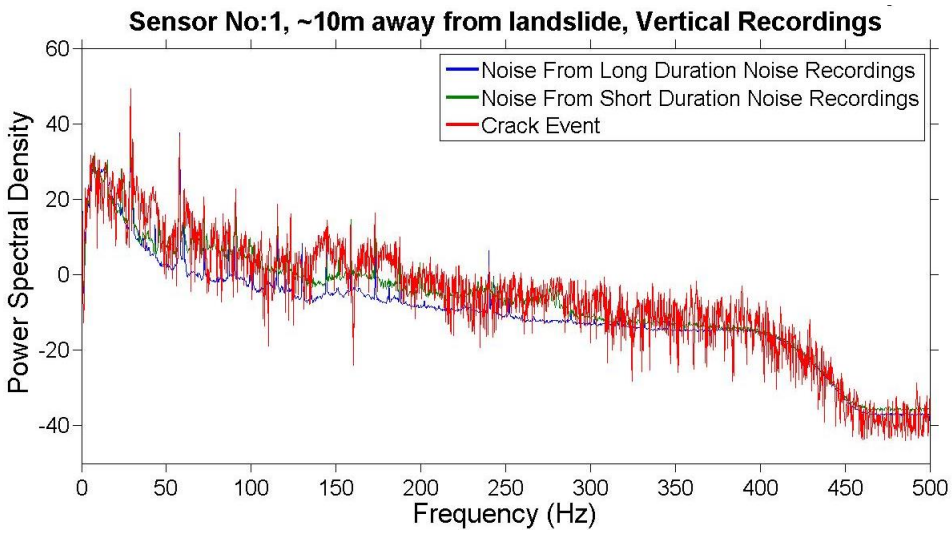

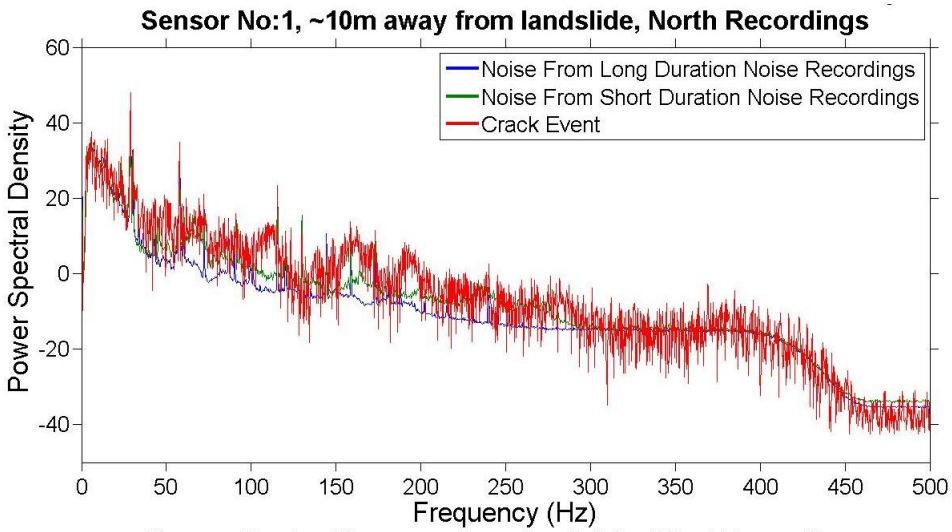

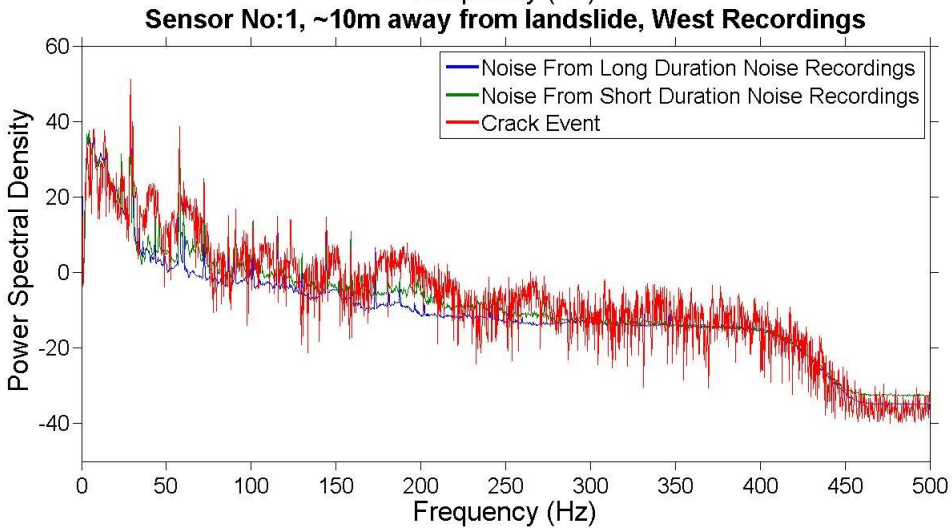

b) Sensor No2

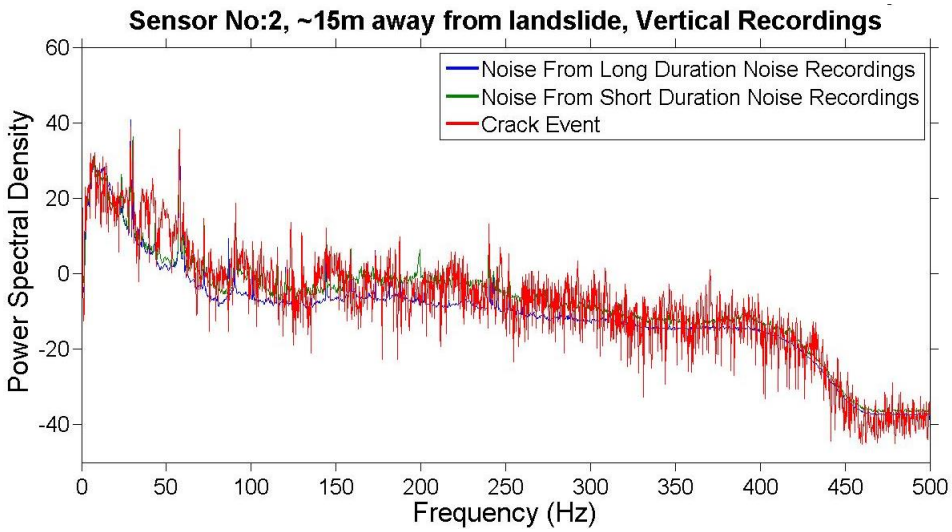
Sensor No:2, ~15m away from landslide, Vertical Recordings
Noise From Long Duration Noise Recordings
Noise From Short Duration Noise Recordings
Crack Event
Power Spectral Density
Frequency (Hz)

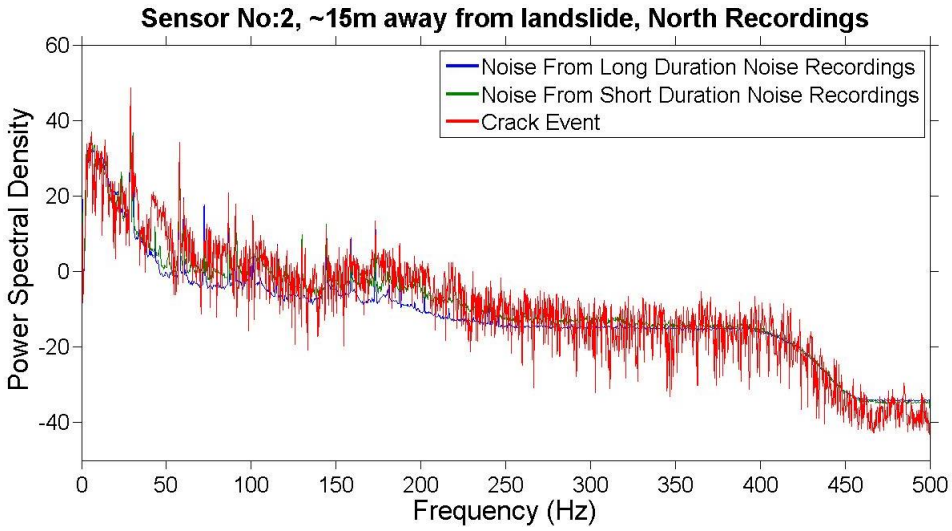
Sensor No:2, ~15m away from landslide, North Recordings
Noise From Long Duration Noise Recordings
Noise From Short Duration Noise Recordings
Crack Event
Power Spectral Density
Frequency (Hz)

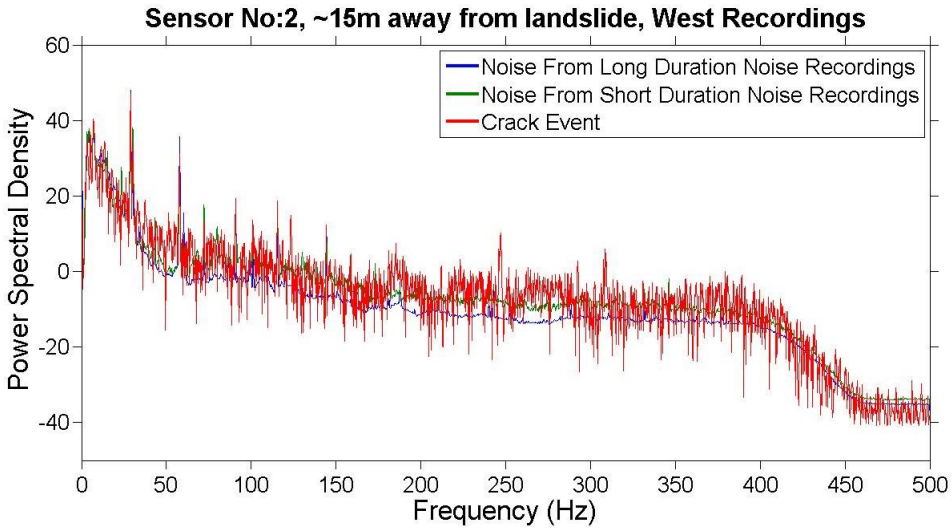
Sensor No:2, ~15m away from landslide, West Recordings
Noise From Long Duration Noise Recordings
Noise From Short Duration Noise Recordings
Crack Event
Power Spectral Density
Frequency (Hz)

c) Sensor No3

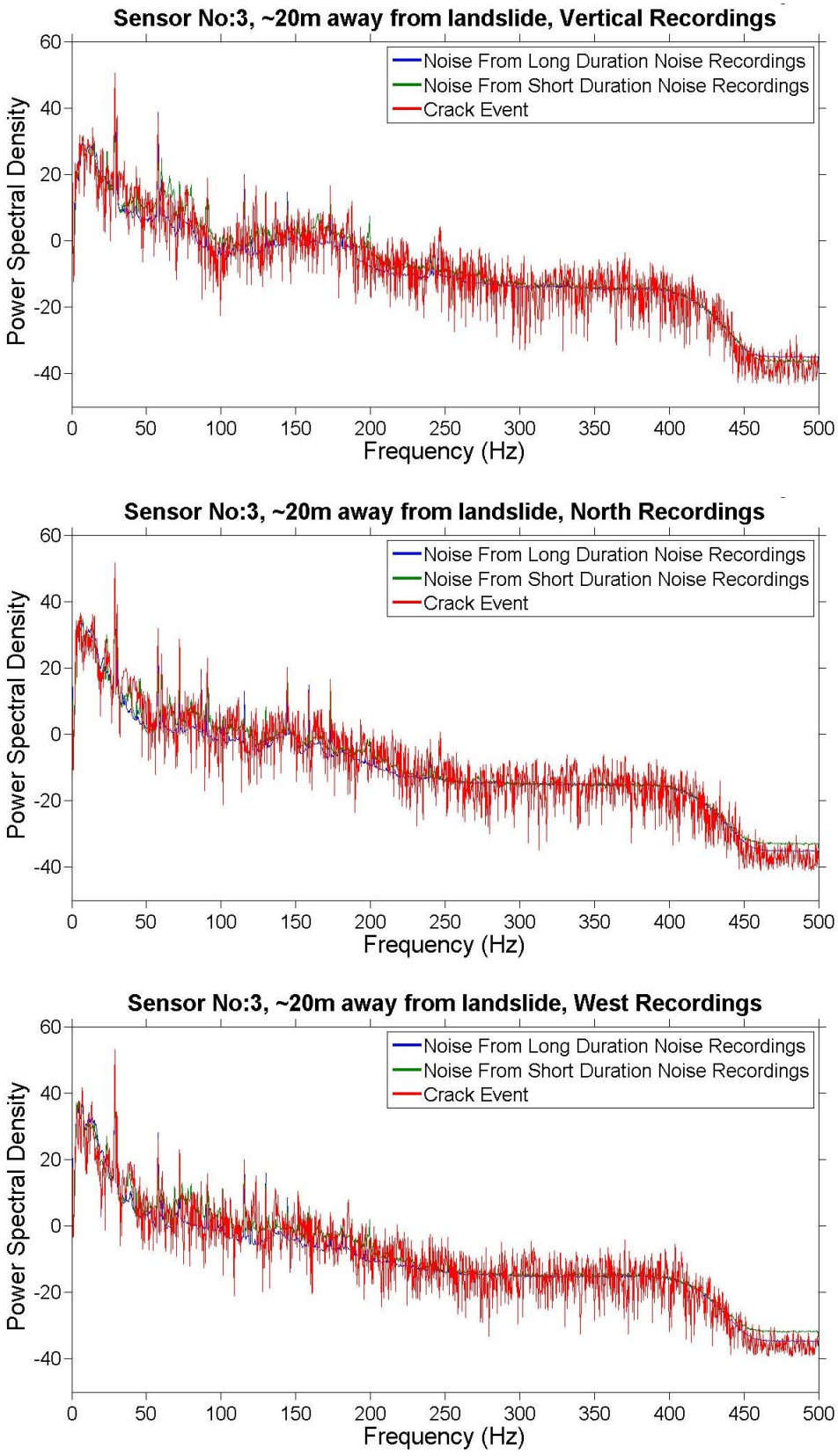
Sensor No:3, ~20m away from landslide, Vertical Recordings
Noise From Long Duration Noise Recordings
Noise From Short Duration Noise Recordings
Crack Event
Power Spectral Density
Frequency (Hz)
Sensor No:3, ~20m away from landslide, North Recordings
Noise From Long Duration Noise Recordings
Noise From Short Duration Noise Recordings
Crack Event
Power Spectral Density
Frequency (Hz)
Sensor No:3, ~20m away from landslide, West Recordings
Noise From Long Duration Noise Recordings
Noise From Short Duration Noise Recordings
Crack Event
Power Spectral Density
Frequency (Hz)

d) Sensor No11

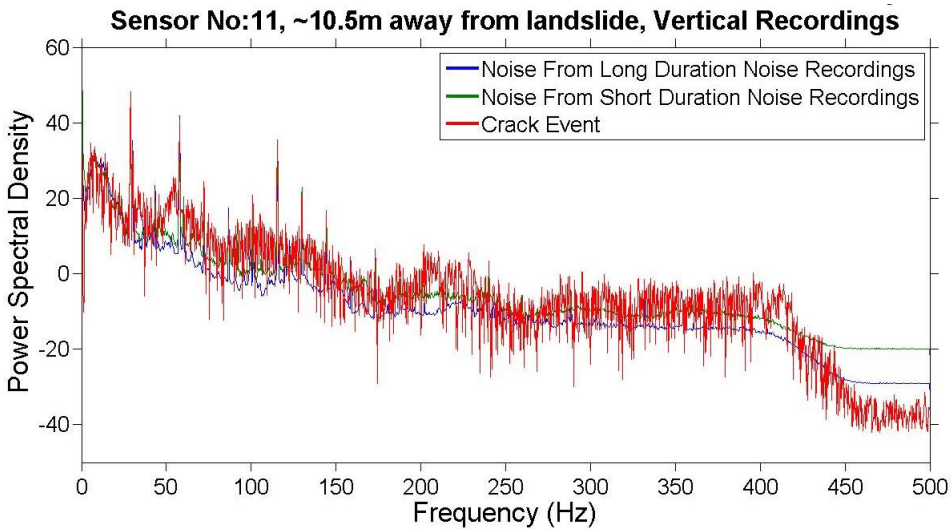

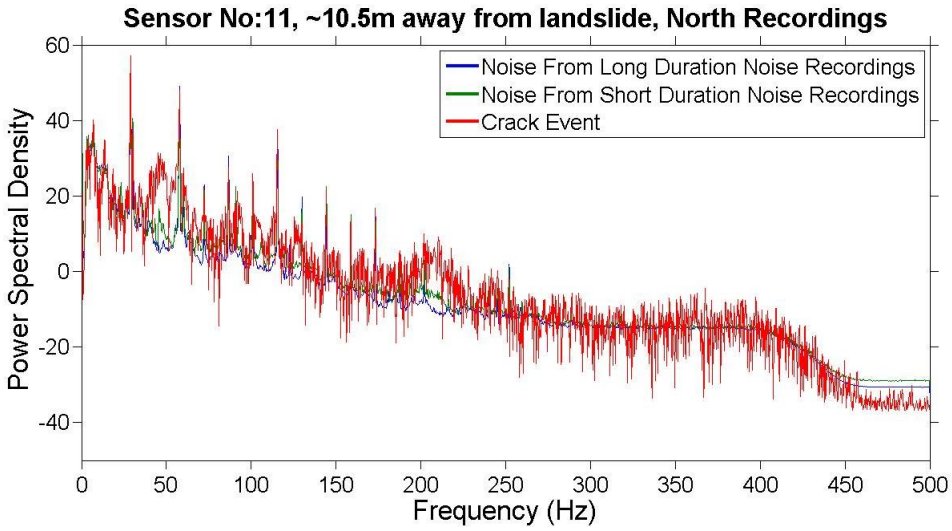

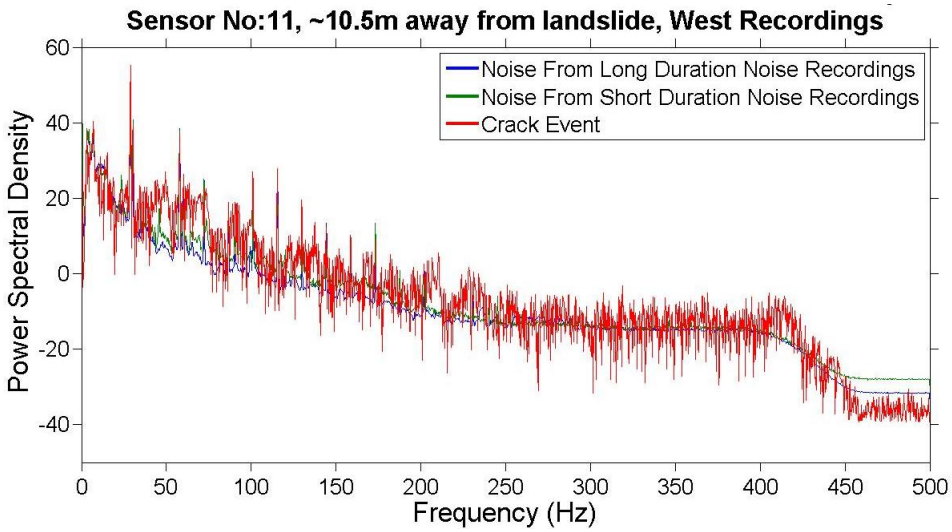

C3.2 Additional PSD graphs for FT2: Soil block topple and fall

C3.2.1 Additional PSD graphs of FT2 No1 event presented at Figure 8.23

a) Vertical Component

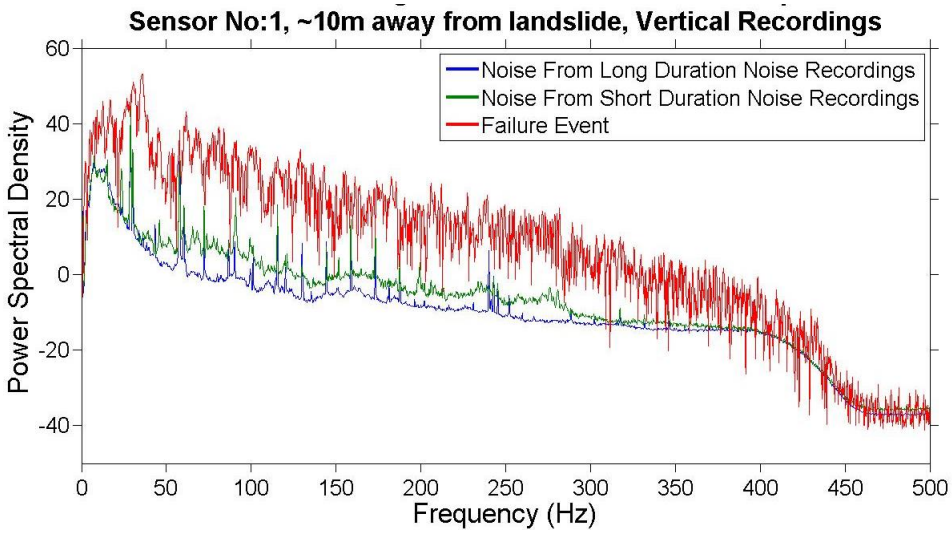

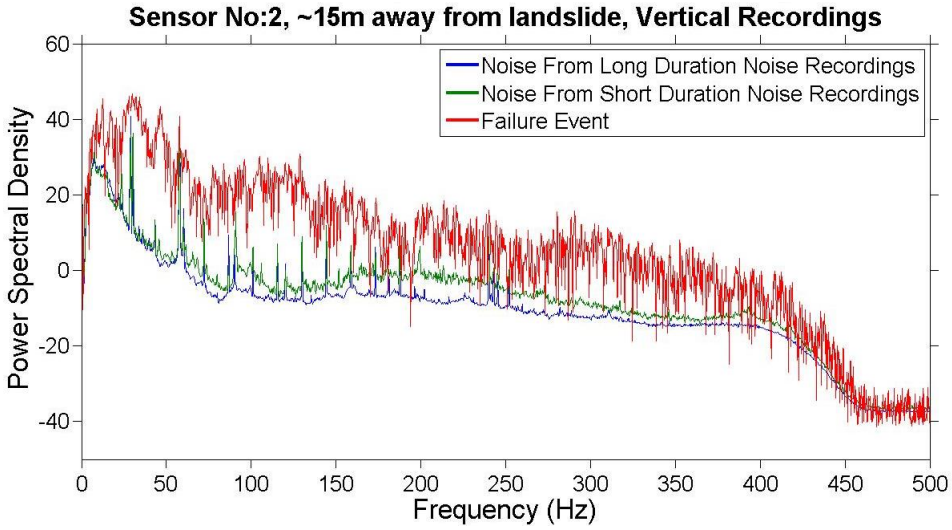

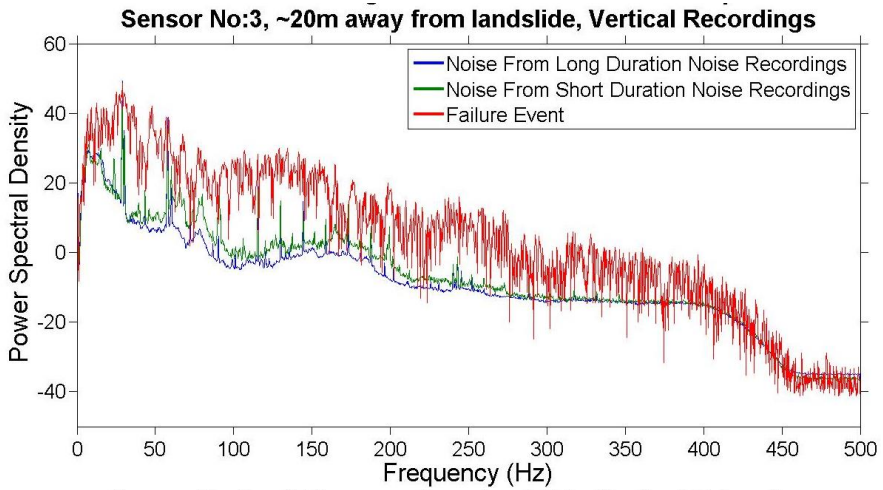
Sensor No:3, ~20m away from landslide, Vertical Recordings
Noise From Long Duration Noise Recordings
Noise From Short Duration Noise Recordings
Failure Event
Power Spectral Density
Frequency (Hz)

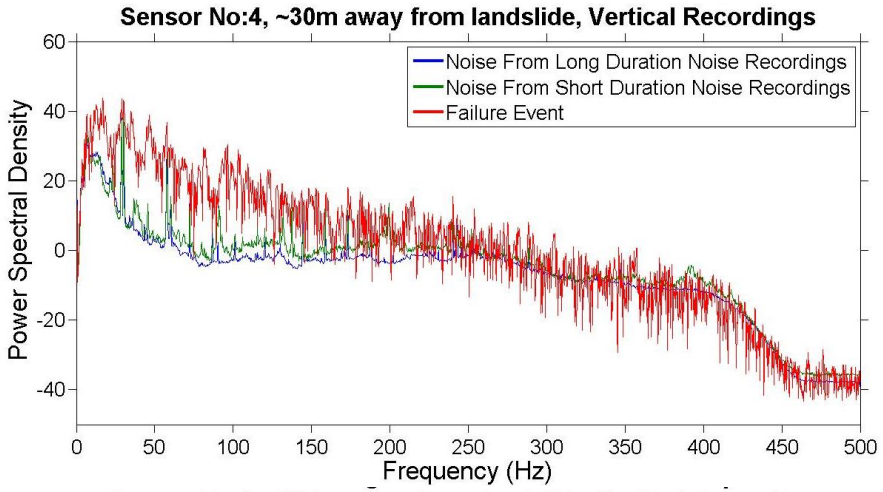
Sensor No:4, ~30m away from landslide, Vertical Recordings
Noise From Long Duration Noise Recordings
Noise From Short Duration Noise Recordings
Failure Event
Power Spectral Density
Frequency (Hz)

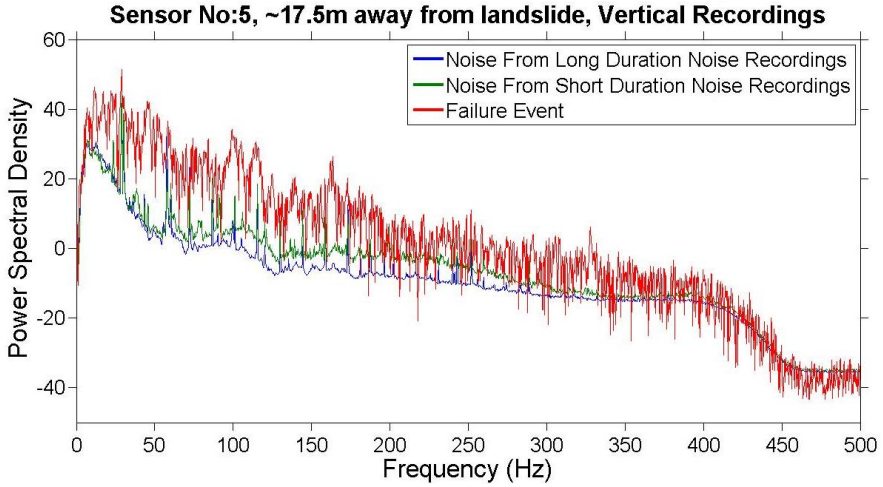
Sensor No:5, ~17.5m away from landslide, Vertical Recordings
Noise From Long Duration Noise Recordings
Noise From Short Duration Noise Recordings
Failure Event
Power Spectral Density
Frequency (Hz)

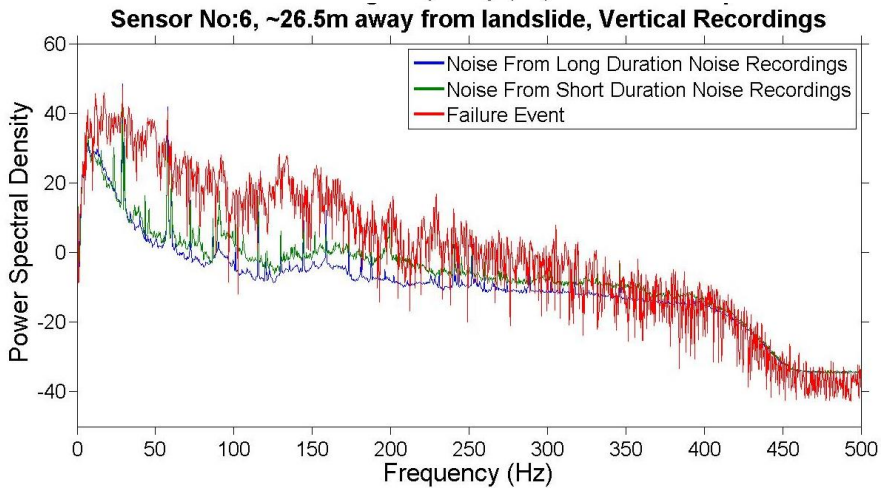
Sensor No:6, ~26.5m away from landslide, Vertical Recordings
Noise From Long Duration Noise Recordings
Noise From Short Duration Noise Recordings
Failure Event
Power Spectral Density
Frequency (Hz)

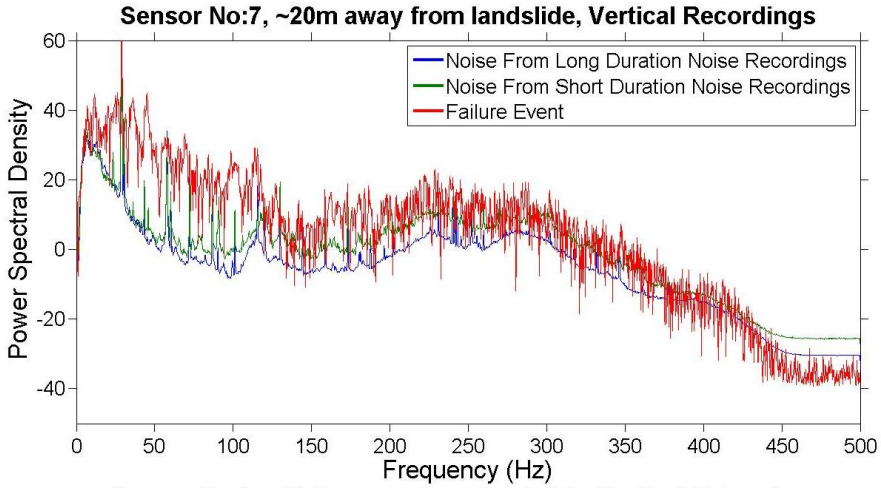
Sensor No:7, ~20m away from landslide, Vertical Recordings
Noise From Long Duration Noise Recordings
Noise From Short Duration Noise Recordings
Failure Event
Power Spectral Density
Frequency (Hz)
60
40
20
0
-20
-40
0
50
100
150
200
250
300
350
400
450
500

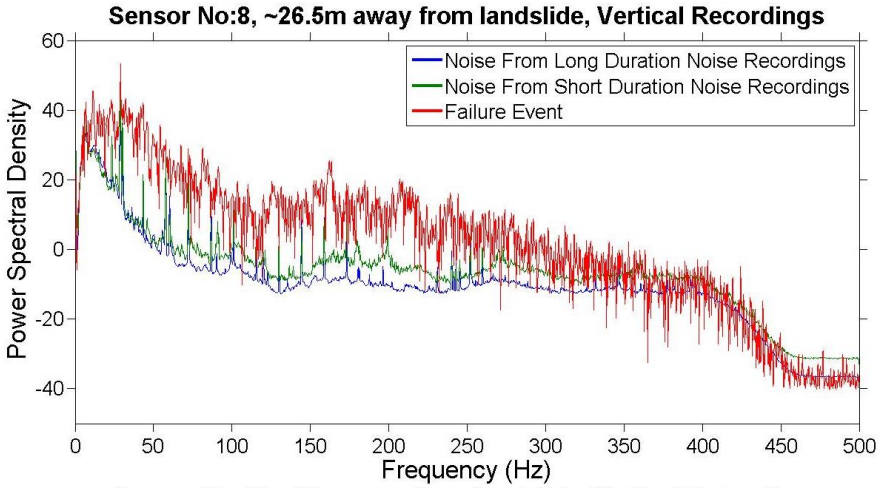
Sensor No:8, ~26.5m away from landslide, Vertical Recordings
Noise From Long Duration Noise Recordings
Noise From Short Duration Noise Recordings
Failure Event
Power Spectral Density
Frequency (Hz)
60
40
20
0
-20
-40
0
50
100
150
200
250
300
350
400
450
500

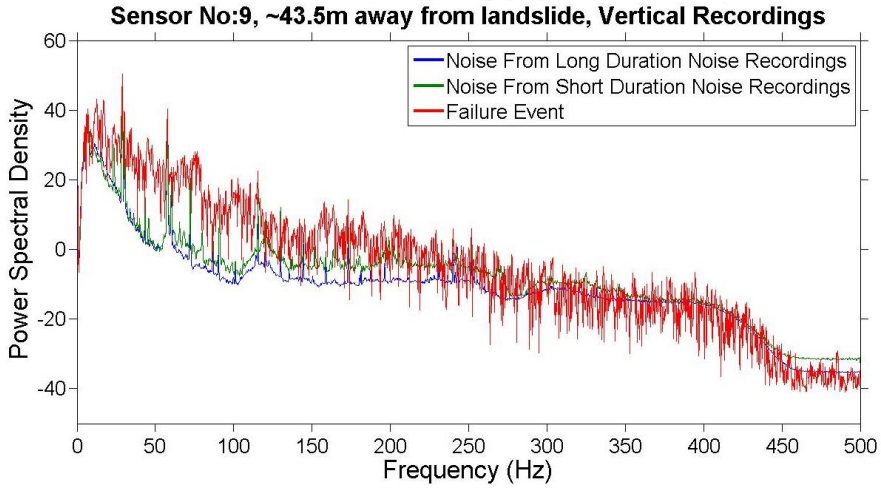
Sensor No:9, ~43.5m away from landslide, Vertical Recordings
Noise From Long Duration Noise Recordings
Noise From Short Duration Noise Recordings
Failure Event
Power Spectral Density
Frequency (Hz)
60
40
20
0
-20
-40
0
50
100
150
200
250
300
350
400
450
500

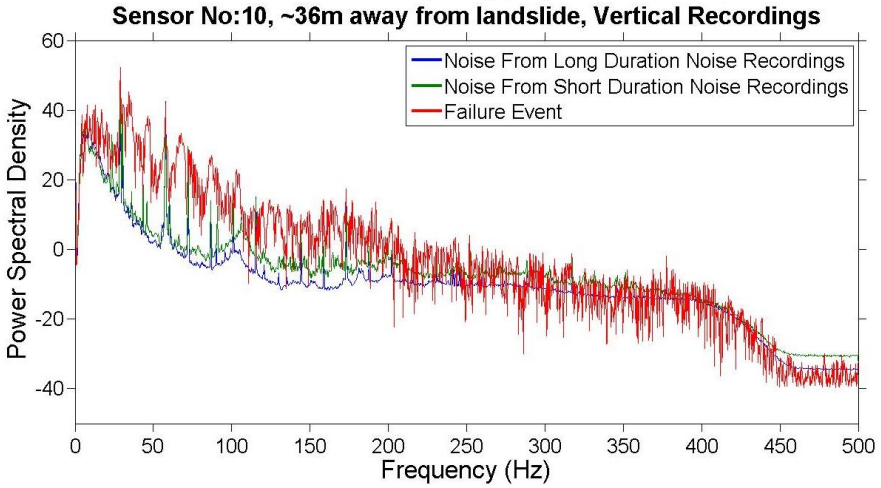
Sensor No:10, ~36m away from landslide, Vertical Recordings
Noise From Long Duration Noise Recordings
Noise From Short Duration Noise Recordings
Failure Event
Power Spectral Density
Frequency (Hz)
60
40
20
0
-20
-40
0
50
100
150
200
250
300
350
400
450
500

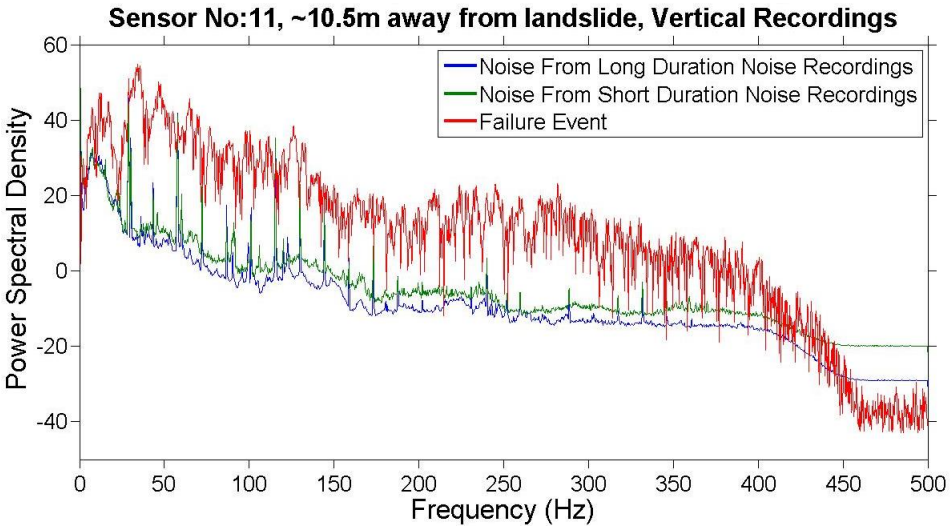

b) North-South Component

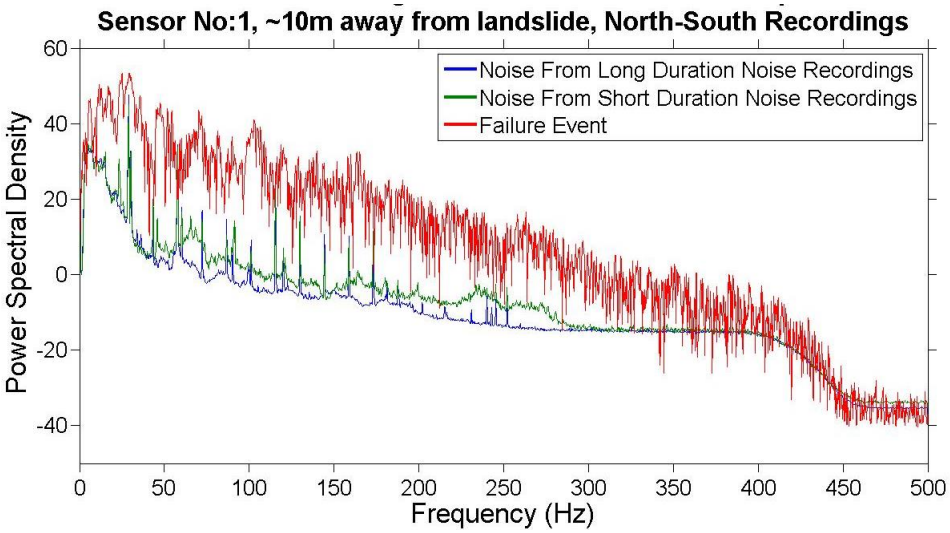

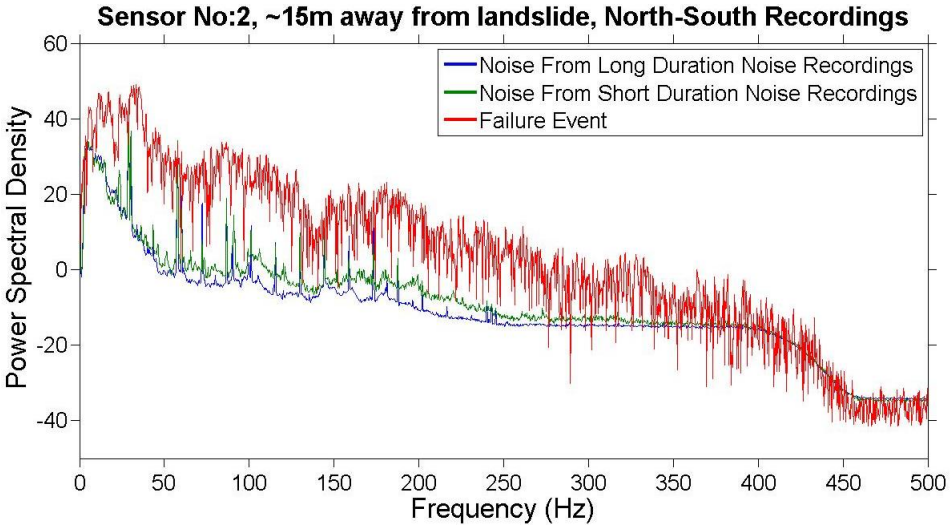

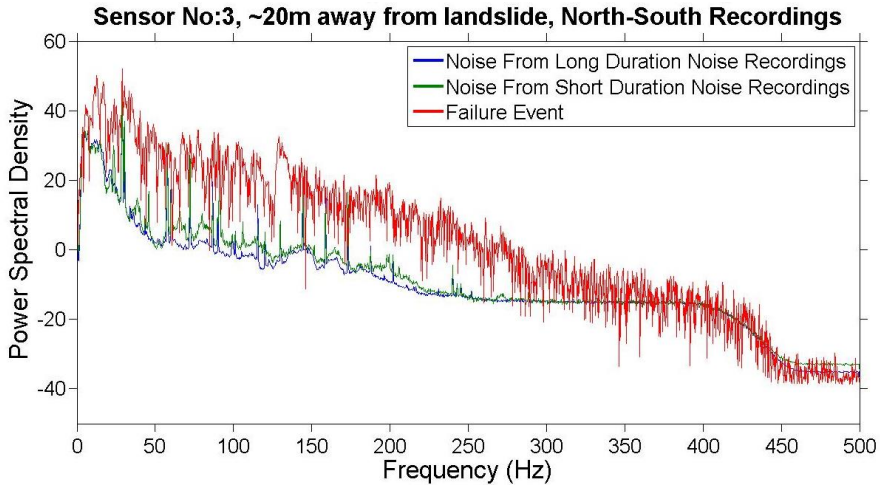
Sensor No:3, ~20m away from landslide, North-South Recordings
Noise From Long Duration Noise Recordings
Noise From Short Duration Noise Recordings
Failure Event
Power Spectral Density
Frequency (Hz)
60
40
20
0
-20
-40
0
50
100
150
200
250
300
350
400
450
500

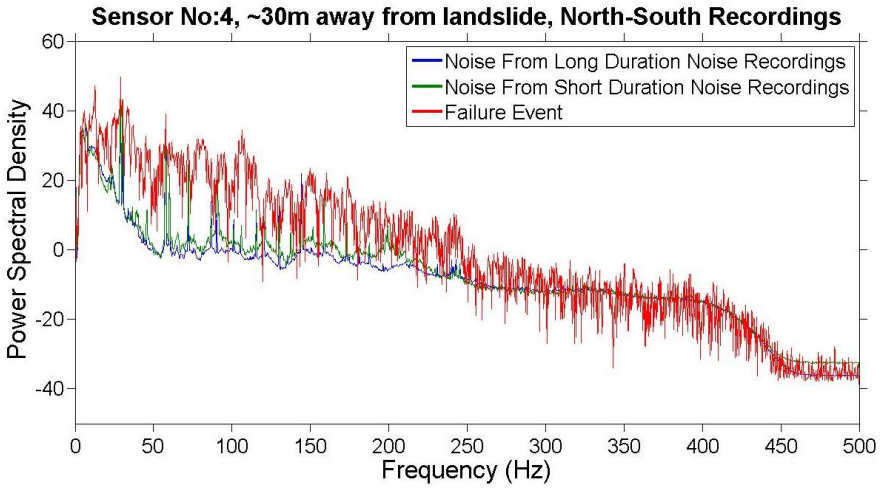
Sensor No:4, ~30m away from landslide, North-South Recordings
Noise From Long Duration Noise Recordings
Noise From Short Duration Noise Recordings
Failure Event
Power Spectral Density
Frequency (Hz)
60
40
20
0
-20
-40
0
50
100
150
200
250
300
350
400
450
500

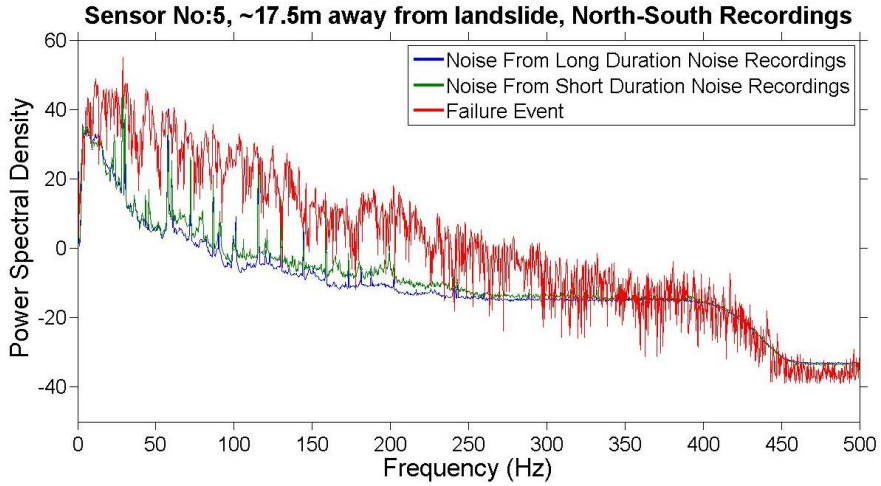
Sensor No:5, ~17.5m away from landslide, North-South Recordings
Noise From Long Duration Noise Recordings
Noise From Short Duration Noise Recordings
Failure Event
Power Spectral Density
Frequency (Hz)
60
40
20
0
-20
-40
0
50
100
150
200
250
300
350
400
450
500

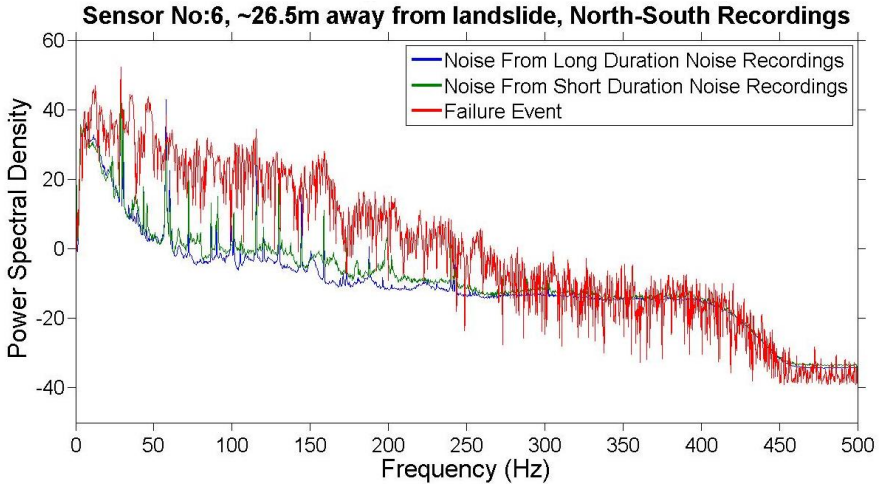
Sensor No:6, ~26.5m away from landslide, North-South Recordings
Noise From Long Duration Noise Recordings
Noise From Short Duration Noise Recordings
Failure Event
Power Spectral Density
Frequency (Hz)
60
40
20
0
-20
-40
0
50
100
150
200
250
300
350
400
450
500

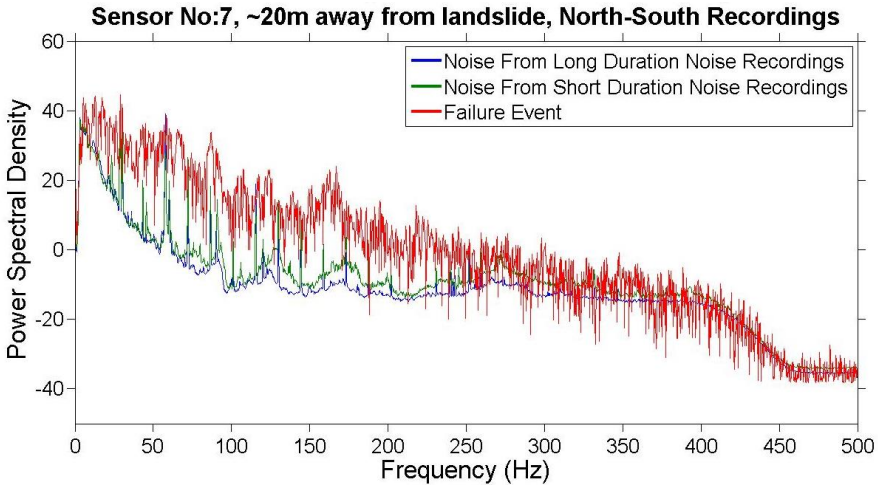
Sensor No:7, ~20m away from landslide, North-South Recordings
Noise From Long Duration Noise Recordings
Noise From Short Duration Noise Recordings
Failure Event
Power Spectral Density
Frequency (Hz)

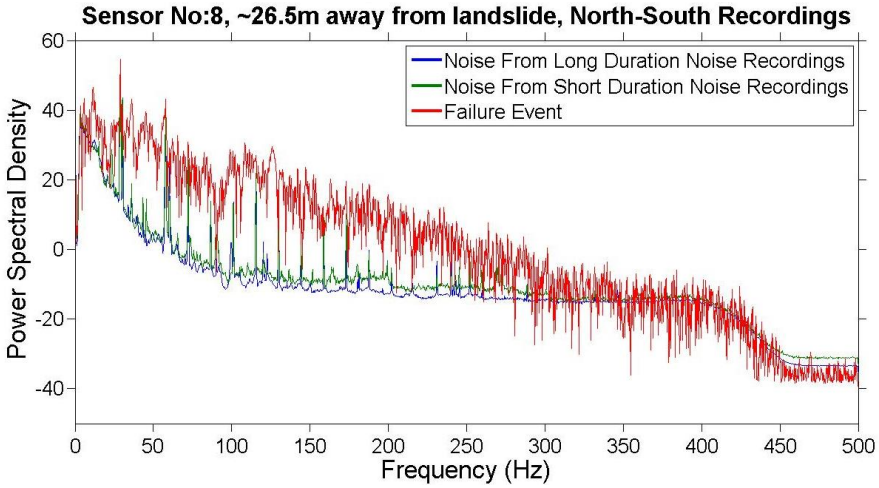
Sensor No:8, ~26.5m away from landslide, North-South Recordings
Noise From Long Duration Noise Recordings
Noise From Short Duration Noise Recordings
Failure Event
Power Spectral Density
Frequency (Hz)

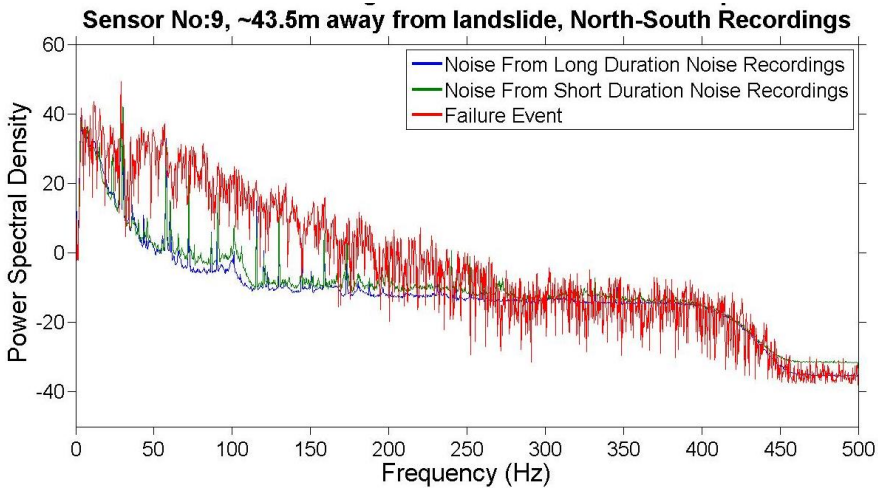
Sensor No:9, ~43.5m away from landslide, North-South Recordings
Noise From Long Duration Noise Recordings
Noise From Short Duration Noise Recordings
Failure Event
Power Spectral Density
Frequency (Hz)

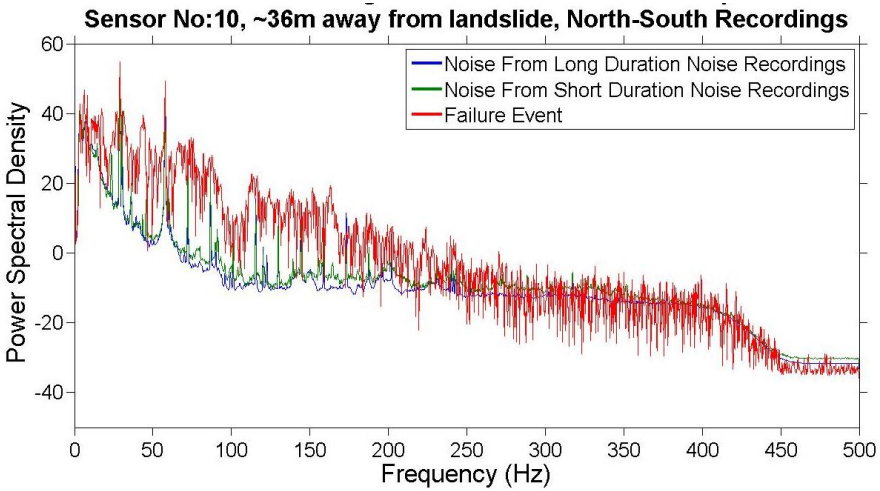
Sensor No:10, ~36m away from landslide, North-South Recordings
Noise From Long Duration Noise Recordings
Noise From Short Duration Noise Recordings
Failure Event
Power Spectral Density
Frequency (Hz)

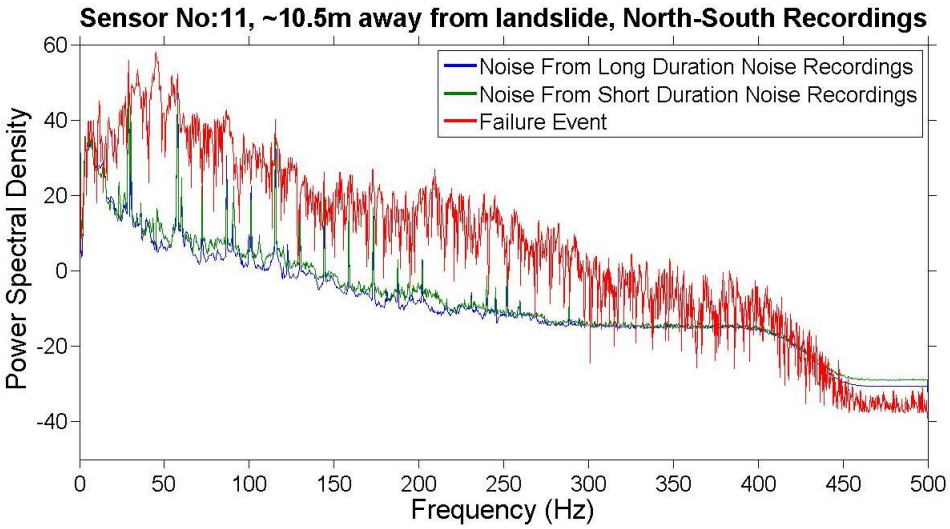

c) East-West Component

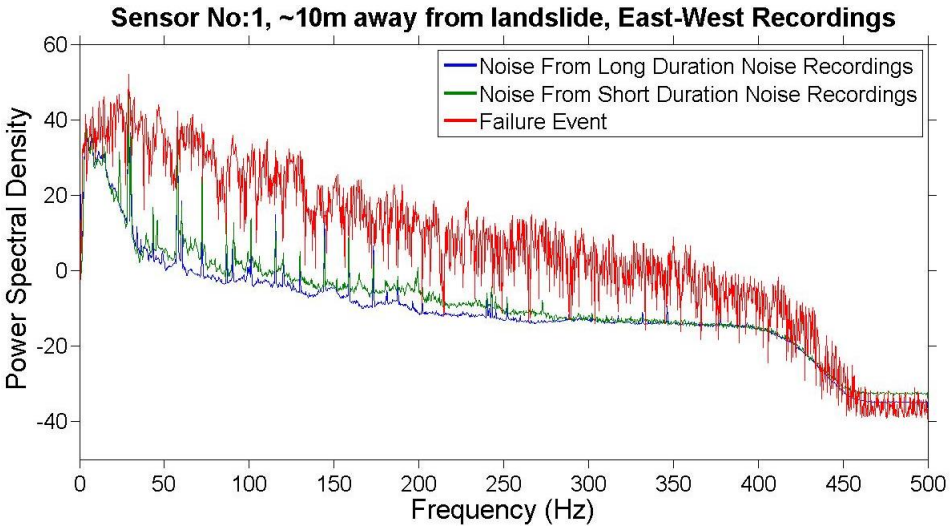

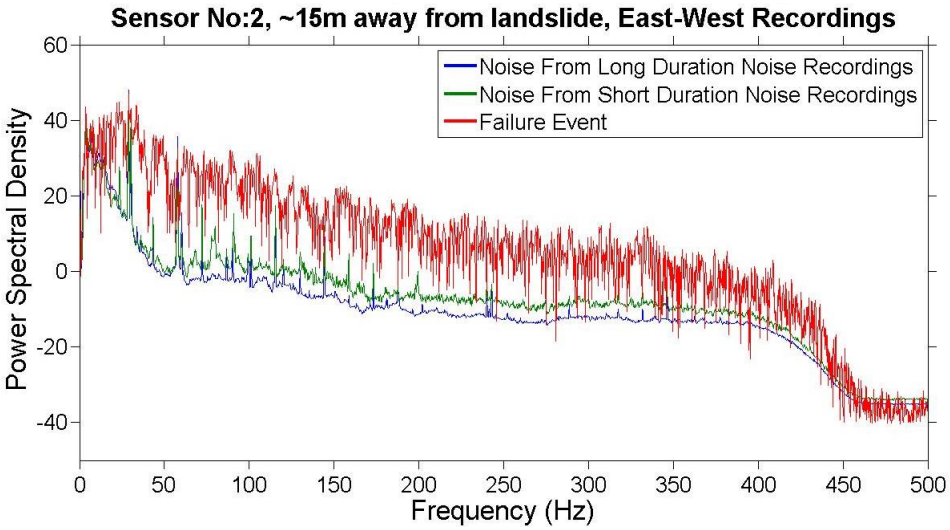

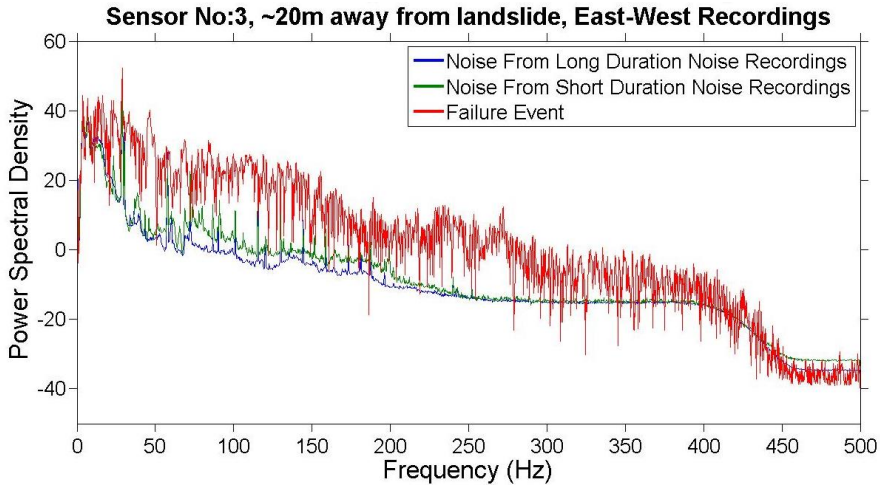
Sensor No:3, ~20m away from landslide, East-West Recordings
Noise From Long Duration Noise Recordings
Noise From Short Duration Noise Recordings
Failure Event
Power Spectral Density
Frequency (Hz)
60
40
20
0
-20
-40
0
50
100
150
200
250
300
350
400
450
500

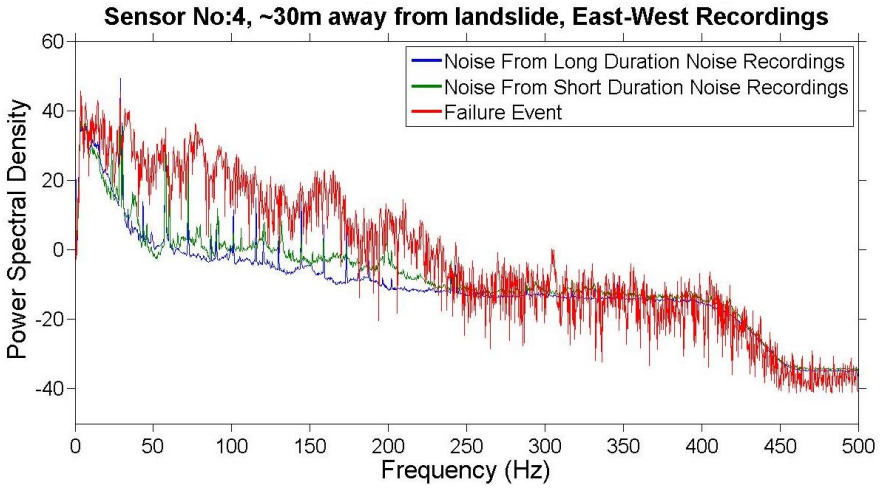
Sensor No:4, ~30m away from landslide, East-West Recordings
Noise From Long Duration Noise Recordings
Noise From Short Duration Noise Recordings
Failure Event
Power Spectral Density
Frequency (Hz)
60
40
20
0
-20
-40
0
50
100
150
200
250
300
350
400
450
500

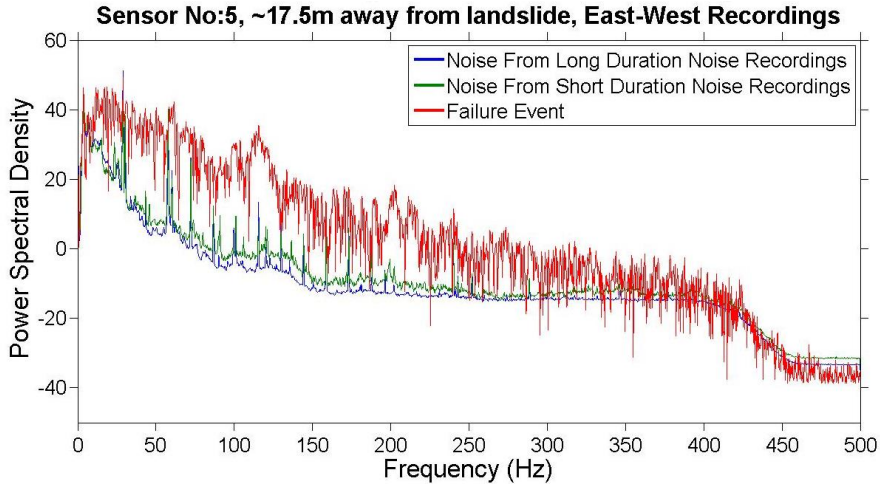
Sensor No:5, ~17.5m away from landslide, East-West Recordings
Noise From Long Duration Noise Recordings
Noise From Short Duration Noise Recordings
Failure Event
Power Spectral Density
Frequency (Hz)
60
40
20
0
-20
-40
0
50
100
150
200
250
300
350
400
450
500

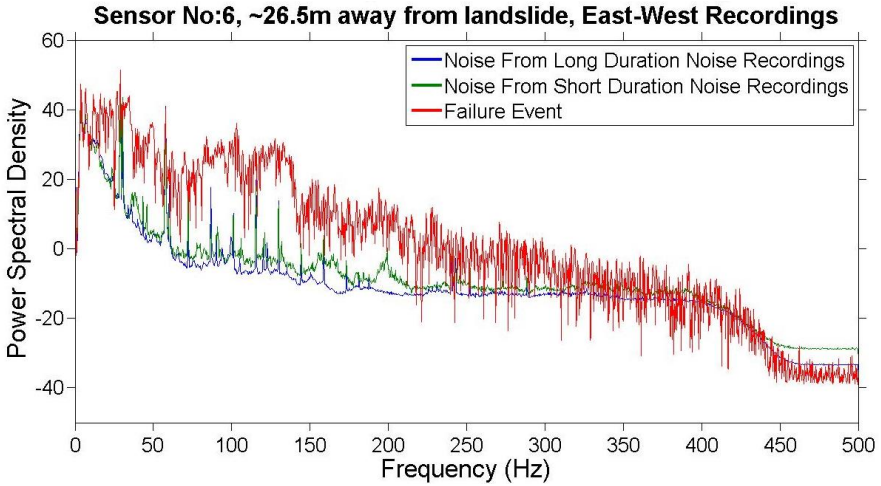
Sensor No:6, ~26.5m away from landslide, East-West Recordings
Noise From Long Duration Noise Recordings
Noise From Short Duration Noise Recordings
Failure Event
Power Spectral Density
Frequency (Hz)
60
40
20
0
-20
-40
0
50
100
150
200
250
300
350
400
450
500

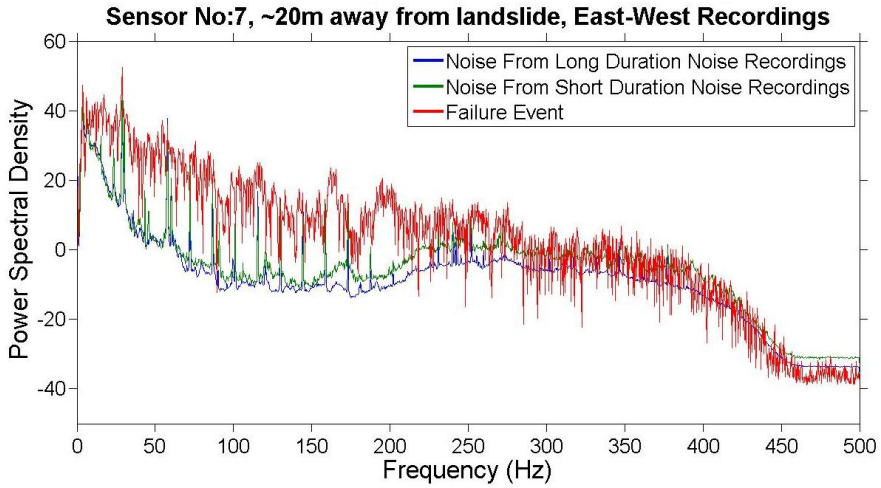
Sensor No:7, ~20m away from landslide, East-West Recordings
Noise From Long Duration Noise Recordings
Noise From Short Duration Noise Recordings
Failure Event
Power Spectral Density
Frequency (Hz)

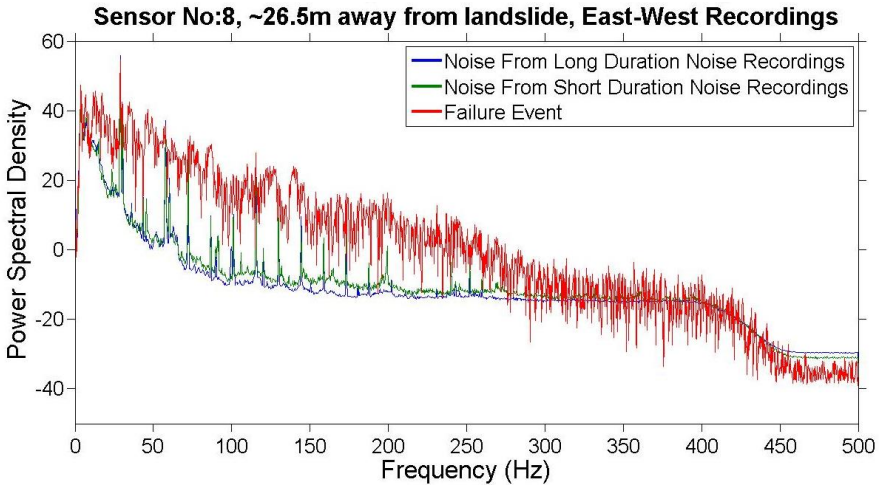
Sensor No:8, ~26.5m away from landslide, East-West Recordings
Noise From Long Duration Noise Recordings
Noise From Short Duration Noise Recordings
Failure Event
Power Spectral Density
Frequency (Hz)

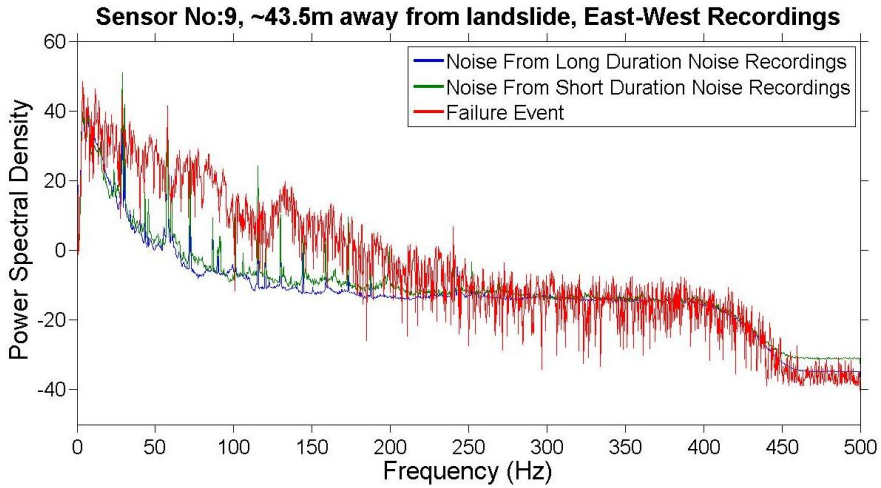
Sensor No:9, ~43.5m away from landslide, East-West Recordings
Noise From Long Duration Noise Recordings
Noise From Short Duration Noise Recordings
Failure Event
Power Spectral Density
Frequency (Hz)

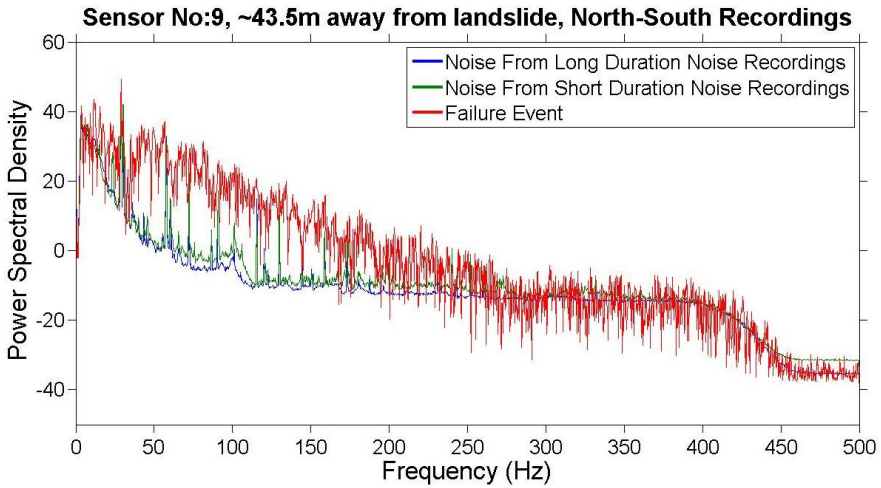
Sensor No:9, ~43.5m away from landslide, North-South Recordings
Noise From Long Duration Noise Recordings
Noise From Short Duration Noise Recordings
Failure Event
Power Spectral Density
Frequency (Hz)

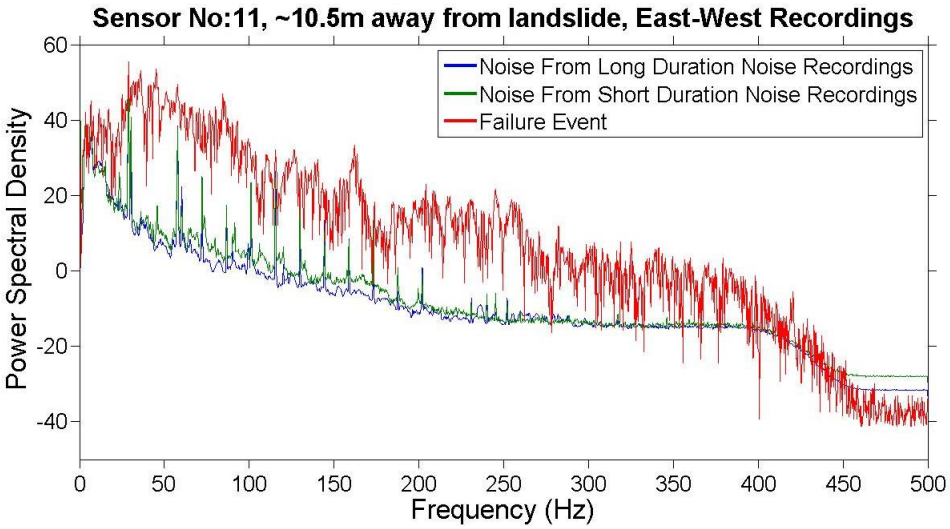

C3.2.2 Additional PSD graphs of FT2 No2 event presented at Figure 8.24

a) Vertical Component

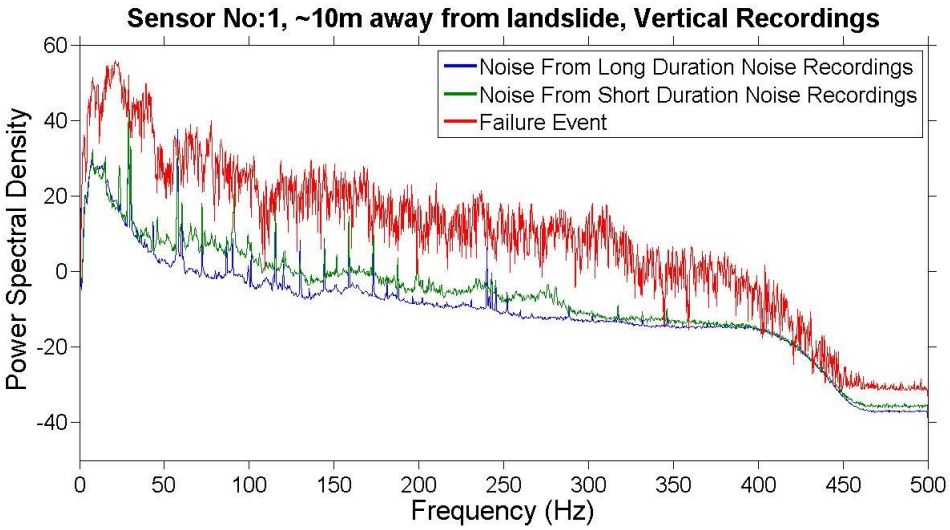

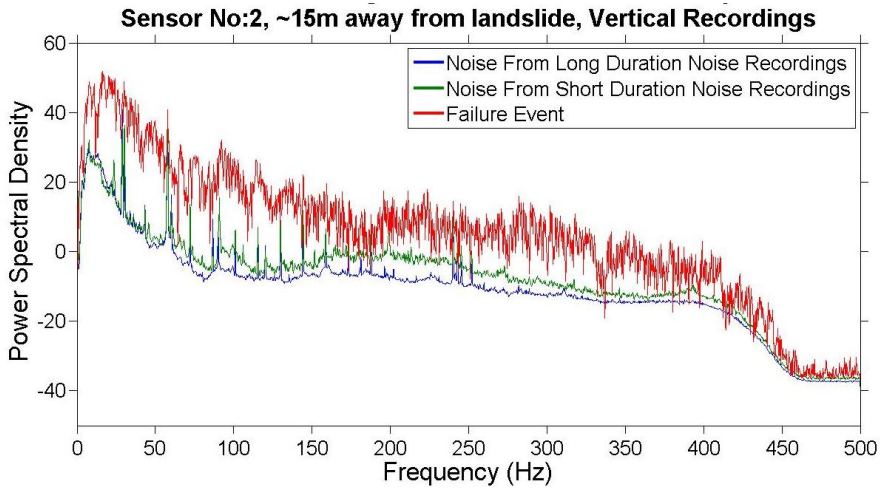
Sensor No:2, ~15m away from landslide, Vertical Recordings
Noise From Long Duration Noise Recordings
Noise From Short Duration Noise Recordings
Failure Event
Power Spectral Density
Frequency (Hz)
60
40
20
0
-20
-40
0
50
100
150
200
250
300
350
400
450
500

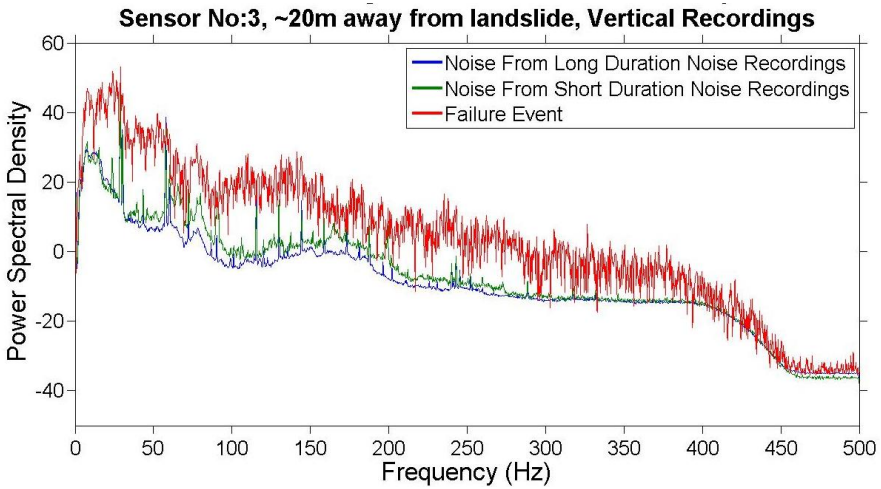
Sensor No:3, ~20m away from landslide, Vertical Recordings
Noise From Long Duration Noise Recordings
Noise From Short Duration Noise Recordings
Failure Event
Power Spectral Density
Frequency (Hz)
60
40
20
0
-20
-40
0
50
100
150
200
250
300
350
400
450
500

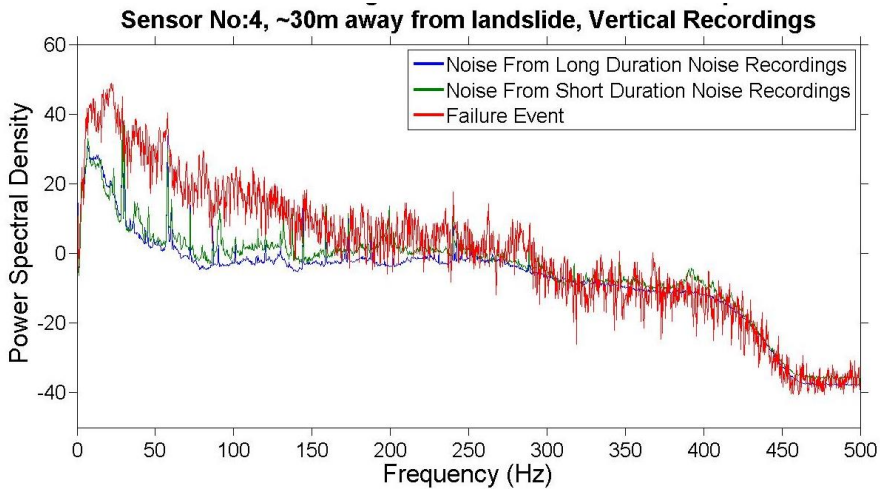
Sensor No:4, ~30m away from landslide, Vertical Recordings
Noise From Long Duration Noise Recordings
Noise From Short Duration Noise Recordings
Failure Event
Power Spectral Density
Frequency (Hz)
60
40
20
0
-20
-40
0
50
100
150
200
250
300
350
400
450
500

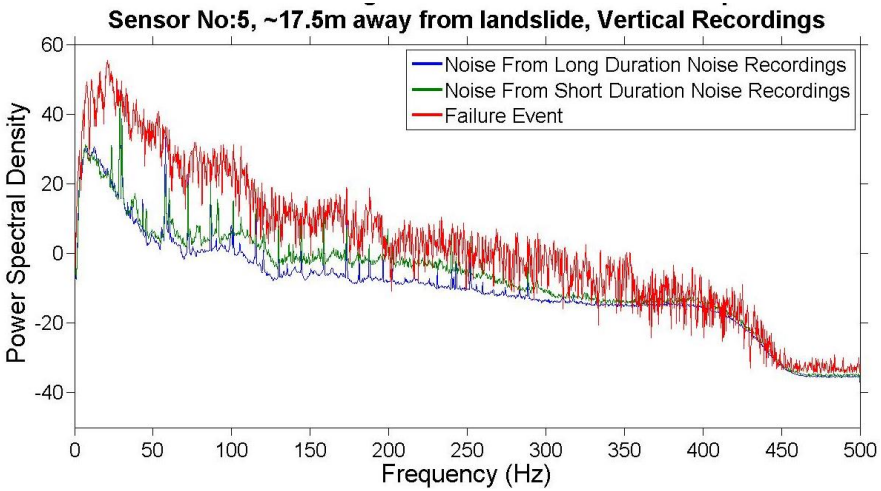
Sensor No:5, ~17.5m away from landslide, Vertical Recordings
Noise From Long Duration Noise Recordings
Noise From Short Duration Noise Recordings
Failure Event
Power Spectral Density
Frequency (Hz)
60
40
20
0
-20
-40
0
50
100
150
200
250
300
350
400
450
500

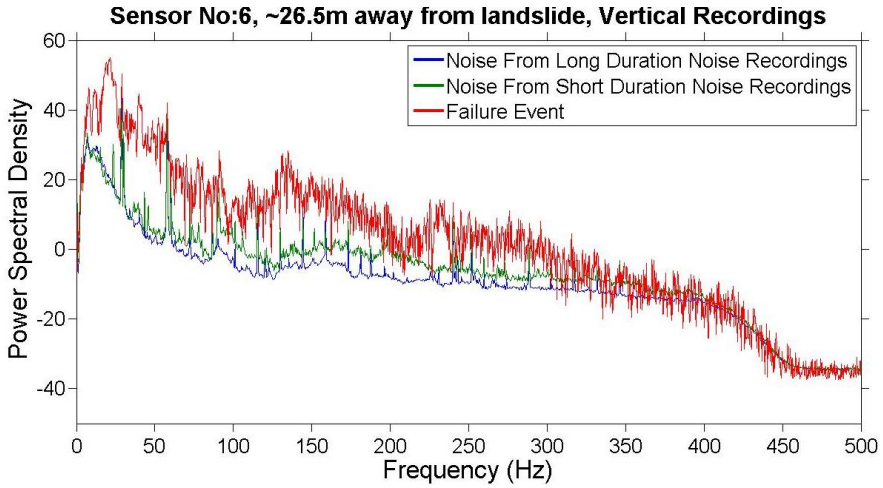
Sensor No:6, ~26.5m away from landslide, Vertical Recordings
Noise From Long Duration Noise Recordings
Noise From Short Duration Noise Recordings
Failure Event
Power Spectral Density
Frequency (Hz)

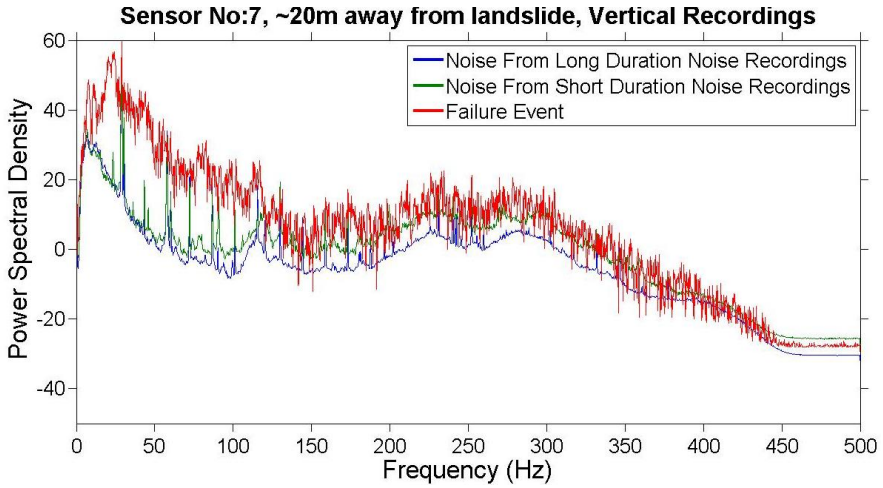
Sensor No:7, ~20m away from landslide, Vertical Recordings
Noise From Long Duration Noise Recordings
Noise From Short Duration Noise Recordings
Failure Event
Power Spectral Density
Frequency (Hz)

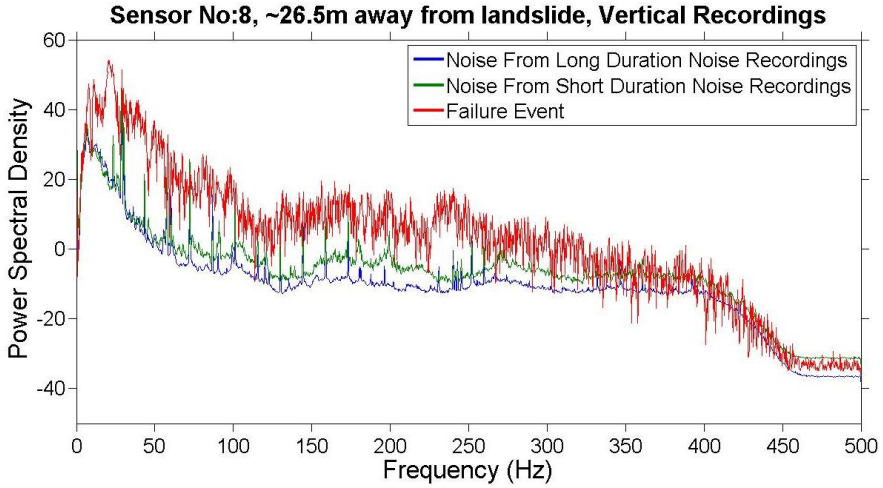
Sensor No:8, ~26.5m away from landslide, Vertical Recordings
Noise From Long Duration Noise Recordings
Noise From Short Duration Noise Recordings
Failure Event
Power Spectral Density
Frequency (Hz)

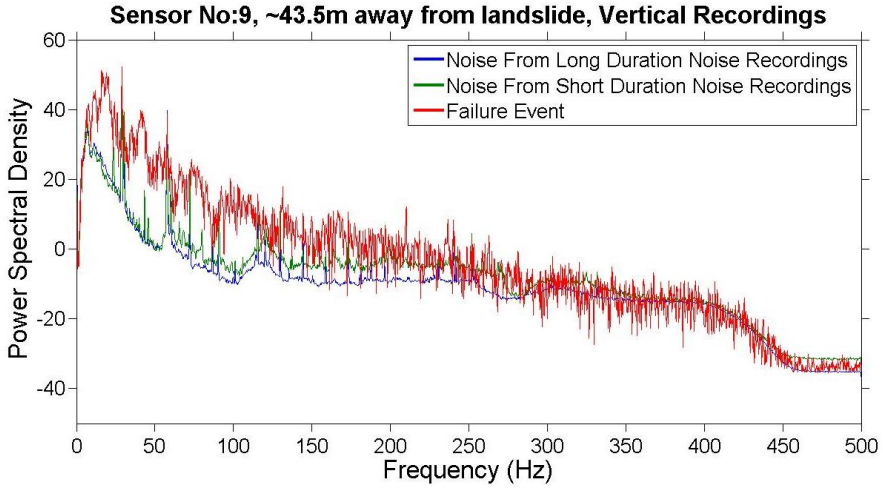
Sensor No:9, ~43.5m away from landslide, Vertical Recordings
Noise From Long Duration Noise Recordings
Noise From Short Duration Noise Recordings
Failure Event
Power Spectral Density
Frequency (Hz)

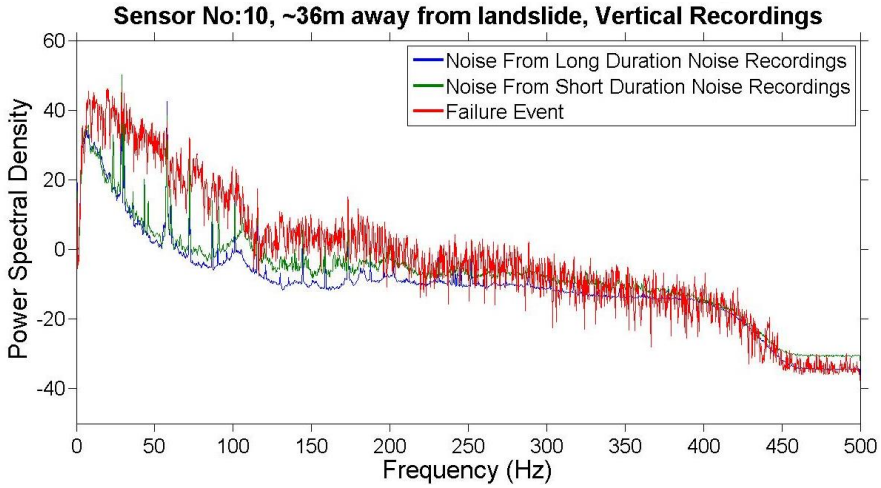

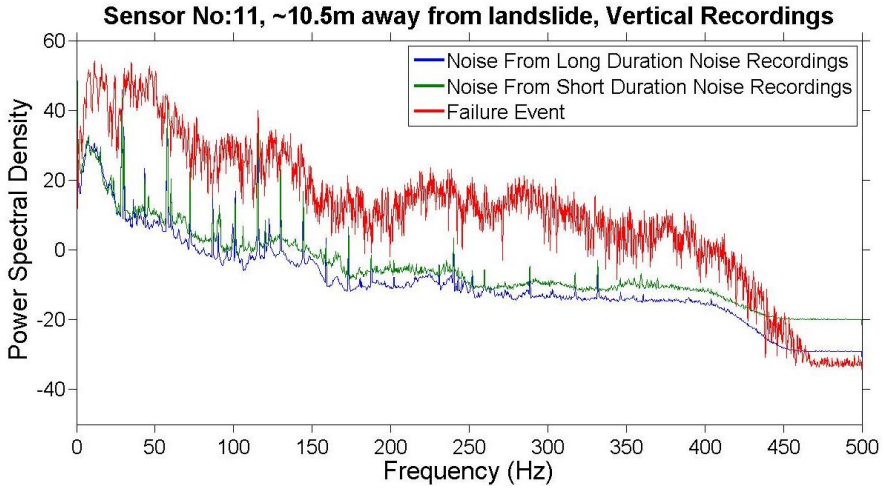

b) North-South Component

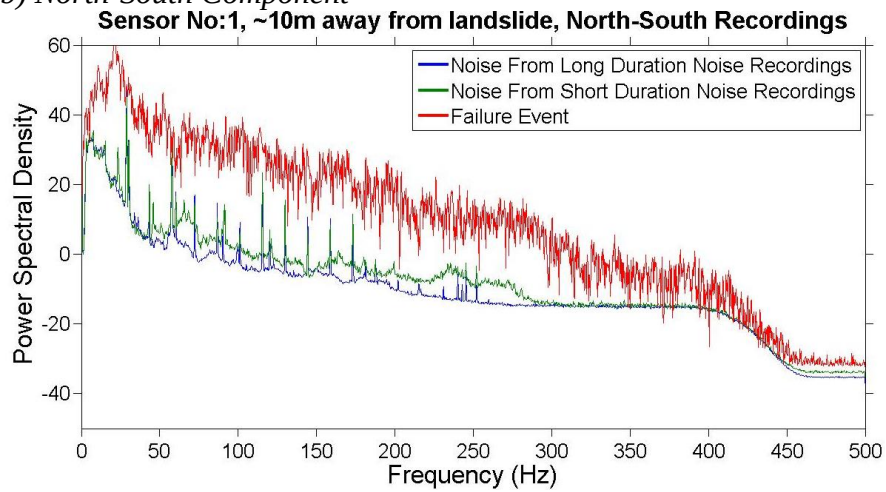

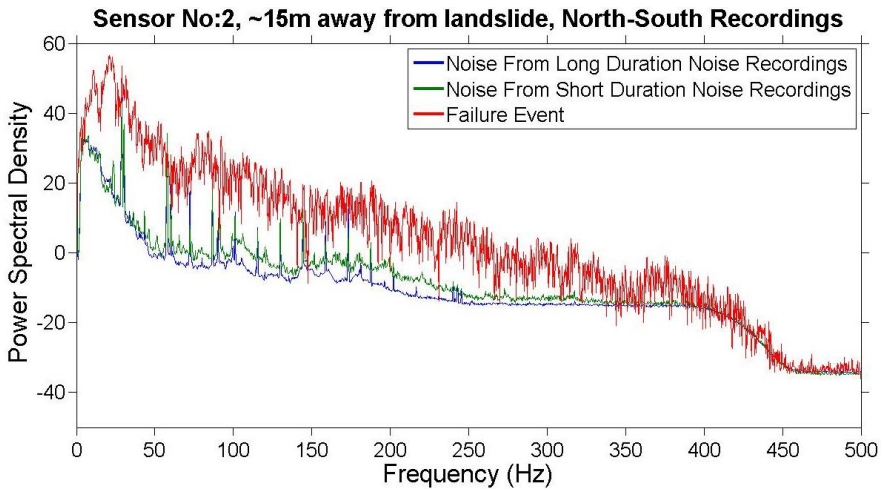

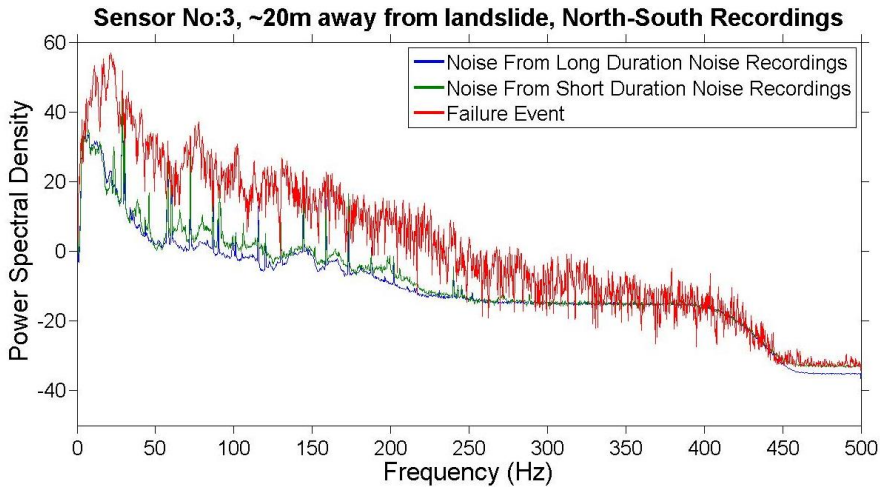
Sensor No:3, ~20m away from landslide, North-South Recordings
Noise From Long Duration Noise Recordings
Noise From Short Duration Noise Recordings
Failure Event
Power Spectral Density
Frequency (Hz)

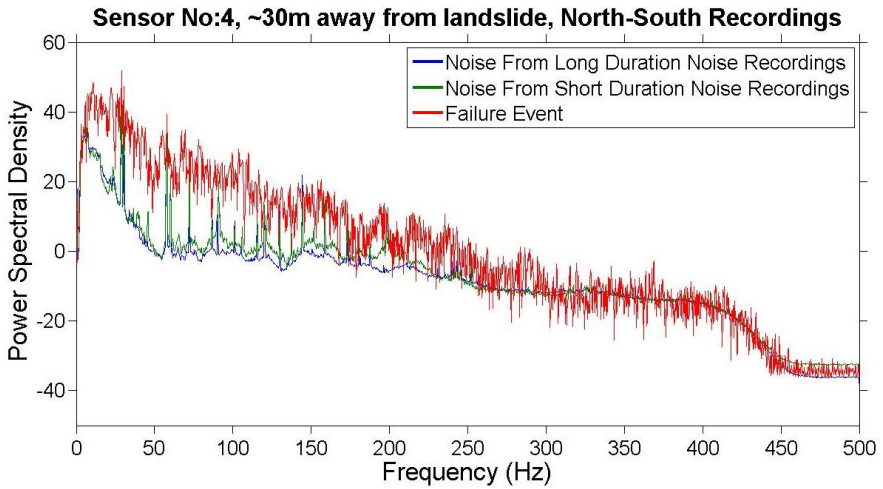
Sensor No:4, ~30m away from landslide, North-South Recordings
Noise From Long Duration Noise Recordings
Noise From Short Duration Noise Recordings
Failure Event
Power Spectral Density
Frequency (Hz)

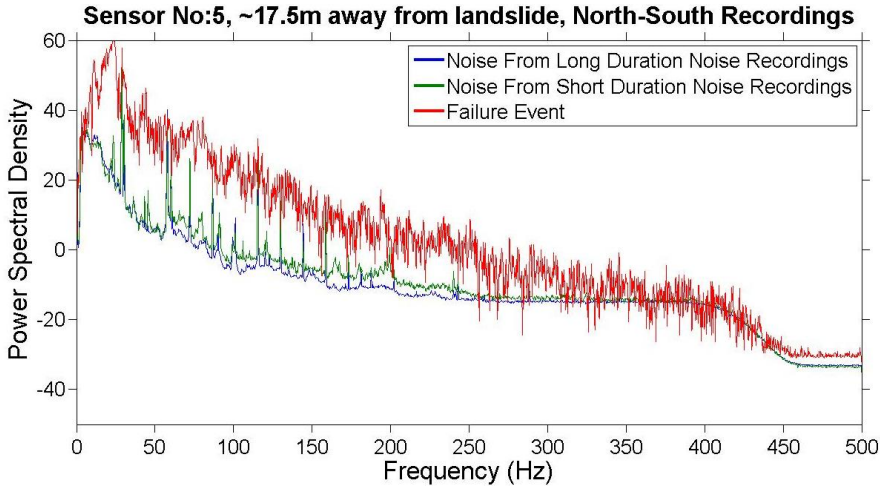
Sensor No:5, ~17.5m away from landslide, North-South Recordings
Noise From Long Duration Noise Recordings
Noise From Short Duration Noise Recordings
Failure Event
Power Spectral Density
Frequency (Hz)

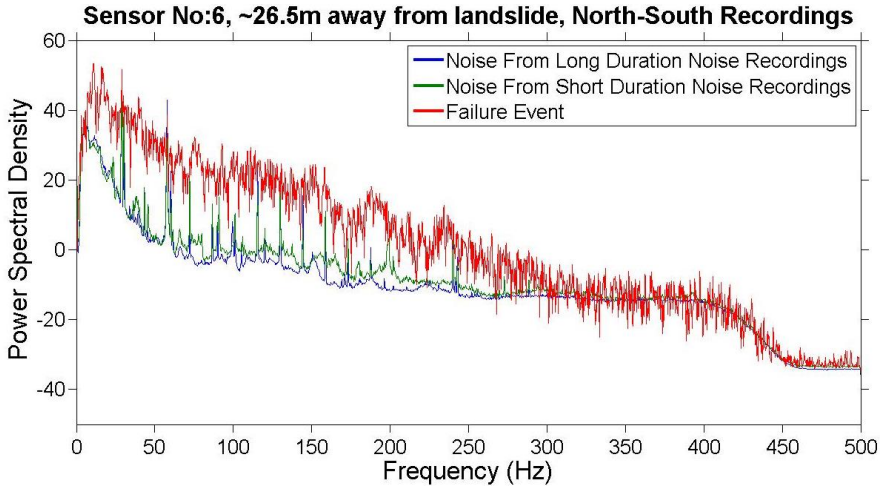
Sensor No:6, ~26.5m away from landslide, North-South Recordings
Noise From Long Duration Noise Recordings
Noise From Short Duration Noise Recordings
Failure Event
Power Spectral Density
Frequency (Hz)

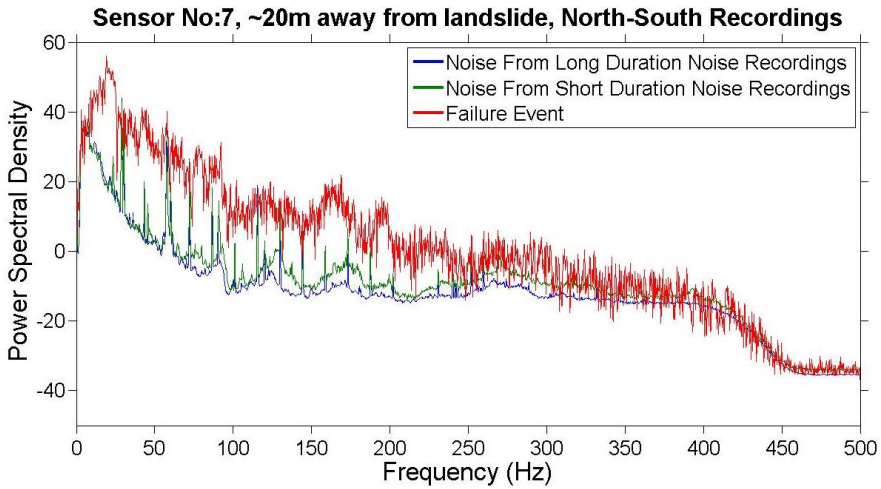
Sensor No:7, ~20m away from landslide, North-South Recordings
Noise From Long Duration Noise Recordings
Noise From Short Duration Noise Recordings
Failure Event
Power Spectral Density
Frequency (Hz)

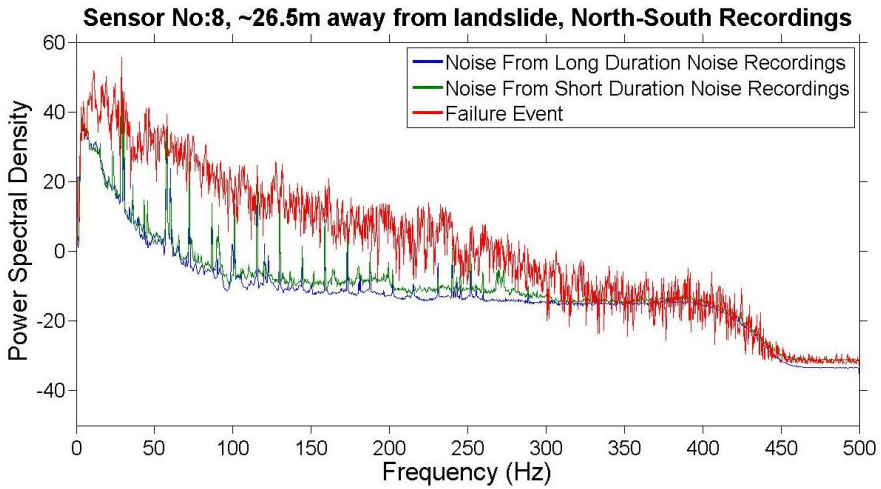
Sensor No:8, ~26.5m away from landslide, North-South Recordings
Noise From Long Duration Noise Recordings
Noise From Short Duration Noise Recordings
Failure Event
Power Spectral Density
Frequency (Hz)

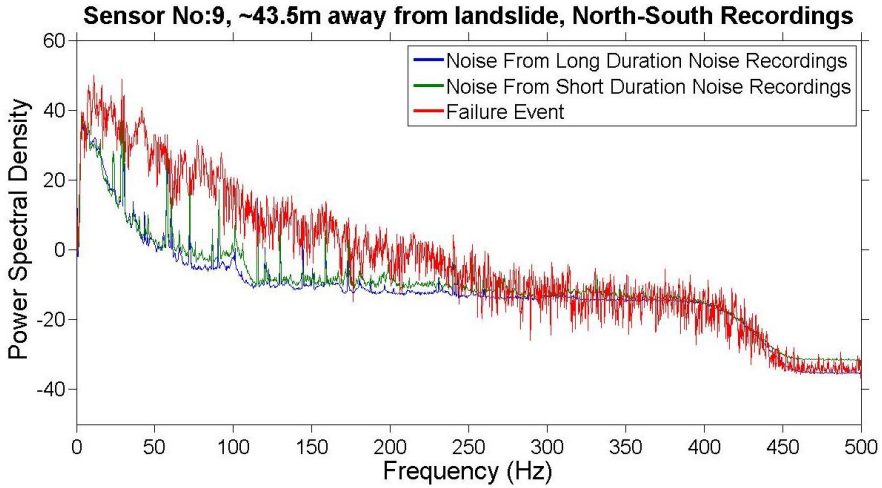
Sensor No:9, ~43.5m away from landslide, North-South Recordings
Noise From Long Duration Noise Recordings
Noise From Short Duration Noise Recordings
Failure Event
Power Spectral Density
Frequency (Hz)

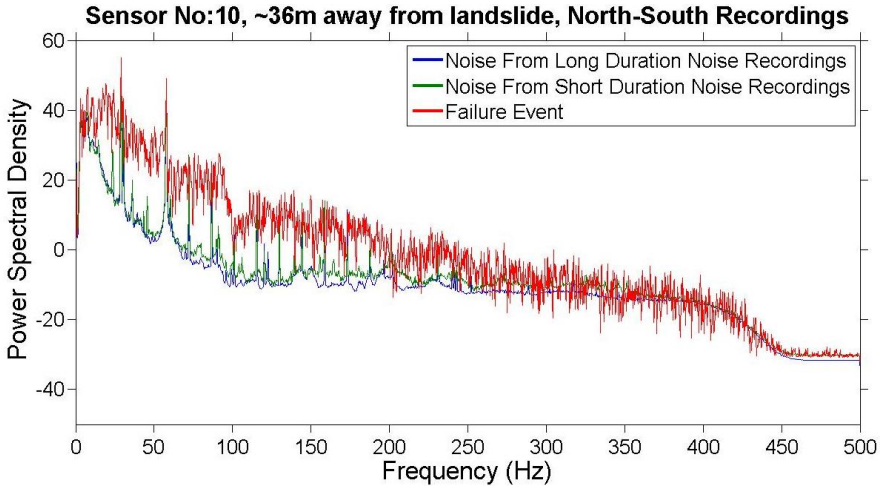
Sensor No:10, ~36m away from landslide, North-South Recordings
Noise From Long Duration Noise Recordings
Noise From Short Duration Noise Recordings
Failure Event
Power Spectral Density
Frequency (Hz)

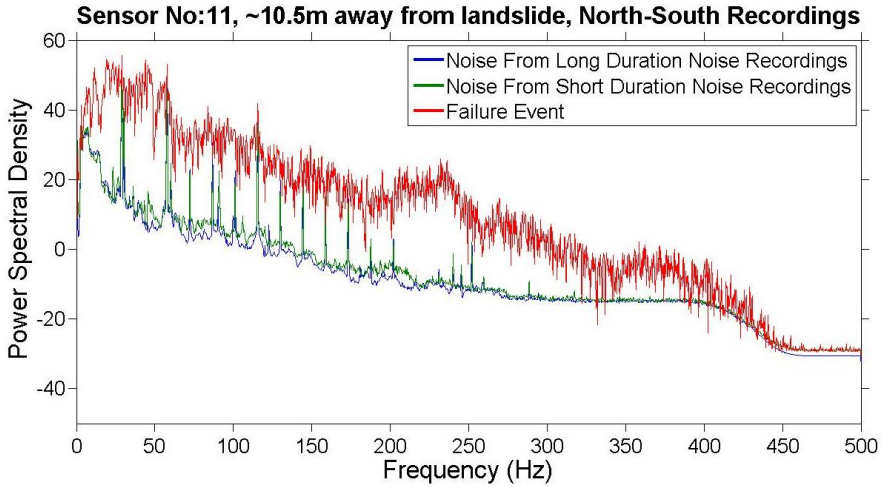

c) East-West Component

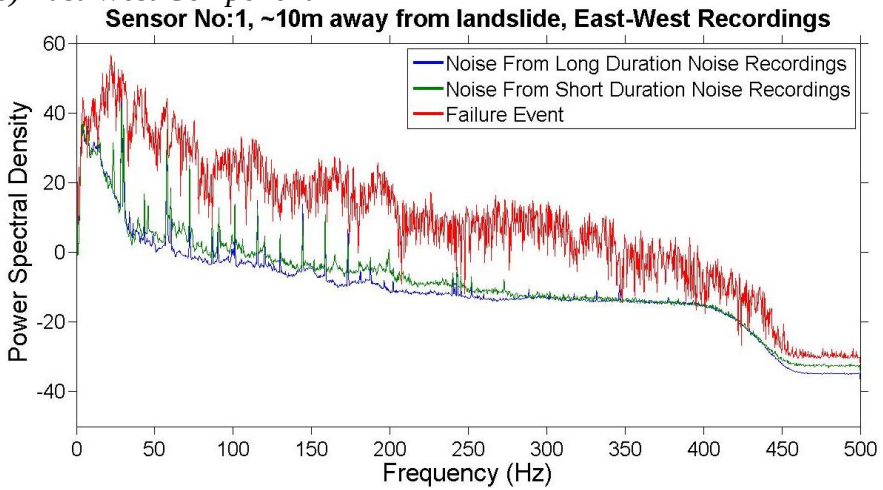

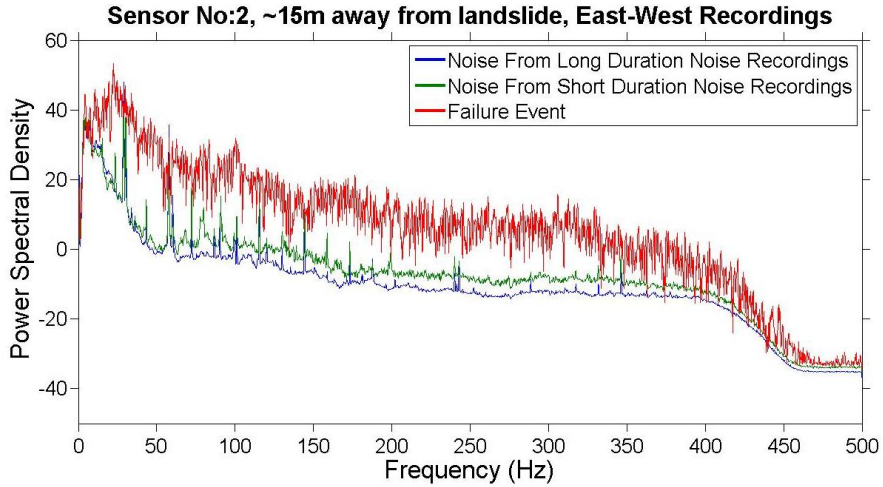

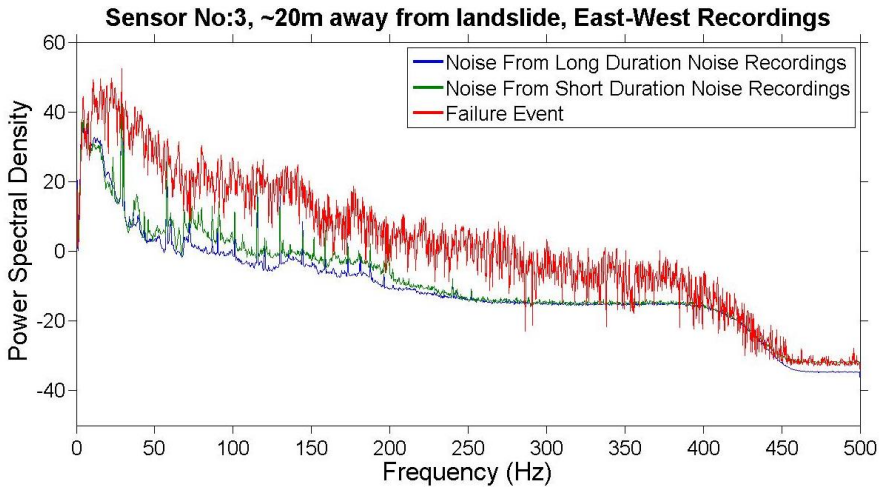
Sensor No:3, ~20m away from landslide, East-West Recordings
Noise From Long Duration Noise Recordings
Noise From Short Duration Noise Recordings
Failure Event
Power Spectral Density
Frequency (Hz)
60
40
20
0
-20
-40
0
50
100
150
200
250
300
350
400
450
500

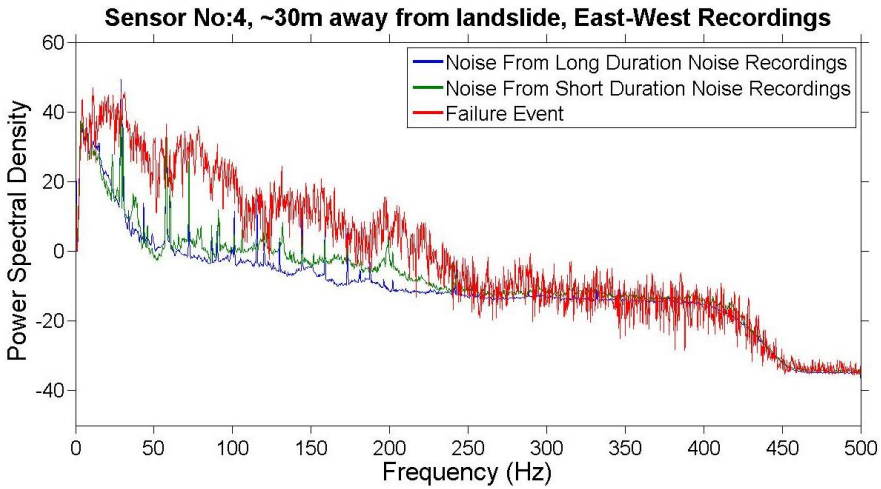
Sensor No:4, ~30m away from landslide, East-West Recordings
Noise From Long Duration Noise Recordings
Noise From Short Duration Noise Recordings
Failure Event
Power Spectral Density
Frequency (Hz)
60
40
20
0
-20
-40
0
50
100
150
200
250
300
350
400
450
500

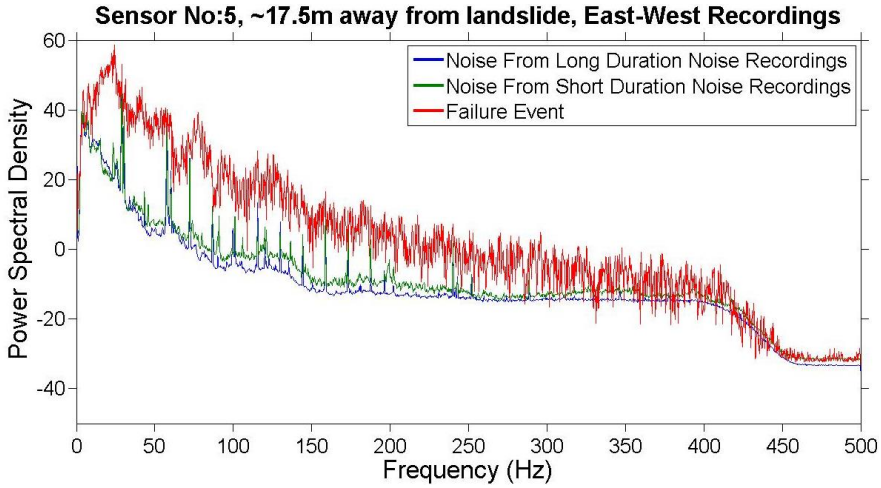
Sensor No:5, ~17.5m away from landslide, East-West Recordings
Noise From Long Duration Noise Recordings
Noise From Short Duration Noise Recordings
Failure Event
Power Spectral Density
Frequency (Hz)
60
40
20
0
-20
-40
0
50
100
150
200
250
300
350
400
450
500

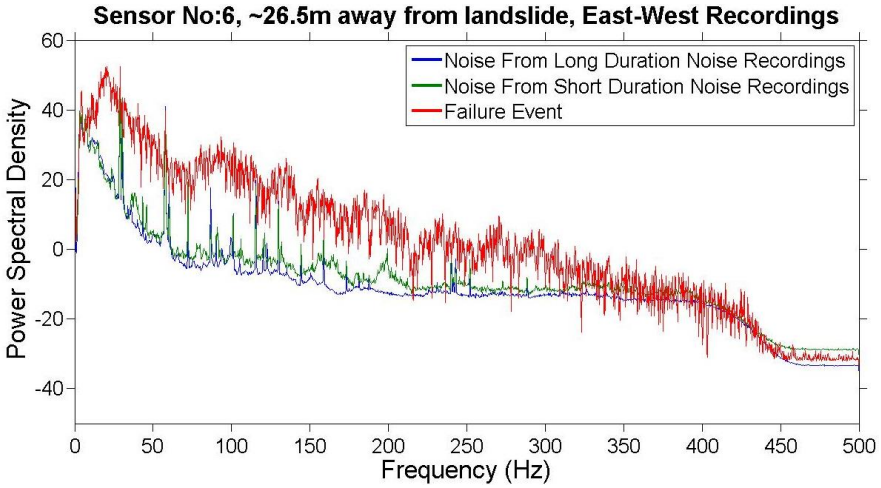
Sensor No:6, ~26.5m away from landslide, East-West Recordings
Noise From Long Duration Noise Recordings
Noise From Short Duration Noise Recordings
Failure Event
Power Spectral Density
Frequency (Hz)
60
40
20
0
-20
-40
0
50
100
150
200
250
300
350
400
450
500

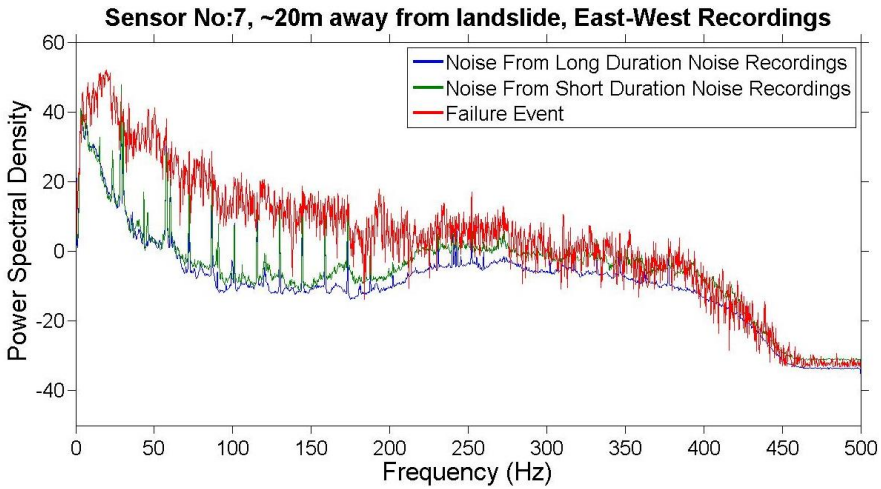
Sensor No:7, ~20m away from landslide, East-West Recordings
Noise From Long Duration Noise Recordings
Noise From Short Duration Noise Recordings
Failure Event
Power Spectral Density
Frequency (Hz)

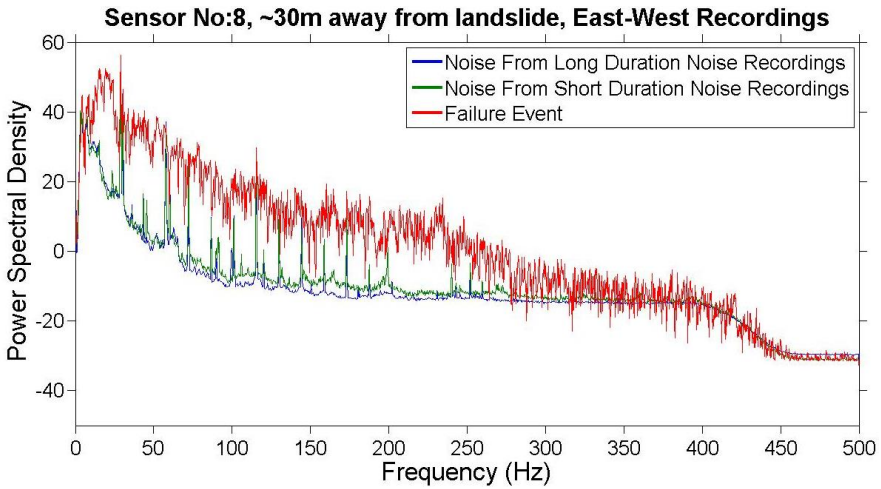
Sensor No:8, ~30m away from landslide, East-West Recordings
Noise From Long Duration Noise Recordings
Noise From Short Duration Noise Recordings
Failure Event
Power Spectral Density
Frequency (Hz)

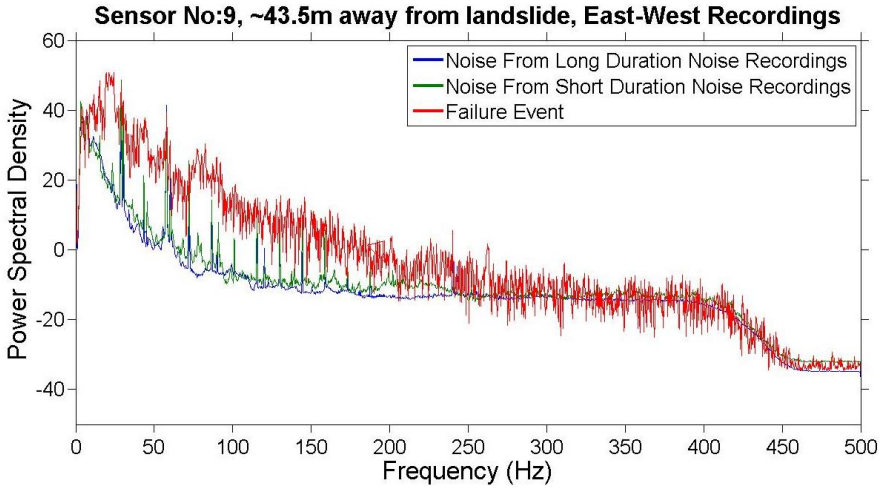
Sensor No:9, ~43.5m away from landslide, East-West Recordings
Noise From Long Duration Noise Recordings
Noise From Short Duration Noise Recordings
Failure Event
Power Spectral Density
Frequency (Hz)

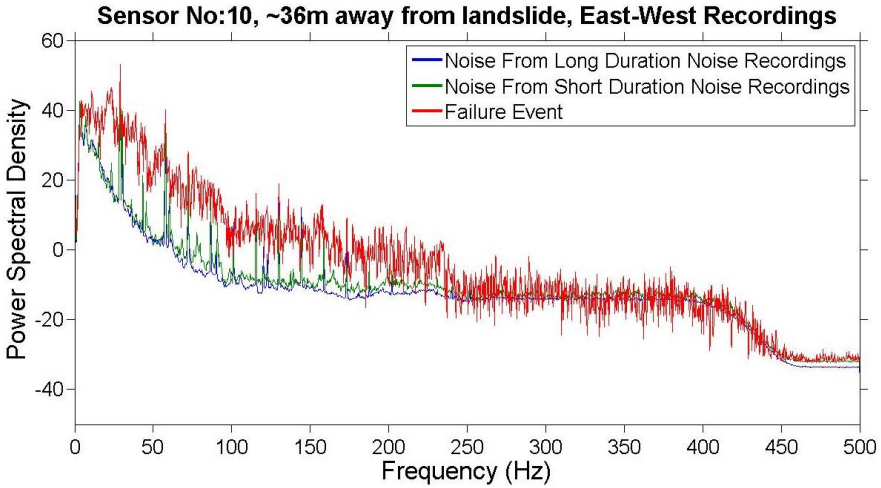
Sensor No:10, ~36m away from landslide, East-West Recordings
Noise From Long Duration Noise Recordings
Noise From Short Duration Noise Recordings
Failure Event
Power Spectral Density
Frequency (Hz)

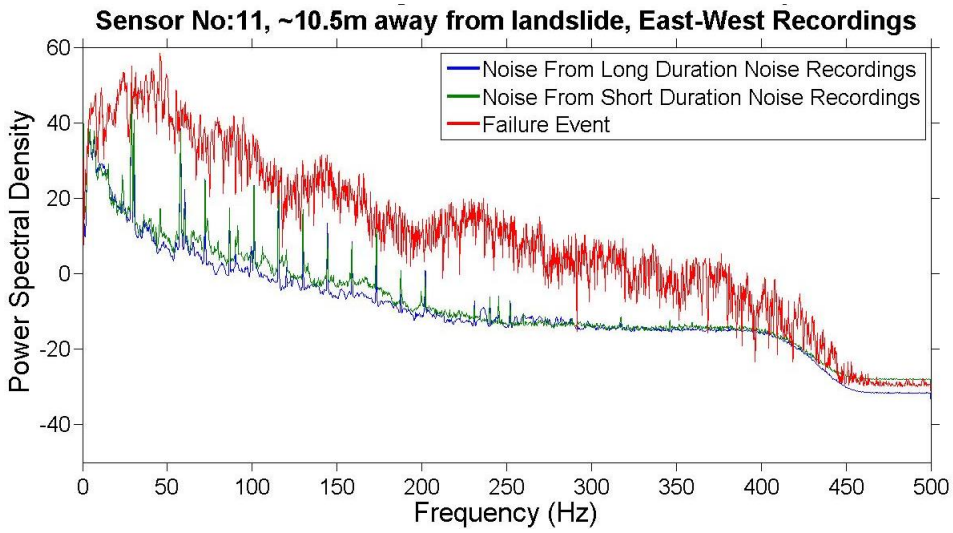

C3.3 Additional PSD graphs for FT3: Soil Block Fall

C3.3.1 Additional PSD graphs of FT3 No1 event of Experiment L1 presented at Figure 8.23

a) Vertical Component

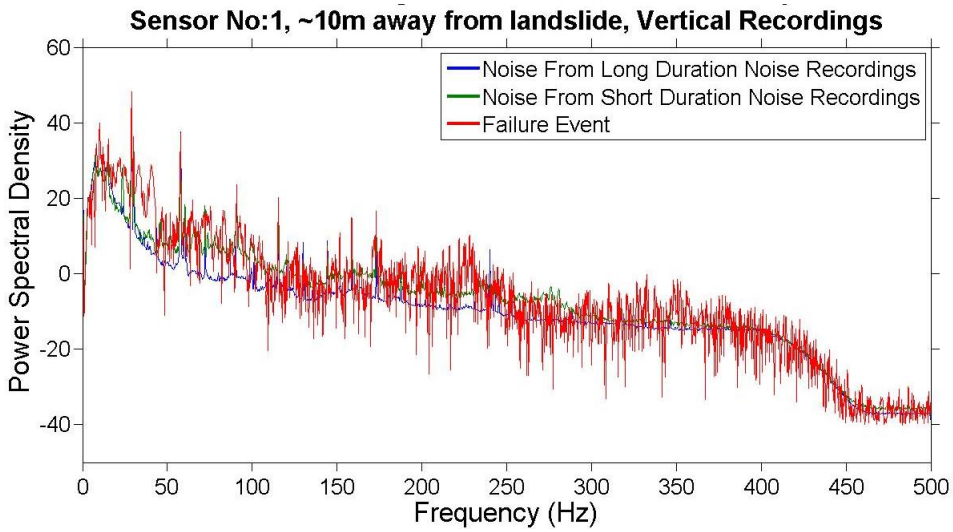

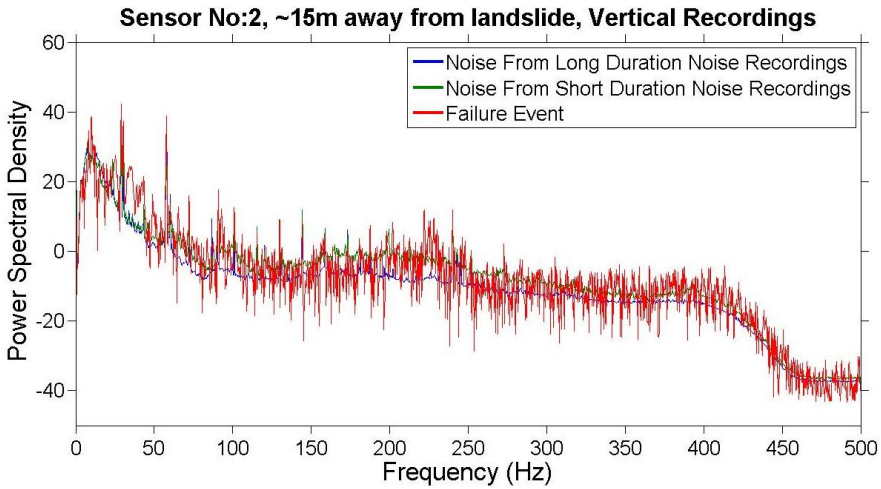
Sensor No:2, ~15m away from landslide, Vertical Recordings
Noise From Long Duration Noise Recordings
Noise From Short Duration Noise Recordings
Failure Event
Power Spectral Density
Frequency (Hz)

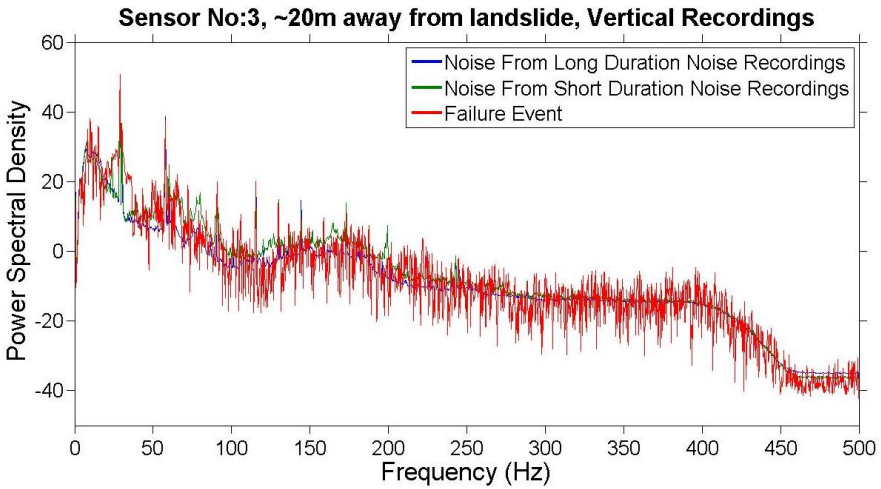
Sensor No:3, ~20m away from landslide, Vertical Recordings
Noise From Long Duration Noise Recordings
Noise From Short Duration Noise Recordings
Failure Event
Power Spectral Density
Frequency (Hz)

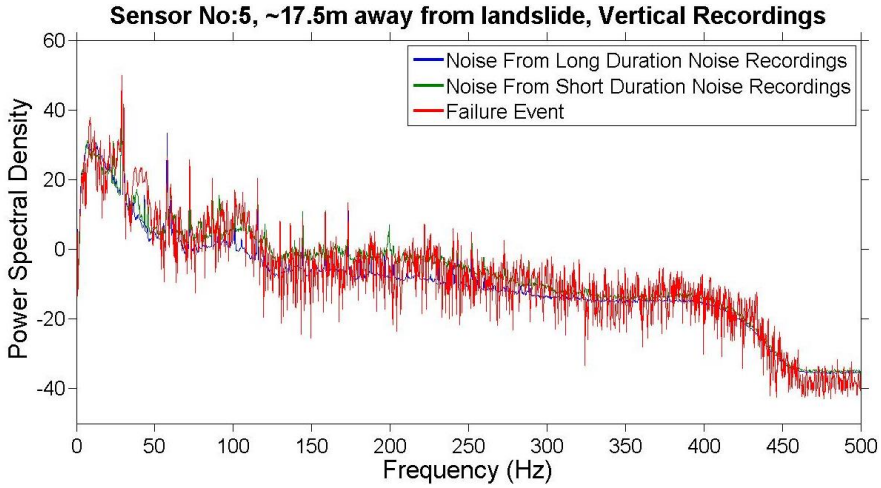
Sensor No:5, ~17.5m away from landslide, Vertical Recordings
Noise From Long Duration Noise Recordings
Noise From Short Duration Noise Recordings
Failure Event
Power Spectral Density
Frequency (Hz)

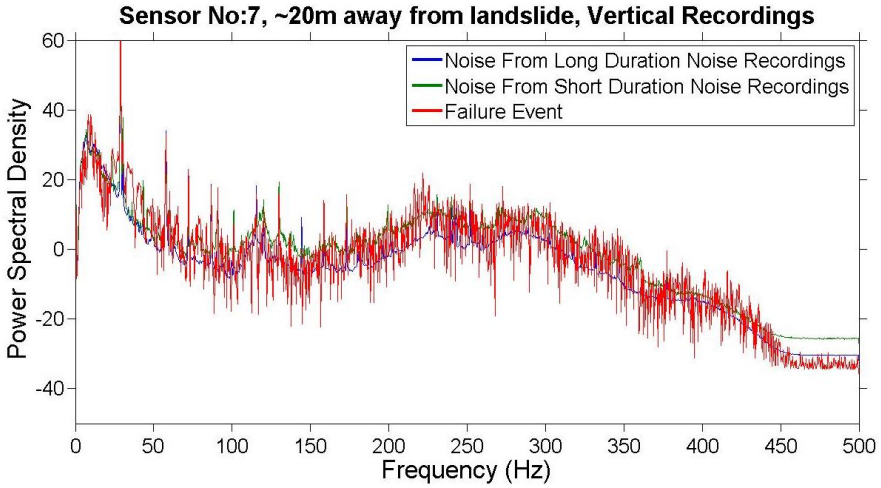
Sensor No:7, ~20m away from landslide, Vertical Recordings
Noise From Long Duration Noise Recordings
Noise From Short Duration Noise Recordings
Failure Event
Power Spectral Density
Frequency (Hz)

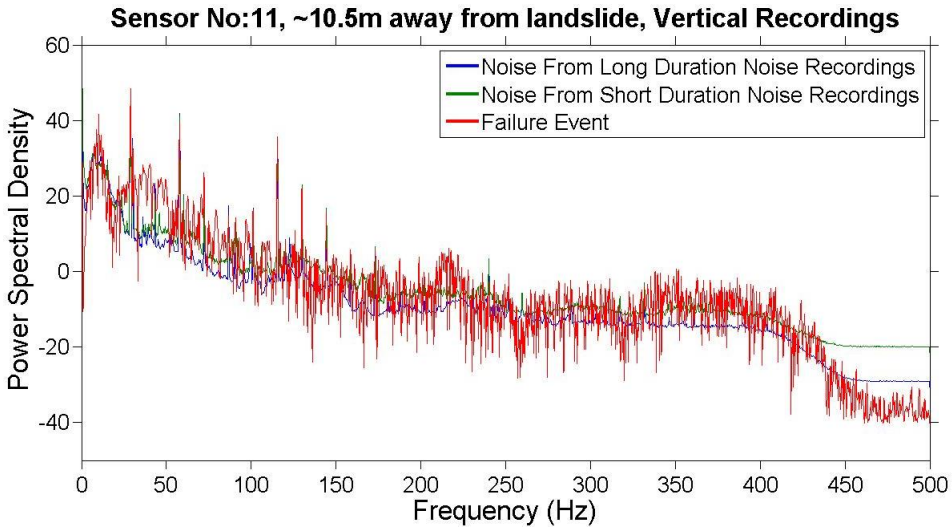

b) North South Component

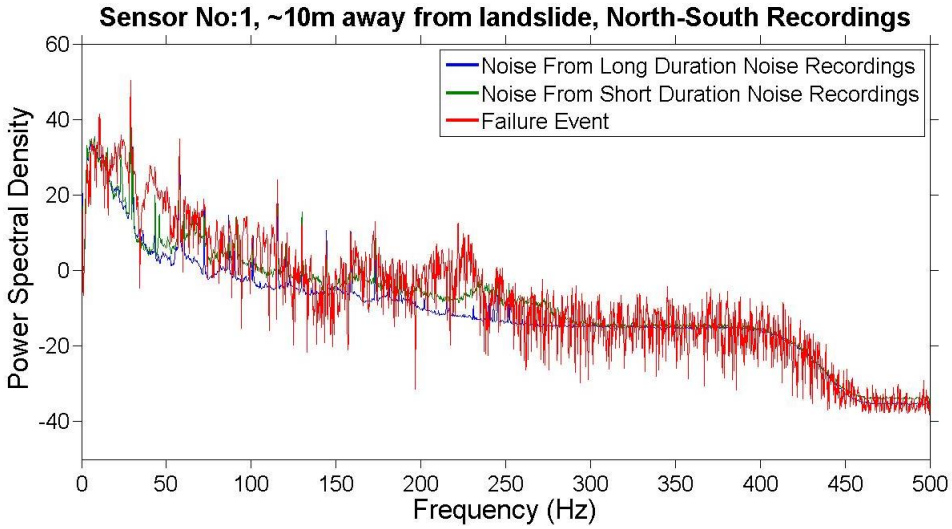

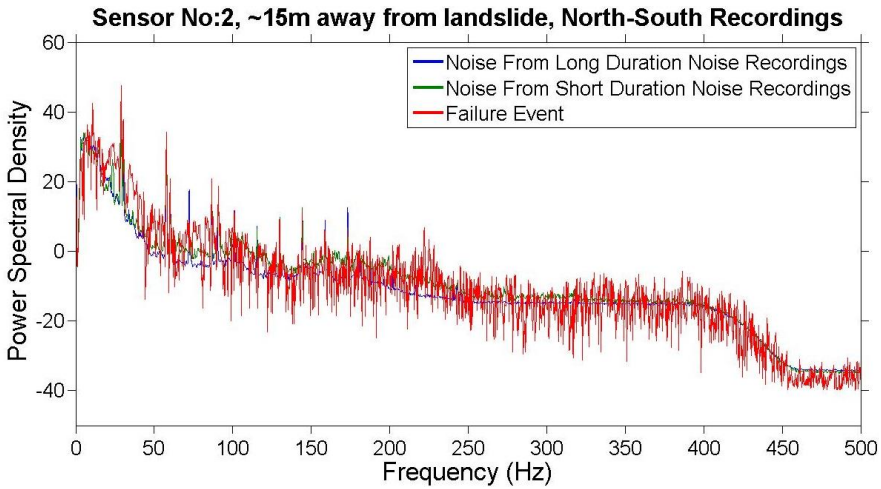
Sensor No:2, ~15m away from landslide, North-South Recordings
Noise From Long Duration Noise Recordings
Noise From Short Duration Noise Recordings
Failure Event
Power Spectral Density
Frequency (Hz)

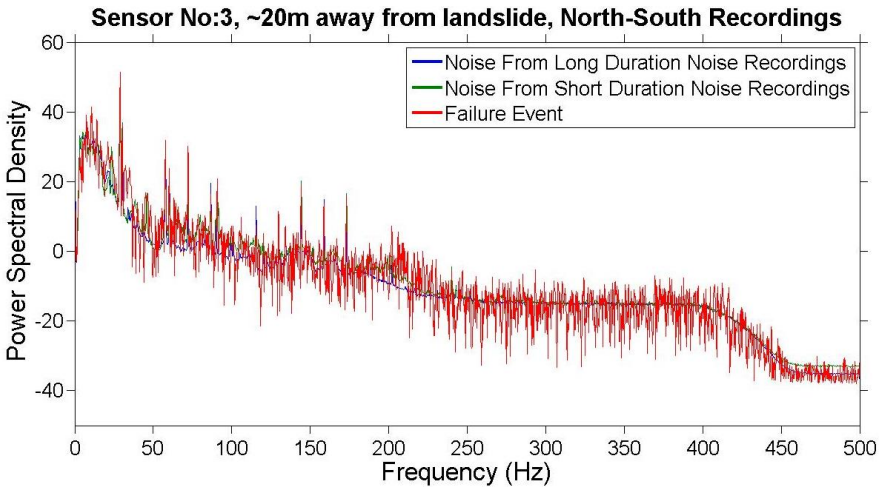
Sensor No:3, ~20m away from landslide, North-South Recordings
Noise From Long Duration Noise Recordings
Noise From Short Duration Noise Recordings
Failure Event
Power Spectral Density
Frequency (Hz)

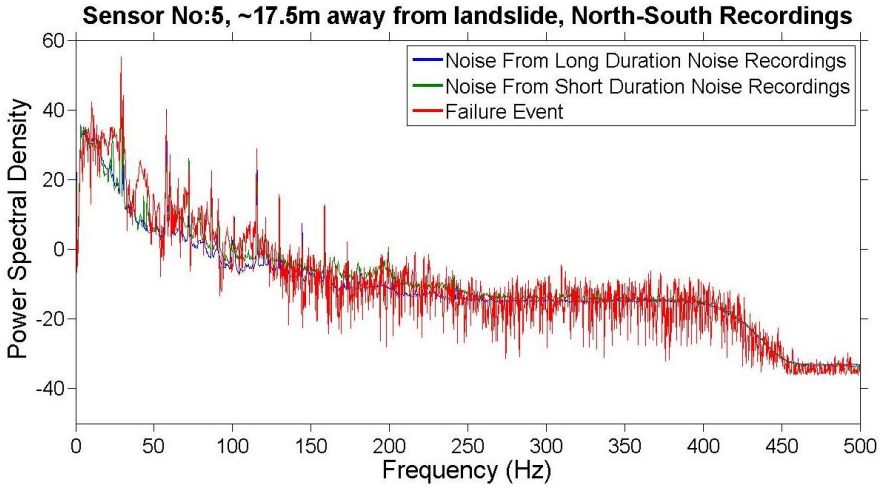
Sensor No:5, ~17.5m away from landslide, North-South Recordings
Noise From Long Duration Noise Recordings
Noise From Short Duration Noise Recordings
Failure Event
Power Spectral Density
Frequency (Hz)

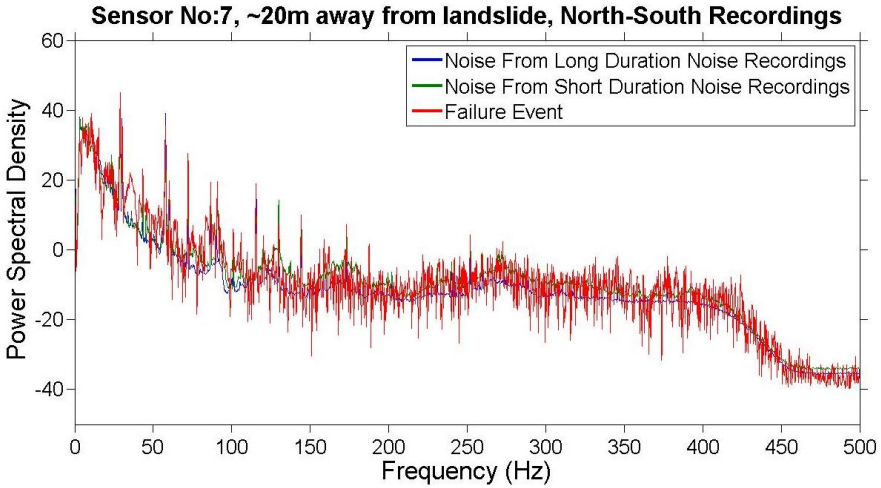
Sensor No:7, ~20m away from landslide, North-South Recordings
Noise From Long Duration Noise Recordings
Noise From Short Duration Noise Recordings
Failure Event
Power Spectral Density
Frequency (Hz)

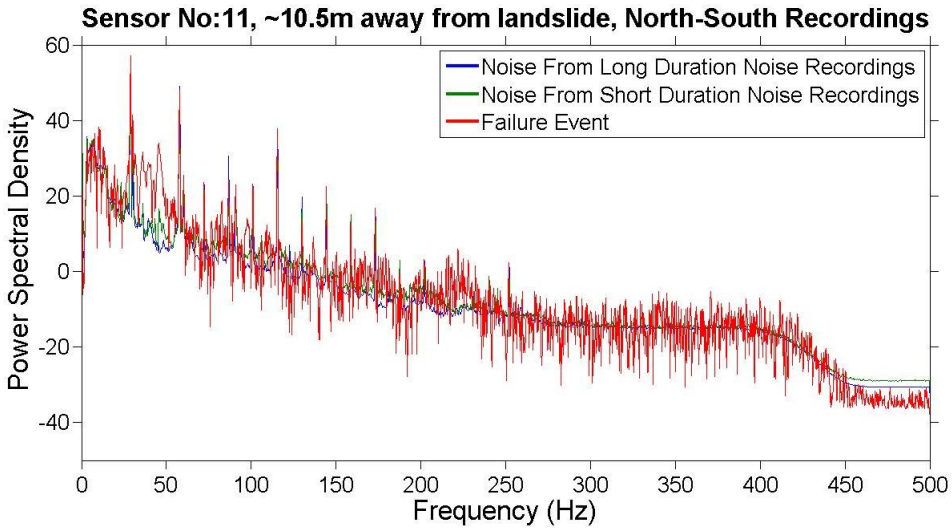

c) East-West Component

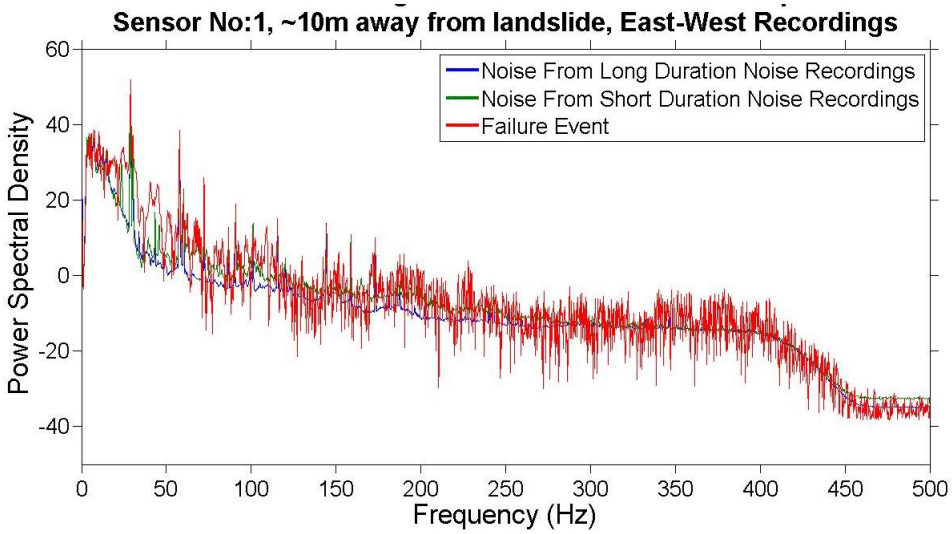

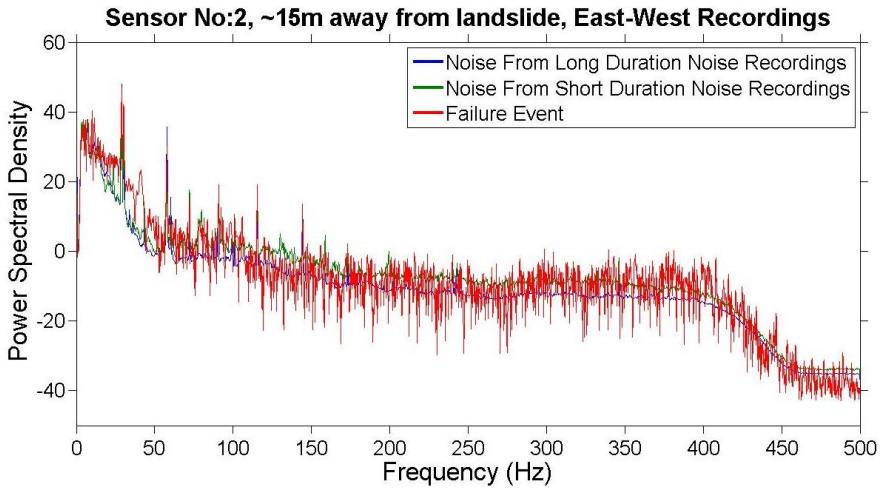
Sensor No:2, ~15m away from landslide, East-West Recordings
Noise From Long Duration Noise Recordings
Noise From Short Duration Noise Recordings
Failure Event
Power Spectral Density
Frequency (Hz)

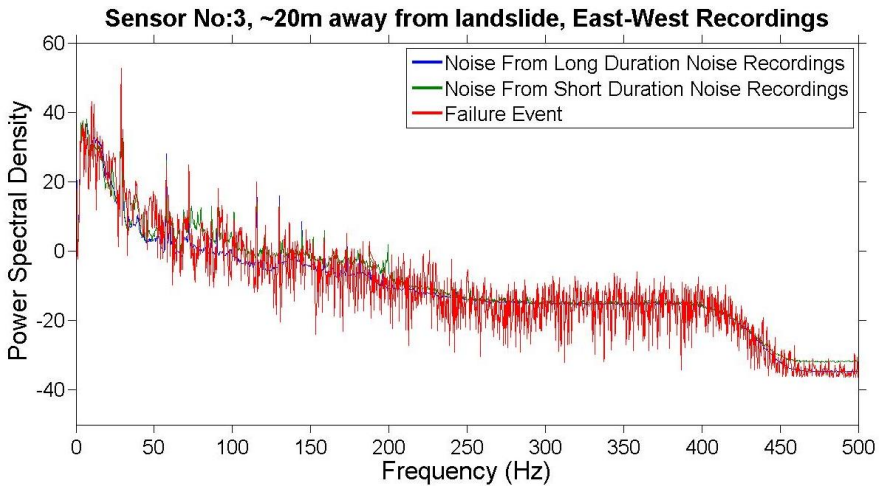
Sensor No:3, ~20m away from landslide, East-West Recordings
Noise From Long Duration Noise Recordings
Noise From Short Duration Noise Recordings
Failure Event
Power Spectral Density
Frequency (Hz)

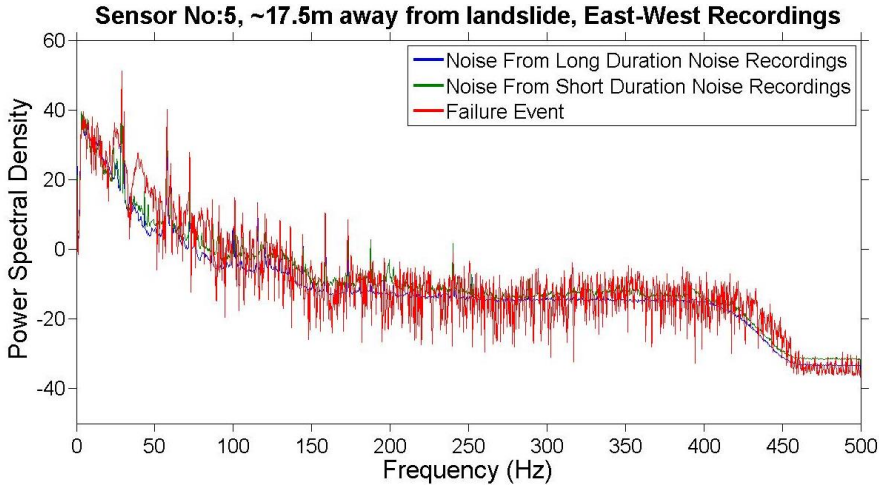
Sensor No:5, ~17.5m away from landslide, East-West Recordings
Noise From Long Duration Noise Recordings
Noise From Short Duration Noise Recordings
Failure Event
Power Spectral Density
Frequency (Hz)

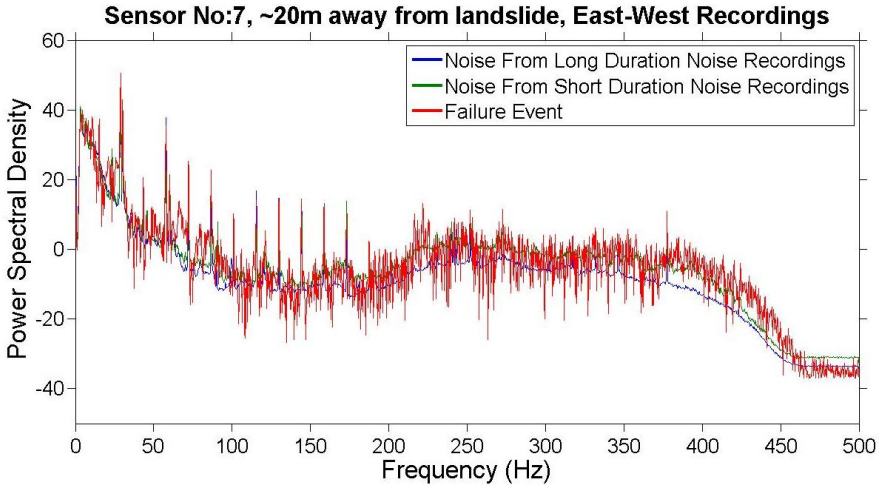
Sensor No:7, ~20m away from landslide, East-West Recordings
Noise From Long Duration Noise Recordings
Noise From Short Duration Noise Recordings
Failure Event
Power Spectral Density
Frequency (Hz)

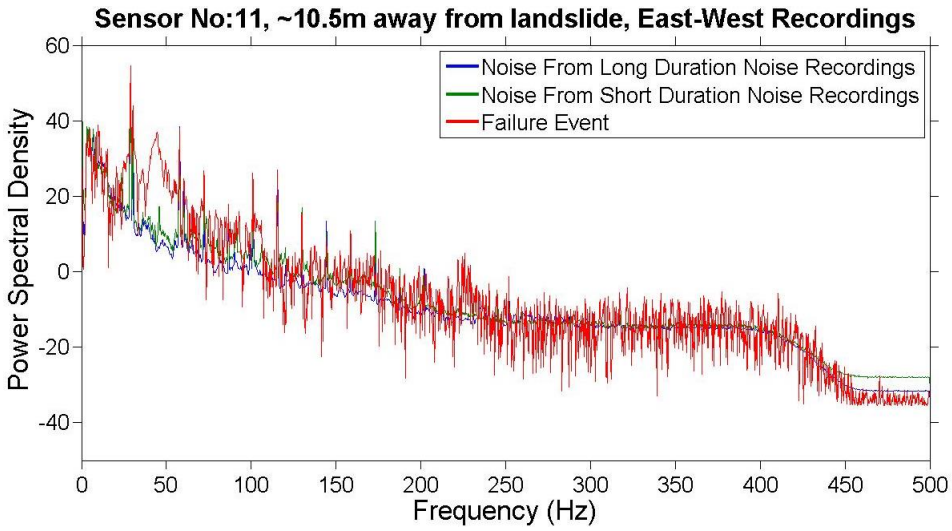

C3.3.2 Additional PSD graphs of FT3 No3 event of Experiment L1

a) Vertical Component

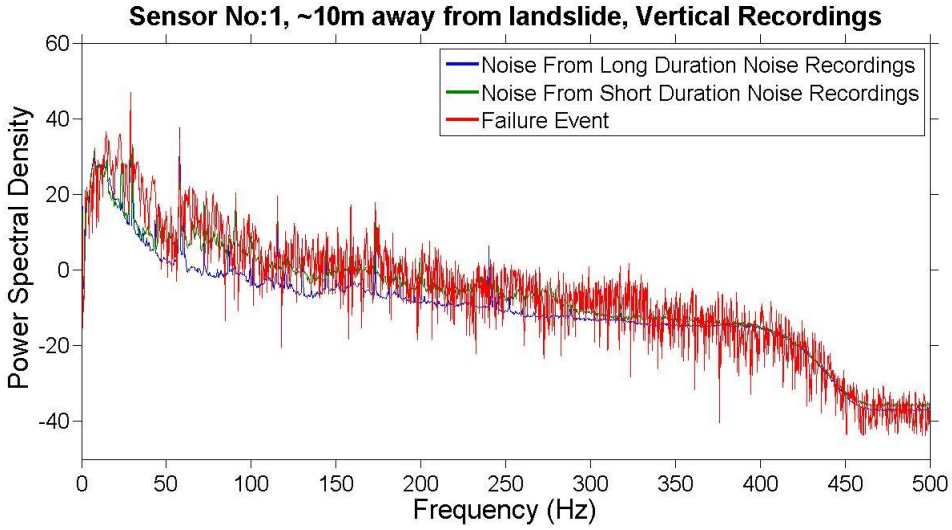

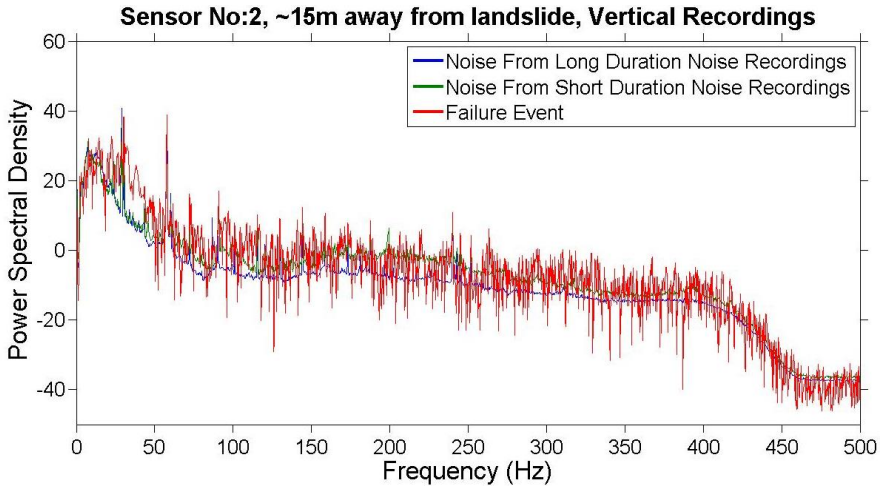
Sensor No:2, ~15m away from landslide, Vertical Recordings
Noise From Long Duration Noise Recordings
Noise From Short Duration Noise Recordings
Failure Event
Power Spectral Density
Frequency (Hz)

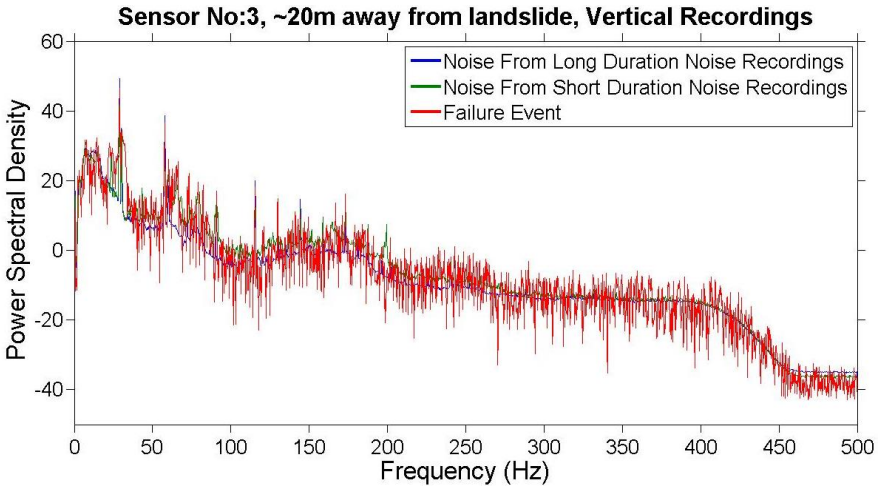
Sensor No:3, ~20m away from landslide, Vertical Recordings
Noise From Long Duration Noise Recordings
Noise From Short Duration Noise Recordings
Failure Event
Power Spectral Density
Frequency (Hz)

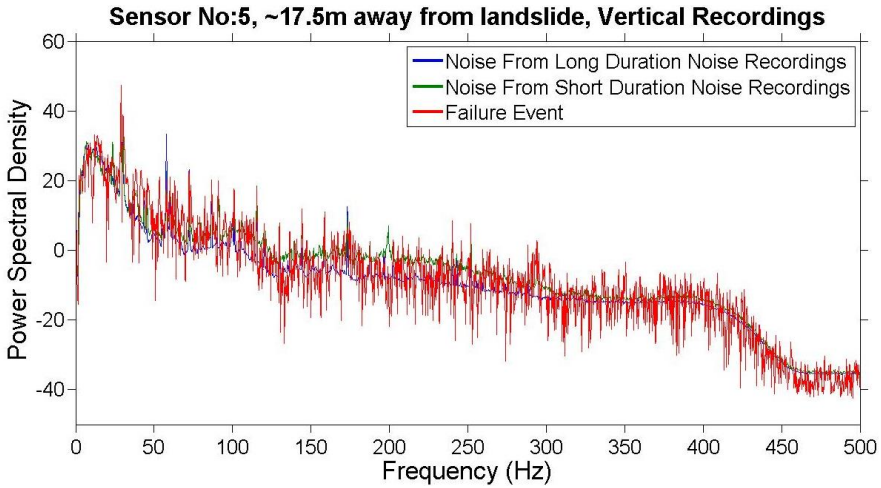
Sensor No:5, ~17.5m away from landslide, Vertical Recordings
Noise From Long Duration Noise Recordings
Noise From Short Duration Noise Recordings
Failure Event
Power Spectral Density
Frequency (Hz)

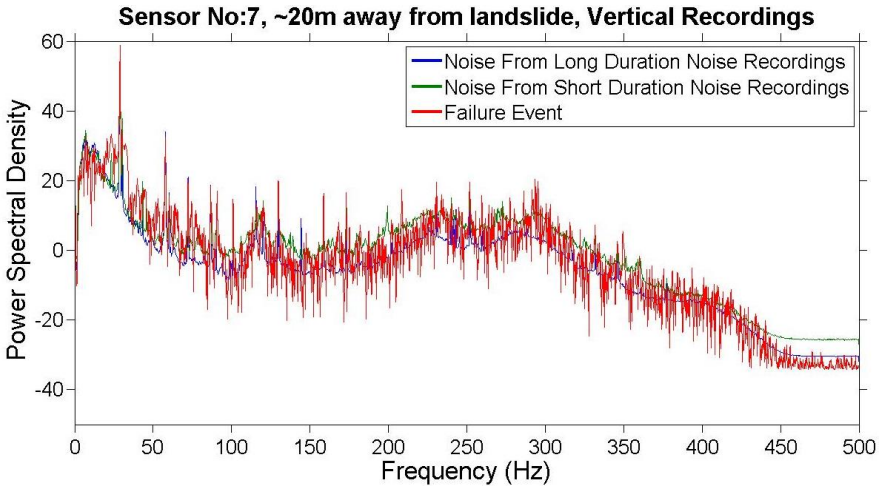
Sensor No:7, ~20m away from landslide, Vertical Recordings
Noise From Long Duration Noise Recordings
Noise From Short Duration Noise Recordings
Failure Event
Power Spectral Density
Frequency (Hz)

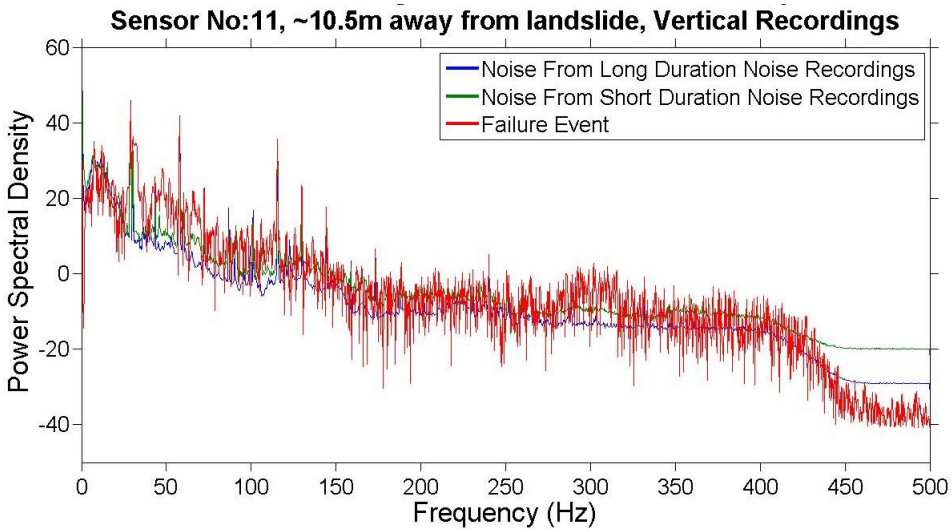

b) North-South Component

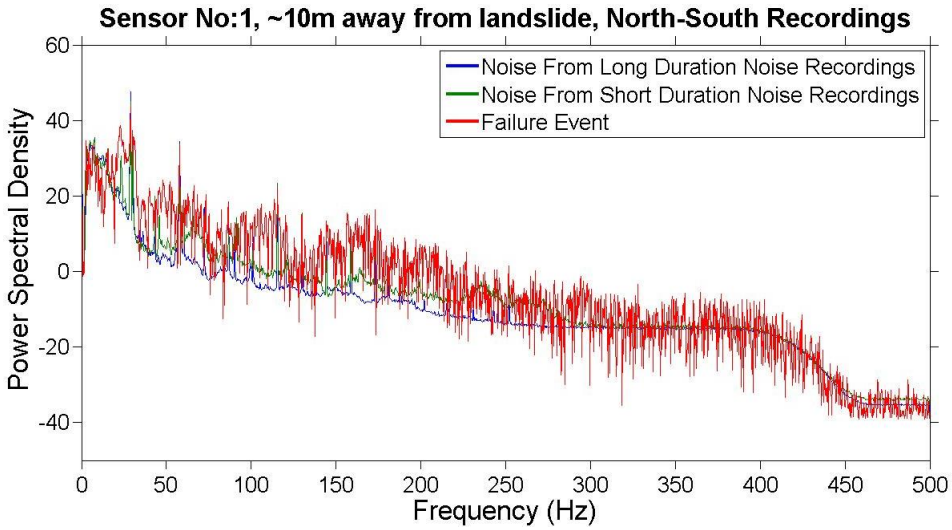

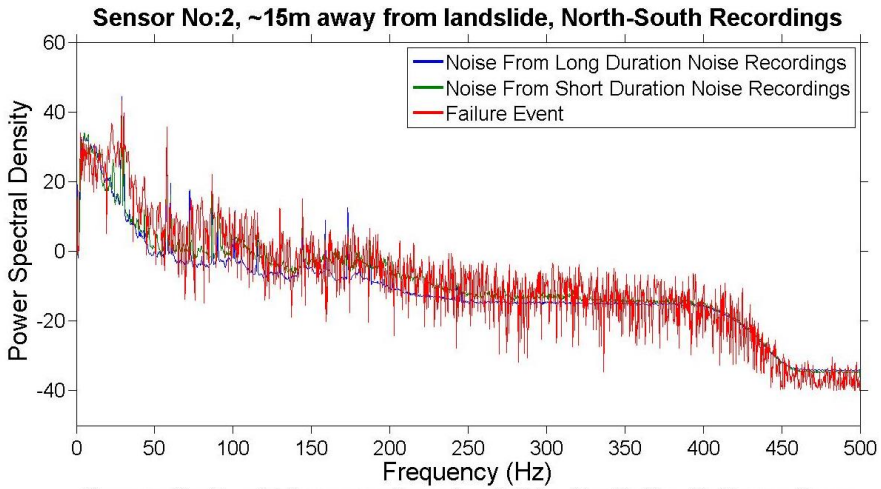
Sensor No:2, ~15m away from landslide, North-South Recordings
Noise From Long Duration Noise Recordings
Noise From Short Duration Noise Recordings
Failure Event
Power Spectral Density
Frequency (Hz)

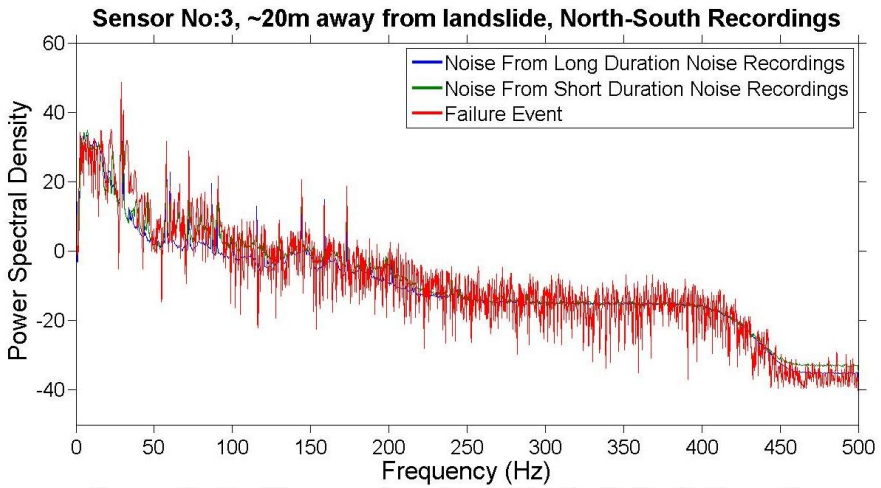
Sensor No:3, ~20m away from landslide, North-South Recordings
Noise From Long Duration Noise Recordings
Noise From Short Duration Noise Recordings
Failure Event
Power Spectral Density
Frequency (Hz)

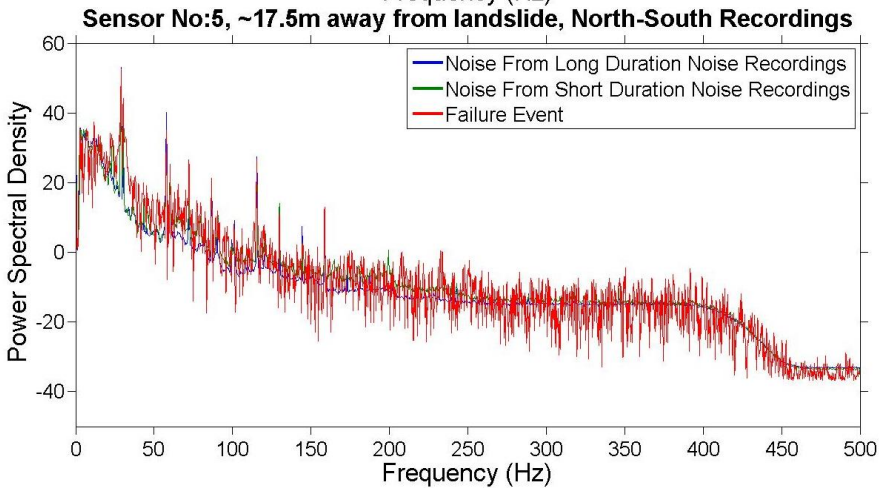
Sensor No:5, ~17.5m away from landslide, North-South Recordings
Noise From Long Duration Noise Recordings
Noise From Short Duration Noise Recordings
Failure Event
Power Spectral Density
Frequency (Hz)

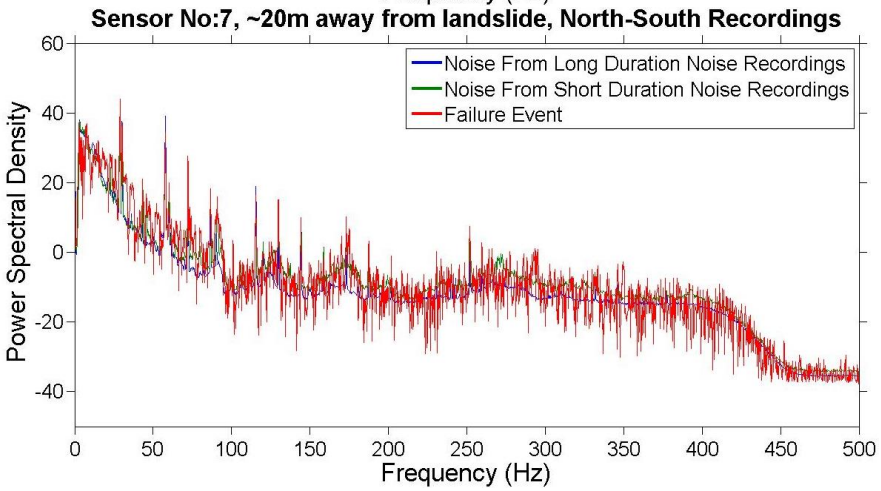
Sensor No:7, ~20m away from landslide, North-South Recordings
Noise From Long Duration Noise Recordings
Noise From Short Duration Noise Recordings
Failure Event
Power Spectral Density
Frequency (Hz)

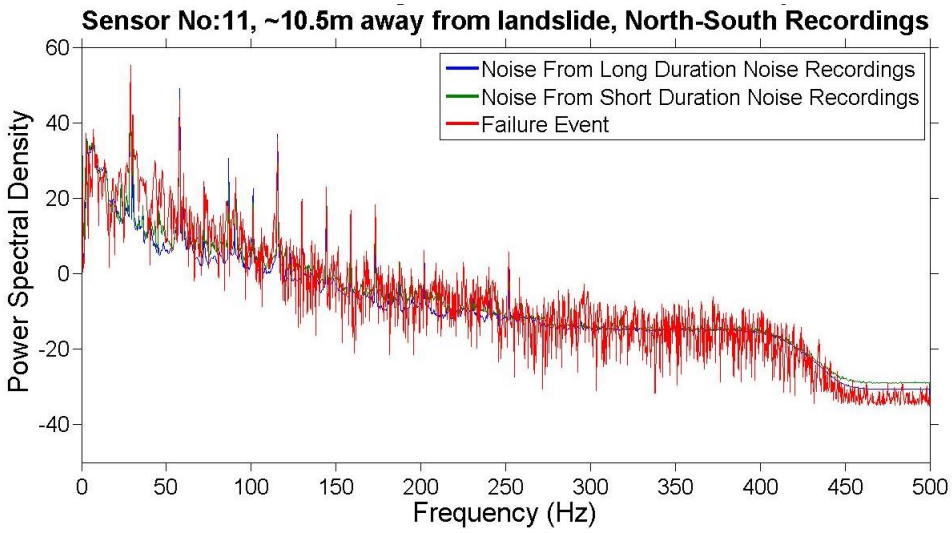

c) East-West Component

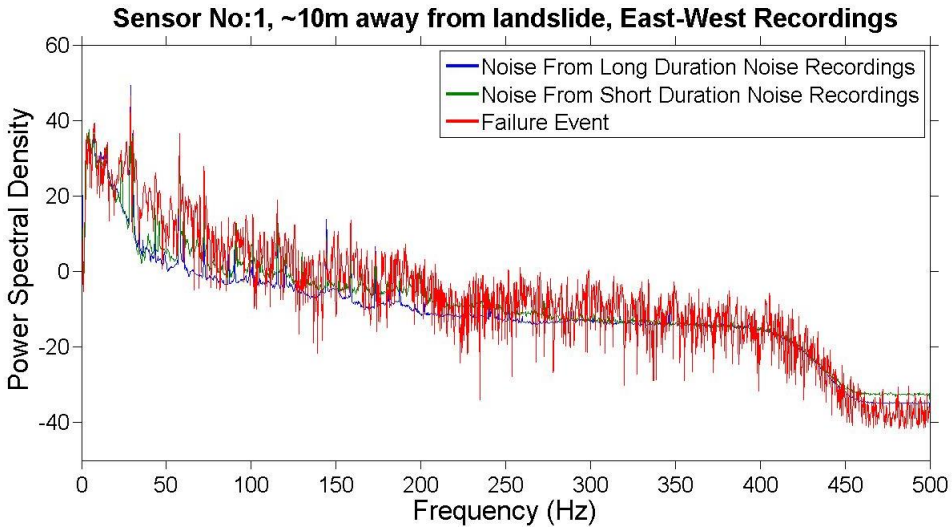

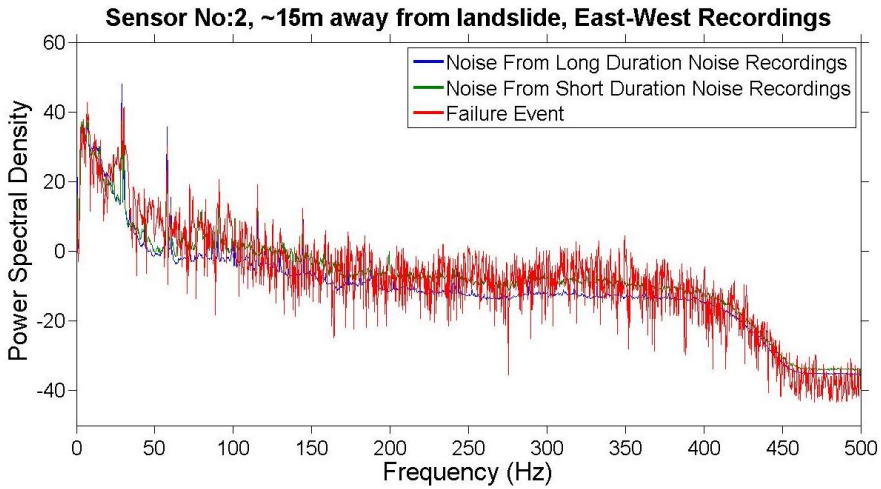
Sensor No:2, ~15m away from landslide, East-West Recordings
Noise From Long Duration Noise Recordings
Noise From Short Duration Noise Recordings
Failure Event
Power Spectral Density
Frequency (Hz)

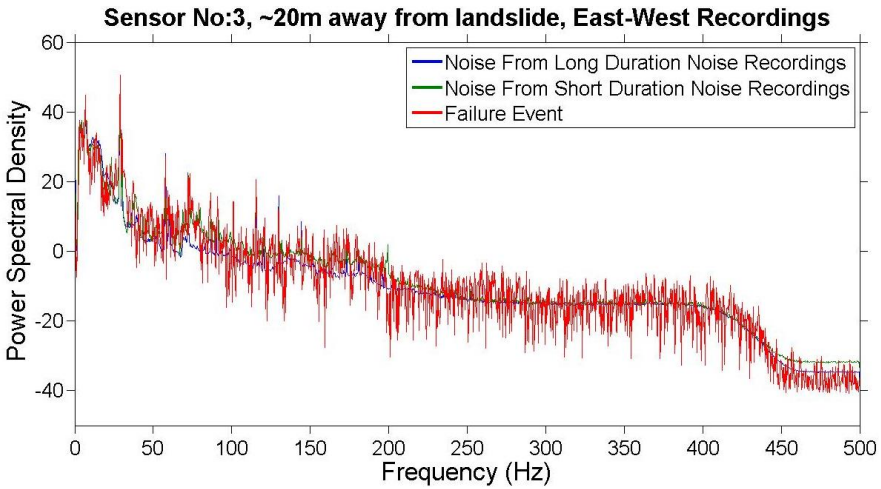
Sensor No:3, ~20m away from landslide, East-West Recordings
Noise From Long Duration Noise Recordings
Noise From Short Duration Noise Recordings
Failure Event
Power Spectral Density
Frequency (Hz)

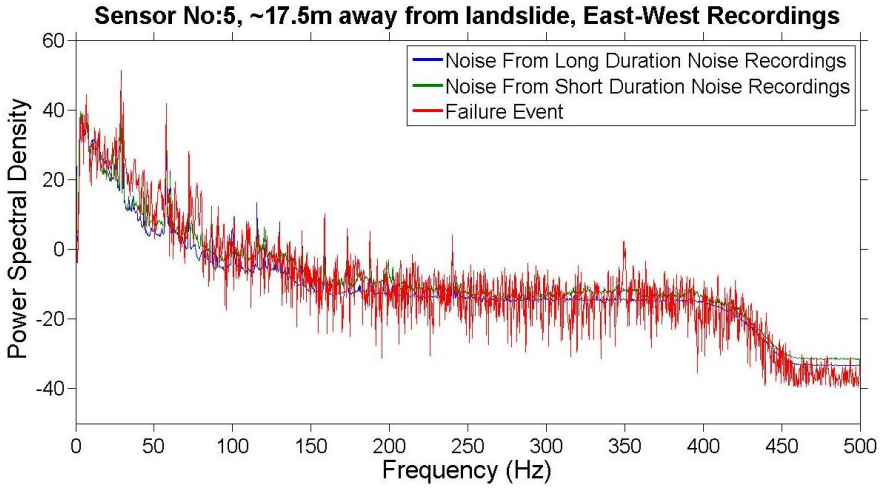
Sensor No:5, ~17.5m away from landslide, East-West Recordings
Noise From Long Duration Noise Recordings
Noise From Short Duration Noise Recordings
Failure Event
Power Spectral Density
Frequency (Hz)

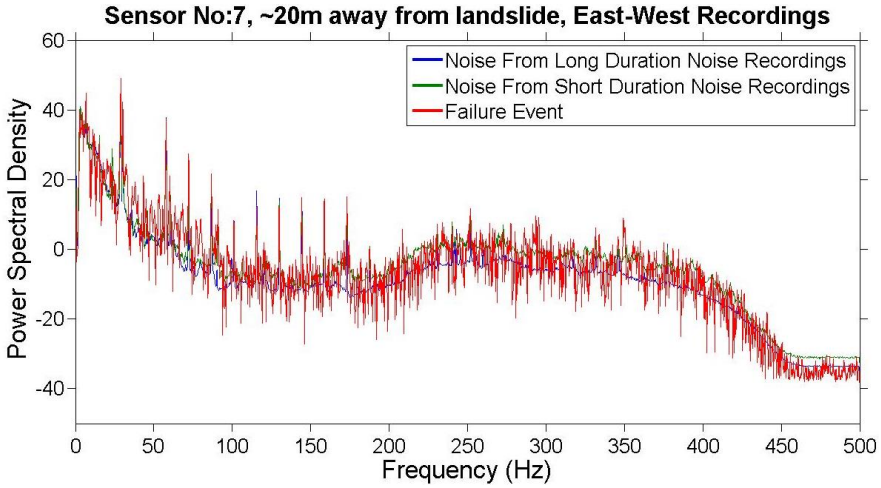
Sensor No:7, ~20m away from landslide, East-West Recordings
Noise From Long Duration Noise Recordings
Noise From Short Duration Noise Recordings
Failure Event
Power Spectral Density
Frequency (Hz)

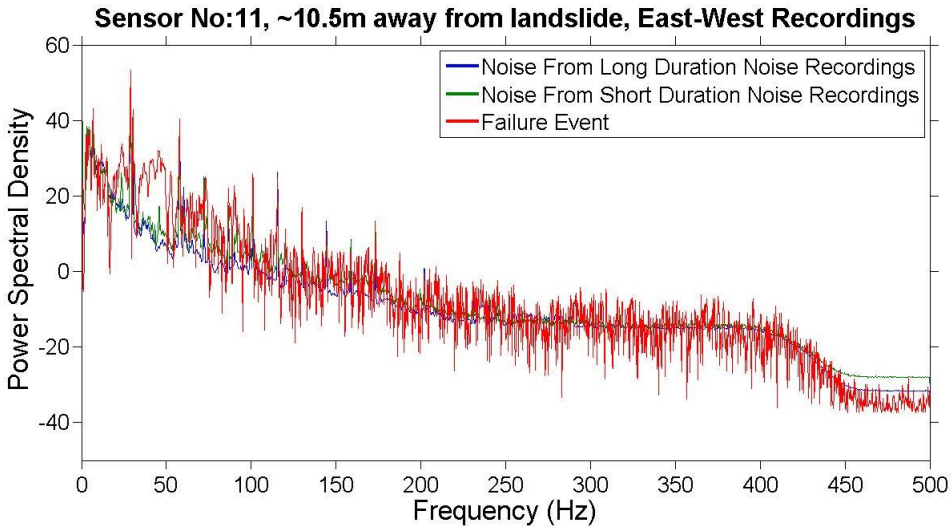

C3.3.3 Additional PSD graphs of FT3 No2 event of Experiment L1 presented in Figure 8.24

a) Vertical Component

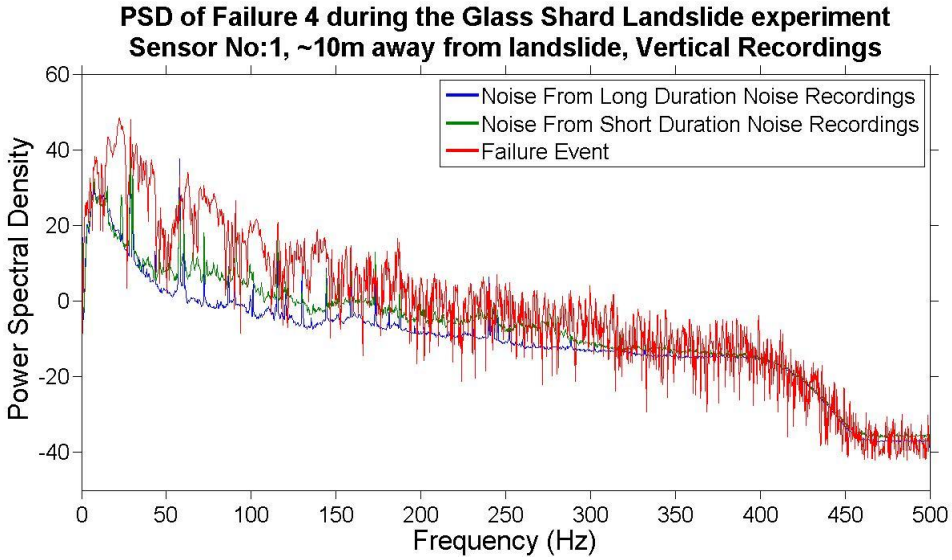

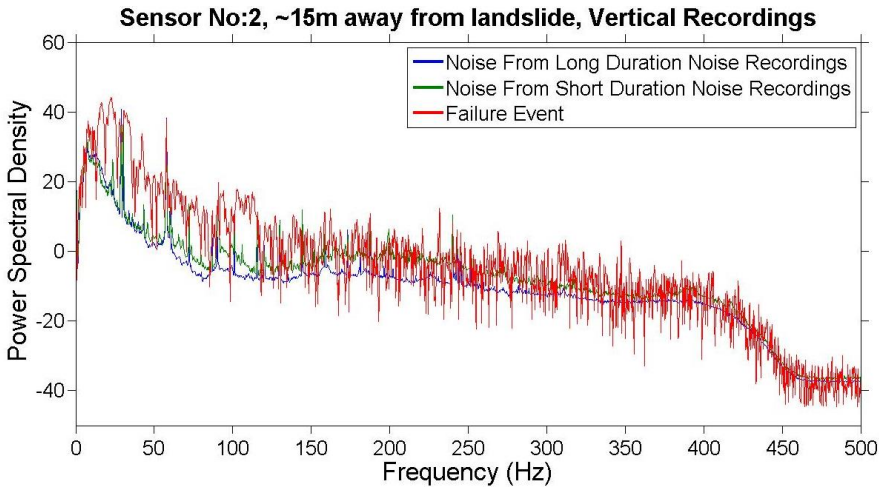
Sensor No:2, ~15m away from landslide, Vertical Recordings
Noise From Long Duration Noise Recordings
Noise From Short Duration Noise Recordings
Failure Event
Power Spectral Density
Frequency (Hz)
60
40
20
0
-20
-40
0
50
100
150
200
250
300
350
400
450
500

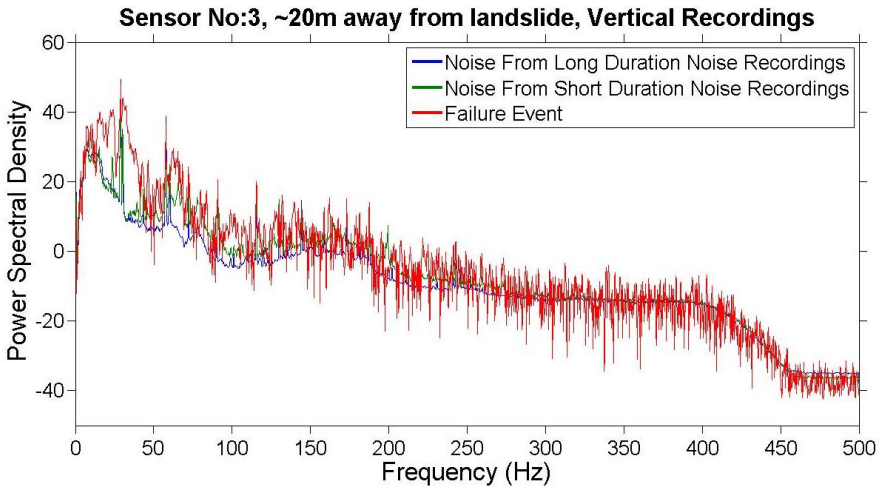
Sensor No:3, ~20m away from landslide, Vertical Recordings
Noise From Long Duration Noise Recordings
Noise From Short Duration Noise Recordings
Failure Event
Power Spectral Density
Frequency (Hz)
60
40
20
0
-20
-40
0
50
100
150
200
250
300
350
400
450
500

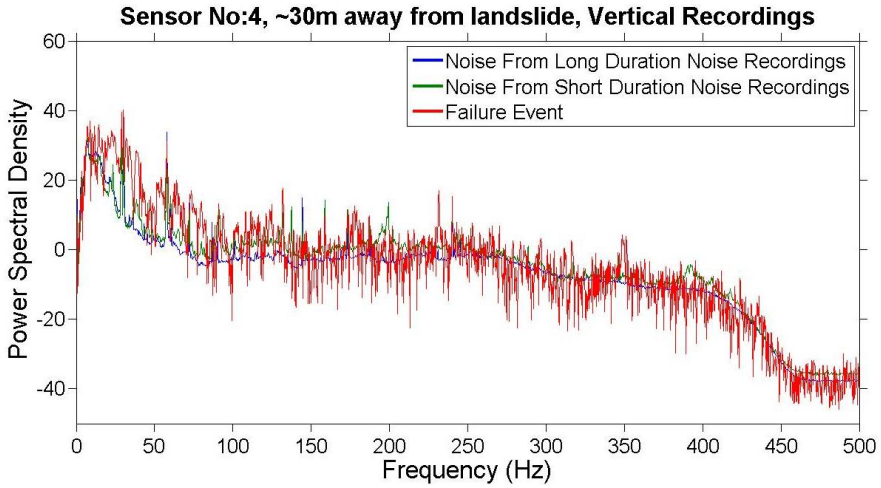
Sensor No:4, ~30m away from landslide, Vertical Recordings
Noise From Long Duration Noise Recordings
Noise From Short Duration Noise Recordings
Failure Event
Power Spectral Density
Frequency (Hz)
60
40
20
0
-20
-40
0
50
100
150
200
250
300
350
400
450
500

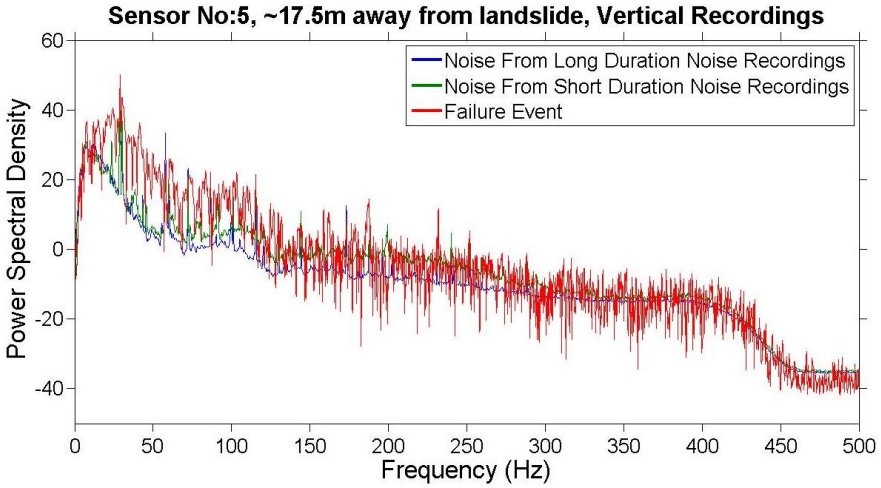
Sensor No:5, ~17.5m away from landslide, Vertical Recordings
Noise From Long Duration Noise Recordings
Noise From Short Duration Noise Recordings
Failure Event
Power Spectral Density
Frequency (Hz)
60
40
20
0
-20
-40
0
50
100
150
200
250
300
350
400
450
500

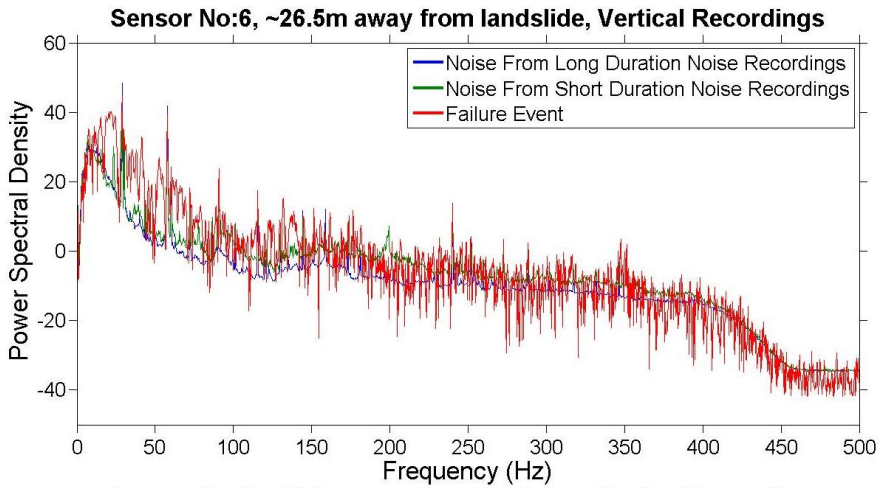
Sensor No:6, ~26.5m away from landslide, Vertical Recordings
Noise From Long Duration Noise Recordings
Noise From Short Duration Noise Recordings
Failure Event
Power Spectral Density
Frequency (Hz)

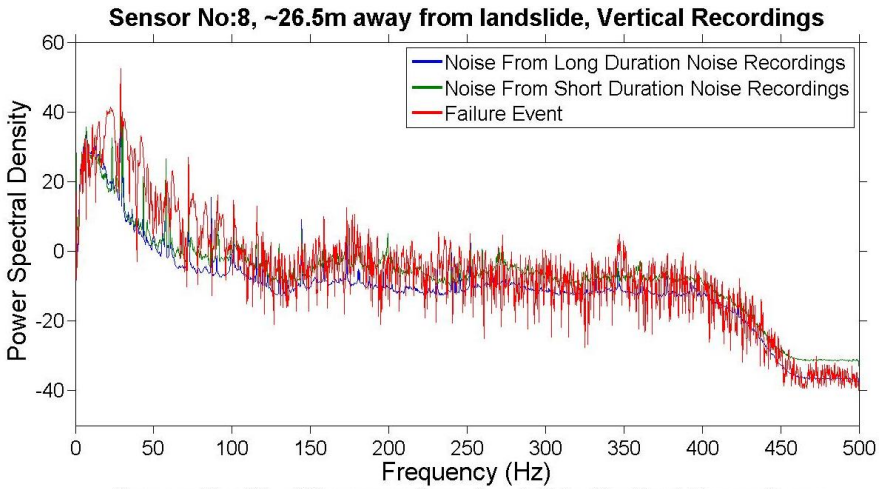
Sensor No:8, ~26.5m away from landslide, Vertical Recordings
Noise From Long Duration Noise Recordings
Noise From Short Duration Noise Recordings
Failure Event
Power Spectral Density
Frequency (Hz)

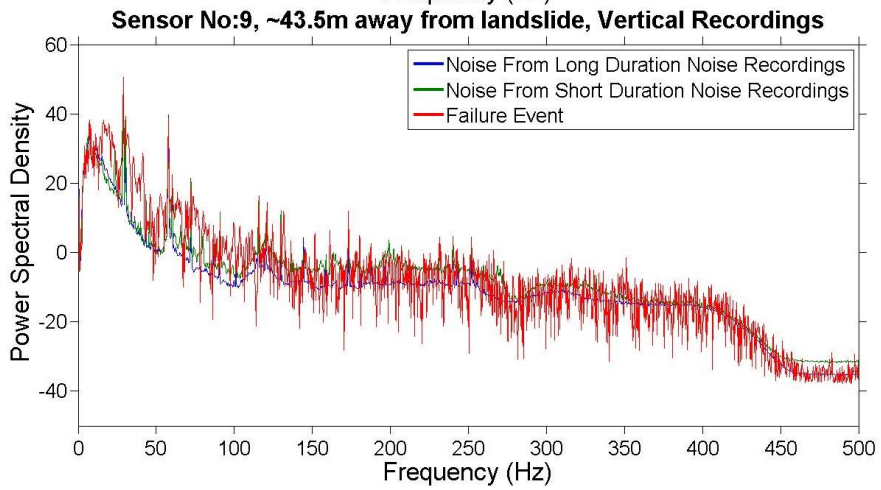
Sensor No:9, ~43.5m away from landslide, Vertical Recordings
Noise From Long Duration Noise Recordings
Noise From Short Duration Noise Recordings
Failure Event
Power Spectral Density
Frequency (Hz)

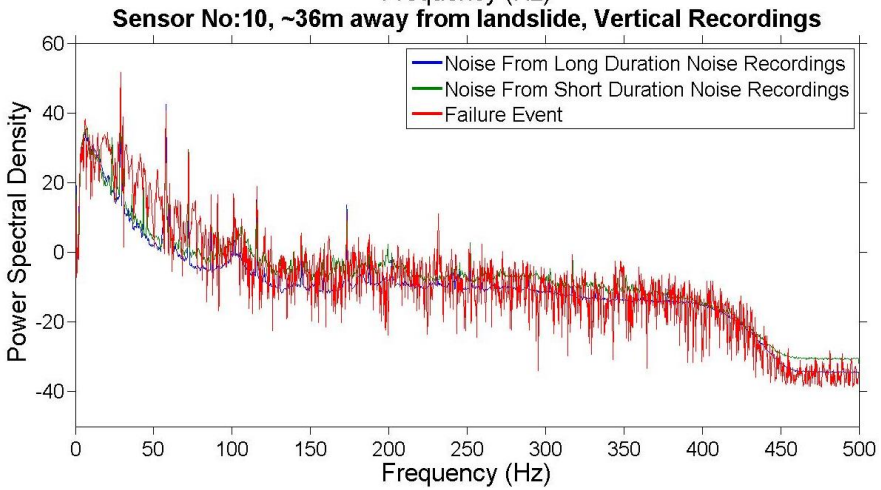
Sensor No:10, ~36m away from landslide, Vertical Recordings
Noise From Long Duration Noise Recordings
Noise From Short Duration Noise Recordings
Failure Event
Power Spectral Density
Frequency (Hz)

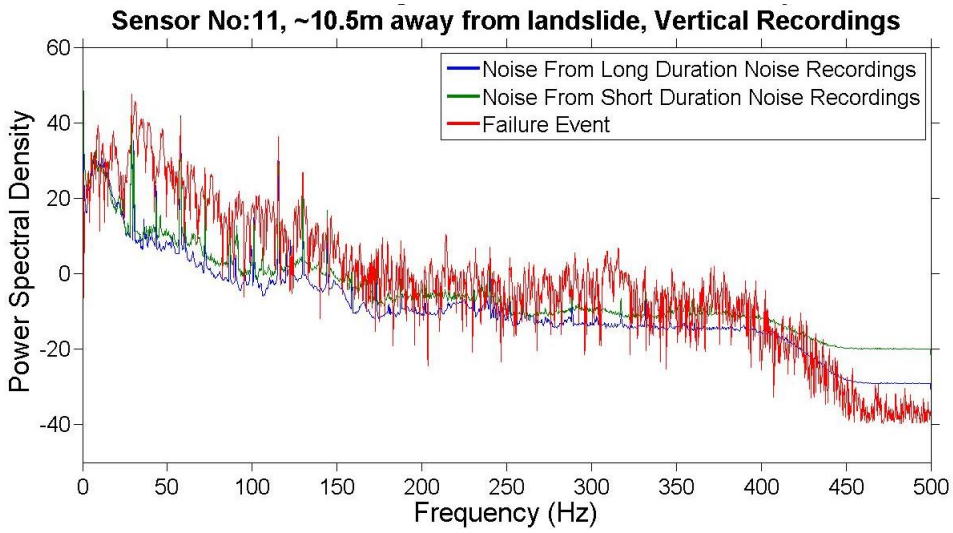

b) North-South Component

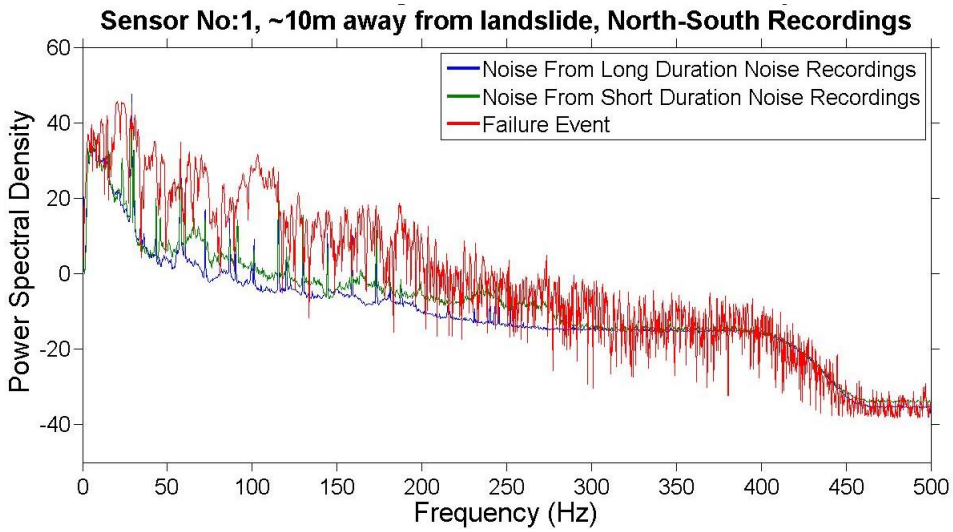

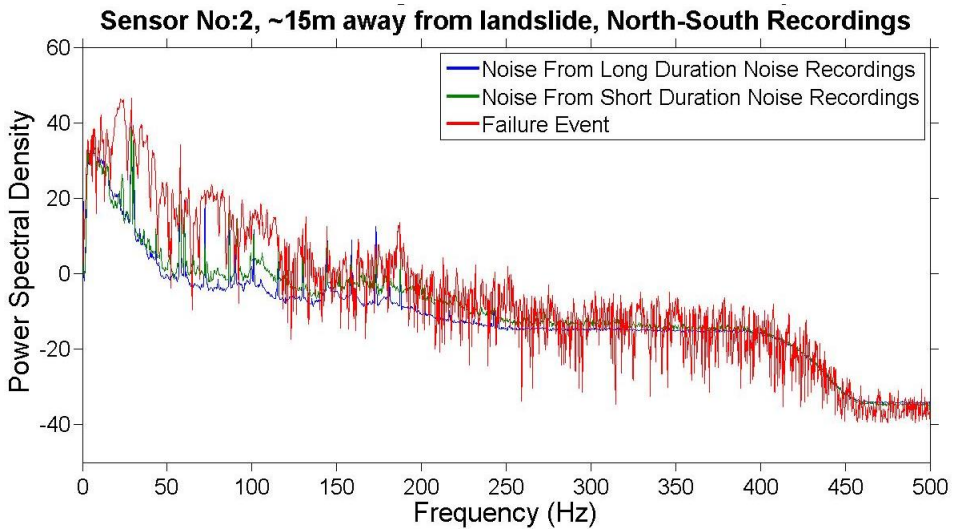

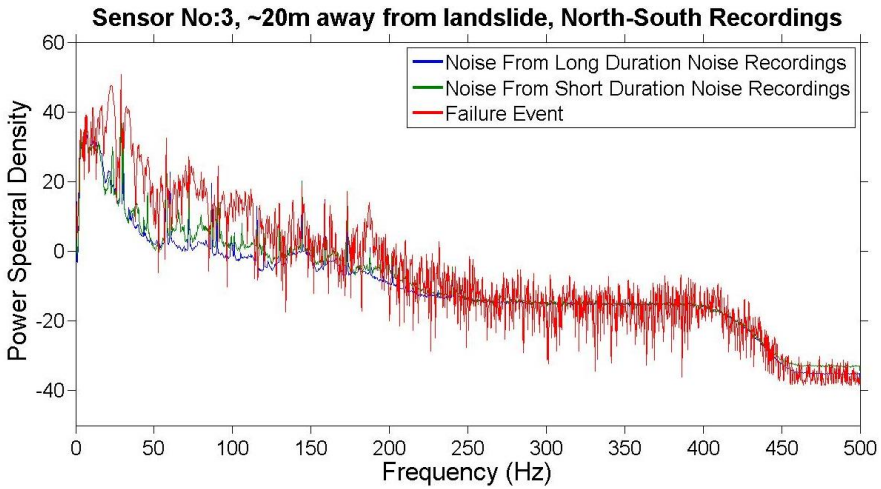
Sensor No:3, ~20m away from landslide, North-South Recordings
Noise From Long Duration Noise Recordings
Noise From Short Duration Noise Recordings
Failure Event
Power Spectral Density
Frequency (Hz)

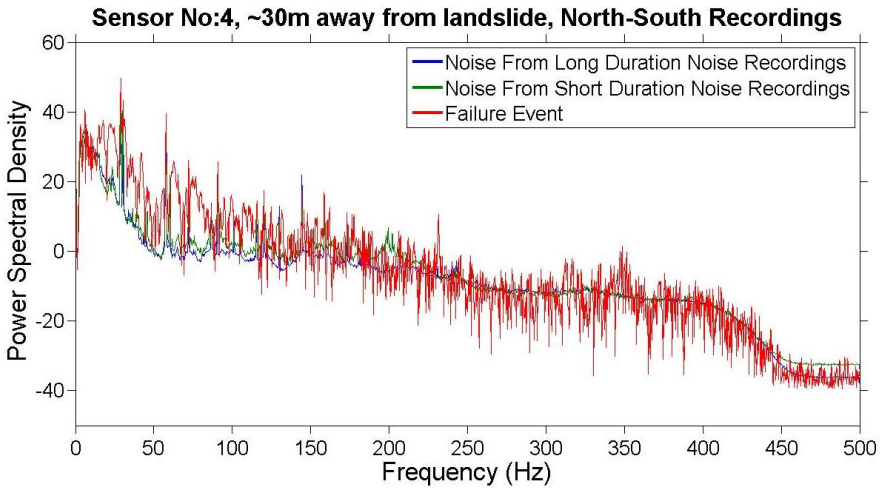
Sensor No:4, ~30m away from landslide, North-South Recordings
Noise From Long Duration Noise Recordings
Noise From Short Duration Noise Recordings
Failure Event
Power Spectral Density
Frequency (Hz)

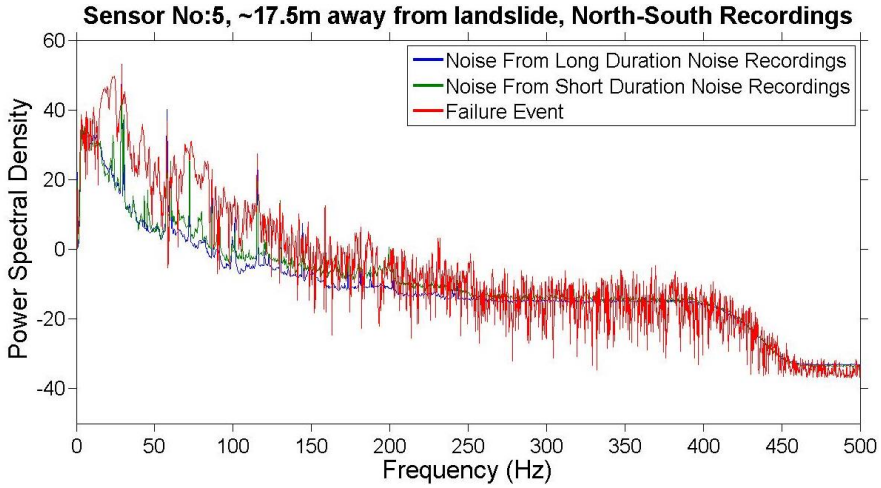
Sensor No:5, ~17.5m away from landslide, North-South Recordings
Noise From Long Duration Noise Recordings
Noise From Short Duration Noise Recordings
Failure Event
Power Spectral Density
Frequency (Hz)

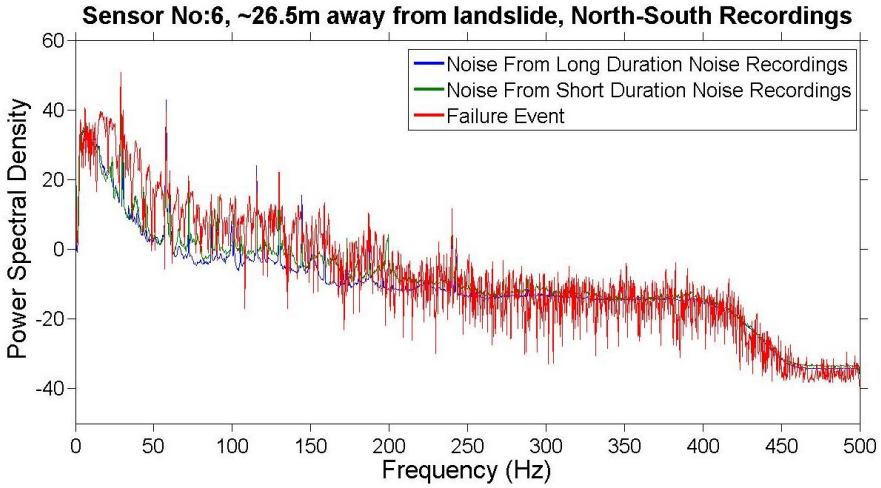
Sensor No:6, ~26.5m away from landslide, North-South Recordings
Noise From Long Duration Noise Recordings
Noise From Short Duration Noise Recordings
Failure Event
Power Spectral Density
Frequency (Hz)

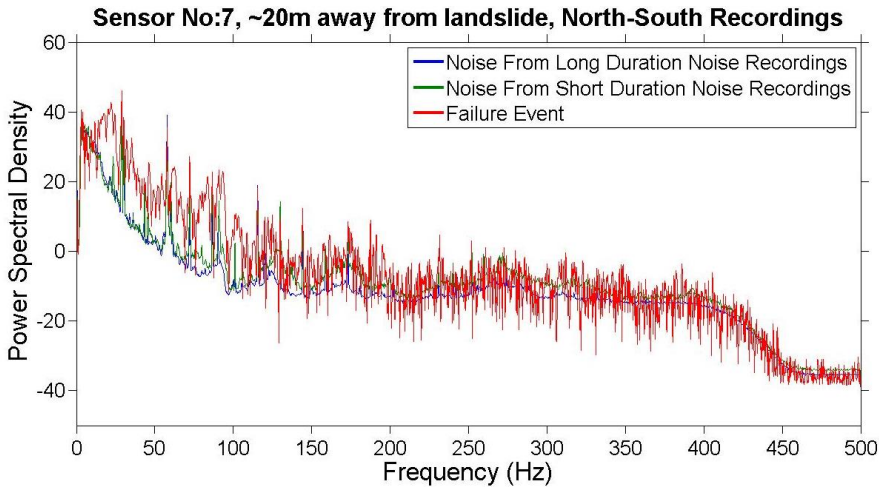
Sensor No:7, ~20m away from landslide, North-South Recordings
Noise From Long Duration Noise Recordings
Noise From Short Duration Noise Recordings
Failure Event
Power Spectral Density
Frequency (Hz)
60
40
20
0
-20
-40
0
50
100
150
200
250
300
350
400
450
500

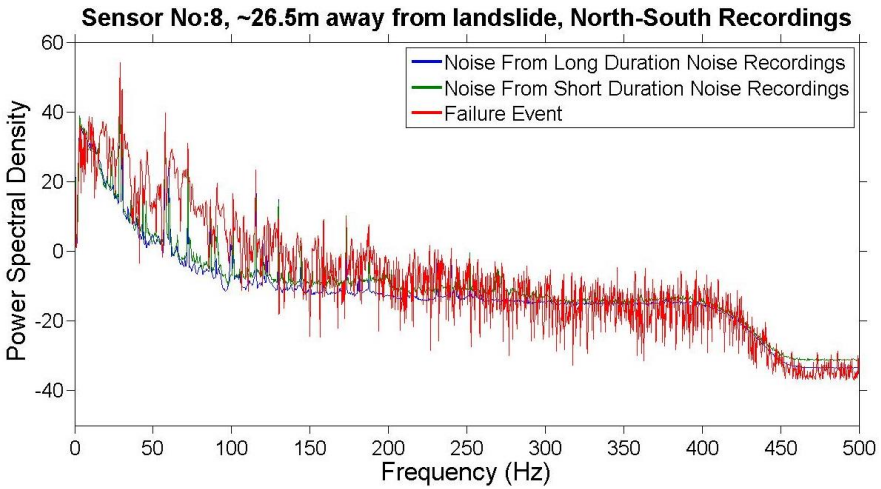
Sensor No:8, ~26.5m away from landslide, North-South Recordings
Noise From Long Duration Noise Recordings
Noise From Short Duration Noise Recordings
Failure Event
Power Spectral Density
Frequency (Hz)
60
40
20
0
-20
-40
0
50
100
150
200
250
300
350
400
450
500

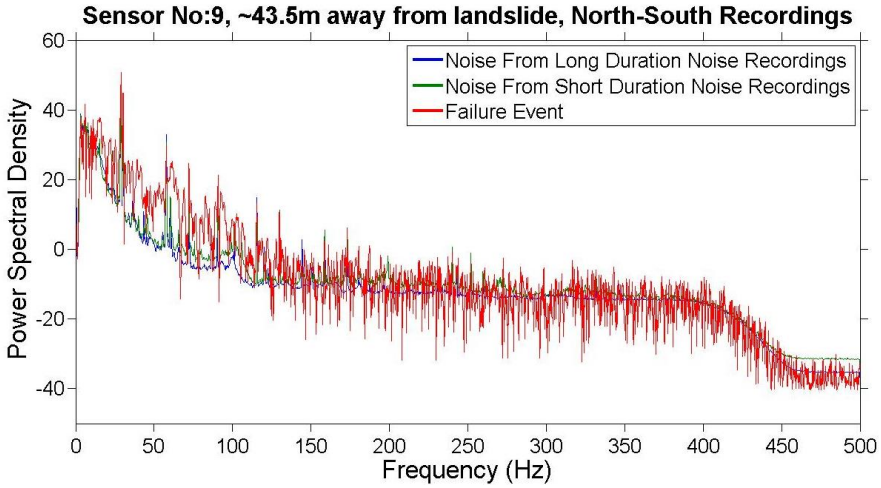
Sensor No:9, ~43.5m away from landslide, North-South Recordings
Noise From Long Duration Noise Recordings
Noise From Short Duration Noise Recordings
Failure Event
Power Spectral Density
Frequency (Hz)
60
40
20
0
-20
-40
0
50
100
150
200
250
300
350
400
450
500

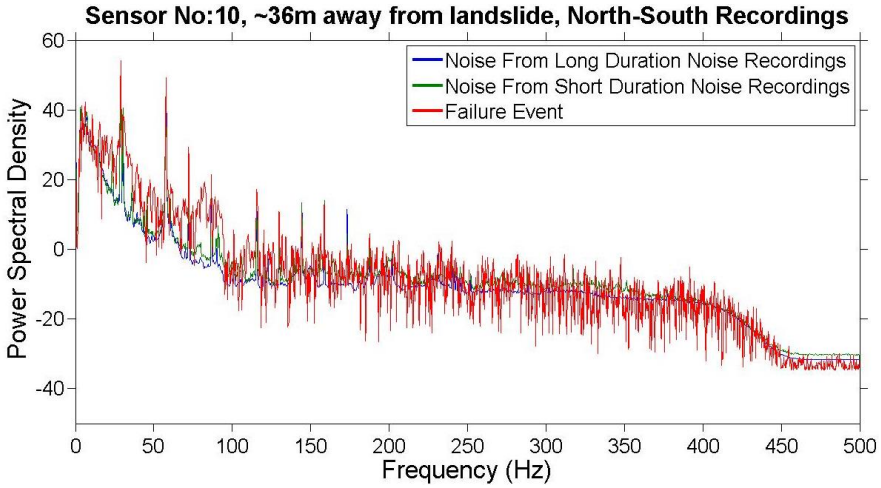
Sensor No:10, ~36m away from landslide, North-South Recordings
Noise From Long Duration Noise Recordings
Noise From Short Duration Noise Recordings
Failure Event
Power Spectral Density
Frequency (Hz)
60
40
20
0
-20
-40
0
50
100
150
200
250
300
350
400
450
500

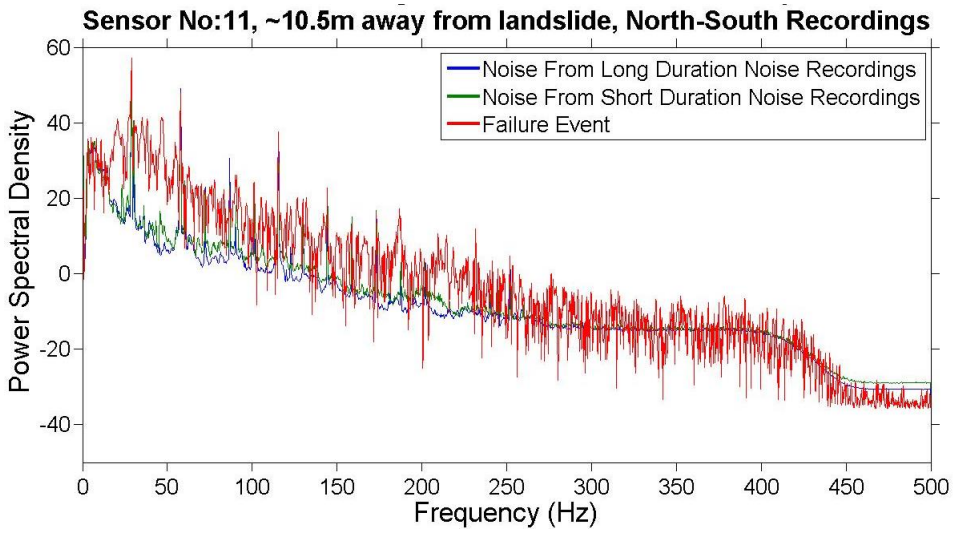
Sensor No:11, ~10.5m away from landslide, North-South Recordings
Noise From Long Duration Noise Recordings
Noise From Short Duration Noise Recordings
Failure Event
Power Spectral Density
Frequency (Hz)
60
40
20
0
-20
-40
0
50
100
150
200
250
300
350
400
450
500

c) East-West Component

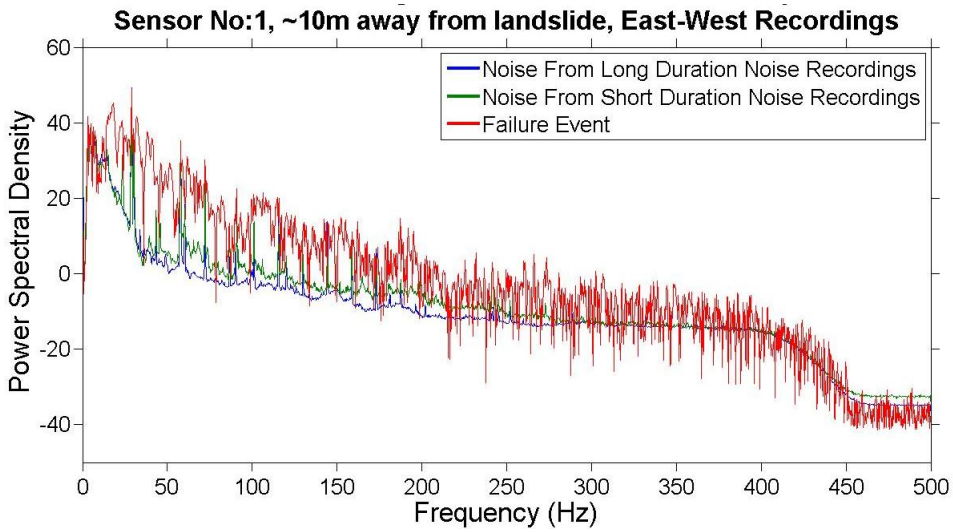

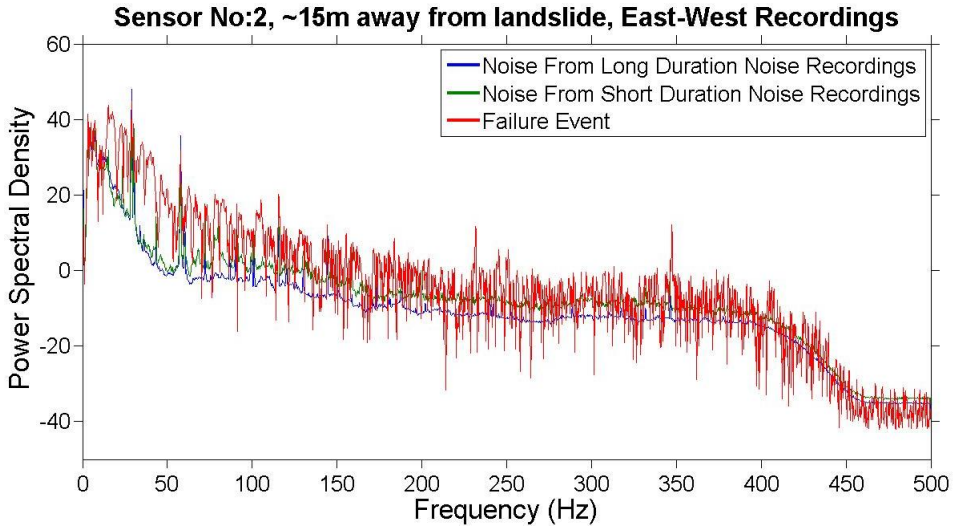

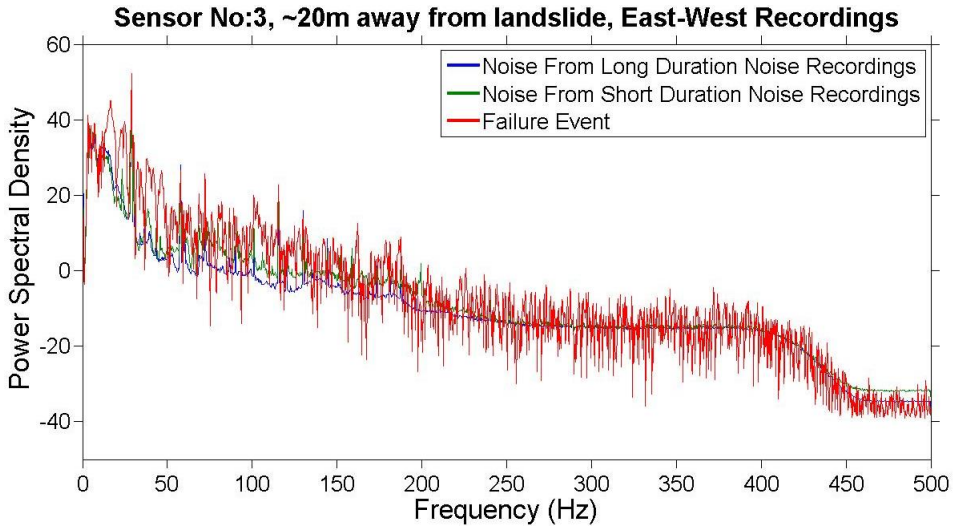

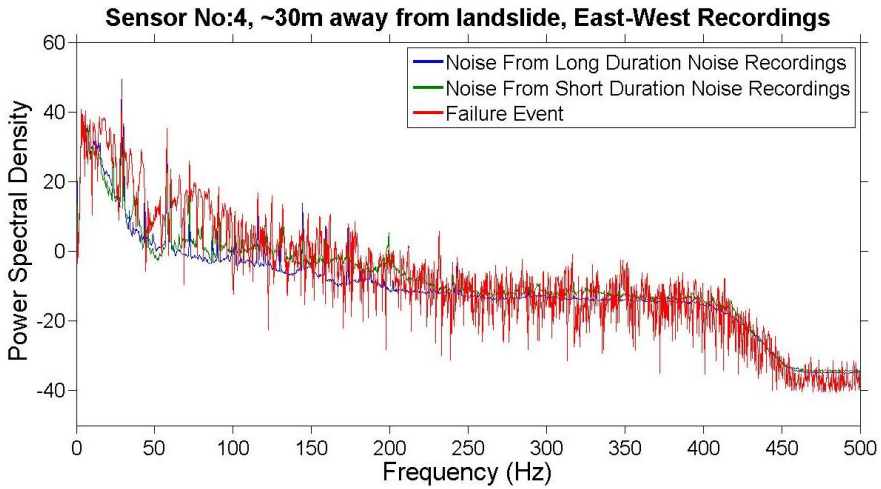
Sensor No:4, ~30m away from landslide, East-West Recordings
Noise From Long Duration Noise Recordings
Noise From Short Duration Noise Recordings
Failure Event
Power Spectral Density
Frequency (Hz)
60
40
20
0
-20
-40
0
50
100
150
200
250
300
350
400
450
500

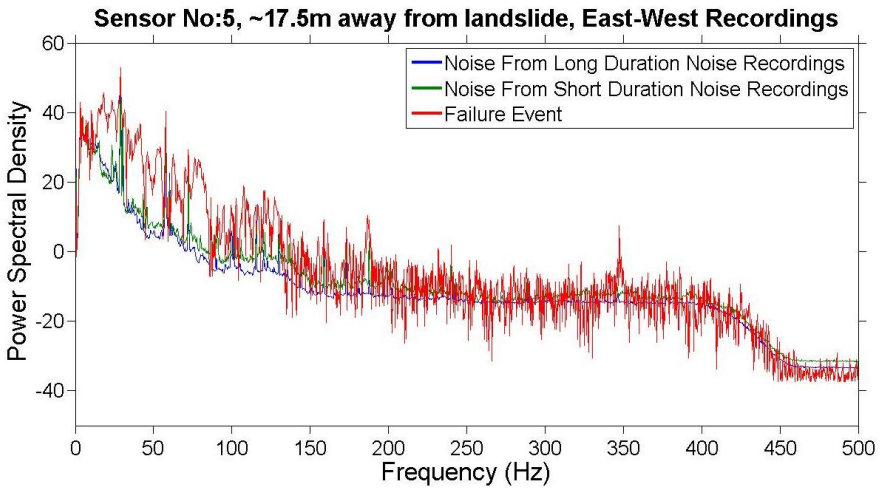
Sensor No:5, ~17.5m away from landslide, East-West Recordings
Noise From Long Duration Noise Recordings
Noise From Short Duration Noise Recordings
Failure Event
Power Spectral Density
Frequency (Hz)
60
40
20
0
-20
-40
0
50
100
150
200
250
300
350
400
450
500

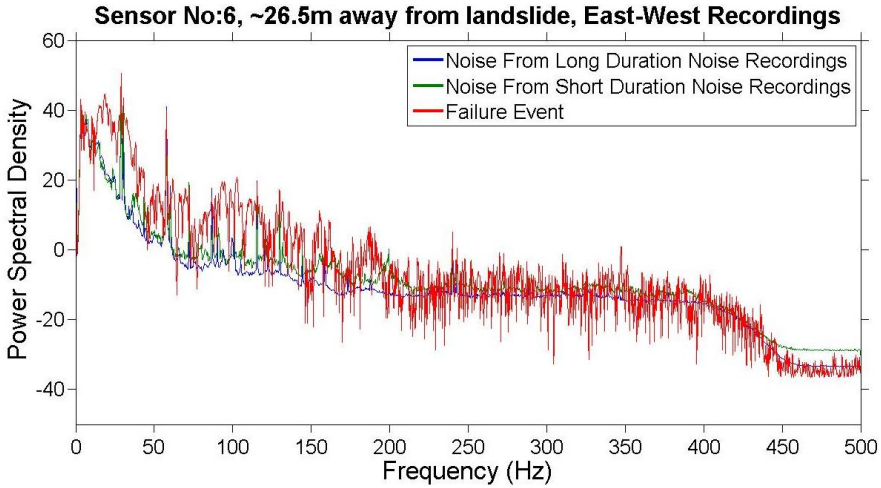
Sensor No:6, ~26.5m away from landslide, East-West Recordings
Noise From Long Duration Noise Recordings
Noise From Short Duration Noise Recordings
Failure Event
Power Spectral Density
Frequency (Hz)
60
40
20
0
-20
-40
0
50
100
150
200
250
300
350
400
450
500

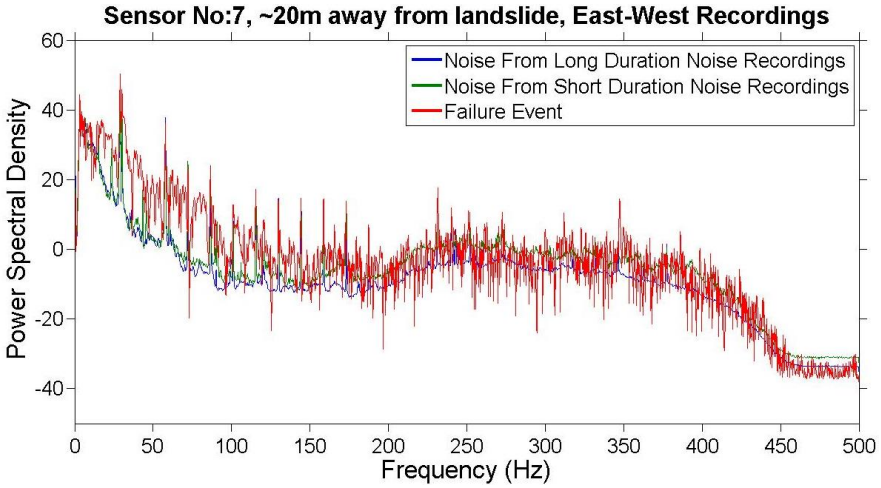
Sensor No:7, ~20m away from landslide, East-West Recordings
Noise From Long Duration Noise Recordings
Noise From Short Duration Noise Recordings
Failure Event
Power Spectral Density
Frequency (Hz)
60
40
20
0
-20
-40
0
50
100
150
200
250
300
350
400
450
500

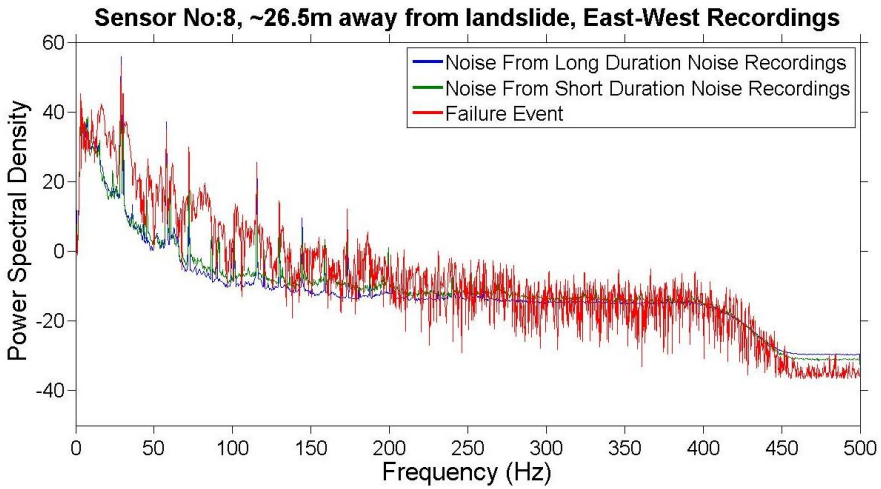
Sensor No:8, ~26.5m away from landslide, East-West Recordings
Noise From Long Duration Noise Recordings
Noise From Short Duration Noise Recordings
Failure Event
Power Spectral Density
Frequency (Hz)

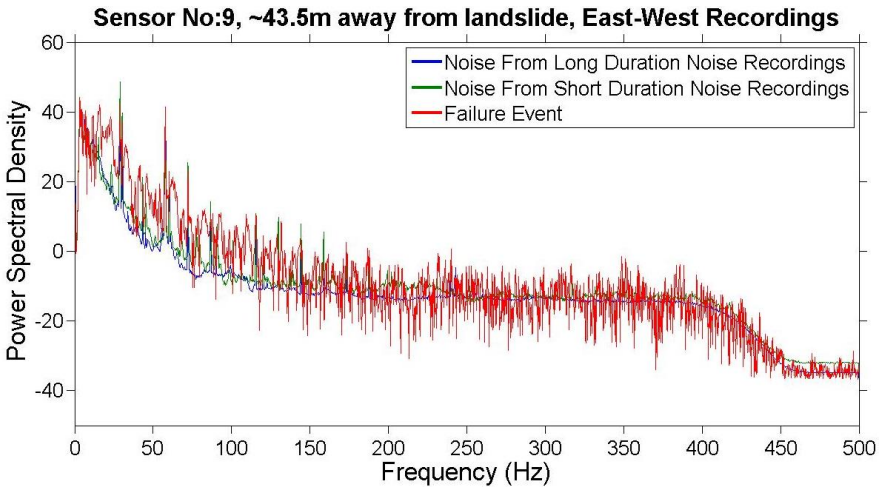
Sensor No:9, ~43.5m away from landslide, East-West Recordings
Noise From Long Duration Noise Recordings
Noise From Short Duration Noise Recordings
Failure Event
Power Spectral Density
Frequency (Hz)

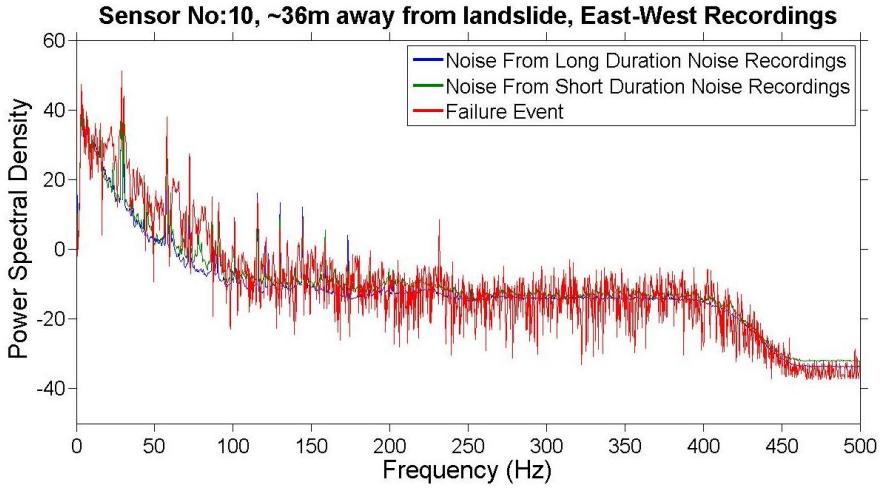
Sensor No:10, ~36m away from landslide, East-West Recordings
Noise From Long Duration Noise Recordings
Noise From Short Duration Noise Recordings
Failure Event
Power Spectral Density
Frequency (Hz)

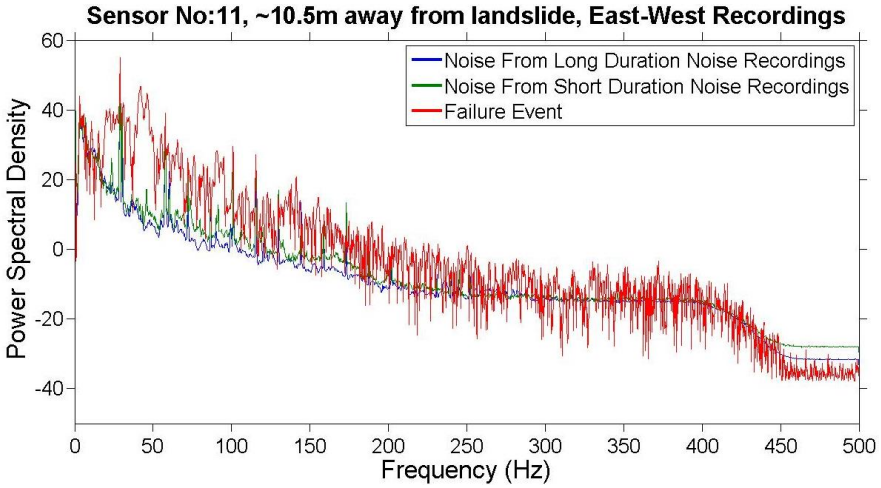
Sensor No:11, ~10.5m away from landslide, East-West Recordings
Noise From Long Duration Noise Recordings
Noise From Short Duration Noise Recordings
Failure Event
Power Spectral Density
Frequency (Hz)